IFMBE Proceedings

Yuri Dekhtyar • Alexei Katashev
Linda Lancere (Eds.)

Volume 38

International Symposium on Biomedical Engineering and Medical Physics, 10–12 October, 2012 Riga, Latvia

Springer

IFMBE Proceedings 38

Series Editor

R. Magjarevic

For further volumes:
http://www.springer.com/series/7403

The International Federation for Medical and Biological Engineering, IFMBE, is a federation of national and transnational organizations representing internationally the interests of medical and biological engineering and sciences. The IFMBE is a non-profit organization fostering the creation, dissemination and application of medical and biological engineering knowledge and the management of technology for improved health and quality of life. Its activities include participation in the formulation of public policy and the dissemination of information through publications and forums. Within the field of medical, clinical, and biological engineering, IFMBE's aims are to encourage research and the application of knowledge, and to disseminate information and promote collaboration. The objectives of the IFMBE are scientific, technological, literary, and educational.

The IFMBE is a WHO accredited NGO covering the full range of biomedical and clinical engineering, healthcare, healthcare technology and management. It is representing through its 60 member societies some 120.000 professionals involved in the various issues of improved health and health care delivery.

IFMBE Proceedings Vol. 38
Yuri Dekhtyar, Alexei Katashev, and Linda Lancere (Eds.)

International Symposium on Biomedical Engineering and Medical Physics, 10–12 October, 2012, Riga, Latvia

Springer

Editors
Prof. Yuri Dekhtyar
Biomedical Engineering and Nanotechnologies Institute
Riga Technical University
Riga
Latvia

Alexei Katashev
Biomedical Engineering and Nanotechnologies Institute
Riga Technical University
Riga
Latvia

Linda Lancere
Biomedical Engineering and Nanotechnologies Institute
Riga Technical University
Riga
Latvia

ISSN 1680-0737
ISBN 978-3-642-34196-0
DOI 10.1007/ 978-3-642-34197-7
Springer Heidelberg New York Dordrecht London

e-ISSN 1433-9277
e-ISBN 978-3-642-34197-7

Library of Congress Control Number: 2012949359

The IFMBE Proceedings is an Official Publication of the International Federation for Medical and Biological Engineering (IFMBE)

Printed on acid-free paper

Springer is part of Springer Science+Business Media (www.springer.com)

IFMBE

Welcoming address from the IFMBE

Celebrating any anniversary, whether of a human or of an institution, reminds all the involved of preparing it and teaches the invited guests the history preceding the jubilee. Riga Technical University has, no doubt, a rich history and a 150 years long experience in research and teaching of technical sciences. Being the first technical university in the Russian Empire, Riga Technical University remained a leading research and education institution in the Baltic area. The development of Biomedical Engineering at the RTU as a scientific field began more than 30 years ago and since then it has been growing very fast. When we speak of biomedical engineering, we pay respect to the past, but we also look into the future. There are many indicators of global growth of biomedical engineering as a science and as a profession, e.g. the labor market for biomedical engineers in the United States is presumed to have the highest rate of growth of 75 percent among engineering professions in the following years.

At the RTU, biomedical engineering activities are founded at the Institute of biomedical engineering and nanotechnologies. For a number of years, study programmes in Medical Engineering and Medical Physics are taught at bachelor, master and Ph.D. level. Extensive research is present primarily in biomaterials, biocompatibility and applications of various microscopic and spectroscopic methods in biomedical applications. The Institute is carrying several international research projects.

Latvian Medical Engineering and Physics Society is the national BME society affiliated to the International Federation for Medical and Biological Engineering (IFMBE). I believe that many of the international contacts of the members of the Latvian MEMP Society have contributed to the successful development of biomedical engineering at RTU. The Society has very successfully organized the IFMBE co-sponsored 14th Nordic-Baltic Conference on Biomedical Engineering and Medical Physics in 2008 and from that time many BM engineers keep in their memories also the beautiful city of Riga.

It is my special pleasure to welcome all participants of the International Symposium on Biomedical Engineering and Medical Physics. I am sure you are going to enjoy the scientific presentations and discussions during the Symposium but also those less formal meetings in the picturesque streets of ancient Riga.

Finally, on behalf of the Federation, let me offer sincere congratulations for the 150th Anniversary of the Riga Technical University to all researchers, teachers and students!

Ratko Magjarević
President, IFMBE

LMIFB

The Proceedings presents the reports delivered at the International Symposium on Biomedical Engineering and Medical Physics ISBEMP-2012, held in Riga, Latvia, 10–12 October, 2012.

The ISBEMP-2012 was organized under the IFMBE umbrella in the frame of the jubilee International Conference of the Riga Technical University (RTU) dedicated to its 150 anniversary.

The RTU was established as the first technical university in the former Tsarist Russia. The university became the centre of science and exerted a tremendous influence on economy and life both in Tsarist Russia and the Baltic region.

Now the RTU is the largest technical university in Latvia and has leader positions in different fields, biomedical engineering and medical physics being one of them.

The ISBEMP-2012 was aimed to emphasize the high role of academia in the modern economy and progress related to biomedical engineering and physics. The ISBEMP-2012 was targeted to assist in development and strengthening of international scientific, business and personal contacts and cooperation.

The previous similar international meetings provided in Riga *(International Scientific Conference Biomedical Engineering and Microtechnologies dedicated to the 140 anniversary of RTU, 2002; the 14th Nordic-Baltic Conference on Biomedical Engineering and Medical Physics, 2008)* demonstrated the great interest to visit the capital of Latvia with its deep scientific, historical and cultural traditions.

The ISBEMP-2012 presented 112 reports connected to different topics of the Biomedical engineering and medical physics field.

The organizers of the Symposium are deeply indebted to the participants for their outstanding presentations and discussions.

Co-chairmen of the Symposium

Yuri Dekhtyar

Prof., Riga Technical University, Latvia

Alexei Katashev

Prof., President of the Latvian Medical Engineering and Physic Society (LMIFB)

Annotation

The Proceedings presents the reports delivered at the International Symposium on Biomedical Engineering and Medical Physics ISBEMP-2012, held in Riga, Latvia, 10–12 October, 2012.

The ISBEMP-2012 was organized under the IFMBE umbrella in the frame of the jubilee International Conference of the Riga Technical University (RTU) dedicated to its 150 anniversary.

The articles collected at the Proceedings are rubricated to:

- general approaches, epidemiology and education
- Sensors, instrumentation and telemedicine
- Diagnostics, imaging, expert systems
- Biophysics and physiology, drug delivery and molecular diagnostics
- Radiation therapy and diagnostics, dosimetry and QA
- Biomechanics, Rehabilitation and Prostheses
- Biomaterials, micro- nano- materials
- Bioimplants, tissue engineering, nanomedicine and nanotoxicity

The ISBEMP-2012 Committees

The Organizing Committee

Aldis Balodis, Prof. (Latvia)
Karina Dudina, MSc (Latvia)
Aleksejs Kataševs, Prof. (Latvia) - chairman Prof.
Marina Romanova, MSc, PhD student (Latvia)
Maksims Šneiders, MSc (Latvia)
Viktorija Vendiņa, MSc, PhD student (Latvia)

The Program Committee

Diana Adliene, Prof. (Lithuania)
Iulian Antoniac, Prof. (Romania)
Gerhard Artmann, Prof. (Germany)
Igor Axenovich, Dr.Med (Hungary)
Csaba Balazsi, Prof. (Hungary)
Marom Bikson, Prof. (USA)
Yuri Dekhtyar, Prof. (Latvia) – chairman
Arzum Erdem, Prof. (Turkey)
Renars Erts, Doc. (Latvia)
James Goh, Prof. (Singapore)
Natalia Golnik, Prof. (Poland)
Hans Joachim Hein, Dr.rer.nat. habil. (Germany)
Timo Jamsa, Prof. (Finland)
Djordje Janackovic, Prof. (Serbia)
Vladimir Kasyanov, Prof. (Latvia)
Wlodzimierz Klonowski, Prof. (Poland)
Igor Khlusov, Prof. (Russia)
Ivars Knets, Prof. (Latvia)
Leszek Kubisz, Prof. (Poland)
Ivars Lacis, Prof. (Latvia)
Linda Lancere, MSc, PhD student (Latvia) – secretary
Juris Lauznis, MSc (Latvia)
Cornelius Lewis, Prof. (UK)
Pierre-Noel Lirsac, Dr. (France)
Arunas Lukosevicius, Prof. (Lithuania)
Ratko Magjarevic, Prof. (Croatia)
Jaakko Malmivuo, Prof. (Finland)
Zigurds Markovics, Prof. (Latvia)
Jose Miguel Martin Martinez, Prof. (Spain)
Kalju Meigas (Estonia)
Ion Mihailescu, Prof. (Romania)
Franco Milano, Prof. (Italy)
Pawel Olko, Prof. (Poland)
Peter Pushko, Dr. (USA)
Erik Palcevski, Dr. (Latvia)
Nicolas Pallikarakis, Prof. (Greece)
Marta Wasilewska-Radwanska, Prof. (Poland)
Miriam Rafailovich, Prof. (USA)
Anatoly Rozenfeld, Prof. (Australia)
Rachel Sammons, Dr. (UK)
Wolfgang Schüler, Prof. (Germany)
Andrejs Skagers, Prof. (Latvia)
Jos A.E. Spaan, Prof. (The Netherlands)
Janis Spigulis, Prof. (Latvia)
Frank Stein, Dr. (Germany)
Jenia Vassileva, Prof. (Bulgaria)
Vladimir Varchena, MSc (USA)
Todorka Vladkova, Prof. (Bulgaria)
Yuri Volkov, Prof. (Ireland)
Jan Maria Wojcicki, Prof. (Poland)

The List of Reviewers and Sub-reviewers

Diana Adliene (Lithuania)
Iulian Antoniac (Romania)
Igor Axenovich (Hungary)
Csaba Balazsi, (Hungary)
Marom Bikson (USA)
Anna Bistrova (Latvia)
Yuri Dekhyar (Latvia)
Arzum Erdem (Turkey)
Renars Erts (Latvia)
James Goh (Singapore)
Natalia Golnik (Poland)
Hans Joachim Hein, Dr.rer.nat. habil. (Germany)
Timo Jamsa (Finland)
Djordje Janackovic (Serbia)
Vladimir Kasyanov (Latvia)
Wlodzimierz Klonowski (Poland)
Igor Khlusov (Russia)
Ivars Knets (Latvia)
Leszek Kubisz (Poland)
Ivars Lacis (Latvia)
Igor lackovich (Croatia)
Linda Lancere (Latvia)
Juris Lauznis (Latvia)
Cornelius Lewis (UK)
Pierre-Noel Lirsac (France)
Ratko Magjarevic (Croatia)
Jaakko Malmivuo (Finland)
Zigurds Markovics (Latvia)
Kalju Meigas (Estonia)
Franco Milano (Italy)
Laura Neimane (Latvia)
Pawel Olko (Poland)
Peter Pushko (USA)
Nicolas Pallikarakis (Greece)
Marta Wasilewska-Radwanska (Poland)
Marina Romanova (Latvia)
Anatoly Rozenfeld (Australia)
Rachel Sammons (UK)
Andrejs Skagers. (Latvia)
Jos A.E. Spaan (The Netherlands)
Janis Spigulis. (Latvia)
Frank Stein (Germany)
Zoran Tiganj (France)
Jenia Vassileva. (Bulgaria)
Vladimir Varchena (USA)
Viktoriya Vendina (Latvia)
Yuri Volkov (Ireland)
Jan Maria Wojcicki (Poland)

Logos


International Symposium on Biomedical Engineering and Medical Physics
ISBEMP
Riga,
10-12 October 2012


IFMBE

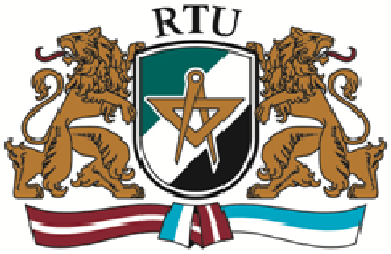
RTU


LMIFB

Table of Contents

Generality, Epidemiology and Education

Sensors, Instrumentation and Telemedicine

Diagnostics, Imaging, Expert Systems

Biophysics and Physiology, Drug Delivery and Molecular Diagnostics

Radiation Therapy and Diagnostics, Dosimetry and QA

Biomechanics, Rehabilitation and Prostheses

Biomaterials, Micro- Nano- Materials

Bioimplants, Tissue Engineering, Nanomedicine and Nanotoxicity

DEFECTS OF FIELD STRUCTURES

I.I. Demidova

Institute of Mathematics and Mechanics, SPbGU, Sankt-Petersburg, Russia
E-mail: maria_ib@mail.ru

Abstract—The different state of the system depending from the mechanical properties FS, its dimensions, the acting and the boundary conditions are analyzed. The redistribution of the stress state is discussed. It's necessary to project the medical apparatus for the detecting of the different FS's defects.

Keywords— **field structure, modelling, stress, defects, cracks**

INTRODUCTION

The field structures (FS) around the living biosystems are known from ancient times. Peoples detected such fields by hands and the different devices (the metallic frame, the ticker and others). The biolocation method is noticed from the Egyptian reed which totals 5000 years. Many scientists from Aristotel to modern world had the inretest to the ticker. It's notable that the presence of the field around the living systems was discovered from ancient times as demonstrated the nimbus on the money of the Kushan Empire (1 century BCE) (fig.1) and later on the icons beginning with the Y1centurie. The shamans from Asia and Africa treated by hands (fig.2). From the end of the X1X century many scientists studied the physical properties of the FS and showed that the weak radiation controls all processes in the living world.

Fig. 1. Budda'nimbus http://ru.wikipedia.org/wiki/

Fig.2. Visit to shaman http://mustagclub.ru/blog/

Fig.3. The field around hand http://ktispb.ru

Herewith the dependence of the changing of FS is noted both the outer and the inner parameters. The connection between the organism diseases and the changing of the state of FS is determined. Now Elektroakupunktur nach Voll, the method Bioelectrography, the Adaptometry and others are used [1] (fig.3). In addition the instruments for the registration of FS in during time and under the interaction of man with the plants are designed. But the practice shows that under the investigation of the FS by the candle the areas of the irregular concentration are detected. It's necessary to define its. In this report the different defects of the FS are discussed from the point of view of the mechanics of the solid bodies using the methods of the photoelasticity [2].

The concept of the strength, the hardness was known to peoples from ancient times. English anthropologist R.H. Dart (1925) supposed that the first culture was the culture the osteo- odonto- ceratic culture, as the bones and the teeth was the first instruments for the agriculture and the defence. The first ideas about the biomechanics were suggested by Aristotle (384-322 years BC). In 1638 year Galileo Galilee (1564-1643) tried to base the connection of the bone form with the applied efforts. In 1866 year the prof. doctor G.H. Meyer from Zurich and prof. Culmann from Zurich Polytechnic School showed on the example of the hip bone that the texture of the bone tissue corresponds to the mechanical laws. In particular the paths of the trabecules of the sponge tissue coincide with the lines of the maximum stresses – the Wolff 'law.

11. THE STRESS STATE OF THE BIOSYSYEM

The natural constructions have the complicated structure with the time changing of the physical –mechanical properties α_k of the tissues and different mechanical, physical and chemical actions β_k of the environment. It is to note that the parameters α_k are interrelations i.e. every parameters of α_k is the function of the all others internal parameters, the environment parameters β_j of and time t

$$\alpha_k = f(\alpha_1, \alpha_2, ..., \alpha_{k-1}, \beta_j, t).$$

All parameters α_k have the value limitations for the normal functioning of the living system.

$$\beta_{k**} < \beta_{k*} < \beta_k < \beta_k^{*} < \beta_k^{**}, \quad \alpha_{ki\,**} < \alpha_{ki\,*} < \alpha_{ki} < \alpha_{ki}^{*} < \alpha_{ki}^{**},$$

Where the parameters with one asterisk define the area with normal function of the living system and the parameters with two asterisks – critical values. In such state the

Y. Dekhtyar et al. (Eds.): *International Symposium on Biomedical Engineering and Medical Physics*, IFMBE Proceedings 38, pp. 1–4, 2013.
DOI: 10.1007/978-3-642-34197-7_1

system reduce the own activity or the system is dead. The index "i" shows the individual values of the living system. These values may be differed on the degree. For the solving such problems the system analysis is used, all factors which influence on the state and the functioning of the biosystem are revealed. The general view of the equation system of the solid body mechanics including the changing of all factors and the anisotropic of the tissue structure is very complicated. For the studying of the functioning of the biosystem, for the revealing of the zones with the fracture defects the different methods of the physical and the mathematical simulation are applied. For the investigation of the stress state for the rigid tissues of the elements of the living constructions under the mathematical simulation Lame's problem is used [3]. The stress state in the sphere under uniform temperature with boundary conditions is examined $\sigma_r = p_0, \quad r = b, \sigma_r = p_i, \quad r = a$.

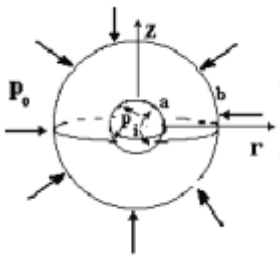

$$\sigma_r = \frac{p_i a^2 - p_0 b^2}{b^2 - a^2} - \frac{a^2 b^2}{r^2}\frac{p_i - p_0}{b^2 - a^2},$$

$$\sigma_\theta = \frac{p_i a^2 - p_0 b^2}{b^2 - a^2} + \frac{a^2 b^2}{r^2}\frac{p_i - p_0}{b^2 - a^2}$$

Fig. 4. Model - sphere	Fig. 5. The decision of Lame'problem

According to the Levi – Michell'theorem the stress distribution depends from the pressure p_0, p_i, and the sizes a and b and doesn't depends from the material properties [2] (fig. 4-6). From this decision it's follows that if the pressure p_0 acts only then the hoop stress σ_θ is tensile and the radial stress σ_r is compressive. The value σ_θ is more than stress σ_r. The existence the tensile hoop stress leads to the appearance of the construction fracture for the materials with the low strength, par example, the crust rupture of the trees (fig. 8).

The stress difference ($\sigma_r - \sigma_\theta$) will be

$$\sigma_r - \sigma_\theta = -\frac{2a^2 b^2}{r^2}\frac{p_i}{b^2 - a^2}.$$

According to the Werthgeim law the birefringence will be

$$\delta \cos 2\varphi = C(\sigma_r - \sigma_\theta) = -2C\frac{a^2 b^2}{r^2}\frac{p_i}{b^2 - a^2}$$

Where is the C- optical constant for material. Hence the geometrical locus will be the circles (fig.7). In this case the inner pressure was done by the press fitted the polymer ring from the optical sensitivity on the disk.

It's noticed that the pressure of the biosystems has the own structure par example the outer pressure p_0 consists from atmospheric p_a, light p_s , information p_{ln} pressures and others $p_0 = f(p_a, p_s, , p_{ln}, , ...)$, then the inner pressure has several components $p_i = f(p_{blk}, p_{lk}, p_{ск}, ..)$, where p_{bl} - the pressure in the blood, p_l – in the lymph, $p_{ск}$ - in the cell and others. The parameter k marcs the dependence from the man organ.

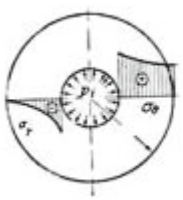

Fig. 6. The stress distribution σ_r and σ_θ	Fig. 7. The interference pattern in the ring	Fig. 8. The crust rupture of the oak tree

111. Applications of the Lame's problem to the FS

It's known that the FS is formed on the stage of the appearance of the living construction. This system is unique search less and very complicate. About the properties of the FS are reputed too little: the weight of the man FS is 2-30 gr, the mechanical properties are nonelasticity. Through this system the information are transmitted. The tissues of the FS are situated in the constant vibration process.

If the outer pressure acts on the biosystem, then the system brings the influence to the environment i.e. some physical field appears around the biosystem.

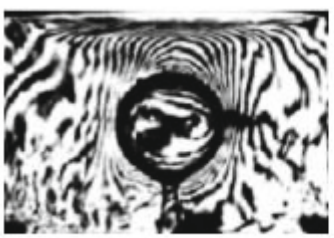

Fig.9. The interference pattern in the model with the sphere inclusion	Fig. 10.The problem about the acting the concentrate force

Biosystem function under limited changing parameters of construction. In the solution of the Lame' problems the inner boundary $r = a$ will be the outer surface of the biocon-

struction and the outer boundary $r = b$ will be boundary generated under the construction forming. In the polarize light this field will be as the interference fringes in the polymer matrix around the glass sphere inclusion [4] (fig. 9).

The degree of this acting on the value and the radius is certainly small in comparison with the dimension of the Universe – 4-5 radius of the body, but when the living systems occur among closely spaced groups the value of this acting will be perceptibly. The model with uniform stress distribution on the boundary is the ideal model for the cell, organ and organism. On the practice the stress distribution may be irregular. Such state may be cause by the different reasons.

IY. THE MODELLING OF THE DEFECTS IN THE FS

The influence of the idea. In the present tense the scientists recognize that the idea has the material nature, the idea – the energy. As model the problem about the acting the concentrate force may be suggested. In this case the stress concentration is appeared and the pressure of the FS is changed. If the pressure changing wiil be long and after the unloading time for the recovery will be short then the deformations of the FS will be remain. In the organism the health problem may be appear as the cell sensitivities are not equal and the pressure limits of the cells exist. An example is the actor impersonation in the theatre. Thus the man can influence on the own stress state of FS. As this takes place, the pressure changing of the FS goes to the changing of the FS deformation properties and using the analogy with polymer materials –the pressure increasing leads to the rising hardness [5]. In the FS the fracture may be appear as on the model (fig.11) under the limitation of the outer bounder.

The influence of the outer acting on the bioconstruction. The pressure changing of the FS may be from the changing of the surrounding media: gradients pressure and temperature, much information, others parameters.

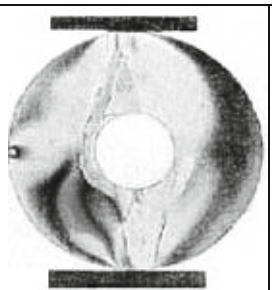

Fig.11. The ring fracture

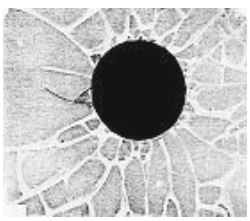

Fig.12. The cracks in the matrix around the inclusion [6]

Hence, the deformation properties will be change and the FS fracture is possible as on the model with inclusion after very rapidly cooling [6] (fig. 12).

The changing of FS from the acting of other bioconstruction. For the demonstration of the relationship of the living systems the models problems about the stress state in the composite models with the inclusions are suggested. For the decision of this problems the photoelasticity and photothermoviscoelasticity is used [7]. Using the isoclines of these methods the lines of the maximum stresses may be draw. On the figures 13, 14 the isoclines of the model with 4 inclusions and the mitomic cells of the brain.

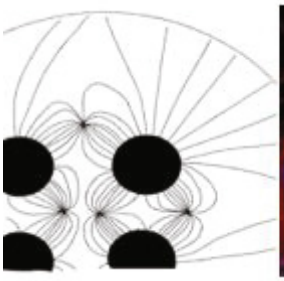

Fig. 13. The isoclines in the model with 4 inclusions

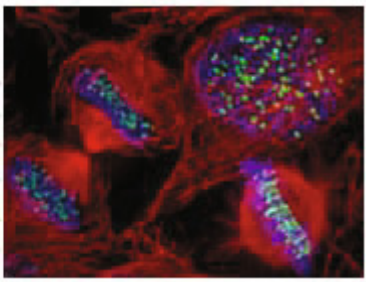

Fig.14. The mitomic cells of the brain http://ru-micromir.livejournal.com/40497.html

For the model with the inclusions the stress state will be change, the stress concentration is increasing. In the investigating models the polymer inclusions had the preliminary deformation. Under the curing namely the hitting the inclusion deformation changed and the polymer matrix had the deformation.

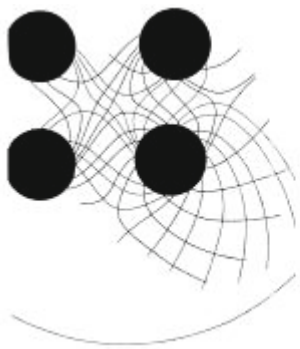

Fig.15. The slipping lines for the model

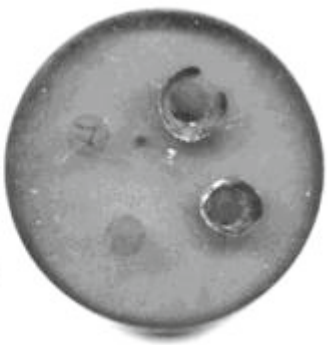

Fig.16. The cracks as the logarithmic spiral

Some models had the cracks as the logarithmic spiral (fig.15, 16). Such cracks may be appearing under the growth, under the function of the living system. These cracks limit the information perception, new stress state and the reconstruction around the cells will be. Some departure from the norm of the behavior and the contracting a disease may be appearing.

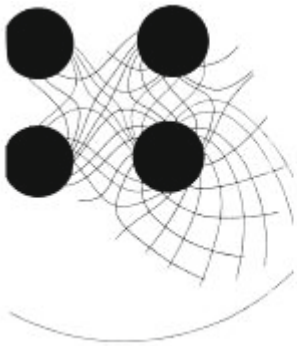

Fig.15. The slipping lines for the model

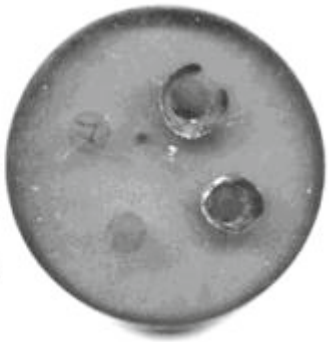

Fig.16. The cracks as the logarithmic spiral

The suggested models are the base for the biomechanical interpretation of the fear and depressing state and some diseases as one variant of a stroke.

Y. CONCLUSIONS

Thus the application of the mechanical problems allows to explain several phenomena under the diagnosticating of the different man state. It's necessary to project the medical apparatus for the detecting of the different FS's defects.

V1. REFERENCES

1. Korotkov K.G. Base of the GRV bioelectrography. SPbGITMO. 2001
2. Froht M.M. Photoelasticity. 1948. 1-2vol.
3. Timoshenko S.P., Gaudier D. Theory of elasticity. 1975. 576 p.
4. Demidova I.I. Biomechanical applications of the Lame'problem. Reports of V11 International conference "The strength problems of the materials and construction on the transport". 2008. SPb.P.56-63
5. Aibinder S.B., Tjunina E.L. Introduction to theory of polymer friction. Riga. Zinatne. 1978. 224 p.
6. Theocaris P.S., Paipetis S.A. Shrinkage stresses in three - dimensional two -phase systems.// J. Strain Anal. 1973. v. 8 N 4. P. 286 -293.
7. Bugakov I.I., Demidova I.I. Method of photothermoviscoelasticity. L. SpbGU. 1993. 160 p.

System Pattern of Consciousness Functioning

S. Dadunashvili

GeorgianTechnicalUniversity, Tbilisi, Georgia

Abstract — **This paper presents results of researches system pattern of consciousness functioning. To describe different levels of consciousness, the concept "Diagramme of consciousness" is introduced. All evolving World, perceived by us, consider as set of working programs. Programs are characterized by discrete and continual semantic components. It sets senses of the program. We will consider that all possible senses are initially packed and placed in a continuum. Representation about compressed elements assuming as a basis of the semantic field concept. Differentiation of senses set not by division, bat as procedure of scaling specify on all field. Occurrence as a result of scaling of system of preferences, selectivity in an estimation of various sites of a field, creates preconditions unpacking of senses and program generation.**

The consciousness of the person acts in the World as a set of programs carriers of senses. Senses are initially set in the potential, not shown form and concrete unpacking of senses is represented free possibility for the person.

Expand the description of a basis of Entity of the World, postulating, that in its sources there is a semantic field and rudiments of aptitude. The actual personal consciousness in phenomenal life of the person, not only occupies certain position in hierarchical system of revealing senses, but also co-exists to quite certain concrete environment of aptitude. Aptitude is an internal fundamental principle of any life and all processes accompanying it. Evolution of aptitude of actual consciousness is comprehension gradually increasing on quality it underlying and pan-united fundamental principles of any concrete empirical life, both in individual manifestation, and in all its world's a whole, and also disclosing by consciousness effect totality of coexistence with the primordial nature of the Reality.

Keywords — **Consciousness, senses, continuum, semantic field, rudiments of aptitude.**

I. Introduction

All evolving World, perceived by us, we would consider as set of working programs. When we study biosphere - separate individuals, species and other component of biospheres turn out as mediums of programs. When we consider a technosphere, we find programs in all artificial systems. When we study ethnic and social systems, we detect programs in manifestations of human consciousness, directed on formation and fixing of communicative relationships [1,2,3].

Programs are characterized by discrete and continual semantic components, last of which is not visible us directly. It sets senses of the program. We will consider that all possible senses are initially packed and placed in a continuum, same as all real numbers on the real numerical axis are pressed. The senses placed in a continuum are unpacked, not shown potentialities, this just semantic field where is absent preference system.

The pattern of a mathematical continuum carries representation about compressed elements, which assuming as a basis of the semantic field concept and are not giving in discrete splitting. Therefore, differentiation of senses will be set not by division, bat as procedure of scaling specify on all field. Scaling procedure consists in assignment to different sites of a semantic field of a certain extent. It means, that to any site of a field can be attributed the weight, equivalent to the area under extent curve, sharing to a respective site. Thereby there is a distribution across the field of normalized extent density. Extent function represents the "eyepiece" through which the person can observe closely a semantic field and scan it.

Occurrence as a result of scaling of system of preferences, selectivity in an estimation of various sites of a field, creates preconditions unpacking of senses and program generation. In the program, senses always specified selectively, and semantics of each concrete program is specified by those weight parities, which are defined by the function of a measure. Use of this function allows making senses commensurable on the importance for the person, thus, senses, being by the nature qualitative, finding the quantitative characteristic.

The semantic field is not localized somewhere in space of physical action, it does not change and in general is out of time. Concentrating the attention to the nature of senses, we find out them in everpresent indissoluble integrity, it defines using conception about continuum — the set which does not have empty places. Thus, the semantic continuum is an Entity, and it scaling unpacking – multiple. Therefore, the semantic continuum becomes involved to being and, thus, is shown in plurality of the World. The main thing is it, that an Entity becomes plural not through crushing, but

Y. Dekhtyar et al. (Eds.): *International Symposium on Biomedical Engineering and Medical Physics*, IFMBE Proceedings 38, pp. 5–10, 2013.
DOI: 10.1007/978-3-642-34197-7_2

through set by function of a measure scaling. Unpacking of a semantic continuum through scaling is a procedure not breaking its integrity.

II. Two sources non-locality of consciousnesses

The consciousness of the person acts in the World as a set of programs carriers of senses. Its nature is special — flexible, mobile, dynamical, capable to changes. The consciousness to openly World, co-operating with it, consciousness control the self-nature. The consciousness appears as transcending instrument, which is connecting different levels the Worlds and carrying out in it system-forming function.

The basis of differentiation of consciousness and brain considers the statement that the brain is spatially extent, but the consciousness does not possess this quality [4]. However, the spatial perception of a physical reality is set not so much by the World surrounding us, but as initially set to consciousness ability to perceive the World spatially ordered. Entity is not in space as in a certain neutral receptacle, but organizes spatiality of the World by the active presence at it. The spatiality is in the World in that degree in what the space is found out by that entitativ which designs a life and existence.

For geometrize representations about consciousness and to create an evident image of a semantic field, it must be admitted that senses are primary by it nature. I.e. to admit, that base senses are set initially, similarly as admits primary preconceived of fundamental physical numerical constants.

Senses are initially set in the potential, not shown form and concrete unpacking of senses is represented free possibility for the person. When the person addresses to a semantic continuum, it scans senses not mechanically, but acts as the active creator unpacking a continuum of senses. The semantic continuum finds actualization when the person sets on it a certain system of preference, addressing to measure function.

Actualization of a semantic continuum occurs like self-acting. The unpacked senses keep property of non-locality and manifestation through generated programs. Even at external logicality, the program is perceived by the person as process of depth experience and each person can execute the same program differently.

Let's expand the description of a basis of Entity of the World, postulating, that in its sources there is a semantic field and rudiments of aptitude (see fig. 1). Aptitude is a natural ability to exist and a natural ability to do something. When we learn the rudiments of something, we learn the most essential things about it.

The semantic environment is always formed *by collective* of the individual, isolated concrete-empirical actors peripherally influence against each other. Empirical existence organization formed as a result of this interaction, inseparably connected not only to existence and phenomenology of multiple collective, but also it is found out not otherwise, as through its means —in aggregate processes made in collective.

The actual personal consciousness in phenomenal life of the person, not only occupies certain position in hierarchical system of revealing senses, but also co-exists to quite certain concrete environment of aptitude.

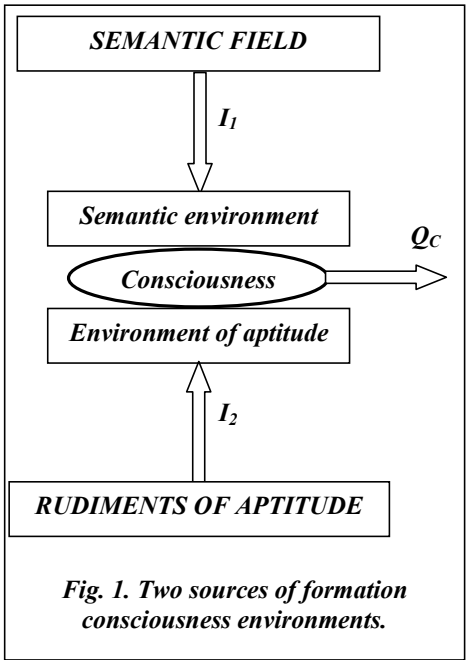

Fig. 1. Two sources of formation consciousness environments.

Exists of environment of aptitude is original and it is found out in phenomenal processes both the isolated individuals, and composite collectives. Environment of aptitude in itself is independent from concrete empirical, as an element of rudiments of aptitude, it always possesses own actuality and concreteness and that precedes all phenomena and processes of the phenomenal World, including peripheral manifestations of the semantic environment.

Aptitude is an internal fundamental principle of any life and all processes accompanying it. Evolution of aptitude of actual consciousness is comprehension gradually increasing on quality it underlying and pan-united fundamental principles of any concrete empirical life, both in individual manifestation, and in all its world's a whole, and also disclosing by consciousness effect totality of coexistence with the primordial nature of the Reality.

In evolution of aptitude, consciousness of the person moves not in the peripheral nature of the Reality and aspires not to explanation of system and the World mechanism as its diverse hierarchical detection, but gravitates directly to essence of life in itself. In this process the consciousness of the person departs from all individual, isolated and differentiated and entirely becomes isolated in contemplation of a stream of a life passing in the underlying. It is not cognition process, there is no relation knower to coming outside, i.e. there is not division into the subject and object and all of them subsequent mutual relations.

Here the subject and object coincide in identity, here the cycle of cognitive process not only becomes the closed (self-contained) and single act of direct contemplation, here not only knower, knowable and scope of knowledge are coincide, but also most this process becomes inseparable from basic essence of a life and its expansion in prolongation. Therefore, aptitude conducting is identical to feeling of a life; it is familiarizing with its rhythm, it is a deliverance from chaining to the form and the organization, it is a direct perception of the Life.

In one's own aptitude constituent empirical consciousness of the person joins in that or any other environment exclusively on underlying of his empirical existence as detection of degree of a susceptibility to internal aptitude of Life. Belonging to environment is caused only by internal self-feeling of the person of a rhythm of the Life. In this retirement, the person finds sensation of completeness and likeness with the rudiments of Life poured in the World.

Being localized, the person at the same time feels that at its retirement there is also something infinitely more higher, than he himself is. This higher, nonlocal, is present as well at many other related to it individuals that is why here arises special, direct communication uniting invisible bonds of people, and communication incomparably fuller, true and valid, than all rough and obvious connection in the world of the passing phenomena.

The environment of aptitude is defined in the native nature as essential dynamic and permanent harmonious conjugation of unity to multiplicity. Underlying of the environment of aptitude in prestanding to empirical consciousness reveals as system of transcendental conditions of life and effective experience of a life in environment of aptitude of any consciousness being in it. In other words, the environment of aptitude affects any concrete empirical consciousness irrespectively its quantitative and qualitative condition and besides its own active potency.

In aptitude, specific tonalities of its underlying define the effective nature of concrete consciousness living in it, its position in hierarchy of a susceptibility and, according to it, singularity this environment of aptitude.

Distinction of the World and chaining consciousnesses of individuals to the certain qualitative hierarchical status, is overcome by dynamic process of a life — perceptions and realizations of intuitive revelations pan-united rudiments of aptitude and a semantic field. The nature of intuition is essentially dynamical, and it reveals in mutual relations of realities of various hierarchical orders.

In semantic environment intuition ($\boldsymbol{I_1}$, fig. 1) is that creative source which help overcomes coherence with a certain grade level of a hierarchical structure of the World, realities of higher orders are perceived and dynamic switching in the higher environment in harmony with increase of the qualitative status of consciousness is happen.

In the environment of aptitude, the help of intuition ($\boldsymbol{I_2}$, fig. 1) is happen overcoming of coherence with a susceptibility of the certain environment of aptitude and creative inclusion in the higher order environment.

Between intuitions of a semantic field and rudiments of aptitude ($\boldsymbol{I_1}$ and $\boldsymbol{I_2}$) there is rather essential difference. In the semantic environment the hierarchical structure and all system of steps of the organization of senses ascending on the qualitative status is a phenomenal reality, in the environment of aptitude similar conformity is the hierarchy of a susceptibility set for any concrete consciousness only transcendental. From here directly follows, that in the semantic environment actually are realities of various orders, and in the environment of aptitude has life the single aptitude reality, which is only variously perceived by concrete empirical consciousnesses, depending on actual development of their conductors.

In the environment of aptitude, owing to it pan-united, cannot be discontinuity in phenomenological being of intuitions. Here the rudiments of intuition not only are continuous in itself but also continuous in essence process of evolutive mastering of its realities by actual concrete-empirical consciousness of the person. Any development in aptitude is not formation of the new realities, not consistently ascending conjugation to individual kinds of concrete life of the higher orders, but only ability development to perceive underlying prestanding of consciousness eternal in itself actual and perfect rudiments of aptitude. In each concrete condition, the empirical consciousness of the person perceives rudiments of aptitude according to development of the susceptibility, the conductors, and in consequence of it appears in the certain environment of aptitude.

The intuition ($\mathbf{I_2}$) is intuition of a life in itself. It reveals not ascending chain of concrete action of cognition, but incorporation in underlying of all observable processes. Moreover, degree of the successes reached in it defines an accessory of the person to this or that concrete environment of aptitude. Level of the successes reached in it, defines an accessory of the person to concrete environment of aptitude.

In semantic environment, the accessory to it is caused by organizational level of actual consciousness, i.e. by condition of its instruments of the cognitive and active actions directed on empirical as periphery of the World. Staying in the environment of aptitude is caused by τονος' of consciousness lives, i.e. degree of its susceptibility of aptitude, an internal - fundamental principle of its concrete life.

Aptitude in itself is rudiments of the unconscious. The aptitude *coexistence* of consciousness with rudiments becomes objectified and actual only at its disclosing as product of the semantic field defining evolutionary activity of consciousness under the hierarchical law. Only in this process, primordial aptitude receives the true place in the perspective of the World.

In the course of evolution of consciousness of the person, revelation of aptitude intuition not only become objective actual realities through activity of semantic intuition, but also the first empirically also are caused by the second. The empirical consciousness only in so far as is capable to exist and reply actually to rudiments of aptitude, as concrete comprehension of it is represented as free possibility. The bigger hierarchical level of consciousness in the semantic environment, the, accordingly, is realized larger approach to the Reality and that it is capable to apprehend higher kinds of the environment of aptitude.

III. THE DIAGRAMME OF CONSCIOUSNESS AND LANGUAGE OF PRELOGICAL THINKING

The consciousness nature as system-forming object should have multilevel structure. The schematic structure and the diagramme of functioning of human consciousness are shown in fig. 2.

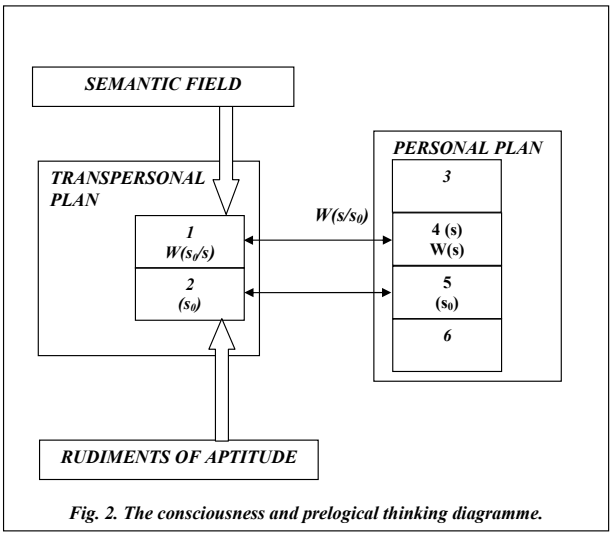

Fig. 2. The consciousness and prelogical thinking diagramme.

Let's consider consciousness structure on supra-individual level.

The first, separately opposable metalevel — metaconsciousness level. This level, for which one sources of non-locality serves semantic field, is not included into the semantic-body organization of the person. Metaconsciousness level already belongs to the transpersonal plan — to the collective consciousness co-operating with personal consciousness of the person. At this level, there is a self-acting generation of semantic impulses bearing a creative charge and starting unpacking of senses.

Level (1) acts as semantic trigger - timeless, self-acting operating and consequently not shown for individual.

The second level represents the bottom layer of collective consciousness. There are archetypes of the collective unconscious. Formation of it is defined by non-local rudiments of aptitude, "breathing" according to the law of his existence. Keeping existence continuity, it is a source for perception identically adjusted consciousnesses, and is imprinted in them in the form of similar archetypes. These archetypes of the unconscious remain at elimination separate individual consciousnesses. ***Live it is not lost in the Reality.***

The consciousness rest on unconscious, it is permanent grows from unconscious and comes back to it [5]. Consciousness exist like a wave crest over the wide and deep basis. The world of unconscious is hidden from our direct look and learns something about unconscious we can only by means of consciousness. In each conscious action of our life, especially in each act of generation of creative impulses participates present in us unconscious.

Supra-individual consciousness acts in the form of two-layer structure. The bottom layer is the world of the fixed archetypes, it is as a protective cover supra-individual consciousnesses; the top layer — area of generation of creative impulses. The input in it is carried out through a protective cover of collective unconscious where archetypes act in a role of starting keys.

Let's consider consciousness structure on the personal plan:

The third, top level is that layer of individual consciousness, where senses are exposed to disclosing through the formal logic. It is level of logic thinking. Stating the thoughts, we use formal logic, but the formal logic is only dialogue means between the people, carrying out binding function in the process of communications.

The fourth level is level of prelogical thinking, where those initial parcels and postulates on which actually logic thinking is based are developed, and which then (at level 3) are comprehended by formal logic. It is the level of creative activity, on which realized generation of senses as an

independent goal. Level (4) serves as a conductor of action of the trigger (1).

Processing at the fourth level also is internal — semantic habit of the person. At this level, senses find the effective force.

The fifth level are basement of consciousness, there is a sensual contemplation of forms. There the meeting with archetypes of the collective unconscious is carried out. Level (5) is connected with level (2).

The sixth, bottom level — is a physical body. It is level which defines general somatic condition of the person. In consciousness and thinking the direct connection of the individual with the Reality is broken, however a body remains in the Reality. The corporality serves communication of consciousness with a physical body and maintenance of consciousness of the individual.

Level (3,4,5) show in fig. 2, represent actually consciousness of the person. A consciousness part — levels (4) and (5) identify with unconscious. This unconscious is generated not by an inclination, instinctive by the nature, but is a product of perception of rudiments of aptitude. Creative activity is started at collision of levels (5), (6) is direct with level (3).

Those, changed conditions of consciousness, in which the transpersonal psychology is interested now, arise at switching-off the top, logically structured level. Switching-off is carried out by the directed influence on a body — by relaxation, touch deprivation, breath regulation. Everything is exposed to operating influence, that can change own rhythm. In this system of representations the body, becomes one of consciousness levels.

Thus, determinative in consciousness structure is allocation of levels (1) and (4), responsible for process prelogical thinking, playing a main role in consciousness functioning. By means of the processes proceeding at these levels, senses in consciousness are revealing.

To disclosure the processes occurring at level of prelogical thinking, it is necessary to develop the language adequate to these processes. For this purpose, on semantically filled continuum building measure function $W(s)$, which scans a semantic field, for giving of significant scales to its separate sites (s). Value $W(s)$ named a semantic charge of a site. Creative prelogical thinking, muffling one senses and strengthening others, transfers results of scaling to level (3). However, as soon as the situation varies, there is a redistribution of the scales, setting the importance of senses.

Function $W(s)$ change and evolution at some level of aptitude susceptibility of consciousness (s_0), occurs by influence of a creative charge on personal consciousness of the person. Self-acting generation of the semantic impulses bearing a creative charge is expressed in self-acting occurrence of the filter $W(s_0/s)$ which occurs at supra-individual level (1) of consciousnesses.

Conditional function of a measure $W(s_0/s)$ — arises in consciousness at certain level of aptitude susceptibility of consciousness (s_0) and at scanned value (s). Thus, argument of the functions $W(s_0/s)$, carrying out a filter role, it is considered (s), a (s_0) - serves as a starting key.

Filter $W(s_0/s)$ influence on personal consciousness of the person occurs by *multiplicate* interaction to initial function $W(s)$:

$$W(s/s_0)=kW(s_0/s)W(s) \quad (1)$$

where $W(s/s_0)$ – the conditional function of a measure defining semantics of the new program, arising after operation of starting key (s_0);
k – a normalization constant, which gets out so that density size of normalize measures was in an interval [**0, 1**].

In expression (1) operations have *numerical* character – in the right part there is the sign on multiplication having numerical disclosing, hence language defined by this expression it appears numerical.

Expression (1) contains two premises - $W(s)$ and $W(s_0/s)$ from which's with necessity the program with new semantics $W(s/s_0)$ follows. Expression (1) generates the language of senses bearing in an explicit form two origins supplementing each other: continuous (from a semantic field) and discrete (defined in the value of susceptibility by consciousness of rudiments of aptitude).

Expression (1) is applied to the senses, which are blurred on a semantic continuum, i.e. both premises and carry a consequence arising from them not atomic, but blurred character and the second of premise carries caused by a situation (s_0), instead of categorical character. Thus, language is arranged so, that in its programs possibility of occurrence of atomic senses is excluded: function over a semantic continuum is set through density of normalized measures, from here follows, that possibility of occurrence of atomic sense is equal to zero.

Language appears free from the law excluded third; accordingly, it is free from rigid differentiation of the true and falsity. As that is represented true, and that is represented false, is constructed on the same semantic continuum and differs only in measure value. Absence of the law excluded third opens space for intuition action.

IV. Conclusions

Semantic work of consciousness (Q_C) on creation of new programs is determined by product of quantity of a current

semantic charge on quantity of the semantic status of consciousness, which is defined by the susceptibility environment of aptitude reached by consciousness. Process of work on finding of new senses is intuitive and based on regulating role of intuitions (I_1 and I_2) in consciousness functioning.

Consciousness as the semantic system is opened – it is opened to the transpersonal plan on which crop up filters generating further language of prelogical thinking. Hereby come into existence mechanism expanding borders of personal consciousness up to transpersonal level, and supra-individual consciousness acquire concreteness.

Supra-individual consciousness, the carrier of senses, through the person localized in a body, reaches possibility of interaction with real, ready to social action in Reality, created substantially by senses imprinted in the person.

References

1. Dadunashvili S.A. (1996) Monitoring of Technoevolution Processes. – Bulletin of the Georgian Academy of Sciences, № 2(153), Tbilisi, 1996. p. 210-214.
2. Dadunashvili S.A. (1997) System-forming models in biosphere and a noosphere. – Proceedings of GTU, №3 (414), Tbilisi, 1997. p. 224-232.
3. Dadundshvili S. A. (2003) Simulation of the process of etnogenesis. - Georgian Engineering News, 2003, №4, c.150-159.
4. Dadunashvili S.A. (2005) Coordinate system for representation of the information phenomena. - Georgian Engineering News, 2005, No.1, p. 36-47.
5. Charles R. Card (1996) The Emergence of Archetypes in Present-Day Science And Its Significance for a Contemporary Philosophy of Nature - *Dynamical Psychology,* 1996

Author: Dadunashvili Sergo
Institute: Georgian Technical University
Street: Kostava 77
City: Tbilisi
Country: Georgia
Email: dadu@gtu.ge

Mission and Social Impact of the Multidisciplinary School of Engineering in Biomedicine

M. Wasilewska-Radwańska[1], E. Augustyniak[2], and P. Augustyniak[1]

[1] AGH University of Science and Technology, Multidisciplinary School of Engineering in Biomedicine, Kraków, Poland
[2] AGH University of Science and Technology, Faculty of Humanities, Kraków, Poland

Abstract — **The Multidisciplinary School of Engineering in Biomedicine was founded in AGH University of Science and Technology for the purpose of education of biomedical engineering students. This paper discusses the extensions of the MSIB's mission and impact to the local society resulted from independent information policy. Broadening of awareness of the new profession was mainly targeted on college scholars and prospective employers in order to help in human flow management. Beyond the study track, MSIB implemented a biomedical engineering-specific professional culture having impact on students' competences demonstrated by voluntary and extramural students' activities. All these examples prove a high impact of the School on new professionals, their job opportunities and local society benefiting from their work.**

Keywords — **biomedical engineering, BME education, multidisciplinary learning, education quality, learning organization.**

I. Organizational principles of MSIB

The Multidisciplinary School of Engineering in Biomedicine (MSIB) is an independent department of the AGH University of Science and Technology (AGH-UST) and has been in operation since the academic year 2005-2006 [1]. Although MSIB has been formed on the basis of the staff formally employed by five faculties, it is treated as a separate part of the AGH-UST and has its own students. Formally, MSIB's structure is similar to that of other faculties. It is governed by a Programme Board of 18 persons. This Board, approved by the University Senate, is made up of professors with not less than a DSc degree who are teaching at MSIB, as well as of an adequate representation of students. At present, the professors represent five faculties:

- Faculty of Electrical Engineering, Automatics, Computer Science and Electronics,
- Faculty of Materials Science and Ceramics,
- Faculty of Mechanical Engineering and Robotics,
- Faculty of Metals Engineering and Industrial Computer Science, and
- Faculty of Physics and Applied Computer Science.

One of the Board's tasks is to recommend to the Rector appointments for the Head and the Deputy Head of the School. The appointed Head is also President of the Board. The main responsibility of the Board is to supervise the education process, assure its highest quality, verify and, if necessary, correct academic curricula, prepare staff assignments and implement other objectives of the School. The Head also represents the MSIB in the University Board on par with deans of other faculties.

From the student's viewpoint, there is no organizational difference between the faculty and the Multidisciplinary School. Both have a Dean's Office, a staff of qualified teachers, a social support system and a Student Council. As far as education is concerned, the rights and responsibilities of the Head of the School are identical to those of a Dean, the only difference being that research is carried out in laboratories in various faculties run by individual professors rather than in the organizational framework of MSIB. The agreement between the universities gives students the opportunity to attend lectures of six medicine-oriented lectures (e.g. anatomy, physiology, medical deontology, history of medicine), and to participate in laboratory exercises in the Faculty of Medicine at Collegium Medicum (Medical College) of the Jagiellonian University. This cooperation is mutually beneficial since it provides an alternative, i.e. medicine-based viewpoint, for our medical colleagues and medicine students [2], [3]. Postgraduate studies and technology-oriented teaching projects are also offered by some lecturers from AGH-UST for medicine students or medical doctors. The organizational chart of a multidisciplinary school is innovative and rarely implemented by universities, therefore the university funds' distribution mechanisms are often inadequate.

The BME teaching in the MSIB AGH-UST is programmed accordingly to legal regulations including national standards for academic teaching by the Ministry of Science and Higher Education [4] and to the guidelines of Bologna Process (including the Educational Credits Transfer System). The current offer consists of (fig. 1):

- a single 1-st degree (Bachelor/Engineer) 7 semester track,
- five domain-oriented 2-nd degree (Master) 3 or 4 semester tracks,
- a single 3-rd degree (Doctoral) 8 semester track.

Y. Dekhtyar et al. (Eds.): *International Symposium on Biomedical Engineering and Medical Physics*, IFMBE Proceedings 38, pp. 11–14, 2013.
DOI: 10.1007/978-3-642-34197-7_3

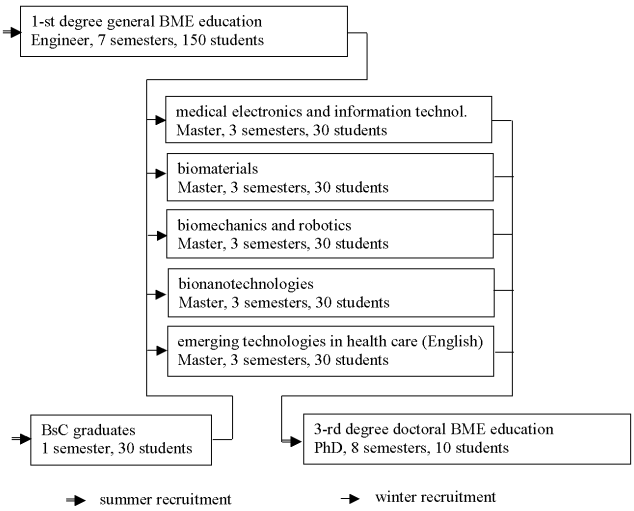

Fig. 1 Education tracks scheme for biomedical engineering at MSIB AGH-UST.

II. Management of Human Flow

A. Independent Information Policy

One of the most important advantages of the School is the prerogative to create and implement the independent information policy. This tool can be used not only for administrative purposes, but can help in creating a public understanding of "biomedical engineering". This issue is of particular importance in countries like Poland, where tradition of regular academic education in this domain has started recently. The information policy is primarily used by universities to inform prospective candidates about admittance conditions or facts about studying. However, due to the independence, the message not integrated with other faculties within a department may be also addressed to a general public and support the awareness of a new profession. In that case the information policy became a tool of social mission which extends far beyond the standard understanding of higher education [5].

Within the mission of MSIB four main directions were identified as targets of information policy:

- candidates, being the input of institutional human flow,
- employers, being the output of institutional human flow,
- students, being recipients of knowledge, skills and social competences as well as partners within a common corporate culture [6],
- society, being indirectly concerned by the outcome of biomedical engineering and requiring information as tax payers

B. Cooperation with Undergraduate Scholar Institutions

Biomedical engineering falls within areas of interest of several subjects in the college: mathematics, physics, biology, chemistry etc.. Therefore the existence and aims of university education for new professionals require to be communicated to both youth and teachers.

Thanks to the corporate culture in MSIB, the understanding of information policy by students is demonstrated by their help in college communication meetings, university open days or science festivals. In the same spirit, we encouraged students to join academic professors in a project of editing an introductory review book to biomedical engineering. As in case of personal contacts, besides the enthusiasm, the main advantage of students' help is their veracity supported by use of age-specific language register.

Certainly, the candidates' information and websites are also provided, since these conservative information carriers are more persistent, easier to consult and commonly accessible. However, organizing an informative event with support from colleges' authorities is also beneficiary for students as a practical verification of their social competences.

C. Competitions for Individuals – Seeking for the Most Involved Candidates

Long discussion were devoted to a question of relation of candidate skills to education efficacy. In our practice, we rather opt for admittance of domain-devoted individuals than best-scored school leavers. Since no specific college subject is directly related to the study, we analyzed feasibility conditions of high school competition in bioengineering. The country-wide competition is targeted to undergraduates and aimed at supporting the interest for the biomedical engineering, spreading the idea of bioengineering as a profession and university faculty as well as identification and recruitment of the most talented and oriented individuals to the university. Such goal is difficult to achieve mainly because of low social awareness of the idea of bioengineering, systematic abandoning of the physical and biological subjects in colleges, and low population of teachers prepared for supporting their pupils beyond the range of their duties.

Such competition was for years an accompanying event of the International Conference BioMedTech Silesia organized by Foundation of Cardiac Surgery Development in Zabrze. Despite of its long standing tradition, the competition was not formally recognized by Polish Ministry of

Education and therefore the laureates may not be officially get preferential admittance for a public university.

D. Cooperation with Prospective Employers

This aspect of university information policy is usually limited to tracking of the graduates' careers. The commonly accepted success scores like first job salary or initial unemployment duration are hardly representative in case of a new profession. In MSIB we extended the understanding of "educational offer" and "educational product" by the way typical to other commercial offers and products. In that spirit, during the International Trade Fair of Medical Equipment and Instruments SALMED 2012 held in Poznań from 14-th to 16-th March 2012, we presented the educational offer of MSIB, concerning the education of professionals for technical support of medicine in the faculty of biomedical engineering. Our offer was proposed along with offers of other exhibitors of equipment, solutions and services (e.g. training, publishing) for health care.

Our participation in Fair as an exhibitor was mainly targeted at communicate to widely represented manufacturers of medical instrumentation, doctors and officers of health care management about the knowledge, skills and competences of our graduates. Similarly to the products presented in their intended actions, our graduates were presenting their attitudes in a practical way by means of completed Engineer Diploma Projects. Despite only two example projects were presented, the opinion of professional approach and high merit was equally attributed to other projects completed at MSIB. In result of the presentation, the MSIB acquired in visitors' eyes a connotation of quality education continuously adapted to the demands of job market.

E. Promotion of the School and Self-promotion of Students

The Fair was an unprecedented opportunity to promote the MSIB as educational institution as well as for self-promotion for involved graduates. Thanks to the corporate culture insisting on staff-student partnership [6], the graduates motivated by their commitment actively prepared and performed the exposition, at the same time being main beneficiaries of the event. They got numerous remarks and directions on their projects and also some offers concerning further development, application and employment. Even in worst case, including a fair exhibitor experience in a CV is not common to university graduates.

The other part of institutional promotion targeted at future graduates is the summer apprenticeship of one month duration. During this period students are participating in industrial, health care or scientific project not only making their first steps towards professional experience, but also representing the university with their knowledge, skills and competences.

III. Impact to the social competences

A. Competences in BME-Related Areas

Identifying of profession-specific needs for social competences and setting educational standards also belong to the extended mission of MSIB. Besides other particularities, striving for the technical excellence and ethical background belong to key competences of bioengineer.

Working in a team with the doctor, nurse and pharmacist, the biomedical engineer is a representative for all technology-related ideas, and is expected to solve issues in this area. No other application of technology could be compared as having a direct relation with the human, his well-being and fundamental values, as the support of life. Consequently, a particular presumption of excellence is distinguishing the biomedical engineer among other engineers. Moreover, since the technology is currently fast enlarging the ability and efficiency of medicine, it also bears a particular responsibility for unfortunate medical acts.

The engineer is rarely as closely related to the human in various life circumstances (birth, adolescence, impairment, disease, pain, death and others), as the biomedical engineer. Therefore, particular education forms should stress on attitudes supporting the understanding of the human in general. Since the engineering in biomedicine is always a part of medical act, simultaneous or intended in the future, the ethical background proper for the medicine should be also a mandatory element of lectures and practice in the BME educating institute.

B. Competences Concerning Multidisciplinary Education

Due to the fact of cooperating of professors from different departments of AGH-UST and medical doctors, the multidisciplinary education is and inherent feature of MSIB [7]. As the university may be considered as an archetype of future workplace, this idea is consequently propagated to the expected educational competences.

Biomedical engineering, as relatively new discipline bridges the gap between the medicine and technology, and applying various technological achievements directly influences the quality of life. Consequently, a single medical act involves multiple actors, many of which, essentially the engineers, usually remain behind the scene. Their cooperation may success only if all share some common understandings about their roles and mutual dependencies. Moreover, the medical act has to be as appropriate as possible, what - among the other aspects - requires the technical

excellence and high ethical awareness of participating engineers. Finally, the clinical engineer frequently works shoulder to shoulder with medics in emergency and under the pressure of time, where common feelings, ideas and behavior are decisive, not only improving factors for the final result. Therefore understanding within a multidisciplinary team definitely belongs to key aspects of BME-related professional culture.

IV. Impact to the local society

A. Broadening the Awareness of Health and Prevention

In our society health prevention is considered substantially rarer than leisure or comfort. This opens a new area of MSIB mission and its social impact. Health promotional events targeted at general public attract people of any age thanks to interesting equipment demonstrated in its everyday use. The public take the opportunity to familiarize with technology supporting health care, to learn about purpose and backgrounds of particular devices and therefore weaken all unpleasant connotations with disease. Future biomedical engineers get involved in broad education and benefit from the chance to develop their communication skills.

B. Articulating the Need of New Profession

There is an urgent and important need for the development of medical technology because of the poorer quality of social health services in Poland compared with those in highly developed EU countries. Since local industry was rather undeveloped, Poland is now highly influenced by international corporations. Their sales- or service representatives are not independent in research and development or human resources management. We estimate the number of local medical technology-related enterprises to be about 100, but most of them (40%) were very small businesses, so-called micro-enterprises, having 1-5 employees, or small enterprises (30%) with 6-50 employees [8].

In response of the ageing society and with support from European funding, some health care institutions in Poland was recently equipped with last achievements of technology substantially rising the quality of medical services. This equipment need to be operated and maintained by local staff. We are encouraging the graduates to take this opportunity to join international research and development teams in both universities and company milieus.

C. Voluntary Actions towards Disabled or Elderly

As shown by statistical surveys, biomedical engineering students belong to the most involved in voluntary actions organized for disabled or elderly people. Institutional support of their activity in hospitals, hospices or homeless refugees also belongs to MSIB mission in the society. Besides encouragement, this support has a form of ECTS credits awarded similarly to the study workload (1 ECTS credit corresponds to 25-30 working hours). Performing such duties, students acquire competences impossible to learn in pure academic conditions.

Acknowledgment

This work was founded from the AGH-University of Science and Technology, grant no. 11.11.120.612.

References

1. Wasilewska-Radwańska M, Augustyniak P. (2010) Multidisciplinary school as a BME teaching option, [in:] Olaf Dössel, Wolfgang C. Schlegel (eds.) World congress on Medical physics and biomedical engineering. Springer, R. Magjarevic (ed.) IFMBE Proceedings, ed. vol. 25 pp. 200-203.
2. Monzon JE (2005) The Challenges of Biomedical Engineering Education in Latin America. 27th Annual International Conference of the Engineering in Medicine and Biology Society, IEEE-EMBS, 2005, pp2403-2405
3. Schwartz MD (1988) *Biomedical Engineering Education*, in: Webster J.G (ed), Encyclopedia of medical Devices and Instrumentation, Wiley, New York, 1998, pp392- 403
4. Ministry of Science and Higher Education, Educational Standards for Higher Education, No 49 Biomedical Engineering (in Polish) 2007
5. Wasilewska-Radwanska M, Augustyniak E, Tadeusiewicz R, Augustyniak P. (2012) Educational Opportunities in BME Specialization - Tradition, Culture and Perspectives [in:] Dhanjoo N. Ghista (ed.) Biomedical Science, Engineering and Technology, InTech, 2012, pp. 559-584.
6. Augustyniak E, Augustyniak P. (2010) From the foundation act to the corporate culture of a BME Teaching Institute. Proceedings of the 32nd annual international conference of the IEEE Engineering in Medicine and Biology Society, 2010, pp. 319-322.
7. Wasilewska-Radwanska M, Palko T (2008) Actual State of Medical Physics and Biomedical Engineering Education in Poland. 14th Nordic-Baltic conference on Biomedical Engineering and Medical Physics : Riga, Latvia, June 16–20, 2008 : abstracts / IFMBE Riga Technical University, cop. 2008. — ISBN 978-9984-32-231-5, 2008, p121
8. Augustyniak P. (2011) Adaptive Approach to BME Teaching at the AGH-UST [in:] Piotr Augustyniak (ed.) Biomedical Engineering Educational Offer Review, Bio-Algorithms and Med-Systems 3/2011, 73-84

Author: M. Wasilewska-Radwanska
Institute: AGH-University of Science and Technology
Street: 30, Mickiewicz Ave,
City: 30-059 Krakow
Country: Poland
Email: radwanska@novell.ftj.agh.edu.pl; ETP@efomp.org

Approach to the Silicon Sensor with Pre-threshold Electron Emission Readout to Detect Exhaled Breath Gases

Yuri Dekhtyar, Kristine Perovicha, and Alexander Soudnikovich

Biomedical Engineering and Nanotechnologies Institute, Riga Technical University,
1 Kalku Street, Riga LV1658, Latvia

Abstract — **Preliminary diagnosis of human diseases such as cancer and diabetes is possible via the detection of violate organic compounds (VOCs) contained in exhaled breath gases. A pre-threshold electron emission yield from a solid emitter depends on the gas molecules adhered to the emitter, if the electron work function is influenced. The paper demonstrates that pre-threshold electron emission from a silicon solid emitter could be employed to detect exhaled VOCs.**

Keywords— **exhaled breath gas, silicon gas detector, electron emission.**

I. Introduction

According to medical research, patients with cancer, diabetes and COPD have very specific violate organic compounds (VOC) in their exhaled gases [1-3]. For cancer patients the concentrations of VOCs such as benzene, acetone, toluene, pentane and hexane, which are the metabolites of cancer cells, are very specific.

Presently the detecting techniques succeed to identify approximately around 200 of VOCs at the nano – piko-molar concentration [1,2]. However, increasing the detecting technique's sensitivity to alterations of the VOCs concentration will significantly improve the reliability of the diagnostics.

Since detecting techniques typically consist of a VOCs detector and equipment to amplify and record signal, there are two ways to enhance sensitivity: improving the detector and advancing the quality of the equipment.

The latter is boosted by signal processing algorithms and circuitry decisions improvement. However, to get a better detector, the derivation of the signal (S) supplied by the detector on the VOCs concentration (C) is the most important property.

The function S(C) could be written as:

$$S(C) = S(C_0) + (C - C_0)\frac{dS}{dC} + (C - C_0)^2\,\frac{d^2S}{dC^2} + \cdots \quad (1)$$

C_0 – value of C at that vicinity that S is derived.

The accuracy of S(C) is high when the nonlinear elements of the formula are kept. This can be achieved when the highly indexed derivations provide significant impact even when the difference (C-C_0) is small. Such conditions are available, if the VOCs detector demonstrates nonlinear, preferably parabolic, dependence S on C. The pre-threshold emission of electrons gives such opportunity.

Photoelectron emission (PE) current density (I) generally obeys the equation:

$$I = A(h\nu - \varphi)^m \quad (2)$$

A – coefficient of proportionality;
$h\nu$ – energy of the photon that excites the electron [eV];
m –coefficient that deals with transitions between the initial and final states of the electron, m>1[4], φ – electron work function.

If the emitter attaches to the electrically active molecules, the value of φ depends on their concentration. Looking at the first approach

$$\varphi(C) = \varphi(C = 0) + \Delta\varphi(C), \quad (3)$$

$\Delta\varphi\ (C)$– the increment of φ resulting from C,

$$\Delta\varphi(C) = \frac{\Delta\sigma(c)l}{2\varepsilon\varepsilon_0}, \quad (4)$$

$\Delta\sigma$ - surface charge density increment, influenced by C;
l - emitting electron main free path within the emitter;
ε - electrical permittivity of the matter that the electron escapes from;
ε_0- electrical permittivity of vacuum.

Because of the above, I is a parabolic (m>1) function of C and I fits in (1). However to get the Δφ response on C, the value of ε should not be large.

The alteration of φ can also give a contribution to the weak thermoelectron emission (TE). Its electron current density I_T obeys Richardson - Dushman formula:

$$I_T(C) = B \cdot T^2 \cdot \exp\left(\frac{-\varphi(C)}{kT}\right) \quad (5)$$

B - coefficient;
K - Boltzmann constant;
T - temperature K.

Y. Dekhtyar et al. (Eds.): *International Symposium on Biomedical Engineering and Medical Physics*, IFMBE Proceedings 38, pp. 15–18, 2013.
DOI: 10.1007/978-3-642-34197-7_4

To compare the sensitivities of I and I_T on the C alteration, the derivation dI/dφ and $dI_T/d\varphi$ can be weighted:

$$\frac{\partial I}{\partial \varphi} = Am \cdot (h\nu - \varphi)^{m-1} \quad (6)$$

$$\frac{\partial I_T}{\partial \varphi} = B \cdot T^2 \cdot \exp\left(-\frac{\varphi}{kT}\right) \cdot \left(-\frac{1}{kT}\right) \quad (7)$$

For instance, comparison of (6) and (7) can be written as

$$\frac{\left|\frac{dI_T}{d\varphi}\right|}{\left|\frac{dI}{d\varphi}\right|} > 1 \quad (8)$$

$$\frac{B \cdot T^2 \cdot \exp\left(-\frac{\varphi}{kT}\right)}{kTAm \cdot (h\nu - \varphi)^{m-1}} > 1 \quad (9)$$

When $I = I_T$:

$$B \cdot T^2 \cdot \exp\left(-\frac{\varphi}{kT}\right) = A(h\nu - \varphi)^m \quad (10)$$

And (9) is transformed to:

$$\frac{(h\nu - \varphi)}{kT} > m \quad (11)$$

This means that the TE is preferred to detect VOCs, if the condition (11) is right.

Because of the Fermi statistics, the emitting electron energy uncertainty cannot be less than kT. Therefore if the PE mode is applied, the photon energy should be selected as:

$$(h\nu - \varphi) > kT \quad (12)$$

The present paper is directed to identify the capability of PE and TE to detect VOCs. The gases of benzene and isopentane were selected as examples that are typical of lung cancer patients [1-3].

II. Materials and methods

The magnitude of φ of the doped semiconductors is influenced if the electrically active molecules are adsorbed [5]. The crystalline silicon (Si) specimens having n- and p-type conductivity were selected for the experiments (Table 1). This in addition to the above was motivated because:

- the PE of Si is provided due to indirect photoinduced electron transitions, m = 2.5 [4].
- the value of ε is small, $\varepsilon = 11.9$ [5].

Table 1 Electrical resitance of the Si specimens.

Type	Electrical resistance, Ω·cm	Legend
p-Si, doped with Boron	0.0005	SHB – 0.0005
	1	SHB-1
n-Si, doped with Phosphorus	0.0014	SEP-0.0014
	5	SEP-5

The specimens were prepared from Si crystals mechanically (cutting, grinding, polishing) reaching a mirror like surface. The thickness of the specimens was equal to 0.2 mm and they were sized to approximately 1x1 cm^2. The specimens were then cleaned with batiste tampon soaked in 96% ethanol. After this, the specimens were placed in the PE spectrometer, described in details in [6]. The magnitudes of I were detected in vacuum conditions (10^{-1} Pa) at room temperature and a hν range of 4.5-6 eV. The peculiarities of I(hν) spectra were observed at 5 eV. After that the specimens were annealed in the same spectrometer in 10^{-1} Pa at + 600 C°, the I was detected simultaneously at 5 eV. Annealing was interrupted when I stabilized. After that the PE spectra were detected as above.

The TE was measured from the specimens. The measurements were provided in the spectrometer [4] in vacuum condition 10^{-1} Pa. The specimens were heated from the room temperature until + 400 °C with a heating rate of 0.3°C/sec.

Next the specimens were placed into Petri dishes (volume 0.08 cm^3). The volume of 125 µl of the liquid benzene (dipole moment D=0 D [7]) or isopentane (dipole moment D=0.29 D [8]) was dripped inside the Petri dishes using single-channel pipette, then the dishes were sealed with their covers. The liquids were completely evaporated in less than 10 minutes. The specimens were exposed in the closed dish for longer than those 10 minutes. After the exposure the specimens were placed in the above spectrometer to detect PE or TE.

The differences of the measured emission currents densities before and after exposure were calculated as ΔI and ΔI_T for PE and TE, correspondingly.

In addition the exposure depended increment of the total emitted charge was numerically calculated as:

$$Q = \int_{4.5\ eV}^{6\ eV} \Delta I(h\nu)\, d(h\nu) \quad (13)$$

And

$$Q_T = \int_{20\ C}^{400\ C} \Delta I_T(T)\, dT \quad (14)$$

The same specimens were exposed in gas several times. However, to restore the specimens after each experiment

they were restored to the initial state: annealing at 600 ºC during 20 minutes. As the result I (at hν = 5 eV) was reached at the magnitude of the initial specimens.

III. Results

Fig. 1-4 demonstrates ΔI and ΔI_T for exposure of the specimens in benzene and isopentane, correspondingly.

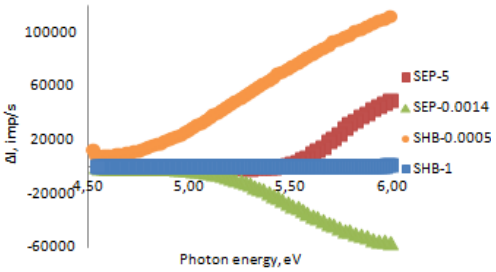

Fig. 1 ΔI of PE in bezene, exposure time 30 min.

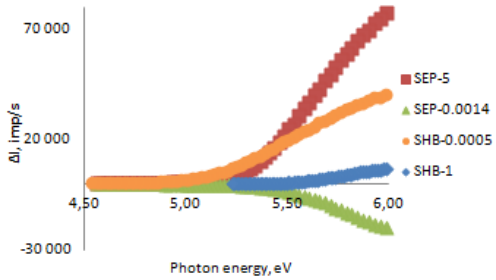

Fig. 2 ΔI of PE in isopentane, exposure time 30 min.

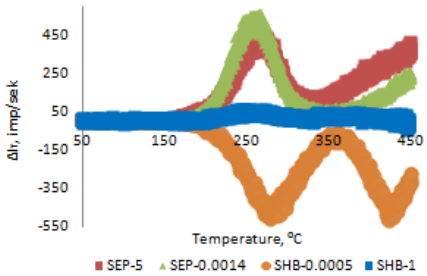

Fig. 3 ΔI_T of TE in benzene, exposure time 30 min.

As seen from the figures above, SHB-0.0005 material shows strong PE and TE emission curemt with benzene and isopentane. SEP-0.0014 shows lower PE current after exposure for both VOC's, which is represented as negative ΔI(hv).

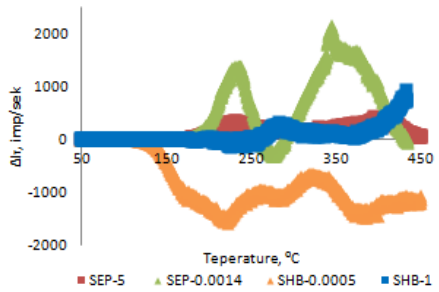

Fig. 4 ΔI_T of TE in isopentane, exposure time 30 min.

Fig. 5-6 demonstrates Q and Q_T changes, depending on different type of Si specimen and gases in exposure time 30 min.

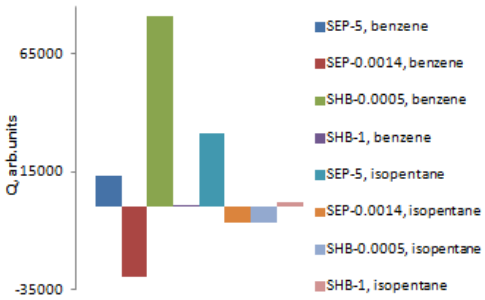

Fig. 5 Q for different types of Si, experiments with benzene and isopentane, exposure time 30 min.

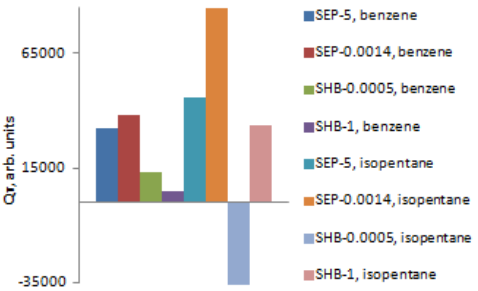

Fig. 6 QT for different types of Si, experiments with benzene and isopentane, exposure time 30 min.

30 minutes of the exposure time was chosen as minimal as liquid benzene and isopentane evaporated totally (during 10 minutes). The spectra differences corresponding to 10 minutes of the specimens presence in the atmosphere by the evaporating liquid are represented as Q, Q_T.

Fig. 7-8 reflects influence of the exposure on Q and Q_T.

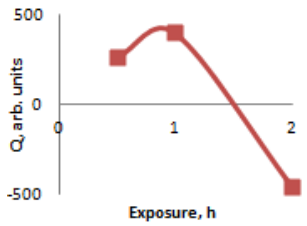

Fig. 7 Q in dependence on exposure time in benzene, SHB-1.

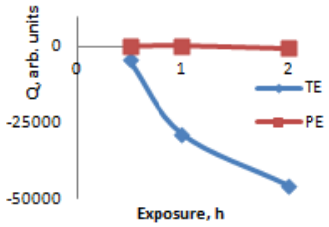

Fig. 8 Q (PE) and Q_T (TE) in dependence on exposure time in benzene, SHB-1.

The value of Q_T depends on the exposure time stronger than Q, since heating is performed to whole specimen area. As a result detected signal was stronger.

IV. Conclucions

1. Pre-threshold PE and TE were explored to supply signals depending on the exposure of a solid Si emitter in gases with different polarities of the molecules. The isopentane molecules having a higher polarity give stronger impact in experiments with TE (Fig. 7).

2. TE is stronger influenced by the exposure in the benzene and isopentane gas atmospheres (Fig. 5).

3. Further experiments are necessary to provide more knowledge on the sensitivity of the electron emission based technique to detect VOCs.

References

1. Wang C, Sahay P (2009) Breath Analysis Using Laser Spectroscopic Techniques: Breath Biomarkers, Spectral Fingerprints, and Detection Limits. Sensors 9, 8230-8262
2. Shirau M, Touhaza K (2011) The scent of disease volatile organic compounds od the human body related to disease and disorder. Oxford J, The Journal of Biochemistry 3, 257-266
3. Mandis A (1983) The diagnostic potential of breath analysis. Clin Chem. 29:5 – 15
4. Akmene R J, Balodis A J, Dekhtyar Yu D, Markelova G N, Matvejevs J V, Rozenfelds L B, Sagalovičs G L, Smirnovs J S, Tolkačovs A A and Upmiņš A I (1993) Exoelectron emission spectrometer complete set of surface local investigation. Poverhnost, Fizika, Himija, Mehanika 8:125 -128
5. Kane E (1962) Theory of photoelectric emission from semiconductor ctors. Phys Rev 127:131-141
6. Sagalovich G L, Dekhtyar Yu D (1987) Photostimulated exoelectron emission from crystalline silicon containing edge dislocations and point defects. Physica Status Solidi(a) 102, 665-677
7. Isopentane at http://www.microkat.gr/msdspd90-99/Isopentane.htm, 30.04.2012
8. Benzene at http://en.wikipedia.org/wiki/Benzene, 30.04.2012

MEMS Accelerometer-Based Heart Monitoring System with Myocardial Fixation

F. Tjulkins, A.T. Nguyen, M. Andersen, and K. Imenes

HiVe - Vestfold University College, IMST – Department of Micro and Nano Systems Technology, Horten, Norway

Abstract — **The drawbacks of existing post-operative heart monitoring systems create the demand for novel methods of monitoring patients heart activity. The continued advances in the field of micro electromechanical systems (MEMS) make it possible to create a heart monitoring system using commercially available sensors and develop a mission specific package for it. In this paper an early prototype of such a system system is described.**

Keywords — **encapsulation, heart monitoring, accelerometer, MEMS.**

I. Introduction

In the modern world, heart surgery, such as the coronary bypass grafting, is an everyday occurrence. In large hospitals, multiple operations may be carried out daily. To monitor for complications a diagnostic system is necessary. It has been reported that graft occlusion happens in 4% of patients immediately after closure of the wound [1]. Established monitoring techniques have a number of drawbacks: electrocardigraphy (ECG) can be unspecific [2], echosonography and angiography are accurate [3] but provide only intermitted monitoring. A sensitive, specific, reliable tool for continuous monitoring and detection of graft occlusion and ischemia in post-operative period is necessary.

An efficient heart monitoring system, based on a compact tri-axial accelerometer was developed by Hogskolen i Vestfold in cooperation with Intervention Centre at Oslo University Hospital [4]. The system demonstrated capability for rapid heart function change detection [5 – 8]. Despite excellent results obtained in clinical trials both on animal subjects and human beings the system is held back from clinical application by the relatively large size which means the patient's chest has to be open for implant removal. In order to make the clinical application of this system possible, the sensor must be able to work in a closed chest setting and be extracted from the patient without additional surgical procedures, in a similar fashion to temporary epicardial pacing leads (heartwires). With the advance of MEMS accelerometers, highly compact tri-axial acceleration sensors like the CMA3000 (VTI, Finland) and BMA250 (Bosch, Germany), both just 2x2x0.95mm, are now available. These sensors can make a backbone of an implantable heart monitoring providing a suitable packaging solution is provided.

Previously, the sensor was sutured on top of the left ventricle, in the current project the implant is fixed inside the myocardium of the left ventricle, same way as temporary myocardial ECG probes. See Figure 1. In order to make this system possible, it is necessary to provide both electrical interconnection and biocompatible encapsulation. For the electrical interconnection a set of decoupling capacitors is necessary, as well as leads to connect the sensor to an external data acquisition unit. The encapsulation must be biocompatible and provide both fixation and stabilisation for the implant. See Figure 2.

In this two methods of electrical interconnection were used: a flex substrate that doubles up as a cable and a microribbon cable with a separate substrate. The sensor was overmoulded with medical grade silicone using a mould form. Silicone moulding is a well-developed technique and allows control over the end devices parameters: the shape, the surface and mechanical properties.

Compared to the previous generation system the size has to be reduced as much as possible yet things like package mechanical properties and ability to standup to the environment inside the human body also play a paramount role.

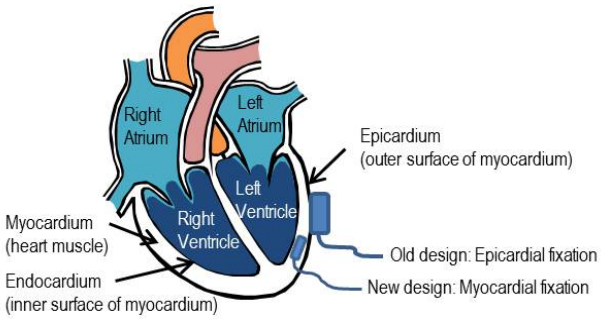

Fig. 1 Cross section of the heart showing the old and the new method of implant fixation.

Y. Dekhtyar et al. (Eds.): *International Symposium on Biomedical Engineering and Medical Physics*, IFMBE Proceedings 38, pp. 19–22, 2013.
DOI: 10.1007/978-3-642-34197-7_5

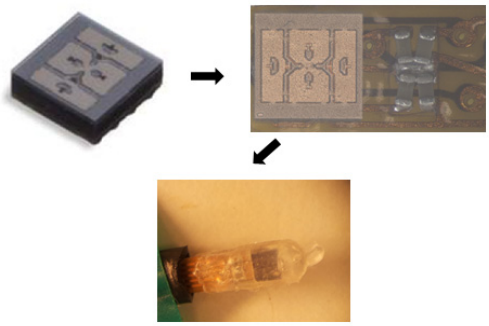

Fig. 2 CMA3000 sensor, CMA3000 mounted on a flex substrate with capacitors, an early prototype - sensor mounted and encapsulated with silicone.

II. Materials and Methods

A. Sensor

Previous generations of the accelerometer based heart monitoring system used a number of different sensing solutions: first a hybrid 3-axis sensor constructed from two 2-axis ADXL-202 (Analog Devices, USA) accelerometers perpendicular to each other [5], in later stages a single 3-axis accelerometer, the KXM52-1050 was used [4][8] and finally, a compact three-axis accelerometer was developed in-house [9]. However, the rapid advance of MEMS accelerometers made the in-house designed sensor obsolete. The availability of micro-miniature, commercial sensors allows to save time on developing a sensor and focus on developing a mission-specific package. The sensor selected for this system is the CMA3000 3-axis ultra-low power accelerometer. As of writing this article, this sensor, along with the near identical BMA250 (Bosch, Germany) is the most compact 3 axis accelerometer on the market. The sensor is a capacitive, 3-axis, MEMS accelerometer, it features both SPI and I^2C interfaces, user selectable measurement ranges, sampling rates and frequency response, low current consumption and is RoHS compliant. The standard interface and compatibility with LabWiev (National Instruments, USA) makes the sensor compatible with the previously made signal processing and interpretation software [5][10].

B. Electrical Interconnection

To operate the sensor requires not just leads but also a set of decoupling capacitors. A set of capacitors would require a compact substrate and an additional interconnection between substrate and cable. Two approaches have been taken: a flexible cable with an integrated substrate and a separate substrate with a microribbon cable.

Table 1 Specifications of the CMA3000 capacitive 3-axis accelerometer.

Parameter	Units	CMA3000
Range	G	±2 or ±8
Sensitivity	V/g	Vdd/6 or Vdd/24
Operating Voltage (Vdd)	V	1.7-2.7
Noise @ 100hz and @ 400hz	µg/√Hz	300 or 600
Bandwidth	Hz	20 or 80
Cross-axis sensitivity	%	1

C. Microribbon and Substrate

An attractive solution for providing an electrical interconnection in implantable systems is the Microribbon (Temp-Flex Cable, USA) cable. This cable was tried out in a previous study [11]. For this project the isolation on the end of the cable was stripped by O2 plasma and bonded to an alumina (Al_2O_3) substrate with gold interconnect layout (Mectro AS, Horten, Norway). The bonding was achieved using Epotek 353ND biocompatible, nonconductive epoxy. See Figure 3.

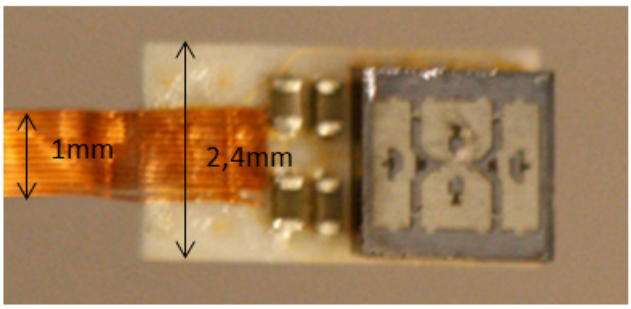

Fig. 3 The sensor attached to a substrate with capacitors and the micro ribbon cable.

D. Flexible Printed Circuit

Another design for the electrical interconnection between the accelerometer and the data acquisition system is the integrated design. There is a union of substrate and cable using a polyimide-based flexible printed circuit (Figure 4) which has been used recently in implantable medical devices [12 - 14]. A double-sided circuit design is selected to have a high aspect ratio between the length and the width of the circuit with 2.4 mm in width and 500mm in length. The drawback of this interconnect system is the larger width but the benefits are high mechanical robustness of the circuit system, reduction of interconnection resistance and capacity for mass-production.

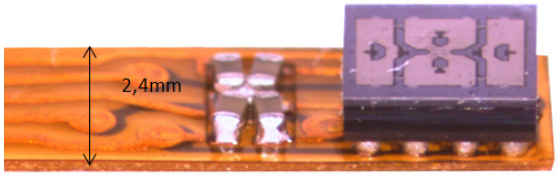

Fig. 4 The integrated design of cable and substrate.

E. Encapsulation

The encapsulation is a critical component in this project, as factory-made encapsulation of the CMA3000 sensor is not biocompatible and is not meant for use in an environment such as the inside of a human body. Silicone was chosen because it is a well-established bio inert, biocompatible material and is relatively easy to prototype and process. The silicone used in this project is Elastosil R 4001/40 from Wacker Chemie AG (Germany). The same silicone was used in previous stages of the project [4] and has proven to be an excellent solution.

The full 165^{O}C temperature was used when press curing the mock-up containing an inert sensor, for the devices containing functioning sensors the curing temperature would have to be lowered and curing time increased.

Table 2 Elastosil 4001/40 properties.

Parameter	Units	Elastosil 40001/40
Appearance		Clear
Press cure	Min @ ^{O}C	15 @ 165
Cure catalyst		Platinum
Tensile strength	N/mm^2	11
Elongation at break	%	940

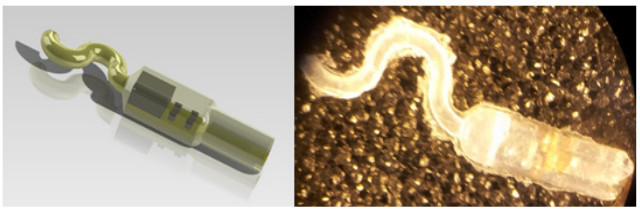

Fig. 5 On the left – a CAD drawing of the encapsulated sensor, on the right – an early prototype.

The encapsulation consists of three parts: main body containing the sensor, a zig-zag attachment similar to the ones found on temporary epicardial pacing leads, in order to improve the fixation of the implant and an overmould of outgoing leads to facilitate seamless transition from the myocardium to outside – this could be a channel or a surgical drainage tube. See Figure 5.

III. Summary

The existing packaging techniques make it possible to create a highly compact sensor package. The sensor is yet to undergo clinical testing which will point out the weak points and preferable techniques but the fact that the system can be made so compact using mostly commercially available tools and components bodes well for developing similar systems in the future.

Acknowledgements

The authors would like to thank Svein Mindrebøe from Vestfold University College (HiVe) for manufacturing the mould form, the team at Oslo University Hospital Intervention Centre and the packaging group at Institute of Microsystem Technology.

References

[1] Hol P. K.,Lindgaas P. S., Lundblad R, et al. 2004 Intraoperative angiography leads to graft revision in coronary artery bypass surgery. Ann Thor. Surg. 78:502-505.

[2] Gianrossi R, Detrano R, Mulvihill D, Lehmann K, Dubach P, Colombo A, McArthur D and Froelicher V 1989 Exercise-induced ST depression in the diagnosis of coronary disease: a meta-analysis Circulation 80 87–98.

[3] Edvardsen, T. Urheim, S. Skulstad, H. Steine, K. Ihlen, H. Smiseth, O. A. Quantification of left ventricular systolic function by tissue Doppler echocardiography: added value of measuring pre- and postejection velocities in ischemic myocardium Circulation 105 2071-2077.

[4] K. Imenes, K. Aasmundtveit, E. M. Husa, J. O. Høgetveit, S. Halvorsen, O. J. Elle, P. Mirtaheri, E. Fosse, and L. Hoff, "Assembly and packaging of a three-axis micro accelerometer used for detection of heart infarction," *Biomedical Microdevices,* vol. 9, pp. 951-957, 2007.

[5] O. J. Elle, S. Halvorsen, M. G. Gulbrandsen, L. Aurdal, A. Bakken, E. Samset, H. Dugstad, and E. Fosse, "Early recognition of regional cardiac ischemia using a 3-axis accelerometer sensor," *Physiological Measurement,* pp. 429-440, 2005.

[6] P. S. Halvorsen, A. Espinoza, L. A. Fleischer, O. J. Elle, L. Hoff, R. Lundblad, H. Skulstad, T. Edvardsen, H. Ihlen, and E. Fosse, "Feasibility of a three-axis epicardial accelerometer in detecting myocardial ischemia in cardiac surgical patients," *The Journal of Thoracic and Cardiovascular Surgery,* vol. 136, pp. 1496-1502, December 1, 2008 2008.

[7] P. S. Halvorsen, L. A. Fleischer, A. Espinoza, O. J. Elle, L. Hoff, H. Skulstad, T. Edvardsen, and E. Fosse, "Detection of myocardial ischaemia by epicardial accelerometers in the pig," *Br. J. Anaesth.,* vol. 102, pp. 29-37, January 1 2009

[8] L.A. Fleisher, P. S. Halvorsen, L. Hoff, E Fosse, O.J. Elle. Epicardial acceleration measured using a single chip 3-axis accelerometer. NBC 2008, proceedings 20, pp 221-224, 2008.

[9] Desmulliez, M. ; Hoff, L. ; Elle, O.J. ; Fosse, E. Design and fabrication of a minituarized three-axis accelerometer for measuring heart wall motion. Electronics, Circuits and systems, ICECS 2008, pp 194 – 197.
[10] Hoff L., Elle O. J., Grimnes M. J. Et al. (2004) Measurement of heart motion using accelerometers. Proceedings of 26th annual international conference IEEE Eng. In Med. And Biol society 26:2049-2051
[11] Imenes K., Aasmundtveit K., Bjornsen G., Moreno P., et al. Micro ribbon cable bonding for implantable device.(2008) Proceedings of ESTC 2008 conference. 1-4.09.2008. pp 265-270.
[12] Jörg-Uwe Meyer et al., "High Density Interconnects and Flexible Hybrid Assemblies for Active Biomedical Implants", *IEEE Transactions on Advanced Packaging,* Vol. 24, No. 3, August 2001.
[13] S. Kisban et al., "Microprobe Array with Low Impedance Electrodes and Highly Flexible Polyimide Cable for Acute Neural Recording", *Proceedings of the 29th Annual International Conference of the IEEE EMBS Cité Internationale,* Lyon, France August 23-26, 2007.
[14] S. Kisban et al., "Hybrid Microprobes for Chronic Implantation in the Cerebral Cortex ", *30th Annual International IEEE EMBS Conference Vancouver, British Columbia,* Canada, August 20-24, 2008

Author: Fjodors Tjulkins
Institute: Institute of Microsystem Technology
Street: Raveien 197
City: Borre
Country: Norway
Email: ft@hive.no

The Biotelemetry Lessons Innovation – Low Power RF

Martin Cerny[1], Marek Penhaker[1]

[1] VSB – Technical University of Ostrava/ Dept. of Cybernetics and Biomedical Engineering

Abstract— **The biotelemetry lessons are taught at VSB - Technical University Ostrava since 2007. This course is designed for students of bachelor's degree and wants the task is familiar with the possibilities of transmission of biomedical data both wired and wireless communication. Given that the communications are rapidly developing, this subject upgraded with new laboratory tasks. The new one deals about Low Power RF technologies. This laboratory task shows how to use the wireless technology which wasn't designed form biomedical usage into biomedical engineering praxis.**

Keywords— **Low power RF, Biotelemetry, CC1111.**

I. Introduction

The subject biotelemetry is designed as a practical subject for students of bachelor study. The number of hours is 1 hour lecture and two hours of practical exercises per week. In this course, students are acquainted with different methods of data transmission.

The course is divided into ten chapters, which corresponds to the number of lectures per semester. The first four chapters focus on the history of telemetry, an introduction to biosignals measurements, biosignal measurement methods, types of biomedical sensors and standards for the modulation signal. The next chapter discusses the steps of the A / D conversion. Another part of the lecture is devoted to the basics of communication such as serial and parallel data transfer, synchronous and asynchronous data transmission, multiplex, taxonomy networks, network topology and the ISO-OSI model. Other chapters deal with specific technologies and standards for wired and wireless data transfer. Students will learn about the standards RS232, parallel communications, USB, FireWire, Ethernet and GPIB. The wireless technologies are recited mainstream technologies such as Bluetooth, ZigBee, Wi-Fi, GSM and GPRS. Finally, students are familiarized with the possibilities of practical applications and systems, remote home care [2].

Practical laboratory tasks are an important part of the course. Since the beginning of teaching this course are part of the job, dealing with types of signal modulation standards RS232, Bluetooth, ZigBee and wireless transmission of data on the ISM frequencies. Each of the jobs created by the connection uses wireless technology and medical devices or circuits for measurement of biological signals. All proposed and realized instrument is our laboratory of Biomedical Engineering. Most OEM modules are used for the measurement of biological signals such as temperature, blood pressure, ECG and plethysmography. They are also used basic electrical wiring for example, ECG measurements, which were conducted in our laboratory. Wireless communication is realized by commercial wireless modules that can be built into industrial products. On the receiving side (PC) is used the board that students can see real hardware. Although each exercise is focused on other issues, there is a link between exercises within the meaning of the measured and the type of data transmitted - biosignals. Student can identify differences between similar technologies, their range and power consumption. Used equipment is designed for students to understand and secure, but also to resist their unqualified interference [1].

II. Low power RF

Low Power RF technologies are technological solutions for data transfer over short distances with the least energy consumption. They are very useful in applications with data transmission over short distances without the need to transfer larger volumes of data. For typical RF technology is that it can be in sleep mode for 95% of the time. In this mode, consumption is reduced to the minimum possible boundary moving at 0.5 mA. For the transition from sleep mode devices require 300 ms or less. The device consumes less than 16 mA and 20 mA during data transmit. This enables to reduce overall consumption and increase battery life of wireless sensing element. Another trend in the low RF power is also a way of dealing with hardware. Important are hardware solutions that bear the SoC (System on Chip). On one chip thus is a complete solution to the wireless module in the form of a full microprocessor with many peripherals and RF front end.

To familiarize students with these solutions, the role laboratory has been created that uses the CC1111 SoC with an indication from Texas Instruments. The CC111x has been chosen because of it uses other standards than other devices, and its proposed power consumption is very low. The next advantage is the student familiar microprocessor architecture-8051.

Y. Dekhtyar et al. (Eds.): *International Symposium on Biomedical Engineering and Medical Physics*, IFMBE Proceedings 38, pp. 23–25, 2013.
DOI: 10.1007/978-3-642-34197-7_6

CC1111 SoC is low power RF solution with low power consumption in sub-communicating 1 GHz band, designed for low power wireless applications such as home automation and transmission or discontinuous data streams. CC1111 includes a complete RF interface and the standard 8051 microcontroller with up to 32kB Flash memory and up to 4KB of RAM. CC1111 contains in addition to the standard peripherals Full-Speed USB 2.0 interface.

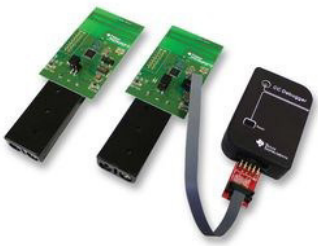

Fig. 1 CC111x Evaluation Kit

RF part is based on CC1101 with a sensitivity of-110 dBm at 1.2 kBaud, programmable data rate up to 500kBaud, programmable output power to 10 dBm for all supported channel frequency. Communication is possible at frequencies from 300 to 348 MHz, 391-464 MHz and 782-928 MHz. Consumption of the device is in RX: 16.2 mA @ 1.2 kBaud, TX: 15.2 mA @ -6 dBm output power. Power consumption in sleep mode 0.3 uA in PM3 (the operating mode lowest power consumption) and 0.5 uA in PM2 (operating mode is the second lowest power consumption when the dog on a timer or external interrupt).

The microprocessor core is built on 8051 by Texas Instruments with DMA. There is 8/16/32 kB in variations in system programmable flash memory and RAM 1/2/4kB. Also includes two USART, one 16-bit timer module with DSM, three 8-bit timers, 7-12bit AD converter with up to eight inputs and Full Speed USB Controller with 1kB FIFO memory. In addition, software Compatible with other chips from Texas Instruments.

Supply voltage is from 2V to 3.6V, dimensions 6 x 6 mm QFN 36 package[3].

III. Laboratory task

There were purchased for a set of development modules and development kits CC111x with CC1111 for the purposes of laboratory tasks. In addition, a laboratory for the realization of the role of biological signal simulator is purchased, a source of test signals in the measurement of biological chain.

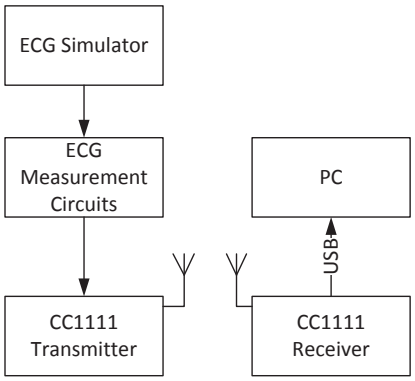

Fig. 2 Measuring Chain

The bioamplifier circuit was designed and implemented, which allows one lead ECG measurement. Bioamplifier is built on Texas Instruments INA126 and OPA2335. Its properties are sufficient to fully purpose laboratory tasks. Supply voltage is 3V, the low drop over stabilizer. The measured signal voltage levels are 0-3V, which can be easily digitized CC1111 modules.

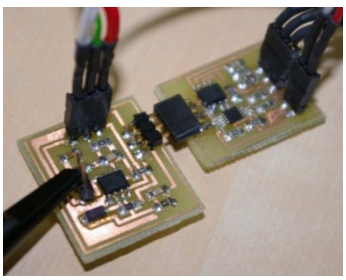

Fig. 3 ECG Bioamplifier

Because this laboratory task is in bachelor study, there were finished the complete procedure, how to work with CC111x modules. From the first initial steps with quick start programs from TI, follows the firs “Hello World” program to the tests of communication establishment. The last part is main program for ECG measurement with CC111x

The step-by-step procedure is provided, how to create new IAR project with specified module. This part is the most appreciated by students, because it helps them to understand to structure of IAR.

There was programmed software program in IAR studio for the purposes of laboratory task. The program allows continuous measurement of signal with selectable sampling frequencies. The program also allows you to set wireless parameters such as transmit power. Two programs were implemented for the broadcast part, one with power management (use of sleep modes) and one without. Students in

the lab can determine what influence the use of sleep modes on overall consumption measuring and transmitting devices. The measuring module is capable of sampling the signal at the input of your A / D converter with adjustable frequency. In the implementation of laboratory tasks, students not only transmit information wirelessly, but also can assess the impact of changes in sampling frequency measurements. He also implemented a simple software configuration for wireless communication between wireless modules. With this program, students can set the communication parameters such as baud rate and transmit power.

To view the data in the PC software was created, which shows the measured data and allows users to save them to text files. The assay procedure of laboratory task is shown in the picture below.

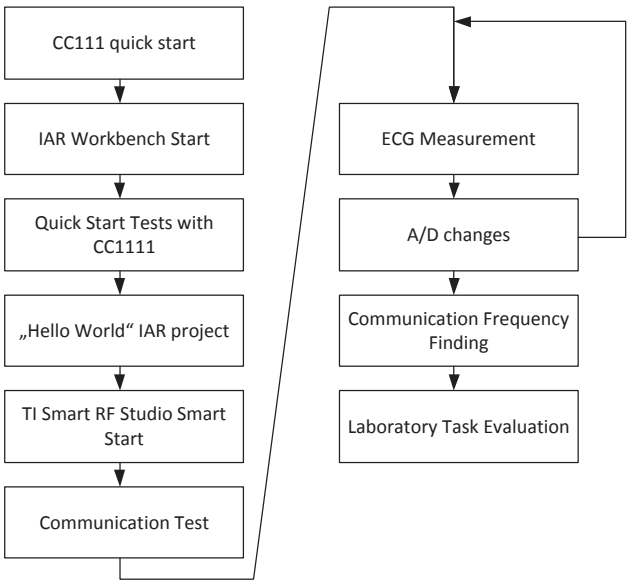

Fig. 4 Laboratory Task Scheme

One important part of this laboratory task is the work with SmartRF studio. This software tool from TI allows students to change parameters of wireless communication easily. After that students can better understand to communication protocols and possibilities of proposed wireless technology.

The changes of A/D parameters supports the orientation of students in the C code for microprocessor, because they need to find the right place for the change inside the commented code. The A/D changes show the consequences of Shannon theorem in praxis.

IV. Conclusion

Although the Biotelemetry lessons are optional part of the study plan, it passes the standard 70% of students in the year of the field of biomedical techniques. The course also enters students of other disciplines, which is offered in this subject the teachers can offer subjects. Innovation labs content of the subject is still relevant and reflects the developments in telecommunications technology and its application in bio-telemetry data. Created laboratory task is ready for were tested and reactions of students are really positive.

Acknowledgment

The work and the contributions were supported by the project SP2012/114 “Biomedical engineering systems VIIII” and TACR TA01010632 “SCADA system for control and measurement of process in real time”. Also supported by project MSM6198910027 Consuming Computer Simulation and Optimization. The paper has been elaborated in the framework of the IT4Innovations Centre of Excellence project, reg. no. CZ.1.05/1.1.00/02.0070 supported by Operational Programme 'Research and Development for Innovations' funded by Structural Funds of the European Union and state budget of the Czech Republic.

References

1. Zhang, G.-Z. Body Sensor Network.(2006) 1.ed.. London: Springer Verlag, 2006. ISBN 978-1-84628-272-0.
2. Cerny, M., Penhaker, M. Biotelemtry.(2008) In 14th Nordic – Baltic Conference on Biomedical Engineering and Medical Physics IFBME, 16.-20.6.2008 Riga, Latvia. Riga: Riga Technical University, 2008. s.118. ISBN 978-9984-32-231-5.
3. CC111x Low-Power SoC (2008) (System-on-Chip) with MCU, Memory, Sub-1 GHz RF Transceiver, and USB Controller[online], 2008 USA :Texas Instruments, id SWRS033G.

Use macro [author address] to enter the address of the corresponding author:

Author: Martin Cerny
Institute: VSB – Technical University of Ostrava
Street: 17. listopadu 15
City: Ostrava
Country: Czech Republic
Email: martin.cerny@vsb.cz

Source Localization Based on Ictal Electroencephalographic Recordings

Narayan Puthanmadam Subramaniyam[1,4], Jukka Peltola[2], Jarno M.A.Tanskanen[1,4], Katrina Wendel-Mitoraj[1,4] Jari Hyttinen[1,4] and Jaakko Malmivuo[3]

[1] Tampere University of Technology/Department of Biomedical Engineering, Tampere, Finland
[2] Tampere University Hospital/Neurology Unit, Tampere, Finland
[3] Tampere University of Technology, Professor Emeritus, Tampere, Finland
[4] BioMediTech, Tampere, Finland

Abstract— **Accurate source localization of the epileptogenic regions require EEG data that reflect only the epileptic activity. Isolating the ictal activity from the other artifacts and normal background activity of the brain is a challenge. In this work we apply independent component analysis to first obtain independent source signals from ictal recordings of one patient having severe seizure. From these independent signals, epileptic source activity was isolated. The isolation was based on the high level of synchronicity between the components using spectral coherence as a measure at ictal-dominant frequencies. EEG data was then reconstructed by only considering the components with high synchrony to reflect the seizure activity. This reconstructed EEG data reflected the ictal patterns more clearly and was used as an input for source localization algorithm. The results indicate the cortical origins of the seizure onset and its further spread. ICA method along with spectral coherence can be used to obtain EEG data relevant only to epileptic activity. The information on the cortical origins of seizure can be further enhanced by using this clean EEG data to perform source localization.**

Keywords— **Epilepsy,ICA,Spectral Coherence, EEG, Source Localization.**

I. Introduction

Epilepsy is a neurological disorder affecting up to 1% of the total world population. It is characterized by seizures that are recurrent in nature [1]. Electroencephalography (EEG) is a very useful diagnostic tool that can reveal characteristic findings of seizure in its recordings [2]. EEG is also non-invasive, cost-effective and a very simple procedure. In patients with intractable epilepsy, resection surgery is a preferred treatment option, requiring localization of epileptogenic regions [3].

Localization of epileptogenic regions using non-invasive EEG data is an inverse problem, which is ill-posed in nature. The sources can be modeled either as single dipole or distributed dipoles. Several methods have been studied and proposed to localize the epileptogenic region using EEG data [4-6]. Physiological and anatomical constraints are needed to achieve a reasonable solution. Due to the ill-posed nature, regularization is often required in such problems. Many methods exist in literature to choose the regularization parameter, with L-curve and generalized cross validation (GCV) method being the most popular.

Independent component analysis (ICA) is a statistical technique that is commonly used in cleaning of EEG data. ICA decomposes a multivariate data into components that are both statistically independent and non-gausssian [7]. ICA has been applied successfully to decompose EEG as well as magnetoencephalography (MEG) data. The basic assumptions made are a) sources are statistically independent b) mixing at the sensors is linear and instantaneous and c) stationarity of mixing and independent components (IC).

Selection of independent components that represent seizure or abnormal brain activity is usually done by visual inspection of their corresponding scalp topographies. This can be a tedious process if there are many independent components. Also it is a highly subjective method prone to human errors. It is generally agreed that synchronization of different brain areas play an important role during seizure onset and its further spread [8, 9]. There appears to be an increase in local synchrony between cortical regions involved in seizure onset. This synchrony is higher than it is for normal and post ictal activity [10]. Based on these assumptions, other automatic methods to select relevant ICs have been proposed, for e.g. using phase locking value which gives the strength of synchronization between signals [11].

In this work, we utilize ictal recordings of a single patient, representing a severe seizure. The ictal period was subjectively identified by trained neurophysiologist. We apply ICA method to decompose the EEG into ICs. Since the ictal EEG has a characteristic pattern and are dominant in certain frequency range [13, 14], we have chosen spectral coherence as a measure of strength of synchronicity as it can be calculated in frequency domain. By measuring the spectral coherence of ICs at ictal-dominant frequency and averaging them, the components relevant to seizures can be automatically selected. By modifying the mixing matrix

Y. Dekhtyar et al. (Eds.): *International Symposium on Biomedical Engineering and Medical Physics*, IFMBE Proceedings 38, pp. 26–30, 2013.
DOI: 10.1007/978-3-642-34197-7_7

(defined in Section II B) the EEG is reconstructed. The reconstructed EEG is then used as an input for the source localization algorithm to determine the regions involved in seizure onset and its spread.

II. Materials and Methods

A. Data and pre-processing

The Video-EEG from one patient was recorded using a 25 electrodes based on 10-20 system. Two zygomaticus electrodes Pg1 and Pg2 were placed on the left and right side respectively. The reference electrode was placed between Pz and Cz. A sampling rate of 256 Hz was used. The recording consists of approximately 4 minutes of EEG data consisting of pre-ictal, ictal and post-ictal segments. The onset of seizure (Approximately from 36 seconds into the recording) was subjectively identified by a trained neurophysiologist from the Tampere University Hospital (TaUH). A bandpass filter (0.1 – 70 Hz) was used to filter the data and the line noise (50 Hz) was removed using a notch filter. The filtered ictal EEG segment lasting from 36 seconds to 76 seconds is shown in Fig 1.

Fig. 1 Ictal EEG beginning at approximately 36 seconds into the recording and ending at 95 seconds (A duration of 40 seconds).

B. Independent Component Analysis

ICA is a computational method which is used to separate multiple mixtures of signals into statistically independent components. A random vector $\mathbf{x} = [\, x_1, x_2, x_3, \ldots, x_m]^T$ is assumed to be a linear combination of components vector $\mathbf{s} = [\, s_1, s_2, s_3, \ldots, s_p]^T$ given by the equation

$$\mathbf{x} = \mathbf{A}\mathbf{s} \tag{1}$$

Where, A is the mixing matrix. ICA aims at finding the de-mixing matrix **W** such that

$$\mathbf{s} = \mathbf{W}\mathbf{x} \tag{2}$$

There are several separation algorithms based on ICA and in this work we have used the FastICA implementation [12].

C. Identification of seizure-related components

After decomposing the EEG data into independent components, only those components were selected that were responsible for seizure generation, thus excluding the background activity and artifacts. This was done by computing the spectral coherence in frequency domain through the Fast Fourier Transformation (FFT) between every pair of independent components.

The spectral coherence between two signals x and y is given by

$$C_{xy} = \frac{|S_{xy}(f)|^2}{S_{xx}(f)S_{yy}(f)} \tag{3}$$

Where $S_{xy}(f)$ is cross spectrum between the signals x and y at a particular frequency f. $S_{xx}(f)$ and $S_{yy}(f)$ are the auto power spectra at a particular frequency f. A hanning window of 1 second with 20% overlap was used. The spectral resolution was fixed at 0.5 Hz. The spectral coherence was calculated at the frequency range of 3.5 – 10 Hz, which mainly corresponds to ictal EEG activity [13, 14].

The computed spectral coherence in the mentioned frequency range was averaged for each component pair. The independent components with highest spectral coherence meant a high level of synchronicity between the components. These components are likely to be relevant to the epileptic activity. The columns of the mixing matrix **A** corresponding to these components are retained, setting the rest to zero and the EEG is reconstructed according to equation (1).

D. Volume conductor model

We constructed an average head model using the boundary element method (BEM) implementation in freely distributed MATLAB package software BrainStorm [15]. The Montreal Neurological Imaging (MNI) template in BrainStorm was used for this purpose. The BEM head model consisted of sub-regions like scalp, outer-skull, inner-skull and brain. Each region was assigned a constant conductivity. The method transforms field equation (Poisson's equation) to surface integral equation. The electrodes were warped on the scalp surface of the model as seen in Fig 2.

E. Source Localization

Using the reconstructed EEG signals, the cortical activity was reconstructed by solving the EEG inverse problem. The

relationship between the source activity and the EEG data can be expressed by the linear equation [16],

$$\mathbf{d} = \mathbf{Lj} + \mathbf{n} \tag{4}$$

Where, **d** is the measured EEG activity, **j** is the cortical source activity and **L** is the so called lead-field matrix that represents the relationship between the source and sensor (EEG) activity. Every j^{th} column of the lead-field matrix describes the potential distribution across all the scalp electrodes and generated by a j^{th} unit dipole. The estimated solution to the cortical activity is given by

$$\tilde{\mathbf{j}} = \arg min \left(\|\mathbf{d} - \mathbf{Lj}\|_p^s + \alpha \|\mathbf{Mj}\|_p^s \right) \tag{5}$$

Where s and p are the order of the norm. The matrix **M** is known as the compatible matrix and the parameter α is known as the regularization parameter. The equation (5) reduces to the standard Tikhonov regularization [17] when **M** is chosen to be identity matrix with s and p equal to 2. The standard solution to the equation of Tikhonov regularization is given as

$$\tilde{\mathbf{j}} = (\mathbf{L^T L})^{-1} \mathbf{L^T d} \tag{6}$$

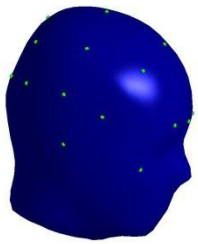

Fig. 2 Electrodes on the scalp surface including two zygomaticus electrodes according to 10/20 system

Another relationship between true and estimated current sources can be given as [16]

$$\tilde{\mathbf{j}} = \mathbf{Gd} = \mathbf{GLj} = \mathbf{Rj} \tag{7}$$

Where, **R** is the resolution matrix. By applying the inverse operator **G** to the signal covariance matrix **C**, the cortical current strength at every location can be divided by the noise at that location. This approach is known as dynamic Statistical Parametric Mapping (dSPM) and is explained in more detail elsewhere [16]. These equations were implemented in BrainStorm [15] toolbox to estimate the cortical current strength from EEG data.

III. Results

The independent components of the ictal EEG segment are shown in the Fig 3. The frequency-averaged spectral coherence matrix is shown in Fig 4. The variation in the coherence values for each channel pair is color-coded.

It can be seen from the Fig 4 that there are high levels of synchronicity are seen between components 19 and 18, 23 and 13. Retaining the columns corresponding to these components in mixing matrix and setting the rest to zero, EEG data is reconstructed which is shown in Fig 6. It can be seen from Fig 5 that the ictal patterns are more clearly evident when compared to the ictal EEG data in Fig 1.

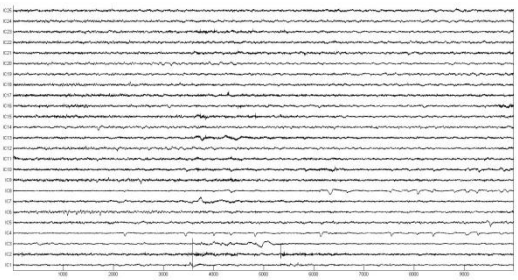

Fig. 3 Independent components obtained using after applying ICA decomposition to ictal segment of EEG data.

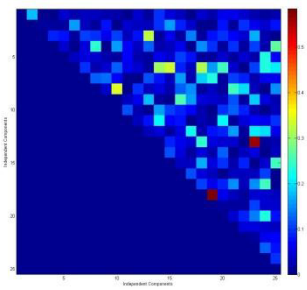

Fig. 4 Frequency-averaged spectral coherence matrix between every IC pair. The color variation from red to blue represents maximum to minimum synchronicity.

Source localization is performed on the reconstructed EEG using dynamic statistical parametric method (dSPM) implemented in BrainStorm [15]. The cortical origins of the seizure onset, its bilateral spread and finally a left discharge are shown in Fig. 6. Only the regions with cortical strength which is greater than or at least 70 % the maximum value

are highlighted in Fig 6. Based on the inputs by the neurophysiologist, three time points were selected pertaining to seizure onset, mid-ictal period (where bilateral spreading is seen) and left discharge, after which there was no further temporal evolution of the seizure.

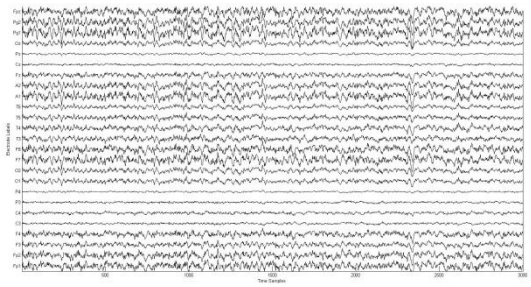

Fig. 5 Reconstructed EEG data after modifying the mixing matrix based on level on synchronicity between ICs

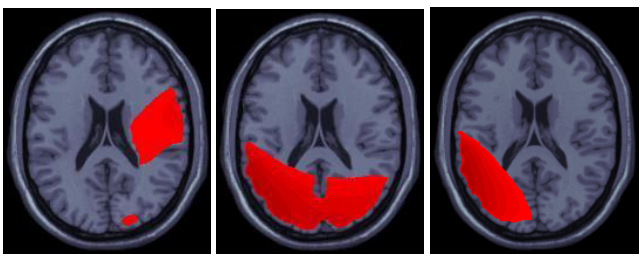

Fig. 6 From left to right – Seizure onset, bilateral spreading and final left discharge. The orientation of the axial slice is (L-R).

IV. Discussion and Conclusion

In this work we have demonstrated that by using ICA along with spectral coherence the components relevant to epileptic activity can be isolated. Further it was demonstrated that, by reconstructing the EEG using only the relevant independent components, cortical origins of seizure activity can be extracted by source localization.

Increase in local synchrony during epileptic seizure onset is not uncommon. Previous research work has supported this hypothesis [8-10]. Also studies have shown that, before the onset of seizure, other areas detach themselves from the cortical areas involved in seizure as result of which, during the seizure onset these areas become isolated and in synchrony. The phase coherence between the cortical areas has also been found to decrease in the post-ictal period.

In future, we will explore the possibilities of applying similar measures on the estimated cortical current data from pre-ictal, ictal and post-ictal period to derive functional networks and their connectivity during these periods. This will give an insight on how some cortical areas are detached before seizure onset and how other areas recruited during seizure onset.

Acknowledgment

The work is supported by the International Graduate School for Biomedical Engineering and Medical Physics (iBioMEP), Oulu, Finland and Department of Biomedical Engineering, Tampere University of Technology, Tampere, Finland. Special thanks to the EEG staff at Tampere University Hospital for providing and segmenting the EEG data.

References

1. Hauser W.A., Kurland L.T. (1975) The Epidemiology of Epilepsy in Rochester, Minnesota, 1935 Through 1967. Epilepsia , 16, pp. 1–66
2. Noachtar S, Remi J (2009) The role of EEG in epilepsy: A critical review. Epilepsy & Behaviour 15, 22-33
3. Stern Y, Neufeld M, Kipervasser S, Zilberstein A, Fried I, Teicher M, Adi-Jhapa E (2009) Source Localization of Temporal Lobe Epilepsy Using PCA-LORETA Analysis on Ictal EEG Recordings. J Clin Neurophysiol. 26:109-116
4. Michel C.M., Lantz G, Laurent S, Grave de Peralta R., Landis T, Seeck M (2004) 128-Channel EEG Source Imaging in Epilepsy: Clinical Yield and Localization Precision. J Clin Neurophsiol 21:71-83
5. Plummer C, Harvery S.A., Cook M (2007) EEG Source Localization in focal epilepsy: Where are we now? Epilepsia, 49: 201–218
6. Lantz G, Grave de Peralta R, Spinelli L, Seeck M, Michel CM (2003) Epileptic source localization with high density EEG: how many electrodes are needed? Clinical Neurophysiology 114:63-69
7. Hyvärinen A, Karhunen J, Oja E (2001) *Independent Component Analysis*. Wiley Interscience, 481 pages.
8. Mormann F, Lehnertz K, David P, Elger CE (2000) Mean phase coherence as a measure of phase synchronization and its application to the EEG of epilepsy patients. Physica D 114,pp.358-369
9. Dominguez LG, Wennberg RA, Gaetz W, Cheyne D, Snead OC, Velazquez PLJ (2005). Enhanced Synchrony in Epileptoform Activity? Local Versus Distant Phase Synchronization in Generalized Seizures. J. Neurosci, 25(35) :8077.8084
10. Van Quyen M Le (2005) Anticipating epileptic seizures: from mathematics to clinical applications. C R Biol 328(2) 187:198
11. James CJ, Gupta D (2009) Seizure Prediction for Epilepsy using a Multi-Stage Phase Synchrony based System. Engineering in Medicine and Biology Society, Annual International Conference of IEEE,pp.25-28
12. Hyvärinen A, Oja E (200) Independent Component Analysis. Neural Networks 13(4-5):411-430
13. Darcey TM, Williamson PD (1985). Spatio-temporal EEG measures and their application to human intracranially recorded epileptic seizures. Electroenceph Clin Neurophysiol 61:573-87
14. Quian Quiroga R, Blanco S, Rosso OA, Garcia H, Rabinowicz A (1997) Searching for hidden information with gabor transform in Generalized Tonic Clonic Seizure. Electroenceph Clin Neurophysiol 103:434-9

15. Tadel F, Balliet S, Moscher JC, Pantazis D, Leahy M (2011) Brainstorm : A User Friendly Application for EEG/MEG Analysis. Computational Intelligence and Neuroscience. vol. 2011, Article ID 879716, 13 pages . doi:10.1155/2011/879716
16. Hauk O, Wakeman DG, Henson R (2011) Comparison of noise normalised minimum norm estimates for MEG analysis using multiple resolution metrics. Neuroimage 54:1966-1974
17. Tikhonov AN (1963) Solution of incorrectly formulated problems and regularization method. Soviet Math. Dokl:pp 1035-1038. English translation of Dokl Akad Nauk SSSR 151:501-504

Author: Narayan Puthanmadam Subramaniyam
Institute: Department of Biomedical Engineering / BioMediTech
Street: Biokatu 6
City: Tampere
Country: Finland
Email: narayan.ps@tut.fi

Development of New Mobile Telemedicine Screening Complex

Z. Markovitch[1], J. Lauznis[1], G. Balodis[1], A. Katashev[2], and I. Markovitcha[1]

[1] Riga Technical University/ Faculty of Computer Science and Information Technology, Riga, Latvia
[2] Riga Technical University/ Faculty of Mechanics and Engineering, Institute of Biomedicine and Nanotechnologies, Riga, Latvia

Abstract — **Public health is one of key priorities of any European Union country. It is necessary to do research work for development of new set of mobile, portable medical device complex for preventive examinations which could be effectively used by family doctors, at schools for children's health tests, sports medicine needs or even at work and at home.**

Team of authors in frames of ERDF supported project is working on development of new portable telemedicine preventive health care device complex. The new device complex will include equipment for testing vision, hearing, blood pressure, spirometry, pulse oximetry, digital thermometry, digital phonendoscopy, electrocardiogram, anthropometric measurements, urine and blood analysis and will include interactive diagnostic questionnaire. The system will consist of 2 parts – the mobile diagnostics part which takes examinations of patient and analysis center part with specialists which makes diagnosis based on those examinations.

The new product will make preventive health diagnostic more accessible to wide range of potential patients. It will save time and costs associated with taking tests for preventive diagnostics.

Keywords — **Telemedicine, mobile, screening, diagnostics, e-health.**

I. Introduction

Public health is one of key priorities of any European Union country, including Latvia, (the EU Charter of Fundamental Rights Section 35 provides that every person has a right to preventive health care and medical treatment). This means not only high quality and high levels of treatment of diseases, but also the timely diagnosis and prevention.

An important role here is regular preventive examinations that can be taken by the family doctor, if he is provided with the necessary medical technologies. Currently investigations and analysis are usually carried out by health care institutions, because only in very rare cases, family doctor has the necessary diagnostic equipment and skills of evaluation of the information obtained in the investigations. Often the tests are carried out at different times and in institutions, which may be located a considerable distance from the residence of the person under investigation. Thus additional time and resources of the patient and the employer is being spent time on the way to examination centers and waiting for the results as well as for re-appointment with the doctors for collection and assessment (by the Central Statistical Bureau data on the reasons that prevented consulting with specialist doctors, 23.7% respondents indicated that they could not afford it, 23.6% of respondents wanted to wait, because maybe the problem will disappear by itself, while 19.4% of respondents could not find time [1]).

That is why many people refuse to seek further but necessary tests before any diagnosis of illness or refuse to perform tests because of the above mentioned financial and time delays. This in turn causes direct damage to the country, in both cases declining GDP and tax payments, increasing the potential for sickness and disability payments. Moreover, from the direct and indirect losses if the person neglected diseases, dies.

II. The Aim of the Project

To solve the above-defined problem, it is necessary to develop a new mobile telemedicine screening complex (MTSK) with analysis and advice center software, which will eliminate the existing system deficiencies and will be substantially better than existing systems.

It is necessary to do research work for development new set of mobile, portable medical device complex for preventive examinations, which would be significantly better from a functional, user-friendliness and cost point of view, compared to the existing prototypes, and could be effectively used by family doctor's, at schools for children's health tests, sports medicine needs including competitions, or even at work and at home, as well as analytical and advisory center(s) for competent interpretation of and responses by use of modern data communication technologies (Internet, mobile communications), as well as geographical location determination and communication.

Development of new mobile telemedicine screening complex and consultancy center software:

1. A hardware and software necessary for recording and analysis of 10-14 parameters, thereby increasing the effectiveness of complex diagnostic. Reduce the prototypical size, weight and power consumption, in line with the concept of portable devices. Therefore, the essential investigations could be performed at the family doctor's office, at home, at school or even at work. Reducing equipment

Y. Dekhtyar et al. (Eds.): *International Symposium on Biomedical Engineering and Medical Physics*, IFMBE Proceedings 38, pp. 31–34, 2013.
DOI: 10.1007/978-3-642-34197-7_8

manufacturing and maintenance costs will decrease the price of services.

2. Establish the necessary subjective level of information and extracting form (Diagnostic Questionnaire), which form a further examination needs for a given patient. Therefore, in the project it is necessary to study the questionnaires optimal size and structure for obtaining and processing information in a small (short) time interval.

3. A method of optimal allocation of resources between MTSK and Analysis Center should be found. The study would answer what software resources are to be deployed on "local" computer so that in the event of limited communication and Internet access it will give some diagnostics, and in what way information transfer and analysis to the center will take place for the assessment and decision making. There should possibility to supplement the system with new functions and to reconcile with other systems of information exchange level, like state telemedicine and e-health agencies. Similarly, the system must have increased security to meet the internationally recommended standards for the exchange of medical information and patient data protection, telemedicine and e-health. Study needs to be done for the best auto-positioning and communications applications from the side of the analysis center, to permit the use of a complex emergency service or rescue missions.

III. Research to be carried out in the project

The project complies with the industrial research, as in all the planned new product development phases are foreseen that the activities and sub-activity consists of research and analysis aimed at obtaining new knowledge and techniques which will be used in the development of new product's hardware components and software creation and product development as a whole.

The optimal technical solution development for registration of at least 6 subsequent physiological parameters, will be realized as modular or single box pilot sample device, based on newest technologies in field:

- Electrocardiogram (ECG);
- Spirometry (Spiro);
- Pulse oximetry (SpO2);
- Blood pressure, registration using non invasive method (NIBP) [6, 7, 8];
- Digital thermometry (contact or contactless measurement of body temperature);
- Digital phonendoscopy (heart and lung-tone registration);

Industrial research of MTSK modules is based on team previous experience in local and international projects [2, 3, 4, 5, 6, 9, 10].

In addition to mentioned above, extended research to include new features in MTSK is provided, as follows:

- Methodology and the optimal solution for computer based vision and hearing test, including hardware.
- Development of new anthropometric data recording system includes set of parameters for selected detection system. System operation is based on the anatomical point recognition in real time from patient's picture. The system will replace the current physician held sliding calipers and measuring tapes. In research work necessary algorithms will be developed, which will become the basis for system performance, and algorithm-based measurement error will be evaluated.
- Exploring the possibility of setting up simplified strip express analysis module. Possibility of using commercially available camcorders will be analyzed for the purpose of express analysis of stripes, or simple, special-design creation. During the research will be looking for correct stripe lighting conditions and also video camera or sensor type selection will be carried out, in order to get the system which allows quantitative urine (at least 10 parameters) and blood (at least 2 parameters) analysis of the strip.
- Analysis of the feasibility of adding dermascope module. Possibility of using commercially available video cameras for dermascopy will be analyzed. Similar as in the preceding paragraph, lighting options (with different spectrum) will be analyzed in order to allow the skin formation macro photography regardless of external lighting conditions.
- Fat-muscle ratio measurement method development by means of complex impedance measurement method or another. Will study the possibility to combine it with a physiological recorder module is being developed.
- Design of optimal solution for data transfer and location module. Automatic registration of system's location and on-demand transfer of information obtained using wireless technology. Latest technology available will be explored and optimal system performance algorithms will be designed.
- Study for MTSK interactive diagnostic questionnaire design. The study will establish the optimal size and structure of the questionnaire; the evaluation algorithm will be developed to process information in a short time interval, and analysis and testing of the questionnaire and algorithm will be performed.
- Study for development of MTSK data acquisition and analysis software. In the study effective information exchange schemes, technical solution designs and software for optimal allocation of resources between the complexes and analysis center will be developed. As

well as the principles of the system of cooperation with other information sources and databases, in the framework of e-health concept, as well as a study for the best auto-positioning and communications applications from the side of the analysis center, which would allow complexes to be used in the emergency service or rescue missions.

System overall schematic and information flow is shown below in Fig.1.

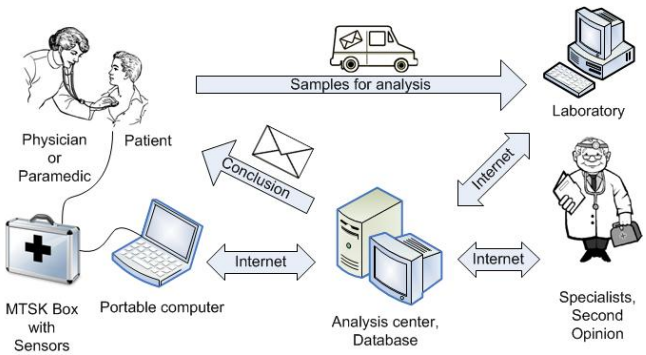

Fig. 1 MTSK overall schematic and information flow.

IV. Results

MTSK Module research and development and experimental design is generally finished and includes modular design in level of tested schematics to record ECG, spirometry, audiometry, NiBP and SpO2. Last two are based on OEM modules, being adapted in software level to fit general concept and data exchange protocols. This research includes also wireless data transmission options and methods to provide data integrity and safety.

Methodology for computerized vision and hearing testing is realized for vision test as software for Windows based computers providing it by means Landolt C ring method (standard ISO 8596:1994, [11]), originally adapted to fit PC screen size, resolution and distance to test person. Additionaly, color vision tests are added, if in patriciular cases they may have important impact on individual behavior (some professions) and to prevent potential accidents in case if it fails.

Hearing test hardvare is completed up to schematics, taking into account software to be developed.

MTSK data acquisition and analysis software is completed in the level of information exchange protocol development between components of system, data base structure, its design rules and test software for concept approval.

MTSK interactive diagnostic questionnaire is developed in the concept and algorithm level, and some samples (for differential diagnostics) or particular cases for diagnosis, as for tachyarrhythmia, elderly people, heart (mal)failure; still real software is under development and tests.

Development of basics of new anthropometric data recording system has almost finished its research and experimental test phase, results are promising, as acceptable algorithms for compensation of distortions from low-cost cameras are found (relatively acceptable, in max, deviation complies with standard requirements), but research will continue.

Research work is not finished (ends, according to plan in 12.2013), and presented are only preliminary results up to day.

V. Conclusions

The results of the research when finished and system pilot sample may be used to develop industrial model of MTSK. In this case a new product will be offered, being significantly advanced and more economical in use, compared to those currently in the market. Similarly, if the main concept of the project is lead to market, this product will offer new opportunities to telemedicine service, being better compared to the currently available.

This will tap new markets or increase existing market share because today there is no equipment provided with the planned new parameters in the market and the functionality of the system as a whole. Consequently, the potential Latvian producer has the opportunity to fill the empty market share.

Quality of goods or services will improve because the study of MTSK development plans not only to increase the number of recorded parameters, but also increase the quality of usage. This is resulting from the research of new and innovative solutions and information obtained in the analysis and interpretation of the project.

Acknowledgment

Project is supported and financed thanks to European Regional Development Fund, agreement Nr: 2011/0007/2DP/2.1.1.1.0/10/APIA/VIAA/008

References

1. Central Statistical Office at http://www.csb.gov.lv/csp/events/?mode=arh&period=11.2009&cc_cat=471&id=10914 #Central Statistical Office
2. Korsakas S, Vainoras A, Lauznis J, Markovitcs Z, Gargasas L, Markovitc I, Poderys J, Jurkonis V, Ruseckas R, Miskinis V, Juodenas G, Balodis G, Strelcs V. The Human Health Wireless Monitoring and Warning System. Proceedings of conf. “Biomedical Engineering”, Kaunas University of Technology, Kaunas, Lithuania, 2007, pp. 236 – 239.

3. Korsakas S, Vainoras A, Lauznis J, Markovitch Z, Gargasas L, Markovitcha I, Poderys J, Jurkonis V, Ruseckas R, Miskinis V, Juodenas G, Balodis G, Strelcs V. The Remote Mobile Monitoring System for Patients with Cardiac Risk. Proceedings of conf. "Biomedical Engineering", Kaunas University of Technology, Kaunas, Lithuania, 2006, pp. 123 – 126.
4. Balodis G, Lauznis J, Markovitch Z. Real Time ECG Transmission Using Wireless LAN. Proceedings of conf. „Applied Information and Communication Technologies", Latvia University of Agriculture, Jelgava, Latvia, 2008, pp. 106 – 109.
5. Balodis G, Lauznis J, Markovitch Z. Use of Mobile Phone for Transmitting Electrocardiogram in Real Time, Proceedings of Biomedical Engineering, Kaunas, Lithuania, 2008, pp. 97–100.
6. Balodis G, Markovitch Z, Lauznis J, Development of online blood pressure monitoring system using wireless mobile technologies. Proceedings of conf. "Biomedical Engineering", Kaunas University of Technology, Kaunas, Lithuania, 2009, pp. 190 – 193.
7. Ruxer J., Mozdzan M., Baranski M., Wozniak-Sosnowska U., Markuszewski L. "White coat hypertension" in type 2 diabetic patients, Arch. Med. Wewn. Poland, 2007, pp. 452.-455.
8. Myers MG. Ambulatory blood pressure monitoring for routine clinical practice, Hypertension, USA, 2005, pp. 483.-484.
9. Balodis G, Lauznis J. Development of wireless ECG recorder based on Bluetooth technology. Proceedings of conf. „Advanced Engineering Design", Prague, Czech Republic, 2006, pp. 80 – 85.
10. Shuvalova L, Lauznis J, Katashev A, Katasheva J and Markovicha I. (2007) Impact of Bluetooth Technology on Registration of Electrocardiograms. Proceedings of conf. Biomedical Engineering. Kaunas University of Technology, pp. 257-260.
11. ISO 8596:1994 Ophthalmic optics – Visual acuity testing – Standard optotype and its presentation.

Author: Z. Markovitch
Institute: Riga Technical University, Faculty of Computer Science and Information Technology
Street: Meza str. 1/3
City: Riga
Country: Latvia
Email: zigurds.markovics@rtu.lv

The System Designed for Elderly Vital Signals Monitoring

A. Vainoras[1], L. Gargasas[1], L. Bikulciene[1,2], V. Jurkonis[1], and R. Ruseckas[1]

[1] Institute of Cardiology, Lithuanian University of Health Sciences, Kaunas, Lithuania
[2] Department of Applied Mathematics, Kaunas University of Technology, Kaunas, Lithuania

Abstract — **The main aim of this work was developing the hardware and software of system for simultaneously recording and on-line analysis of physiological and biomechanical processes: three ECG leads, two oxygen saturation and three accelerometer signals. The developed algorithms allow input signals pre-processing, recognition of ECG waves, measurement of ECG parameters, calculates oxygen saturation values and evaluates patient activity from the accelerometer signals in real time. The decision about patient state changes from the calculated parameters is made using the convolution of Mealy and Moore automata. In case of appearance of dangerous situation pocket computer sends the alarm signal to patient and analysis results to physician server. Decision making about person functional state will be performed by principles which are based on methodology of distributed intellect. Physician computer makes more detailed analysis of person functional state off-line by using multi-stage non-linear analysis methods and evaluation of complexity changes as measure of human organism status. The developed mobile patient recorder and software were tested by voluntary elderly patients. The exceptional feature of developed data monitoring system is analysis of multi processes in some functional connections of investigated persons. Integrated assessment of person functional state is adapted for user requirements in individual level. If patient is in danger situation or needs external help, the data could be sent to medical service center.**

Keywords — **monitoring system, ECG, complex systems, Mealy and Moore automaton.**

I. Introduction

Recent advances in medical information technologies as well as technological advances in wireless networking, microelectronics, sensors, and the Internet allow us to change the way health care services are deployed and delivered [1]. Focus on prevention and early detection of disease or optimal maintenance of chronic conditions promise to augmented existing health care systems that are mostly structured and optimized for reacting to crisis and managing illness [2-7]. In these latter years more and more studies showed credibly that during obsolescence processes the complexity of functional state decreases, and herewith the person potential of adaptation decreases also [8]. Therefore the development and adaptation for use in practice of new methods for evaluation of complexity was one of aim of this work. It is likely that early assessment of complexity changes will enable to start earlier usage of preventive means with intention to preclude the manifestation of various disorders in human organism. Another possibility for performing of preventive task could be estimation of values of individual physical activity, necessary for every person and their use in practice with aim to decrease the level contrary – having too small physical activity and of risk for overdose of physical activity, and on the ineffective impact on person's health. This prospective method designed for safety of elderly at home is a new diagnostic technology, and development of this technology is one of ITEA2 08018 GUARANTEE project goals [9].

II. Materials and Methods

Architecture of system. The system consists of three levels: the lowest level encompasses a mobile patient recorder (MPR), the second level is the personal server, and the third level encompasses a network of remote server for medical experts. The MPR consists of intelligent sensors for simultaneously recording and wireless transmission of three ECG leads, three accelerometer signals (ACS), one plethysmogram (PPG) and oxygen saturation (SpO2) channel. The personal server is Internet enabled digital assistant (PDA) with real time data analysis software. The remote server is network with personal computers (PC), off-line data analysis software and data base.

The architecture of human monitoring and analysis system is presented in Figure 1.

Fig. 1 Architecture of system.

Y. Dekhtyar et al. (Eds.): *International Symposium on Biomedical Engineering and Medical Physics*, IFMBE Proceedings 38, pp. 35–38, 2013.
DOI: 10.1007/978-3-642-34197-7_9

Algorithms. The ECG analysis algorithm consists of complexes identification, parameters measurement and classification of ECG complexes. Requirements for long ECG recordings recognition algorithms are: adaptation to a wide QRS complex amplitude change, adaptation to a wide variation of RR intervals, adaptation to various signal quality, elimination of artifacts.

In order to avoid the wide QRS complex amplitude and RR interval variations, the QRS wave detection algorithm to ECG record of 10 seconds duration was applied. First, noise levels in the three channels are defined. The channels, whose noise level does not exceed the noise level of the threshold, other were filtrated by digital filter. Next, the detection procedure of QRS wave point-by-point to entire ECG record was applied to determine begin and end of wave strips.

ECG waves and complexes (P, QRS, ST-T) recognition method is based on a scalar function $T(t)$ and consists of a vector signal $W = Y_k(t)$, where k – number of simultaneous ECG channels. The transformation $T(t)$ is multiphase function nearly to zero in the ECG isoelectric line and significantly different from zero in parts of the ECG complexes. The function $T(t)$ is normalized according to the amplitude. In order to improve resistance to noise, the function $T(t)$ is additionally filtered with the moving average filter. Then the detection of function $T(t)$ sections performed, with assumed existence of QRS complexes. The logical algorithm combines these segments into a single segment – called „QRS“ section, separates it in the different parts and excludes false T waves in QRS complexes. Segments, where the fixed ends of the T wave were determined, are evaluated by Bazett's formula:

$$QTc = \frac{QT}{\sqrt{RR}}. \quad (1)$$

T-wave end is determinate in the next stage. P wave of ECG is searched only in cardio cycles in which the QRS complex was identified.

All measured parameters can be divided into amplitude parameters (P, Q, R, S, T wave abnormalities from isoline) and temporal parameters (wave length in milliseconds: the total length of the QRS complex, the electrical negativity DAV time, P-Q interval, Q-T interval and RR interval).

Decision-making about person functional state is performed by principles which are based on methodology of distributed intellect. First of all the above-mentioned on-line analysis of processes is made, and subject to its results (dangerous status) more detailed analysis of person functional state are performed off-line by using multi-stage nonlinear analysis methods and evaluation of complexity changes as measure of human organism status. The primary task of this work was developing on-line data ECG analysis algorithms and software.

Fig. 2 Example of decision making.

The criteria of ECG parameters for elderly functional state evaluation are rule based and depend on individual elderly vital signs values. The monitoring system makes a main decision about patient state changes from the calculated parameters by using convolution of Moore and Mealy automata [10]. According to received analysis results the software forms warning signals (green, yellow, red) to patient. In case of appearances of dangerous situation for patient, the software sends the results of analysis to physician. The example of decision making and signal sample is presented in Figure 2.

III. Results

Biomechanical and physiological signal acquiring device allows recording simultaneously three ECG leads, three accelerometers and two oxygen saturation channels. Low power three channel ECG amplifier is built using INA333 Micro-Power (50mkA), zero-drift, rail-to-rail output instrumentation amplifier produced by Texas Instruments. This instrumentation amplifier has RFI filtered inputs with very high input impedance, which typically is about 100GΩ. Baseline reference is regulated from microcontroller by using cheap 4 channel digital to analog converter DAC104S085. Analog signals are sampled by 4-channel, ultra low noise, 24-bit sigma-delta analog to digital converter (ADC) AD7193 from Analog Devices. Main microcontroller

is MSP430F5438, which at regular time intervals (500 samples/second) samples incoming signals and preprocesses acquired signals. Photoplethysmography signal is acquired using PureSAT 8000R reflectance sensor and NONIN OEM III module for signal preprocessing. Biomechanical data, acceleration in X, Y, Z axes, are measured by digital accelerometer ADXL346 (Analog Devices Inc.). Accelerometer is mounted inside logger unit and has programmable sensitivity ranges from *2g* up to *16g*, thus allowing wide range of movement to be recorded without disruption. As of now, acceleration sensitivity range is selected manually, but it should be possible to select it automatically with the intelligent preprocessing inside firmware. Gathered data is being accumulated into internal buffers while its size achieves page size in MicroSD card storage. Then the data buffers are transferred to MicroSD card file system and / or transferred by Bluetooth wireless link to PDA or PC for analysis. MicroSD card capacity is 1GB, however any standard card with FAT32 file system is suitable.

Fig. 3 PDA setup screenshot.

Bluetooth module is BlueMod+P25/G2 class 2, Bluetooth v2.0+EDR made by Stollmann E+V GmbH. This module is able to communicate via Health Device Profile (HDP) thus it fits medical devices category. Powerful and lightweight Li-ion battery allows long time recording, minimum expected time for real time data acquisition is 24 hours. Charging of battery is accomplished by using MCP73832. It is simple Li-ion battery charger, which allows recharging of the battery by plugging device to standard USB port or wide range of mobile chargers with MiniUSB connector.

The mobile patient recorder was tested by elderly volunteers. Algorithms were developed by Microsoft Visual Studio 2008 Professional Edition. Operating system – Windows Mobile 6.5. The experimental program was developed for algorithm verification and correction in Windows 32-bit environment using the Borland compiler. PDA setup screenshot analysis is presented in Figure 3 as well as PDA results analysis screenshot is presented in Figure 4.

Description of Figure 3: **100 Hz** - high frequency filter on/off, **Reject 50 Hz** - reject filter on/off, **Drift remove** - isoline drift filter on/off, **50 Hz** – 50 Hz high frequency filter on/off, **ST after S** - point position after S [ms], **P before R** - P point position before R [ms], **ST Limit** - allowable ST shift limit [mV], **HR max** - allowable Heart Rate max [1/min], **Cancel** – discard changes, **Save OK** – accept changes.

Fig. 4 PDA results screenshot.

Description of Figure 4: **dHR** – Heart Rate deviation, **dDQRS** – deviation of QRS complex duration, **dST** – ST segment deviation, **dSPO** – deviation of SPO2, **dACS** – deviation of ACS. Red color – danger, Blue color – warning, Green color – OK. By moving slider bar we can see any recorded time point. OK button for exit from there.

IV. Conclusions

The presented work reflects three main results: developed hardware of monitoring system, proposed data analysis, with decision algorithms and developed software.

The developed hardware of monitoring system consists of intelligent sensors for synchronous acquisition and wireless transmission of three ECG leads, three axes accelerometer, plethysmography and oxygen saturation data channels.

The new feature of developed human data monitoring system is capability to analyse multi processes in some functional connections of investigated persons. Integrated assessment of person functional state is adapted for user requirements in individual level. If patient is in danger or needs external help, the data could be sent to medical service center.

Acknowledgment

This study was supported by Agency for International Science and Technology Development Programs in Lithuania, project ITEA2 08018 GUARANTEE.

References

1. Drew B. J., Califf R. M., Funk M. et al. (2004) Practice Standards for Electrocardiographic Monitoring in Hospital Settings. Circulation 2004; 110: 2721-2746.
2. Pinna G. D., Maestri R., Johnson P. et al. (2005) Long-term Home Telemonitoring of Vital Signs and Cardiorespiratory Signals in Chronic Heart Failure Patients: the Challenge of the HHH Project. Folia Cardiologica 2005; 12, Suppl. D:338-345.
3. Braga F., Forlani C., Signorini M. G. (2005) A Knowledge Based Home Monitoring System for Management and Rehabilitation of Cardiovascular Patients. Computers in Cardiology; 32: 41-44.
4. Dranca L., Goni A., Rodriguez J., Burgos A., Illarramendi A. An On-Line Ischemia Monitoring Algorithm for Mobile Devices. Computers in Cardiology 2005; 32: 861-864.
5. Otto Ch., Milenkovič A., Sanders C., Jovanov E. (2006) System Architecture of a Wireless Body Area Sensor Network for Ubiquitous Health Monitoring. Journal of Mobile Multimedia;1(4):307-326.
6. Zheng J. W., Zhang Z. B., Wu T. H. and Zhang Y., (2007) A wearable mobilhealth care system supporting real-time diagnosis and alarm. Medical & Biological Engineering & Computing; 45: 240-255.
7. Lobodzinski S. S., Laks M. M. (2008) Comfortable textile-based electrocardiogram systems for very long-term monitoring. Cardiology Journal 2008; 15: 477-480.
8. Science of the Heart, at http://www.heartmath.org/ - Institute of HeartMath.
9. A Guardian Angel for the Extended Home Environment.. http://www.itea2.org/project/index/view/?project=1140
10. .Sliupaitė, Z.Navickas, L.Gargasas (2006). Data stream control in e-medicine using the convolution of Meally and Moore automata". Biomedical engineering: proceedings of the conference. Kaunas: Technologija, p. 288-293.

Author: Liepa Bikulciene
Institute: Institute of Cardiology of Lithuanian University of Health Sciences
Street: Sukileliu av. 17
City: Kaunas
Country: Lithuania
Email: Liepa.bikulciene@ktu.lt

Pilot Clinical Study of Novel Ultrasonic Hydration Monitor for Infants

A. Tatarinov[1], N. Sarvazyan[1], D. Gardovska[2], L. Eihvalde[2], and I. Kreicberga[3]

[1] Artann Laboratories, Trenton, NJ, USA
[2] Children Clinical University Hospital, Pediatric Department, Riga, Latvia
[3] Riga City Maternity Hospital, Riga, Latvia

Abstract — **Findings from a pilot clinical study of a novel Infant Hydration Monitor (IHM) are presented. IHM is a portable device measuring ultrasound velocity (USV) through the leg muscles in young infants to monitor changes of their hydration status. Study in newborns revealed that USV in their muscles is lower than in adults, indicating higher water content in the tissue by an average of 12%. Observed cases of short term changes of USV can be explained by hydration changes during applied hydration therapy or water detention regiments.**

Keywords — **Ultrasound velocity, hydration, muscle, pediatrics.**

I. Introduction

An infant's hydration status is one of the most critical pieces of information that guides medical team's health assessment and management of babies with diseases involving affected homeostasis [1]. Early detection of water imbalance in neonates can unhide presence of underlying diseases such as diabetes, heart failure or kidney dysfunction so they can avoid possible complications. Infants of all ages, suffering from diarrhea and vomiting commonly accompanying infections, caused by viruses like rotavirus or bacteria like salmonella, can become dangerously dehydrated if signs of dehydration are not recognized and rehydration treatment not applied in time [2]. The opposing treatment strategies for dehydration vs. water intoxication make it especially important that any water imbalance is identified early and correctly.

Meanwhile, there is a lack of instrumental tools to evaluate the hydration status rapidly and quantitatively. Usually, diagnostics is based on vital signs such as dry skin, sunken eyeballs, lack of tears when infant cries, dry gums, increased pulse rate and etc. Frequently, these signs are not specific and objective. They do not allow monitoring of hydration changes in short term scale.

The technology being currently developed at the Artann Laboratories (NJ, USA) is based on the dependence of ultrasound velocity (USV) on the tissue composition. It was demonstrated that USV in soft biological tissues is principally determined by its molecular composition, the water content being the main determinant, while the structural and intracellular interactions are of minor influence. The muscle tissue is the major volumetric water depot of the body, where the water content is 70-85%. The tissue loses up to 40% of water during severe dehydration [3], and thus can serve as a representative indicator of total body hydration. Since short term changes of the muscle composition can occur mostly due to changes of fluids content, this type of tissue was chosen as the object for measurements. Laboratory experiments on 'in vitro' animal muscle tissues showed linear dependence of USV on water content with a slope of 2.5-3 m/s per 1% of water loss [4]. A potential of USV measurements to monitor peripheral edemas in adults has been previously demonstrated [5]. Based on this background, a prototype of ultrasonic Infants Hydration Monitor (IHM) has been designed. The objectives of current pilot study conducted in Riga hospitals were 1) to examine applicability of IHM in infants; 2) to obtain feedback from the medical personnel about convenience of operation and 3) to establish clinical confirmation of IHM sensitivity to possible hydration changes in neonates during their first days of life and in older infants during infection diseases with respect to body dehydration and rehydration.

II. Methods and Subjects

A. Infants Hydration Monitor (IHM)

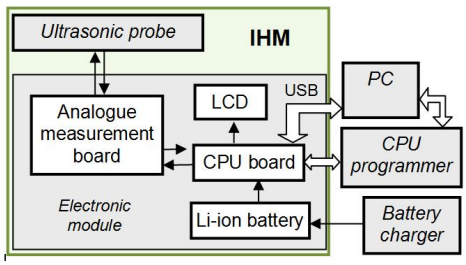

Fig. 1 Block diagram of IHM.

IHM measures USV in through transmission mode by a couple of emitter and receiving transducers placed opposite each other. Measurement accuracy of IHM is constrained

Y. Dekhtyar et al. (Eds.): *International Symposium on Biomedical Engineering and Medical Physics*, IFMBE Proceedings 38, pp. 39–42, 2013.
DOI: 10.1007/978-3-642-34197-7_10

within 3 m/s to discriminate 1% of hydration changes. IHM is designed as a compact, lightweight, battery-fed device with rapid processing, taking only a few seconds per measurement. It does not require special training and is very practical in both in hospitals and underserved, rural and field settings. For easy use the electronic unit with LCD is wrist-mounted and connected with the probe by a short cable.

The device consists of two circuitries: an analogue board and a controller board with LCD (Fig. 1). The emitting transducer is excited by a 20V rectangular pulse and produces a short ultrasonic signal at 3MHz frequency propagating through muscles. The circuitry has a master clock for setting pulse repetition frequency and a system of comparators allowing records of the first zero crossing of the received signal in a predefined time window. Measurement of ultrasound propagation time is performed by a voltmeter measuring charge of a saw-tooth voltage generator synchronized with pulse generation. Thus, the measured output voltage is proportional to ultrasonic propagation time. The processor calculates the ultrasound velocity by using the calibration data recorded in memory and the measured time-of-flight of the ultrasonic pulse. Bench tests of IHM using pure water and gelatin solutions showed measurement accuracy better than 1 m/s.

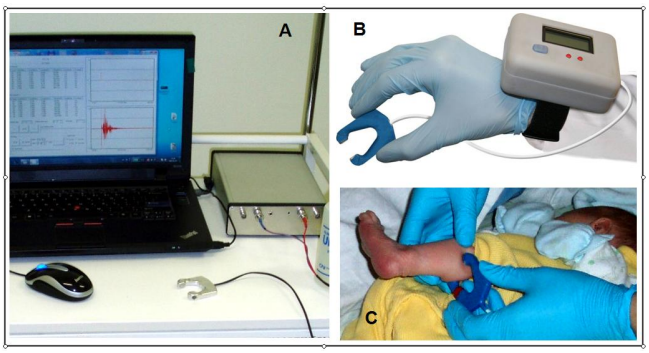

Fig. 2 IHM: A – laptop based setup; B – portative wrist-mounted device; C – application of ultrasonic probe to infant's calf.

To have both viewing and analysis of raw ultrasonic signals, a measurement setup included a digital acquisition board and a laptop PC (Fig. 2A). The setup simulated output and input parameters of the "blind" IHM circuitry. The portable version used wrist-mounted electronic module (Fig. 2B). Both IHM modalities were used in the study.

The measurement site we defined for the IHM is the middle of infant's calf. This anatomical site characterized by a large bulk of muscle tissue. The ultrasonic probe is made of metallic bracket-type frame to provide stiffness of the transducers base. The probe is applied to the leg with slight compression of the tissue (Fig. 2C). Acoustic gel is used as lubrication.

B. Study Program and Subjects

The pilot clinical studies were conducted in Latvian children hospitals under review and approval of the Medical Ethics Committee of the Riga Stradinsh University obtained on 6 October 2011.

The purpose of study at the Riga Maternity Hospital (RMH) was to evaluate the applicability of IHM in newborns and to get a statistically significant set of USV data in newborn muscle tissues. In total, 42 newborns with gestational ages of 34-42 weeks were examined during 1st and 2nd days of life.

A second study has been initiated in the Department of Infectious Diseases at the Children Clinical University Hospital (Riga) (CCUH). Young children between 1 and 5 years of age admitted to the hospital and suffering from diarrhea caused by viral infections like rotavirus and gastroenteritis were examined during the successive periods of intravenous infusion therapy. In this study, 21 children were examined, 10 of them with acute respiratory infections and 11 with gastroenteritis and rotavirus. Examinations were performed multiple times during children's stay at the hospital.

III. Results

A. USV Measurements Obtained in Newborn Children

Table 1 Comparison of USV in calves of newborn children and adults.

Gender	Newborns			Adults [5]			ΔUSV, m/s	p
	n	USV, m/s	SD, m/s	n	USV, m/s	SD, m/s		
Males	23	1534	19	60	1583	16	49	<0.001
Females	19	1541	11	67	1561	16	20	<0.001
Both	42	1537	14	127	1572	21	35	<0.001

Comparison of average USV in calf muscles of newborns and adults in respect of gender is shown in Table 1. USV values in adults with no leg edemas were provided from our earlier published data [5]. This study showed that USV is significantly lower in newborns than in adults, consistently for both genders.

USV had moderate correlation with body weight (Pearson linear correlation coefficient r=-0.60). The smallest and lean infants (weight < 3 kg, n=4) had USV in the highest values range, or >1540 m/s, but the largest ones (weight >4.5 kg, n=2) had the lowest USV (<1510 m/s).

No prominent correlation with postnatal body weight loss and changes of USV in muscle during 1st day of life was

found. No evidential dehydration symptoms were revealed in the examined babies in RMH. However, several cases were observed, where USV notably increased indicating possible water loss. A simultaneous increase of USV in two newborn sisters-twins of low gestational age (34 weeks) occurred after a one-day stay in neonatal incubator with an integrated heater. The USV changes were several times higher than the measurement deviation in 4 repeat tests and corresponded to water loss to 2.5-3.5%.

No adverse events were reported in the study. The clinical operators further did not report any concerns about the convenience of bracket-type probe application. If the probe was positioned properly, ultrasonic signals of sufficiently high amplitude were received resulting in signal-to-noise ratios comparable to that obtained in test experiments in water.

B. Changes of USV in Infants with Infection Diseases

There were no children with the symptoms of severe dehydration among the study group at the CCUH. However some of the children enrolled in the study had mild dehydration symptoms such as fever, dry skin and increased pulse rate. USV varied among the enrolled patients within the range of 1504 to 1565 m/s.

In 9 children, USV changes were followed from the moment before infusion start and after 4 hours of its application. In 4 of the cases, USV decreased by 4-13 m/s, in 4 children USV was within ±3 m/s considered as the allowable measurement error, and in 1 child it increased on 14 m/s. Measurements performed for the children that received higher doses of infused fluids resulted in lowering of USV.

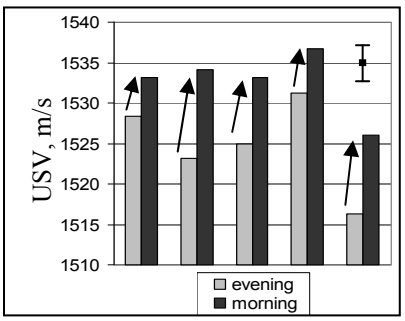

Fig. 3 USV changes in 5 acute infection patients after night without receiving intravenous rehydration therapy. Vertical bar shows measurements error as SD in 4 repetitions.

In 5 children, data were collected on the evening of the 1st day after rehydration therapy and early the next morning of the 2nd day without infusion therapy having been administered during the night. Fig. 3 shows changes of USV in the examined patients. In all of them, USV increased by 5-11% corresponding to a 2-4% water loss.

IV. Discussion

This pilot clinical study provided several findings confirming sensitivity of IHM to changes in hydration of young children. The baseline shift of USV on 35 m/s lower in neonates than in gender matched adults corresponds to about 12% higher water content in muscles of newborns. This finding is consistent with the accepted clinical knowledge of elevated body hydration of newborns of that order [6].

Cases of USV increase in newborns during their stay in incubators with warming controls and in children with infection diseases during night sleep can be explained by insensible water loss achieving 2-4%.

Wide individual variation of USV in infants significantly exceeding the short-term changes induced by dehydration was observed. This limitation defines application of IHM for assessment of relative changes of hydration status from the initial individual baseline. At the same time substantially high USV values could potentially indicate dehydration in the absolute scale.

Average standard deviation in 3 repeated measurements with probe repositioning during one examination was 3.0 m/s corresponding to deviation of water content of 1%. Deviations of less than 3.0 m/s (0.5-2.9 m/s) occurred in 65% of the measurements however about 15% of measurements had deviations exceeding 5 m/s. The measurement error is explained primarily by the probe positioning artifacts, such as, wrong orientation of the probe in relation to the leg's anatomical axis and baby's movement during examination. Special efforts to standardize the application procedure and minimize positioning errors should be undertaken in the future development.

One of the causes of the measurement error could be related to the undefined pressure applied to the tissue which can be different depending of the muscle thickness. To minimize the variability of this pressure, the measurements are made at the moment when a reliable signal above a predefined threshold is achieved while inserting the probe over the calf from its lower thinnest part. Such measurement procedure provides automatic normalization of the contact pressure. However, the effect of variable contact pressure is not very significant because it is experimentally shown in our bench studies on excised animal tissues that tissue deformation up two 20% negligibly affects the ultrasound velocity measurement because Poisson's ratio of soft tissue is close to 0.5.

Further studies can be designed to include continuing observation of dehydrated patients to verifying IHM measurement data with other methods of hydration assessment such as urine and/or blood osmolality tests.

REFERENCES

1. Oh W (1997) Fluid and electrolyte management. In: Fanaroff AA, Martin RJ, eds. Neonatal-Perinatal Medicine: Diseases of the Fetus and Infant. 6th ed. St. Louis, MO: Mosby; 1997:622-38
2. Finberg L (2002) Dehydration in infancy and childhood. Pediatr Rev 23:277-82.
3. Hamilton B, Schwartz R (1935) The composition of tissues in dehydration. J Biol Chem 109:745-753
4. Sarvazyan A, Tatarinov A, Sarvazyan N (2005) Ultrasonic assessment of tissue hydration status. Ultrasonics 43:661-671
5. Topchian A, Tatarinov A, Sarvazyan N, Sarvazyan A (2006) Ultrasound velocity in human muscle in vivo: perspective for edema studies. Ultrasonics 44:259-264
6. Bianchetti MG, Simonetti GD, Bettinelli A (2009) Body fluids and salt metabolism - Part I. Ital J Pediatr 35:36-42.

Author: Alexey Tatarinov
Institute: Artann Laboratories
Street: 1459 Lower Ferry Rd
City: Trenton, NJ
Country: USA
Email: tatarinov@artannlabs.com

The Differential Oscillometric Method Can Be Used for Recording Beat-to-Beat Arterial Pressure Patterns from Radial Arteries

J. Talts, R. Raamat, K. Jagomägi, and J. Kivastik

Department of Physiology, University of Tartu, Tartu, Estonia

Abstract — **The aim of this pilot study was to investigate the feasibility of the differential oscillometric technique to record beat-to-beat mean arterial pressure patterns from radial arteries (MAPrad). MAPrad was recorded by an experimental device in 9 healthy subjects during rest, light physical exercise and local cooling. Simultaneously, the finger beat-to-beat mean arterial pressure pattern (MAPfin) and the fingertip skin blood flow by the laser Doppler flowmetry were registered. Results demonstrated that the group-averaged beat-to-beat MAPrad recordings had a high similarity to related MAPfin recordings (r=0.92; range 0.86 to 0.98). However, the dynamic radial-to-finger blood pressure difference was found to vary in some subjects as a result of intensive vasoconstriction. In further development attention should be paid to proper positioning of the local pad-type cuffs to avoid overestimation of the radial pressure.**

Keywords — **Oscillometric beat-to-beat blood pressure, continuous noninvasive mean arterial pressure, vasoconstriction.**

I. Introduction

Conventional oscillometric monitors measure systolic and diastolic blood pressures (SBP and DBP, respectively), while some of them also provide mean arterial pressure (MAP) values. Approximately 30–60 s are needed for getting a reading.

An application of the oscillometric method for beat-to-beat MAP measurement was reported in [1]. Briefly, unlike the volume-clamp finger monitors (e.g., Finapres, Portapres, Finometer), in which the cuff pressure rapidly follows the instantaneous intraarterial pressure [2], in the modified oscillometric finger instrument the cuff pressure follows the mean intraarterial pressure for every cardiac cycle. In this case, according to Marey's principle, maximum oscillations appear in the occluding cuff and those can be used as an input signal for the servo system. For higher reliability, the modified oscillometric instrument uses a differential servo system and it operates with two cuffs on adjacent fingers with pressures shifted from the mean pressure value in both directions to a small extent. In this differential version the principle of maximum oscillations becomes the principle of the equality of amplitudes of simultaneous volume oscillations in the two adjacent finger cuffs.

A number of studies have compared the differential oscillometric finger instrument to the volume-clamp finger monitor under several physiological conditions [4, 5]. However, we did not find data in the literature on the use of the differential oscillometric method to measure beat-to-beat MAP profiles from radial arteries.

This study presents preliminary results of an experimental application of the differential oscillometric technique to record beat-to-beat MAP from radial arteries. The measured radial pressure patterns are compared to those recorded simultaneously from the finger arteries applying the same principle of measurement.

II. Methods and materials

A. Experimental Design and Protocol

Our study group included 9 volunteers, five females and four males, aged 17 to 68. They had no history of vascular disease. Research Ethics Committee of the University of Tartu approved the study and written informed consent to take part was obtained from all subjects.

The subject was lying with both hands resting at heart level on a support (Fig.1). Before starting the measurement session, the brachial right-left difference was determined by simultaneous applying of two Microlife BP A100 monitors (Microlife AG, Switzerland). Only subjects who had the simultaneously measured SBP or DBP differences between two hands less than 5 mmHg were included in the study.

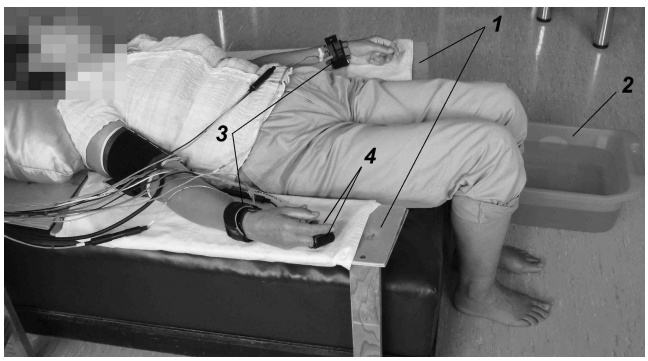

Fig. 1 Illustration of the experimental setup: 1 – hand support, 2 – basin with water at 12°C, 3 – radial cuffs, 4 – finger cuffs and a laser Doppler sensor.

Y. Dekhtyar et al. (Eds.): *International Symposium on Biomedical Engineering and Medical Physics*, IFMBE Proceedings 38, pp. 43–46, 2013.
DOI: 10.1007/978-3-642-34197-7_11

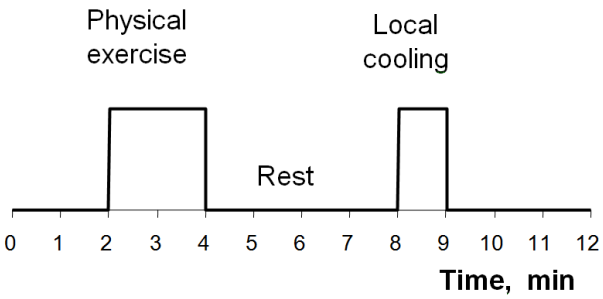

Fig. 2 Schematic presentation of the experimental protocol.

The experiment contained three different physiological conditions: rest, light physical exercise (static leg raise for 2 min) and local cooling (immersion of legs into water at 12°C for one minute). The experimental protocol is illustrated by Fig. 2.

Measurements were carried out at room temperature 25–26°C. Continuous noninvasive recording of three variables was performed: finger beat-to-beat mean arterial pressure (MAPfin), radial beat-to-beat mean arterial pressure (MAPrad) and fingertip skin blood flow by laser Doppler flowmetry (LDF).

MAPfin was measured by the UT9201 physiograph (University of Tartu, Estonia) that applies the differential oscillometric method briefly described afore. Two finger cuffs of the UT9201 instrument were attached to the second phalanges of the middle and ring fingers of the right hand.

MAPrad was recorded by an experimental device which also applies the differential oscillometric principle. Like the differential finger monitor, the radial instrument uses two cuffs with pressures shifted from the mean arterial pressure to a small extent in both directions. One of the cuffs was placed on the left and the other on the right radial artery. The local pad-type cuffs were adjusted in a way that they compress the underlying radial artery while the ulnar artery and veins remain open [6]. This enabled blood supply to sites more distal to the wrist and did not affect the simultaneous finger blood pressure measurement. Using palpation, the radial cuffs were positioned at the place of maximum pulsation. The subjects were asked not to move their hands during measurements.

Peripheral blood flow was recorded by a laser Doppler instrument (MBF3D, Moor Instruments, Axminster, Devon, UK). LDF flux signal was used to reveal the peripheral blood flow changes capable of influencing the peripheral blood pressure measurement. The laser Doppler probe was placed on the pulp of the fifth finger of the right hand (i.e. closer to the ulnar artery).

B. Signal Processing and Data Analysis

The analog signals from the finger and radial MAP monitors as well as from the laser Doppler flowmeter were digitized by an analog-to-digital converter (16-bit accuracy, sampling rate 200 Hz) and transferred to the computer.

The results of finger blood pressure measurement are often evaluated against radial measurement [7, 8]. In the present study, vice versa, we validated the MAPrad patterns obtained by the new device against the simultaneously recorded MAPfin patterns. Similarity between the MAPrad and MAPfin patterns was assessed by observing them visually and by using Spearman's correlation analysis.

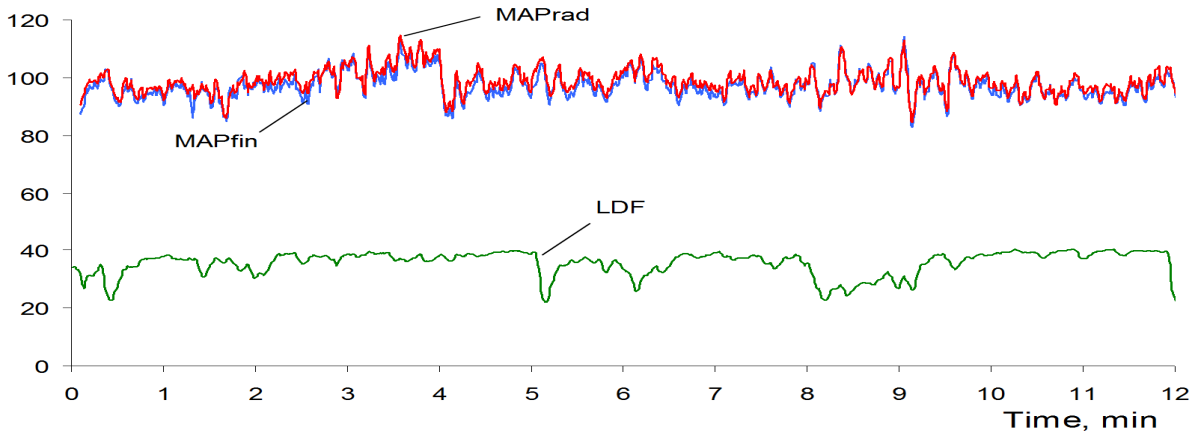

Fig. 3 Original beat-to-beat recording in Subject 9 with radial mean arterial pressure (MAPrad) and finger mean arterial pressure (MAPfin) close to each other. The fingertip laser Doppler flowmetry signal (LDF) is also shown. Pressure signals are given in mmHg, the laser Doppler signal is in arbitrary units (au).

III. Results

The individual and group-averaged characteristics of correlation between MAPrad and MAPfin are listed in Table 1. The median of the correlation coefficient (r) for the whole group was 0.92. All the individual correlation coefficients were highly significant ($p<0.005$).

Fig. 3 demonstrates an original recording in Subject 9 with MAPrad and MAPfin situated close to each other (the radial-to-finger pressure gradient was 1-3 mmHg). Fig. 4 is a recording in Subject 7 having a larger radial-to-finger pressure difference of about 10-13 mmHg. Fig. 5 shows differences between MAPrad and MAPfin during local cooling in one subject who had an intensive vasoconstriction.

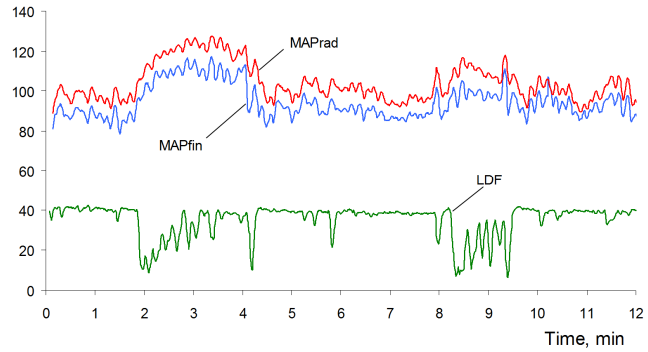

Fig. 4 A recording similar to Fig.3 in Subject 7 showing a noticeable persistent difference between radial and finger mean arterial pressures.

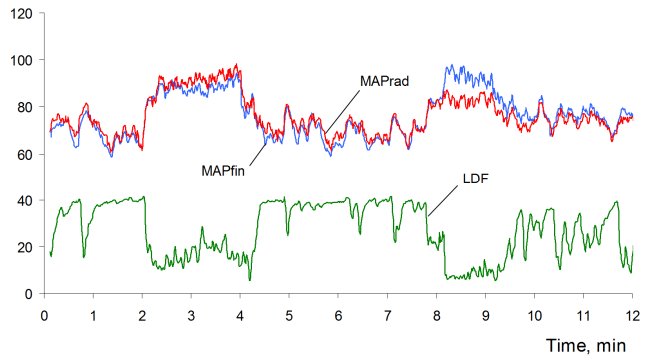

Fig. 5 A recording similar to Fig.3 in Subject 1 demonstrating the influence of an intensive vasoconstriction during local cooling.

Table 1 Individual and group-averaged correlation coefficients (r) between the radial mean arterial pressure (MAPrad) and the finger mean arterial pressure (MAPfin).

Subject	Correlation coefficient			
	Total	Exercise	Rest	Local cooling
1	0.92	0.84	0.95	0.59
2	0.93	0.91	0.93	0.40
3	0.91	0.91	0.90	0.94
4	0.98	0.98	0.95	0.87
5	0.90	0.91	0.96	0.73
6	0.86	0.89	0.87	0.91
7	0.97	0.88	0.91	0.90
8	0.87	0.93	0.89	0.54
9	0.96	0.96	0.96	0.97
Min	0.86	0.84	0.87	0.40
Max	0.98	0.98	0.96	0.97
Median	**0.92**	**0.91**[a]	**0.93**	**0.87**[a]

[a] – no significant difference compared to Rest ($p>0.05$, Wilcoxon signed rank test). All the individual correlation coefficients were highly significant ($p<0.005$).

IV. Discussion

The study demonstrated that the measured radial beat-to-beat MAP recordings had a high similarity to related finger MAP recordings. MAPrad revealed responses in the same direction as MAPfin and almost any change in MAPfin was also seen in MAPrad. The median r for all the pairs of comparison was 0.92 (Table 1). At the same time a little lower correlation was noticed for exercise and local cooling compared to the resting condition (0.91, 0.87 and 0.93, respectively). However, this difference did not reach the level of statistical significance.

Fig. 3 shows typical responses in simultaneously recorded MAPrad, MAPfin and LDF in Subject 9. It can be detected by visual observation that the time series of finger and radial MAP were in good agreement with each other throughout all the stages of the experiment (r=0.96).

We suppose that a noticeable difference between the radial and finger MAP levels in Subject 7 (Fig. 4) had no physiological origin and it was caused by our little

experience in radial cuff handling. When positioning the local pad-type radial cuffs, palpation was used to find the place of maximum pulsations of the arterial wall. However, it turned out that this methodology specified the place located about 10-15 mm proximal from the optimum measurement point for some male subjects. As a result, the radial artery was not correctly pressurized by the local pad-type cuff, leading to overestimation of the radial pressure.

To avoid this, it is reasonable to use palpation while keeping in mind that the optimum measurement point is usually located at the very distal end of the radial bone [9,10]. However, despite the noticeable shift in pressure levels, the shape of compared time series in Subject 7 remained highly similar (r=0.97).

Some differences observed between the simultaneous radial and finger MAP recordings can be explained by different measurement sites. It is generally known that the finger blood pressure compared to the radial or brachial pressure is more influenced by the changing peripheral vascular tone [11,12]. Subject 1 had a very intensive vasoconstriction during local cooling (note a steep fall in the LDF signal at 8 min). As a result, the MAPfin signal showed an inadequate response: the MAPfin signal was even higher than that of MAPrad. The possible explanation is that the oscillometry was affected by the cold-induced vasoconstriction, which caused a change of the finger pressure-volume relationship [13-15].

V. Conclusions

The study demonstrated the possibility of using the differential oscillometric technique to record beat-to-beat MAP from radial arteries. However, attention should be paid to the proper compression of the radial artery to avoid overestimation.

Acknowledgment

This study was supported by the Estonian Science Foundation (grant 7723) and the Estonian Ministry of Education and Research (SF0180125s08).

References

1. Reeben V, Epler M (1983) Indirect Continuous Measurement of Mean Arterial Pressure. In: Ghista DN (ed.) Advances in Cardiovascular Physics, vol.5, Cardiovascular Engineering. Part II: Monitoring. Karger, Basel, 1983, pp 90−118
2. Wesseling KH (1991) Finapres, continuous noninvasive finger arterial pressure based on the method of Peñáz. In: Rüddel H, Curio I (ed.) Non-invasive continuous blood pressure measurement. Peter Lang, Frankfurt am Main, Bern, New York, Paris, 1991, pp 9–17
3. Raamat R, Jagomägi K, Talts J (2008) Continuous recording of the oscillometric mean arterial pressure by the differential servo system with two photoplethysmographic sensors, Proc. 8th IEEE Int. Conf. on Bioinformatics and Bioengineering BIBE, Athens, Greece, 2008, pp 1–4
4. Jagomägi K, Talts J, Raamat R et al. (1996) Continuous non-invasive measurement of mean blood pressure in fingers by volume-clamp and differential oscillometric method. Clin Physiol 16:551–560
5. Raamat R, Jagomägi K, Talts J et al. (2001) Continuous mean arterial pressure measurement in the fingers: the influence of local arm cooling. Med Biol Eng Comp 39:584–589
6. Raamat R, Talts J, Jagomägi K, Kivastik J (2010) Comparison of oscillometric pulse amplitude envelopes recorded from the locally compressed radial arteries. Med Eng Phys 32:1124–1130
7. Gibbs NM, Larach DR, Derr JA (1991) The accuracy of Finapres noninvasive mean arterial pressure measurements in anesthetized patients. Anesthesiology 74:647–652
8. Stokes DN, Clutton-Brock T, Patil C et al. (1991) Thompson JM, Hutton P. Comparison of invasive and non-invasive measurements of continuous arterial pressure using the Finapres. Br J Anaesth 67:26–35
9. Lu W, Tsukada A, Shiraishi T, Sasaki K (2001) Indirect arterial blood pressure measurement at the wrist using a pad-type square cuff and volume-oscillometric method. Front Med Biol Eng 11:207–219
10. Kim JP, Kim YH, Bae S et al. (2009) Factors affecting the accuracy of volume-oscillometric blood pressure measurement during partial pressurization of the wrist, EMBC 2009, Annual International Conference of the IEEE, pp 721–724
11. Pinna GD, Maestri R, Mortara A (1996) Estimation of arterial blood pressure variability by spectral analysis: comparison between Finapres and invasive measurements. Physiol Meas 17:147–169
12. McAuley D, Silke B, Farrell S (1997) Reliability of blood pressure determination with the Finapres with altered physiological states or pharmacodynamic conditions. Clin Auton Res 7:179–184
13. Baker PD, Westenskow DR, Kück K (1997) Theoretical analysis of non-invasive oscillometric maximum amplitude algorithm for estimating mean blood pressure. Med Biol Eng Comput 35:271–278
14. Raamat R, Talts J, Jagomägi K, Länsimies E (1999) Mathematical modelling of non-invasive oscillometric finger mean blood pressure measurement by maximum oscillation criterion. Med Biol Eng Comput 37:784–788
15. Raamat R, Talts J, Jagomägi K, Kivastik J (2011) Errors of oscillometric blood pressure measurement as predicted by simulation. Blood Pres Monit 16:238–245

Author: Jaak Talts
Institute: Department of Physiology
Street: Ravila 19
City: Tartu
Country: Estonia
Email: jaak.talts@ut.ee

Revealing Small Hidden Changes in Human EEG by Higuchi's Fractal Dimension

M. Bachmann, A. Suhhova, J. Lass and H. Hinrikus

Department of Biomedical Engineering, Technomedicum, Tallinn University of Technology, Ehitajate Rd 5, 19086 Tallinn, Estonia

Abstract— **The aim of this study was to detect extremely small hidden changes in human EEG by non-linear Higuchi's fractal dimension (HFD). As a source of small alterations in the EEG the modulated 450 MHz microwave radiation at different modulation frequencies (40 and 70 Hz) was applied at the level of exposure much lower than the health protection limits. The EEG was recorded for a group of 15 subjects during 40 minutes (1 min off, 1 min on). The signals in the P3-P4 EEG channels were selected for comparison. The HFD method revealed significant change at 40 Hz modulation frequency. The trend of changes but no statistically significant effect was detected at 70 Hz modulation frequency. The results confirm that the microwave effect depends on modulation frequency. More specific algorithms are needed for discrimination of the effect in future investigations.**

Keywords— **EEG, EMF, Higuchi's fractal dimension.**

I. Introduction

During last decades understanding the brain activity has became a topic of major interest. Computers are already in our pockets and soon everything should work just by thinking of it. However, at present, even several mental disorders are evaluated by the help of questionnaires revealing subjective symptoms since there is no objective means for evaluation.

In addition, the wide use of wearable computers and mobile phones places us into electromagnetic field (EMF). The permanent presence of the EMF causes public concern. Health effects of the EMF are still under discussion and necessity for independent research in the area is underlined even by the European Parliament [1]. Main reasons for doubts in the influence of the EMF are the hidden feature of the effects and diverse sensitivity of persons to the EMF which makes the effect very difficult to detect.

As EEG is quite easily available, cost effective and reflects the ongoing activity, it is a valuable method getting objective information about changes in brain physiology. In addition, it is believed that EEG exhibits also complex behavior [2, 3] and hence has patterns with different complexities. Therefore the nonlinear measures can be a good alternative to more frequently applied linear methods.

Therefore, this study is oriented to clarify two questions: 1) can the nonlinear EEG analysis based on Higuchi's fractal dimension (HFD) reveal the EMF effect at conditions where the linear analysis failed and 2) does the effect really depend strongly on the modulation frequency as reported in our previous studies [4,5]. We have previously shown the effect of microwave exposure at modulation frequency 40 Hz applying linear [6] and non-linear methods [7]. On the other hand, attempts to detect the effects at modulation frequency 70 Hz by linear methods were not as successful [6]. Therefore, in this study both modulation frequencies will be used along with a sham recording for comparison, to discover whether Higuchi's FD is powerful enough to detect small hidden changes in EEG at both modulation frequencies.

As the effect of exposure to microwave radiation is extremely difficult to detect, the periodic exposure to microwave radiation is used in this study to influence human EEG. The aim of the work is to detect as small changes in EEG as possible by using two different modulation frequencies.

II. Materials and methods

A. Subjects

The experiments were carried out on a group of healthy volunteers consisting of 15 young persons (aged 21–24), eight male and seven female.

All the subjects selected were without any medical or psychiatric disorders. A questionnaire and a clinical interview were used to evaluate their physical and mental condition (tiredness, sleepiness) before the experiment. The persons who declared tiredness or sleepiness before the experiment were excluded.

EEG recording was performed for a subject during a day between time interval 9:00 a.m. to noon. The room of the experiments was dark and the subjects were lying in a relaxed position, eyes closed, and ears blocked during the experiments.

After the recordings they were asked how they were feeling during the experiment. The subjects reported neither alertness nor any strain experienced during the recordings. The experiments were conducted with understanding and written consent of each participant.

Y. Dekhtyar et al. (Eds.): *International Symposium on Biomedical Engineering and Medical Physics*, IFMBE Proceedings 38, pp. 47–50, 2013.
DOI: 10.1007/978-3-642-34197-7_12

B. Exposure

Microwave radiation at the non-thermal level of field power density was selected to be identical to that in our previous studies [5].

The experimental study was performed according to recording protocol identical for all subjects. All subjects passed two recording protocols with microwave exposure and sham.

Exposure conditions were the same for all subjects in the group. The 450-MHz electromagnetic radiation was generated by the Rohde & Swartz signal generator model SML02.

The RF signal was 100% pulse-modulated by the Rohde & Swartz pulse modulator SML-B3 at 40-Hz frequency, duty cycle 50%. The signal from the generator was amplified by the Dage Corporation power amplifier model MSD-2597601. The generator and amplifier were carefully shielded. The 1-W electromagnetic radiation output power was guided by a coaxial lead to a 13-cm quarter-wave antenna NMT450 RA3206 by Allgon Mobile Communication AB, located close to the ear 10 cm from the skin on the left side of the head. The Central Physical Laboratory of the Estonian Health Protection Inspection measured the spatial distribution of the electromagnetic radiation power density by the Chauvin Arnoux Fieldmeter CA 43 field strength meter. The used measurement equipment passed calibration by the Estonian Technical Surveillance Authority. The calibration curves of dependence of the field power density on the distance from the radiating antenna were obtained from these measurements performed under real experimental conditions. The average field power density of the modulated microwave at the skin from the left side of the head was 0.16 mW/cm^2, as estimated from the measured calibration curves. During the experiments, the stability of the electromagnetic radiation level was monitored by an IC Engineering Digi Field C field strength meter. The specific energy absorption rate (SAR) was calculated using SEMCAD software. The calculated spatial peak SAR averaged over 1 g has its maximum 0.303 W/kg in middle of the left hemisphere near the left ear [8].

C. Recording protocol and equipment

The protocol with exposure lasted 40 min, during which the resting eyes closed EEG was continuously recorded.

For the duration of every even minute of the recording the subject was exposed to microwave at modulation frequency 40 or 70 Hz. The pair of successive reference minute followed by exposed minute was an exposure cycle (Figure 1).

Cycle			
Resting/reference segment 60 s		Exposure segment 60 s	
First half-period 0-30 s	Second half-period 30-60 s	First half-period 0-30 s	Second half-period 30-60 s
Comparison interval		Comparison interval	

Fig. 1 Recording cycle.

Twenty exposure cycles were applied during a recording: first ten exposure cycles were performed at first and ten last at second modulation frequency. Selection of 40 or 70 Hz as first or second modulation frequency was randomly assigned.

Sham recording session used the same protocol, except that the microwave power was switched off. For each recording session, the exposure conditions were randomly assigned between subjects.

Cadwell Easy II EEG measurement equipment was used for the EEG recordings. The EEG was recorded using 19 electrodes, which were placed on the subject's head according to the international 10–20-electrode position classification system. The channels chosen for analysis were P3-P4 with the reference electrode Cz.

The artefacts at the modulation frequencies were removed from the EEG signals by off-line filtering during the pre-processing of the signals in the LabVIEW programming and signal-processing environment. The recorded EEG signals were stored on a computer in 0.5–38 Hz frequency band at an 80-Hz sampling frequency.

D. EEG analysis

Higuchi's algorithm calculates FD of time series directly in the time domain [9]. It is based on a measure of length *L(k)* of the curve that represents the considered time series while using a segment of k samples as a unit.

The value of FD was calculated according to the following algorithm [9]. From the given time series: *X(1), X(2), X(3), ..., X(N)* a new series X_k^m is constructed as:

$$X_k^m : X(m), X(m+k), X(m+2k), \ldots, X\left(m + int\left(\frac{N-m}{k}\right)k\right), \qquad m = 1,2,\ldots,k.$$

The length $L_m(k)$ of every curve X_k^m is calculated according to the formula:

$$L_m(k) = \frac{1}{k}\left[\left(\sum_{i=1}^{int\left(\frac{N-m}{k}\right)} |X(m+ik) - X(m+(i-1)k)|\right)\frac{N-1}{int\left(\frac{N-m}{k}\right)k}\right]$$

The length *L(k)* of the curve for time interval *k* is defined as average over *k* values of $L_m(k)$, *m=1,2,...,k*. If *L(k)* scales like $L(k) \sim k^{-FD}$, the curve has FD, which is calculated using linear regression of the graph:

$$\ln\big(L(k)\big) \sim ln\left(\frac{1}{k}\right)$$

according to the following formula:

$$FD = \frac{n\sum(x_k y_k) - \sum x_k \sum y_k}{n\sum(x_k^2) - (\sum x_k)^2},$$

where $x_k = ln\left(\frac{1}{k}\right)$, $y_k = \ln L(k)$, $k = k_1, \ldots, k_{max}$, and *n* denotes the number of *k*-values for which the linear regression is calculated ($2 \le n \le k_{max}$).

FD was calculated in 400 samples (5 s) window, and the window was shifted by 40 samples (0.5 s) with parameter $k_{max} = 8$. As it was previously found, the EMF effects appear mainly during the first half-period of the segment [5]. Therefore the HFD was calculated for every first half-period (30 s), giving 111 FD values for every microwave exposure half period and for every reference half-period.

Averaging over ten exposure cycles was performed.

III. RESULTS AND DISCUSSION

Figure 2 indicates the difference averaged over all subjects and all recording cycles between exposed and reference segments first half-periods for sham, microwave exposed at 40 Hz and microwave exposed at 70 Hz recordings.

As can be seen, the FD difference is negative for sham recordings. As there was no exposure, this indicates the normal behavior of Higuchi's FD in time. However, the decrease between uneven and even segments was not statistically significant. As the recordings were quite long, those non-significant negative changes in FD might still indicate the possible decline in the level of subjects' alertness [10].

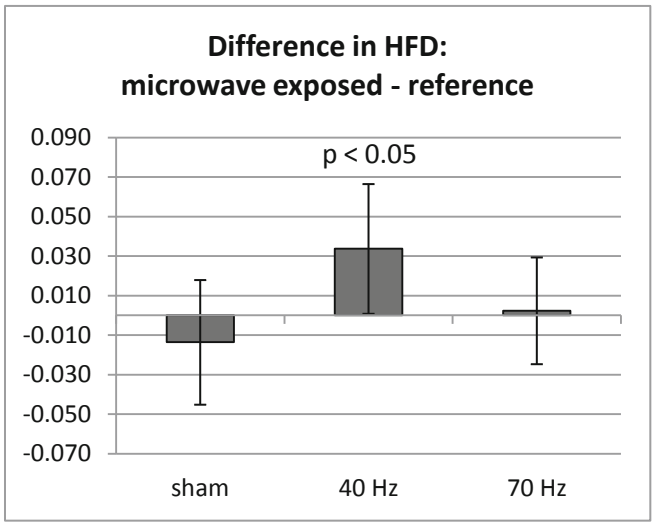

Fig. 2 Average difference in Higuchi's FD between microwave exposed half periods and reference half-periods: sham recordings, recordings at modulation frequency 40 Hz and recordings at modulation frequency 70 Hz.

The statistically significant positive difference in FD can be seen at modulation frequency 40 Hz. This indicates that the FD is higher for microwave exposed segments compared to reference segments. Therefore, exposure leads to more complicated character of neuronal oscillations compared to resting conditions.

The statistically insignificant difference between exposed and reference segments is close to zero at modulation frequency 70 Hz. Being insignificant, it can still indicate a trend of changes by keeping the subjects alertness at almost constant level in contrast to sham situation in case the FD was reduced.

Figure 3 presents the average Higuchi's FD values for reference half-segments. In case there would be any long-lasting microwave effects, the reference segments would be contaminated for microwave exposed recordings. The average FD value at modulation frequency 40 Hz is highest but not significant. This might indicate some contamination. If this is the case then the actual effect of microwave exposure is rather stronger.

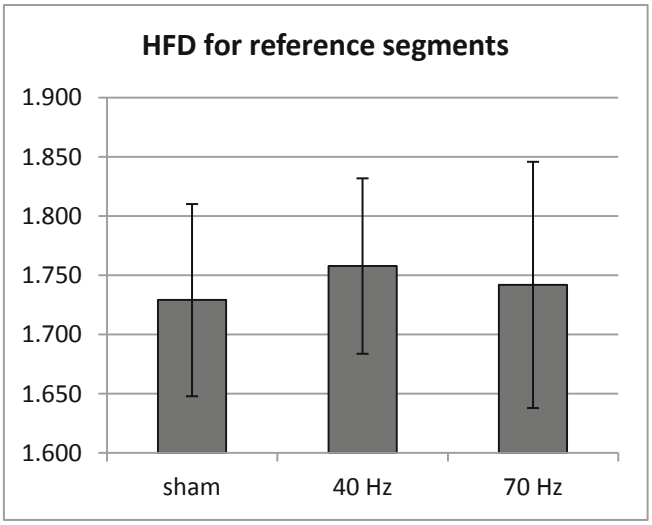

Fig. 3 Average Higuchi's FD for reference segments: sham recordings, recordings at modulation frequency 40 Hz and recordings at modulation frequency 70 Hz.

The Higuchi's fractal dimension was proved to reveal statistically significant changes on a group level at the modulation frequency 40 Hz [7]. However, at modulation frequency 70 Hz the method, like previously used linear methods [6], did not differentiate any statistically significant change on a group level. Despite that, the linear methods revealed changes for individual subjects at 40 Hz (4 subjects) as well as at 70 Hz (2 subjects) modulation in our previous study [6]. It seems that 70 Hz modulation frequency causes particularly small changes and in smaller number of subjects. Higuchi's fractal dimension has been proved to provide good discrimination of small changes at the group level [7]. However, in current study the HFD did not provide better discrimination of trends of alterations compared to linear method in conditions of decreasing individual sensitivity. This could be due to the small number of subjects and thus needs to be investigated in further study. The fact that it is extremely difficult to find changes in EEG at 70 Hz modulation frequency demonstrate again the modulation frequency dependence of the microwave exposure effects reported also in our previous study [5].

IV. CONCLUSIONS

The results indicate that the Higuchi's fractal dimension can discriminate the effect at 40 Hz modulation frequency. However, while increasing the modulation frequency to 70 Hz, no statistically significant effect was detected. Consequently, the Higuchi's fractal dimension was not able to detect trends of microwave effects on a group level at the higher modulation frequency where the linear method also failed. The results support the previous findings that the microwave effect depends on the modulation frequency. More specific algorithms are needed for discriminations of trends in further investigations.

ACKNOWLEDGMENT

The research has been supported by the Estonian targeted financing project SF0140027s07 and by the European Union through the European Regional Development Fund.

REFERENCES

1. Council of Europe, Parliamentary Assembly, Resolution 1815, 2011. The potential dangers of electromagnetic fields and their effect on the environment.
2. Korn H, Faure P (2003) Is there chaos in the brain? II. Experimental evidence and related models. C R Biol 326(9):787-840
3. Stam CJ (2005) Nonlinear dynamical analysis of EEG and MEG: review of an emerging field. Clin Neurophysiol 116(10):2266-301
4. Hinrikus H, Bachmann M, Lass J (2011) Parametric mechanism of excitation of the electroencephalographic rhythms by modulated microwave radiation. International Journal of Radiation Biology 87(11):1077 - 1085
5. Hinrikus H, Bachmann M, Lass J, Tomson R, Tuulik V (2008) Effect of 7, 14 and 21 Hz modulated 450 MHz microwave radiation on human electroencephalographic rhythms. International Journal of Radiation Biology 84(1): 69 - 79.
6. Bachmann M, Tomson R, Kalda J, Säkki M, Lass J, Tuulik V, Hinrikus H (2007) Individual Changes in Human EEG Caused by 450 MHz Microwave Modulated at 40 and 70 Hz. The Environmentalist 27(4): 511 – 517
7. Hinrikus H, Bachmann M, Karai D, Klonowski W, Lass J, Stepien P, Stepien R, Tuulik V (2011) Higuchi's fractal dimension for analysis of the effect of external periodic stressor on electrical oscillations in the brain. Medical & Biological Engineering & Computing 49(5):585-591
8. Hinrikus H, Bachmann M, Lass J, Karai D, Tuulik V (2008) Effect of low frequency modulated microwave exposure on human EEG: individual sensitivity. Bioelectromagnetics 29:527 - 538
9. Higuchi T (1988) Approach to an irregular time series on the basis of the fractal theory. Phys D 31:277–283
10. Klonowski W, Olejarczyk E, Stepien R. (2005) Sleep-EEG Analysis Using Higuchi's Fractal Dimension, International Symposium on Nonlinear Theory and its Applications NOLTA' Bruges, Belgium, 2005. pp. 222–225

Author: Maie Bachmann
Institute: Tallinn University of Technology
Street: Ehitajate Rd 5
City: Tallinn
Country: Estonia
Email: maie@cb.ttu.ee

LED Based Dual Wavelength Heterochromatic Flicker Method for Separate Evaluation of Lutein and Zeaxanthin in Retina

M. Ozolinsh[1] and P. Paulins[2]

[1] Institute of Solid State Physics, University of Latvia, Riga, Latvia
[2] Department of Physics and Mathematics, University of Latvia, Riga, Latvia

Abstract — **The decrease of density and consequentially optical density of macular pigment serves as a diagnostic mean for a number of ophthalmological pathologies, particularly as a risk factor for age related macular degeneration. Macular pigment absorbs light in short wavelength blue spectral range. Thus the optical density of macular pigment can be detected by various optical – both objective and subjective psychophysical techniques. Latter techniques use eye and brain visual pathways as spectral sensitive optical detector and decision maker, and exploit perception facility to process information flow in a unique manner to create various perception illusions. The psychophysical methods of detection of optical density of macular pigment include heterochromatic flicker photometry and minimum illusory motion photometry. We develop and employ a heterochromatic flicker photometry method where LEDs are used as visual stimuli. LED emission maximum wavelengths in blue spectrum region are chosen in range 445-460 nm, that corresponds to spectrally resolved maxima of light absorption for two types of macula pigments – lutein and zeaxanthin or in spectral range 500-510 nm, where lutein and zeaxanthin absorption have decay, that for both type of pigments have a detectable shift. Statistical dispersion of the results allows to use the difference between results of psychophysical measurements obtained for different LEDs to estimate the concentration of lutein and zeaxanthin in human retina.**

Keywords — **Macular pigment, lutein, zeaxanthin, heterochromatic flicker photometry, light emitting diodes.**

I. Introduction

The central area of retina in the eye – macula has the highest density of photoreceptors, a lack of blood vessels, and macula is the thinnest part of retina plexiform layer system. Besides the macula layer contains the macula pigment, actually two proteins - lutein and zeaxanthin [1]. These proteins absorb light in blue spectrum region, scatter and reflect yellow, and therefore macula is called the yellow spot of retina. These proteins are found only in retina, they take part in metabolism of retinal processes and hypothetically act as a shield against influence of ultraviolet radiation in central vision area [2,3]. During the last decades studies of macular pigment are intensified, because the deficit of macular pigment can promote developing age related macular degeneration AOMD – one of the most often hard eye pathologies of elder population [4,5]. Macular pigment *in vivo* can be detected by a variety of techniques, mainly optical, due to spectral selective light absorption or luminescence [6-8]. Other possibility to diagnose macular pigment in retina is psychophysical methods, when the patient analyzes own visual perception and a psychophysical decision serves as a detection tool. Two kinds of visual perception peculiarities can be used in such psychophysical measurements – heterochromatic flicker photometry and minimum motion illusion (apparent motion photometry)[9-11].

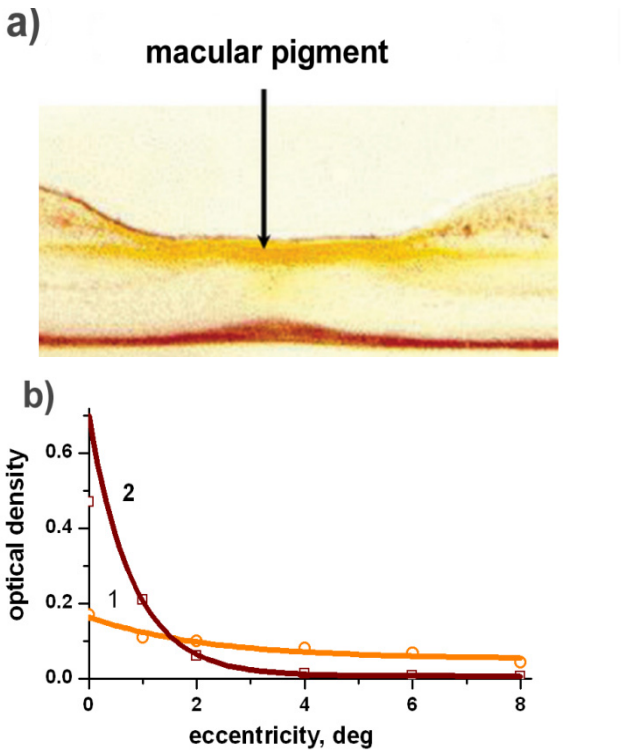

Fig. 1 a.Macular pigment in the area of central vision of retina. Macular pigment absorbs blue radiation and scatters yellow [3]. b.Optical density of macular pigment: lutein - curve 1, zeaxanthin – curve 2 (data from [1]).

Y. Dekhtyar et al. (Eds.): *International Symposium on Biomedical Engineering and Medical Physics*, IFMBE Proceedings 38, pp. 51–54, 2013.
DOI: 10.1007/978-3-642-34197-7_13

Both of them are based on finding the equiluminance of spectrally different light sources, and on the dependence of this equivalence on the eye eccentricity [11-13]. Various experimental and commercial devices are quoted in literature to measure macular pigment optical density using these two methods [4,14,15]. The spectrally sensitive light attenuation by macular pigment and the axial symmetry of this phenomenon allow to distinguish the effect by using chromatic stimuli in psychophysical studies. Moreover macular pigment can be divided into two main constituent parts – lutein and zeaxanthin [7]. Another carotenoid mesozeaxanthin is the third component of the macular pigment and is only found in small amounts at the macula center. Lutein and zeaxanthin normally is consumed at ratio 5:1, and concentration of zeaxanthin prevails most at the macula center [16].

Lutein and zeaxanthin have differences in absorption spectrum. It is possible to differentiate their content in retina analyzing attenuation of light with different spectral content. We have developed a method to separate contributions of macular pigments into total absorption. The main task of present studies was to select proper spectral characteristics of LED light sources used in the method to reach the best selectivity and to carry out psychophysical tests of the experimental device.

II. Experimental

Two light emitting bars placed symmetrically to viewing direction served as stimuli. A pair of red and blue power LEDs was attached at each end of the bars. The bars had special light scattering surfaces, so the luminance of internally illuminated bar surfaces were practically constant (see more in [17]). One colour luminance of the bars was kept at constant level, and other colour luminance was changed by controlling the DC current. Luminance varied in the range 30-90 cd/m^2. Bars were placed at distance 1-1.5 m. Distance between bars was changed so the eccentricity of locally excited retina areas was 3-8 degree. Visible area of the bars was 15x30 mm. All other scene was a screen by neutral background oblique illuminated by an incandescent light. Luminance was calibrated by *Minolta CS-100A* chronometer. Emission spectra were measured by *Ocean Optics USB4000* spectrometer.

Subjects' task was to find the optimum flicker frequency, then to reach by two way staircase method the subjective sense of perceived minimum flicker. Two persons participated in the experiments. They had no ophthalmologic pathologies.

Subjects did that adjusting blue LED current. At least 40 measurement series were made to obtain statistically significant data.

Results were compared for the pairs with three different excitation wavelengths of blue LEDs. For that we used XR7090-AM-L1 type LEDs [18]. Royal blue LED with λ_{max} = 450 nm was chosen as a reference emission. Fig.2 shows the spectrum of this royal blue LED stimuli together with retina pigments absorption spectra. So far wavelength light stimuli red led with λ_{max} = 670 nm was used.

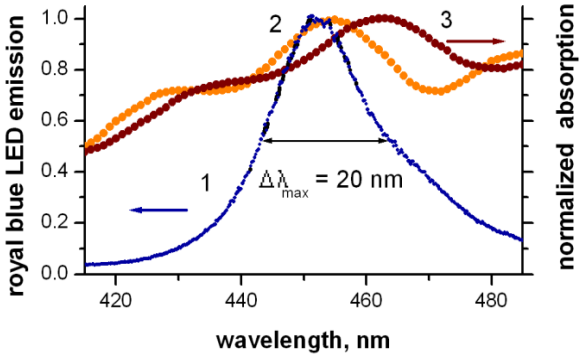

Fig. 2 Measured royal blue LED with λ_{max} = 450 nm emission halfwidth (curve 1) and normalized lutein (2) and zeaxanthin (3) pigment light attenuation (data from [7]).

III. Results and Discussion

We have measured emission spectra of the miniature LED sources of different providers. Characteristics of red LEDs have less significance, because their emission lies in spectral region, where the spectral selectivity plays no significant role. The most essential was the emission line halfwidth of blue LEDs. Using of LED with small halfwidth allows on a selective basis to adjust the position in spectrum, where absorption of lutein and zeaxanthin differs at highest extent. That concerns especially region 440-460 nm, where a number of pronounced maxima and minima can be found in lutein and zeaxanthin spectra, and also spectral region 490-510 nm, where pigment absorption has decay, but which is shifted by 10 nm for lutein and zeaxanthin. Three typical kinds of InGaAs blue LED emission spectrum lies within this emission wavelength: royal blue, blue and cyan. The measured halfwidth of royal blue LED (Fig.2) is around 20 nm at peak emission wavelength 445-450 nm (Fig. 3). Close to these diodes in emission spectra are blue LEDs with $\lambda_{max}\approx$460 nm. Cyan LEDs have peak wavelength 495-510 nm and much wider emission spectra. When processing measured LED emission data together with absorption quoted in literature, one can find a factor of merit of this psychophysical method – emission ratio $ER_{LU/ZE}$

$$ER_{LU/ZE} = \frac{[\Sigma s_1(\lambda) \times tr_{LU}(\lambda)]/[\Sigma s_1(\lambda) \times tr_{ZE}(\lambda)]}{[\Sigma s_2(\lambda) \times tr_{LU}(\lambda)]/[\Sigma s_2(\lambda) \times tr_{ZE}(\lambda)]}, \quad (1)$$

– where $s_1(\lambda)$ and $s_2(\lambda)$ are emission intensities of a pair of blue LED, $tr_{LU}(\lambda)$ and $tr_{ZE}(\lambda)$ are light transmission through lutein and zeaxanthin. Fig. 4 shows the blue spectrum range with depicted emission of two kind of diodes - royal blue (λ_{max} =450 nm – curve 1rb) and cyan (λ_{max} =502 nm – curve 2cy), and corresponding retina excitation by light passing through equal thickness of lutein and zeaxanthin pigments (curves 1lu, 1ze, 2lu, 2ze). Calculations give values for $ER_{LU/ZE}$ = 1.46 (royal blue – cyan pair) and 1:1.6 (royal blue – blue LED pair). We found such values of figure of merit sufficient for a psychophysical evaluation of the level of concentration and the ratio of lutein and zeaxanthin content.

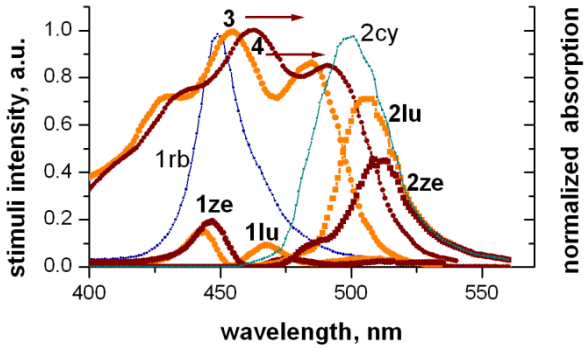

Fig. 3 Red-blue heterochromatic flicker photometry blue stimuli LEDs emission spectra – royal blue (1rb) and cyan (2cy). Curves (1lu and 2lu, 1ze and 2ze) show both LED excitation illumination passing through equal thickness of lutein or zeaxanthin to retina. Curves 3 and 4 show lutein and zeaxanthin pigment light attenuation.

Method was used to find isoluminance for red – royal blue and red – cyan spectral pairs at retina eccentricity 4-8 deg. At these conditions absorption in blue spectrum range mainly is determined by lutein and reveals itself for red – blue spectral pair. We found statistically significant difference in the spectral dependence over all measured eccentricity range (isoluminance was obtained for royal blue stimulus at stimuli luminance more than 30% higher than for cyan). In Fig.4 the dependence of eye sensitivity to blue at royal blue – red stimuli isoluminance conditions is depicted. Error bars correspond to confidence level 95%.

Increasing of eye sensitivity to excitation at royal blue wavelength and corresponding its increase with eccentricity agrees with dominant role of lutein as macula pigment at eccentricities measured experimentally.

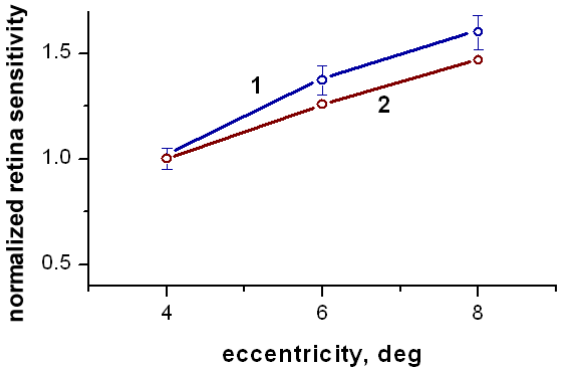

Fig. 4 Normalized retina sensitivity to blue stimuli radiation dependence on retinal eccentricity for red-blue heterochromatic flicker isoluminance condition (curve 1 – subject PP, 2 - MO). Blue stimuli wavelength 450 nm. Data are normalized to the eye sensitivity at eccentricity 4 deg.

Experiments were done without special nutrition and medicine intake [19]. Mentioned can seriously affect the body carotenoid balance and therefore the non-normalized experimental data. Further measures to calibrate method should be undertaken. Considerable improvement of the method would be the implementation of a narrow band light source. That allows selective to fix the absorption parameters of lutein and zeaxanthin. Here one can use the diode pumped solid state DPSS laser at wavelength 445 nm. LEDs have a relative broad distribution of λ_{max}, that influences the data uncertainty.

IV. Conclusions

Emission characteristics of LEDs available in market both for red and blue spectral range allow to design devices to detect changes of concentration of macular pigments lutein and zeaxanthin and to evaluate their specific contribution in total light extinction using psychophysical detection methods. The dispersion of measurement results confirms statistical significance of reasonable psychophysical measurement resolution. One can improve the method suitability replacing at least one LED excitation light source with portable DPSS laser (wavelength 445 nm).

Acknowledgment

Paulis Paulins has been supported by the European Social Fund within the project “Support for Doctoral Studies at University of Latvia”.

REFERENCES

1. Berendschotj TJM (2010) Imaging the Macular Pigment. In: Medical Retina – Focus on Retinal Imaging, Spaide RF. (Ed.),1st Edition:51–68; DOI: 10.1007/978-3-540-85540-8_6
2. Trieschmann M, van Kuijk FJGM, Alexander R, et al. (2008) Macular pigment in the human retina: histological evaluation of localization and distribution. Eye 22:132–137
3. Snider LI (2008) Evidence Supports New Approaches for Reducing the Risk of Macular Degeneration. Cont Educat Issue: November 2008:S1–S8; http://www.visioncareeducation.com/article.aspx?article=102340&a=om
4. Bartlett H, Howells O, Eperjesi F (2010) The role of macular pigment assessment in clinical practice: a review. Clin Exp Optom 93:300–308
5. Beatty S, Boulton M, Henson D, et al. (1999) Macular pigment and age related macular degeneration. Br J Ophthalmol 83:867–877; doi:10.1136/bjo.83.7.867
6. Howells O, Eperjesi F, Bartlett H (2011) Measuring macular pigment optical density in vivo: a review of techniques. Graefes Arch Clin Exp Ophthalmol 249:315–347; DOI: 10.1007/s00417-010-1577-5
7. van de Kraats J, Kanis MJ, Genders SW, van Norren D (2008) Lutein and zeaxanthin measured separately in the living human retina with fundus reflectometry. IOVS 49:5568–5573
8. Delori FC, Goger DG, Hammond BR, et. al. (2001) Macular pigment density measured by autofluorescence spectrometry: comparison with reflectometry and heterochromatic flicker photometry. J Opt Soc Am A Opt Image Sci Vis 18:1212–1230
9. de Kinkelder R, van der Veen RLP, Verbaak FD, et al. (2011) Macular pigment optical density measurements: evaluation of a device using heterochromatic flicker photometry. Eye 25:105–112; doi:10.1038/eye.2010.164
10. Anstis S, Cavanagh P (1983) A minimum motion technique for judging equiluminance. In: Colour vision: Psychophysics and physiology, London: Academic Press, 155–166
11. Mellerio J, Ahmadi-Lari S, van Kuijk FJGM, et al. (2002) A portable instrument for measuring macular pigment with central fixation. Cur Eye Res 25:37–47
12. Moreland JD (2004) Macular pigment assessment by motion photometry. Arch Biochem Biophys 430:143–148
13. Robson AG, Holder GE, Moreland JD, Kulikowski JJ (2006) Chromatic VEP assessment of human macular pigment: comparison with minimum motion and minimum flicker profiles. Vis Neurosci 23:275–283
14. http://www.brainvoyager.co.uk/catalog/metropsis/MP.html
15. van der Veen RLP, Berendschot TTJM, Hendrikse F, et al. (2009) A new desktop instrument for measuring macular pigment optical density based on a novel technique for setting flicker thresholds. Ophthal Physiol Opt 29:127–137
16. Thurnham DI (2007) Macular zeaxanthins and lutein – a review of dietary sources and bioavailability and some relationships with macular pigment optical density and age-related macular disease. Nutrition Res Rev 20:163–179
17. Ozolinsh M, Martín I, Lauva D, Karitans V (2011) Howard-Dolman test at different opponent colour stimuli. J Modern Opt 58:1749–1754
18. http://datasheet.octopart.com/XR7090-AM-L1-0001-Cree-datasheet-8398722.pdf ; Cree® XLamp® XR LED Data Sheet
19. Qin L, Bartlett H, Griffiths HR, et al. (2011) Macular pigment optical density is related to blood glutathione levels in healthy individuals. Invest Ophthalmol Vis Sci 52:5029–5033

Author: Maris Ozolinsh
Institute: Institute of Solid State Physics
Street: 8 Kengaraga
City: Riga
Country: Latvia
Email: ozoma@latnet.lv

The Analysis of Finger Photoplethysmographic Waveform in Healthy Volunteers and Diabetes Patients

K. Pilt, K. Meigas, K. Temitski, and M. Viigimaa

Tallinn University of Technology / Technomedicum / Department of Biomedical Engineering, Tallinn, Estonia

Abstract — **Six indices has been extracted from finger photoplethysmographic (PPG) signal to characterize the changes in PPG waveform, which are caused by the stiffness of blood vessels. The indices are measured from PPG signal at the locations of the second derivative signal peaks and normalized with PPG signal amplitude. The finger PPG signals from healthy volunteers and diabetes patients were filtered, two times differentiated, normalized in length, and averaged before the second derivative wave peaks were detected and the indices were calculated. The correlation relationships between normalized indices and age were found $r = -0.81$, $r = -0.85$, $r = 0.87$ for indices PPGa, PPGb, and PPGd respectively.**

Keywords — **Photoplethysmography, signal processing, arterial stiffness, second derivative method.**

I. Introduction

It is important to determine the cardiac risk of a patient in advance to prevent premature death [1]. The risk factors for cardiovascular diseases are associated with the increasing stiffness of the arterial wall. Among the other factors the arterial stiffness increases with age, hypertension, and diabetes mellitus [2]. It has been found that a decrease in small arterial compliance appears with the structural changes in the large arteries [3]. Photoplethysmographic (PPG) waveform analysis has been used as one method for the estimation of peripheral arterial stiffness [4].

Photoplethysmography is a non-invasive optical method that can be used to detect blood volume changes in smaller arteries and peripheral vessels at different body locations [5]. The PPG sensor consists of the light source, which is often red or infrared, and photodetector. Photodetector can be placed adjacent to the light source (reflection mode) or to the opposite side of the measured volume (transmission mode). The light is emitted from the LED to the skin and a small fraction of light intensity changes are received by a photodetector.

The AC component of the PPG signal is synchronous with the heart rate and depends on changes in the pulsatile pressure and pulsatile blood volume. Although the origins of the waveform components of the AC signal are not fully understood, it is generally accepted that they can provide valuable information about the cardiovascular system.

The AC component of the PPG signal is characterized by a systolic and diastolic part, which are separated by an inflection point or notch. Different parameters have been extracted from the PPG signal to estimate the cardiovascular risks [6]. The AC component waveform of the finger PPG signal can be analyzed by second derivative method [7]. The method is used to quantify the changes in the signal, which can be caused, besides the other factors, also by the stiffness changes in the microvascular bed. The SDPPG waveform amplitudes of the distinctive waves ‘a’, ‘b’, ‘c’, ‘d’, and ‘e’ were analyzed, which are situated in the systolic part of the heart cycle (Fig. 1). In this study also the sixth wave has been used and it is named as ‘f’.

The locations of the second derivative distinctive waves can be used to detect the characteristic points on the PPG signal waveform (Fig. 1). The aim of this study was to investigate the correlation between the PPG waveform parameters and age. In addition the parameters are compared between the healthy volunteers and diabetes patients.

II. Methods

The finger signal has been registered by using commercially available Envitec F-3222-12 clip sensor. It consists of LED and photodetector, which are placed opposite to each other. The photodetector registers the transmitted light intensity changes through the finger. The LED consists of two light sources, which are in the infrared and red spectrum region. In this study the infrared LED was used as it resulted with the PPG signal with higher signal-to-noise ratio. The Envitec sensor is connected to the lab-built PPG module.

The output signal from PPG module is digitalized with National Instruments PCI MIO-16-E1 data acquisition card with sampling frequency of 1 kHz. The PPG signal is monitored in online and recorded through program, which is written in LabVIEW environment [8]. The registered signals are analyzed in MATLAB environment.

The PPG signal was filtered with low- and high-pass FIR filters in order to separate DC component and high frequency noise. The cut-off frequencies for the low- and high-pass filters were selected as 30 Hz and 0.5 Hz, respectively. Both

Y. Dekhtyar et al. (Eds.): *International Symposium on Biomedical Engineering and Medical Physics*, IFMBE Proceedings 38, pp. 55–58, 2013.
DOI: 10.1007/978-3-642-34197-7_14

filters were designed using window method, with the Hamming window function, where the corresponding filter orders were chosen as 500 for the low-pass and 4000 for the high-pass filter.

As follows, the PPG signal was differentiated two times. The Smooth Noise Robust Differentiator (SNRD) was used, because this kind of differentiation suppresses also the higher frequencies [9]. In this study the fifth order of the SNRD was used. Higher frequency components need to be suppressed with FIR filter even after the SNRD.

In practice, biosignals such as PPG, which are related to the heart activity, are recurring but not periodic. This means that the harmonic components of the two consecutive recurrences of the PPG signal and its derivatives can be situated at different frequencies. In this study the low-pass filter was used with static edge-frequency. By this follows that certain numbers of harmonic components are passed and all the others are suppressed. The lengths of the PPG signal recurrences are then normalized to ensure that all the harmonic components are processed in the same way. All the recurrences of PPG signal were limited equally with six harmonical components, which have been found as optimal for the SDPPG signal analysis in the previous study.

Firstly, the PPG signal was resampled in such a way that one of the selected recurrence length was 1s, which corresponds to the pulse frequency of 1 Hz. The fundamental frequency is situated at 1 Hz and all the other components lay at the frequency multiples of 1Hz. Secondly, the signal was filtered with Parks-McClellan optimal equiripple FIR (PM) filter with edge frequency of 6Hz and width of transition-band was 1Hz. The maximum allowable errors, i.e. ripples, for the pass- and stop-band were set at 0.001. The resampling and filtering was also carried out with the second derivative of the PPG signal. Thirdly, the copy of selected recurrence was aligned with other normalized and filtered recurrences from this PPG signal. The 50 per cent level of the PPG signal raising front was used as the reference point for the alignment of the recurrences. Furthermore, the second derivative was moved according to the movement of the PPG signal recurrences. The resampling, filtering and aligning processes outlined above have been carried out separately for every recurrence in PPG signals. As a result the normalized and averaged PPG signal and its second derivative waveforms were calculated from processed recurrences. The six waves ‘a’, ‘b’, ‘c’, ‘d’ ‘e’, and ‘f’ were detected from normalized and averaged SDPPG signal (Fig. 1).

The values of the characteristic points were measured from the PPG signal in the locations of the SDPPG waves. The values of PPG signal characteristic points represent the difference in amplitude between detected point of a PPG waveform and the baseline and it is measured in arbitrary units. For the comparisons between the different signals the characteristic points are normalized with PPG signal amplitude (PPGmax-PPGmin). The normalized characteristic points are the indices, which are named respectively to the SDPPG waves as follows: PPGa, PPGb, PPGc, PPGd, PPGe, and PPGf.

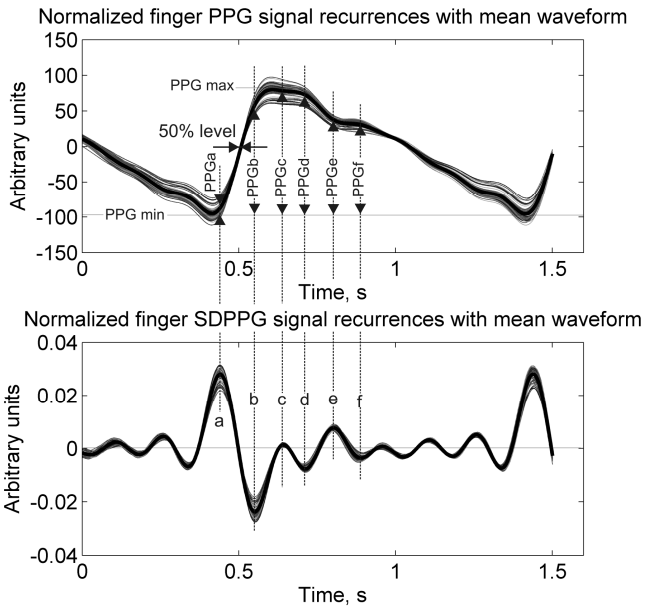

Fig. 1 Finger PPG signal and second derivative of PPG signal with detected peaks ‘a’, ‘b’, ‘c’, ‘d’, ‘e’, and ‘f’. Normalized finger PPG signal recurrences are given with thin gray lines and calculated mean waveform is given with bold line (upper figure). Normalized finger SDPPG signal recurrences are given with thin gray lines and calculated mean waveform is given with bold line (lower figure).

It is difficult to determine the stiffness of the blood vessels in the vascular bed of finger. In this study we used the Arteriograph (TensioMed, Budapest, Hungary) measurements as reference to determine the pulse wave velocity (PWV) in aorta. PWV is related to the stiffness of aorta through Moens-Korteweg equation. With the increased PWV in aorta we can assume that also the stiffness of the blood vessels in finger has been increased.

The PPG signal registration and measurements with Arteriograph were performed on 11 volunteers (10 males and 1 female with mean age of 36 year) and on 4 diabetic patients (all females with mean age of 52 year). All the healthy volunteers were minimally once per week dealing with some physical training or activity. The subject was in the supine position for at least 20 minutes before the measurements and this position also remained constant during the registration of the signals. The room temperature was kept constant at around 23 degrees Celsius during the experiments.

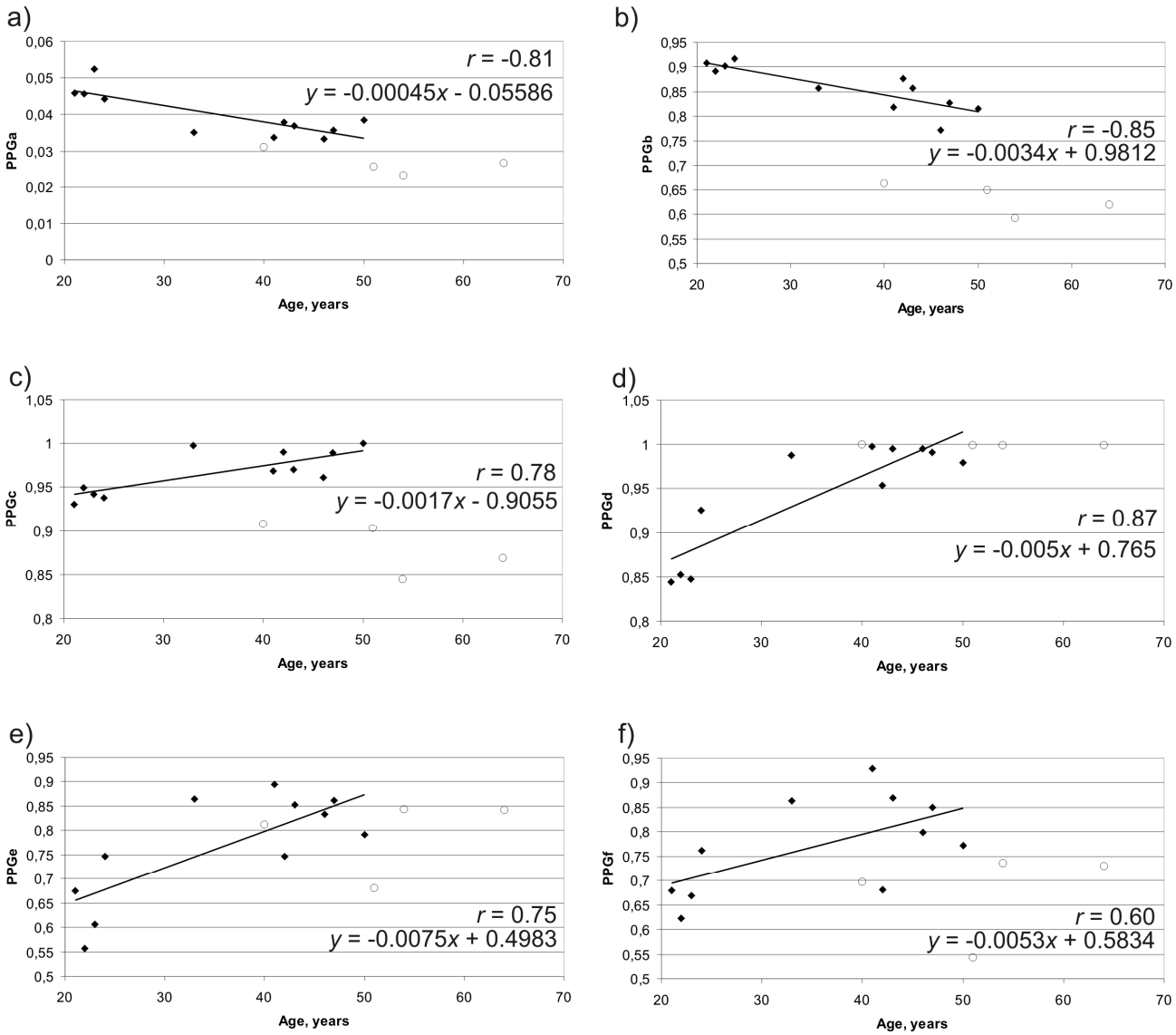

Fig. 2 The relationship between the normalized indices of PPG signal a) PPGa, b) PPGb, c) PPGc, d) PPGd, e) PPGe, f) PPGf and age with regression lines and correlation coefficients.

Firstly, the Arteriograph measurement was carried out and the average aortic PWV were calculated automatically by the TensioClinic (TensioMed, Budapest, Hungary) program. It was followed by the 1 minute long PPG signal registration from left hand index finger. The above described signal processing was carried out for every registered signal and the normalized indices PPGa, PPGb, PPGc, PPGd, PPGe, and PPGf were detected from the normalized and averaged PPG waveform.

III. Results

The average PWV for the healthy volunteers was 6.78 ± 0.80 m/s and for diabetes patients 12.23 ± 1.27 m/s. There was no significant correlation found between age and PWVs for healthy volunteers.

The relationships between normalized indices of the PPG signal and age are given in Fig. 2. The data points of healthy volunteers are given with diamonds and for diabetes

patients with circles. The normalized indices PPGa and PPGb have relatively high negative correlation to the age r = -0.81 and r = -0.85 respectively. The normalized indices PPGc, PPGd, PPGe, and PPGf have positive correlation to the age r = 0.78, r = 0.87, r = 0.75, and r = 0.60 respectively. The correlation coefficients were calculated by using only the data points from the healthy volunteers. For each index the regression model was proposed, which was, similarly to the correlation coefficients, calculated by using data points from healthy volunteers. The regression models for each index has been given in Fig. 2.

IV. Discussion

High positive correlation between age and aortic PWV has been reported before as the stiffness of the arteries increases with age [10]. Still the positive correlation was not found in this study. It can be due to the number and narrow age range of the volunteers, who participated in the study. In addition the volunteers were dealing regularly with physical activities, but each of them in a different level. Healthy volunteers had aortic PWVs below 8m/s. The diabetes patients had PWVs over 10 m/s, which are relatively high and it shows the stiffening of the aorta.

The relatively high correlation coefficients were found between normalized indices of finger PPG signal and age. The lowest correlation coefficients had indices PPGe and PPGf, which are characterizing the diastolic wave of the waveform. These results were unexpected as there are studies, which are showing a good correlation between the diastolic wave amplitude and age.

The highest correlation was found with PPGd index. It is visible that PPGd nears to one, while the age increases. The PPGd value can not rise above one as the parameter is normalized. With older subjects the PPGd index is limited and can not be used to characterize the stiffness of the vessels. In case of diabetes patients the PPGd value is one.

The PPGc is limited with one as well. It can be expected that in case of stiffer arteries the PPGc value is increased. In case of diabetes patients the PPGc value has been unexpectedly decreased. It can be assumed that PPGc may have parabolic relationship to the age and in case of older healthy persons the PPGc value starts to decrease.

There is negative correlation between PPGa and PPGb indices and age. The values of PPGa and PPGb are noticeably lower for the diabetes patients than for healthy volunteers. However for the PPGb the difference is highest.

It can be assumed that the changes in the index finger vascular bed, which are caused by the stiffening of the blood vessels, can be described with PPG waveform indices PPGa, PPGb, and with limitations PPGc and PPGd. However, the number of subjects with stiffer blood vessels has to be increased to make more general conclusions. In addition peripheral arteries oriented reference method should be used for the determination of the vessel stiffness.

Acknowledgment

This work was supported by the Estonian Science Foundation Grant no. 7506, by the Estonian targeted financing project SF0140027s07, and by the European Union through the European Regional Development Fund.

References

1. Khoshdel A R, Carney S L, Trevillian P, Gillies A (2010) Evaluation of arterial stiffness and pulse wave reflection for cardiovascular risk assessment in diabetic and non-diabetic kidney transplant recipients. Iran J Kidney Dis. 4:237-243
2. Kimoto E, Shoji T, Shinohara K, et al. (2006) Regional arterial stiffness in patients with type 2 diabetes and chronic kidney disease. J Am Soc Nephrol 17:2245-2252
3. Cohn J N, Duprez D A, Grandits G A (2005) Arterial elasticity as part of a comprehensive assessment of cardiovascular risk and drug treatment. Hypertension 46:217–220
4. Millasseau S C, Ritter J M, Takazawa K, Chowienczyk P J (2006) Contour analysis of the photoplethysmographic pulse measured at the finger. J Hypertens 24:1449-1456
5. Allen J (2007) Photoplethysmography and its applications in clinical physiological measurement. Physiol Meas 28:R1-R39
6. Korpas D, Hálek J, Dolezal L (2009) Parameters describing the pulse wave. Physiol Res. 58:473-479
7. Takazawa K, Tanaka N, Fujita M, Matsuoka O, Saiki T, Aikawa M, Tamura S, Ibukiyama C (1998) Assessment of vasoactive agents and vascular aging by the second derivative of photoplethysmogram waveform. Hypertension 32:365-370
8. Pilt K, Meigas K, Viigimaa M, Temitski K, Kaik J (2010) An experimental measurement complex for probable estimation of arterial stiffness, Conf. Proc. IEEE Eng. Med. Biol. Soc., Ann. Int. Conf. IEEE Eng. Med. and Biol. Soc., Buenos Aires, Argentina, 2010, pp 194-197
9. Holoborodko P (2008) Smooth noise robust differentiators at http://www.holoborodko.com/pavel/numerical-methods/numericalderivative/smooth-low-noisedifferentiators/
10. Ohmori K, Emura S, Takashima T (2000) Risk factors of atherosclerosis and aortic pulse wave velocity. Angiology 51:53-60

Author: Kristjan Pilt
Institute: Department of Biomedical Engineering
Street: Ehitajate tee 5
City: Tallinn, 19086
Country: Estonia
Email: kristjan.pilt@cb.ttu.ee

Measurement of Changes in Skin Conductance Evoked by Musical Stimuli

Edward Gorzelanczyk[1], Piotr Podlipniak[2], and Piotr Walecki[3]

[1] Institute of Psychology, Polish Academy of Sciences, Warsaw, Poland
[2] Adam Mickiewicz University, Poznan, Poland
[3] Jagiellonian University Medical College, Krakow, Poland

Abstract — **In order to determine objective components of the subjects, who is listening to music, emotional state, changes in skin conductance while exposure to musical stimuli was measured. The changes in skin conductance, demonstrating the activity of the autonomic nervous system, were treated here as a marker of affective response to presented musical stimuli. Reactions to different musical stimuli differ both in terms of the number of peaks, mean amplitude and the decay of reaction. "Mute" stimulus, in which the dynamics of musical stimulus is being gradually decreased, elicits in the subjects the strongest response, characterized both by the greatest number of peaks and the highest average amplitude of responses. The weakest psychogalvanic response, with the lowest number of peaks and the average amplitude of response, is evoked by a "slowing down" stimulus, in which the pace of musical stimuli is gradually decreasing. The stimulus combining the features of "mute" and "slowing down" incentives, in which both the dynamics and the pace are gradually decreasing, causes a very weak, galvanic skin response in comparison to other stimuli, both in terms of the number of peaks and the average amplitude of responses. It is possible that a gradual decrease in tempo, with (or without) a gradual mute, acts soothing to the subjects and causes a reduction in the sympathetic nervous system activity.**

Keywords — **skin conductance, musical stimuli, autonomic nervous system.**

I. Introduction

Music is often used to influence emotions of a listener in advertisements or movies (Cohen, 2000). Singing, being probably the oldest form of musical expression (Gorzelańczyk, 2003; Gorzelańczyk and Podlipniak, 2006), is a natural way of calming children. However it can also be a demonstration of force in excessive emotional disclosure during musical concerts or sport events. The relationship of music with emotions can be seen in almost all aspects of its use. Therefore, understanding the relationship between music and emotional reaction induced by it would create the possibility to use music as an effective stimulus for specific emotional states. Intuitively recognized relationship between music and emotions is not confirmed by reliable scientific evidence. It was found that listening to music involves affective reaction (Becker, 2004). Different properties of musical waveforms can cause different emotional response. A specific affective reaction may indicate the occurrence of certain characteristics of the listener's emotional state (Juslin and Sloboda, 2001). On the other hand, evaluation of the emotional impact of music is dependent on individual experience and culture (Becker, 2004). The results of the research indicate that the features of music such as speed and sound pressure level (SPL) are used in a similar manner and in similar emotional contexts in different cultures (Balkwill and Thompson, 2004).

II. Objectives

The aim of the study is to determine whether the tempo and intensity of sounds in music stimuli evoke skin conductance change. The observation of such similarities could indicate the existence of universal human patterns of affective response to specific features of sound. To determine the components of the music listener's emotional state in this study changes in the conductivity of skin were measured. The changes in skin conductance, showing activity of the autonomic nervous system, were treated as a marker of affective responses to musical stimuli.

III. Materials and methods

The study was conducted in 54 subjects. The age of the individuals was between 19-22 years. In the test eight different music waveforms were presented. During the presentation of musical stimuli electrical conductivity of skin was measured. It is assumed that the value of electrical conductivity (EC) is related to the autonomic nervous system activity while listening to musical stimuli.

The electrodermal reaction for each musical stimulus was described by three variables read and calculated from the graph of skin conductance changes in time:

- the number of peaks - the number of local maxima, calculated for the time window 20 ms;
- the average amplitude of reaction – the quotient of the total amplitude for a stimulus and the number of peaks;

Y. Dekhtyar et al. (Eds.): *International Symposium on Biomedical Engineering and Medical Physics*, IFMBE Proceedings 38, pp. 59–62, 2013.
DOI: 10.1007/978-3-642-34197-7_15

- the decay of reaction - the local maximum after 50 ms of its occurrence.

To measure the electrical conductivity of skin psychogalvanometer UNISAR v.03 with the original software was used. This device allows recording of skin conductance at a frequency of 10 times per second. During the measurement disposable electrodes were used in the ECG measurement. To calculate the number of peaks, mean amplitude of response and its decay specially developed for this research software was used.

In order to test the statistical significance of differences in electrodermal reaction for eight musical stimuli the analysis of variance was performed. The measurements, used repeatedly for three variables, were: the number of peaks, the mean amplitude of reaction, and the decay of reaction. The analysis of post-hoc Fischer's LSD test (Least Significant Difference) was performed.

Seven stimuli were prepared in musical notation and saved as MIDI files. The first musical stimulus is the first part of the symphony A major, Mozart's KV-114 in an arrangement for piano (called *basic theme*). The second stimulus is a modified version of the first theme, in which the tempo was gradually increased (*accelerando*). In the third stimulus slowing down (*diminuendo*) was applied progressively. In the next two stimuli the dynamics of the music (sound intensity) was changed and it was gradually increasing into the fourth stimulus (*crescendo*) and decreasing (*decrescendo*) in the fifth stimulus. In the sixth and the seventh musical stimuli the changes in time and dynamic were made. The sixth musical stimulus is getting louder and faster and the seventh musical stimulus is becoming more and more quiet and slow. The eighth musical stimulus is a part of Mass Amando Ivancic.

A simplified description of the stimuli is presented in Table 1.

Table 1 Musical stimuli.

Changes	id	Description	
	1	*basic theme* - symphony A major, Mozart's KV-114	
time	2	*accelerando*	acceleration
	3	*diminuendo*	slowing down
dynamic	4	*crescendo*	volume up
	5	*decrescendo*	mute
dynamic and time	6	*accelerando* & *crescendo*	acceleration and volume up
	7	*diminuendo* & *decrescendo*	slowing down and mute
	8	Mass Amando Ivancic	

IV. Results

In Tables 2 and 3 the results of the analysis of variance with repeated measurements were presented.

Since the analysis of variance F tests indicated the existence of statistically significant differences between means for all variables, post-hoc tests were performed to determine which mean differences are statistically significant (Tables 4-6).

The largest number of peaks were found when subjects were listening to a "mute" (*decrescendo*) musical stimulus, which significantly differed from the response to a "volume up" (*crescendo*), "acceleration and mute" (*accelerando & crescendo*) musical stimulus and the response to a part of the mass. The second one, in terms of the number of peaks, is a reaction to a *part of the mass*, which differs significantly from responses to the *basic theme*, "slowing down" (*diminuendo*), and "slowing down and mute" (*diminuendo & decrescendo*) musical stimuli. The stimulus which had the smallest number of peaks is the "slowing down" (*diminuendo*) stimulus and the *basic theme* stimulus. "Volume up" (*crescendo*) musical stimulus had a greater number of peaks compared to the number of peaks when listening to the *basic theme* and "slowing down" musical stimulus, but they were not significantly statistically different. The reaction to *the part of the mass* differed significantly from the response to the other stimuli such as: *diminuendo*, *decrescendo & diminuendo*, and the *basic theme*, which caused the least number of peaks . As for the number of peaks, one of the highest average amplitude is observed in response to *decrescendo*, which is significantly different from the responses to *diminuendo*, *diminuendo*, *decrescendo & diminuendo*. The highest average amplitude was found when listening to *a part of the mass*, which is not only statistically significantly different from the responses to *decrescendo & crescendo*. In contrast to the number of peaks the high levels of average amplitude of response were found for the *basic theme*. The highest value of decay of reaction was observed for *basic theme* and the second highest value of decay - for *accelerando*, but the difference between this reaction and the reaction to other music stimuli are not statistically significant. The third highest value of decay was found for *a part of the mass*. The higher was the value of the decay of reaction, the slower was the decay rate.

Table 2 Multivariate Tests of Significance Sigma-restricted parameterization. Effective hypothesis decomposition.

	Test	Value	F	Effect df	Error df	p
Intercept	Wilks	0.026	4861.2	3	389.0	0.0000
Musical stimuli	Wilks	0.899	2.006	21	1117.5	0.0046

Table 3 Test of SS Whole Model vs. SS Residual.

	Multiple R	Multiple R2	Adjusted R2	SS Model	df Model	MS Model	SS Residual	df Residual	MS Residual	F	p
peaks	0.2099	0.0441	0.026945	155.9	7	22.27	3382.0	391	8.650	2.5744	**0.0132**
amplitude	0.2463	0.0607	0.043840	0.139	7	0.02	2.2	391	0.006	3.6069	**0.0009**
decay	0.1267	0.0161	-0.001487	7720.7	7	1102.9	471016.1	391	1204.6	0.9156	0.4942

Table 4 Probabilities for Post Hoc Tests. LSD test, variable: **peaks**. Error: Between MS = 8.6497, df = 391.00.

	Musical stimulus	{1} 3.3396	{2} 3.9184	{3} 3.4792	{4} 4.2745	{5} 5.1961	{6} 4.2449	{7} 3.6000	{8} 4.8750
1	basic theme		0.3214	0.8119	0.1059	**0.0014**	0.1212	0.6536	**0.0091**
2	accelerando	0.3216		0.4626	0.5453	**0.0305**	0.5829	0.5905	0.1100
3	diminuendo	0.8119	0.4626		0.1795	**0.0039**	0.2006	0.8390	**0.0206**
4	crescendo	0.1059	0.5453	0.1795		0.1144	0.9599	0.2499	0.3106
5	decrescendo	**0.0014**	**0.0305**	**0.0039**	0.1144		0.1067	**0.0067**	0.5875
6	accelerando & crescendo	0.1212	0.5829	0.2006	0.9599	0.1067		0.2760	0.2921
7	diminuendo & decrescendo	0.6536	0.5905	0.8390	0.2499	**0.0067**	0.2760		**0.0325**
8	Mass Amando Ivancic	**0.0091**	0.1100	**0.0206**	0.3106	0.5875	0.2921	**0.0325**	

Table 5 Probabilities for Post Hoc Tests. LSD test, variable: **amplitude**. Error: Between MS = 0.00551, df = 391.00.

	Musical stimulus	{1} 0.13292	{2} 0.13351	{3} 0.11576	{4} 0.13831	{5} 0.15834	{6} 0.12063	{7} 0.10937	{8} 0.16719
1	basic theme		0.9679	0.2465	0.7110	0.0815	0.4039	0.1084	**0.0210**
2	accelerando	0.9679		0.2395	0.7464	0.0952	0.3908	0.1065	**0.0260**
3	diminuendo	0.2465	0.2395		0.1315	**0.0046**	0.7467	0.6706	**0.0008**
4	crescendo	0.7110	0.7464	0.1315		0.1738	0.2342	0.0508	0.0538
5	decrescendo	0.0815	0.0952	**0.0046**	0.1738		**0.0115**	**0.0010**	0.5537
6	accelerando & crescendo	0.4039	0.3908	0.7467	0.2342	**0.0115**		0.4510	**0.0022**
7	diminuendo & decrescendo	0.1084	0.1065	0.6706	0.0508	**0.0010**	0.4510		**0.0001**
8	Mass Amando Ivancic	**0.0210**	**0.0260**	**0.0008**	0.0538	0.5537	**0.0022**	**0.0001**	

Table 6 Probabilities for Post Hoc Tests. LSD test, variable: **decay**. Error: Between MS = 1204.6, df = 391.00.

	Musical stimulus	{1} 215.81	{2} 208.74	{3} 204.13	{4} 204.38	{5} 201.92	{6} 205.11	{7} 202.31	{8} 209.17
1	basic theme		0.3048	0.0922	0.0941	**0.0420**	0.1207	**0.0493**	0.3379
2	accelerando	0.3048		0.5137	0.5304	0.3263	0.6049	0.3575	0.9511
3	diminuendo	0.0922	0.5137		0.9717	0.7510	0.8899	0.7954	0.4773
4	crescendo	0.0941	0.5304	0.9717		0.7202	0.9164	0.7649	0.4928
5	decrescendo	**0.0420**	0.3263	0.7510	0.7202		0.6459	0.9543	0.2992
6	accelerando & crescendo	0.1207	0.6049	0.8899	0.9164	0.6459		0.6888	0.5647
7	diminuendo & decrescendo	**0.0493**	0.3575	0.7954	0.7649	0.9543	0.6888		0.3287
8	Mass Amando Ivancic	0.3379	0.9511	0.4773	0.4928	0.2992	0.5647	0.3287	

V. Discussion

The results of this study indicate that physiological responses to each musical stimulus vary in the number of peaks, the average amplitude of reaction and the decay of reaction.

The “mute” musical stimulus, in which the dynamics of the music progressively decreased, produces largest response in subjects, characterized by the greatest number of peaks and the highest average amplitude of response. The lowest psychogalvanic reaction – the lowest number of peaks, and the lowest average amplitude response, were in the "slowing down" musical stimulus, in which the tempo is gradually released. A musical stimulus, combining features of both of these incentives, called "mute and slowing down", in which both dynamics and tempo are gradually reduced, produces, in comparison to other stimuli, a small number of peaks, and low average amplitude of response.

It is possible that gradual slowing of tempo with a gradual mute calms the subjects, thus reducing the activation of the sympathetic nervous system (Gorzelańczyk et al, 2012). This observation is consistent with the view that slow tempo of music is one of the characteristics of low-intensity emotions such as sorrow (Balkwill and Thompson, 1999; Juslin and Sloboda, 2001). Slow tempo is also a universal feature of the biological function of calming children. The use of music for these purposes is treated as a possible cause of the evolutionary selection of human musical ability (Dissanayake, 2008, 2009; Falk, 2009). Association of slowing down in music and the reduction in activation of the sympathetic nervous system may have older evolutionary reasons related to sound communication and motor expression of mammals (Dissanayake, 2008). The change of tempo is an important element of the universal form of emotional communication characteristic of a large group of mammals called expressive phrasing (Merker, 2003). Tempo is expressed as the integral component of motoricity and it has also played an important role in the evolution of language (Gorzelańczyk, 2003; Falk, 2009).

VI. Conclusions

A clear response of the sympathetic nervous system to a certain musical stimulus does not mean that it is always related to emotions, or that it is a part of the conscious experience of subjects related to listening to these stimuli. Therefore, future studies should use the tools to identify the content of the subjects’ experience when listening to stimuli.

References

1. Balkwill L-L, Thompson W F, Matsunaga R (2004) Recognition of emotion in Japanese, Western, and Hindustani music by Japanese listeners. Japanese Psychological Research 46(4): 337-349.
2. Becker J (2004) Deep Listeners: Music, Emotion, and Trancing. Indiana University Press, Bloomington.
3. Cohen A J (2000) Development of Tonality Induction: Plasticity, Exposure and Training. Music Perception 17: 437-459.
4. Dissanayake E (2008) If Music Is The Food of Love, what about Survival and Reproductive Success? Musicae Scientiae Special issue: 169-195.
5. Falk D (2009) Finding Our Tongues: Mothers, Infants and the Origin of Language. Basic Books, New York.
6. Gorzelańczyk E J (2003) Neurobiology and the Evolution of Human Culture and Language. Acta Neuropsychologica 1(4): 436-448.
7. Gorzelańczyk E J, Podlipniak P (2006) Poszukiwanie uniwersalnych mechanizmów przetwarzania muzyki (Searching for universal processing mechanisms of the music). In: Człowiek – jego bioelektroniczna konstrukcja a percepcja muzyki. Cieszyn (in polish).
8. Gorzelańczyk E J, Podlipniak P, Walecki P. (2012) The Skin Conductivity Changes as a Marker for the Affective Response to Tonal Music Stimuli, Conference Proceedings Book International Psychological Applications Conference and Trends, InPACT.
9. Juslin P N, Sloboda J A (ed.) (2001) Music and Emotion. Theory and research Oxford: Oxford University Press.
10. Merker B (2000) Synchronous chorusing and human Origins. In: Walilin N L, Merker B, Brown S (ed.) The origins of music, London, MIT Press, pp. 315-327.

Use macro [author address] to enter the address of the corresponding author:

Author:	Piotr Podlipniak
Institute:	Adam Mickiewicz University
Street:	Wieniawskiego 1
City:	Poznan
Country:	Poland
Email:	podlip@poczta.onet.pl

Evaluation of Atrophic Edentulous Maxillary Alveolar Bone with Cone Beam Computed Tomography (CBCT) in Postmenopausal Women

L. Neimane[1], A. Skagers[2], and A. Slaidina[3]

[1] Department of Dental and Maxillofacial Diagnostic Radiology, RSU Institute of Stomatology, Riga, Latvia
[2] Department of Dental and Maxillofacial Surgery, RSU Institute of Stomatology, Riga, Latvia
[3] Department Prosthodontics, RSU Institute of Stomatology, Riga, Latvia

Abstract — **This radiological study was designed to compare atrophic alveolar bone of maxilla among female patient in postmenopausal age with CBCT. Patients were divided in three groups considering T–score of osteodensitometric analysis. All patients were completely edentulous in maxilla and had their maxillofacial area scanned with CBCT. The results of the study indicated that osteoporosis group had a higher alveolar bone in maxilla, but least bone density. This study suggests that it CBCT measurements correlate with osteodensitometric analysis data.**

Keywords — **CBCT, bone density, osteoporosis, post-menopausal.**

I. Introduction

In cases of dental implant surgery quality and quantity of the bone is essential. The amount of alveolar bone alters during lifetime. Relevant atrophy of alveolar bone takes place after tooth extraction. Atrophy of alveolar bone is observed also in cases of paradontosis. Depending on severity of paradontosis, duration and treatment the degree of atrophy is different. The bone quality depends on different metabolic and hormonal factors. Quality of whole skeleton depends on calcium and phosphate metabolism. Similarly whole skeleton is influenced by ostoporotic disease, which is characterized with reduced bone density and defects in microarchitectonic of the bone. Due to these influences strength of the bone reduces [1;2]. Also bone of the jaws and alveolar processes are influenced by the generalized onset of osteoporosis. However, literature data are controversial in evaluation of the osteoporosis influence on implantation. Also diagnosis of osteoporosis if facial skeleton using dental panoramic method is unequivocal, where mandibular bone is investigated [3;4;5]. The investigation of reduced density maxillary bone with CBCT has not been explored. In this study atrophic maxillary alveolar bone of postmenopauseal female was investigated with CBCT.

II. Materials and Methods

There were thirty one female patients included in this study. They were previously investigated with dual energy x-ray absorptiometry (DEXA) to measure bone density in lumbal vertebra and hip bone. Considering results of DEXA measurements patients were divided in to three groups: norm, osteopenic and osteoporosis group.

All patients were completely edentulous in the maxilla and they were examined with CBCT before implant therapy. Radiological examinations were done with I – CAT Next Generation (Imaging Science, USA). There was standardized protocol used for all patients: field of view 13 cm, 0.3 vox. The data were processed with I - CAT Exam Vision program.

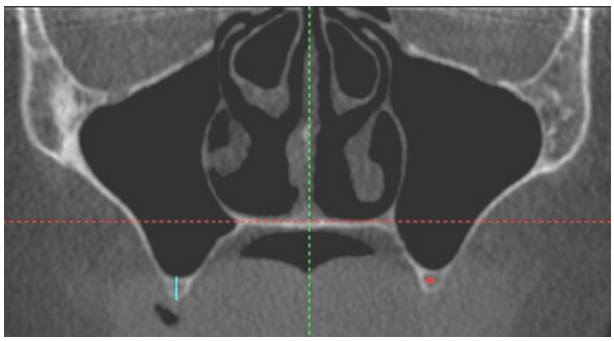

Fig. 1 Positioning and measuring - in left side measuring of density and in right side measuring of heights of maxillary alveolar bone.

The alveolar bone was measured in both sides of maxilla after reconstruction in coronal view. The scans were positioned so the hard palate is parallel to the floor and facial midline visualizing in through nasal spine and middle of nasaofrontal suture and it is perpendicular to the floor. In axial view the, to avoid rotation, through intermaxillar suture were positioned to be parallel to the sagittal plane. The maxillary bone was examined in the view were also maxillary sinus ostia was seen. In alveolar bone it

Y. Dekhtyar et al. (Eds.): *International Symposium on Biomedical Engineering and Medical Physics*, IFMBE Proceedings 38, pp. 63–65, 2013.
DOI: 10.1007/978-3-642-34197-7_16

correspond the region of second premolar and first molar. The alveolar bone height (mm) and density (HU) was measured (Fig. 1). The density measurement field was 1 square milimiter.

The results were summarized and analyzed with Microsoft Office Excel 2007. The descriptive statistics were used and Bartell's test for equal variance and one-way ANOVA test were used.

III. Results

There were eleven (35%) patients in norm group, nine (30%) in osteopenic and 11 (35%) in osteoporotic group. The average age in norm group was 68.54 ± SD 10, osteopenic 74.22 ± SD 8.02 and osteoporotic 73.09 ± SD 7.14.

The alveolar bone heights in millimeters were measures in both sides of maxillary alveolar bone. The average measurement of all three groups is shown in Table 1. There was no statistically significant difference between groups found in bone heights measurements.

Table 1 The height of edentulous maxillary alveolar bone (mm).

	Right	Left
Norm group	5.38 ± SD 3.72	4.71 ± SD 3.85
Osteopenic group	5.38 ± SD 3.10	6.49 ± SD 3.80
Osteoporotic group	6.50 ± SD 2.71	6.32 ± SD 2.85

The alveolar bone density was measured in the same sites as height. The average bone density of all three groups is shown in Table 2. There was no statistically significant difference between groups found in bone density measurements. However, there is tendency that complies with DEXA analysis of the groups.

Table 2 The radiodensitometry of edentulous maxillary alveolar bone (HU).

	Right	Left
Norm group	142.45 ± SD 224.78	200.73 ± SD 346.68
Osteopenic group	89.00 ± SD 185.42	130.22 ± SD 251.69
Osteoporotic group	38.55 ± SD 211.96	28.72 ± SD 116.92

IV. Discussion

This was radiological study to investigate if there is difference in maxillary alveolar bone height and density among postmenopausal female patients. No patient history, medications used or timing and reason of teeth loss were evaluated.

The alveolar bone is subjected to changes whole life. The changes and atrophy occur by physiological reasons that in some cases are intensified by pathological reasons. The physiological atrophy of alveolar bone is more often met in adults after 40 years of age [6]. Reich et al. found statistically significant difference between age of patient and atrophy of posterior alveolar maxillary bone. Atrophy of posterior maxillary alveolar bone is influenced also by maxillary sinus pneumatization. The pneumatization takes place whole life. Marked pneumatization is seen after molar tooth loss [7].

In this study the bone heights between groups did not differ significantly. However, there were little bit higher scores for osteoporotic and osteopenic groups. It could be speculated that the reason for that was different timing and reasons for teeth loss. If patient would have had paradontosis than, probably, the bone height would be less. Also coarse extraction manner could have influenced bone loss. In this study patient history was not taken in account.

The bone density is influenced by osteoporotic activity in the body. Osteoporosis more often is observed in female patients in postmenopausal age. It is accepted that osteoporosis is systemic condition which is characterized by loss of bone mass and mineral density and increased risk of bone fracture. However, the relationship between skeletal and maxillary bone mass is limited [8]. Bornstein et al. suggested that for implant placement in maxillary atrophic bone clinical local investigation has higher informative value then detected bone density of peripheral bones. There are controversial and discrepant data about detection of osteoporosis changes in maxillary and mandibular bones. Other authors have found that there is reduced bone density in posterior segments of maxillary alveolar bone [9].

The CBCT scans are commonly performed before dental implantation. This investigation is of high value if patient have atrophic alveolar bone. The individual anatomical variation and amount of the bone can be seen. The measurement of the bone density with CBCT method has comparative not exact value due to the image acquisition technique [10;11;12]. There are studies done and more are on the way to develop algorithm to attain exact HU measures with CBCT [13;14].

In this study there were no statistically significant difference found between groups in bone density measurements. However, there were positive tendency, supporting DEXA results that osteoporotic group had lowest mean value and norm group highest. Considering that the bone height was the lowest in norm group and supposing that reason for that is timing of teeth extraction it could be concluded that influence of reduced bone density in peripheral bones correlates with bone density of the jaw

bones. In this study there was limited number of subjects investigated. More research is needed to support CBCT use in alveolar bone density detection. With the development of the algorithm for precise HU values obtained by CBCT the problem of detecting exact alveolar bone density will be solved.

V. Conclusion

1. The highest maxillary bone optical density is in group with normal T score, detected by osteodensitometry.
2. The bone density detected with CBCT correlate with osteodensitometric data of peripheral bones.
3. The height of the maxillary alveolar bone does not correlate with the maxillary bone density and DEXA results of peripheral bones.
4. This is preliminary study and more research is needed to evaluate CBCT as bone density measurement tool in facial region.

References

1. Peck WA, Burkhard P, Christensen C (1993) Consensus decelopment Conference: diagnosis, prophylaxis and treatment of osteoporosis. Am J Med. 94:645-50.
2. NIH Consensus Development Panel on Osteoporosis prevention, diagnosis and theraphy. (2001) JAMA 285: 785-795.
3. Klementti E, Kolmakov S, Kroger H (1994) Pantomography in the assesment of the osteoporosis risk group. Scand J Dent Res. 102:68-72.
4. Horner K, Devlin H, Harvey L (2002) Detecting patients with low skeletal bone mass. J Dent. 30 (4): 171-5.
5. Ozola B, Slaidina A, Laurina L.et al. (2011) The influence of bone mineral density and bony mass index on resorption of edentulous jaws. Stomatologija. 13:19-24.
6. Reich K, Huber C, Lippnig W et al. (2011) Atrophy of the residual alveolar ridge following tooth loss in a historical population. Oral Dis. 17: 33-44.
7. Sharan A, Madjar D (2008) Maxillary sinus pneumatization following extractions: a radiographic study. Int J Oral Maxillofac Implants. 23:48-56.
8. Bornstein MM, Cionica N, Mombelli A (2009) Systemic conditions and treatments as risk for implant therapy. Int J Oral Maxillofac Implants. 24: 12-27.
9. Rosen CJ, Glowacki J, Bilezikian JP (1999) The aging skeleton. Academic Press, California.
10. Armstrong RT. (2006) Acceptability of cone beam ct vs. multi-detector CT for 3D Anatomic model construction. AAOMS. 64:37.
11. Miles DA, Danforth RA. (2007) A clinician's guide to understanding cone beam volumetric imaging (CBVI). Available from www.ineedce.com
12. Lee S, Gantes B, Riggs M et al. (2007) Bone density assessments of dental implant sites: 3. Bone quality evaluation during osteotomy and implant placement. Int J Oral Maxillofac Implants. 22: 208–212.
13. Mah P, Reeves TE, McDavid WD (2010) Deriving Hounsfield units using grey levels in cone beam computed tomography. Dentomaxillofacial Radiology. 39: 323–335.
14. Vannier MW (2003) Craniofacial computed tomography scanning: technology, applications and future trends. Orthod Craniofac Res. 6: 23–30.

Laura Neimane
RSU Institute of Stomatology
Dzirciema iela 20
Riga, LV 1007
Latvia
laura.neimane@inbox.lv

Comparison of Microsphere Models for Calculation of Backscattered Ultrasound Spectra

R. Jurkonis and A. Lukoševičius

Kaunas University of Technology / Biomedical Engineering Institute, Kaunas, Lithuania

Abstract — **It was assumed that commercially available clinical ultrasound diagnostic systems could be modified to provide additional information about tissue microstructure after additional spectral analysis of backscattered ultrasound signals. Proper processing of echoscopy signals would enable diagnostic systems for quantitative characterization of tissues at sub-resolution level. The possibilities and limitations of this approach were considered theoretically by calculation of spectra of back scattered ultrasound waves from tissue models which are taking into account size and acoustic properties of cells - the main scattering centers of ultrasound. It is assumed that cells in tissue could be simulated as microspheres submerged in fluid. In the present paper the empirical and analytical theoretical models were adopted and compared. Using two models (F.L. Lizzi et .al. 1997; and G.E. Trahey et .al. 1998) spectra were calculated for viable cell of different sizes in the frequency range 5-15 MHz. Comparison of simulation results have shown, that Faran-Trahey model has possibility to take into consideration scatterer elasticity (Poisson's ratio), while the Lizzi model - does not. It was shown that calculation approaches for diffraction effects are different, but comparable by results. Theoretical calculations have shown good relation of backscattering spectra slope with scattering microsphere diameter for both models analyzed.**

Keywords — **ultrasound, backscattered spectra, tissue characterization, Faran's theory, spherical scatterers.**

I. Introduction

Ultrasound B-scan visualization is the common mean for representation of biological tissue structure. B-scan image presents amplitudes of reflected waves from tissue inhomogeneities. But spectral information contained in backscattered ultrasound signals usually are not available from conventional ultrasound B-scan diagnostic systems, therefore open ultrasound systems had been developed [1, 2]. It has been found that ultrasound backscattered spectrum methods [3, 4] could be used for development of quantitative tissue characterization systems [5, 6, 7]. Theoretical method for estimation of random media structural properties was developed in [8] while experimental verification of approach is reported with viable biological cells [9, 10, 11].

It was assumed that commercially available clinical ultrasound diagnostic systems could be modified to provide additional information about tissue structure after additional analysis of non-detected (radio-frequency (RF)) backscattered signals. Our trial study [12] on analysis of ultrasound RF signals from the phantom have proved that spectral information of backscattered signals could give qualitatively new information about structure of the phantom. Particularly the non-conventional parametric maps were presented using distribution of mean instantaneous frequency and bandwidth of radiofrequency backscattered signal showing increased resolution of a phantom structure.

The remaining problem is a development of tissue characterization method taking into account size and acoustic properties of cells, which are the main scattering centers in biological tissues [8]. We consider the theoretical possibilities and limitations of tissue characterization in sub-resolution level since there are no reports comparing available models of ultrasound spectra backscattered by microspheres.

The aim of present paper is to adopt and compare available theoretical calculations of backscattered ultrasound spectra for modeling of tissue microstructure.

II. Models of Backscattered Ultrasound Spectra for Microspheres

A. Empirical Model

Using empirical approach the total ultrasound power scattered from small targets is determined by relationship between the diameter d of target and the wavelength λ of the wave. For targets that are much smaller than a wavelength ($d<<\lambda$), power function of scattered ultrasound is $W_s \sim d^6/\lambda^4 \sim d^6 f^4$. This frequency dependency is often referred as Rayleigh scattering [13]. Cobbold et al [14] has introduced the normalized size of scatterer $ka=a\omega/c$, a – is scatterer radius ($d/2$), ω – angular frequency, c – speed of ultrasound. In [14] is shown the monotonically increasing frequency dependence of backscattering when ka is from 0.01 to 0.5, which is described as Rayleigh scattering (by power low f^4). The transition from Rayleigh scattering (i.e. higher slope) zone to more complex resonant scattering is occurring from around ka=0.5. This transition zone is of present research interest.

Y. Dekhtyar et al. (Eds.): *International Symposium on Biomedical Engineering and Medical Physics*, IFMBE Proceedings 38, pp. 66–69, 2013.
DOI: 10.1007/978-3-642-34197-7_17

Theoretical framework for spectrum analysis relates backscattered spectra with morphology of tissue [15, 16]. The tissue sample is treated as an ensemble of weak scatterers (Born approximation). It is assumed also that scatterers are statistically homogeneously distributed in focal volume of diagnostic transducer. Power spectrum backscattered by the ensemble of scatterers was expressed empirically by F.L. Lizzi et. al. [5]:

$$S(f)=185Lq^2a^6CQ^2f^4\frac{e^{-(3.487fa)^2}}{1+2.66(qfa)^2}; \quad (1)$$

where: $L=cT/2$ – is the distance corresponding to the width of Hamming window applied for signals from region of interest, T – is the time duration of window; $q=A/R$ – is normalized transducer geometry parameter, A – radius of transducer aperture, R – is the distance of region of interest from transducer, a - is the radius of scatterer, C – effective concentration of scatterers, $Q=(Z-Z_0)/Z_0$ – relative acoustic impedance of scatterer with respect to surrounding (Z_0).

B. Analytical Model

The second - analytical approach is adapted from Faran's theory developed for microsphere scatterers [17]. Model of the sound scattering spectra in fluid by isotropic spherical scatterers of solid materials was solved by Faran and corrected by Hickling [18]. The complex amplitude of pressure in the scattered wave at large distances from the microsphere could be calculated [19]:

$$P_s(t,k_3,\Theta)= \quad (2)$$
$$=\frac{P_0a}{2r}\left[\frac{2}{k_3a}\sum_{n=0}^{\infty}(-1)^n(2n+1)\sin(\eta_n)e^{-j\eta_n}P_n(\cos\theta)\right]e^{-jk_3(c_3t-r)}$$

here: P_0 – is the incident pressure, a – sphere radius, c_3 and k_3 –sound speed and the wave number in surrounding fluid accordingly, Θ - observation angle, r – distance between sphere and observation point, P_n – Legendre polynomial; n – order of the solution; η_n – Faran phase shift angle of the n^{th} scattered wave, ρ_1 and ρ_3 are densities of sphere and surrounding fluid, σ is a Poisson's ratio of sphere material.

C. Problem of Input Constants for Calculation

Proper modeling of backscattering spectra from tissue requires knowledge of cells' model constants. In present research Chinese hamster ovary (CHO) cells were chosen, as they would be available for experimental verification [20]. Looking for constants of CHO cells we reviewed available references. We have found that reported sizes of CHO cells have specified mean diameters from 12 μm [21] to 14.46±2.14μm [22], while researchers at [23] report mean diameter to be 15μm. One publication [24] presents, that size of these cells is variable: mean diameter in 9 days culture time decreased from 15.21 μm to 14.02 μm. In recent model [25] of backscattering the radius of CHO cells was taken 6.8±0.7 μm, the acoustical impedance of the cytoplasm - 1.55±0.09 MRayl and the impedance of the nucleus was 1.63±0.03 MRayl. The most complicated is a specification of Poisson's ratio of CHO cells material modeled by sphere. Some researchers tried to use Poisson's ratio in range of (0.20-0.499) [26] or (0.1-0.49) [27] when modeling backscattered spectra. Other researchers tried to establish whether live cells acoustically could be better concerned as a solid or fluid object. Measurements performed by Baddour et al 2005 [28] at frequencies 10–65 MHz on cells with different relative nucleus sizes have shown that for cells having a nucleus-to-cell volume ratio of 0.50, the backscattering response was better modeled with an elastic sphere model. For the cells in which this ratio was 0.33, the backscattering showed good agreement with the theoretical solution for a fluid sphere. Falou et al 2008 [29] modeled the ultrasound backscattering from non-nucleated biological specimen in frequency range 10–62 MHz. The measured backscattering response from individual sea urchin oocytes was compared with theoretical predictions. A good agreement was found between the experimental and theoretical results suggesting that the non-nucleated oocytes are of fluid nature. The mean density of CHO cells was calculated to be 1.051 kg/m^3 [30]. It was found from [31] that for CHO cells the nucleus occupy 22% of the total cell volume. Therefore we assumed that fluid sphere method for CHO cells modeling could be chosen in empirical and analytical models of backscattered ultrasound spectra. During calculations all acoustical properties of media and cells where kept constant. Only the diameter of cell model – microsphere - was varied to examine how spectral features are related to the size of scatterrer.

III. Results of Modelling

Empirical and analytical models we calculated in MATLAB environment. For calculation of Faran model of fluid type microsphere we adopted implementation by R. E. Baddour [32]. The calculated curves of power spectra functions are presented in Fig. 1 with their linearly approximated parameters (Fig. 1. c). Results show that for small scatterers (e.g., 4 μm), the exponential term and denominator of equation (1) are near to unity, so Rayleigh spectra proportional to f^4 and f^6 are observed (see Fig.1a). As the scatterer size increases, the spectra become less positively sloped; for scatterers larger than 112 μm, spectra can become negatively sloped, i.e., low frequencies are scattered more strongly than higher frequencies. Lizzi model (Fig.1a)

shows monotonic functions of power spectra. In general the spectral magnitude increases with increase of scatterer size. From Faran model (Fig.1b) power spectra could obtain peaks that represent resonant vibration modes of scaterring object. Resonant pattern is expected for spheres with larger diameter.

Calculated backscattering spectra could be approximated linearly in the frequency range from 5 to 15 MHz. Linear approximations resulted in two scalar parameters of spectra: intercept (the level of approximating line at frequency of 0 Hz expressed in dB) and slope (steepness of approximating line expressed in dB/MHz). These scalar parameters are dependent on diameter of microspheres as it is presented in Fig. 1c. Evaluating results of backscattered spectra calculations we can note that both models - Lizzi (empirical) and Faran (analytical) have shown similar general dependences. When the size of scatterer is increasing the magnitude of spectra is increasing but the slope is decreasing from positive to negative. Spectral slope could be assumed as first priority parameter related with scatterer size.

IV. Discussions and Conclusion

Comparing both model calculation methods could be pointed out, that Faran model has possibility to include scatterer elasticity (Poisson's ratio) into consideration, while the Lizzi model does not. But this advantage of Faran model is difficult to apply practically, because the Poisson ratio of cell material is difficult to measure and it is rarely found in references. Therefore Lizzi model could be sufficient to model biological scaterrers, while the phantom microparticles which could be well specified in size and material mechanical properties could be accurately simulated with Faran model. Calculation approaches of diffraction effects in Faran and Lizzi models are different. Calculating Lizzi model the aperture size (A) is taken into account that together with depth range (R) simulates diffraction effect of source transducer. Calculating Faran model source transducer diffraction is not taken into account, but instead is calculated amplitude loss of spherical wave at observation point. (It is assumed that spherical wave is backscaterred by microsphere). Therefore amplitudes of backscattered spectra calculated by Lizzi model (A=6mm, R=23mm) were similar to those calculated by Faran model at r=0,5 mm distance from microsphere.

Intercept and slope of spectrum curves are useful for tissue characterization, since method developed in [16] estimates slope of approximated and system compensated backscattering power spectra to calculate size of scatterers while estimated scatterer size could be used to calculate acoustical density (CQ^2) from spectral intercept [5].

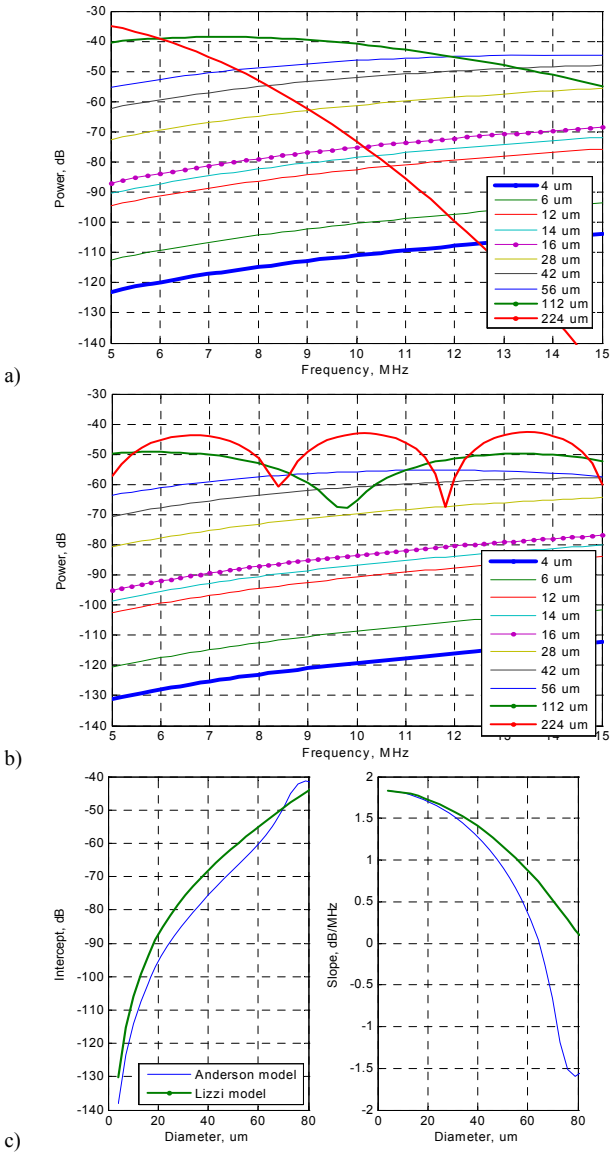

Fig. 1 Model calculated backscattered power spectra for micro sized scatterers: a) when acoustical density is set to unity (CQ^2=1) in model by Lizzi [7] (A=6mm, L=1mm; R=23mm) with indicated diameters; b) model by Faran with in saline (c_3=1497 m/s; ρ_3= 1.0046 kg/m^3) suspended microsphere fluid type [29] scatterers (c_{1CHO}=1520 m/s; ρ_{1CHO}=1.051 kg/m^3; σ_{1CHO}=0.35) of indicated diameters; c) intercept and slope parameters of linearly approximated power spectra's from models by Lizzi and Faran.

Concluding theoretical calculations it could be stated that both models (Lizzi and Faran) predicted backscattering spectra slope relation with scattering microsphere size. The Faran model is taking into account elastic features of scaterring microsphere therefore backscaterring spectra could be predicted accurately if properties of scaterrers are known precisely.

ACKNOWLEDGMENT

This research was supported from Agency for International Science and Technology Development Programmes in Lithuania, EUROSTARS project E!4297 – NICDIT "A Non-Invasive Expert System for Diagnosis of Intraocular Tumours".

REFERENCES

1. Raišutis R, Tumšys O, Deksnys V (2010) The prototype of ultrasonic imaging system–attachment for diagnosis of human eye tumours. Ultragarsas (Ultrasound), 65(2):42-46
2. Mari J M, Cachard Ch (2007) Acquire real-time RF digital ultrasound data from a commercial scanner. Electronic Journal "Technical Acoustics" 3:1-16, http://ejta.org/en/mari1
3. Feleppa E J, Lizzi F L, Coleman D J, Yaremko M M (1986) Diagnostic spectrum analysis in ophthalmology: a physical perspective. Ultrasound Med Biol 12(8):623-631
4. Lizzi FL, Astor M, Kalisz A, Liu T, Coleman D J, Silverman R, Ursea R, Rondeau M (1996) Ultrasonic spectrum analysis for assays of different scatterer morphologies: theory and very-high frequency clinical results, Ultrasonics Symposium. IEEE Proceedings, San Antonio, TX , 1996, vol 2, pp 1155–1159
5. Lizzi F L, Astor M, Liu T, Deng Ch, Coleman D J, Silverman R H (1997) Ultrasonic Spectrum Analysis for Tissue Assays and Therapy Evaluation. Int J Imaging Syst Technol 8:3-10
6. Oelze M L, Zachary J F (2006) Examination of cancer in mouse models using high-frequency quantitative ultrasound. Ultrasound Med Biol 32(11):1639-1648
7. Mamou J, Coron A, Hata M, Machi J, Yanagihara E, Laugier P, Feleppa E J (2010) Three-dimensional high-frequency characterization of cancerous lymph nodes. Ultrasound Med Biol 36(3):361-375
8. Insana M F, Wagner R F, Brown D G, Hall T J (1990) Describing small-scale structure in random media using pulse-echo ultrasound. J Acoust Soc Am 87(1):179-192
9. Baddour R E, Sherar M D, Hunt J W, Czarnota G J, Kolios M C (2005) High-frequency ultrasound scattering from microspheres and single cells. J Acoust Soc Am. 117(2):934-943
10. Kolios M C, Czarnota G J, Lee M, Hunt J W, Sherar M D (2002) Ultrasonic spectral parameter characterization of apoptosis. Ultrasound Med Biol. 28(5):589-597.
11. Davros W J, Zagzebski J A, Madsen E L (1986) Frequency-dependent angular scattering of ultrasound by tissue-mimicking materials and excised tissue. J Acoust Soc Am, 80(1):229–237
12. Jurkonis R, Daukantas S, Janušauskas A, Lukoševičius A, Marozas V, (2009) Synthesis of parametric map from raw ultrasound B-scan data. Electronics and Electrical Engineering 6(94):109-112
13. Hoskins P R, Thrush A, Martin K, Whittingham T A (2003) Diagnostic ultrasound: physics and equipment. Ashford Color Press Ltd, Gosport, ISBN 1841100420
14. Cobbold R S C (2007) Foundations of biomedical ultrasound. Oxford University Press, New York, , ISBN 0195168313
15. Lizzi F L, Greenebaum M, Feleppa E J, Elbaum M, Coleman D J (1983) Theoretical framework for spectrum analysis in ultrasonic tissue characterization. J Acoust Soc Am 73(4):1366-1373
16. Lizzi F L, Ostromogilsky M, Feleppa E, Rorke M, (1986) Relationship of Ultrasonic Spectral Parameters to Features of Tissue Microstructure. IEEE Trans Ultr Ferr Freq Contr 33(3):319-329
17. Faran J J (1951) Sound scattering by solid cylinders and spheres. J Acoust Soc Am 23:405-418
18. Hickling R (1952) Analysis of echoes from a solid elastic sphere in water. J Acoust Soc Am 34:1582-1592
19. Trahey G E, Anderson M E, Soo M S (1998) Microcalcifications as elastic scatterers under ultrasound. IEEE Trans Ultr Ferr Freq Contr 45:925-934
20. Tamošiūnas M, Čepurkienė K, Šatkauskienė I, Jurkonis R, Šatkauskas S (2009) The mocrobubble concentration study for the sonoporation effectiveness in vitro. Proc. of Intern. Scientific – Practical Conf. Virtual Instruments in Biomedicine, Klaipėda, Lithuania, 2009, pp 80-87
21. Pinto R C V, Medronho R A, Castilho L R (2008) Separation of CHO cells using hydrocyclones. Cytotechnology 56(1): 57–67
22. Beckman CoulterTM (2003) VI-Cell Instrument Overcomes Limitations of Manual Methods. Figure 6. CHO cell diameter distribution. Genetic Engineering News, Vol.23, No.10, May, 2003, http://www.beckmancoulter.com/literature/Bioresearch/AR-9725A.pdf
23. Kostner S, Vellekoop M J (2006) Optical Detection of Different Single Biological Cells in an Integrated Projection Cytometer. 5th IEEE Conference on Sensors, Daegu, Korea, 2006, pp 113 – 116
24. Yi Han, Xing-Mao Liu, Hong Liu, Shi-Chong Li, Ben-Chuan Wu, Ling-Ling Ye, Qu-Wei Wang, and Zhao-Lie Chen (2006) Cultivation of Recombinant Chinese Hamster Ovary Cells Grown as Suspended Aggregates in Stirred Vessels. J of Bioscience and Bioengineering 102(5):430–435
25. Teisseire M, Han A, Abuhabsah R, J P Blue, Sarwate Jr S O'Brien W D Jr (2010) Ultrasonic backscatter coefficient quantitative estimates from Chinese hamster ovary cell pellet biophantoms. J Acoust Soc Am 128(5):3175-3180
26. Choi A P C, Zheng Y P (2005) Estimation of Young's modulus and Poisson's ratio of soft tissue from indentation using two different-sized indentors: finite element analysis of the finite deformation effect. Med Biol Eng Comput 43:258-264
27. Boudour T, Ohayon J, Arntz Y, Finet G, Picart C, Tracqui Ph (2006) An extended modeling of the micropipette aspiration experiment for the characterization of the Young's modulus and Poisson's ratio of adherent thin biological samples: Numerical and experimental studies. Journal of Biomechanics 39:1677–1685
28. Baddour R E, Kolios M C (2007) The fluid and elastic nature of nucleated cells: implications from the cellular backscatter response. J Acoust Soc Am 121(1):EL16-22 DOI: 10.1121/1.2401224
29. Falou O, Baddour R E, Nathanael G, Czarnota G J, Kumaradas J C, Kolios M C (2008) A study of high frequency ultrasound scattering from non-nucleated biological specimens. J Acoust Soc Am 124(5):EL278-83 DOI: 10.1121/1.2987462
30. Anderson E C, Petersen D F, Tobey R A (1970) Density invariance of cultured Chinese hamster cells with stage of mitotic cycle. Biophysical Journal 10:630-645
31. Anderson R G, Orci L, Brown M S, Garcia-Segura L M, Goldstein J L (1983) Ultrastructural analysis of crystalloid endoplasmic reticulum in UT-1 cells and its disappearance in response to cholesterol. J Cell Sci 63:1-20
32. Baddour R E, Dept. of Medical Biophysics, University of Toronto, Canada. MATLAB implementation of Anderson's solution of sound scattering from a fluid sphere (Anderson, V.C., JASA 22:426-431, 1950)., http://www.ieee-uffc.org/ultrasonics/software.asp

New Fractal Methods for Diagnosis of Cancer

W. Klonowski, M. Pierzchalski, P. Stepien and R.A. Stepien

Nalecz Institute of Biocybernetics and Biomedical Engineering, Polish Academy of Sciences, Warsaw, Poland

Abstract— **We have proposed two new fractal methods that may be helpful in diagnosis of cancer. To reduce computational complexity, 2-D images of tumors are firstly preprocessed following our methods to form 1-D sequences that are subsequently analyzed using Higuchi fractal dimension. The first method, Image Signature's Fractal Dimension, is based on analysis of 1-D sequence called the signature of the tumour mass contour. The second method, Image Landscapes' Fractal Dimension, is based on analysis of two 1-D sequences called the horizontal and vertical landscapes. Both methods are easy and quick and we demonstrated that they may be successfully applied in oncology to support pathologist's diagnosis.**

Keywords— **fractal dimension, image analysis, signal processsing, breast cancer, Anal Intraepithelial Neoplasia**

I. Introduction

Fractal methods can be very useful for quantitative assessment and classification of images used for medical diagnostics, such as mammograms or histological slides. Here we present two fractal methods that may be supportive for diagnosis of cancer. To reduce computational complexity we preprocess 2-D images to form 1-D sequences that are subsequently analyzed using Higuchi fractal dimension method (cf. [1]). Higuchi fractal dimension, D_f, is calculated directly from the data series, without embedding the data in a phase space [2]. D_f always takes values between 1 and 2, The problem with fractal dimension is that the same notion is used to denote different quantities. There were several attempts to apply fractal dimension methods for cancer diagnostics and differentiation, but in most cases it was either the so called *box fractal dimension* or the *Fourier fractal dimension* calculated indirectly through the power spectrum of 2-D image [3]. But usefulness of Higuchi fractal dimension in analysis of digital images is more and more noticeable [4].

II. Methods

A. Image signature's fractal dimension (ISF) method

A contour on an image is specified in any rectangular coordinate system by the set of pairs (x_i , y_i) such that the pairs for i-1, i, i+1 correspond to the consecutive points (pixels) belonging to this contour for any $i = 1 , \dots , I$; the first point $i = 1$ may be chosen arbitrary and the point $i = I + 1$ coincides with the point $i = 1$ i.e. the contour is a closed planar curve.

We transform Cartesian coordinates of the 2-D contour to be analyzed into 1-D series r_i that we call this contour's *signature* what is in fact the set of polar r-coordinates of all contour points. First we calculate the arithmetic averages, x_0 and y_0, of Cartesian coordinates of all contour points and the contour's signature r_i ($i = 1 , \dots , I$) is given by:

$$r_i = \sqrt{(x_i - x_0)^2 + (y_i - y_0)^2} \tag{1}$$

We present here application of *ISF* method in analysis of breast masses contours in mammograms. Di Giovanni et al. [5] demonstrated a significant association between fractal measurements and breast tumor characteristics. Recently Florindo and Bruno [6] analyzed closed contours by mapping them on complex signals and then calculating their fractal dimension using Fourier transform, the method that is more complicated and error-prone due to 'time-frequency' transformation than direct calculation using Higuchi algorithm.

B. Image landscapes' fractal dimension (ILF) method

Since changes in the texture visible on histopathological slides depend on the type and the grade of eventual tumor quantitative assessment of such images should play a very important role in diagnosis and grading of tumors. For this purpose we apply another fractal method (cf. [7]), *ILF* method. The method is based on constructing from the analyzed 2-D image two 1-D sequences that we call *landscapes.*

Digitized grayscale images are stored in the form of matrices where matrix elements can take on values from $g_{min} = 0$ for a black pixel up to $g_{max} = (2^b - 1)$ for a white pixel, where b denotes the number of bits ($g_{max} = 255$ for $b = 8$). Most color images are overlays of three monochrome images. In this paper we will analyze only gray-scale images.

First the analyzed color image is transformed into a gray-scale one. Then stepping through a gray value image length of N pixels and height of M pixels row by row we calculate

Y. Dekhtyar et al. (Eds.): *International Symposium on Biomedical Engineering and Medical Physics*, IFMBE Proceedings 38, pp. 70–73, 2013.
DOI: 10.1007/978-3-642-34197-7_18

the sum of the gray values in each row, G_m *(m = 1, ... , M)*, and dividing so obtained numbers by the largest of them, G_R , we obtain the *horizontal landscape, hgs,*

$$NGS_m = G_m / G_R \in [0,1] \qquad m = 1,\ldots,M \qquad (2)$$

where

$$G_m = \sum_{n=1}^{N} g_{mn} \;; \quad G_R = \max(G_m) \qquad m = 1,\ldots,M$$

Similarly, stepping through the same image column by column we calculate the sum of the gray values in each column, G_n *(n = 1, ... , N)*, and dividing so obtained numbers by the largest of them, G_C , we obtain the *vertical landscape, vgs*

$$NGS_n = G_n / G_C \in [0,1] \qquad n = 1,\ldots,N \qquad (3)$$

where

$$G_n = \sum_{m=1}^{M} g_{mn} \;; \; G_C = \max(G_n) \qquad n = 1,\ldots,N$$

Normalization in (2) and (3) is convenient but not really necessary since Higuchi fractal dimension is invariant with respect to scaling of the data.

We present here application of *ILF* method to differentiate clinical cases of three grades of *Anal Intraepithelial Neoplasia* (AIN). AIN is a disease that is characterized by epithelial dysplasia and can lead to anal carcinoma. Recently Phinyomark et al. [8] used our method of landscapes to reduce computational complexity of 2-D microscopic images of breast cancer, but for estimation of their fractal dimension they used critical exponent analysis (CEA) method.

III. Examples of applications

A. ISF analysis of breast mass contours in mammograms

The contours of 111 breast masses found in mammograms were supplied to us by R.M.Rangayyan. The diagnostic classification of the masses was based upon biopsy. The contour of each mass was manually drawn by an expert radiologist specialized in mammography and verified independently by another radiologist. R.M.Rangayyan and T.M.Nguyen used fractal analysis of contours of those masses to differentiate between malignant and benign tumors. They computed fractal dimensions of the contours applying either the ruler method or the box counting method [9]. Again, we used Higuchi algorithm for analysis of contours' signatures - the method is simpler and leads to comparable results [10,11].

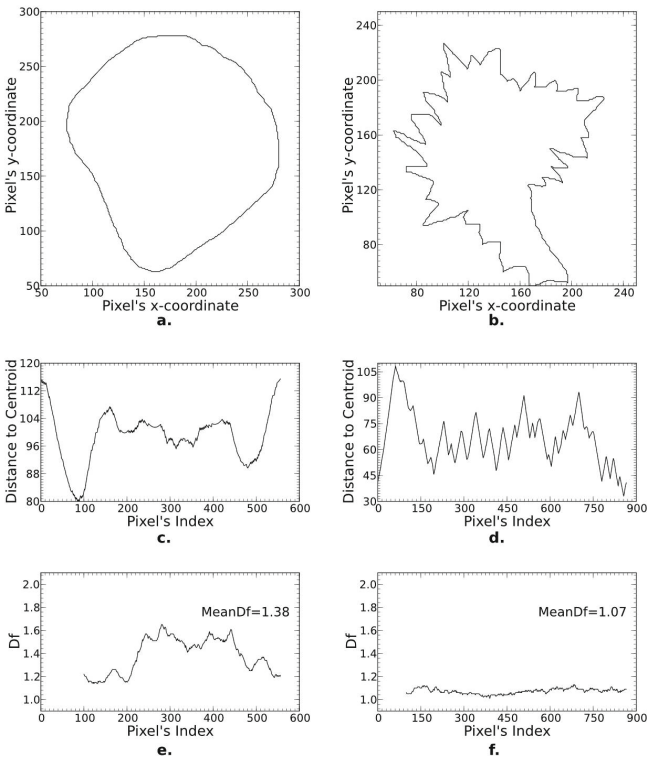

Fig. 1. Contours of a benign mass (a) and of a malignant breast tumor (b); their signatures, respectively (c) and (d); and Higuchi fractal dimension of these signatures, respectively (e) and (f) [10]

In the studied data most of the benign masses were well-circumscribed whereas most of the malignant tumors were spiculated. But there also existed circumscribed malignant and speculated benign masses. While the contour of a circumscribed breast mass (Fig. 1 a**.**) seems to be more regular than the contour of a spiculated breast tumor (Fig. 1b.) fractal dimension of the malignant breast tumors (Fig. 1f.) is lower than fractal dimension of benign breast masses (Fig. 1e.). If the contours are zoomed up one may observe that these of benign masses show many more small irregularities than those of malignant tumors. That is why signature of a benign mass shows many small 'fluctuations' while that of a malignant tumor does not so leading to differences in their fractal dimensions.

For assessment of performance of Higuchi fractal dimension for differentiation of benign masses from malignant tumors analysis of *Receiver Operating Characteristic curve* (ROC) (cf. [12]) was used showing that Higuchi fractal dimension well differentiates circumscribed masses while ruler method [9] well differentiates spiculated masses [11]. So, these two methods when combined well classify all breast masses.

B. ILF analysis of histopathological images of AIN

Classification of AIN into three grades (AIN1, AIN2, AIN3, with AIN3 being the highest grade with the highest risk for invasive anal carcinoma) is widely used but there is considerable interobserver variation in AIN grading.

We have analyzed 120 histological slices of abnormal anal tissues 36 of AN1, 56 of AIN2, 28 of AIN3. Microscopic images of eosin stained slices were of dimension 749x579 pixels (579 rows, *M=579,* 749 columns, *N=749*; cf. Eqs. (2) and (3)) each [13]. These color images were transformed to the 8-bit gray scale.

We have produced two landscapes for each image and analyzed these landscapes with Higuchi algorithm using parameter k_{max}=8 (cf. [13]). Fig. 2. shows an example of the *ILF* analysis of one histological slice classified by a trained pathologist as AIN1. Since we used a sliding window of the length 100 (cf. [13]) moved in each step 1 point (pixel) to the right we have the first value assigned to the 100^{th} pixel. So, for the horizontal landscape we calculated the mean value, D_h , of *hgsDf* from 480 values; similarly, for the vertical landscape we calculated the mean value, D_v , of *vgsDf* from 650 values. For further consideration we calculated for each slide fractal dimension *Df* (shown on the top of the figure) - the average of D_h and D_v .

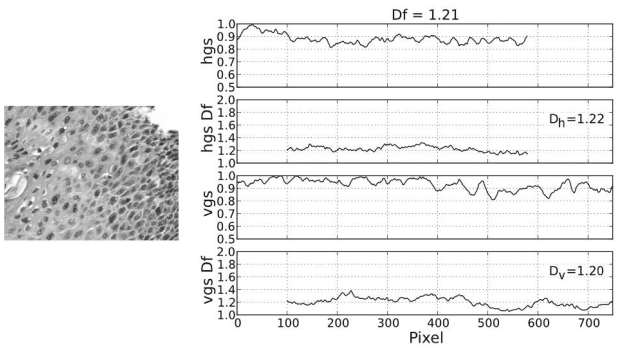

Fig. 2 Example of *ILF* analysis of one histological slice (AIN1).

After calculating *Df* for each of the 120 cases we calculated mean values and standard deviations for each of the three AIN's grades. The results are shown in Fig. 3. With increasing grade of dysplasia the value of *Df* increases accordingly. Statistically, the three groups are disjoint. It is obvious that the differences between AIN's grades are statistically significant.

Using ROC analysis we get the following cut-off values for discrimination between three AIN grades:

$$Df < 1.2172 \quad \text{for AIN1}$$
$$1.2172 < Df < 1.2460 \quad \text{for AIN2}$$
$$1.2460 < Df \quad \text{for AIN3}$$

and statistical analysis confirms that *Df* well discriminates between AIN grades [13]

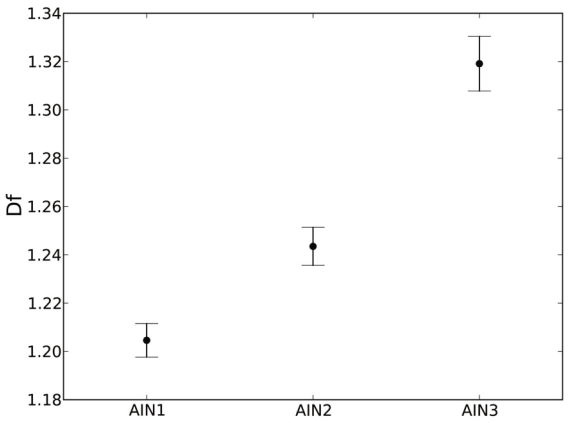

Fig.. 3 Differentiation of three AIN-grades using *ILF* analysis [13]

Many images under investigation show inherent background noise [14]. In this case the artifacts are white spots. Therefore, we repeated the calculations with the background subtracted by the rolling ball method [15]. It turned out that subtraction of the background did not improve the results substantially (cf. [13]).

IV. CONCLUSIONS

The presented fractal methods of image analysis may have broad medical application.

The *ISF* method of analysis of contours of breast masses in mammograms may help in differentiating between mammographic images of benign masses and of malignant tumors in screening medical examinations. The method is quick – one may analyze the whole signature at once to calculate Higuchi fractal dimension of the signature.

The *ILF* method is also easy and quick and it may be successfully applied for differentiation between AIN stages. The proposed method is not restricted to the grading of AIN. It can easily be adapted to other histological specimen. Another major advantage is that image segmentation is not necessary. Usually, image segmentation introduces subjective parameters such as threshold values and furthermore fully automatic algorithms are rare and mostly fail because of slide to slide color or brightness variations. The method could be used for training purposes during education or as an auxiliary method in order to support pathologists' decisios.

Acknowledgements

This work was supported in part by the Nalecz IBBE PAS statutory activity 4.4/st/12. We thank Prof. R.M.Rangayyan (University of Calgary, Alberta, Canada) for data of contours of breast masses. We also thank Prof. R.Sedivy (Centre of Pathology Danube Private University, Krems, Austria) and Prof. H.Ahammer (Medical University of Graz, Austria) for images of AIN.

References

1. Klonowski.W (2007) From conformons to human brains: an informal overview of nonlinear dynamics and its applications in biomedicine. Nonlinear Biomedical Physics 1: 5, Available from: http://www.nonlinearbiomedphys.com/content/pdf/1753-4631-1-5.pdf
2. Klonowski W (2002) Chaotic dynamics applied to signal complexity in phase space and in time domain. Chaos Solitons Fract 14:1379–1387
3. Ahammer H, Kroepfl JM, Hackl C, Sedivy R (2011) Fractal dimension and image statistics of anal intraepithelial neoplasia, Chaos Soliton Fract 44:86–92
4. Ahammer H (2011) Higuchi Dimension of Digital Images, PLoS ONE 6(9) e24796. DOI:10.1371/journal.pone.0024796
5. P. Di Giovanni P, Ahearn TS, Semple SIK, Lovell LM, Miller I, Gilbert FJ, Redpath TW, Heys SD, Staff RT (2012) The biological correlates of macroscopic breast tumour structure measured using fractal analysis in patients undergoing neoadjuvant chemotherapy, Breast Cancer Res Treat, preview DOI 10.1007/s10549-012-2014-8,
6. Florindo JB, Bruno OM (2011) Closed contour fractal dimension estimation by the Fourier transform. Chaos Solitons Fract 44:851-861
7. Klonowski W, Olejarczyk E, Stepien R (2005) SEM Image Analysis for Roughness Assessment of Implant Materials, in: Computer Recognition Systems, Kurzynski M, Wozniak M, Puchala E, Zolnierek A (Eds.) Springer Verlag, Berlin, Heidelberg, pp.553-560.
8. Phinyomark A, Jitaree S, Phukpattaranont P, Boonyapiphat P (2012) Texture Analysis of Breast Cancer Cells in Microscopic Images Using Critical Exponent Analysis Method. Procedia Engineering, 32:232-238 8
9. Rangayyan RM, Nguyen:TM (2007) Fractal Analysis of Contours of Breast Masses in Mammograms. J Dig Imag 20:223-237
10. Klonowski W. Stepien R, Stepien P (2010) Simple fractal method of assessment of histological image for applications in medical diagnostics, Nonlinear Biomedical Physics 4:7. Available from : http://www.nonlinearbiomedphys.com/content/pdf/1753-4631-4-7.pdf
11. Stepien R, Stepien P. (2010) Analysis of Contours of Tumor Masses in Mammograms by Higuchi's Fractal Dimension Biocyb Biomed Eng 30:49-56. Available from : http://www.ibib.waw.pl/bbe/bbefulltext/bbe_30_4_049_ft.pdf
12. MedCalc® for Windows - statistics for biomedical research software manual, Version 12, MedCalc Software (2011). Available from: http://www.medcalc.org/download/medcalcmanual.pdf
13. Klonowski W, Pierzchalski M, Stepien P, Stepien R, Sedivy R, Ahammer H (2012) Application of Higuchi fractal dimension in analysis of images of *Anal Intraepithelial Neoplasia* Chaos Solitons Fract, submitted
14. Ahammer H, De Vaney TTJ (2005) The influence of noise on the generalized dimensions. Chaos Solitons Fract 25:707–717.
15. Sternberg S (1983) Biomedical Image Processing. IEEE Computer 16:22-34

Author: Wlodzimierz Klonowski
Institute: Nalecz Institute of Biocybernetics and Biomed. Eng. PAS
Street: 4 Trojdena St
City: Warsaw
Country: Poland
Email: wklon@ibib.waw.pl

A Surface Smoothing Method for a 3D Model of a Medical Object

M. Kovalovs[1], A. Sisojevs[2], and A. Glazs[3]

[1] Riga Technical University/Department of Image Processing and Computer Graphics, PhD student, Riga, Latvia
[2] Riga Technical University/Department of Image Processing and Computer Graphics, Assistant, Riga, Latvia
[3] Riga Technical University/Department of Image Processing and Computer Graphics, Professor, Riga, Latvia

Abstract — **This paper describes a method to smoothen the surface of a Medical object's 3D model. This method is intended to be used on model that was obtained by a triangulation algorithm, but it also can be used on a model that was obtained by a marching cubes algorithm. The basic principle behind this algorithm is that it adjusts the position of the vertices of a 3D model relative to the neighboring vertices, thus evening the rough edges. This method was tested on the model of human head, which was acquired by computer tomography and it showed considerable visual improvement of the model.**

Keywords — **smoothing algorithm, medical object, visualization.**

I. Introduction

The 3D visualization of a medical object is an important aspect of medical image analysis and research. Analysis and visualization of different medical images, which were obtained by computer tomography (CT) or magnetic resonance imaging (MRI), is important to medical research and clinical practice. Some the most important initial phases of medical image processing are tasks of extraction and analysis of different image regions (a medical object or a pathology zone). In relation to this, a necessity to solve the task of 3D visualization of the region of interest emerges in computer diagnostics. The ability to visualize the orientation, position, size of structures in medical images can be vital to researchers and physicians. In order to obtain a 3D model of the region, the medical image must first be segmented, following the region extraction from the medical image. Afterwards, the control points must be selected on the contour of the extracted region, and then these control points are used for 3D visualization.

Although there are methods that allow segmentation and visualization of the medical image [1][2], the existing approaches of 3D visualization are not always able to provide a high-quality smooth surface of the 3D model. The resulting 3D models have a distinct aliasing effect.

This paper proposes a method to smoothen the 3D model of a medical object that was obtained by a control point triangulation algorithm or a marching cubes algorithm. The proposed method adjusts the position of the vertices in the 3D model, resulting in a better quality of surfaces of the 3D model.

II. Proposed method

The surface of a 3D model is usually described by vertices that are joined into triangles. The basic principle of the smoothing algorithm is to adjust the position of these vertices to even out the sharp edges that might appear between the triangles.

The proposed method works by sequentially taking every vertex in the 3D model and finding all the vertices that are connected to this vertex. Then a new vertex is determined, which is located exactly in middle of all the vertices that are connected to the original vertex. Finally a new 3D model is created by using all the newly generated vertices, while preserving the connections between the original vertices. Figure 1 shows a visual example of this method.

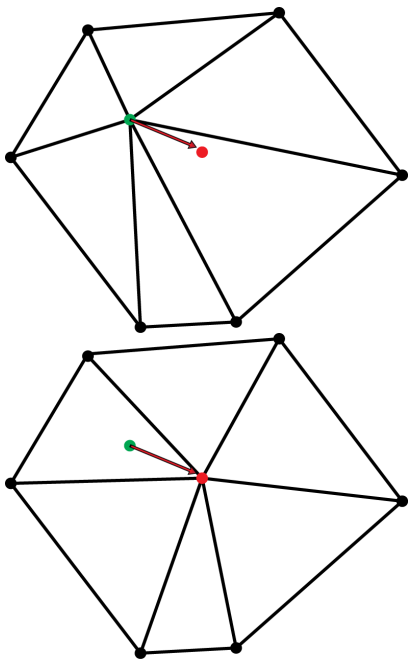

Fig. 1 Vertex position adjustment, where green point is the original vertex and the red point is the generated vertex

Y. Dekhtyar et al. (Eds.): *International Symposium on Biomedical Engineering and Medical Physics*, IFMBE Proceedings 38, pp. 74–77, 2013.
DOI: 10.1007/978-3-642-34197-7_19

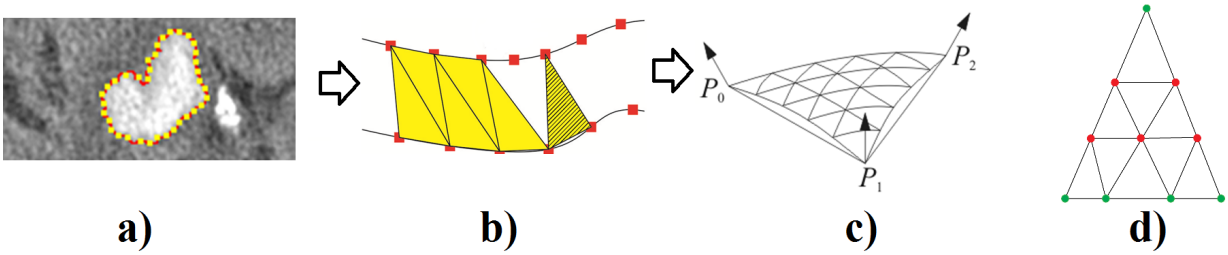

Fig. 2 a) Control point selection, b) Triangulation algorithm, c) Bezier triangle, d) The Bezier triangle that is used in the modified smoothing algorithm, where the red vertices are adjusted by the smoothing algorithm and the green points remain unaffected.

A. Using the Proposed Method on a 3D Model That Is Generated by a Triangulation Algorithm (Polygonal Model)

The model that is generated by the triangulation algorithm is created in two steps [1].

1. The control points are selected on the contour of the medical object.
2. The mesh of the 3D model is formed by triangulating the acquired control points.

To improve the quality of the 3D model every triangle is converted into the Bezier triangle[3] which creates additional triangles.

Figure 2 illustrates the creation process of the 3D model using the triangulation algorithm (Fig. 2.a) and the Bezier triangles (Fig . 2.c).

One of the flaws of this method is that, while it smoothes out the original model, in the process the model might lose some of its detail. To solve this problem the method can be slightly modified to preserve the detail of the original model.

The modified smoothing method works by adjusting only those vertices that were created by the Bezier triangles, so those vertices that belong to the original triangles remain unaffected. This preserves the core structure of the original model, while smoothing the additional triangles created by the Bezier triangles. Figure 2.d illustrates which vertices remain unaffected by the modified smoothing algorithm.

Figure 3 illustrates the results of both smoothing methods that were used on a model of human head, where a) is the original model that was created using the triangulation algorithm on the medical images that were acquired with computer tomography, model b) shows the same model after the original triangles were converted into Bezier triangles, thus creating additional triangles and improving the amount of detail of the original model, c) and d) shows the same model after the proposed smoothing method was used, where the position of points of the Bezier triangles is adjusted to smooth out the 3D surface. From these results it is clearly seen that the proposed method provides a much more detailed and smooth surface, while the modified method provides a slightly less smooth surface, but it preserves the basic structure of the original model.

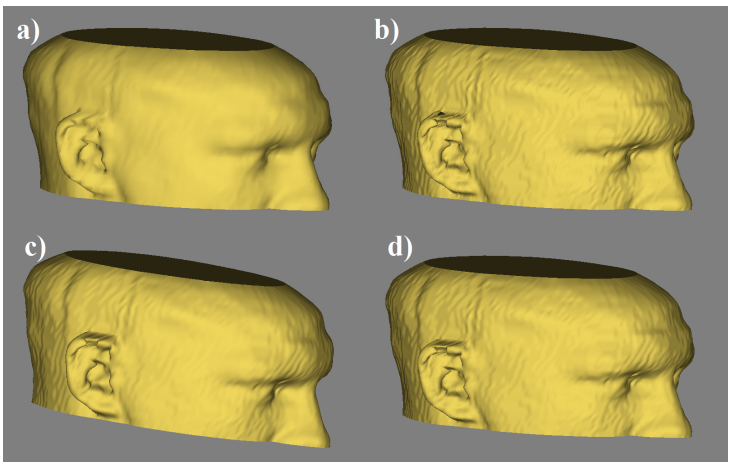

Fig. 3 a) The Original 3D model, b) Bezier triangle model, c) Proposed smoothing method, d) Modified smoothing method

B. Using the Proposed Method on a 3D Model That Is Generated by a Marching Cubes Algorithm.

Marching cubes is a computer graphics algorithm, which was developed by W. E. Lorensen and H. E. Cline,[2] for extracting a polygonal mesh of a surface from a three-dimensional scalar field (sometimes called voxels). The marching cubes algorithm is one of the most popular 3D modeling algorithms in medical visualizations.

The algorithm works by taking eight neighbor locations at a time (thus forming an imaginary cube) on the medical images, then determining the polygon(s) needed to represent the part of the surface that passes through this cube. The individual polygons are then fused into the desired surface. This is done by creating an array of possible polygon configurations within the cube. Figure 4 shows the 14 unique polygon configurations.

One of the main flaws of the marching cubes algorithm is that the surface of the 3D model created by this algorithm has a distinct aliasing effect. The proposed smoothing method considerably improves the quality of the 3D model by mostly removing the aliasing effect. Figure 5 illustrates the results of using the proposed method on the 3D models of two human heads that were created using the marching cubes algorithm on the medical images that were acquired with computer tomography. It is clearly seen that proposed method (Fig. 5.b, Fig. 5.d) smoothes out the aliasing effect, that was created by the marching cubes algorithm (Fig. 5.a, Fig 5.c).

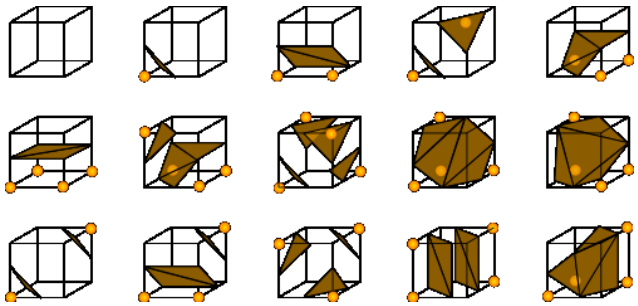

Fig. 4 Possible polygon configurations of the marching cubes algorithm.

III. Experiments

The proposed method was tested on a real medical object. The object in the experiment was a model of a human head fragment, which was created from an array of 31 medical images, acquired with the computer tomography.

The result of the proposed method was compared with the original 3d model, which was created using the triangulation algorithm and a model created by the 3D imaging software 3D-Doctor[4]. Figure 6 illustrates the comparison of various methods, where it is clearly seen that, when used on a 3D model that was created by the triangulation algorithm the proposed method smoothes out the surface of the model while creating additional detail and that the surface is considerably smoother than that of model created with 3D-Doctor program, which has a distinct aliasing effect.

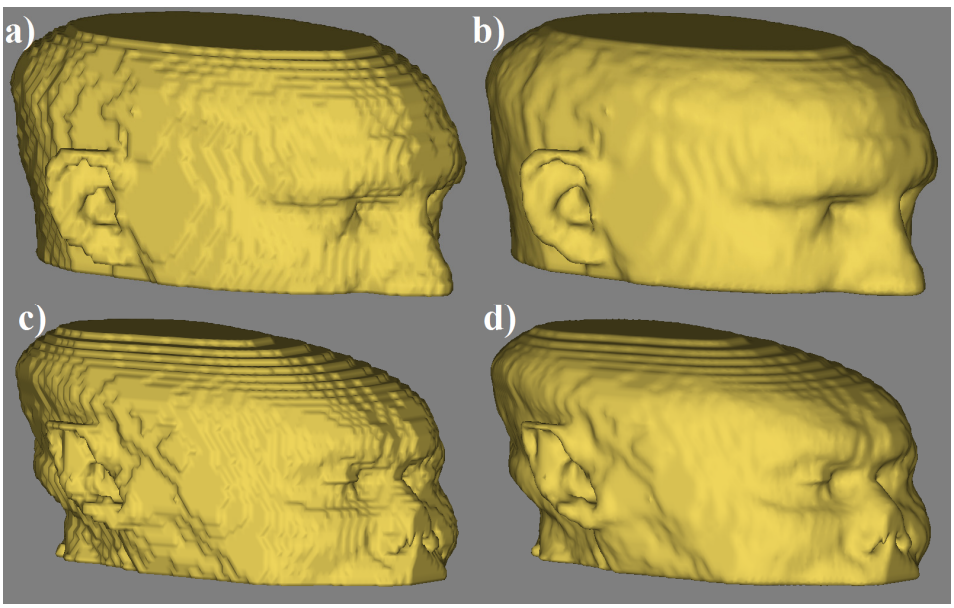

Fig. 5 a) and c) The original model created by the marching cubes algorithm, b) and d) Proposed smoothing method.

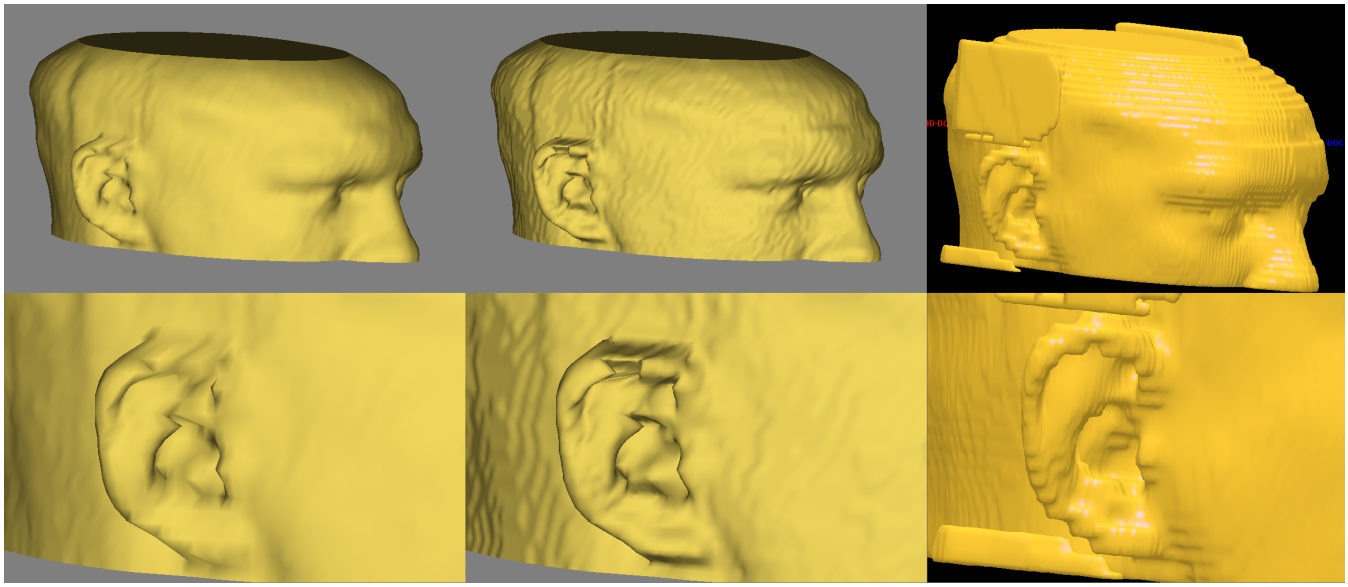

Fig. 6 Comparison of different models. Left - Triangulation (polygonal) model, middle – proposed method, right - 3D Doctor.

IV. Conclusions

This paper proposes a method to smoothen the surface of a medical objects 3D model. The proposed method have been tested on 3D models, that were created using medical images of a brain acquired by computer tomography.

The proposed method shows considerable visual improvement when used on the model created with the triangulation algorithm or the marching cubes algorithm. The proposed method was also compared with the 3D imaging software 3D-Doctor and it gave a better visual result. The surface of the model is smoother without an aliasing effect. Overall, the proposed smoothing method shows stable results in visualization and may be implemented in medical software to provide better 3D visual quality of the reconstructed medical object.

References

1. Bolochko K., Kovalovs M., Glaz A. (2011) Medical Image 3D Visualization by Vector Based Methods. IADIS MCCSIS CGVCVIP 2011 Proc., Rome, Italy.
2. Lorensen W.E. and Cline H.E. (1987) Marching Cubes: a high resolution 3D surface reconstruction algorithm. SIGGRAPH Proc. Computer Graphics, Vol. 21, No. 4, pp 163-169.
3. Sisojevs A, Kovalovs M, Glazs A, (2012) Medical Image 3D visualization method based on the Bezier triangles. IADIS MCCSIS CGVCVIP 2012 Proc. (in press)
4. Able Software Corp. 3D-DOCTOR, FDA 510K cleared, vector-based 3D imaging, modeling and measurement software, http://www.ablesw.com/3d-doctor/

Author: Mihails Kovalovs
Institute: Riga Technical University, Department of Image Processing and Computer Graphics
Street: Meza Street 1/3
City: Riga
Country: Latvia
Email: mihails.kovalovs@rtu.lv

Author: Aleksandrs Sisojevs
Institute: Riga Technical University, Department of Image Processing and Computer Graphics
Street: Meza Street 1/3
City: Riga
Country: Latvia
Email: aleksandrs.sisojevs@rtu.lv

Author: Aleksandrs Glazs
Institute: Riga Technical University, Department of Image Processing and Computer Graphics
Street: Meza Street 1/3
City: Riga
Country: Latvia
Email: glazs@rtu.lv

Ontology Driven Decision Support System Architecture for Gait Analysis

Ivan Turcin, Vladimir Ergovic, and Marko Lackovic

IBM Croatia, Miramarska 23, 10000 Zagreb, Croatia

Abstract — **This paper presents role of domain ontology in construction process and architecture of medical data warehouse and decision support system based on provided ontology. Domain described is in part of musculo-skeletal system of the lower limbs. In this paper we preset a way how to combine generics data mining method with data warehouse model and domain ontology in order to build intelligent system for gait analysis. This paper describes specific domain ontology of lower limbs and a ways how this ontology is mapped to data warehouse models and steps in decision support system creation.**

Keywords — **Data warehouse, ontology, expert system, lower limbs, data mining.**

I. Introduction

In a number of decision support systems knowledge representation and result interpretation based on the queries over large data warehouse is important problem. Medical domain is characterized by the abundance of existing expert knowledge and practically each of its specializations has a constantly growing and interacting number of relevant guidelines. A long-term goal is knowledge representation in a form that can be used by systems supporting medical decision making. One of these domains is gait analysis or in our case musculo-skeletal system of the lower limbs. We have explored methods and tools available together with generic data mining method as basis method to follow during construction process. So far there were only few researches regarding systematic development of data warehouse models based on ontologies and only one regarding ontology design for musculo-skeletal system of the lower limbs. These researches however didn't give full description of data warehouse and data mining construction process for specific domain of human gait. One of the questions which stayed unanswered is the role of the ontology in method and model. Since the idea behind the ontology is re-usage, we have selected existing ontology as reference for our project. This paper shows integration of the domain ontology with generic data mining method and data warehouse. Our approach includes demographic data (categorical, numerical data) and time sequence data (human gait variables, trial specific variables, etc) of individual classes (joints, muscles [1, 2, 3].

II. Ontology background

Ontology is an explicit and structured specification of a concepts and semantic, intelligent relation in a field, where conceptualization is also the abstract model of real phenomena. Today usage of ontologies in medicine is mainly focused on the representation and organization of medical terminologies. Physicians developed their own specialized languages and lexicons to help them store and communicate general medical knowledge and patient-related information. Such terminologies, optimized for human processing, are characterized by a significant amount of implicit knowledge. Medical information systems, on the other hand, need to be able to communicate complex and detailed medical concepts unambiguously [1,4]. This difficult task can be achieved by constructing medical domain ontology for representing medical terminology such as GALEN [4,5]. This large ontology of medical terms, anatomy and drugs is translated into OWL (Ontology Web Language) and it has about 20 MB in size. OWL is most used standard ontology languages today, and it is based on XML format. From an AI (Artificial Intelligence) perspective therefore, ontology is not only a discipline, but also the outcome of the activity of ontological analysis and modeling. This is why we can speak of "ontology of lower limbs". This ontology is example of the so-called "domain ontology", whereas "foundational ontology" represent domain-independent concepts like objects, events, processes. Some benefits of using ontologies are: interoperability, re-usage, data and knowledge integration and sharing. There is skepticism about the impact that ontologies may have on the design and maintenance of real-world systems. Considering the size and complexity of medical ontologies we see issues regarding design and maintaince of the large ontologies. That is why we focus on domain driven ontology. We examined OSMMI (Ontologie du Systeme Musculo-squelettique des Membres Inferieurs) as ontology for our project in Laboratory of Biomechanics in favor of GALEN and other more complex ontologies [1].

Y. Dekhtyar et al. (Eds.): *International Symposium on Biomedical Engineering and Medical Physics*, IFMBE Proceedings 38, pp. 78–81, 2013.
DOI: 10.1007/978-3-642-34197-7_20

III. Proposed architectural approach

Decision support system construction has multiple approaches. Since our goal is data mining system for gait analysis, we started with generic data mining method which comprises seven steps [6]:

- Defining the issue in a precise statement.
- Defining the data model and the data requirements.
- Sourcing data from all available repositories and preparing the data.
- Evaluating the data quality
- Choosing the mining function and defining the mining run
- Interpreting the results and detecting new information.
- Deploying the results and the new knowledge.

Following the method we have defined issues regarding gait disorder based on knee injuries. This step is more oriented to specific issue and in data warehouse we want to cover more broad data which is in domain of musculoskeletal system of the lower limbs. In second step we have examined existing conceptual data models based on medical domain ontologies. Regarding our domain and interest in gait analysis we have found muscular, skeletal and nervous data facts of the proposed model most interesting. Conceptual data model of skeletal system with fact table and related dimension is shown in Fig 1. In gait analysis this is not optimal solution because additional effort is needed to integrate multiple fact tables and querying becomes more difficult since there exists multiple fact tables for each system. Proposed model from Fig 1 also has denormalized, coarse grained fact table, not suitable for storage of large time series data.

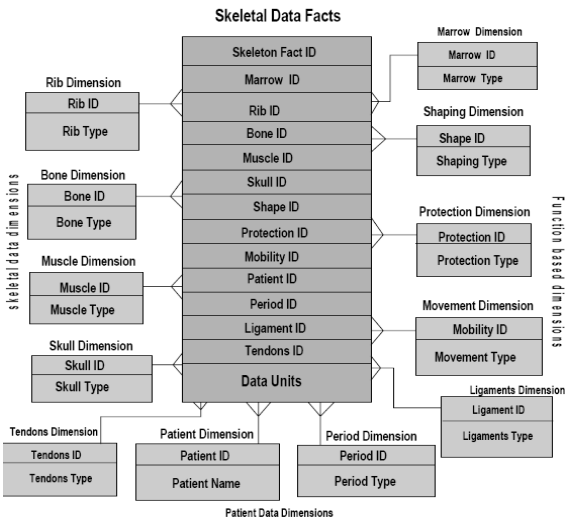

Fig. 1 Skeletal System Multidimensional Ontology (Data warehouse) [2].

In our case, average reading included 10 different parameters sampled at 10 ms for 20 seconds period of movement that produced around 20000 samples for one movement pattern including five steps, without additional temporal and demographic dimensions needed in analysis. Data warehouse is temporal model where measures are organized, collected, and represented as facts which are hold in fact tables. This structural approach enables interpretation of measures in a given context [7]. Facts become more meaningful when enriched using different dimensions, for example time, demographic and anthropometric parameters, vocabulary, etc. Since chorons used in gait analysis are placed on milliseconds scale proposed skeletal fact table becomes candidate for slow-vary dimension table. Ontology is useful input to data modeling and it gives possibility to share the common comprehension of the structure of information and it allows reuse of the implicit knowledge. Presented model although based on one of the ontologies does not satisfy gait analysis requirements since it is too generic. In construction process we used some ideas from it but we based our model on other ontology – OSMMI. OSMMI classes with relationships between them are illustrated with UML (Unified Modeling Language) stereotypes in Fig 2 [1].

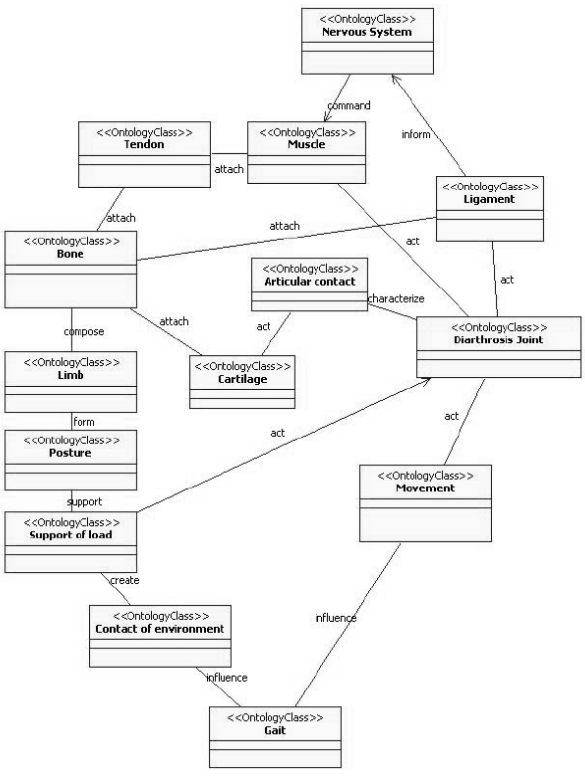

Fig. 2 General overview of the OSMMI.

OSMMI includes 14 parts (classes). These include: Nervous system, Ligament, Muscle, Tendon, Cartilage, Bone, Limb, Posture, Support of load, Diarthrosis Joint, Movement, Articular contact, Contact of environment and Gait. Semantic of OSMMI is described by relations summarized in table 1 [1].

Table 1 OSMMI relations.

Name	Description
inform	the ligaments inform the nervous system about active signals
command	the nervous system command the muscles
attach	the muscles are attached to the bones through the tendons; the cartilages and the ligaments are attached to the bones
compose	limb is composed by the different bones which correspond to a particular function in gait
act	the muscles, the support of load, the movement, and the ligaments act on the diarthrosis joint; cartilage act the articular contact
influence	limbs form the correspondent posture
support	posture is supported by the support of load;
create	support of load is created by the contact of environment
characterize	the articular contact characterize the diarthrosis

Classes are divided into subclasses for finer insights and classification of individual classes for gait analysis. Semantic is based on different relations that make it suitable for implementation in the traditional relational databases, but not for analytical databases. Typical data units held in fact table include measurement of several variables from trial including muscles, bones, ground reaction forces, etc. In our approach we initially include all variables which are part of the typical trial in one large fact table. Justification of this approach is that data in its nature is time series based and additional information is stored in slow vary dimension like trial since it can hold descriptive information (after operation it can be artificial hip as well). Ontology classes are all candidates for dimension tables. Initially this approach creates star like structure, but we need to keep in mind that ontology is formed from the classes and some of these classes have subclasses like posterior ligament (which have two subclasses: arched poplity, oblique poplity), patellar aileron (which again have two subclasses: patellar external aileron, patellar internal aileron) and these classes form snowflake schema. All these data can be derived and conceptualized into ontologically derived data dimensions, based on these categories, functions and activities of human body systems. Simulation models can be deduced based on metadata and data warehousing approaches. An important aspect of human gait is learning the relationship between body structures and their location as interpreted through palpation of relevant landmarks. This examination eases the task of relating knowledge, observation and palpation to make or confirm diagnoses. The conceptualization of data and information has a definite role in the logical and intelligent design of databases and data warehouses in which information is described as an inventory [8] and an asset to the system. Two types of systems are interpreted: machine based (ontology perspective) and natural systems such as human anatomy. Integrated human anatomy [9] is a natural built-in system with well connected entities or dimensions. Dimensions analogous to entities can be described, conceptualizing the relationships. Several associated data dimensions are conceptualized using ontology and stored as metadata. Volume of dimensions from real world situations can be interpreted through ontology stored in meta-data as shown with Fig 3 [6].

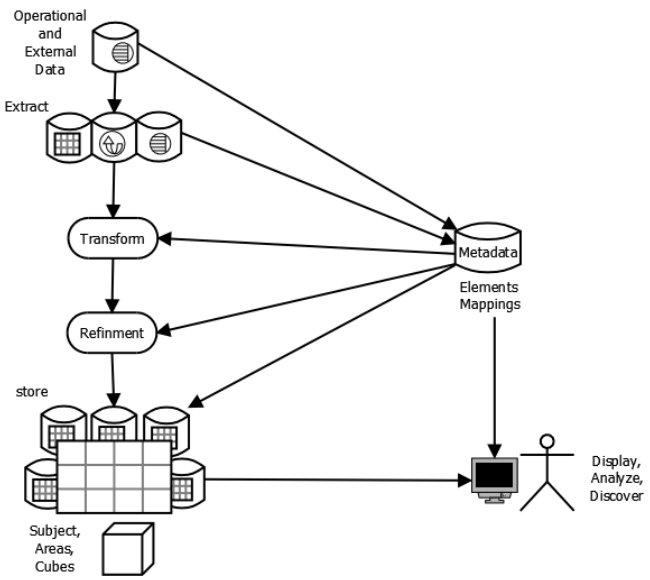

Fig. 3 Metadata in system context.

Data sourcing and preprocessing comprises the stages of identifying, collecting, filtering and aggregating (raw) data into a format required by the data models. Evaluation of the data model requires validation of chosen variables, handling of outliers and missing values and removal of redundant variables. Ontology based ETL (Extract Transform and Load) is a tool which handles both of these steps. There are several papers that recommend ontology as a tool for selecting appropriate data mining which is part of choosing the mining function step. The results from performing any type of data mining can provide a wealth of information that can sometimes be difficult to interpret and this interpretation is done by business metadata where ontology is stored. In most cases data mining creates mathematical

representations of the data that we call models. These models are very important, because they not only provide a deeper insight of patients but can themselves be deployed in, or (re) used by other systems.

IV. Discussion and conclusion

Although there are numerous obvious benefits of using ontologies in process of decision support system construction such as standardization of terms, knowledge sharing and re-usage, data warehouse model validation and support the indispensable integration of knowledge and data, practitioners should still be focus on specific domain. We were able to build data warehouse model based on OSMMI in a week avoiding numerous questions regarding data requirements and model. Our model has 3 fact tables, 18 dimension tables (based on the ontology classes, 4 which are slowly-vary dimensions) and additional meta-data tables. We re-used ontology in ETL, data refinement and in result interpretation. OWL is interesting XML based language that combined with XSLT (Extensible Stylesheet Language Transformations) enables automatic generation of dimension tables, metadata and skeleton of fact tables. Meta-data and dimension tables can be as well, automatically populated with terms and relationships implicitly stored in OWL for purpose of result interpretation. However we have found that the biggest advantage of ontology is in ETL and in result interpretation.

Acknowledgment

The results presented are the product of scientific projects “Noninvasive measurements and procedures in bio-medicine”, “Automated motion capture and expert evaluation in the study of locomotion” and “Real-life data measurement and characterization”, realized with the support by The Ministry of Science, Education and Sports, Republic of Croatia.

References

1. Dao T et al: Ontology of the musculo-skeletal system of the lower limbs, Proceedings of the 29th International Conference of the IEEE EMBS; 2007 Aug 23-26; Lyon, France; p. 386-389.
2. Nimmagadda S et al: Ontology based data warehouse modeling and managing ecology of human body for disease and drug prescription management, Proceedigns of the 2nd International Conference IEEE DEST 2008; 2008 Feb 26-29; Phitsanulok; p. 212-220.
3. Arnold A et al: Computer modeling of gait abnormalities in cerebral palsy: application to treatment planning, Theoretical Issues in Ergonomics Science, Vol 6, No. 3-4, May-August 2005, 305-312.
4. Rector A L et al: Unifying Medical Information using an Architecture Based on Descriptions, Proceedings of the 14th Annual Symposium on Computer Applications in Medical Care , SCAMC 90, 1990, IEEE Computer Society Press, Los Alamitos, California , pp 190-194.
5. Rector A L et al: The GALEN High Level Ontology, In: Fourteenth International Congress of the European Federation for Medical Informatics, MIE-96, Aug. 19-22 2006, Copenhagen, Denmark
6. Baragoin C et al. Mining Your Own Business in Health Care, San Jose, IBM; 2001.
7. Medved V et al: Towards a High Performance Expert System for Gait analysis, Proceedings of the 4th European Congress for Medical and Biological Engineering; 2008 Nov 23-27; Antwerp, Belgium; p. 2105-2108.
8. Tokosumi et al: Medical Ontologies as a Knowledge Repository, Proceedings of the 2007 IEEE/ICME International Conference on Complex Medical Engineering; 2007 May 23-27; Beijing; p. 487-490.
9. Moore K, Dalley A. Clinically Orientated Anatomy, Pennsylvania: Lippincott Williams and Wilkins; 1999.Smith J, Jones M Jr, Houghton L et al. (1999) Future of health insurance. N Engl J Med 965:325–329

Author: Ivan Turcin
Institute: IBM Croatia
Street: Miramarska 23
City: Zagreb
Country: Croatia
Email: ivan.turcin@hr.ibm.com

Sequential and Structural Biophysical Aspects of Combinatorial Oligo FISH in Her2/neu Breast Cancer Diagnostics

D. Zeller[1], N. Kepper[1,2], M. Hausmann[1], and E. Schmitt[1,3]

[1] Heidelberg University, Kirchhoff Institute for Physics, Im Neuenheimer Feld 227, Heidelberg, Germany
[2] Heidelberg University, Bioquant, Im Neuenheimer Feld 267, Heidelberg, Germany
[3] Georg-August-University, Institute for Numerical and Applied Mathematics, Lotzestraße 16-18, Göttingen, Germany

Abstract — **Fluorescence in situ Hybridization (FISH) is an important tool in medical diagnostics to determine the genetic status to monitor tumor progression in breast cancer. The newly developed method of COMBO-FISH allows a more refined diagnosis by using a set of short oligonucleotides which cluster at the Her2/neu gene and indicate the multiplicity of amplification. A careful image analysis of the fluorescence microscopic image also provides insights in the nanolocal nuclear architecture. Designing a set of short oligonucleotides which can form triple helical structures with double stranded DNA and cluster exclusively at the Her2/neu gene locus is based on the analysis of the sequence of the whole human genome, while understanding the properties of the hybridization process, namely its kinetics and energetics, depends on the detailed knowledge of the dynamics of the molecular interactions which are exemplified by molecular dynamics simulations of triplex forming oligonucleotides.**

Keywords — **Human genome, sequence analysis, triplex forming oligonucleotide, molecular dynamics simulation, nuclear architecture.**

I. Introduction

In diagnostics and therapy, it has become more and more important to have reliable means of detecting the patient's individual status to apply appropriate medical treatment. It has become routine to investigate the cellular conditions by Fluorescence in situ Hybridization (FISH) which is a method to label specific genetic regions by introducing into the cell nucleus long DNA strands complementary to the desired genetic region [1-3]. The strand, carrying fluorescent dyes, binds to the denatured DNA single strand of the chromosome. The fluorescence signals are detected by microscopic imaging and after appropriate image analysis, a detailed picture of the nucleus is achieved [4, 5]. In this way, aberrations of genetic status, like gene duplication, translocation, or loss can be detected [6-9]. For specific diseases, numbers like gene multiplication are important indicators for progression of the disease or success of treatment, as it is the case for the Her2/neu (ERBB2) gene amplification during breast cancer development [10-12]. In this case, the genetic status of lymphocytes is determined.

In addition to the application by the bed side practitioner, such methods are used in research and development to investigate the micro- and nanolocal structural changes within the cell nucleus to get a clearer impression of the molecular basis of disease and to model the biophysical foundations of chromosomal and genetic ontogeny [13, 14]. Unfortunately, FISH in its original form is not very well suited for such investigations for several reasons. On the one hand side, the FISH probe strands are rather long, several hundred to thousands or even millions of bases, which have a strong interaction with the DNA region to be investigated. On the other hand side, the cell specimen has to be denatured to introduce the strands into the nucleus and to provide single stranded chromosome DNA. This procedure destroys the genuine chromosomal architecture. Therefore, the method of COMBinatorial Oligo FISH (COMBO-FISH) was developed to overcome these drawbacks [15-17]. Here, a set of short oligonucleotides in the range of 15 to 30 bases length is chosen and hybridized to the nuclear DNA. In the first place, the method was designed for Triplex Forming Oligonucleotides (TFOs), which bind via Hoogsteen triplets to double stranded DNA, to avoid the necessity to denature the specimen. But as interphase DNA also shows a lot of single strands, the method can also be applied with short oligonucleotides which do not form triplex structures.

Here, we describe the triplex forming COMBO-FISH set which has been developed for the special application to Her2/neu breast cancer diagnostics and therapy control. We will put special emphasis on the combinatorial methods used for the design of the COMBO-FISH probe set and on the biophysical structural problems associated with the hybridization process.

II. COMBO-FISH probe set design for HER2/neu

To design a triplex forming COMB-FISH probe set, several short oligonucleotides are selected which have the capability to form triplex structures with double stranded DNA, that is, the oligo strand intercalates into the major groove of double stranded DNA. This imposes manifold

Y. Dekhtyar et al. (Eds.): *International Symposium on Biomedical Engineering and Medical Physics*, IFMBE Proceedings 38, pp. 82–85, 2013.
DOI: 10.1007/978-3-642-34197-7_21

restrictions on the single oligo chosen. It has to be of a length between 15 and 30 bases, and, for classical Hoogsteen pairing, the sequence has to consist either of T's and C's solely or of A's and G's exclusively. We would like to remark here that there are also other sequence combinations which slightly differ from these patterns, but this is still matter of ongoing research both in theory and experiment. In addition, experiments have shown that too many bases of the same kind in sequence destabilize the structure and lead to low hybridization efficiency.

Furthermore, we have to select enough different oligos carrying one or two dyes each to get a detectable signal under fluorescence conditions. For standard microscopical equipment, the lower bound of the number of oligo strands is about 20, when they are hybridized to a DNA region not longer than 250 kb, which we then call a colocalizing COMBO-FISH probe set. On the other hand, we want the probe set to be uniquely identifying the desired genetic region, here the Her2/neu gene. Therefore, the oligo strands, which bind to a lot of genomic locations due to the mere combinatorics of the vast human genome (3.7 Gb), are not allowed to form clusters of more than 6 oligo strands within 250 kb chromosomal length elsewhere in the genome.

In consequence, the task is clear: Find at least 20 oligo sequences of length 15 to 30 bp within the DNA region of the Her2/neu gene, such that anywhere else in the genome within 250 kb at most 6 of them colocalize. For this task, C-programs have been written [18] which extract all possible sequences regarding the above mentioned subsequence restrictions from the human genome, which amounts to about 3 percent of the genome base number, and to perform the search for such oligo sets.

III. Sequential Features of Her2/neu Gene Locus

The genomic locus of the Her2/neu gene extends from base 3118545 to base 3159067 in positive strand direction on contig 5 of chromosome 17 as deposited in the 2011 read of the reference human genome of NCBI. With a length of 40523 bases, it consists of the join of 30 exons which are expressed in different mRNA variants. Flanking genes are PGAP3 (base position 3101527 to 3118462, length 16936 bp) at a rather short distance of 82 bases downstream and ORB3 (synonym C17orf37, bases 3159561 to 3160940) of length 1380 at 493 bases upstream on the complementary strand. It should be noted that there is a micro RNA (MIR4728, base position 3156884 to 3156971, length 88 bp) between exon 26 and 27 within the Her2/neu gene itself. Another important gene for cancer diagnostics is GRB7 (length 9387 bases) at distance 7343 downstream.

The locus of Her2/neu contains 35 sequences consisting of T's and C's exclusively with a minimum length of 15 bases, the longest being a sequence of 35 A's and one G. As for COMBO-FISH the direction of the strand is not of any relevance, and as A's and G's are complementary to T's and C's, we restrict the search to T/C-stands (polypyrimidines), on either strand, of course. Several of these oligo strands contain multiple C- or T-regions, and those with a sequence of more than 7 bases of the same kind are excluded, leaving 16 possible candidates for a COMBO-FISH probe set. Two sequences of 28 and 26 bases, respectively, are truncated to 20 bases. As a cluster of 16 oligo strands would be at the lower limit of detectability, anyway, the set is augmented by 10 additional oligo strands in the range to base 3102000 upstream, the whole set now spanning a region of about 57000 bases.

Having determined all binding locations of these probe candidates, a cluster analysis is performed and subsequently probes are removed from the set, until no clusters with more than 6 oligo strands within 250 kb are remaining. This final set consists of 13 strands on the Her2/neu gene and 7 strands in the region up to 6520 bases upstream. The sequences in 5' to 3' strand direction on the Her2/neu locus are listed in Table 1. If reverted to 3'-5'-direction, they are suitable for TFO COMBO-FISH.

Table 1 TFO Sequences on Her2/neu Locus.

No.	Sequence	Length (bp)
1	aaggagaaaaggagga	16
2	gaggggagaagggagg	16
3	cctcctctctctccc	15
4	gggaaggagaagaggaagg	19
5	ccctcctccttcctct	16
6	agaggaagagaagaa	15
7	cccttctttcctctctcctt	20
8	ccctttctcctccccc	20
9	tctcttttcctttctcttcc	20
10	aaaggaagagaagaa	15
11	ccccttccctcct	16
12	ccccccttcctctcctctt	19
13	gggagggaagagagaaagag	20
14	gaagagagggagaaag	16
15	ggggaagaggaggggg	16
16	gagaaggaaggagagag	17
17	ctttctctcctccct	15
18	cctctttcctcctctc	16
19	tccttccctcccctct	17
20	gaagggagggaagggg	16

IV. Structural Features of Her2/neu Gene Locus

Several protocols have been designed for the experimental application of triplex forming oligonucleotides to DNA and RNA, e.g. for gene silencing. Depending on the usage of polypyrimidines (T/C sequences) or polypurines (A/G

sequences), different physiological conditions are needed. In both cases, the necessary pH is prohibitive for live cell experiments which could show the natural dynamics of nuclear architecture and chromosomal movement during the cell cycle. It has therefore been a continuous effort to fine tune the experimental details to enable more physiological conditions.

One way of changing hybridization conditions is to modify the backbone of the hybridization probe. Exchanging the sugar phosphate backbone of DNA by a peptide like strand called PNA [19] reduces electrostatic repulsion of the strands. Other possible modifications include locked nucleic acids LNA [20] which contain a sugar modification, or the introduction of further aromatic side strands into the hybridization probe which intercalate with the DNA double strand, so called twisted intercalating nucleic acids, TINAs [21]. The basis for considerations concerning the modification of triplex forming COMBO-FISH probe sets is the knowledge of the kinetics and energetics of the binding process.

In order to understand the hybridization behaviour, we have performed molecular dynamics simulations for short oligonucleotides bound to double stranded DNA. Such simulations impose statistical molecular forces on a starting configuration, here in water solution, to model the dynamical behaviour in such an environment. As a starting structure, we chose a crystal structure of a TFO of six bases intercalating into the major groove of the corresponding double stranded DNA well extending beyond the binding region. The TFO sequence is CTCTCT, a motive which is contained in three of the 20 COMBO-FISH probes designed for Her2/neu. Details of the molecular dynamics simulation will be published elsewhere.

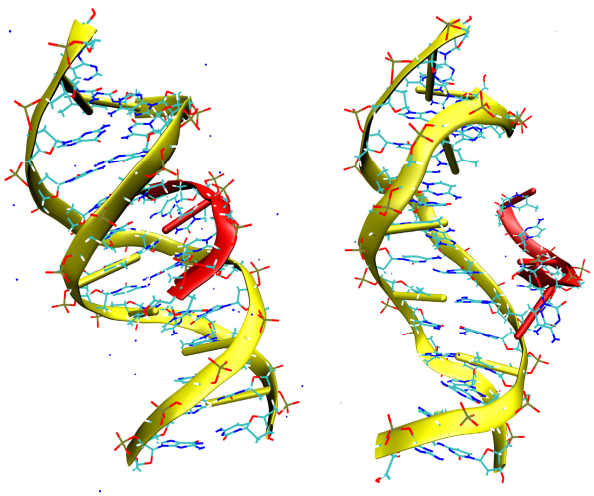

Fig. 1 Left: TFO starting structure 1BWG, Right: after 20 ns.

Two snapshots of the simulation are depicted in Figure 1, which shows the starting configuration 1BWG [22] in the protein data bank PDB with additional water molecules (Left). Performing several runs with varying initializations of the statistical fluctuations, we observed different dynamical behavior of the the triplex structure. The triplex forming oligonucleotide can stay within its binding groove, or it will loose its binding contacts and drift away (Fig. 1 Right, after 20 ns). This indicates that six oligonucleotides may be a critical length for the stability of the alternating CT repeated sequence.

V. Discussion and Conclusion

Fluorescence in situ Hybridization (FISH) has become an important tool in medical diagnostics. In our example here, tumor progression in breast cancer is monitored by the observation of the status of the Her2/neu gene. Indicators for the patients state of health are numbers like the amplification or translocation of the gene [23-25]. Though commercial kits for labeling Her2/neu are widely used in clinics and laboratories nowadays, a more detailed analysis of the Her2/neu chromosomal status could improve the results [26-27]. As opposed to commercial kits, which use rather large single DNA strands for hybridization, the newly developed method of COMBO-FISH is based on a set of short oligonucleotides which cluster at the genomic location to be labeled. In fact, the method has proven to be successful in several experiments [7, 15-17] in the investigation of the abl/bcr gene loci regarding numerical parameters like gene amplification and also geometrical measurements like size and compactification of the chromosomal elements. Furthermore, the use of PNA as backbone for the sequence was the key feature in an experiment with a single probe labeling a multiply repeated sequence in a centromere.

Here we design a set of COMBO-FISH oligos for the Her2/neu gene to measure and indicate the multiplicity of an amplification. Preliminary experiments have shown that a careful analysis of the microscopic image of a lymphocyte specimen also provides insights in the nanolocal nuclear architecture and allows conclusions on parameters like gene compactification and the form of genetic territories [28] as already shown for abl/bcr [17]. Understanding the properties of the hybridization process, namely its kinetics and energetics, in order to optimize the physiological and biochemical conditions of the hybridization experiment depends on the detailed knowledge of the dynamics of the molecular interactions. Here, further research is required e.g. by extended molecular dynamics simulations of triplex forming oligonucleotides including dye molecules as they are appearing in COMBO-FISH probe sets.

ACKNOWLEDGMENT

The authors greatly acknowledge financial support by the BMBF, grant 13N11163 COMBO-FISH, to Michael Hausmann. Eberhard Schmitt wants to thank in particular Cathrin M. for her encouraging judgement of the beauty of computations and Jenny W. for her never ceasing aid in making this beauty visible.

REFERENCES

1. Sreekantaiah C (2007) FISH panels for hematologic malignancies. Cytogenet Genome Res 18:284-296
2. Halling K, Kipp B (2007) Fluorescence in situ hybridization in diagnostic cytology. Hum Pathol 38:1137–1144
3. Tibiletti M (2007). Interphase FISH as a new tool in tumor pathology. Cytogenet Genome Res 118:229–236
4. Cremer M, Gasser F, Lanctot C et al. (2000) Multicolor 3D fluorescence in situ hybridization for imaging interphase chromosomes. Methods Mol Biol 463:205–239
5. Ronneberger O, Baddeley D, Scheipl F et al. (2008) Spatialquantitative analysis of fluorescently labeled nuclear structures: Problems, methods, pitfalls. Chromosome Res 16:523–562
6. Wiech W, Stein S, Lachenmaier V et al. (2009) Spatial allelic imbalance of BCL2 and chromosome 18 in non-neoplastic and neoplastic cervical squamous epithelium. European Biophysics Journal 38:793 – 806
7. Schwarz-Finsterle J, Stein S, Großmann C et al. (2005) COMBO-FISH for focussed fluorescence labelling of gene domains: 3D-analysis of the genome architecture of abl and bcr in human blood cells. Cell Biol. Intern 29:1038–1046
8. Rauser S, Weis R, Braselmann H et al. (2007) Significance of HER2 low-level copy gain in barretts cancer: Implications for fluorescence in situ hybridization testing in tissues. Clin Cancer Res 13:5115–5123
9. Gajda M, Camara O, Oppel S et al. (2008) Monitoring circulating epithelial tumor cells (cetc) during primary systemic chemotherapy including trastuzumab for early prediction of outcome in patients with Her2/neu-positive tumors. Ann Oncol 19(12):2090–2091
10. Stein S, Riede F, Schmitt E et al. (2006) The nuclear architecture of Her2neu and centromere 17 in ductal breast carcinoma and non-neoplastic ductal epithelium. Cell Proliferation 39:353–354
11. Tubbs R, Pettay J, Swain E et al. (2006) Automation of manual components and image quantification of direct dual label fluorescence in situ hybridization (FISH) for HER2 gene amplification. A feasibility study. Appl Immunohistochem Mol Morphol 14(4):436–440
12. Bolzer A, Kreth G, Solovei I et al. (2005) Three-dimensional maps of all chromosomes in human male fibroblast cell nuclei and prometaphase rosettes. PloS Biol 3:e157
13. Kozubek K, Lukasova E, Jirsova P et al. (2002) 3D structure of the human genome: order in randomness. Chromosoma 111:321–331
14. Lanctot C, Cheutin T, Cremer M et al. (2007) Dynamic genome architecture in the nuclear space: regulation of gene expression in three dimensions. Nat Rev Genet 8:104–115
15. Hausmann M, Winkler R, Hildenbrand G et al. (2003) COMBO-FISH: specific labelling of nondenatured chromatin targets by computer-selected DNA oligonucleotide probe combinations. Biotechniques 35:564–577
16. Schwarz-Finsterle J, Stein S, Großmann C et al. (2007) Comparison of triplehelical COMBO-FISH and standard FISH by means of quantitative microscopic image analysis of abl/bcr genome organisation. J Biophys Biochem Meth 70:397–406
17. Grossmann C, Schwarz-Finsterle J, Schmitt E et al. (2010) Variations of the spatial fluorescence distribution in ABL gene chromatic domains measured in blood cell nuclei by SMI microscopy after COMBO-FISH labelling. in: A. Méndez-Vilas, and J. Díaz Álvarez, (Eds.), Microscopy: Science, Technology, Applications and Education, Formatex Research Center, Badajoz, 688-695
18. Schmitt E, Wagner J, Hausmann M (2012) Combinatorial Selection of Short Triplex Forming Oligonucleotides for Fluorescence in situ Hybridisation COMBO-FISH. Journal of Computational Science, epub 2011
19. Brandt O, Feldner J, Stephan A et al. (2003) PNA-microarrays for hybridisation of unlabelled DNA-samples. Nucleic Acids Res 31:e119
20. Petersen M, Wengel J (2003) LNA: a versatile tool for therapeutics and genomics. Trends Biotechnol 21(2):74–81
21. Géci I, Filichev V, Pedersen E (2006) Synthesis of Twisted Intercalating Nucleic Acids Possessing Acridine Derivatives. Thermal Stability Studies. Bioconjugate Chem 17(4):950–957
22. Asensio JL, Brown T, Lane AN (1999) Solution conformation of a parallel DNA triplex with 5' and 3' triplex-duplex junctions. Structure 7:1-11
23. Cremer T, Cremer C (2001) Chromosome territories, nuclear architecture and gene regulation in mammalian cells. Nat Rev Genet 2:292–301
24. Erenpreisa J, Kalejs M, Cragg M. (2005) Mitotic catastrophe and endomitosis in tumour cells: An evolutionary key to a molecular solution. Cell Biol. Intern 29:1012–1018
25. Kosak S, Groudine M. (2004) Form follows function: the genomic organization of cellular differentiation. Genes Dev, 18:1371–1384
26. Sexton T, Schober H, Fraser P et al. (2007) Gene regulation through nuclear organization. Nat Struct Mol Biol, 14:1049–1055
27. Schmitt E, Stein S, Hausmann M (2009) Conception of an image data base for cell nuclei and geometric algorithms for diagnosis and therapy monitoring. Studies in Health Technology and Informatics 147:251-256
28. Müller P, Schmitt E, Jacob A et al. (2010) COMBO-FISH enables high precision localization microscopy as a prerequisite for nanostructures analysis of genome loci. International Journal of Molecular Sciences 10 (11):4094-4105

Use macro [author address] to enter the address of the corresponding author:

Author: Eberhard Schmitt
Institute: Kirchhoff Institute for Physics
Street: Im Neuenheimer Feld 227
City: D-69120 Heidelberg
Country: Germany
Email: eschmitt@kip.uni-heidelberg.de

Magnetic Properties of Lewis Lung Carcinoma and Antitumor Magneto-Sensitive Complex

V.E. Orel[1], A.D. Shevchenko[2], A.V. Romanov[1], A.P. Burlaka[3], S.N. Lukin[3,4], E.P. Sidorik[3], and E.F. Venger[4]

[1] National Cancer Institute, 33/43 Lomonosov Street, 03022, Kyiv, Ukraine
[2] G.V. Kurdyumov Institute for Metal Physics, 36 Academican Vernadsky Blvd., 03680, Kyiv-04142, Ukraine
[3] R.E. Kavetsky Institute of Experimental Pathology, Oncology and Radiobiology, 45 Vasil'kovsky Street, 03022, Kyiv, Ukraine
[4] V.E. Lashkaryov Institute of Semiconductor Physics, 45 Nauki Pr., 03028, Kyiv, Ukraine

Abstract — **In this study we have examined endogenous magnetic characteristics of Lewis lung carcinoma** of C57BL/6 mice **and mechano-magneto-chemical synthesized magneto-sensitive complex (MC) consisted of magnetic nanoparticles Fe_3O_4 with KCl and antitumor antibiotic anthracycline doxorubicin (DR). Magnetic properties were studied by the method of vibrating magnetometry and electron spin resonance spectroscopy. Lewis lung carcinoma on 14 day after inoculation is weak soft ferromagnetic with saturation magnetic moment m_s = + 0.187 emu/g in contrast to diamagnetic environment tissues (m = – 0.002 emu/g). Lewis lung carcinoma had higher concentration of paramagnetic centers compared to environment tissue. Maximal concentration of paramagnetic centers was observed in MC samples (10^{18} mg^{-1}). The g-factor for MC increased up to 2.64. DR after mechano-magneto-chemical treatment is paramagnetic (m = + 0.068 emu/g at H = 3000 Oe) in contrast to conventional drug which is diamagnetic (m = – 0.200 emu/g).**

Keywords — **Lewis lung carcinoma, doxorubicin, magnetic nanoparticles, magnetic properties.**

I. Introduction

Iron is a central element in the metabolism of normal and malignant cells. Abnormalities in iron and ferritin expression have been observed in many types of cancer. Three main iron components encountered in the human host are: haemoglobin-bound iron in the blood, which exhibits nearly paramagnetic behaviour, ferritin, the iron storage protein and magnetite (Fe_3O_4) and/or maghemite (γ-Fe_2O_3). Ferritin is the primary intracellular iron storage protein and is one of the major proteins of iron metabolism. Human meningiomal brain tumor tissues contain an order of magnitude higher concentration of ferrimagnetic particles than non-tumor hippocampi. Although these tumors are well vascularized, it is not known whether blood supply plays a role in this higher concentration yet. Iron distribution in the brain is heterogeneous. However, the formation rate of ferrimagnetic magnetite and/or maghemite appears to be higher in the tumor tissue [1]. Although the presence and biological origin of this material is clear, little is known about the distribution or metabolic function of ferromagnetic minerals in vertebrate tissue during experimental malignant process.

It is known that the ferric oxide content, which is a ferromagnetic, can be stored in Lewis lung carcinoma. This tumor originated spontaneously as a carcinoma of the lung of a C57BL mouse. Most of the ferromagnetic crystals in Lewis lung tumor had coercivity from 20 to 30 mT. Control samples of muscle and connective tissue from normal C57BL/6 mice displayed only very weak coercivity of 32 pT [2]. It's phenomena is not specific for malignant tumor. There aren't detected remanences in human tissues in normal stomach, gastric carcinoma, colon carcinoma, and renal carcinoma. Lots of tumors have high internal concentrations of the iron storage protein ferritin [3].

Magnetic nanoparticles offer some attractive possibilities in biomedicine. Firstly, they have controllable sizes ranging from a few nanometers up to tens of nanometers, so their sizes match those of biological entities of interest. Indeed, they can be coated with biological molecules to make them interact with or bind to a biological entity, thereby providing a controllable means of "tagging" them. Secondly, the magnetic nanoparticles obey Coulomb's law and can be manipulated by an external electromagnetic field gradient. This "action at a distance", is combined with the inherent ability of electromagnetic fields to penetrate into human tissue, opens up lots of applications involving the transport and/or immobilization of magnetic nanoparticles, or magnetically tagged biological entities. This way they can be made to deliver a package, such as an anticancer drug to a targeted region of the body, such as a tumor. Thirdly, the magnetic nanoparticles can be made to resonantly respond to a time-varying electromagnetic field, with advantageous results related to the transfer of energy from the exciting field to the nanoparticle. For example, the particle can be made to heat up, which leads to their use as hyperthermia agents, delivering toxic amounts of thermal energy to targeted areas such as tumors; or as chemotherapy and radiotherapy enhancement agents, where a moderate degree of tissue warming results in more effective malignant cell destruction. These, and many other potential applications, can be applied in biomedicine as a result of the special physical properties of magnetic nanoparticles [4].

Y. Dekhtyar et al. (Eds.): *International Symposium on Biomedical Engineering and Medical Physics*, IFMBE Proceedings 38, pp. 86–89, 2013.
DOI: 10.1007/978-3-642-34197-7_22

The synthesis of magneto-sensitive complex (MC) consisted of magnetic nanoparticles Fe_3O_4 with KCl and antitumor antibiotic anthracycline doxorubicin (DR) [5] is based on the integration of two known methods: mechano-chemical synthesis [6] and synthesis of enzymes in a micro-reactor with magnetic elements [7]. The principle of the mechano-chemical synthesis is based on the fragmentation and formation of an ensemble of paramagnetic centers, such as free radicals in the complex nanoparticle structure. A free radical is any atom or molecule that has a single unpaired electron in an outer shell. Most biologically-relevant free radicals are highly reactive in cancer treatment. The principle of the magneto-chemical synthesis is concerned with the magnetic properties of chemical compounds. Magnetic properties arise from the spin and orbital angular momentum of the electrons contained in a compound. Compounds are diamagnetic when they contain no unpaired electrons. Molecular compounds that contain one or more unpaired electrons are paramagnetic. This increases the drug activity and therapeutic synergism in cancer treatment [8].

In this regard, it need to be known the magnetic properties of Lewis lung carcinoma and MC of the nanoparticles Fe_3O_4 with KCl and organic antitumor drugs are able to predict the effects of their interaction during treatment. For years there have been many reports of observations of weak spontaneous magnetization near room temperature in organic compounds. Magnetic order at room temperature in metal-free carbon-based structures remains one of the exciting issues in fundamental and applied research across all scientific disciplines [9]. However, the lack of reproducibility in some cases, hinder the understanding of this effect to biological tissues and pharmaceuticals with a heterogeneous chemical composition.

In this study we have examined endogenous magnetic characteristics of Lewis lung carcinoma (3LL), mechano-magneto-chemically synthesized MC and mechano-magneto-chemically treated anthracycline antitumor antibiotic doxorubicin (DR).

II. Materials and Methods

A. Experimental Animals and Tumor Transplantation

In the study 10 C57BL/6 male mice weighing 19 ± 1 g bred in the vivarium of National Cancer Institute (Kyiv, Ukraine) were used. The transplantation Lewis lung carcinoma was performed according to the established procedure. The tumor and environment tissue (muscle and connective tissue) of mice of Lewis lung carcinoma were surgically removed from hind limb on 14 day after inoculation of the neoplasm. We have studied the lyophilized Lewis lung carcinoma and environment of the tumor tissue of C57Bl/6 mouse.

B. Mechano-Magneto-Chemical Treatment

MC consisted of the nanoparticles Fe_3O_4 (International Center for Electron Beam Technologies of E.O. Paton Electric Welding Institute, Ukraine) with diameters in the range 20–40 nm, KCl and DR(Pfizer, Italy) were processed in high-precision mechano-magneto-reactor (NCI, Ukraine). Mechanical processing was performed by vertical vibrations of the chamber at a frequency of 36 Hz and an amplitude of 9 mm for 5 min using mechanical energy of 20 W/g. Simultaneously, electromagnetic irradiation at 42 MHz by an induction coil with 75 W initial power and permanent magnets with magnetic field intensity 25 Oe for 5 min, was applied [5]. Mass concentration of DR in MC was 33.3%.

C. Magnetic Studies

The magnetic properties were studied by "Vibrating Magnetometer 7404 VSM" ("Lake Shore Cryotronics Inc.", USA) with magnetic fields up to 13 kOe. The magnetometer's sensitivity is 10^{-7} emu, and that allowed measurements of magnetic moment of samples weighing milligrams to be performed.

D. Electron Spin Resonance (ESR) Spectroscopy

The registration of ESR spectra and the assessment of paramagnetic centers' concentration in the samples were performed using an updated computer-controlled electron spin resonance spectrometer RE-1307, which has a cylinder microwave resonator with the mode H_{011} at the frequency 9.15 GHz. The microwave power radiation was 40 mW and the magnetic field modulation frequency was 100 kHz. The samples with diameter of 4.5 mm and lengths 40 mm were placed in a quartz Dewar. ESR spectra of the samples were recorded at liquid nitrogen temperatures (77 K) together with a constant standard of intensity (ions Cr^{3+} in Al_2O_3).

III. Results and Discussion

A. Magnetic Studies

Magnetic properties of investigated samples are shown in Table 1. Hysteresis loop of Lewis lung carcinoma and MC is represented at Fig. 1 and 2 respectively. Obtained results testify that Lewis lung carcinoma had properties of weak soft ferromagnetic in contrast to diamagnetic environment tissues. Both Fe_3O_4 and MC was soft ferromagnetic. Saturation magnetic moment for tumor was appreciably smaller compared to Fe_3O_4 and MC (in 289 and 63 times accordingly). Conventional DR was the diamagnetic. Mechano-magneto-chemical treatment increased saturation magnetic moment m_s of DR and it turned into paramagnetic.

B. ESR Spectroscopy

Lewis lung carcinoma had higher concentration of paramagnetic centers compared to environment tissue (Fig. 3, Table 2), while preserving the availability of all the known components of the ESR spectrum for biological objects [10]. Maximal concentration of paramagnetic centers was observed in MC samples (Fig. 4). The *g*-factor for MC increased up to 2.64. It is known that conventional Fe_3O_4 nanoparticles are characterized by ESR signals with typical *g*-factors 2.08 and 2.19 [11]. Qualitative change in ESR spectrum for DR samples is not observed (Fig. 5). The data suggest that the concentration of paramagnetic centers with $g = 2.003$ in DR, which acquired the properties of the paramagnetic under influence of mechano-magneto-chemical treatment increase in comparison with conventional DR which is diamagnetic.

Table 1 Magnetic properties of the samples.

Examined object	Saturation magnetic moment m_s, emu/g	Magnetic field H_{ms} at m_s, Oe	Coercivity *Hc*, Oe
Conventional DR, diamagnetic ($m = -0.200$ emu/g)	–	–	–
Mechano-magneto-chemically treated DR, paramagnetic ($m = +0.068$ emu/g at $H = 3000$ Oe)	–	–	–
Fe_3O_4, soft ferromagnetic	54.006	7200	39.193
MC, soft ferromagnetic	11.781	12000	45.659
Lewis lung carcinoma, soft ferromagnetic	+ 0.187	2000	0.362
Environment tissues of Lewis lung carcinoma, diamagnetic ($m = -0.002$ emu/g)	–	–	–

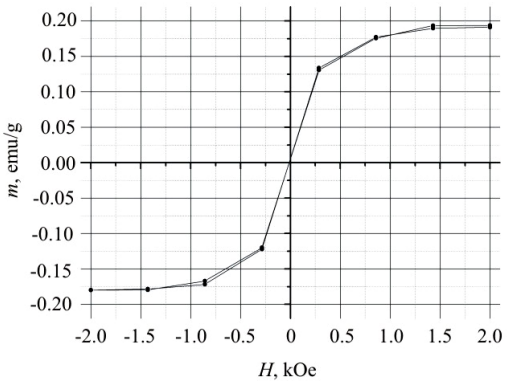

Fig. 1 Hysteresis loop of Lewis lung carcinoma at 300 K, *H* – magnetic field.

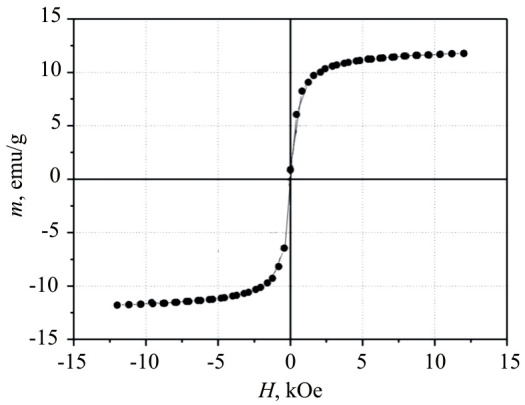

Fig. 2 Hysteresis loop of magneto-sensitive complex at 300 K, *H* – magnetic field.

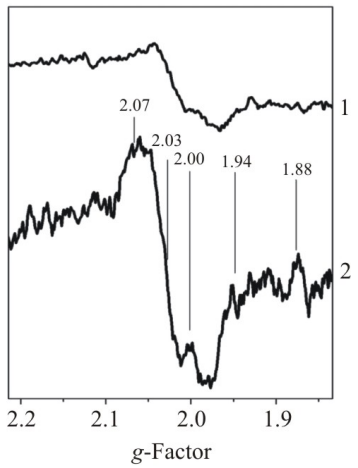

Fig. 3 ESR spectra of lyophilized tissue: environment tissue of Lewis lung carcinoma C57Bl/6 mouse from hind limb (1); Lewis lung carcinoma (2).

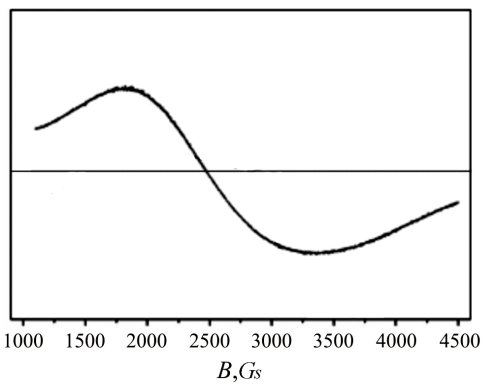

Fig. 4 ESR spectrum of mechano-magneto-chemically synthesized magneto-sensitive complex.

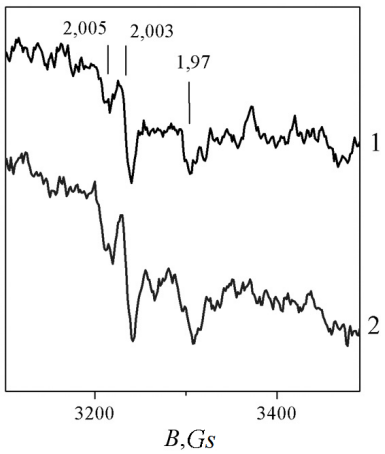

Fig. 5 ESR spectra of doxorubicin: 1 – conventional doxorubicin; 2 – mechano-magneto-chemically treated doxorubicin.

Table 2 The concentration of paramagnetic centers (C, mg^{-1}).

N	Sample	g-factor	Paramagnetic centers concentration
1	Conventional DR	2.003	$8 \cdot 10^{13}$
2	Mechano-magneto-chemically treated DR	2.003	10^{14}
3	MC	2.64	10^{18}
4	Lewis lung carcinoma	2.03	10^{15}
5	Environment tissues of Lewis lung carcinoma	2.03	$3 \cdot 10^{14}$

The g-factors in ESR spectrum for biological samples are shown according to [10]: 1.88 – FeS protein S-3 in the electron transport chain succinate dehydrogenase of mitochondrial complex; 1.94 – FeS protein N2 in the electron transport chain NADH: ubiquinone oxidoreductase of mitochondrial complex; 2.00 – ubisemiquinone; 2.03 – complexes NO-FeS-protein N2 in the electron transport chain of mitochondria; 2.07 – component of the triplet ESR signal of heme and nonheme protein.

IV. Conclusion

In this paper, it was demonstrated that Lewis lung carcinoma on 14 day after inoculation had hysteresis loop typical for was weak soft ferromagnetic in contrast to diamagnetic environment tissues. However, ferromagnetic properties aren't specific for malignant tumor [1, 2]. The concentration of paramagnetic centers in Lewis lung carcinoma is about three times greater than the concentration in environment tissue. Maximal concentration of paramagnetic centers was observed in MC samples. Also DR after mechano-magneto-chemical treatment is paramagnetic in contrast to conventional drug which is diamagnetic.

In future we are planning to study nonlinear dynamics of magnetic properties of MC components, Lewis lung carcinoma and its environment over time after tumor inoculation. It will advance our understanding of possible singularities in magnetic properties during interaction MC components with tumor and tumor microenvironment**.** Whereas only 10–15% of the total amount of nanoparticles introduced into a patient [12] reached tumor, this information would be able to increase the efficiency of drug delivery technologies.

Acknowledgment

We are grateful to Dr. N.N. Khranovskaya and O.V. Skachkova for assistance in preparing of biosamples.

References

1. Brem F, Hirt A, Winklhofer M et al. (2006) Magnetic iron compounds in the human brain a comparison of tumor and hippocampal tissue. J Royal Soc Interface 3:833–841
2. Kirschvink J, Tabrah F, Batkin S (1982) Ferromagnetism in two mouse tumours. J Exp Biol 101: 321–326
3. Dörner M, Silverstone A, Nishiya K et al. (1980) Ferritin synthesis by human t lymphocytes. Science 209:1019–1021
4. Pankhurst Q, Connolly J, Jones S et al. (2003) Application sofmagnetic nanoparticles in biomedicine. Appl Phys D36:R167–R181
5. Orel V, Shevchenko A, Mel'nik Y et al. (2010) Physicochemical characteristics of magnetosensitive nanocomplex obtained by mehanomagnetochemical technology of dry synthesis. Metallofiz Noveishie Tekhnol 32:1157–1167
6. Gutman E (1998) Mechanochemistry of materials. Int Science Publishing, Cambridge
7. Kuramitz H (2009) Magnetic microbead-based electrochemical immunoassays. Anal Bioanal Chem 394: 61–69
8. Walter H, Wampler L, Stablein D et al. (1982) Drug activity and therapeutic synergism in cancer treatment. Cancer Res 42:2963
9. Makarova T, Sundqvist B, Esquinazi P et al. (2001) Magnetic properties of carbon structures. Nature 413: 718–722
10. Blumenfeld L (1981) Problems of biological physics. Springer-Verlag, Berlin
11. Köseoglu Y, Ysildiz F, Kim D et al. (2004) ESR studies on superparamagnetic Fe_3O_4 nanoparticles. Phys Stat Sol C1:3511–3515
12. Amiji M (2007) Nanotechnology for Cancer Therapy. CRC Press, Boca Raton

Author: Valerii E. Orel
Institute: National Cancer Institute
Street: 33/43 Lomonosova Str
City: Kyiv
Country: Ukraine
Email: v-orel@voliacable.com

The Modelling of Cell Membrane Electrodynamics

Jānis Valdmanis

Institute of Physics University of Latvia
32 Miera str., Salaspils, LV-2169, Latvia
jvaldman@sal.lv

Abstract — **Main electrical processes in cells are defined by membranes. The membrane maintains a biochemical environment inside the cell that differs from the outside one, keeping the electrical potential negative inside the cell and organizing the selective transport across the surface. In the paper, it is attempted to explain the cell membrane electrodynamics using modelling experiments with magnetic dipoles. It is shown that the membrane has a definite symmetry or handenness. In addition, a characteristic mechanism of the excited state physics is given. The modelling experiments have also shown that a membrane with different symmetry can exist. Since the electrical processes in these cases are different, such cells could be dangerous to organisms. The recent knowledge of physical processes in a carbon sheet just of one atom thick and its biophysical aspects are discussed.**

I. Introduction

In recent years, researchers very actively investigate one-atom-thick crystalline and plane (2D) systems. An example on the crystalline element is the buckyballs also known as C_{60} that had been discovered in 1985 [1].There is not only C_{60}, but a whole family of related molecules. Carbon atoms are connected by electrical (quantum mechanical) forces and form a periodical structure.

Examples of plane 2D systems are graphene, graphane and graphyne. Since the physical processes in such systems are at starting positions, there are no review monographs, but all interesting effect one can find by clicking in the internet. The main characteristics of such 2D systems are the one-atom-thick layer and the periodic character of structure. Graphene and graphyne are electrical conductors. The conductivity is realized by electrons. There are some new specific effects, which allow electrons to be massless and transferred along the film surface with very a high speed. Graphene has a hexagonal structure, but graphyne is a combination of hexagons and tetrahedrons [2]. In comparison with graphene and graphyne, graphane is an electrical insulator because its electron bonds are saturated with some atom (usually H) absorbed on the film surface. There are no free electrons and no electrical conductivity. Another interesting effect is that on the film surface there locally exists a region strained in a particular way that influences the electron transfer character. The electrons start rotating around the strained zone, and physically it is like existence of a strong local magnetic field [3].

II. Results of Modelling Experiments

Due to some analogy between electric and magnetic characteristics in modelling experiments, small magnetic balls were used. In this case, main forces between balls are dipole-dipole interactions. Magnetic balls of 5 mm in diameter and maximum induction of 100 mT are used. We will start with a model of C_{60} molecule known as the buckyballs. There are 20 hexagonal and 12 pentagonal elements, which make approximately a round surface (fig. 1).

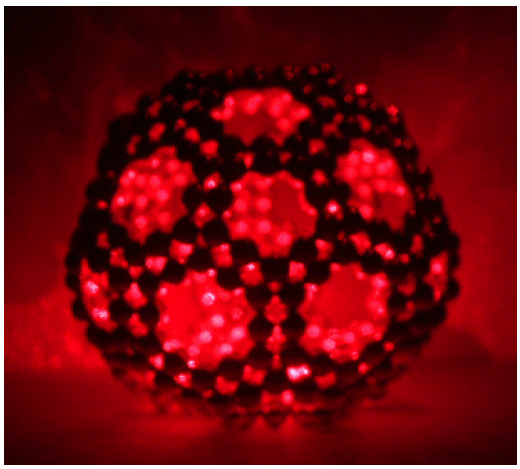

Fig. 1 The model of magnetic buckyballs with definite symmetry.

If we try to complete the plane elements, the hexagon is still plane, but pentagons can make either a convex or a concave structure. In each element in the central part, there is a channel that could be modelled for outside–inside communications (fig.2).

Y. Dekhtyar et al. (Eds.): *International Symposium on Biomedical Engineering and Medical Physics*, IFMBE Proceedings 38, pp. 90–92, 2013.
DOI: 10.1007/978-3-642-34197-7_23

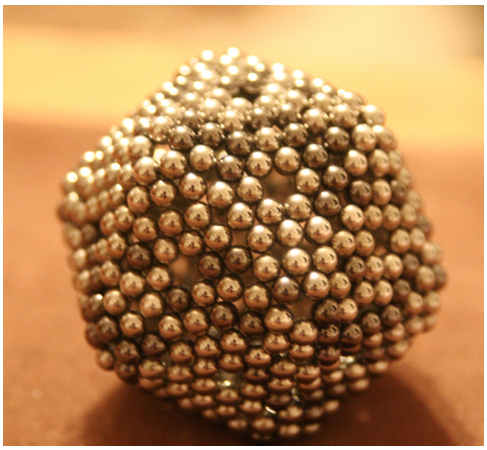

Fig. 2 The buckyballs membrane model with all 12 pentagons in the convex state.

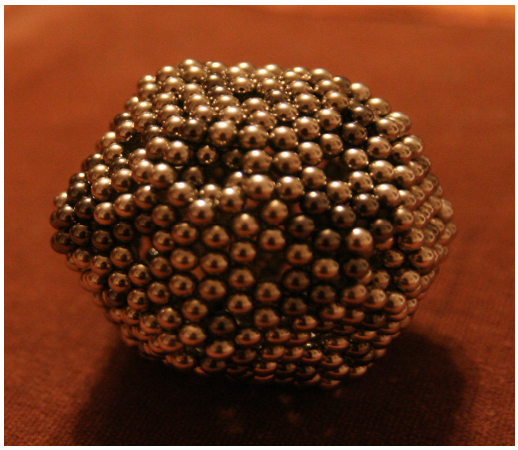

Fig. 3 The membrane model when three pentagons are in the concave state.

If there appears some local or global membrane straining actions, the pressure increases inside the cell and an ion current is generated from inside to outside. Another possibility is the current generator by regular pentagon changes from convex to concave configuration. In fig. 3, three pentagons are shown in the concave state.

The current pulse generates a magnetic field around the flow. Such field tries to conserve the current value and initiate the known "overshoot" effect. Due to the small geometry of the pump channel, which is also an electrical current dimension, there could appear resonant effects [4]. In fact, the electrical current retains the potential inside the cell and goes to the initial negative value with a small returning "overshoot". There are two important things. First, all elements in figs.2, 3 are with the same symmetry. Second, it is possible to decrease the geometry of the elements by going to polyhedrons. It means to decrease the size of the balls and increase the number of the elements. Therefore, we can have also a molecular dimension. The communication across the membrane is realized by ions or by dipole particles. Taking into account many specific effects of electrons in such one-atom-thin film, an important role of electrons for communications along the membrane surface as well as for global communication between cells in the organism as a whole is acknowledged.

The model (figs. 2, 3) has a definite symmetry, let us say left-handed. It is possible to use the same elements to manage buckyballs with a right-handed symmetry. There will be no difference visually, but the changes can initiate differences in communication and interaction processes. By splitting the process, such abnormal cell will generate cells with the same symmetry. Such membranes and cells could be dangerous to organisms. In the modeling experiments, we used the magnetic dipole, but there is analogy with the electrical one. In the membrane, we have a normal electric field. We can suppose that there is also a magnetic field around the electric field.

How to destroy the cell membrane? In the modelling experiments, it is realized by taking out separate elements step by step. Another way is to increase the pressure inside the cell that will initiate the cell decay in separate elements. In modelling experiments, it is possible to make a two-layer model as well as an onion type one.

III. Conclusion

The carbon film investigation is just at starting position, and every day brings some new surprising physical results. We focus on some interesting processes, which could occur in biomembranes. The structure of the carbon sheet as well as C_{60} is made by atoms. In biomembranes, we have molecular complexes. In the modelling experiments, we have used macro dipoles. It seems that there is a physical analogy and no influence of the dimension scale. Modelling experiments with magnetic dipoles allow to extend the results also to systems with electrical dipoles. There are enormous experimental and theoretical data in cells membranes science, and the discussed results could only serve as ideas that would stimulate future investigations.

References

1. I.Peterson. *Atoms in buckyball cage*. Science News, February 27, 1993, p.193.

2. Daniel Malko, Christian Neiss, Francesc Viñes, and Andreas Görling. Competition for Graph*ene: Graphynes with Direction-Dependent Dirac Cones. Rev. Lett. 108, 086804 (2012) [4 pages].*

3. Antonio H. Castro Neto. *Another Spin on Graphene Science.* 15 April 2011: Vol. 332 no. 6027 pp. 315-316.
4. Janis Valdmanis, Aleksandrs Cipijs. *On the mechanism of low frequency bioelectromagnetism*. The14-th Baltic Conference on Biomedical Engineering and Medical Physics, 2008, pp.347-349.

Entering the Nano-Cosmos of the Cell by Means of Spatial Position Determination Microscopy (SPDM): Implications for Medical Diagnostics and Radiation Research

M. Hausmann[1], P. Müller[1], R. Kaufmann[1] and C.Cremer[2]

[1] Kirchhhoff-Institute for Physics, University of Heidelberg, Im Neuenheimer Feld 227, 69120 Heidelberg, Germany
[2] Institute for Molecular Biology, University of Mainz, Ackermannweg 4, 55128 Mainz, Germany

Abstract— **During the last 20 years fluorescence light microscopy has made an enormous progress towards fluorescence nanoscopy in order to elucidate the nanostructural organization of cellular machineries beyond classical limits of resolution in light microscopy. One of these novel techniques is Spatial Position Determination Microscopy (SPDM), an approach of molecular localization microscopy based on the application of specific fluorescence labelling of cellular structures by means of dyes that undergo reversible photobleaching resulting in blinking effects during image acquisition. This blinking allows spectral separation of individual molecules and thus precise localization and distances measurements far below the diffraction limited resolution of an objective lense. Here, the principles of this technique are presented and the imaging power is demonstrated by several examples of nano-analyses in various cell systems. It is shown how receptor clusters of Her2/neu change their morphology in different tumour cell types depending on the degree of overexpression. From the distribution of the m164 protein, nano-structural information of the endoplasmatic reticulum and the nuclear membrane can be obtained after murine cytomegalovirus infection. SPDM analysis of the distribution of nucleosomes in cell nuclei in comparison to computer models can give insights into the nano-architecture of cell nuclei and its conformation changes after radiation exposure and during DNA repair processes. Finally, first approaches of SPDM and Combinatorial Oligonucleotide Fluorescence In Situ Hybridization (COMBO-FISH) indicate that nano-analyses of chromatin conformation of gene target sites will become feasible.**

Keywords— **localization microscopy, Spatial Position Determination Microscopy, nanostructures of membranes, organization of the endoplasmatic reticulum, chromatin conformation changes**

I. Introduction to SPDM

A serious impediment to exploit the potential of light microscopy to study cellular structures has been the conventional optical resolution due to diffraction limits of the objective lenses used. Using visible light the resolution limit described as the smallest distance between two discriminable object points results at about 200 nm laterally and 600 nm axially and can be calculated by the Abbe–Rayleigh criterion. Novel microscopic techniques, however, enable effective optical resolutions down to about 20 nm or even better [1]. One of these high resolution techniques is localization microscopy based on the fundamental concept of using fluorophores that can be switched between two different spectral states to achieve a temporal isolation and thus a spatial separation of signals. This allows the determination of positions of fluorophores and their spatial distances even if they are below the conventional optical resolution. During the last few years localization microscopy has been established in a series of embodiments as for instance photoactivated localization microscopy (PALM), fluorescence-activated localization microscopy (FPALM), stochastic optical reconstruction microscopy (STORM) etc. (see references in [1]). Many of these embodiments require photo-switchable fluorochromes.

Spatial Position Determination Microscopy (SPDM) originally also called Spectral Precision Distance Microscopy (SPDM), was developed in the mid 1990s as an early localization microscopy approach [2] with a localization precision of 50 nm or even better in 3D conserved cell nuclei [3, 4]. In this early version spectral separation was obtained by different signatures like colours of emission.

The nowadays applied improved version [5, 6] is still using conventional fluorophores (e.g. fluorescent proteins or Alexa dyes). The applied dyes, however, can be switched to a “dark” state by a light induced reversible photobleaching process. The stochastic recovery of the fluorophores from this “dark” state to the bright state can be interpreted as “blinking” and allows optical isolation of individual molecules, although they show the same emission spectrum. Taking a time series of images of a given region of interest and merging all localization values of blinking molecules into one image results in high resolution, structural information of a given object.

Y. Dekhtyar et al. (Eds.): *International Symposium on Biomedical Engineering and Medical Physics*, IFMBE Proceedings 38, pp. 93–95, 2013.
DOI: 10.1007/978-3-642-34197-7_24

II. Applications of SPDM

So far SPDM has found a broad spectrum of biological/biophysical and biomedical applications in 2D and 3D localization microscopy [1].

In the following some typical examples are presented and summarized:

a) Certain types of breast cancer are characterized by an overexpression of erbB-2 which can be associated by a copy number increase of the Her2/neu gene on chromosome 17. In order to study tumour typical conformational changes of erbB-2 receptor clusters on cell membranes different mamma carcinoma cell lines and cells of a breast biopsy of a healthy donor were analyzed. The characterization of the erbB-2 distribution yielded typical receptor clusters with a mean diameter of 67 nm independently from the cell line (Fig. 1). Statistical analyses of the receptor antibody distances within the clusters revealed significant differences in clustering of erbB-2 between the different cell lines [7]. Moreover, by means of two colour 3D-imaging of erbB-2 clusters and erbB-3 clusters an indirect stimulation of erbB-2 after Neureguline stimulation of erbB-3 could be verified by typical structural changes within the respective receptor clusters.

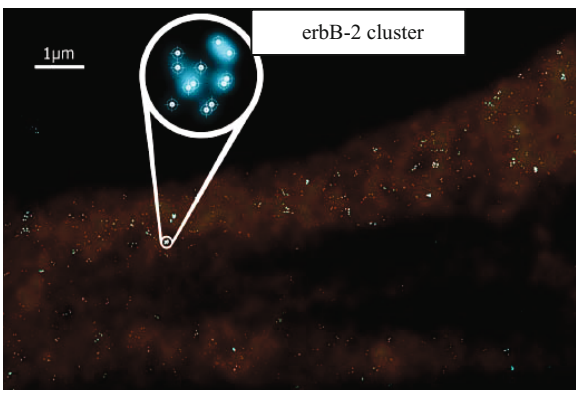

Fig. 1 Image section of a cellular membrane after specific antibody labelling of erbB-2 receptors. SPDM can resolve the molecular organization of the receptor clusters as shown by the enlarged insert. The erbB-2 cluster shown here has a diameter of 82 nm.

b) The importance of CD8 T-cells for the control of cytomegalovirus (CMV) infection has raised interest in the identification of immunogenic viral proteins as candidates for vaccination and immunotherapy. Gene m164 of murine CMV thought to represent a 'host adaptation' gene involved in virus-host interaction. The m164 protein was analyzed by SPDM as a membrane glycoprotein with exceptional intracellular trafficking dynamics, moving within the endoplasmatic reticulum (ER) and the outer nuclear membrane [1].

c) A combined approach of SPDM and statistical methods was used to interpret the nuclear nanostructure after specific labelling of all nucleosomes by green fluorescent proteins (GFP) (Fig. 2). The results show that different mechanisms of expression of the same nuclear protein type lead to significantly different patterns on the nanoscale below 200 nm nucleosome distances and to pronounced differences in the detected compressibility of chromatin [8].

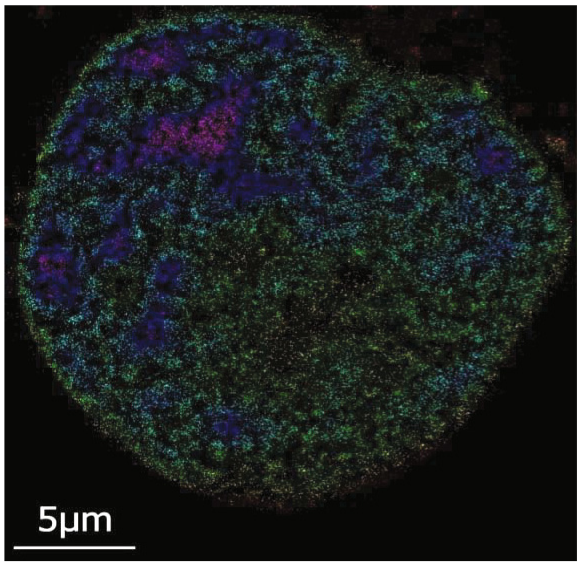

Fig. 2 Image section of a cell nucleus after specific labelling of the nucleosomes by GFP. About 70,000 individual signals can be discriminated by SPDM and their distances can be calculated. In this image the colour code from green to blue, violet represents a measure for the number of neighbouring signals within an environment of 200 nm.

d) The same cells expressing nucleosomal labels by GFP were used. Combining this labelling with specific antibody labelling against heterochromatic or euchromatic regions in the cell nucleus revealed typical chromatin rearrangements after exposure to ionizing radiation between 0.5 Gy and 4.0 Gy. Preliminary results indicate that during repair processes heterochromatic clusters could be reconstituted. Euchromatic rearrangemants may be dose dependent.

e) With the completeness of genome data bases, it has become possible to develop a novel FISH (Fluorescence In Situ Hybridization) technique called COMBO – FISH (COMBinatorial Oligo FISH). In contrast to other FISH techniques, COMBO – FISH makes use of a bioinformatic approach for probe set design. By means of computer genome data base search, several oligonucleotide stretches of typical lengths of 15 – 30 nucleotides can be selected in such a way that all uniquely colocalize at the given genome target. For a probe repetitively highlighted in centromere 9, the specific locus was clearly discriminated by the signal intensity. Individual signals were detected with localization accuracy in the range of 10-20 nm. These results indicate that COMBO-FISH probes with blinking dyes are well suited for SPDM which will open new perspectives on molecular nanostructure analysis of the genome [9].

III. CONCLUSION

SPDM is a novel technique of localization microscopy that allows imaging of single molecule positions in 3D conserved cells after specific labelling of nanostructures. The localization precision in the nanometer range results in an effective optical resolution one order of magnitude below the conventional diffraction limited resolution. For biomedical applications SPDM has the advantage that it can be implemented in standard microscopic systems so that objects can be analyzed under different detection modi without changing the instrument. Moreover, specimens can be prepared according to standard protocols and with well established dyes and labelling strategies. These advantages will open new perspectives in biological and biophysical research as well as in medical diagnostics.

ACKNOWLEDGMENT

The financial support of the BMBF (Bundesmisterium für Bildung und Forschung) and the BMU (Bundesministerium für Umwelt, Energie und Reaktorsicherheit) are gratefully acknowledged. SPDM and COMBO-FISH are patents of M.H and C.C.

REFERENCES

1. Cremer C, Kaufmann R, Gunkel M, et al. (2011) Superresolution imaging of biological nanostructures by Spectral Precision Distance Microscopy (SPDM). Review. Biotech. J. 6: 1037-1051
2. Cremer C, Hausmann M, Bradl J, Rinke B (1996) German Patent DE 196 54 824.1; European Patent EP 0 946 855 B1; US-Patent 6,424,421 B1
3. Esa A, Edelmann P, Kreth G, et al. (2000) Three-dimensional spectral precision distance microscopy of chromatin nanostructures after triple-colour DNA labelling: a study of the BCR region on chromosome 22 and the Philadelphia chromosome. J. Microsc. 199: 96 – 105
4. Rauch J, Knoch TA, Solovei I, et al. (2008) Lightoptical precision measurements of the active and inactive Prader-Willi Syndrome imprinted regions in human cell nuclei. Differentiation 76: 66-82
5. Lemmer P, Gunkel M, Baddeley D, et al. (2008) SPDM – light microscopy with single molecule resolution at the nanoscale. Appl. Phys. B 93: 1-12
6. Lemmer P, Gunkel M, Weiland Y, et al. (2009) Using conventional fluorescent markers for far-field fluorescence localization nanoscopy allows resolution in the 10 nm range. J. Microsc. 235: 163-171
7. Kaufmann R, Müller P, Hildenbrand G, et al. (2011) Analysis of Her2/neu membrane protein clusters in different types of breast cancer cells using localization microscopy. J. Microsc. 242: 46-54
8. Bohn M, Diesinger P, Kaufmann R, et al. (2010) Localization microscopy reveals expression-dependent parameters of chromatin nanostructure. Biophys. J. 99: 1358-1367
9. Müller P, Schmitt E, Jacob A, et al. (2010) COMBO-FISH enables high precision localization microscopy as a prerequisite for nanostructure analysis of genome loci. Int. J. Molec. Sci. 11: 4094-4105

Author: Prof. Dr. Michael Hausmann
Institute: Kirchhoff-Institute for Physics
Street: Im Neuenheimer Feld 227
City: 69120 Heidelberg
Country: Germany
Email: hausmann@kip.uni-heidelberg.de

Cardiosynchronous Transcutaneous Electrical Nerve Stimulation

Z. Bredriha[1], J. Lauznis[1], and P. Butlers[2]

[1] Riga Technical University, Riga, Latvia
[2] Riga Stradins University, Riga, Latvia

Abstract — **Cardiosynchronous transcutaneous electrical nerve stimulation device is new technology. In our studies we use electrical nerve stimulation 200ms after R-wave with 125ms long bipolar pulses package to decrease Rate - Pressure product. The aim of the present study is technical elaboration of the innovative ECG R-wave triggered transcutaneous nerve stimulation prototype device to further perform the feasibility studies of such a neurostimulation technology.**

Keywords — **blood pressure, electrical nerve stimulation, heart rite.**

I. Introduction

Transcutaneous electrical nerve stimulation applied to human afferent nerves (auricular branch of vagus, trigeminal nerve, median nerve) has been widely used as therapeutic tool in cardiology for a treatment of angina pectoris, hypertension and other diseases associated with elevated sympathetic neural system activity [1]. However typical stimulation intensity (electrical current) frequently exceeding motor threshold (causes muscle contractions) which leads to adverse, in fact opposite, side effect of stimulation - reflexively increasing sympathetic outflow during stimulation (somato-sympathetic reflex) which can significantly reduce the therapeutic efficiency of stimulation.

Transcutaneous electrical nerve stimulation is used for ischemic heart disease therapy [2]. This stimulation decreases sympathetic activity heart workload and myocardial oxygen consumption because on that we use rate pressure product for control parameter which characterizes heart workload and myocardial oxygen consumption. Stimulation always has a side effect – somatosympathetic reflex, therefore there is a need to optimize stimulation mode.

Recent studies [3] have demonstrated that augmentation of the sympathetic activity can be reduced if the intermittent sensory stimulation pulse is applied during each cardiac cycle with the time delay 200-400ms after ECG R-wave. Moreover previous pilot study shows that applying of such a cardio synchronous stimulation mode to the afferent nerve endings in human auditory canal results in significant lowering of arterial systolic pressure if the initial arterial pressure values were elevated.

Till now there is no such noninvasive neurostimulation device with which it is possible to decrease high sympathetic neural system activity and myocardial oxygen consumption. There is developed TENS device by CardioLa [4] [5]. Device stimulates skeletal muscles and makes heart load easier by pumping blood. It is not possible to use it in long term because muscles get tired. Therefore a stimulator for long term use is needed.

II. Materials and methods

According to aim prototype device for transcutaneous nerve stimulation was developed by INTEGRIS, Ltd and RTU, Latvia and tested in pilot experiments.

Equipment used in pilot experiment is: ECG monitor with R-wave pulse output – Cardiac Trigger Monitor, Model 3100, IVY, USA; Digital Storage Oscilloscope – TDS 2002B, Tektronix, USA; ECG Phatom 320, M&S, Germany (only for preparations work); prototype device - Experimental Synchronous Programmable Electrostimulator (Experimental stimulator) developed by INTEGRIS, Ltd and RTU, Latvia. Experimental stimulator (prototype device) is forming pulses during each cardiac cycle with the changeable time delays and pulse packet length. As well pulse amplitude is changeable. For experiment device was programmed to generate train of bipolar stimulation pulses, with pulse length 1ms and 4ms pause between them. Pulse count in train (packet length) and delay time from trigger pulse (formed by ECG R-wave) can be changed using one of 7 different patterns. Amplitude of pulses is adjustable from 0 to 15V with limited maximum current at 10mA.

To test device and concept we provided 2 physiological experiments (with time delay and without it after R-wave) for one person with elevated blood pressure. Pilot experiments schematic is shown in figure 1. Stimulation was done for the person who had initial average systolic blood pressure 153 and heart rate 84. To show and record processes we used storage oscilloscope, Fig.1 (2). Fig.1 (1) represents Cardiac Trigger monitor to synchronize microcomputer with ECG R-wave. Experimental stimulator uses LiPo battery with 1100 mAh capacity Fig.1 (4) for independent

Y. Dekhtyar et al. (Eds.): *International Symposium on Biomedical Engineering and Medical Physics*, IFMBE Proceedings 38, pp. 96–98, 2013.
DOI: 10.1007/978-3-642-34197-7_25

power supply. Voltage converter Fig.1 (5) provides stabile 5V for microcomputer (Fig.1 (3)) and isolated stimulation pulse former. According to the experiment program isolated pulse former Fig.1 (6) provides required signal form and current intensity.

The ECG signal was taken from chest electrodes and simulation signal was applied to vagus nerve by special ear electrodes (Fig.1) that were made only for this experiment.

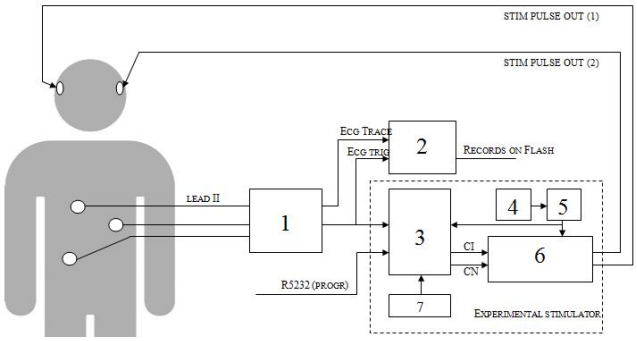

Fig. 1 Pilot Experiment schematic.

Pilot experiments were made for 2 simulation signal pauses after the R-wave: in first experiment simulation provided 25 pulses (0.5ms positive pulse, 0.5ms negative pulse, 4ms pause) 200ms after R-wave, pulse current 6mA ±5%, figure 2 shows Oscilloscope screen.

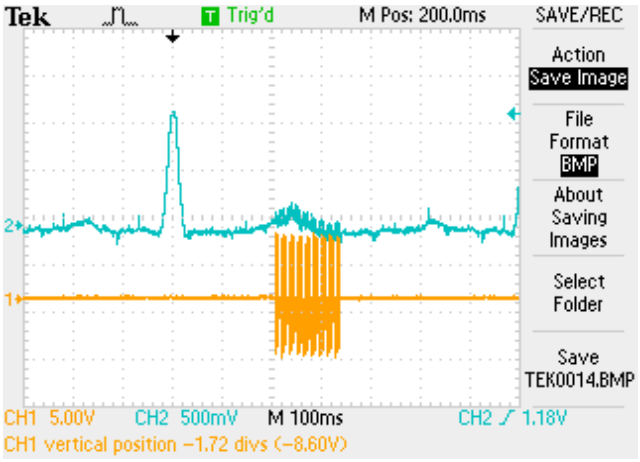

Fig. 2 Oscilloscope screen in first experiment.

In second experiment stimulation provided 25 pulses (0.5ms positive pulse, 0.5ms negative pulse, 4ms pause) with R-wave pulse current 9mA ±5%, figure 3 shows Oscilloscope screen.

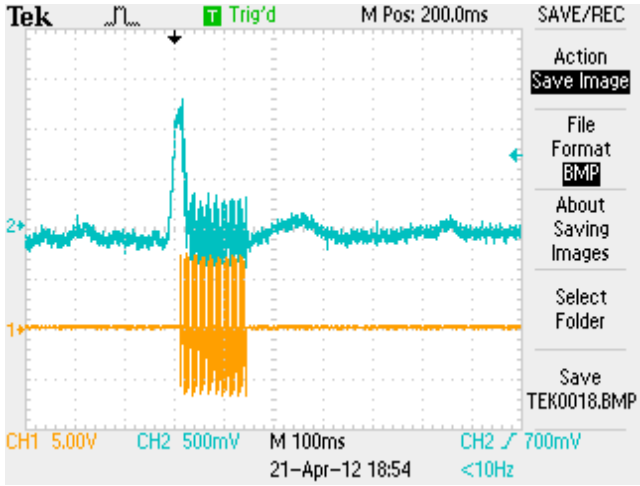

Fig. 3 Oscilloscope screen in second experiment.

Patient was measured for systolic blood pressure SBP diastolic blood pressure and pulse rate PR in 1 minute interval for 25 minutes during the stimulation. From measured data we can compute (1) Rate-Pressure Product RPP (beats per minute (bpm) multiplied (*) by systolic blood pressure in mmHg), that characterizes heart workload and myocardial oxygen consumption.

$$RPP = SBP \times PR \,/100 \tag{1}$$

III. Results

Pilot experiments shows that innovative ECG R-wave triggered transcutaneous nerve stimulation prototype device is working properly and is user friendly. Device is programmable to obtain different pulse length, delay time (7 different patterns) and pulse amplitude.

Prototype device was used in two pilot experiments for vagus nerve stimulation with 200 ms delay after R-wave, see figure 4, and right after R-wave see figure 5.

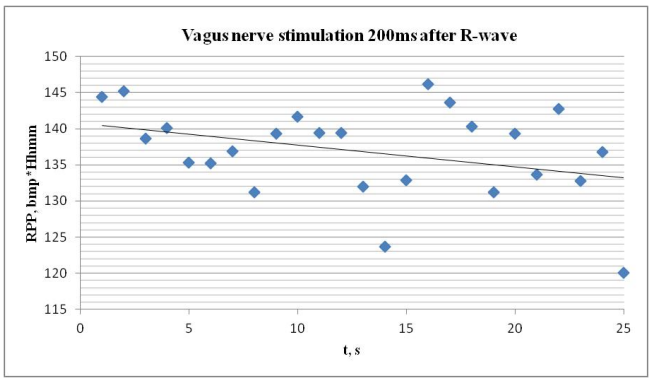

Fig. 4 Stimulation 200ms after R-wave.

This stimulation causes approximately 12% RPP decrease in last 10 minutes. Moreover second experiment where stimulation was right after R-wave RPP didn't show changes (figure 5).

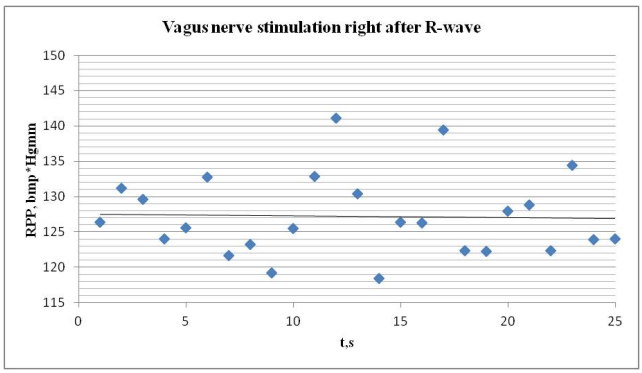

Fig. 5 Stimulation right after R-wave.

IV. Conclusion

1) According to our aim new transcutaneous nerve stimulation prototype device was designed and built having possibility to synchronize it with ECG monitor. Experiments proved possibility to change delay after R-wave, pulse package length and pulse amplitude. Device is programmable so we can change all pulse parameters and number of pulses in package.
2) Primary hypothesis was accepted during pilot experiment, RPP dynamic depends on stimulation mode. The most rapid decline is when the intermittent burst stimulation is 200 ms after R-wave.
3) Experiments should be continued with different pulse parameters and delay time to obtain optimal results.

References

1. P. J. Schwartz , G. M. De Ferrari, A. Sanzo, M. Landolina, R. Rordorf, C. Raineri, C. Campana, M. Revera, N. Ajmone-Marsan, L. Tavazzi, A. Odero, Long term vagal stimulation in patients with advanced heart failure First experience in man European Journal of Heart Failure 10 (2008) 884–891
2. Zamotrinsky AV, Kondratiev B, de Jong JW. Auton Neurosci. 2001 Apr 12;88(1-2):109-16. Vagal neurostimulation in patients with coronary artery disease. http://www.ncbi.nlm.nih.gov/pubmed/11474540
3. J Neurosci. 2009 Feb 11;29(6):1817-25. Following one's heart: cardiac rhythms gate central initiation of sympathetic reflexes. http://www.ncbi.nlm.nih.gov/pubmed/19211888
4. http://www.cardiola.com/
5. P. Tozzia, A.F. Cornoa, L.V. Lapanashvilib, L.K. von Segesser Muscular counterpulsation: preliminary results of a non-invasive alternative to intra-aortic balloon pump European Journal of Cardio-thoracic Surgery 26 (2004) 726–729

Novel Concepts of "Niche-Relief" and "Niche-Voltage" for Stem Cells as a Base of Bone and Hematopoietic Tissues Biomimetic Engineering

I.A. Khlusov[1], Yu. Dekhtyar[2], M.Yu. Khlusova[1], E.A. Gostischev[1], Yu.P. Sharkeev[1], V.F. Pichugin[1], and E.V. Legostaeva[1]

[1] Scientific Educational Center "Biocompatible Materials and Bioengineering", Tomsk Polytechnic University, Siberian State Medical University, Institute of Strength Physics and Materials Science, Siberian Branch, Russia Academy of Sciences, Tomsk, Russia
[2] Riga Technical University, Riga, Latvia

Abstract — **An affect of relief features and quantitative variables of artificial surfaces on structural-functional status of human lung prenatal stromal cells (HLPSC) and remodeling of Balb/c mice bone/bone marrow system have been studied. Implants with rough (Ra>2 μm) calcium phosphate micro-arc coatings have structural-functional sites (micro-regions) named "niches-relief" which are necessary for maturation and differentiation of HLPSC into secreting osteoblasts in short-term culture. Maximal remodeling of mouse bone/bone marrow system in 45-day subcutaneous heterotopic test in vivo is also noted under optimal parameter (average index of cellular alkaline phosphatase area to artificial micro-region area is about 43 %) of osteogenic niche in vitro. Probable physical mechanism of osteogenic niche functioning has been determined. It correlates with increasing of electron work function (φ) supplied with a negative charge of calcium phosphate nanorelief in the sockets (artificial "niches"). "Niche-voltage" concept for bone tissue biomimetic engineering was proposed.**

Keywords — **Calcium phosphate coatings, artificial micro-territories, cell culture, mice, electron work function.**

I. Introduction

Currently, a lot of publications, mainly as hypotheses, were dedicated to niches for hemopoietic stem cells (HSC). Multipotent mesenchymal stromal cells (MMSC) are treated as important cell component of HSC niches [1].

At the same time, the circumstance that discussion of existence of niches determining fate of MMSC themselves just appears in literature sets at gaze [2]. Pilot experimental data about existence and dimensions of niches for osteogenic differentiation of MMSC, their close dependence on quantitative variables of bone mineral substance relief were recently obtained by us [3].

As early as in 1964 A.S. Curtis and M. Varde [4] supposed the most important role of surface topography and geometry in determination of cell behavior. According to [5], scientists are only at the beginning of understanding of their effect.

In this connection, investigation of the relief features effects of model mineral matrix on structural-functional conditions of human MMSC and remodeling of bone/bone marrow system in mice was of great interest.

II. Specimens

A. Titanium Specimens with Calcium Phosphate (CP) Coating Preparation

Pure titanium specimens (diameter 12 mm, thickness 1 mm) with bilateral rough (Ra>2 μm) CP coatings were used as artificial substrate for MMSC cultivation. Coatings were applied on titanium by means of anode-spark (microarc) oxidation method in 10 % phosphoric acid solution containing suspension of nano-sized (20 – 40 nm) synthetic HAP particles with stoichiometric composition $Ca_{10}(PO_4)_6(OH)_2$ [6]. Smooth CP surfaces (Ra<1 μm) were formed by means of high-frequency magnetron sputtering of CP target electrode [7].

B. Artificial Surfaces Investigation

Morphology and ultimate composition of CP coatings were estimated by Quanta 200 ESEM FEG scanning electronic microscope (SEM) (FEI Company, USA) with an Oxford Inca Energy Dispersive X-ray (EDX).

Roughness of CP coatings was evaluated by means of Talysurf 5-120 measuring system (Taylor-Hobson, UK, resolution 10 nm). Ra (μm) index was determined.

An alteration of electron work function (φ) was estimated by photoelectron emission (soft ultraviolet prethreshold mode) technique from the surface nanolayer. An increment of the electron work function (φ) was an index on potential alteration. An auto correlation function of the voltage distribution over the specimens' surface was calculated on a base of Kelvin probe measurements. These manipulations were carried out as described earlier [8].

Y. Dekhtyar et al. (Eds.): *International Symposium on Biomedical Engineering and Medical Physics*, IFMBE Proceedings 38, pp. 99–102, 2013.
DOI: 10.1007/978-3-642-34197-7_26

III. In vitro experiments

A. Short-Term Cell Culture

Culture of human lung prenatal stromal cells (HLPSC, "Stem cells bank" Co Ltd., Tomsk) was used in experiments as MMSC source. HLPSC differentiation into alkaline phosphatase (ALP) positive cells secreting osteocalcin was established by us earlier [3].

For cells cultivation on titanium discs with CP coating we used following medium's composition: beta-glycero phosphate (10 mM), ascorbic acid (50 μg/ml), dexamethasone (10^{-6} M), L-glutamine (280 mg/l), gentamicin sulphate (50 mg/l), HEPES buffer (10 mM), 20% fetal bovine serum, 80% DMEM/F12 (1:1) medium.

Discs were placed in plastic wells (area 1.77 cm^2) of 24-well plate (Orange Scientific, Belgium). Cell suspension (1 ml) in concentration of $3x10^4$ viable karyocytes in complete cultural medium was added.

B. Cytochemical Assay

Discs with adherent cells were removed in 4 days and air-dried. Adherent cells fixation was carried out in formalin vapor during 30 sec. Fixed cells were stained for alkaline (ALP) and acid phosphatase (ACP) by means of azo-coupling method. Naphthol- ASMX-phosphate, fast garnet salt (Lachema, Czechia) was used. Other specimens with adherent cells were prepared to SEM.

C. Immunoenzyme and Biochemical Analyses

Concentrations of calcium and inorganic phosphorus, ALP activities in intercellular liquids (supernatants) were estimated by Roche Hitachi 911 Analyzer according to standard colorimetric method.

Osteocalcin (OC) levels were measured in cell supernatants by "sandwich" ELISA.

IV. In vivo experiments

A. Heterotopic Osteogenesis Test

20 BALB/c male mice were used in heterotopic (ectopic) bone formation experiments. Investigations were carried out with consent of Local Ethics Committee of Siberian State Medical University (Verdict No. 948 from 09.02.2009).

We have earlier obtained reproducible results of subcutaneous heterotopic osteogenesis in mice from column of syngeneic bone marrow, preliminary applied on CP surfaces [9]. In current research implants with aseptically applied column of syngeneic bone marrow (average area of marrow was 7.5 mm^2) from femoral bone were subcutaneously introduced into mice under ether anesthesia. For cell adhesion the bone marrow culture was previously precultured on disks during 45 min under 37 °C.

B. Histological Techniques

In 45 days animals were devitalized with ether narcosis. Implants were decalcified. Tissue plates were removed from discs' surface, embedded with wax. Thin (10μm) serial sections in projection perpendicular to implant surface were made and stained with hematoxylin and eosin for histological investigations.

C. Computer Morphometry and Statistical Analysis

Computer morphometry was applied for detection of cell quantity parameters by means of measurement of their optical characteristics. Area and optical density of stained cells were estimated with the use of ImageJ program. Area was expressed in square nanometers, optical density – in standard units of optical density (s.u.o.d.).

Obtained results were expressed as average number (X), 25 % (Q1), and 75 % (Q3) quartiles or statistical deviation (SD). Mann-Whitney U test was used for estimation of statistical significance of sampling differences. Spirman's correlation analysis was carried out for definition of connection between indices being studied.

V. "Niche-relief" concept proposal

Short-term culture of HLPSC with fibroblast-like morphology was used on calcium phosphate (CP) substrates with known topography. According to cell culture (OC, ALP) secretory activity, stromal stem cells interacting with CP discs directly obtained advantage in display of osteoblast-like functional activity in comparison with cells on plastic wells (Fig.1).

CP rough surfaces stimulated formation of three-dimensional culture of HLPSC. Cells staining positively for ACP were located on spheroliths forming relief of CP coatings. ALP stained cells (osteoblast' marker) populated sockets ("niches", Fig.2) of artificial surface.

The ratio of area of cell ALP staining to artificial surface area occupied with stained cell was calculated. S_{ALP}/Sniche index has been established to correlate with CP roughness index (Fig.3). Apparently, artificial "niches" for induction of human MMSC osteogenic differentiation are a structural-functional concept.

These data allowed us to propose "niche-relief" conception for osteogenic differentiation and maturation of stromal stem cells (MMSC). Rough (Ra>2 μm) CP surfaces have own

structure-functional sites (microregions) which were named by "niche-relief" and were able to accelerate in vitro MMSC maturation and differentiation into secreting osteoblasts.

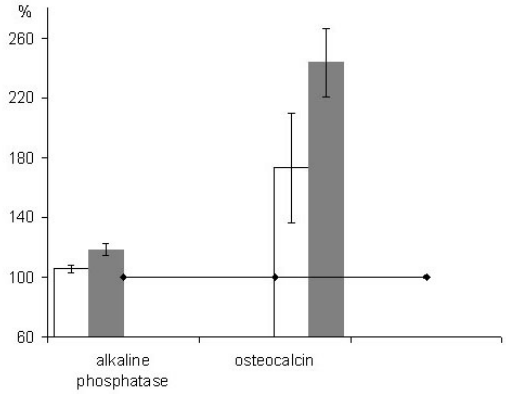

Fig. 1 HLPSC secretory activities on plastics (light columns) and CP coatings (dark columns). Results are presented as mean values and confidence intervals.

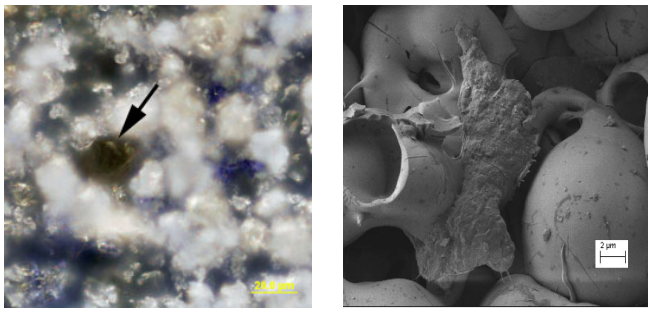

Fig. 2 ALP staining (magnification 1000) and SEM (magnification 10000) of HLPSC in the artificial "niches" of CP surface.

Thus, such CP coatings imitate the surface of remodeling bone tissue. Maximum heterotopic remodeling of mice bone/marrow system in vivo by means of endochondral ossification (Fig.4) was observed under S_{ALP}/Sniche ratio approximately 43 %.

Chemical (inorganic and organic) factors of HSC functioning are known and connected with intercellular calcium level and an activity of extracellular matrix [10]. Current research is devoted to probable physical mechanisms of cell/surface local interaction.

VI. "NICHE-VOLTAGE" CONCEPT PROPOSAL

Our scientific team designed the device for electrostatic potential measurement of low-charged surfaces by means of M. Eguchi method developed. Work area of elevating electrode is 20 square millimeters. CP electrets demonstrated negative charge of surface electrostatic voltage (SEV) with an average range of 45 mV.

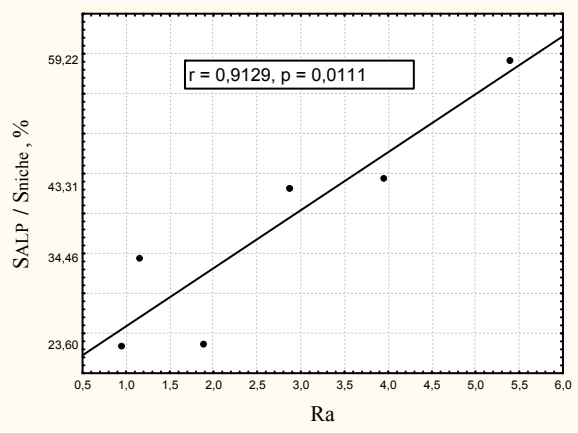

Fig. 3 An interconnection of HLPSC niches with Ra (μm) roughness index.

A direct electrostatic interaction is considered as predictor of cells adhesion to implants [11]. For all this, osteogenic cells have been known to migrate to cathode in electrostatic field [12]. So, it can promote an active cell seeding and spreading.

A correlation (r_S= 0,66; p<0,0004; n=25) of SEV and Ra indices of CP coatings was revealed. Besides, direct regression of Ra and its standard deviation (SD) was noted (Fig. 5).

It can be concluded that a complicacy of CP surface microrelief is accompanied by SEV acceleration.

Logarithmic interconnection of irregularities (SD) of CP coatings nanorelief and voltage estimated from the electron work function measurements was established (Fig.6). The value of φ characterizes a minimal energy that is necessary to supply to an electron to escape it from the solid during photoelectron emission. When the surface acquires the negative charge, φ increases [8].

Increasing φ (negative charge amplitude, respectively) in the sockets (artificial "niches", Fig.2) of CP coatings nanorelief was observed. In this connection, negative voltage of artificial "niches" can be basic physical mechanisms of MMSC moving, seeding and osteogenic differentiation. So, "niche-voltage" concept of biomimetic engineering of bone tissue can't be excluded.

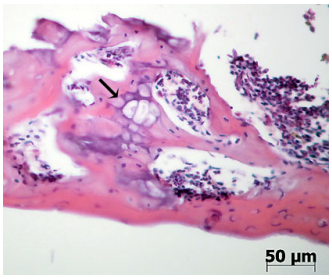

Fig. 4 Mouse bone and marrow formation on CP surfaces in heterotopic test in vivo (field of endochondral ossification is marked by black arrow).

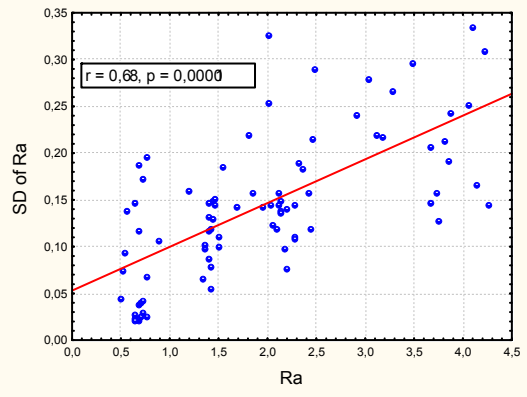

Fig. 5 A connection of Ra (µm) index with its standard deviation (SD).

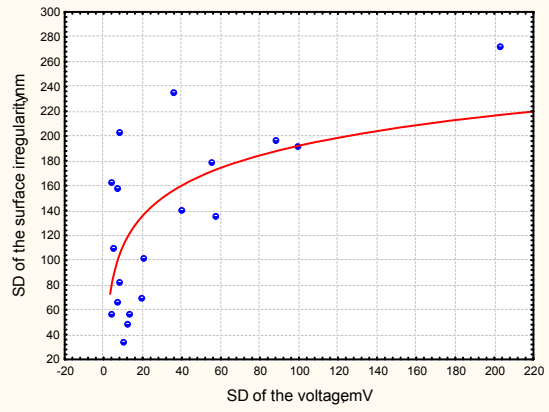

Fig. 6 A connection of nanorelief and voltage indices of CP coatings.

VII. Conclusions

Structural-functional sites (micro-regions) named "niches-relief" are necessary for stromal stem cells maturation and differentiation into osteoblasts in vitro and mouse bone/bone marrow remodeling in vivo.

Probable physical mechanism of osteogenic niche functioning connected with increasing of the electron work function of CP nanorelief in the sockets (artificial "niches") was proposed for prospective bone tissue biomimetic engineering.

Acknowledgment

Authors are deeply indebted to the Federal Goal Program of Russian Federation (grant No 16.512.11.2087).

References

1. Jing D, Fonseca A-V, Alakel N et al. (2010) Hematopoietic stem cells in co-culture with mesenchymal stromal cells – modeling the niche compartments in vitro. Haematologica 95:542-550
2. Kolf CM, Cho E, Tuan RS (2007) Mesenchymal stromal cells. Biology of adult mesenchymal stem cells: regulation of niche, self-renewal and differentiation. Arthritis Res Ther 9: 204-219
3. Khlusov IA, Khlusova MYu, Zaitsev KV et al. (2011) Pilot *in vitro* study of the parameters of artificial niche for osteogenic differentiation of human stromal stem cell pool. Bull Exp Biol Med 150(4):535-542
4. Curtis AS, Varde M (1964) Control of cell behavior: Topological factors. J Natl Cancer Inst 33:15-26
5. Sniadecki NJ, Desai RA, Ruiz SA, Chen CS (2006) Nanotechnology for cell-substrate interactions. Annals of Biomedial Engineering 34:59-74
6. Sharkeev YuP, Legostaeva EV, Eroshenko AYu et al. (2009) The structure and physical and mechanical properties of a novel biocomposite material, nanostructured titanium-calcium-phosphate coating. Composite Interfaces 16:535-546
7. Pichugin VF, Eshenko EV, Surmenev RA et al. (2007) Application of High-Frequency Magnetron Sputtering to Deposit Thin Calcium-Phosphate Biocompatible Coatings on a Titanium Surface. Journal of Surface Investigation. X-ray, Synchrotron and Neutron Techniques 1[6]: 679–82
8. Dekhtyar Yu, Dvornichenko MV, Karlov AV et al. (2009) Electrically Functionalized Hydroxyapatite and Calcium Phosphate Surfaces to Enhance Immobilization and Proliferation of Osteoblasts In *Vitro* and Modulate Osteogenesis In *Vivo,* IFMBE Proceedings vol. 25, World Congress on Med. Phys. & Biomed. Eng., 2009, pp 245–248
9. Khlusov IA, Karlov AV, Sharkeev YuP et al. (2005) Osteogenic Potential of Mesenchymal Stem Cells from Bone Marrow in Situ: Role of Physicochemical Properties of Artificial Surfaces. Bull Exp Biol Med 140:144-152
10. Scadden D.T. (2007) The stem cell niche in health and leukemic disease. Best Pract Res Clin Haematol 20:19-27
11. Smith IO, Baumann MJ, McCabe LR (2004) Electrostatic interactions as a predictor for osteoblast attachment to biomaterials. J Biomed Mater Res A 70: 436–441
12. Ferrier J, Ross SM, Kanehisa J, Aubin JE (1986) Osteoclasts and osteoblasts migrate in opposite directions in response to a constant electrical field. J Cell Physiol 129:283–288

Author: Igor A. Khlusov
Institute: Siberian State Medical University
Street: Moskovsky tract 2
City: Tomsk
Country: Russia
Email: khlusov63@mail.ru

Effects of Heat Stress on the Blood Pressure and Heart Rate Variability in Young Men

K. Jagomägi[1], O. Ates[2,3], J. Talts[1], R. Raamat[1], B. Cotuk[4], A. Burk[2], K. Karelson[2], V. Ööpik[2], T. Traks[1], and J. Kivastik[1]

[1] Department of Physiology, University of Tartu, Tartu, Estonia
[2] Institute of Exercise Biology and Physiotherapy, University of Tartu, Tartu, Estonia
[3] School of Physical Education and Sport, Istanbul University, Istanbul, Turkey
[4] Department of Exercise and Health, Marmara University, Istanbul, Turkey

Abstract — **Eighteen healthy military college cadets and university students were studied by means of a head-up-tilting test (HUT) in normal (temperature 22°, relative humidity 35%) and hot environment (42°C, 18%). During HUT the beat-to-beat mean blood pressure (MBP) and heart rate (HR) were continuously recorded with a differential oscillometric device. The MBP and HR variability were calculated in segments of 5 min using Fast Fourier Transform to obtain high frequency (HF, 0.15–0.4 Hz) and low frequency (LF, 0.04–0.15 Hz) components. In addition to that, we also computed the time domain indices rMSSD and pNN50 for HR variability analysis. Our study revealed that in the heat the mean values of HR were significantly higher in the supine as well as the tilted position compared to the situation in normothermia. At the same time, the mean values of MBP in the supine and tilted positions in normal as well as heat stress condition were not significantly different. The absolute values of LF and HF components of HR variability decreased in hyperthermia, while no significant changes in spectral indices of MBP variability and normalised values of HR variability were observed.**

Keywords — **Heat stress, head-up-tilting, continuous non-invasive mean blood pressure, heart rate variability, blood pressure variability.**

I. Introduction

Cardiovascular autonomic function tests (including head-up-tilting test) have been widely used to assess sympathetic and parasympathetic functions. The normal heart rate and BP response to upright tilt is a modest tachycardia with an increase in heart rate of 10-30 beats per minute. Systolic BP does not fall significantly. Diastolic pressure and mean arterial pressure rise somewhat. Whole-body heat stress compromises the control of blood pressure during an orthostatic challenge, although the extent to which this occurs can vary greatly between individuals [1], [2].

The aim of this study was to explore the effects of heat exposure on heart rate (HR) and mean blood pressure (MBP) variability in response to an orthostatic test (head-up-tilting, HUT) in healthy young male persons.

II. Methods and materials

A. Subjects

Eighteen healthy military college cadets and university students (age 23.4±3.2 years (mean±SD), height 181.1±5.1 cm and weight 80.2±1.2 kg) participated in this study. Approval was acquired from the University of Tartu ethics committee and all subjects provided written informed consent.

B. Head-Up-Tilting (HUT)

HUT was performed in the climatic chamber (Design Environmental Ltd., Gwent, South Wales, UK) twice, one in normal condition (air temperature 22°, relative humidity 35%) and the other in the heat (42°C, relative humidity 18%). The HUT protocol comprised three ten-minute phases: 1) supine baseline, 2) tilting at 70° and 3) resupine. The manually driven tilt-table was supplied with a footboard; during the test subjects were restrained by two Velcro straps placed around the legs and waist. Conversation, other than reporting symptoms, was discouraged.

C. Data Recording

Non-invasive beat-to-beat mean blood pressure was measured by the differential oscillometric device, University of Tartu, Estonia [3], [4]. This instrument applies the modified oscillometric method for measuring continuous mean blood pressure from finger or radial arteries and uses two photoplethysmographic sensors. The sensors were adjusted to the left hand, which was supported by a sling.

As the device was not provided with a height compensation system, corrections were inserted into obtained readings to compensate for the hydrostatic difference between the point of measurement and the heart level (right atrial level in the tilted position and the mid axillar line in the supine position).

Y. Dekhtyar et al. (Eds.): *International Symposium on Biomedical Engineering and Medical Physics*, IFMBE Proceedings 38, pp. 103–106, 2013.
DOI: 10.1007/978-3-642-34197-7_27

In addition to the non-invasive beat-to-beat MBP, the systolic and diastolic blood pressures were measured from the right upper arm by an automatic oscillometric device (Microlife BP A100) in the supine and tilted positions.

Heart rate (HR) was computed as the inverse of the inter-beat interval (IBI) and expressed in beats per minute (bpm).

D. Data Analysis

The analogue signals of blood pressure and heart rate were stored for off-line analysis. All recordings were manually reviewed; spurious artefacts and extra-systolic beats were identified and replaced by linear interpolation. Three subjects presented frequent ectopic heartbeats that precluded variability analysis. Two subjects were eliminated because of an irregular breathing pattern during frequent episodes of falling asleep. Altogether, data from 13 subjects were included in the final analysis.

Group-averaged data were expressed as mean±SE. To test for the presence of significant differences, the Wilcoxon signed rank test was used. A level of significance of 0.05 was applied.

Three 5-minute periods were considered for analysis of heart rate variability (HRV) and mean blood pressure variability (BPV): in the supine position, in the upright tilted position at 70° and in the resupine position. The selection of these periods was based on the decision to obtain measurements of autonomic activity during relatively stable periods.

E. Blood Pressure Variability (BPV) and Heart Rate Variability (HRV)

The mean MBP was used to describe the average level of the MBP time series. For the analysis of the MBP variability, the low frequency power (LF MBP) at frequency range 0.04–0.15 Hz and high frequency power (HF MBP) at frequency range 0.15–0.4 Hz were calculated with the use of Fast Fourier Transformation.

For the inter-beat interval (IBI) time series we used a similar approach as for the MBP signal. However, for spectral HRV analysis, in addition to the low frequency power (LF IBI) and high frequency power (HF IBI), the power of the LF IBI and HF IBI was expressed in normalised units, nu (i.e. the absolute power divided by the total of these two bands). The latter variable was only used for HRV and not for BPV analysis. We also computed the time domain indices rMSSD and pNN50 for HRV.

The results were analysed according to the guidelines of the Task Force of the European Society of Cardiology and the North American Society of Pacing and Electrophysiology [5].

III. Results

A. Hemodynamics

Group-averaged values of IBI, HR and MBP in the supine as well as in the tilted position are given in Tab. 1 and Tab. 2.

The heat significantly increased the mean HR (Tab. 1). The mean IBI in normothermic condition was 997 ms and 778 ms in the supine and tilted position, respectively. In hyperthermic condition, the mean IBI was 930 and 664 ms in the supine and tilted position, respectively. All these changes were statistically significant. The changes from the supine to the tilted position were significant in normal as well as heat stress condition.

Table 1. Group-averaged IBI (HR) responses to head-up-tilting in normothermia and heat stress condition. Inter-beat interval is in ms (corresponding HR in bpm is given in brackets).

	Supine	Tilt	Mean difference
Normothermia	997±52 (60±3)	778±43 (77±4)	219[a] (17)[a]
Heat stress	930±51 (65±4)	664±30 (90±4)	266[a] (25)[a]
Mean difference	67[b] (5)[b]	114[a] (13)[a]	

Values are mean±SE
[a] Significant ($p<0.002$) calculated by the Wilcoxon signed rank test
[b] Significant ($p<0.03$) calculated by the Wilcoxon signed rank test

Table 2. Group-averaged MBP (mmHg) responses to head-up-tilting in normothermia and heat stress condition.

	Supine	Tilt	Mean difference
Normothermia	86±3	92±4	6[b]
Heat stress	82±3	88±3	6[b]
Mean difference	4[a]	4[a]	

Values are mean±SE
[a] Not significant ($p>0.05$) calculated by the Wilcoxon signed rank test
[b] Significant ($p<0.02$) calculated by the Wilcoxon signed rank test

As seen in Tab. 2, hyperthermia did not influence the group-averaged values of MBP significantly. The changes in BP level from the supine to the tilted position were significant.

B. Frequency domain indices of BPV and HRV

The group-averaged values of HRV and BPV analysis are presented in Fig. 1–Fig. 3. Hyperthermia caused a

noticeable decrease in the absolute values of LF and HF components of HRV power (Fig. 1). This change reached the margin of statistical significance for the tilted position ($p<0.04$). At the same time, the normalised LF and HF components in normothermia and hyperthermia (Fig. 2) were not statistically different.

The change from the supine to the tilted position caused the LF and HF components of HRV to decrease (Fig. 1). This change was statistically significant for HF ($p<0.02$) and not significant for LF ($p>0.15$).

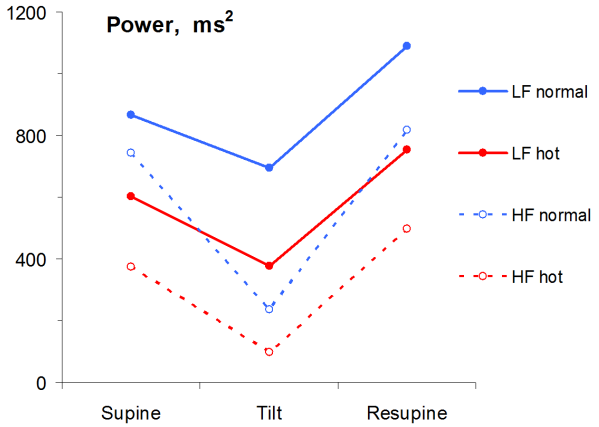

Fig. 1 High and low frequency components of HRV during supine rest, during passive 70° head-up-tilt and during resupine after tilt. Blue line normothermia, red line – heat stress.

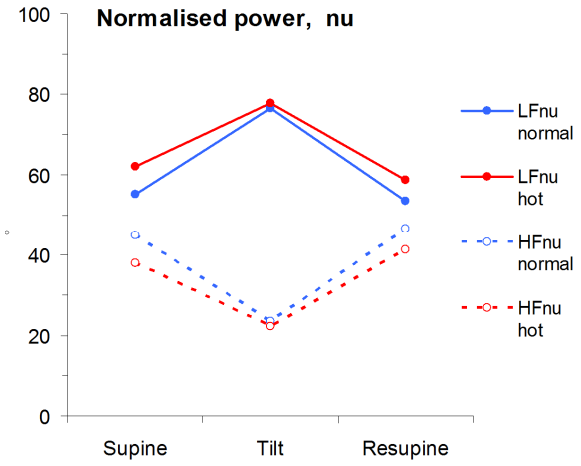

Fig. 2 Normalised high and low frequency components of HRV during supine rest, during passive 70° head-up-tilt and during resupine after tilt. Blue line – normothermia, red line – heat stress.

During tilting the LF (0.04–0.15 Hz) and HF (0.15–0.4 Hz) components of BPV increased compared to supine rest (Fig. 3). Both changes were significant ($p<0.01$).

The BPV indices during hyperthermia were not different from corresponding indices during normothermia ($p>0.1$).

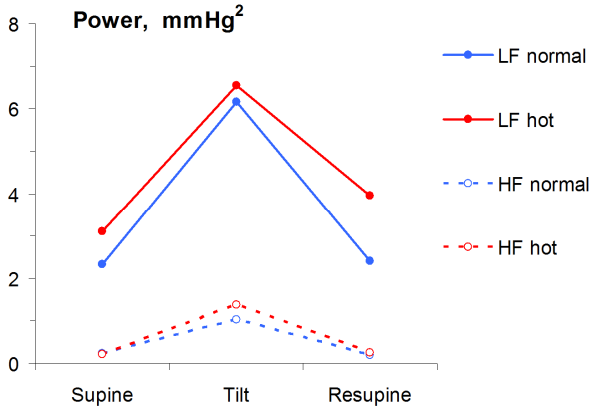

Fig. 3 High and low frequency components of BPV during supine rest, during passive 70° head-up-tilt and during resupine after tilt. Blue line – normothermia, red line – heat stress.

C. *Time Domain Indices of HRV*

As seen in Tab. 3, heat stress caused a noticeable decrease in the time domain parameters rMSSD and pNN50. This change reached the margin of statistical significance for both parameters in the tilted position ($p<0.01$).

Changes in rMSSD and pNN50 from the supine to tilted position were statistically significant both for normo- and hyperthermia ($p<0.005$).

Table 3. Group-averaged time domain indices rMSSD and pNN50 during head-up-tilting in normothermia and heat stress condition.

	Supine		Tilt	
	rMSSD	pNN50	rMSSD	pNN50
Normothermia	65±10	37±6	30±6	9±4
Heat stress	48±9	26±6	19±3	3±2

Values are mean±SE

IV. Discussion

The current study examined if changes in HRV and BPV in response to orthostasis differed in normal and high temperature environment.

In most studies of normal subjects with orthostatic challenge, blood pressure has been monitored with manual or automatic sphygmomanometry. In this study, blood pressure was monitored using a differential oscillometric method [3], [4]. This method allows non-invasive beat-to-beat measurement of the mean blood pressure.

Following the guidelines [5], the heart rate variability is calculated based on the variation in the intervals between adjacent cardiac pulses (inter-beat interval, IBI). The IBI has a nonlinear inverse relation with heart rate: the higher the heart rate, the shorter the inter-beat interval. Shorter IBI values are likely to present less variation in absolute if not relative terms. In other words, the increase in HR decreases HRV parameters, which may lead to a misinterpretation of HRV changes when comparing subjects with different HR levels [6], [7].

Our study demonstrated that during head-up-tilting, HRV decreased as heart rate increased (Fig. 1): this is a consequence of an increased sympathetic activation and reduced vagal control of heart rate. During tilt, the LF component of HRV becomes largely predominant. The total power (i.e. variance) is markedly reduced during tilt and consequently LF and HF powers are both decreased when expressed in absolute units. The use of normalised units (nu) clearly indicates the altered relation between LF and HF during tilt (Fig. 2). Higher resting parasympathetic control of heart rate is usually associated with reduced sympathetic control. In normal subjects, a change from supine to stand causes a shift to greater sympathetic over parasympathetic regulation of cardiac function with a corresponding increase in sympathovagal balance.

In the heat the mean values of HR were higher both in the supine and tilted positions (Tab. 1). A significant HR increase is related to the effect of heat on the sympathetic and parasympathetic systems. The HR response to the tilt test is more pronounced in heat stress condition (Tab. 1).

In hyperthermia the power of LF and HF components of HRV was lower in both positions (Fig. 1)

For the LF MBP there is no parasympathetic influence, and thus LF MBP is a better sympathetic index than LF IBI. An increase in BPV during tilting reflects sympathetically mediated vasomotor BP modulation (Fig. 3).

V. Conclusions

Our study revealed that the head-up tilt-table testing in hot environment resulted in significant changes in hemodynamics. Heat stress increased heart rate in the supine and tilted positions as well as the tilt-induced changes in heart rate. A noticeable decrease in the absolute values of LF and HF components as well as in rMSSD and pNN50 reached the margin of statistical significance for the tilted position. At the same time, no statistically significant changes in normalised spectral indices of heart rate and absolute spectral indices of the mean blood pressure variability were observed.

Acknowledgment

This study was supported by the Estonian Science Foundation (grant 7723); the Estonian Ministry of Education and Research (SF0180125s08) and Estonian Ministry of Defence (grant 456/0709).

References

1. Wilson TE, Crandall CG (2011) Effect of thermal stress on cardiac function. Exerc Sport Sci Rev 39:12–17
2. Cui J, Shibasaki M, Low DA et al. (2011) Muscle sympathetic responses during orthostasis in heat-stressed individuals. Clin Auton Res 21:381–387
3. Reeben V, Epler M (1983) Indirect Continuous Measurement of Mean Arterial Pressure. In: Ghista DN (ed.) Advances in Cardiovascular Physics, vol.5, Cardiovascular Engineering. Part II: Monitoring. Karger, Basel, 1983, pp 90−118
4. Raamat R, Jagomägi K, Talts J Continuous recording of the oscillometric mean arterial pressure by the differential servo system with two photoplethysmographic sensors. IEEE BioInformatics and BioEngineering, Athens, Greece, 2008, pp. 1–4.
5. Task Force of the European Society of Cardiology and the North American Society of Pacing and Electrophysiology Heart rate variability: Standards of measurement, physiological interpretation and clinical use. (1996) Circulation, 93:1043–1065
6. Nieminen T, Kähönen M, Kööbi T et al (2007) Heart rate variability is dependent on the level of heart rate. Am Heart J 154, e13
7. Koskinen T, Kähönen M, Jula A et al. (2009) Short-term heart rate variability in healthy young adults: the Cardiovascular Risk in Young Finns Study. Auton Neurosci 145:81–88

Author: Kersti Jagomägi
Institute: Department of Physiology
Street: Ravila 19
City: Tartu
Country: Estonia
Email: kersti.jagomagi@ut.ee

The Influence of Temperature and Carbon Source on Expression of Recombinant HBcAg

K. Ruģele[1], I. Bērza[2], S. Larsson[3], A. Dišlers[2] and J. Vanags[1]

[1] Institute of General Chemical Engineering, Riga Technical University, Riga, Latvia
[2] Latvian Biomedical Research and Study Centre, Riga, Latvia
[3] Department of Water Engineering and Technology, Riga Technical University, Riga, Latvia

Abstract— **Biotechnological aspects in the field of recombinant protein production are analysed in this work, which includes the investigation of factors for the production of virus like particles (VLPs) formed by recombinant Hepatitis B virus core-antigen (HBcAg) in inducible bacterial (*E. coli*) expression system as well as purification of these particles by gel-filtration and ion-exchange chromatography. Biomass yield and VLP production level depended on the cultivation conditions such carbon source and temperature. As inductor for protein expression lactose was used.**

Keywords— **Recombinant Hepatitis B core-antigen, virus like particles, T5 promoter, expression.**

I. Introduction

The commercial production of recombinant proteins for industrial and medical use has increased significantly in recent years [1,2]. Because of low manufacturing costs, processes using *E. coli* as a producer remain the systems of choice. Examples of recombinant proteins produced in *E. coli* are industrial enzymes (e.g. rennin, amylases, proteases and cellulases) and therapeutic proteins (e.g. filgrastim, insulin, growth hormones, and interferons). Because fermentation facilities for the production of recombinant proteins might be near capacity [3], there is an increasing interest in technologies that maximize the production of recombinant proteins in *E. coli*. Significant improvements have focused on protein expression to increase the productivity of recombinant proteins in *E. coli* [4]: these include improvements in DNA transcription, RNA translation and protein folding and stability. The most probable avenue for future improvements in the production of recombinant proteins in *E. coli* will rely on improvements in fermentation processes and in host metabolism using metabolic engineering strategies [5].

Recombinant protein technology has a significant role in vaccine development. Novel approach in vaccine development is recombinant virus-like particle (VLP) strategy. VLPs are multiprotein structures, consisting basically from virus-derived compounds. These high-molecular structures mimic the organization and conformation of authentic native viruses but lack the viral genome, potentially yielding safer and cheaper vaccine candidates [6]. Because of VLPs repetitive, high density display of epitopes they often are effective in eliciting strong immune responses.

One of the most well-known VLP antigens is Hepatitis B virus core antigen (HBcAg) that was first reported as a promising VLP carrier in 1986 and published in 1987 and even until nowadays it remains one of the most flexible and immunologically most powerful epitope carrier candidates [7].

Biotechnological aspects in the field of recombinant protein production were analysed in this work, which includes the investigation of factors for the production of VLPs formed by recombinant HBcAg in inducible bacterial (*E. coli*) expression system. Expression system *E. coli* RB791 IS104-31 used in this study is based on the expression plasmid pQE60 (Qiagen) basis, where the transcription of HBcAg gene is controlled by T5 promoter and two Lac operators. The use of a commercially available low-copy expression plasmid with the strong promoter T5 (vector pQE60) led to high intracellular HBcAg synthesis levels after optimizing the induction conditions in batch cultures [8].

II. Materials and Methods

A. Bacterial strains and plasmids

E. coli producer used for testing growth and HBcAg expression was RB791/IS104-31 (W3110 lac I^qL8) with expression vector pQE60 (Qiagen), which consisted of promoter of the T5 bacteriophage, two operators of *lac* operon and HBcAg gene.

B. Media composition

The main culture media was 2PY, which consists of Pepton (Reachim – 16g/L, yeast extract (Difco) – 10 g/L, NaCl (Lachema) – 5 g/L (pH 6.8 – 7.0).

Phosphate solution (containing stock solution 125,4 g/L K_2HPO_4 and 23,13 g/L KH_2PO_4) was used for buffering and as a phosphate source.

Y. Dekhtyar et al. (Eds.): *International Symposium on Biomedical Engineering and Medical Physics*, IFMBE Proceedings 38, pp. 107–109, 2013.
DOI: 10.1007/978-3-642-34197-7_28

Antibiotic stock solution was ampicillin (Biochemie) – 50 g/L H_2O. For 100 ml culture media 0,1 ml ampicillin was used..

As carbon source 40% glucose (1 ml/100ml culture media) or 80% glycerol (2,5 ml/100ml culture media) were used.

C. Cultivation conditions

Cultures were grown in sterile 500 ml shake-flasks in an incubator shaker at 200 rpm. The cultivation time was 20-24 hours in two temperatures: 30° C and 37° C. For the experiments 0,2% lactose was used as inductor. Lactose was added with the inoculum in sterile conditions.

D. Methods

The proteins expressed were analyzed on SDS-PAGE followed by Western blot using the specific antibodies. The standard measure of culture growth was the optical density measurement at 560 nm.

III. RESULTS AND DISCUSSION

The Studier auto-induction method [9] was applied as an alternative growing method to increase protein yields. Thus in all the experiments lactose instead of IPTG was used as inductor. .

Cell growth in media containing glucose (and in which no other nutrient is limiting) will continue until glucose becomes depleted or the acid generated by the metabolism of glucose exceeds the buffering capacity of the medium and causes the pH to drop to a level that stops the growth. As long as glucose is present in the growth medium in a sufficient amount, catabolism of other carbon and energy sources that could balance the acid generated by metabolism of glucose is prevented by the phosphoenolpyruvate/ carbohydrate phosphotransferase system (PTS), acting through catabolite repression and inducer exclusion [10,11]. In the absence of glucose, glycerol can support cell growth about as effectively but suppresses the use of other carbon sources less dramatically than glucose by a mechanism affecting cyclic AMP production [12]. Excess glycerol can also generate enough acid to stop growth, but, in contrast to glucose, the presence of glycerol does not suppress the inducing activity found in complex media.

The level of expression of HBcAg by cultivating the producent IS104-31 RB791 at two different temperatures (30º C and 37ºC) and using (i) glucose or (ii) glycerol as two carbon sources, of which (ii) did influence the catabolite repression on the promoter (T5). The variations of temperature can influence the stability of the target protein which in turn, can lead to a higher yield. HBcAg expression was investigated using 0,2 % glucose or 0,5% glycerol at both temperatures indicated.

Table 1 OD measurements in different cultivation times using glucose (glu) and glycerol (gly) as carbon source

Carbon source / Time	Glu, 30ºC	Gly, 30ºC	Glu, 37ºC	Gly, 37ºC
2h	2,40	2,66	4,02	3,64
4h	4,20	3,98	6,02	5,70
6h	6,60	5,84	10,44	9,44
24h	10,52	9,82	14,70	13,25

The cell yield was similar on both substrates however the production at 30ºC was lower both in terms of growth rate and the final concentration compared to that at 37ºC. The expression level after 6 hours was fairly similar in all the experiments however after 24 hours 2-3 times higher expression level was obtained when glycerol was used as the carbon source (Fig. 1). This finding indicates that the expression can be further improved by increasing the cultivation time and the concentration of glycerol. On other hand, the intensity of degradation in the presence of glucose was somewhat lower compared to glycerol.

The level of expression at the lower temperatures was slightly increased when glycerol was used as carbon source whereas the application of glucose resulted in slightly higher expression level at 37°C however also degradation was more pronounced.

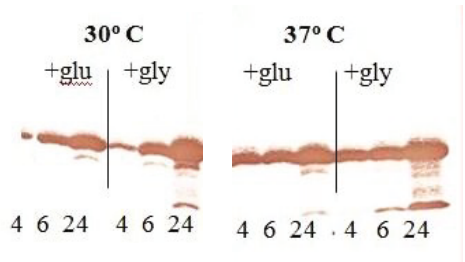

Fig.1. The expression of HBcAg in IS 104-31 RB791 depending on two different temperatures and carbon sources

When the cells were cultivated using glucose as carbon source the tendency of most of protein being insoluble was observed in all the samples, particularly at 30°C.

The cell lysis showed, that the ratio between the HBcAg soluble and insoluble fractions after 24 hours cultivation using glycerol as a carbon source indicate that more of the soluble protein was obtained at the lower temperature. The cultivation at 37°C resulted in a larger fraction of insoluble protein after 24 hours, indicating that lower temperatures favor the production of soluble HBcAg despite that after 6 hours more protein was found in the soluble fraction.

Thus the medium containing glycerol showed a higher potential for expression and contained more soluble protein.

Gel filtration was applied to get a deeper insight in the quality and quantity of the produced HBcAg. The two larger peaks (Fig. 2) indicate the liposaccharides (the first peak) and HBcAg (the second peak), which is higher after the cultivation at 30°C. There was a pronounced third peak at 37°C whereas several smaller peaks, indicating the presence of low molecular weight compounds could be seen after the cultivation at 30°C.

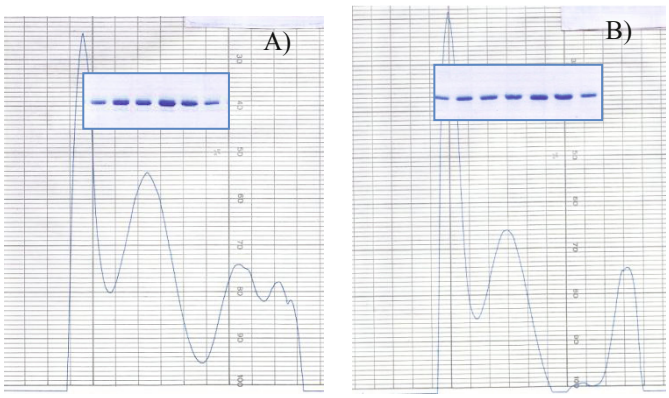

Fig. 2. The graph of gel filtration results and the main fractions. A) Culture cultivated at 30 °C; B) culture cultivated at 37 °C.

The same result can be observed analyzing the distribution of the fractions. At 30°C there was a slightly higher yield of HBcAg and the protein was distributed in fewer fractions (4,5,6,7) compared to the distribution at 37°C (3,4,5,6,7,8).

After gel filtration and ion exchange treatment protein samples with a concentration 14 mg/g cells (30°C) and 11,2 mg/g cells (37°C) were obtained by cultivating the producer *E. coli* RB791 IS104-31 in 2PY medium

To investigate the heterogenity of the produced protein SEM analysis were made and it was concluded that more virus-like particles were obtained in the fraction No. 6 after cultivation at 30ºC compared to the cultivation at 37ºC.

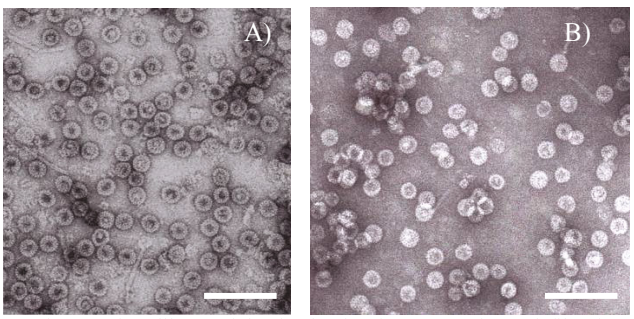

Fig. 3. Virus-like particles in the fraction No.6 after gel filtration of IS104-31 RB 791 cultivation at 30°C (A) and 37ºC (B), magnification 20 000x SEM. Scale bar – 100

IV. CONCLUSIONS

1. The cell yield of the producer *E. coli* RB791 IS104-31 was 30% higher when glucose was added as the carbon source whereas HBcAg expression level was about twice higher when the cells were cultivated in the presence of glycerol.

2. After gel filtration and ion exchange treatment protein samples with a concentration 14 mg/g cells (30°C) and 11,2 mg/g cells (37°C) were obtained by cultivating the producer *E. coli* RB791 IS104-31 in 2PY medium.

3. The cultivation at 30°C resulted in a higher production of HBcAg compared to the cultivation at 37ºC.

ACKNOWLEDGMENTS

We thank Velta Ose for providing the SEM results and Jānis Bogāns for performing the gel filtration and ion exchange treatments.

This work has been partially supported by the National Research Programme of Latvia VPP 7813.

REFERENCES

1. R.Garrett, M.Ch.Grisham. Biochemistry 3rd edition. Thomson Learning, Inc., 2005, 256 pp
2. R.Grabherr, E.Nilsson, G.Striedner, K.Bayer. Stabilising plasmid copy number to improve recombinant protein production. Biotechnol. Bioeng., 2002, 77, 142-147.
3. G.Sawers, M.Jarsch. Alternative regulation principles for the production of recombinant proteins in Escherichia coli. Appl. Microbiol. Biotechnol., 1996, 46:1-9.
4. S.Oehler et.al. Quality and position of the three lac operators of E. coli define efficiency of repression. EMBO J., 1994, 13(14):3348-55.
5. M.Lanzer, H.Bujard, Promoters largely determine the the efficiency of repressor action. Proc. Natl Acad. Sci., USA, 1988.
6. Roldao, A. Virus-like particles in vaccine development. *Expert Rev. Vaccines* , 9(10),1149-1176, 2010.
7. Pumpens P, Grens E. Artificial genes for chimeric virus-like particles. *Artificial DNA: Methods and Applications,* 249-327, 2007.
8. J. Yan, Z.Shou-Feng, M.Ya-Fei, L.Yi-Hui. Effects of lactose as an inducer on expression of *Helicobacter pylori* rUreB and rHpaA, and *Escherichia coli* rLTKA63 and rLTB. World J Gastroenterol, 2004, June 15;10(12):1755-1758.
9. F.W.Studier. Protein production by auto-induction in high-density shaking cultures. Protein Expression and Purification, 41, 207–234, 2005.
10. G.T.Jennings, M.F. Bachmann. The coming of age of virus-like particle vaccines. Biol Chem., 2008, 389:521-36.
11. McAleer et al. Human hepatitis B vaccine from recombinant yeast. Nature 307, 1984, 178–180.
12. P.P.Scaglioni, M.Melegari, J.R.Wands Posttranscriptional regulation of hepatitis B virus replication by the precore protein, *J. Virol*., 1997, 71, 345-353.

Activity of Host Defense Proteins in Rabbit Bone after Pure Hydroxyapatite and Tricalcium Phosphate and Mixed Tricalcium Phosphate/Hydroxyapatite Implantation

J. Vamze[1], M. Pilmane[1], and A. Skagers[2]

[1] Riga Stradins University, Institute of Anatomy and Anthropology, Riga, Latvia
[2] Riga Stradins University, Institute of Stomatology, Riga, Latvia

Abstract — **Inflammation process has significant role in biocompatibility modelling process. Bone loss induced by inflammation is one of the complications after biomaterial implantation into the hard tissue. There is no complete data about time dependent expression of cytokines and defensins into the bone tissue after implantation of biomaterials. The aim of this experiment was to research the changes on distribution and appearance of immune defense profile proteins – Interleukins-1, -8, -10 and human β defensin2 in the lower jaw of rabbits after implantation of pure hydroxyapatite and tricalcium phosphate and mixed tricalcium phosphate/hydroxyapatite produced under different temperatures. Our results revealed that biomaterials – pure and mixed HAP and TCP produced under different temperatures don't make significant difference to IL-1, IL-8, IL-10 and HBD2 production. Bone developing zones and low expression of anti-inflammatory cytokines in experimental tissue with both type of HAP/TCP and with TCP material burned under 1000^0 C possibly indicates better biocompatibility for this material than others used in our study.**

Keywords — **biomaterials, rabbit, Interleukins, human β – defensin.**

I. Introduction

Inflammation process has significant role in biocompatibility modelling process. Bone loss induced by inflammation is one of the complications after biomaterial implantation into the hard tissue. Proinflammatory cytokines interleukin-1 (IL-1) show proosteoclastogenic effects in response to implant-derived wear particles [1]. Interleukin-8 (IL-8) as neutrophil chemotactic factor is often associated with inflammation. IL-8 has been cited as a proinflammatory mediator in gingivitis [2]. Interleukin-10 (IL-10) is an anti-inflammatory cytokine with pleiotropic effects in immunoregulation and inflammation [3]. HBD-2 role in immune defense against oral infection in cases of biomaterial implantation is not completely defined. There is no complete data about time dependent expression of cytokines and defensins into the bone tissue after implantation of biomaterials.

The aim of this experiment was to research the changes on distribution and appearance of immune defense profile proteins – Interleukins-1, -8, -10 and human β defensin2 in the lower jaw of rabbits after implantation of pure hydroxyapatite and tricalcium phosphate and mixed tricalcium phosphate/hydroxyapatite produced under different temperatures.

II. Material and methods

Six Californian male rabbits were used for this study (permission of Animal Ethics Committee of Latvian Food and Veterinary Administration, No. 24, 02.07.2010.). Biomaterials produced in Riga Technical University Biomaterial Innovation and Development centre were used in experiment.

The rabbits received general anaesthesia with Sol. Ketamini (15 mg/kg) and Sol. Dormicum (2 mg/kg), local anaesthesia with Sol. Midazolami (0.5 mg/kg) and Sol. Articaini (5 mg/kg). Intraosseal implantation of following biomaterial in lower jaw tissue was performed: hydroxyapatite (HAP) granules burned under 1000^0C, Tricalcium phosphate/hydroxyapatite (TCP/HAP) burned under 1150^0C, TCP/HAP burned under 1000^0C, pure Tricalcium phosphate (TCP) burned under 1150^0C and pure TCP burned under 1000^0C. The control site was similarly prepared and closed, but no biomaterial was inserted.

After 3 months euthanasia of rabbits by air embolisation was performed. Blocks of bone and soft tissue from experimental and control side were taken out using diamond disc and tissue were prepared for routine morphological study by use of haematoxylin – eosin [4] and for detection of the interleukins: Interleukin 1 (IL-1, working dilution

Y. Dekhtyar et al. (Eds.): *International Symposium on Biomedical Engineering and Medical Physics*, IFMBE Proceedings 38, pp. 110–112, 2013.
DOI: 10.1007/978-3-642-34197-7_29

1:1000, abcam, UK), Interleukin 8 (IL-8, working dilution 1:50, Santa Cruz Biotechnology, Inc), Interleukin 10 (IL-10, working dilution 1:400, abcam, UK) and human β – defensin 2 (HBD2, working dilution 1:100, RD systems, UK) by use of biotin-streptavidin immunohistochemistry [5]. Quantification of immunohistochemically positive structures was done using semi – quantitative evaluation method [6].

III. Results

Biomaterial ingrowth regions during tissue block elimination process was observed in experimental tissue with HAP granules, with both type of TCP/HAP and with TCP material burned under 1150^0. Routine histological examination showed new bone developing zones in experimental tissue with above mentioned biomaterials as well (Fig.1).

Macroscopical signs of inflammation were not detected in none of experimental and control case.

Our study showed low variability of distribution of HBD2 and IL-1, -8 and Il-10. Weak expression of HBD2 was detected in the tissue with pure HAP granules (Fig. 2), but other materials, as revealed immunohistochemical examination, didn't show any impact to immune system response.

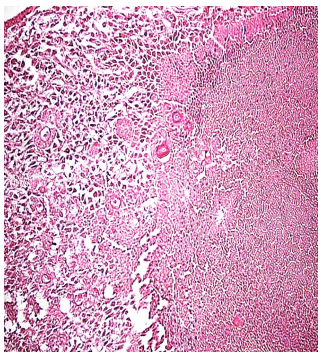

Fig. 1. Bone developing zones in tissue using HAP/TCP burned under 1150^0 C; h/e x250.

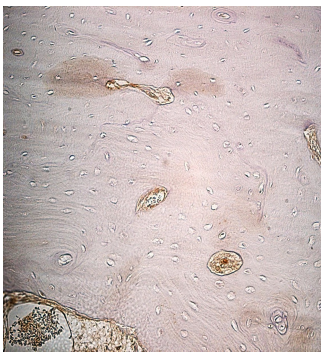

Fig. 2. Some HBD2 positive osteocytes in bone tissue with pure HAP biomaterial; IHC, x250.

Low activity of HBD2 was detected in control tissue as well. The weak expression of IL-1 was observed in bone tissue with HAP/TCP (burned under 1150^0 C), while moderate expression of IL-1 was observed in other experimental material (Fig. 3) and it was equal to control tissue (Fig. 4).

Bone tissue with TCP material (burned under 1150^0C) showed weak expression of IL-8 (Fig. 5), but expression of this interleukin in other experimental bone tissue and control tissue was not detected at all.

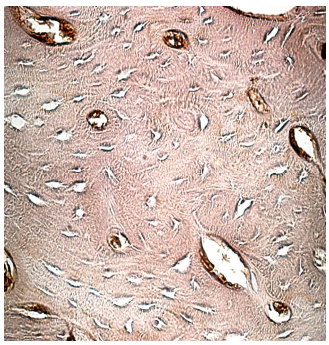

Fig. 3. Moderate numbers of IL-1 positive osteocytes in bone tissue with pure HAP; IHC x250.

Fig. 4. Moderate amount of IL-1 positive osteocytes in bone tissue at the control side; IHC x400.

Expression of anti-inflammatory protein IL-10 was observed in both experimental and control tissue, but it was variable. Moderate amount of IL-10 positive osteocytes was detected in experiment with HAP granules and with TCP burned under 1150^0 C (Fig. 6), what was equal to control tissue. Some IL-10 positive osteocytes were observed in experimental material consisting each of HAP/TCP and pure TCP (burned under 1000^0 C).

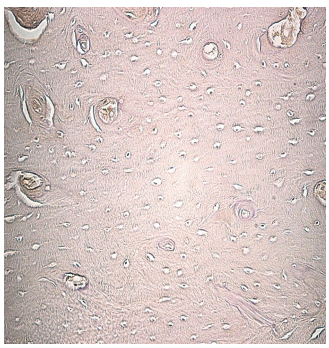

Fig. 5. Some positive IL-8 positive osteocytes in bone tissue using TCP burned under 1150^0 C; IHC x250.

Fig. 6. Moderate amount of IL-10 positive osteocytes in bone tissue using TCP burned under 1150^0 C; IHC x250.

IV. Discussion

Our experimental study showed more extent expression of proinflammatory cytokines than anti-inflammatory one, while macroscopical signs of inflammation were not detected in none of experimental and control case. The expression of proinflammatory cytokine IL-1 was moderate in experimental material and control tissue.

Experimental tissue with such biomaterials as HAP granules and with TCP (burned under 1150^0C) showed influence to increase IL-10 expression. The research of Salma (2009) demonstrates rich expression of IL-10 in contacting bone and soft tissue to pure HAp and HAp saturated with lidocaine after three weeks of implantation [7].

Increase of IL-8 expression in our experiment was detected only in bone tissue with TCP material (burned under 1150^0C), while in experiment with other materials it was not detected at all. Schmidt et al (2003) suggest that differences in material composition do not significantly influence the release of these factors if the materials have similar surface roughnesses [8].

The research of Ninomiya (2001) demonstrates that HAp and HAP/TCP particles are capable of stimulating the expression and secretion of cytokine IL-1 that increase bone resorption, and suggests that particulate debris from implants using these coatings may also increase osteolysis and loss of implants [9].

Our experimental study showed weak activity of HBD-2 and it was detected just in bone tissue with HAP and in control tissue. The controversial data about HBD-2 expression has been described by other authors as well. Thus, in patients with periodontal and peri-implant disease authors detected higher expression of HBD-2 in intact tissue than in diseased one [10]. Madhwani et all (2012) suggest that while host defense proteins – defensin, histatins and cathelicidin reportedly exhibit variable potency against oral bacteria, exposure of hydroxyapatite can markedly influence bacterial viability, composition and microbial aggregation [11].

V. Conclusions

Biomaterials – pure and mixed HAP and TCP produced under different temperatures don't make significant difference to IL-1, IL-8, IL-10 and HBD2 production. Bone developing zones, signs of bone-implant contact and low expression of anti-inflammatory cytokines in experimental tissue with both type of HAP/TCP and with TCP material burned under 1000^0C possibly indicates better biocompatibility for this material than others used in our study.

References

1. Holt G, Murnaghan C, Reilly J, Meek RM (2007) The biology of aseptic osteolysis. Clin Orthop Relat Res 460:240
2. Haake, SK, Huang GTJ (2002) Molecular Biology of the host-Microbe Interaction in Periodontal Diseases (Selected Topics) In: Newman, Takei, Carranza, eds. Clinical Periodontology, Philadelphia: W.B.Saunders Co 162
3. Eskdale J, Kube D, Tesch H, Gallagher G (1997) Mapping of the human IL10 gene and further characterization of the 5' flanking sequence. Immunogenetics 46:120–8
4. Kiernan JA (2008) Histological and Histochemical Methods: Theory and Practice In: Bloxham, UK: Scion 141–174
5. Hsu SM, Raine L, Fanger H (1981) Use of avidin–biotin–peroxidase complex (ABC) in immunoperoxidase techniques: a comparison between ABC and unlabeled antibody (PAS) procedures. J Histochem Cytochem 29:577–580
6. Pilmane M, Luts A, Sundler F (1995) Changes in Neuroendocrine Elements in Bronchial Mucosa in Chronic Lung Diseases in Adults. Thorax 50:551–554
7. Salma I, Pilmane M, Skagers A, Vetra J, Salms G, Berzina-Cimdina L, Serzane R (2009) Early morphofunctional response of contact tissue after intraosal implantation in rabbit jaw of pure synthetic hydroxyapatite (HAp) bioceramic materials and HAp saturated with lidocaine. Stomatologija 11:113–8.
8. Schmidt C, Steinbach G, Decking R, Claes LE, Ignatius (2003) AA IL-6 and PGE2 release by human osteoblasts on implant materials. Biomaterials 24:4191
9. Ninomiya JT, Struve JA, Stelloh CT, Toth JM, Crosby KE (2001) Effects of hydroxyapatite particulate debris on the production of cytokines and proteases in human fibroblasts. J Orthop Res 19:621
10. Bissell J, Joly S, Johnson GK, Organ CC, Dawson D, McCray PB, Guthmiller JM (2004) Expression of beta – defensins in gingival health and in periodontal disease. J Oral Pathol Med 33:278–285
11. Madhwani T, McBain AJ (2012) Compositional modification of nascent in vitro dental plaques by human host-defence peptides. FEMS Immunol Med Microbiol 64:374-81. doi: 10.1111/j.1574-695X.2011.00922.x

Author: Jolanta Vamze
Institute: Riga Stradins University, Institute of Anatomy and Anthropology
Street: Kronvalda bulvaris 9
City: Riga
Country: Latvia
E-mail: jolantavmz@gmail.com

Development of Poly(Vinyl Alcohol) Cryo-Systems with Medicines and Their Comparative Study of Antimicrobial Activity and Cytotoxicity

J. Stasko[1], N. Romanchikova[2], A. Reinis[3], L. Berzina-Cimdina[1], and J. Kroica[3]

[1] Biomaterials Innovation and Development Center, Riga Technical University, Riga, Latvia
[2] Latvian Institute of Organic Synthesis, Riga, Latvia
[3] Department of Biology and Microbiology, Riga Stradins University, Riga, Latvia

Abstract — **The aim of the work was to develop the poly(vinyl alcohol) cryogel systems (PVA_{GS}) with plant extracts (PPe) and simple conventional medicine (Cm), and compare their antimicrobial activity, biocompatibility and cytotoxicity. The stability of gels systems with and without medicines was determined, the gel content and swelling degree were calculated. *In vitro* studies of PVA_{GS}, with and without medicines, microbial contamination risk – the colonization level of the microorganisms and adhesion activity for the use of gel materials for the wound care were detected. PVA_{GS} biocompatibility and cytotoxic properties were examined on cell lines.**

Keywords — **poly(vinyl alcohol), cryogel systems, cytotoxicity, biocompatibility, microbial adherence.**

I. Introduction

Poly (vinyl alcohol) (PVA) gels are research objects for broad spectra of biomaterial development area: tissue engineering, reconstruction, drug delivery, etc. [1-4]. PVA is considered as a nontoxic and biocompatible material [5]. At the same time, PVA has a good ability to form water solution, so excluding the use of organic solvent in the process of gel preparation. Excluding the use of hazardous ingredients (chemical crosslinkers, solvents, catalysts etc.) which have undesirable effect on health [6-7] is very important for development of wound healing materials.

In the recent years, more and more attention is being paid to the development of various application materials the task of which is to foster the healing of burns and at the same time to reduce the risk of an opportunistic infection. Microorganisms, for example, *Ps.aeruginosa, S.aureus, Streptococcus* group A etc. [8] can enter the wound from the microflora of natural flora.

The materials used for wound healing should be stable in the use and have sufficient ability to absorb exudate from the wound. Therefore, one of the most suitable materials for wound healing is gel. However, the gels also should protect the wound especially burn wounds from infection and external contamination. In order to protect cells, the wound healing material must be without high adherence, only in this case the gel can be removed easily without damaging of epithelium cells. A balance must be obtained between antibacterial efficacy and cell proliferation and adhesion.

Nowadays it has been concluded that good results for wound healing can be obtained incorporating medicines in the wound dressing. The use of plant product substances also in traditional medicine has increased in recent years [9-12], as the strong antibacterial agents can hinder the development of new cells, which is retarding the healing process.

As the more efficient and desirable dressing for the healing of burn wounds is in search up to now, the main goal of the research was to develop a biocompatible, stable and functional PVA_{GS} for healing of burn wounds.

In our research work we incorporated PPe and Cm into the PVA_{GS} used for wound healing by years and compared the effects. Therefore the following PPe were chosen: calendula (C), peppermint (P), St.-John`s-wort (JW) [9-11], paste of pine extract (Pro); the following simple Cm was chosen: *Viride nitens* (Vn) and methylene blue (Mb) [13-14].

Moreover, the PPe and Vn in alcohol base were used as ethanol possesses also preservative function, which is very topical for sample storage. We incorporated PPe and Cm in PVA_{GS}, which were prepared by freezing-thawing method [3]. The appropriate approach for development of stable PVA_{GS} with incorporated medicines was found. Therefore, the concentration of PPe and Cm not hindering the development of systems by freezing-thawing method was determined first of all. Additionally, the stability of gel systems was determined and the gel content was calculated. The swelling behaviour of the samples was investigated to establish the capacity to absorb exudate from the wound.

We have also detected the ability of PVA_{GS} to chain microorganisms and the risk of microbial contamination of these biomaterials, as well as the adhesion intensity and the level of colonization of *S.epidermidis* and *Ps.aeruginosa*.

For the determination of PVA_{GS} cytotoxicity and biocompatibility GFP–expressed cell lines PT-67 (mouse embrional fibroblast) and MG-63 (human osteoblast) were used. The cell adherence to the PVA_{GS} were determined as the further prospective is that the developed systems can be easily removed without damaging the epithelium cells.

Y. Dekhtyar et al. (Eds.): *International Symposium on Biomedical Engineering and Medical Physics*, IFMBE Proceedings 38, pp. 113–118, 2013.
DOI: 10.1007/978-3-642-34197-7_30

II. EXPERIMENTAL PART

A. Preparation of PVA_{GS} Samples

Partly crystalline PVA was used (Mw $130 \cdot 10^3$ g/mol, T_m = 225.8 °C, T_g = 76.6°C, degree of crystallinity – 43%). 15 % PVA water solution is chosen for preparation of PVA_{GS} (6h 80°C). The PPe and Cm were added in following concentration: PPe 0.5 and 2.5 w% and Cm 0.15 w% and 0.3 w%. The solution was poured out in moulds and put into closed polyethylene systems, thus providing constant water content in the samples. PVA_{GS} were prepared by freezing (12h at -20°C) followed by thawing (12 h at 20°C), exposed by 1 to 3 freezing-thawing cycles (n_C).

B. Determination of PVA_{GS} Stability

B.1. Gel content

PVA_{GS} were extracted by rinsing to remove the sol fraction by gently mixing until the equilibrium weight of samples. After that, the gels were dried at 105°C and weighed again.

The following calculation was used for determination of the gel content:

$$G_f = \frac{W_D}{W_{PVA_{GS}}} \cdot 100 \quad (1)$$

where: G_f is the gel content, W_D is the weight of dry PVA_{GS} after the removal of sol, W_{PVAGS} – weight of PVA and medicines in the gel system.

B.2. Swelling behavior

The PVA_{GS} were immersed in distilled water and rinsed by mixing. The swollen weight of PVA_{GS} (Ws) was determined by wiping off the surface water with a piece of filter paper. The swelling degree (S) was calculated:

$$S = \left(\frac{W_s - W_i}{W_i} \right) \cdot 100 \quad (2)$$

where: W_i is the initial weight of prepared PVA_{GS}.

C. PVA_{GS} Microbiological Colonization and Adhesion Intensity Studies

PVA_{GS} (size - $1cm^3$) with PPe (C, JW, P, Pro in concentration 0.5 and 2.5%), Cm (Vn, Mb in concentration 0.15% and 0.3%) and without them were incubated in *Ps.aeruginosa* ATCC 27853 and *S.epidermidis* ATCC 12228.

Suspensions from the microbiological cultures of the bacteria were made in 1 ml volume of tryptic soy broth (TSB) in concentration of 10, 10^2, 10^3 and 10^4 (if the sample of the PVA_{GS} possible antimicrobial effect) CFU/ml (colony forming units).

To determine the adhesion of microorganisms, the samples were incubated in the temperature of 37°C for 2 h in all of the above mentioned concentrations of bacteria. To determine the colonization, a pure PVA_{GS} and PVA_{GS} gel with PPe and Cm, which were not expected to have an antibacterial effect, were incubated only with 10^2 CFU/ml (for 24 h at 37°C). The rest of the samples with possible antibacterial effect were cultivated in all concentrations of bacteria made. A scanning electron microscope (SEM) and colonization as well as sonication-plate count method [15-16] to determine the count of colonies were used to evaluate adhesion. The CFU were calculated per 1 mm^2 of the biomaterial surface.

D. PVA_{GS} Biocompatibility and Cytotoxicity Studies

PVA_{GS} sample - 1cm in diameter with PPe (C, JW, P, Pro in concentration 2.5%) and Cm (Vn, Mb in concentration 0.3%) and without them were used for biocompatibility and cytotoxicity studies.

PT-67 (mouse fibroblast, Clontech Laboratories, Inc) and MG-63 (human osteoblast, osteosarcoma) cell lines were obtained from ATCC collection (CRL-1427). Both cell lines were maintained in culture medium DMEM containing 10% fetal bovine serum and 2 mM L-glutamine. Cell lines were incubated in thermostat at 37 °C with 5% CO_2.

For the stable GFP transfection PT- 67 and MG-63 cells were incubated with DOTAP reagent and plasmid pEGFP-N1 for 18 h. After 48 h PT-GFP and MG63-GFP cells were selected in the presence of 500μg /ml G418 (Life Technologies, Inc.).

For biological investigations the samples were sterilized by 96° ethanol for 15 min. Each sample was plated into the well of 24-well tissue culture plate and PT-GFP or MG63-GFP cells were seeded at density 2×10^4 cells/well. The plates were grown in thermostat at 37 °C with 5% CO_2 and humidified atmosphere.

Proliferation assay. After incubation PVA_{GS} with GFP-expressed cell lines for 24h, the samples were washed with phosphate-buffered saline (PBS) and treated with 0.25% trypsine solution for cell detachment. The sample intensive rinsing with PBS and cell number count was done per milliliter.

Cytotoxicity assays. Since the cells were not attached to PVA_{GS}, cell viability was measured in the well around PVA_{GS} samples and, thus, PVA_{GS} cytotoxicity was evaluated.

PVA_{GS} cytotoxicity was detected using a commercial kit (WST-8, Cayman Chemicals). WST-8 assay was done under the manufacturer protocol. Briefly, 2×10^4 were plated into the 24-well microplate. After 72 h WST-8 reagent was added into each well. In 2 h of incubation in thermostat at 37^0 C, the formation of formazan was detected at 450 nm using a microplate reader. All analyses were performed in four wells including medium control.

The results of cytotoxic effect were expressed as percentage of alive cells in the well with the sample, compared to the control – the well without a sample, which was taken as 100% of alive cells. All the results were calculated to the complete well area.

III. Results and Discussion

A. *Determination of PVA_{GS} Stability*

Obtained PVA_{GS} are stable at room temperature. The behaviour and stability of PVA_{GS} were examined. Gel content and swelling determination yield gives important information concerning the stability of PVA_{GS}.

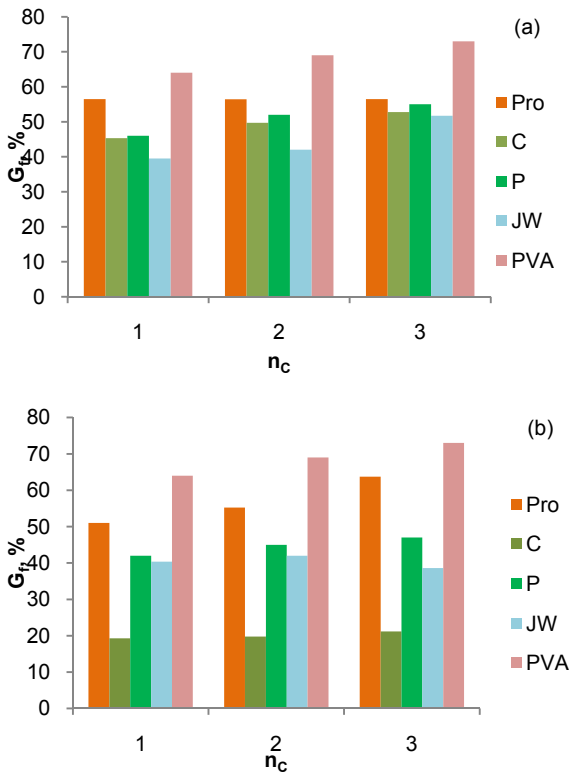

Fig. 1. Correlation of G_f of pure PVA_{GS} and PVA_{GS} with PPe in concentration 0.5% (a) and 2.5% (b) with number of freezing-thawing cycles (n_C).

It is observed that a significant fraction of PVA_{GS} chains were not incorporated into the crosslinked structure of gel systems with PPe, especially, for systems with higher concentration of PPe, for example, with 2.5% of C (Fig. 1). Adding of 0.5% and 2.5% of C the G_f decreased for 10-15% and 15-55%, accordingly. The lowest G_f values were determined for PVA_{GS} (n_C=1) with 0.5% of JW (G_f =19%) and 2.5% of C (G_f = 39%).

The incorporation of Cm did not essentially influence the gel content (Fig. 2) of the systems. It is established, that stable systems can be obtained. Adding of 0.15% and 0.3% of Cm the G_f decreased for 3-10% and 2-15% accordingly. The lower Gf values were determined for PVA_{GS} (n_C=1) with 0.3% Vn (46%).

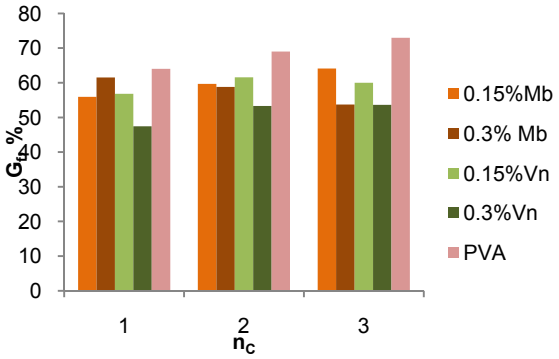

Fig. 2. Correlation of G_f of pure PVA_{GS} and PVA_{GS} with Cm with number of freezing-thawing cycles (n_C).

The swelling behaviour of the samples was investigated to establish the capacity to absorb exudate from the wound. The PVA_{GS} prepared by one cycle of freezing-thawing showed a much more swollen structure than those exposed by three cycles. It indicates that the increasing number of freezing-thawing cycles lead to possible further crosslinking of the samples.

The example of swelling degree as a function of time for PVA_{GS} exposed to 3 freezing-thawing cycles is shown in Fig. 3. It can be seen that in the initial swelling stage, all the PVA_{GS} absorbed water rapidly and the swelling degree increased. It is found out that all medicine incorporation in PVA_{GS}, PPe and Cm, increased the swelling degree.

The highest S values were determined for PVA_{GS} with incorporated of 2.5% of C, S= 55% at the equilibrium.

Raising the number of freezing/thawing cycles the degree of swelling considerably increases during the first five hours. After 48 hours, the equilibrium of swelling degree was noticed for almost all systems. The equilibrium swelling

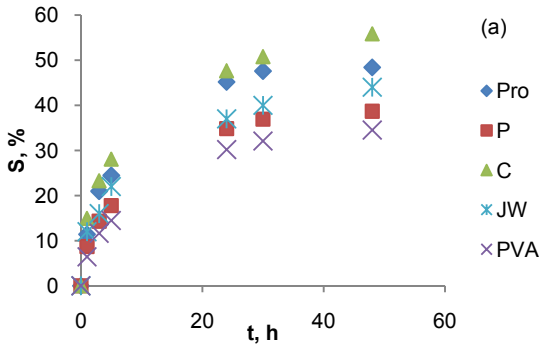

Fig. 3. Relationship between S, % of pure PVA_{GS} and PVA_{GS} with PPe in concentration 2.5% (a) and the time.

degree was significantly increased by addition of PPe, which was due to influence of medicines on system crosslinking.

The results of the experiments of gel stability showed that the most of medicines decreased G_f and increased the S values. It is evident, that the medicines have influence on preparation of systems and crosslinking of macromolecules. However, PVA_{GS} prepared by three cycles of freezing-thawing have a stable structure and relatively high swelling degree also in systems with PPe, where ethanol was used. Moreover, Vn, which is also based on ethanol, almost does not influence the crosslinking of molecules. Therefore, those PVA_{GS} are more suitable for practical application and have been chosen for further microbiological and cell experiments.

B. PVA_{GS} Microbiological Colonization and Adhesion Intensity Studies

The intensity of adhesion on the samples of pure PVA_{GS} was small – in the case of both bacteria adhesion started already at the concentration of 10 CFU/ml, a greater adhesion was observed in the case of *Ps.aeruginosa*. The smallest intensity of adhesion in the case of PVA_{GS} containing antibacterial chemicals was observed while using PVA_{GS} with an addition of 0.3% of the Vn – no adhesion was observed of *S.epidermidis* on the given sample in any of the bacteria concentrations used in the research, while *Ps.aeruginosa* started adhesion only in samples incubated in the concentration of 10^4 CFU/ml.

At the same time, samples of the PVA_{GS} containing the additives of various PPe show almost no effect on the bacterial adhesion, in some cases (JW 2.5% and P2.5%) a delay

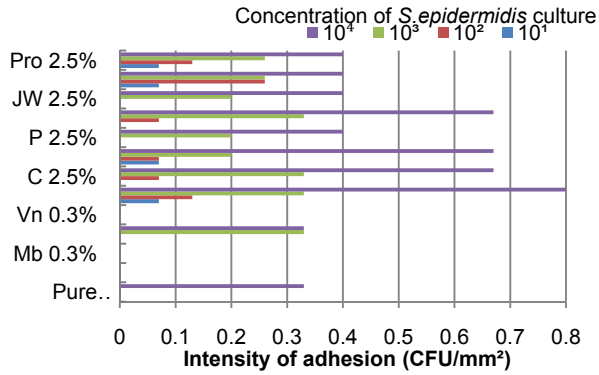

Fig. 4. Intensity of adhesion of *S.epidermidis* on PVA_{GS}, PVA_{GS} with Cm antibacterial additives, PVA_{GS} with PPe gel surfaces CFU/mm^2 after 2 h/37°C ($p<0.05$).

in adhesion of *S.epidermidis* was observed in smaller concentrations (Figures 4 and 5).

The results of the intensity of colonization also show that the best activity against *S.epidermidis* is observed in the samples of PVA_{GS} with Cm (Vn 0.15% and 0.3% as well as Mb 0.3% and to a smaller extent Mb 0.15%). Unfortunately, while using PVA_{GS} with Cm additives, in no case a delay in the growth of *Ps.aeruginosa* was observed. In the samples of PVA_{GS} with the additives of PPe, the observed growing intensity of the bacteria used in the research was such that the colonies in the growth medium were impossible to count (Table 1).

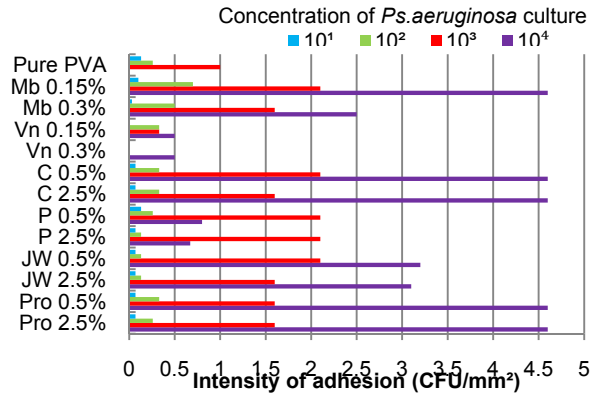

Fig. 5. Intensity of adhesion of *Ps.aeruginosa* on PVA_{GS}, PVA_{GS} with Cm additives, PVA_{GS} with PPe gel surfaces CFU/mm^2 after 2 h/37°C ($p<0.05$).

Table 1. Intensity of bacterial colonization on PVA_{GS}, PVA_{GS} with Cm antibacterial additives, PVA_{GS} with PPe gel surfaces CFU/mm^2 after 2 h/37ºC ($p<0.05$).

	S.epidermidis				*Ps.aeruginosa*			
	10^1	10^2	10^3	10^4	10^1	10^2	10^3	10^4
1	-	3087 ± 9.4	-	-	-	3663 ±13.2	-	-
2	*	*	2 ±0.5	2.7 ±0.6	29040 ±10.2	53380 ±12.1	66725 ±12.2	80070 ±14.2
3	*	*	*	1.3 ±0.25	4710 ±5.1	6280 ±12.3	9420 ±15.3	19625 ±12.2
4	*	*	*	*	20410 ±10.0	20410 ±11.2	40820 ±13.3	39250 ±12.10
5	*	*	*	*	12560 ±14.3	18840 ±10.2	25120 ±19.2	23550 ±15.20

1-Pure PVA_{GS}, 2- Mb 0.15%, 3- Mb 0.3%, 4- Vn 0.15%, 5- Vn 0.3%

*growth not observed
- not performed
for C, P, JW, Pro unable to count - overgrown

The above mentioned results were confirmed visually with the use of the SEM to observe the intensity of colonization for the bacteria used in the research and the possible biofilm as a formation of important virulence properties on the surface of the PVA_{GS}. It was observed that, while using a greater concentration to start the 24 h incubation, *Ps.aeruginosa* also formed the biofilm on the samples of PVA_{GS} with Cm. On the contrary, if the incubation is started in a smaller concentration, the bacteria do not form the biofilm and colonize the PVA_{GS} in a dispersed way.

A not so well defined biofilm was also observed on the PVA_{GS} samples containing PPe additives. In the sample with the additive of C, microcolonies *S.epidermidis* partially covered with glycocalyx were observed, while *Ps.aeruginosa* was colonizing the surface in an even layer of separate cells without the creation of the morphology typical for a classic biofilm.

Ps.aeruginosa and *S.aureus,* especially – methicillin-resistant *S.aureus* can be mentioned as the most important and dangerous microorganisms [17], that can infect burn wounds. Concerning the factors of virulence, we have to take in account both the various factors of adhesion and infection for the above mentioned bacteria and the ability to create biofilm [18-19], that protects the colony of microorganisms from various factors of immunity and therapy, as well as the ability to create strains resistant to antibiotics and, in the case of Pseudomonas – resistance to disinfectants. [8, 20]

We chose matrices of PVA_{GS}, one group of which contained classic antimicrobial agents (Vn, Mb), the second – various PPe additives, that become more and more popular in the composition of the so called "eco- or biotherapy". However, our research shows that PPe cannot compete with the classic antimicrobial agents, for example, the best effect of delaying the colonization and adhesion was shown by systems containing 0.3% of the Vn, as opposed to gels with PPe, which do not decrease adhesion or colonization.

However, being substantiated by the results of microbiology studies we chose PVA_{GS} with 2.5% PPe and 0.3% Cm, to establish the PVA_{GS} influence on epithelium cells.

C. PVA_{GS} Biocompatibility and Cytotoxicity Studies

GFP-expressed PT-67 culture made process of cell visualisation on the samples surface more reliable during the experiments. Microscopy of samples in 72 h showed that during the PT67-GFP cultivation, fibroblast stayed unattached and maintained a spherical shape. Conglomerates were formed around the PVA_{GS} with C cells which were easily removable with gentle rinsing in PBS buffer. Proliferation assay and cell account revealed that cells were not attached either on the sample surfaces, or in the pores. This suggests that cells were unable to bind to the sample surface. To prove that this effect does not result from samples cytotoxic properties, we tested cell viability in the well around PVA_{GS}.

In vitro cytotoxicity assay showed that the presence of the pure PVA_{GS} sample has toxic effect only 11%. The PVA_{GS} with PPe 2.5% Pro, 2.5% JW and especially 2.5% P significantly, about 88%, 97.8% and 100% respectively, reduced the number of alive PT67-GFP cells in the well. Our results showed strong cytotoxic effect of the plant extract on PT67-GFP cell proliferation.

Opposite properties revealed sample PVA_{GS} with 2.5% C - 107.2 % alive cells, which did not influence the PT67-GFP cell viability.

Conventional medicines compound 0.3% Mb was completely, 100% cytotoxic and compound 0.3% Vn repressed about 78% of PT67-GFP cell survival.

We tested cytotoxic effect of Cm and PPe compounds on human osteoblast, as the burns can be deep and affect also bone tissues. Proliferation assay had shown that MG63-GFP cells as well as fibroblast were not attached on the sample surfaces and cytotoxic test determined cell viability in the well around PVA_{GS}. Our studies have shown that osteoblast cell culture MG63-GFP was resistant to PPe compounds, namely, 67.2% to C, 40% to JW and 69.7% to P, but almost 100% sensitive to Cm compounds Mb and Vn.

IV. Conclusions

The stability of PVA_{GS} with and without PPe and Cm prepared by freezing-thawing cycles were investigated. Prepared systems were characterized by gel content and swelling behavior. The results of the experiments of gel stability showed that the most of medicines decrease G_f and

increase the S values. It is evident, that the medicines have influence on preparation of systems and crosslinking of macromolecules. However, PVA_{GS} prepared by three cycles of freezing-thawing have a stable structure and relatively high swelling degree, therefore, those PVA_{GS} are more suitable for practical application and have been chosen for further microbiological and cell experiments.

Microbiology studies showed that *Ps.aeruginosa* chain and colonize the samples of PVA_{GS} more intensively than *S.epidermidis*. The best effect of delaying the colonization and adhesion is shown by PVA_{GS} containing 0.3% of the Vn. At the same time a good effect is also shown by matrices of PVA_{GS} with additive of 0.3% of Mb. An average effect is shown by matrices of PVA_{GS} with additive of 0.15% of Mb and Vn. However, PPe practically does not decrease the adhesion of bacteria and shows a very high level of colonization of bacteria that is practically uncountable.

Proliferation assay and cell account revealed that cells were not attached either on the sample surfaces, or in the pores. This effect is positive for wound care since the new formed fibroblast will not be damaged during the changing process of dressing. The same effect was observed for osteoblast, which is especially acute in the case of deep damage of the skin and underplaying tissues.

Cytotoxicity studies show that pure PVA_{GS} is biocompatible and can be used as biomaterial, for development of wound dressing. PVA_{GS} with Mb and with PPe Pro, P, JW have more pronounced cytotoxicity against human cells PT67-GFP. However, PVA_{GS} with 2.5% C - 107.2 % alive cells and did not influence the PT67-GFP cell viability and therefore use of calendula in wound care materials can be considered.

We guess that the use of PPe for wound treatment in the future is possible in combination with appropriate antiseptic and aseptic techniques. It is more topical as antibiotic mass production and its use in medicine has led to the rapid spread of multi-drug resistant strains of microorganisms in clinics, so development and application of the different PPe products along with conventional antimicrobial therapy will become increasingly important.

Acknowledgment

This work has been partly supported by the European Social Fund within the project “Multidisciplinary Research in Biomaterials Technology of New Scientist Group”, No.2009/0199/1DP/1.1.1.2.0/09/APIA/VIAA/090.

References

1. Peppas NA, Hilt JZ et al. (2006) Hydrogels in Biology and medicine: From Molecular Principles to Biotechnology. Adv Mater 18:1345 – 1360
2. Hoare TR, Kohane DS (2008) Hydrogels in drug delivery: Progress and challenges. Polymer 49:1993 – 2007
3. Peppas NA, Mongia NK (1997) Ultrapure poly(vinyl alcohol) hydrogels with mucoadhesive drug delivery. Eur J Pharm Biopharm 43:51-58
4. Fray M, Pilaszkiewicz A et al. (2007) Morphology assessment of chemically modified and cryostructured poly(vinyl alcohol) hydrogel. Eur Polym J 43:2035–2040
5. Alves MH, Jensen BEB et al. (2011) Poly(vinyl alcohol) physical hydrogels: new vista on a long serving biomaterials. Macromol Biosci 11:1293-1313
6. Hickey AS, Peppas NA. (1995) Mesh size and diffusive characteristics of semicrystalline poly(vinyl alcohol) membranes prepared by freezing/thawing techniques. J Membr Sci 107:229 – 237
7. Ostuka E, Sugiyama M et al. (2011) Formation and destruction of physical crosslinks by mild treatments in chemically crosslinked poly(vinyl alcohol) gels. Polym Bull 67:1215-1226
8. Church D, Elsayed S et al. (2006) Burn Wound Infections. Clin Microbiol Rev 19:403–434
9. Koh HL (2009) Guide to Medicinal Plants: An Illustrated Scientific and Medicinal Approach. Singapore: World Scientific
10. Mukherjee PK, Mukherjee K et al. (2003) Evaluation of Wound Healing Activity of Some Herbal Formulations. Phytother Res 17:265-268
11. Bedi MK, Shenefelt PD (2002) Herbal Therapy in Dermatology. Arch Dermatol 138:232-242
12. Stasko J, Romanchikova N, Reinis A, Berzina-Cimdina L, Kroica J (2012) Microbiological and cytotoxic testing of poly (vinyl alcohol) gel with herbal medicines used for wound care, Proceedings of 24th of European Conference on Biomaterials, Dublin, Ireland, 2011, pp 169-172
13. Zolfaghari PS, Packer S et al. (2009) In vivo killing of Staphylococcus aureus using a light-activated antimicrobial agent. BMC Microbiology 2009, 9:27, (1-8) doi:10.1186/1471-2180-9-27
14. Usacheva MN, Teichert MC et al. (2003) The role of the methylene blue and toluidine blue monomers and dimers in the photoinactivation of bacteria. J Photoch Photobio B 71:87-98
15. Trampuz A, Piper KE et al. (2007) Sonication of removed hip and knee prostheses for diagnosis of infection. N Engl J Med 357:654-663
16. Sampedro MF, Huddleston PM et al. (2010) A biofilm approach to detect bacteria on removed spinal implants. Spine 35:1218-1224.
17. Trafny EA (1998) Susceptibility of adherent organisms from Pseudomonas aeruginosa and Staphylococcus aureus strains isolated from burn wounds to antimicrobial agents. Int J Antimicrob Ag 10:223-228.
18. Stoodley P, Sauer K et al. (2002) Biofilms as complex differentiated communities. Annu Rev Microbiol 56:187-209.
19. Sutherland IW (2001) The biofilm matrix-an immobilized but dynamic microbial environment. Trends Microbiol 9:222-227.
20. Nascimento EG, Sampaio TBM et al. (2009) Medeiros, A.C.; Azevedo, E.P. Evaluation of chitosan gel with 1% silver sulfadiazine as an alternative for burn wound treatment in rats. Act Cirúrg Bras 24:460-465.

Author: Jolanta Stasko
Institute: Biomaterials Innovation and development center
Street: Pulka 3/3
City: Riga
Country: Latvia
Email: Jolanta.Stasko@rtu.lv

An Application of Lévy Metric to Radiotherapy Biological Treatment Plan Optimization

F. Cutanda Henríquez[1] and S. Vargas Castrillón[2]

[1] CNSA, Instituto de Salud Carlos III, Madrid, Spain
[2] Facultad de Medicina, Universidad Complutense de Madrid, Madrid, Spain

Abstract — **Modern Radiation Therapy techniques require novel methods for the computation and evaluation of plans. In this work, we develop the concept of Lévy distances between Dose Volume Histograms for the same volume of interest. It will be shown that Lévy distance is a global property, with a clear geometric interpretation, and rigorous mathematical foundations. A direct application to tumor control probability variation is provided.**

Keywords — **Lévy distance, Dose Volume Histogram, Tumor Control Probability.**

I. Introduction

Modern treatment planning allows achieving complex goals. It is clear that minimum and maximum doses cannot be considered as adequate figures of merit for the quality of a plan, and that is the reason why a complex set of parameters have to be evaluated when an irradiation plan has to be accepted or rejected. Particularly, radiobiological indices are useful tools for this evaluation, as they relate the plan to specific clinical goals. Therefore, it would be of great help in treatment planning evaluation and optimization to easily, even graphically characterize treatment plans, according to the closeness of their indices to a reference value (a goal or a previous result to should be improved). In order to achieve this, a measure of closeness to the objective dose distribution is needed, and it has to be related to the values of the index. In this work, we propose a type of distance between dose volume histograms that can be used for acceptance of absorbed dose distributions.

II. Theoretical background

Volume and dose will be relative to the total volume of the tumour and the prescription dose throughout this work. Given a *DVH* curve, the function *F(z)=1-DVH* is a distribution function for some random variable (absorbed dose for random points inside the tumour in this case). Thus, it belongs to the set of distribution functions *F* where distances can be defined.

In this work, consideration will be paid to the Lévy distance [1]. Given two distribution functions *F* and *G* the Lévy distance between *F* and *G*, $d_L(F,G)$ is:

$$d_L(F,G) = \\ = \inf\left\{\varepsilon \middle| \forall y : F(y-\varepsilon) - \varepsilon \le G(y) \le F(y+\varepsilon) + \varepsilon\right\} \quad (1)$$

It can be proved that this is the definition of a distance in *F*. Moreover, *F* is locally convex and Lévy ball sets (distributions at Lévy distances to F less than R) are convex:

$$\left.\begin{array}{l} d_L(G,F) < R \\ d_L(H,F) < R \end{array}\right\} \Rightarrow \begin{array}{c} \forall \lambda \in [0,1]: \\ d_L(\lambda G + (1-\lambda)H, F) < R \end{array} \quad (2)$$

Lévy distances have a graphical representation. Given *F* and *G*, the Lévy distance between them equals the side of the largest square that can be inscribed between the graphs of *F* and *G*. This is illustrated in Fig. 1.

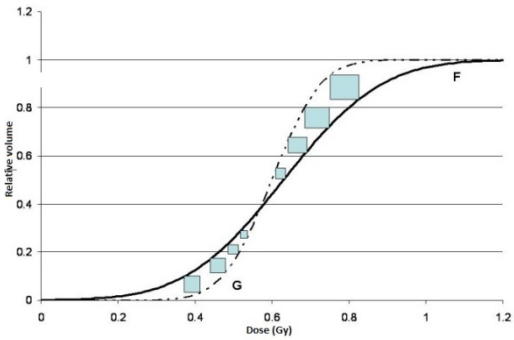

Fig. 1. Lévy distance between distribution functions as the side of the largest square that can be inscribed between both graphs.

If $F_0=1-DVH_0$ and R_0 is a bound for the Lévy distance around F_0, then, for *G* to be within this bound the following inequalities should hold.

$$\forall y : F_0\left(y - R_0\right) - R_0 \le G(y) \\ \forall y : F_0\left(y + R_0\right) + R_0 \ge G(y) \quad (3)$$

Y. Dekhtyar et al. (Eds.): *International Symposium on Biomedical Engineering and Medical Physics*, IFMBE Proceedings 38, pp. 119–122, 2013.
DOI: 10.1007/978-3-642-34197-7_31

In terms of *DVH*:

$$\begin{aligned} \forall y : DVH_0\left(y - R_0\right) + R_0 &\geq DVH(y) \\ \forall y : DVH_0\left(y + R_0\right) - R_0 &\leq DVH(y) \end{aligned} \tag{4}$$

The following figures help understand how these conditions can be fulfilled. In Fig. 2 $R_0=0.1$. As shown by the dashed lines, both conditions are met for these curves.

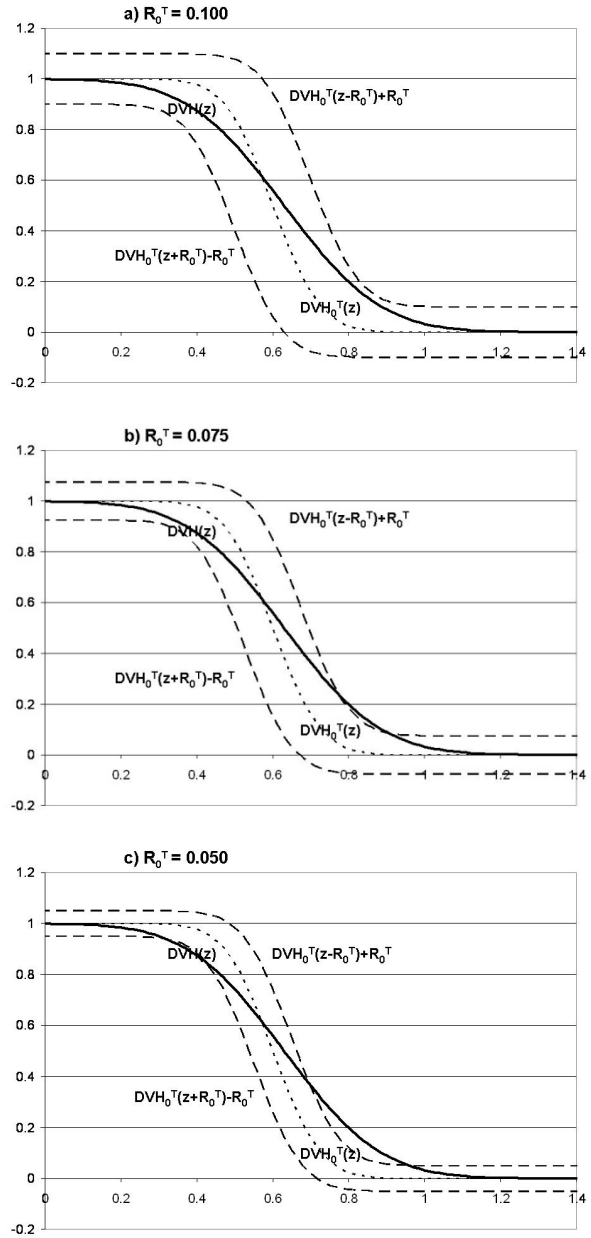

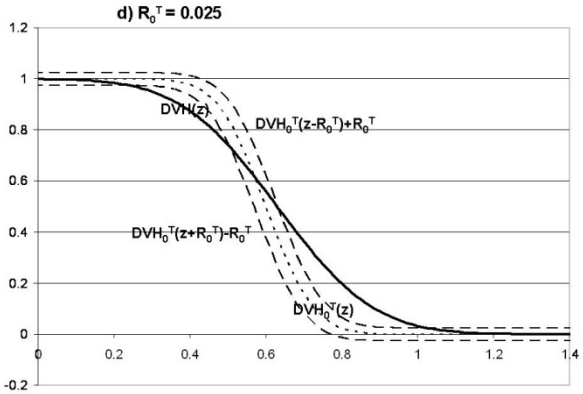

Fig. 2. Illustration of a *DVH*, a desired *DVH* (DVH_0^T), and the two dashed lines defining the boundaries for *DVH* to be at a Lévy distance of R_0 from DVH_0^T. a) $R_0=0.1$ and DVH is closer to DVH_0^T than R_0, b) $R_0=0.075$, c) $R_0=0.05$, d) $R_0=0.025$. In the latter cases the distance is larger than the bound.

If G is closer to F_0 than R_0 the difference between both distribution functions will be:

$$\begin{aligned} \forall y : G(y) - F_0(y) &\leq F_0\left(y - R_0\right) - F_0(y) + R_0 \\ \forall y : G(y) - F_0(y) &\geq F_0\left(y + R_0\right) - F_0(y) - R_0 \end{aligned} \tag{5}$$

according to equations 3.

The problem to be considered is whether or not two *DVHs* within a given Lévy distance correspond to tumour control probabilities inside a certain interval of values. And the inverse problem is to establish the maximum Lévy distance between two *DVHs* in order to fulfil a constraint on *TCP*.

In this context, *TCP* is an operator of the space of distribution functions to the non negative real numbers. If this operator were continuous and differentiable in some way, there would be a clear positive answer to both the direct and the inverse problem. But, first some properties of the space of distribution functions have to be stated.

1.- The Lévy distance induces the weak topology on the space.

2.- The space, with this metric, is locally convex.

3.- The subset of the distribution functions of non negative variables is a subspace, with the induced metric and topology.

Since the set of distribution functions has a structure, it is possible to define continuity. An operator $T: F \rightarrow R$ is continuous in F if, for any $\varepsilon > 0$, there is a value $R > 0$, so that:

$$d_L(F,G) < R \Rightarrow |T(G) - T(F)| < \varepsilon \quad (6)$$

There are several definitions of differentiability of operators which could be applicable; the most suitable of them for this study is the one by von Mises [2]. The operator T is von Mises differentiable at F within certain dominion, if for any G in the dominion the following limit exists, the equation is fulfilled and the function $a(F,y)$ does not depend on G.

$$\lim_{t\downarrow 0} \frac{T(F + t(G-F)) - T(F)}{t} = \int a(F,y) \cdot d(G-F) \quad (7)$$

If this happens, then $a(F,y)$ is the first von Mises derivative of T at F. It is possible to let F vary, and

$$d_1(T(\bullet)) = a(\bullet, y) \quad (8)$$

A linear operator is one defined by the following equation:

$$T_L(F) = \int g(y) \cdot dF(y) \quad (9)$$

for some function $g(y)$. Linear operators have an important property regarding their von Mises derivative:

$$\begin{aligned}
&\lim_{t\downarrow 0} \frac{T(F + t(G-F)) - T(F)}{t} = \\
&= \lim_{t\downarrow 0} \left\{ \frac{1}{t} \cdot \left[\int g(y) \cdot d(F + t(G-F))(y) - \int g(y) \cdot dF(y) \right] \right\} = \\
&= \lim_{t\downarrow 0} \left\{ \frac{1}{t} \cdot \left[t \cdot \int g(y) \cdot d(G-F)(y) \right] \right\} = \\
&= \int g(y) \cdot d(G-F)(y) \qquad (9)
\end{aligned}$$

$g(y)$ does not depend on G. Therefore, for a linear operator $dT_L = g$, and the following formula can be used:

$$T(G) - T(F) \cong \int g(y) \cdot d(G-F)(y) \quad (10)$$

If G is a distribution function within a Lévy distance of R_0 from F_0, according to equations 6, applying the linear operator to both terms and assuming $g(y)>0$ for every y:

$$\begin{aligned}
&T(G) - T(F_0) \cong \int g(y) \cdot d(G - F_0)(y) \leq \\
&\leq \int g(y) \cdot dF_0(y + R_0) - \int g(y) \cdot dF_0(y)
\end{aligned} \quad (11)$$

If T is an operator, and it is continuous, an upper and lower bound can be found on its values for distribution functions at a distance of R_0 from F_0. Moreover, if it is a linear operator, its derivative on G can be easily computed.

III. Practical application for TCP

Using a simple linear-quadratic formula (3), and the mean value of number of clonogens given as datum (N=number of intervals in DVH computation, ρ=clonogen density, V=PTV volume α=radiobiological index),

$$\begin{aligned}
TCP^* &= \exp\left(-N \cdot \rho \cdot V \cdot \sum_i \exp(-\alpha \cdot D_i) \cdot DVH_d(D_i) \right) = \\
&= \exp\left(-N \cdot \rho \cdot V \cdot \int \exp(-\alpha \cdot y) \cdot dG(y) \right)
\end{aligned} \quad (12)$$

In this formula $G(y)=1-DVH_c(y)$ and discrete functions have been considered as continuous.

Defining:

$$T(G) = \int \exp(-\alpha \cdot y) \cdot dG(y) \quad (13)$$

$T(G)$ is a linear operator with $g(y)=\exp(-\alpha y)>0$. Therefore, the relationships described in equations 11 and 12 are applicable. Moreover,

$$\exp\left(-N \cdot \rho \cdot V \cdot \left[T(G) - T(F_0) \right] \right) = \frac{TCP^*(G)}{TCP^*(F_0)} \quad (14)$$

Applying equations 11 and 12, and the TCP^* operator, it is possible to find bounds in terms of R_0 on this ratio.

$$\begin{aligned}
&\frac{TCP^*(DVH)}{TCP^*(DVH_0)} \geq \\
&\exp\left(\sum_{d_i \geq D_p \cdot R_0} -N \cdot \rho \cdot V \cdot e^{-\alpha \cdot d_i} \cdot \left(e^{\alpha \cdot D_p \cdot R_0} - 1 \right) \cdot DVH_d(d_i) \right)
\end{aligned} \quad (15)$$

D_p is the prescribed dose.

Table 1 shows bounds R_0 for a prostate treatment PTV, obtained for equation (15). This equation has been solved numerically via a simple routine for a set of tolerances on TCP variation. Parameter values are: $\rho V=10^4$, $\alpha=0.3$, $D_p=50$ Gy and $N=25$.

Table 1 Lévy bound values to achieve minimum tumor control probability levels in a prostate treatment.

Minimum TCP	R_0
0.995	0.046
0.990	0.082
0.985	0.106
0.980	0.124
0.975	0.138
0.970	0.150
0.965	0.160
0.960	0.168
0.955	0.176
0.950	0.184
0.940	0.194
0.930	0.204
0.920	0.214
0.910	0.222
0.900	0.230

For a minimum TCP goal a bound value can be obtained so that acceptance bands like the ones in Fig 2 can be built on the DVH graph, and therefore used for planning and optimization.

IV. Discussion

The practical example shows how the use of Lévy distance bounds can ensure that plans within the constraints will have TCP values in a predefined interval. R_0 values increase consistently as tolerance on TCP increases, allowing wider variations on DVH.

V. Conclusions

As presented in the theory section, any functional on DVHs can be treated similarly, as long as it shows properties of continuity and differentiability. Particularly, radiobiological indices are continuous functionals, and this method can be applied to some of them.

This novel method allows a straightforward and elegant assessment of TCP variations, it makes possible to design constraints on DVHs ensuring limited variations on TCP.

References

1. Tassi P and Legait S (1990) Complément et Approfondissements sur les Lois de Probabilité in: Théorie des Probabilités en Vue des Applications Statistiques. Editions TECHNIP.
2. Serfling RJ (1980) Von Mises Differentiable Statistical Functions in: *Approximation Methods of Mathematical Statistics*. John Wiley & sons. New York.
3. Kulik C, Mazurier J, Lartigau E (2002). Probabilités de contrôle tumoral et de complications (TCP/NTCP): aspects méthodologiques, physiques et biologiques. Cancer/radiother Suppl 1:155s-165s.

On Usability of Gamma Criteria Distribution for Evaluation of Field-in-Field Treatment Plans in Conformal Radiotherapy

A. Bernans[1] and A. Katashev[2]

[1] P. Stradins University Hospital, Riga, Latvia
[2] Biomedical Engineering and Nanotechnology Institute, Riga Technical University, Riga, Latvia

Abstract — **Hard, dynamic or virtual wedges are often used in conformal radiation therapy to reduce dose inhomogeneity within the target volume. There are restrictions exist in using such field modifiers for large fields due to technical peculiarities of the treatment machine. Field-in-field (FIF) manual segmentation, where one or more subfields are used to achieve dose homogeneity, could solve this problem, but such technique needs to be evaluated and verified first. FIF technique is based on intensity modulated radiation therapy (IMRT) principle, except that the intensity modulation is done manually using direct planning. The aim of this article is to determine whether the gamma criterion evaluation principle is suitable for FIF plans verification. For this study a 17 x 12 cm rectangular 6MV photon beam was used. Rectangular fields, sized 5 x 12, 6 x 8,5 and 3 x 4,3 cm were added as segments for each 17 x 12 cm base field in center. Dose distribution was calculated using treatment-planning system (TPS) to be used as a starting point to make distorted plans with segments displaced in superior, inferior, lateral left and lateral right directions to simulate patient movement or positioning errors during irradiation. Dose distributions for the distorted plans were measured using pixel ionization chambers detector array. The resulting dose distributions were compared to the reference one provided by TPS using gamma criterion. For acceptance criteria ΔDM=3% dose-difference and ΔdM=3 mm distance-to-agreement (DTA) were used and 95% of all pixels should be within this criterion. For some plans, considered in the present paper, 95% threshold was not exceeded even when the displacement reached clinically significant values of 1 cm and even more. Thus, one have to conclude that use of gamma criterion with 95% threshold of number of pixels in agreement is not suitable for FIF plans.**

Keywords — **Field in field, gamma criterion, radiotherapy, verification, IMRT.**

I. Introduction

3D conformal radiotherapy is widely used for patient treatment all over the world. Many treatment planning techniques has been developed to achieve acceptable dose homogeneity across the target volume by using different gantry and collimator angles, forming irregular beam shapes with multi-leaf collimators (MLC) and using beam modifiers like hard, dynamic or virtual wedges. All these features combined with accurate treatment planning system (TPS) three – dimensional analysis can increase dose homogeneity in planning target volume (PTV) and spare organs-at-risk. Wedges can be applied to localizations where the beam has different attenuation rates due patient tissue heterogeneity [1,2].

Not always these modifiers can be applied in patient treatment. For large treatment fields, any kind of wedges is not suitable for using because of the mechanical design of the treatment machines. Limitations of the field sizes, for which the wedges still can be used, can vary for different linear accelerators [3].

Although dynamic intensity modulated radiotherapy (IMRT) becomes more and more popular, simplified techniques still are in use. In [2] has shown, that field-in-field (FIF) technique can significantly reduce dose inhomogeneity in PTV and reduces dose to organs-at-risk.

As any other treatment technique, FIF plans have to be verified. In IMRT field's verification, delivered plans are compared with one calculated by TPS by means of the gamma criteria [6]. Although plan verification usually requires analysis of the gamma criteria distribution over the field, locating "hot spots", where major disagreement is observed. Besides, quantification of the plans "coincidence" may be done by calculating the proportion of the points of the measured distribution, that are close enough to the reference dose distribution to fall within gamma acceptance criteria. Usually, if more then 95% of all points coincide, the fields considered to be coincident as well [2]. In the present paper, gamma criteria distribution method is applied for the verification of the FIF plans.

II. Materials and Methods

A. Detector and Phantom Set Up

Measurements were made, using phantom, composed of the water equivalent 1cm thick PMMA slabs and IBA I'mRT Matrixx pixel ionization chambers detector array. 10 PMMA plates were paced on the array to form 10 cm thick build-up layer, while 5 plates was placed under detector to provide 5 cm thick backscattering layer.

Y. Dekhtyar et al. (Eds.): *International Symposium on Biomedical Engineering and Medical Physics*, IFMBE Proceedings 38, pp. 123–126, 2013.
DOI: 10.1007/978-3-642-34197-7_32

B. *Phantom CT Data Acquisition and Treatment Planning*

Phantom, composed both form PMMA plates and pixel ionization chambers detector array, was scanned using Siemens Somatom Sensation computer tomograph (CT). The pitch of the scanning was 1.5 mm; reconstructed slice thickness was 1 mm. The phantom's CT data was transferred to the Siemens Syngo® RT Oncologist contouring system to draw phantom's contours. Treatment planning was carried out using the Elekta CMS XiO v4.51 treatment planning system. Treatment plans were based on the anterior – posterior (AP) rectangular isocentric field. The size of the field was 17 x 12 cm. For this field 70 monitor units (MU) were prescribed. For each plan base field was copied and additional segmented field was added to the base field to create FIF plan. Segment fields were rectangular, AP aligned and isocentric, with a center aligned with the center of the base field, sized 5 x 12 cm, 6 x 8,5 cm and 3 x 4,3 cm were used. For each segment field 15 MU was prescribed. For each size of the segment field, the simulation of the dose distribution for the whole plan was made [Fig 1].

C. *Field Distortion Modeling and Measurements*

Siemens Oncor Impression Plus linear accelerator with the photon energy 6 MeV was used for measurements. Phantom was positioned manually owing to markers on the detector surface. The segmented fields were provided using multileaf collimator.

To simulate patient misalignment / movement and model field distortion, segment fields was shifted in 1 mm steps in superior, inferior, lateral left and lateral right direction up to distance of 10 mm.

For each position of the segment field, dose distribution over the phantom was measured.

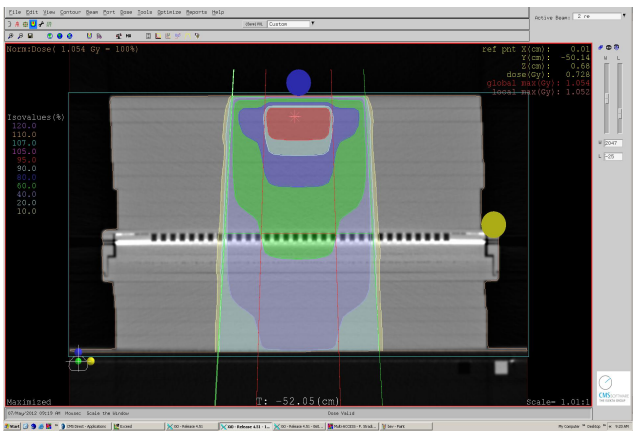

Fig. 1 Simulated FIF field depth dose distribution in transverse plane for segment field 6 x 8.5 cm.

D. *Data Analysis*

Measured dose distributions were compared with the reference, simulated by TPC, using gamma criteria. The dose differences, distances-to-agreement (DTA) and corresponding gamma distributions were evaluated using Omni PRO-I'mRT software. As the acceptance criteria for individual point, ΔD_M=3% dose-difference and Δd_M=3 mm DTA were used [Fig.2]. For two dose distributions to be considered equal, 95% of all pixels should be within this criterion. [4] The chosen criteria are those routinely used in clinic for verification of the IMRT plans.

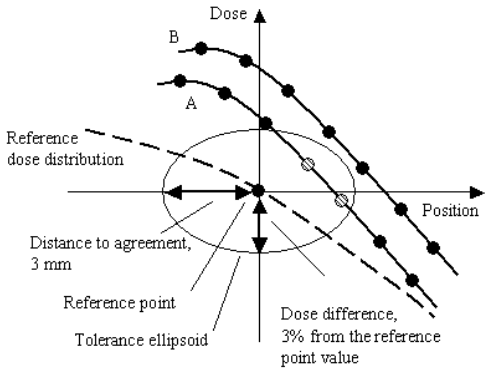

Fig. 2. Geometric representation of the gamma criterion, adopted from [6]. The criterion is satisfied in the reference point for the dose distribution A, because there is at least one point within the tolerance ellipsoid. For the distribution B, the criterion does not met. This mean that reference dose distribution significantly differs from the distribution B at the reference point.

III. Results and Discussion

The distorted dose distributions, measured with the segment field, shifted from its initial position, were compared with reference plans using gamma criterion calculation software. Based on 3 % dose difference and 3 mm DTA acceptance criteria, the gamma distribution was evaluated as the percentage of dose distribution image pixels that pass the tolerance criteria. The percentage of such "passed" or "coincided" pixels for lateral right (+) and lateral left (-) shifts are shown in Figure 3 as function of the segment field shift. As the shifts were performed in direction of shortest sides of the segment field rectangle, shifts greater than 3 mm don't show significant reduction of number of coincided pixels. For each field of interest, the threshold level of 95% was not reached even with lateral shift of 10 mm.

The percentage of pixels, passed gamma criterion for shifts in superior and inferior directions for the same configuration of base and segmented fields is demonstrated at the Figure 4.

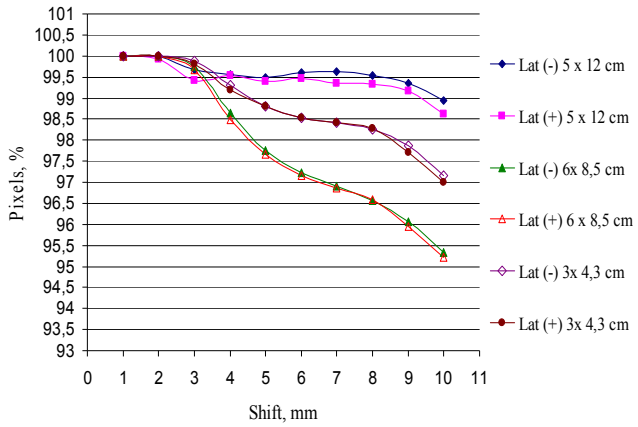

Fig. 5. Number of pixels, passed gamma criterion (3%/3mm) for lateral segment field shifts.

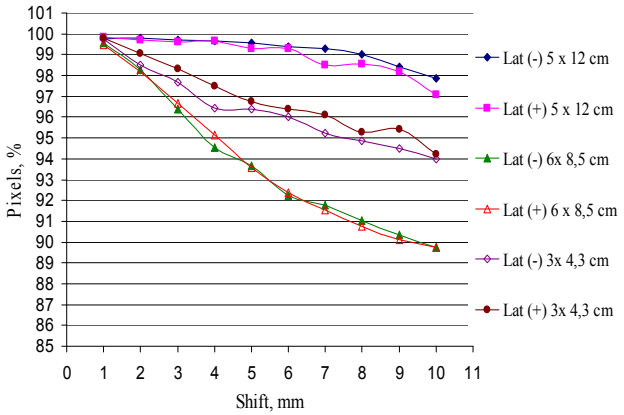

Fig. 3 Number of pixels, passed DTA criterion (mm) for lateral segment field shifts.

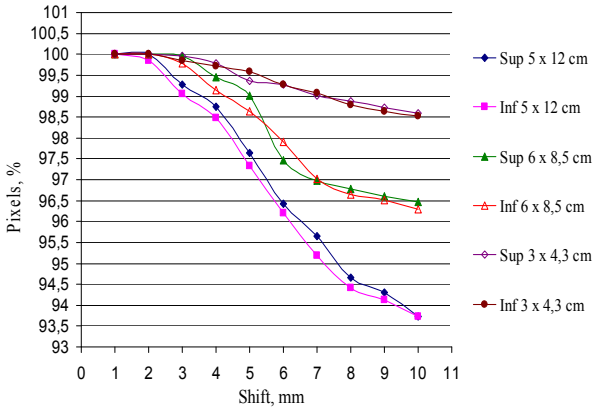

Fig. 6. Number of pixels, passed gamma criterion (3%/3mm) for superior – inferior segment field shifts.

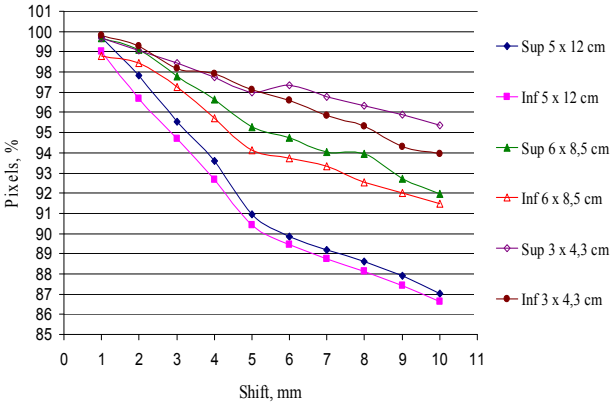

Fig. 4 Number of pixels, passed DTA criterion (3mm) for superior – inferior segment field shifts.

The longitudinal shifts of the largest segment field in the direction of the field's longest side show steeper decrease in the number of "passed" pixels. Nevertheless, even as large shifts as 10 mm for the 6 x 8,5 cm and 3 x 4,3 cm segments do not lead to the percentage drop below 95% threshold. For the largest segment 5 x 12 cm, 8 mm shift required to decrease percentage of passed pixels below 95%, to the 94,66% and 94,42%. for superior and inferior shifts, correspondingly.

The same shifts were analyzed using only DTA criterion, i.e. pixel form the reference distribution pass the criterion, if there is at least one pixel at the distance less then DTA. The DTA based evaluations of the number of passed pixels for lateral and longitudinal shifts are shown in Figure 5 and Figure 6, respectively. The results show that for FIF technique, the criteria, based on the distance discrepancy is more sensitive. The 95% threshold was reached for 5 x 12 cm and 6 x 8,5 cm at lateral and longitudinal shifts of 4 mm. Besides, for the small perimeter field, this method fail to detect discrepancies in the dose distributions for lateral shifts more then 10 mm and for superior – inferior shifts up to 8 mm.

The reason of the poor performance of gamma criteria and DTA criteria seems to be entirely geometrical. FIF technique is characterized large areas of flat dose distributions. In such a case, both gamma and DTA criteria will indicate difference at the edges of segment field. For the segments of small perimeter, the number of pixels affected by shift may just be smaller, then 5%. As an extreme example one may consider segment, whose area is just 2.5% form the total field area. Such a segment may be shifted to any new position, but number of pixels, failed to pass gamma or DTA criteria will not be more then 5%. In general, simple geometrical model may be used to evaluate maximal "significant" shift. Let consider square base field with the size

A and segment field with the size B. Let segment field is shifted by the distance Δ along one of its side. Neglecting penumbras and assuming the field edges are sharp, it easy to calculate area, where dose will be changed in comparison with initial dose distribution:

$$\delta S = 2\Delta B\,, \tag{1}$$

where 2 accounts for two areas: the area in direction of the shift, that becomes irradiated, and area at the opposite side of the segment field, that is not irradiated anymore. Relative part of the field that remained unchanged will be

$$\frac{\delta S}{S} = \frac{2\Delta B}{A^2}\,. \tag{2}$$

Since, to detect discrepancy using 95% threshold, δS/S should become more then 0.05, one could get:

$$\Delta > \frac{0.05A^2}{2B}. \tag{3}$$

For the field 20 x 20 cm and segment field 5x5 cm minimal detectable shift will be 20 mm. If, for any field sizeone will take segment of the same field size (that practically is meaningless), one could get minimal displacement, that in principle may be detected by the gamma criterion distribution method. For 20x20 cm field this displacement is 5 mm, but for 10x10 cm is 2.5 mm. Reduction of the segment field size to half of the base field doubles minimal detectable displacement. For large field 20x20 cm, this displacement will be 1 cm; that is of clinical importance.

IV. Conclusions

This study has demonstrated, that treatment plan validation method, based on the gamma criteria is not effective for conformal field-in-field technique. For small area segments, even the large misalignment of the fields does not lead to significant changes of the percentage of failed pixels. Gamma criterion with dose difference 3%, and DTA 3mm shows poor sensitivity to the misalignment for field-in-field plan evaluations due to small segments perimeters and relatively small ratio between numbers of pixels in field versus number of pixels in shifted area. Even clinically significant shifts of 10 mm pass the 95% threshold level. This could be attributed to the fact, that gamma evaluation method show false positive results in steep dose gradients [5]. Using only DTA evaluations prove that the geometrical evaluations show higher sensitivity, that gamma evaluation, but still significant misalignment may be disregarded for small segment fields. Thus, one have to conclude, that 95% criteria should not be used at all for comparison of dose distribution in field in field conformal radiotherapy and other numerical criterion have to be developed.

References

1. P. Mayles, A. Nahum, J.C. Rosenwald, "Handbook of radiotherapy physics: theory and practice", Taylor & Francis Group, 2007.
2. J.W. Lee, S. Hong, K.S. Choi, "Performance evaluation of field-in-field technique for tangential breast irradiation", Jpn J.Clin Oncol 2008; 38(2), p. 158-163.
3. S.X Chang, J.P. Gibbons "Clinical implementation of non-physical wedges", AAPM refresher course, 1999, p. 13
4. D.A. Low, W.B. Harms, S. Mutic, J.A. Purdy, "A technique for the quantitative evaluation of dose distributions" Medical Physics, 1998, 25 (5), p. 656 – 660.
5. Baptiste Blanpain, David Mercier, "The delta envelope: a technique for dose distribution comparison", Medical Physics, 2009, 36, p. 16
6. T. Depuydt, A. Van Esch & D. P. Huyskens, A quantitative evaluation of IMRT dose distributions: refinement and clinical assessment of the gamma evaluation. Radiotherapy & Oncology, 62(3), 309-19, 2002

Author: Alvis Bernans
Institute: Paul Stradins Univeristy Hospital
Street: Pilsonu 13
City: Riga, LV - 1002
Country: Latvia
Email: alviz@apollo.lv

Author: Alexei Katashev
Institute: Institute of Biomedical Engineering and Nanotechnologies, Riga Technical University
Street: 6k Ezermalas Street
City: Riga, LV-1006
Country: Latvia
Emails: katashev@latnet.lv

Determining the Threshold of Radiotherapy Delivery Error Detection Using Delta4

P. Eizentals[1] and M. Thomas[2]

[1] Biomedical Engineering and Nanotechnology Institute, Riga Technical University, Riga, Latvia
[2] Joint Department of Physics, The Institute of Cancer Research and Royal Marsden NHS Foundation Trust, Sutton, Surrey, UK

Abstract — **Intensity Modulated Radiation Therapy and Volume Modulated Arc Therapy are now widely used in cancer treatment, but due to their complex nature each clinical plan is verified before applying on patient. Many different verification systems are available for this purpose, but because there is no regulation that would make it an obligatory, manufacturers usually don't give such information as devices error detection threshold, repeatability etc. Therefore clinics must carry out tests before using these devices. This article is dedicated to the determining of IMRT/VMAT plan verification systems Delta4 (Scandidos, Uppsala, Sweden) error detection threshold. 10 Head & Neck IMRT and 5 esophagus VMAT clinical plans were modified with intentionally introduced errors and then verified on Delta4. Positioning errors for various moving parts (MLC, Jaws, Collimator and Gantry) together with dose related errors (MU, missing control points) were tested. The resulting gamma index was compared to the one from unmodified plan. A clear detection threshold for IMRT was detected for shift, MU, Jaws, collimator and gantry errors and for VMAT for MU and Jaws errors. No clear error detection threshold within tested error size range was found for the rest of the introduced errors.**

Keywords — **Delta4, Radiotherapy, IMRT, VMAT, Verification.**

I. Introduction

IMRT and VMAT have proven to be reliable radiotherapy treatment techniques, but due to their complex nature every clinical plan must be verified prior to applying on patient [1, 2]. Various systems are available for patient-specific verification, but due to the lack of official regulations related to them manufacturers do not give information about devices error detection abilities. Therefore before using these devices in clinical practice they must be checked by physicists.

Delta^{4PT} is a relatively new device designed for IMRT and VMAT plan verification, and, although there have been several researches [3, 4], but its sensitivity to error detection is still largely unknown. In this study were tested almost all possible geometrical errors and some dosimetrical errors – 3 types of MLC positioning errors, jaws positioning error, monitor units (MU) error, collimator and gantry angle errors and missing control points (for VMAT only).

Delta^{4PT} consists of two orthogonally orientated detector arrays that are crossed under specific degree with total of 1069 p-type silicon diodes which are implemented in a cylindrical polymethylmethacrylate (PMMA) phantom. Detector arrays are distributed in two levels. Central level is 6 x 6 cm square with 0.5 cm spacing between diodes. Outer level is 20 x 20 cm square with 1 cm spacing between diodes. The phantom itself has a diameter of 22 cm and length of 40 cm. It is directly connected to accelerator and measures dose in relation to individual accelerator pulses using the trigger signal. It can also detect the gantry angle by using an inclinometer connected to the gantry head, which allows the device to identify and associate measured dose with separate VMAT control points. Prior to verification clinical RT plan is imported and recalculated in the phantom plan, which consists of a uniform PMMA equivalent cylinder. PMMA cylinder is used instead of CT scan of the phantom to avoid uncertainties due to appearance of the diodes on the CT scan [3]. Gamma index is used to compare and evaluate measurement with reference [5].

II. Materials and Methods

A. Data Acquisition

An approximated method was used instead of an actual verification to fasten the data acquisition process. Errors were introduced by manually modifying the plans outside TPS and then dose distribution was recalculated with Pinnacle3 (Philips Radiation Oncology Systems, Madison, WI). The recalculated plans then were verified with Delta^{4PT} software using slightly different method than standard verification. Instead of irradiating every modified plan to the verification system, only un-modified plan was irradiated, and the modified plans were used as reference data. Such approach helps to get greater amount of data, but can introduced some methodical errors, which were taken into account at data analysis.

B. Introduced Errors

Three different types of MLC positioning errors were introduced – random, systematic and shift. Random error

Y. Dekhtyar et al. (Eds.): *International Symposium on Biomedical Engineering and Medical Physics*, IFMBE Proceedings 38, pp. 127–130, 2013.
DOI: 10.1007/978-3-642-34197-7_33

means one leaf out of position only in one of the segments. Systematic error means that one leaf is out of position in all segments of one field for IMRT and in all segments for VMAT plans. Shift error is simulation of gravity introduced MLC leaf sag, therefore lateral segments were chosen for this error. For VMAT lateral control points were chosen with the sum MU ~10 – 15% from total. MLC leaf positioning errors for up to 5 mm size were introduced.

In MU error extra monitor units were added to one of the segments. All precautions were done to not allow Pinnacle to modify the rest segments at the recalculation.

In jaw error simulation secondary collimator was opened by exact distance, which in this study was 1, 5, 10 and 100mm.

Collimator angle was changed for up to 3°. For IMRT all segments for one of the fields were modified, but for VMAT the error was applied for all segments as the collimator angle in the examined VMAT plans was constant.

Gravity effect was simulated in IMRT gantry error by lowering one of lateral fields by up to 3°. As for VMAT, gantry lag was introduced by gradually increasing the error for up to 3°.

Two types of missing control point error were simulated for VMAT. In the first error type up to three control points were deleted and the total dose was lowered by the amount of deleted control points. In the second type the total amount of monitor units was left intact, letting the TPS to smooth out the difference between the rest control points.

C. Data Analysis

Two methods were used to determine if the error is detected. First is comparison method – the difference between original plans gamma index and the modified plans gamma index was calculated and compared with the size of the error. This way it is possible to see how the gamma index changes according to the error type and size. The error was considered as detected if the difference between original and modified plans gamma index exceeded 5%.

Second method is t-Test for paired two samples for means analysis. In this case null hypothesis was that the means of result for original plan and modified plan are equal ($H: \bar{x} = \bar{y}$) i.e. there is no statistical difference between results. The chosen significance threshold was $\alpha = 0.05$. The resulting p value was then divided into three groups: $p < 0.05$ – error detection group, assumed to have statistical difference between groups meaning that the error is detected; $0.05 \le p \le 0.07$ – near error detection group, the result is close to the determined threshold and although the difference is not statistically significant, it might be clinically significant and $p > 0.07$ – no significant statistical difference between the means of the groups is detected, modified field is assumed to be almost equivalent to the original and no error is detected.

III. Results and Discussion

A. Comparison Data

Every modified field was compared to the original and the results were analyzed as described above. Average differences in gamma index are shown in tables 1 and 2. As it can be seen random and systematic errors are hard to detect even if error size is 5 mm and acceptance criteria 2%/2mm. 2 mm shift error in IMRT plans can be detected with criteria 2%/2mm. As for VMAT, none of MLC positioning errors were detected.

Table 1 Mean γ index difference between original and modified IMRT plans.

Error	Size	Mean Δγ 3%/3mm	Mean Δγ 2%/3mm	Mean Δγ 2%/2mm
Random	0,5 mm	0,01	0,01	0,06
	1 mm	0,03	0,08	0,14
	2 mm	0,03	0,07	0,13
	3 mm	0,03	0,12	0,26
	4 mm	0,06	0,02	0,36
	5 mm	0,04	0,08	0,28
Systematic	0,5 mm	0,02	0,02	0,21
	1 mm	0,03	0,05	0,47
	2 mm	0,1	0,15	0,88
	3 mm	0,29	0,54	1,43
	4 mm	0,51	0,81	2,1
	5 mm	0,73	1,1	2,76
Shift	0,5 mm	0,14	0,26	1,37
	1 mm	0,1	0,21	2,7
	2 mm	1,2	2,19	9,23
	3 mm	5,14	7,1	17,66
	4 mm	11,14	14,91	26,59
	5 mm	18,52	23,3	33,61
Monitor Units	0,5 MU	0,03	0,24	1,25
	1 MU	0,11	1,43	4,81
	2 MU	3,23	9,17	16,92
	4 MU	17,85	23,77	34,55
Jaws	1 mm	0,12	0,23	0,66
	5 mm	2,81	3,54	6,95
	10 mm	6,84	9	13,56
	100mm	29,99	39,84	51,61
Collimator	1°	0,28	0,5	1,68
	2°	1,38	2,1	5,97
	3°	4,2	5,96	11,84
Gantry	1°	0,07	0,05	0,7
	2°	0,58	0,79	3,3
	3°	1,98	2,77	6,09

Dose errors are considerably easier to detect, 2 MU error can be detected using acceptance criteria 2%/3mm for both IMRT and VMAT. In IMRT plans 5 mm Jaws error can be

detected using criteria 2%/2mm, but 10 mm error with criteria 3%/3mm. Surprisingly low impact Jaws error has on VMAT plans, only 100mm error can be detected using criteria 2%/3mm. It might be because esophagus plans have long segments and only few MLC leaves are shielded with jaws.

Collimator error with the given error size was detected only for IMRT plans (2° error with 2%/2mm or 3° error with 2%/3mm criteria). Even less detectable appeared to be gantry error, using acceptance criteria 2%/2mm was mostly was detected only 3° error.

Table 2 Mean γ index difference between original and modified VMAT plans.

Error	Size	Mean Δγ 3%/3mm	Mean Δγ 2%/3mm	Mean Δγ 2%/2mm
Random	0,5 mm	0,1	0,5	0,58
	1 mm	0,22	0,64	0,72
	2 mm	0,42	0,84	0,92
	3 mm	0,6	0,84	0,78
	4 mm	0,96	2,56	2,6
	5 mm	1,16	2,52	2,54
Systematic	0,5 mm	0,16	0,78	0,88
	1 mm	0,22	0,96	1,22
	2 mm	0,44	1,24	1,36
	3 mm	0,6	1,16	1,36
	4 mm	0,86	2,2	2,12
	5 mm	1,08	2,3	2,32
Shift	0,5 mm	0,03	0,45	0,5
	1 mm	0	0,4	0,23
	2 mm	0,03	0,15	0,83
	3 mm	0,13	0,18	1,3
	4 mm	0,28	0,88	1,9
	5 mm	0,33	0,8	2,83
Monitor Units	0,5 MU	0,84	2,82	3,9
	1 MU	1,28	3,28	3,54
	2 MU	3,8	7,24	8,64
	4 MU	12,3	15,68	18,74
Jaws	1 mm	0,28	1,34	1,38
	5 mm	0,2	1,44	1,06
	10 mm	1,26	1,54	1,82
	100mm	4,4	6,8	8,68
Collimator	1°	0,38	1,1	0,72
	2°	0,14	0,5	1,32
	3°	0,44	0,86	2,78
Gantry	1°	0,56	1,8	2,04
	2°	0,44	0,74	1,98
	3°	0,36	1,04	4,36
Control Point 1	-1	9,5	14,08	15,4
	-2	14,85	16,73	18,7
	-3	21,08	23,13	26,88
Control Point 2	-1	0,34	1,08	2,42
	-2	1,4	3,76	5,66
	-3	3,8	5,84	8,64

As for control point errors, the first appeared to be easy detectable, even one missing control point would be usually detected with standard acceptance criteria 3%/3mm, probably because the overall dose change is easy to detect. The second was relatively harder to detect as the dose of the deleted control point smeared out around the PTV. Error starting with two missing control points was detected with criteria 2%/2mm or three control points with criteria 2%/3mm.

Despite the considerable variation in results between plans it is clear that MLC positioning errors described here have relatively low effect on dose distribution compared to dose errors. Similar results were obtained in study by Carver et al. [4].

B. t-Test Data

No statistical difference was detected for Random error plans. Only one IMRT and one VMAT plans had p value close to threshold with error value 5mm ($p = 0{,}06$ for both). No clear error detection threshold can be drawn from Systematic error t-Test data. Only 3 from 10 IMRT plans show error detection at 3mm, 1 plan shows detection at 5mm and the rest show no statistically significant difference between the measurement and reference. As for VMAT, only one plan is close to the threshold with error 5mm ($p = 0{,}05$). For IMRT plans shift error statistical detection threshold is 3 – 4mm. All IMRT plans show statistically significant difference if error is 5mm, 7 from 10 plans are detected to be different with 4mm error and 3 with 3mm error. Only one VMAT plan show response to this error. Almost all (8/10) IMRT plans show statistical difference for monitor units error +4MU, but only one shows with error +2MU (two more are with $p < 0{,}07$). Similar situation is with VMAT plans – 4/5 plans are with p value under threshold with error +4MU and for +2MU 2 from 5 plans $p < 0{,}05$ and 2 plans with $p < 0{,}07$. Only one plan with jaws error 5mm had p value over 0,07 for IMRT, three had p value between 0,05 and 0,07 and the rest under 0,05. For VMAT two from five plans had p value under threshold for 5mm error and four plans for error 10mm. As for the rest types of errors (collimator, gantry, control point), the plan-to-plan variation is too great to define a certain error detection threshold using t-Test for the error sizes examined in this study.

The threshold of error detection can be further clarified by comparing the results of both methods. For random MLC error there was no error detection using both methods with the given error size, therefore it can be said that error detection threshold for such error is still unknown, but must be >5mm. For systematic MLC displacement no error was detected for the tested error sizes with comparison method and only four IMRT plans from ten appeared to be statistically different with error 5mm. This means that also systematic error detection threshold in most cases is >5mm. 2mm

size shift error in IMRT was detected with acceptance criteria 2%/2mm (3mm error with 3%/3mm) using comparison method, but t-Test showed significant amount of different plans (7 from 10) only with 4mm error. As the used α value in t-Test might not be perfect for this study, 3mm was chosen as shift error detection threshold for IMRT. No clear detection threshold for introduced shift type error for VMAT. With both methods for MU error the detection threshold seems to be between +2MU and +4MU. The jaws error detection threshold for IMRT is 5mm. Although 5mm error can be detected only with 2%/2mm, t-Test shows significant difference for over half of the plans at this value. There are still doubts about the VMAT jaws error detection threshold as comparison method detected it only with value 100mm, but t-Test shows that 4 from 5 plans are different with error value 10mm. Collimator angle error detection threshold for the tested IMRT plans appear to be 3°. This error was detected with 2%/3mm and t-Test showed difference for 7 plans. No clear detection for VMAT. Similar results were obtained for gantry angle error. After comparing control point error results for both methods and then analyzing each of the plans with this error, a logical conclusion can be drawn – error detection for this type of error depends on the relative weight of the missing control point therefore it is hard to define an error detection threshold. For most of the tested cases it was -2 control points for both type errors.

IV. Conclusions

Most of possible treatment machine errors were tested in this study to determine their detection threshold with Delta^{4PT} verification phantom. A clear detection threshold for IMRT was detected for errors shift, MU, Jaws, collimator and gantry and for VMAT for errors MU and Jaws. No clear error detection threshold within tested error size range was found for the rest of the errors. Because the sensitivity of the used method due to some uncertainties is lower than normal patient specific verification, the results of this study can be considered as worst case scenario, i.e. if the error was detected in this study, it should be certainly detected in the actual verification. Delta^{4PT} phantom is a useful device for IMRT/VMAT plant pre-treatment verification.

Acknowledgment

This study was possible due to great help from the staff of Joint Department of Physics, The Institute of Cancer Research and Royal Marsden NHS Foundation Trust. Special thanks to Michael Thomas and Jim Warrington.

References

1. Marcus Alber et al. (2008) “Guidelines for the verification of IMRT” ISBN 90-804532-9
2. J. Charles Smith, Sonja Dieterich, Colin G. Orton (2011) “It is STILL necessary to validate each individual IMRT treatment plan with dosimetric measurements before delivery”, Med. Phys. 38:553 – 55
3. Bedford J L et al. (2009) Evaluation of the Delta4 phantom for IMRT and VMAT verification. Phys Med Biol 54(9):N167-76. DOI: 10.1088/0031-9155/54/9/N04
4. Carver A et al. (2011) An analytical approach to acceptance criteria for quality assurance of intensity modulated radiotherapy. Radiother Oncol 100:453-55
5. Low D A, Harms W B, Sasa Mutic, Purdy J A. (1998) “A technique for the quantitative evaluation of dose distributions”, Med Phys 25(5):656-61

Dose Evaluation along the Ir -192 Brachytherapy Source Transportation Path to the Dwell Position Using 2D Film Dosimetry

D. Adliene[1], J. Laurikaitiene[2], K. Jakstas[1,3], V. Rudzianskas[3], and G. Adlys[1]

[1] Kaunas University of Technology, Physics Department, Studentu g. 50, Kaunas, Lithuania
[2] Lithuanian University of Health Sciences, Oncology Hospital, Volungiu g.16, Kaunas, Lithuania
[3] Lithuanian University of Health Sciences, Oncology Institute, Eiveniu g. 2, Kaunas, Lithuania

Abstract — **One of the objectives in brachytherapy is to ensure an accurate and safe dose delivery to a target volume avoiding irradiation to surrounding healthy tissues. 2D film dosimetry is the ideal method for the dose and dose distribution measurements in brachytherapy where steep dose gradients are present; however calibration of films should be performed prior to dose evaluation. Film calibration method in HDR brachytherapy is discussed in the present paper and film calibration curves for radiochromic (Gafchromic® EBT2) and radiographic (Kodak *X*-Omat V) films irradiated by Ir-192 source are provided. It is shown that the doses along the brachytherapy source transportation path to the dwell position evaluated according to the obtained film calibration curves are low and vary from 0.09 Gy to 0.12 Gy. Nevertheless these values are sufficient enough to be considered estimating irradiation doses to surrounding tissues.**

Keywords — **Brachytherapy, Ir-192 source, radiation doses, film dosimetry.**

I. Introduction

Brachytherapy is used to treat patients when tumours are located in special places as it is for example in the case of head and neck cancer patients. This technique has an advantage against external beam radiotherapy treatment since it provides better localization of the dose within a tumour and better protection of healthy tissues. Dose plans for the patient's treatment are usually prepared by a standard treatment planning system, which uses prescribed calculation algorithms. However due to the high dose rate during brachytherapy treatment, dose and dose distribution per procedure has to be known more precise and accurate. Therefore, an accurate dose measurement, or verification technique such as monomer/polymer gel dosimetry, ion chamber, thermoluminescence detector (TLD), and film dosimetry is suggested to verify the outcome of the treatment planning doses and their distribution [1-5].

It is well known [6-8] that film dosimetry is one of most suitable methods to obtain and analyze dose distributions in the areas with the steep dose gradients as it is in the vicinity of brachytherapy sources. The application of films having high special resolution and low spectral (optical) sensibility is also of advantage when photon energy spectrum changes are possible. 2D film dosimetry requires performing of film calibration procedure prior to dose measurements and their analysis [9, 10].

The aim of this work was to discuss film calibration procedure in HDR brachytherapy, to establish film calibration curves for radiochromic (Gafchromic® EBT2) and radiographic (Kodak X-Omat V) films irradiated by Ir-192 source and use obtained calibration curves for the evaluation of the doses along the brachytherapy source transportation path to the dwell position.

II. Instruments and Methods

Two types of films: radiochromic (Gafchromic® EBT2) and radiographic (Kodak X-OmatV) were used in this investigation.

A. Irradiation of Films

Series of both types of films were irradiated with gamma photons emitted from Ir-192 source ($E_\gamma \approx 370$keV) operated in two HDR brachytherapy units: GamaMed iX (Varian) and Microselectron V2 (Nucletron) increasing irradiation dose from 0 Gy to 2.5 Gy in 0.1Gy steps. Irradiation dose values were calculated using standard Ir-192 source activity conversion to dose algorithm. Since one of the objectives in this investigation was to evaluate the actual doses delivered to the irradiated film along the single brachytherapy source transportation path to the dwell position, irradiation was performed using experimental set up shown in Fig.1. Polymethylmethacrylate (PMMA) frame was used for the fixation and alignment of applicator in order to secure the same source - film distance of 5 mm along the source transportation path in all measurements. The same PMMA frame was used for the investigation of dose coherence and dose distribution in the irradiation field when more than one applicator is used and the Ir-192 source is inserted into applicators according to the prescribed sequence (Fig.2).

Y. Dekhtyar et al. (Eds.): *International Symposium on Biomedical Engineering and Medical Physics*, IFMBE Proceedings 38, pp. 131–134, 2013.
DOI: 10.1007/978-3-642-34197-7_34

Irradiated radiographic films were developed in Automatic Development System (ADS) using standard procedure.

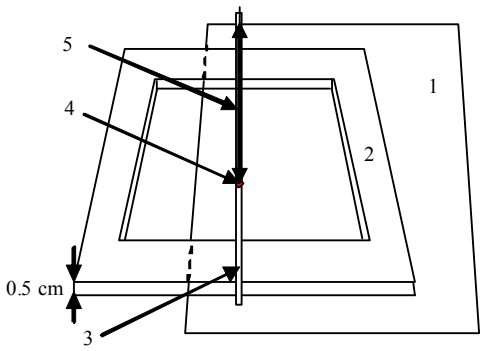

Fig. 1 Experimental set up: 1 – film, 2- PMMA frame, 3- applicator, 4 - Ir-192 source, 5 – source path to the final location (dwell position).

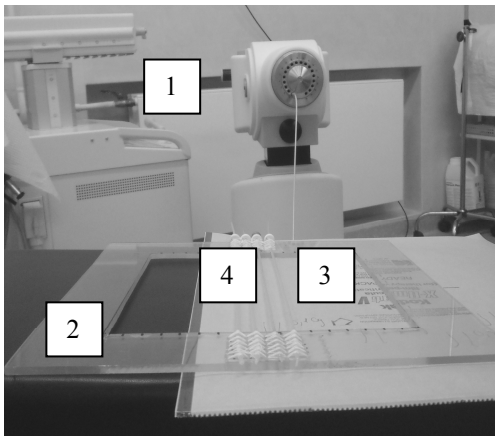

Fig. 2 Experimental set up with fixed and aligned applicators: 1 - brachytherapy unit, 2 – PMMA frame, 3 – film, 4 – applicators.

B. Calibration of Films

It is possible to evaluate irradiation dose using film dosimetry system, however dose calibration curves are needed for the conversion of the film response into dose [9, 11].

Film calibration curves were established: in two ways. In the first case the net optical density (OD) of each irradiated spot (Fig.3) was measured using densitometer iCFilm (Gretag Macbeth). Corresponding dose values were calculated using standard dose calculation algorithm of the brachytherapy unit and the calibration curves "Dose – film net OD" were constructed for each film type.

In the second case irradiated films were scanned and pixel values of the obtained images were evaluated according to the procedure described in our previous paper [10]. Radiographic films were scanned using special Vidar Twain 32 scanner (resolution 300 dpi, depth 8). Radiochromic films were scanned using flatbed scanner Hp LJ 1536 dnf MFP (resolution 1200 dpi). Scanning of radiochromic films was performed > 48 h after the irradiation procedure to ensure that radiochromic films response has been stabilized after the irradiation [12]. Calibration curves "Dose – pixel value" were constructed using pixel evaluation results.

III. Results and Discussions

Examples of the irradiated films with indicated irradiation spots at the dwell positions of the source and clearly seen irradiation tracks corresponding to the source transportation path from the starting position to the dwell location are provided in Fig.3.

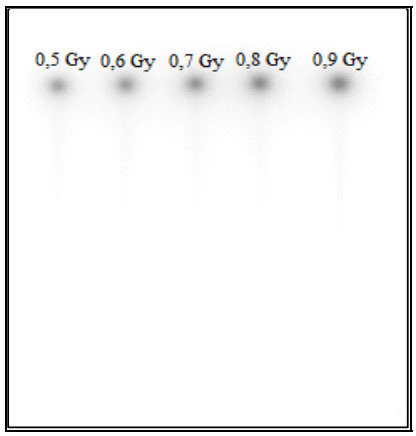

A

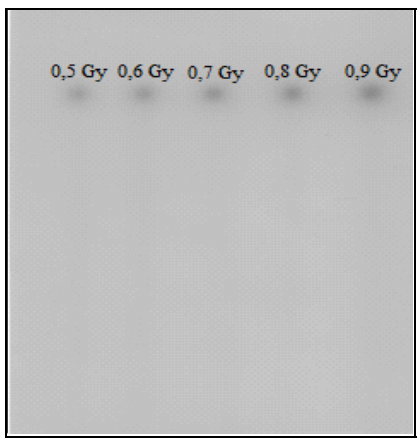

B

Fig. 3 Images of films exposed to different doses: A - radiographic film Kodak X-OmatV, B- radiochromic film Gafchromic® EBT2.

The images of differently exposed films were similar to each other but the relationship between the spot size and irradiation dose and between the spot blackening and irradiation dose (exposure time) was evident. No changes in the irradiation tracks corresponding to the source transportation path from the starting location to the dwell position were observed since brachytherapy source moves with a constant velocity inside the applicator.

Two types of calibration curves were constructed for Ir-192 irradiated radiochromic films (Gafchromic® EBT2) and radiographic films (Kodak X-OmatV) using experimental results obtained in HDR brachytherapy unit GamaMed iX (Varian) and Microselectron V2 (Nucletron). Calibration curves for radiographic films are shown in Fig.4 and calibration curves or radiochromic films are provided in Fig.5. Second order polynomials were used to fit the data.

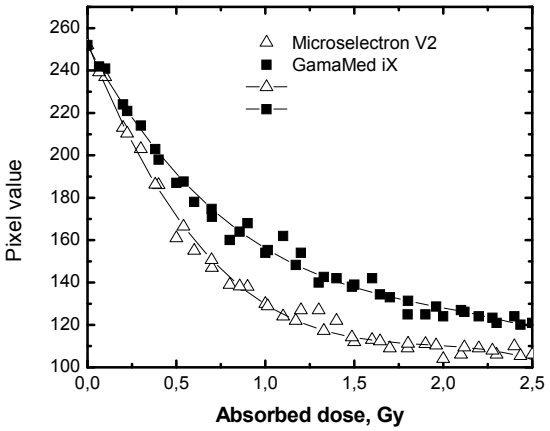

A

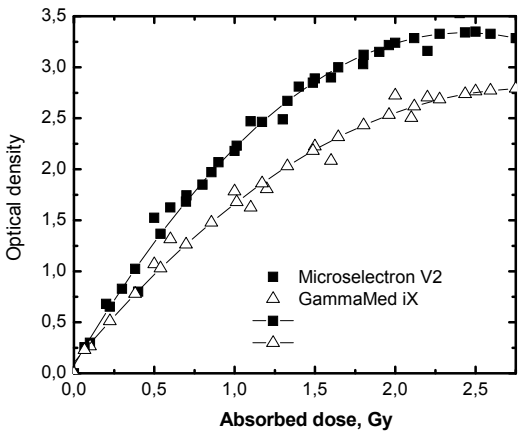

B

Fig. 4 Dose calibration curves for Kodak X-OmatV radiographic films obtained in two different brachytherapy units: A – "Dose - pixel value" curve, B – "Dose net optical density" curve.

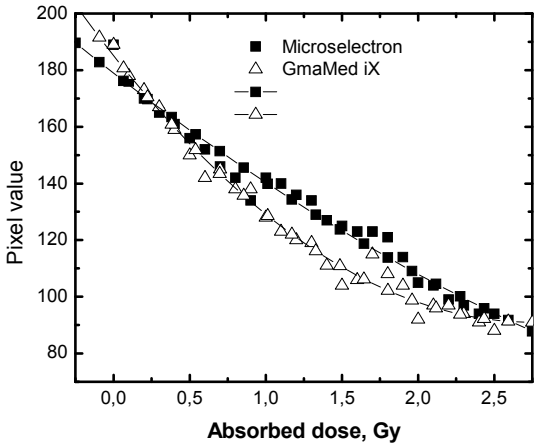

A

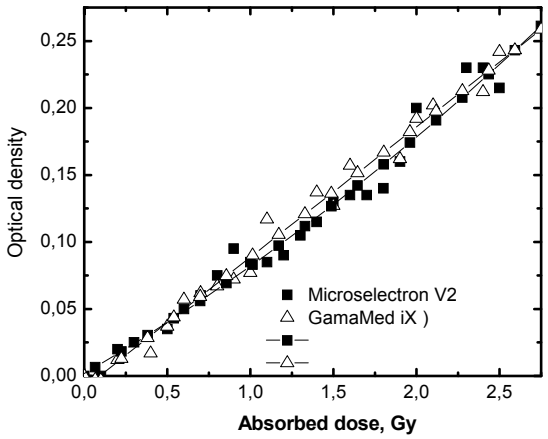

B

Fig. 5 Dose calibration curves for Gafchromic® EBT2 radiochromic films obtained in two different brachytherapy units: A – "Dose - pixel value" curve, B – "Dose net optical density" curve.

It was found that in the case of radiographic films calibration curves obtained in two HDR brachytherapy units differed significantly, especially in the higher dose range. In opposite, only small deviations in calibration curves were observed in the case of radiochromic films. Since the films for the irradiation in different HDR afterloader systems were taken from the same corresponding batch it was to assume that the source calibration accuracy was not the main reason for the observed discrepancies. More over, only small deviations observed in calibration curves of radiochromic films led to the suggestion about the influence of ADS parameters on the reliability of the radiographic film response to the irradiation. Due to this reason application of radiochromic films for 2D dosimetry purposes in HDR brachytherapy is more suitable, as compared to radiographic films and especially in the areas where the steep dose gradients are present.

Calibration curves were used for the evaluation of doses along the source transportation path which was clearly seen in each irradiated film. Since the doses along the track should be low as compared with the tumour treatment doses, track doses are usually neglected and "forgotten" in clinical daily routine. They are not usually calculated using 3D treatment planning systems and possible risk to the patients is not evaluated. Using calibrated 2D film dosimetry system it was found that the "track" doses varied from 0.09 Gy to 0.12 Gy per one single track during irradiation procedure. Despite the evaluated dose values were attributed to the low dose cathegory, these doses should be considered estimating doses to the surrounding tissues.

IV. Conclusions

Dose calibration of radiochromic films (Gafchromic® EBT2) and radiographic films (Kodak X-OmatV) irradiated in two different HDR brachytherapy afterloading systems: GamaMed iX (Varian) and Microselectron V2 (Nucletron) containing Ir-192 source has been performed with a purpose to uses these films for 2D dosimetry in the irradiation fields where steep dose gradients are present and ionization chambers do not work properly. Taking into account that the controlling of processing of the Kodak radiography films is more difficult, for non-experienced users we recommend the use of Gafchromic film for 2D dosimetry.

Performing this investigation dose values along Ir-192 source transportation path have been determined using the established dose calibration curves. It was found that the dose values along one single track varied within the range of 0.09 Gy - 0.12 Gy and were sufficient enough to be considered estimating doses to the surrounding tissues.

Acknowledgment

This work was partially funded by a grant No.MIP-082/2011 "Clinical and physical aspects in head and neck cancer brachytherapy" from the Research Council of Lithuania.

References

1. Jakstas K., Rudzianskas V., Adliene D., et al. Dosimetry methods in HDR brachytherapy. Conf. Proc. Medical Physics in the Baltic States 9, Kaunas, Lithuania, 2011, pp. 130-134
2. Lin M.-H., Huang T.-C., Kao M.-J. et al. (2009) Three dimensional dosimetry in brachytherapy: A MAGAT study. Appl Radiat Isot. 67: 1432-1437
3. Carrara M., Fallai C., Gambarini G., et al. (2010) Fricke gel-layer dosimetry in high dose-rate brachytherapy. Applied Radiation and Isotopes 68: 722–725
4. Laurikaitiene J., Adliene D., Jakstas K., et al. IMRT and brachytherapy for head and neck cancer patients. Conf. Proc. Medical Physics in the Baltic States 9, Kaunas, Lithuania, 2011, pp. 93-97
5. Toye W., Das R., Kron T., et al. (2009) An in vivo investigative protocol for HDR prostate brachytherapy using urethral and rectal thermoluminescence dosimetry. Radiotherapy and Oncology 91:243–248
6. El Barouky J., Fournier-Bidoz N., Mazal A, et al. (2011) Practical use of Gafchromic EBT films in electron beams for in-phantom dose distribution measurements and monitor units verification. Physica Medica 27: 81-88
7. Bazioglou M., Kalef-Ezra J. Dosimetry with radiochromic films:a document scanner technique, neutron response, applications (2001) Applied Radiation and Isotopes 55:339–345
8. Chang L, JyDing H., YowHo S. An innovativemethodfor 192Ir HDR calibration by farmerchamber, V-film, andsolidphantom (2011) Nucl. Instr. and Meth. in Phys. Res. A 646: 192–196
9. Cheunga T., Butsona M.J., Yu P.K.N. Independence of calibration curves for EBT Gafchromic films of the size of high-energy X-ray fields (2006) Applied Radiation and Isotopes 64:1027–1030
10. Medvedevas N., Rutkauskaite I., Adliene D., et al. Application of Gafchromic films for the evaluation of led eye shielding efficiency during superficial X-ray treatment. Conf. Proc. Medical Physics in the Baltic States 9, Kaunas, Lithuania, 2011, pp. 84-88
11. Huet C., Dagois S., Derreumaux S., et al. Characterization and optimization of EBT2 radiochromic films dosimetry system for precise measurements of output factors in small fields used in radiotherapy (2012) Radiation Measurements 47 (1):. 40-49
12. Butson M.J., Yu P.,Cheung T. et al.Radiochromic film for medical radiation dosimetry (2003) Materials Science and Engineering R 41: 61–120

Author: D.Adliene
Institute: Kaunas University of Technology
Street: Studentu g.50
City: Kaunas
Country: Lithuania
Email: Diana.adliene@ktu

Study of Combinations of TL/OSL Single Dosimeters for Mixed High/Low Ionization Density Radiation Fields

L. Oster[1], S. Druzhyna[1,2], I. Orion[2], and Y.S. Horowitz[3]

[1] Physics Unit, Sami Shamoon College of Engineering, Beer Sheva, Israel
[2] Department of Nuclear Engineering, Ben Gurion University of the Negev, Beer Sheva, Israel
[3] Physics Department, Ben Gurion University of the Negev, Beer Sheva, Israel

Abstract — **We have previously demonstrated that the increased response of optically stimulated luminescence (OSL) compared to thermoluminescence (TL) following high ionization density (HID) alpha irradiation is naturally explained via the identification of OSL with the "two-hit" F_2 or F_3^+ center, whereas the major component of composite TL glow peak 5 is believed to arise from a "one-hit" complex defect. This discovery suggested that near-total discrimination between HID radiation and low ionization density (LID) radiation using combined OSL and TL measurements may have significant potential in mixed-field radiation dosimetry In this paper we discuss and compare the potential application of combined OSL/TL measurements using ^{6}LiF:Mg,Ti (TLD-600) or ^{7}LiF:Mg,Ti (TLD-700) and TLD-100 natural isotopic composition) detectors.**

The signal from the dosimeter is given by

$$S_{TL} = a \cdot D_n + b \cdot D_\gamma$$
$$S_{OSL} = c \cdot D_n + d \cdot D_\gamma$$

where S_{TL} and S_{OSL} are the signal intensities for the TL/OSL and D_n and D_γ are the values of the dose deposited in the detector by the neutron (alpha particles) and gamma ray components of the radiation field respectively and a,b,c,d are appropriate calibration constants.

Because b/a is a measure of the accuracy of the measurement of γ dose via TL and c/d is a measure of the neutron dose via OSL we can establish the figure of merit (FOM) as:

$$FOM = \left(\frac{c}{d}\right) \times \left(\frac{b}{a}\right).$$

Beta and alpha particle irradiations were carried out with ^{90}Sr/^{90}Y (~500 keV average energy) and ^{241}Am sources (4.7 MeV) respectively and neutron irradiations were carried out at the PTB (Germany) (E_n = 5 MeV) and RARAF (Columbia University, USA) (E_n = 6 MeV) accelerator facilities. The highest values of the FOM obtained was ~30 for neutron/gamma discrimination and ~110 for alpha/gamma discrimination using OSL/TL - peak 5 measurements in TLD-700.

Keywords — **Thermoluminescence, optically stimulated luminescence, LiF:Mg,Ti, neutron and alpha irradiation, discrimination dosimetry.**

I. Introduction

Accurate/near-total discrimination between high ionization density (HID) radiation (neutrons and heavy charged particles) and low ionization density (LID) radiation (gamma rays and betas) remains a very crucial/important frontier of ionizing radiation dosimetry. This derives from the very high radiobiological effectiveness (RBE) of HID compared to LID radiation. Accurate/effective radiation risk assessment and radiation risk control therefore requires precise/separate determination of the HID and LID components of the radiation field. This requirement is therefore especially important in reactor generated radiation fields, space and air-craft radiation fields, many categories of oncological/clinical applications, accelerator applications and many others. It deserves emphasis that there are no existing practical/small-size/ passive or active dosemeters which have adequate discrimination capability.

The TLDs used in practical dosimetry have high sensitivity, reproducibility, environmental stability, low fading, etc. They are very convenient for measurement of dose, but the application of these dosimeters in real fields of non-monochromatic radiation is problematic. This arises because the response/efficiency of the TLDs depends significantly on the energy of the radiation, leading to possible errors of hundreds of per-cent in the determination of the dose components in the mixed radiation field.

The disadvantages and difficulties inherent to the various types of discrimination mixed-field passive and active dosimeters have been reviewed recently in [1-3].

We have previously demonstrated that the increased response of optically stimulated luminescence (OSL) compared to TL following HID alpha irradiation is naturally explained via the identification of OSL with the "two-hit" F_2 or F_3^+ center, whereas the major component of composite TL glow peak 5 is believed to arise from a "one-hit" complex defect. The preferential population of the F_2 centers (OSL emission band as a function of dose) at high dose by uniformly ionizing beta irradiation arises naturally from the cumulative probability of multiple ionization in a small volume related to the capture cross section of the multiple-hit F_2 trapping centers. This result is of fundamental interest since supralinear behaviour can be predicted for "2-hit" centers by kinetic/statistical models.The association of 2-hit centers with OSL suggests that near-total discrimination between HID radiation and LID radiation using combined OSL and TL measurements may have significant potential in mixed-field radiation dosimetry [4].

Y. Dekhtyar et al. (Eds.): *International Symposium on Biomedical Engineering and Medical Physics*, IFMBE Proceedings 38, pp. 135–138, 2013.
DOI: 10.1007/978-3-642-34197-7_35

In this paper we discuss and compare the potential application of combined OSL/TL, the use of TLD-600 and TLD-700, which can, in principle, serve as ionization density discriminators.

II. Experimental procedure

Samples of TLD-100, TLD-600 and TLD-700 (LiF:Mg,Ti) were used in this work. All the samples were of dimensions 3x3x0.9 mm^3, whitish in colour and fairly opaque. The chips were pre-irradiation annealed at 400 ^oC for one hour in air and then cooled at linear cooling rate of 100 $^oC\ h^{-1}$ to room temperature.

Beta irradiation was carried out with a $^{90}Sr/^{90}Y$ source at a dose rate of ~ 0.13 Gy min^{-1}. Alpha particle irradiations were carried out in air, in close proximity to an ^{241}Am source (4.7 MeV) at a fluence rate of $2.5x10^6$ cm^{-2} sec^{-1}. Neutron irradiations were carried out at the PTB (Germany) (E_n = 5 MeV, gamma dose component is 2.2% of the total dose) and RARAF (Columbia University, USA) (E_n = 6 MeV, gamma dose is ~12.5% of the total dose) accelerator facilities.

The OSL spectra were measured with both a commercial FP-6200 (Jasco) spectrofluorometer with a wavelength resolution of 5 nm, equipped with 150 W Xe-lamp, supported by a Pentium 4 computer and a laboratory set-up, where the luminescence has been excited by the 457 nm (second harmonic) of a Nb:YVO laser (SDL-457-800MFL), spectrally analysed by the monochromator and detecting system of the same spectrofluorometer. The laser beam was transmitted and focused at the crystal face using a fiber-optics system. Appropriate optical filters were applied in order to exclude stray light and second-order effects. The light power on the crystal was 70 μW with the Xe-lamp and up to 400 mW using the laser excitation system and neutral density filters. The incident photon power was measured with a Photodiode Sensor PD300-3W-V1 and an Ophir Nova II microprocessor-based power/energy meter. The OSL spectra were deconvoluted using a commercial "Peak-Fit" non-linear curve fitting program from AISN Software Inc. A Gaussian shape was used to describe the individual emission bands. The TL measurements were carried out using a Harshaw/Bicron Model 3500 TLD reader supported by a Pentium 4 computer. The TL glow curves were deconvoluted into component glow peaks using peak shapes based on first-order kinetics.

III. Results and discussion

Tipical deconvoluted TL glow curves and OSL emission spectra from LiF:Mg,Ti (TLD-600) following beta, alpha and neutron irradiations are shown in Figures 1 and 2. These results are very similar for TLD-100, TLD-600 and TLD-700. The signal from the dosimeter is given by

$$S_{TL} = a \cdot D_n + b \cdot D_\gamma = S_{nTL} + S_{\gamma TL} \quad (1)$$

$$S_{OSL} = c \cdot D_n + d \cdot D_\gamma = S_{nOSL} + S_{\gamma OSL} \quad (2)$$

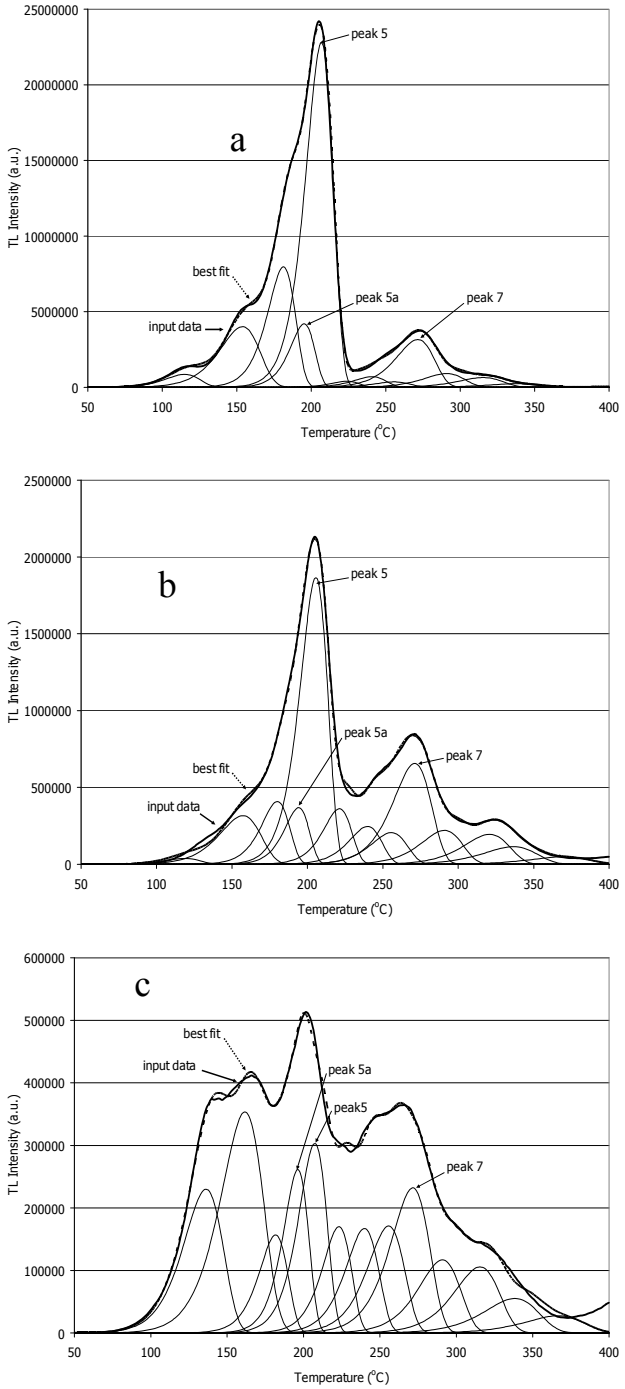

Fig. 1. Typical deconvoluted glow curves of slow cooled (100°C/h) LiF:Mg,Ti (TLD-600) following: a) beta irradiation (10 Gy); b) 5 MeV neutron irradiation (10 Gy); c) 4.7 MeV alpha particle irradiation ($3 \cdot 10^9 cm^{-2}$).

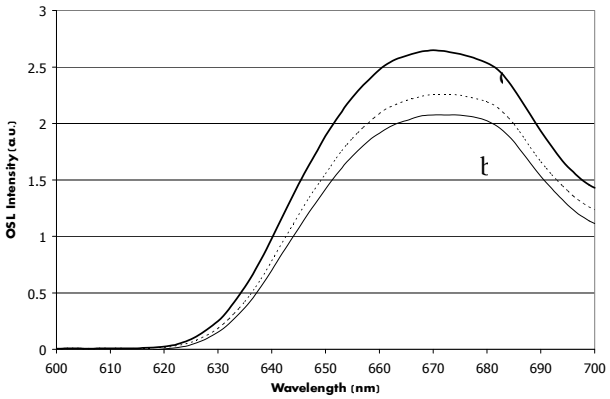

Fig. 2. Typical OSL emission spectra of slow cooled (100°C/h) LiF:Mg,Ti (TLD-600) stimulated by laser illumination (457 nm, 300 mW) following: a) beta irradiation (10 Gy); b) 5 MeV neutron irradiation (10 Gy); c) 4.7 MeV alpha particle irradiation ($3 \cdot 10^9 cm^{-2}$).

where S_{TL} and S_{OSL} are the signal intensities in appropriate units, and D_n and D_γ are the values of the dose deposited in the detector by the neutron (alpha) and gamma ray components of the radiation field respectively.

Because $\left(\frac{b}{a}\right)$ is a measure of the accuracy of the measurement of γ dose via TL and $\left(\frac{c}{d}\right)$ is a measure of the neutron dose via OSL we can establish the figure of merit (FOM) as:

$$FOM = \left(\frac{c}{d}\right) \times \left(\frac{b}{a}\right) \tag{3}$$

Table 1 shows the FOMs for alpha/beta discrimination using OSL/TL-peak 5 measurements (F_2 band at maximum stimulation intensity of 300mW, excitation at 457nm produces **a** broad emission band at ~640 nm) of TLD-100, TLD-600 and TLD-700, following beta (100 Gy) and alpha particle ($1 \cdot 10^9 cm^{-2}$) irradiation. These results demonstrate that an FOM in excess of 100 is achievable with the combined OSL/TL technique. The minimum measurable dose using F_2 OSL is ~1Gy.

Table 1 FOMs for alpha/beta discrimination.

Material	FOM/F 2 center$_2$
TLD-100	70 ± 6
TLD-600	117 ± 11
TLD-700	112 ± 17

The relative TL neutron to gamma efficiency η is given by

$$\eta_{n,\gamma}^{TL} = \frac{S_{nTL} / D_{nTL}}{S_{\gamma TL} / D_\gamma} = \frac{a}{b} \tag{4}$$

Where $S_{nTL} = a \cdot D_{nTL}$ and $S_{\gamma TL} = b \cdot D_\gamma$ are the luminescence signals per irradiated mass for neutrons and gammas (betas) irradiations at absorbed doses D_{nh} and D_γ respectively. S_{nTL} can be derived from the total dosimeter's signal following mixed-field irradiation (eq.1)

$$S_{nTL} = S_{TL} - S_{\gamma TL} \tag{5}$$

Introducing (1) and (5) into (4), we get:

$$\eta_{TL} = \frac{a}{b} = \frac{(S_{\gamma TL} - b \cdot D_\gamma) \cdot D_\gamma}{S_{\gamma TL} \cdot D_{nTL}} \tag{6}$$

And for the OSL

$$\eta_{OSL} = \frac{c}{d} = \frac{(S_{OSL} - d \cdot D_\gamma) \cdot D_\gamma}{S_{\gamma OSL} \cdot D_{nOSL}} \tag{7}$$

From (6) and (7) we derive:

$$FOM = \frac{\eta_{OSL}}{\eta_{TL}} = \left(\frac{c}{d}\right) \cdot \left(\frac{b}{a}\right) = \frac{\left(S_{OSL} - d \cdot D_\gamma\right) \cdot S_{\gamma TL} \cdot D_{nTL}}{\left(S_{TL} - b \cdot D_\gamma\right) \cdot S_{\gamma OSL} \cdot D_{nOSL}} \tag{8}$$

Neutron doses D_{nh} and D_{ni} are different for different detectors/materials (TLD-600 or TLD-700) and equally for the different components (TL peaks 5,7 and OSL) of the same detector. The neutron dose in the detector (for example, TLD-600) was obtained as follows:

$$D_{nTLD-600} = D_n \cdot \frac{K_{TLD600}}{K_{water}} \tag{9}$$

where D_n is the neutron dose component in water (tissue) which, as well as the gamma dose component D_γ, were measured at PTB/RARAF, K_{TLD600} and $K_{water/tissue}$ (PTB/RARAF irradiations) are Kerma Factors of TLD-600 and water/tissue for neutron energies 5 MeV/6MeV [6-8]. Table 2 shows good agreement between our measurements/ calculations of relative neutron/gamma efficiency η and the literature

Table 3 shows the values of the FOMs for TLD-600 and TLD-700. The highest FOM of 30 was achieved using TLD-700. From Tables 1 and 2 one can see that the FOM (obtained in combined OSL/TL measurements) for neutrons is lower than for alpha particles. This lower value may arise from the fact that neutron interactions create recoiling atoms of higher LET and ionisation density due to their lower average energy and higher mass, thereby leading to enhanced saturation effects in the track cores [5].

Table 2 Relative TL neutron/gamma efficiency η.

Detector	Neutron Energy MeV	η	Ref.
TLD-700	5.25	0.094	[9]
	5.3	0.16	[10]
	5.3	0.117	[11]
	4.8	0.132	[12]
	5-6	0.1	[5]
	5	0.12 ± 0.02	This measurement
	6	0.15 ± 0.04	This measurement
	5.98	0.145	[13]
TLD-600	5.3	0.35	[10]
	5	0.25 ± 0.02	This measurement
	6	0.3 ± 0.03	This measurement

Table 3 FOMs for neutron/beta discrimination.

Material	Germany 5MeV 1Gy	Germany 5MeV 10Gy	USA 6MeV 1Gy	USA 6MeV 100Gy
TLD-600		13.6 ±1.7	9.5 ±3.5	9.7 ±1.9
TLD-700	45.8	30 ±5.4	24 ±28	21.5 ±7

IV. Conclusions

The results reported herein demonstrate the potential application of combined OSL/TL measurements in neutron (alpha)-gamma discrimination dosimetry. The OSL/TL dual readout of LiF:Mg,Ti as an ionization density discriminator avoids some of the difficulties [1-3] inherent to the various types of discrimination mixed-field passive dosimeters, and in addition has several advantages:

1. Closeness to tissue equivalence unlike Si based devices.
2. May closely simulate the ionization density dependence of radiation induced DNA radiation damage, eg., ratio of DSBs to SSBs, at the nanometer level in some biological systems
3. Other radiation dosimetry aspects typical to LiF-TLD, eg., low-cost, tiny size, largely immune to radiation damage, insensitivity to dose rate, etc...
4. The preferential excitation of OSL compared to TL following high ionisation density (HID) alpha irradiation, naturally explained via the identification of OSL with the "two-hit" F_2 or F_3^+ center, allows near-total discrimination between HID radiation and low-ionisation density (LID) radiation.
5. This method of discrimination is even more effective than the use of LiF:Mg,Cu,P, which has been proposed as an effective discriminator versus HID radiation in mixed-field dosimetry because of its reduced relative TL response to HID radiation ($\eta_{\alpha\gamma} \sim 0.04$).
6. At lower neutron energies one can expect enhanced the OSL/TL ratio due to the increased ionization density and the same holds for irradiation in water due to the moderating effects on the neutron spectrum. The dependence on neutron energy and irradiation medium are intended for future study.

Acknowledgements

This research was supported by THE ISRAEL SCIENCE FOUNDATION (grant No. 8/09) and INTERNAL FUNDING PROGRAM OF THE SAMI SHAMOON COLLEGE OF ENGINEERING (SCE).

References

1. d'Errico F, Bos A J (2004) Passive detectors for neutron personal dosimetry: state of the art. Radiat Prot Dosim 110: 195-200
2. Nakamura T, Nunimiya T, Sasaki M (2004) Development of active environmental and personal neutron dosemeters. Radiat Prot Dosim 110: 169-181
3. Bos A J, d'Errico F (2006) Some developments in neutron and charged Particle dosimetry. Radiat Prot Dosim 120: 331-336
4. Oster L, Horowitz Y S, Podpalov L (2010) OSL and TL in TLD-100 following alpha and beta irradiation: Application to mixed-field radiation dosimetry Radiat Meas 45: 1130-1133
5. Spurny F (2004) Response of thermoluminescent detectors to charged particles and to neutrons. Radiat Meas 38: 407-412
6. Caswell R S, Coyne J J, Randolph M L (1982) Kerma factors of elements and compounds for neutron energies below 30 MeV. Int J Appl Radiat Isot 33: 1227-1262
7. Singh M S (1979) Kerma factors for neutrons and photons with energies below 20 MeV. Lawrence Livermore Laboratory UCRL-52850: 1-21
8. Alekseev A G, Golovachik V T, Savinsky A K (1986) Kerma equivalent factor for photons and neutrons up to 20 MeV. Radiat Prot Dosim 14: -298
9. Portal G (1978) Etude et Developpement de la dosimetrie par Radiothermoluminescence. CEA Report R4943
10. Scarpa G (1984) New experimental data on the sensitivity to fast neutrons of a number of sintered commercial TL phosphors. Radiat Prot Dosim 6 313-316
11. Wingate C L, Tochilin E, Goldstein N (1967) Response of Lithium Fluoride to neutrons and charged particles. Proc. Int Conf on Luminescence Dosimetry 421-434
12. Furuta Y, Tanaka S (1972) Response of ^{6}LiF and ^{7}LiF thermoluminescence dosimeters to fast neutrons. Nuclear Instruments and Methods 104: 365-374
13. Knipe A D (1984) The photon and neutron calibration of thermoluminescent dosemeters for reactor measurements. AEEW-R 1748

Author: Prof. Leonid Oster
Institute: Sami Shamoon College of Engineering
Street: Bialik/Basel
City: Beer Sheva
Country: Israel
Email: leonido@sce.ac.il

Neutron Field Outside the Room of Linear Medical Accelerator

K. Polaczek-Grelik[1], P. Gandor[1] and A. Orlef[2]

[1] University of Silesia/Medical Physics Department, Katowice, Poland
[2] Center of Oncology – Institute of M. Skłodowska-Curie Memorial/Medical Physics Department, Gliwice, Poland

Abstract— **Neutron radiation field in radiotherapeutic facility is mainly generated as a result of photonuclear reactions (γ,n), occurring when high-energy beam from linear medical accelerators is emitted. The intensity of undesired neutron production is strongly dependent on an accelerator model, i.e. beam type, end-point energy and head materials. Outside the treatment room neutron field is also dependent on the topology of the facility (room surface area, wall composition, maze shape and length, position of the control panel).**

Four linacs working in 20 MV photon mode (600 MU/min), installed in rooms of different size were considered in terms of the occupational neutron dose. The influence of the direction of X-ray beam emission as well as the size of irradiation field and wedge usage on the neutron field behind the treatment room door were investigated.

Prompt gamma neutron activation analysis (PGNAA) has been used for determination of photoneutron fluence outside the treatment room. In situ portable spectrometry system based on semiconductor high purity germanium (HPGe) detector was used. Neutron capture reactions as well as inelastic scattering processes on germanium crystal were observed. The analysis was based on photopeaks count rates selected from registered spectra. Application of neutron energy moderators made of paraffin, allowed for roughly estimation of photoneutron spectra, distinguishing the slow, intermediate and fast components of neutron flux. Ambient dose equivalent H*(10) was estimated with the use of fluence-to-dose conversion coefficients. Additionally neutron dose rate meter LB123 was used. Dose rates 50 cm away from the bunker door were found to be within the range 0.531 – 2.500 μSv/h depending on the linac and direction of 20 MV beam emission. At the operator's console H*(10) was of the order of 0.027 μSv/h.

Obtained results and their agreement with dosimeter indication have shown that PGNAA of HPGe spectrometer could be used in characterization of low rate neutron radiation field.

Keywords— **medical linear accelerator, neutron fluence, neutron ambient dose equivalent, semiconductor spectrometry, occupational dosimetry.**

I. INTRODUCTION

Neutron radiation field around radiotherapeutic high-energy linear accelerator (linac) is strongly dependent on a construction materials chosen by manufacturer and an operating energy. The cross section of nuclear photo effect (γ,n), in which neutrons are mostly produced, has a threshold character and resonance structure characteristic for each isotope. Neutron dose outside the radiotherapeutic room depends not only on the strength of neutron production by a particular linac, but also on the topology of the facility, i.e. wall surface area *S*, wall composition, maze length *L* and shape, bunker door construction, which contribution is often difficult to estimate. Therefore the data found in literature cannot directly serve in occupational neutron dose assessment in a particular case.

The major source of the uncertainty of neutron field investigation is associated with the sensitivity of a method of detecting the low-rate neutron flux in the presence of other radiation types (especially photons) and the poor knowledge of neutron flux energy outside the therapeutic room. Often the lack of the information about neutron spectrum is felt by medical physicists when routine occupational radiation dosimetry is performed. Moreover, standard readout of personal TL dosimeters does not give an accurate information about the neutron component of the dose.

II. EXPERIMENTAL

The aim of this work is to assessed the occupational neutron dose outside the therapeutic room during emission of 20 MV X-ray beam by the Clinac 2300 medical accelerator. The 20 MV nominal potential is one of the highest used nowadays to generate therapeutic X-ray beam. Moreover, the neutron production is higher in this mode than for any other clinically used linac beams (including 23 MeV electrons), as our previous investigations have shown [1].

A. Material

To determine the factors, which influence on neutron field in the pilothouse, four linacs were involved in the study. The geometry of therapeutic rooms and different gantry positions were considered. All studied linacs are installed in rooms with one-band maze of about 8 m long, ended with heavy doors containing paraffin layer surrounded by lead coating. The main information connected

Y. Dekhtyar et al. (Eds.): *International Symposium on Biomedical Engineering and Medical Physics*, IFMBE Proceedings 38, pp. 139–141, 2013.
DOI: 10.1007/978-3-642-34197-7_36

with geometry of accelerator rooms are presented in Table 1. Accelerators in Table 1 are numbered according to the seniority.

All measurements were performed during 20 MV X-ray beam emission with the rate of 600 monitor units per minute (600 MU/min), for the source-surface distance (SSD) equal 100 cm. The three parts of the experiment were the following:

- Investigations of neutron fluence and ambient dose equivalent H*(10) 50 cm from the outer side of the therapeutic room door, performed for the gantry positions of 0° and 90° and the irradiation field size of 10×10 cm^2.
- Measurements of H*(10) at the linac's operational console for the X-ray beam direction of 270° and the irradiation field size of 10×10 cm^2.
- Identification of the factors affecting the neutron dose rate at the outer side of the treatment room door. Hence, the measurements were additionally performed for large 40×40 cm^2, small 0.3×0.3 cm^2 and wedged fields and for 0°, 90° and 270° near the door to the room of linac no 1.

Measurement arrangements are presented in Figure 1. Notation of a gantry movement is described clockwise.

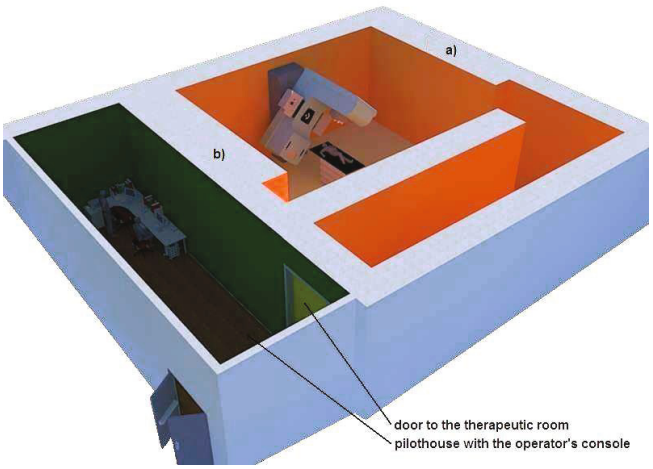

Fig. 1 The visualization of the radiotherapeutic facility with the accelerator room and the pilothouse. The X-ray beam emitted in the direction of wall "a)" means the gantry positioned at 90°, and on the wall "b)" – at 270°.

B. Method

Two methods of neutron ambient dose equivalent determination were used. LB123 monitor gives the information about H*(10) rate of neutrons from thermal up to 20 MeV energy range. High-purity germanium (HPGe) semiconductor spectrometry system, dedicated for *in situ* measurements provided the information about neutron fluence on the base of prompt gamma neutron activation analysis (PGNAA). Registered activation spectrum in the energy range 60 – 2800 keV is presented and described in Figure 2.

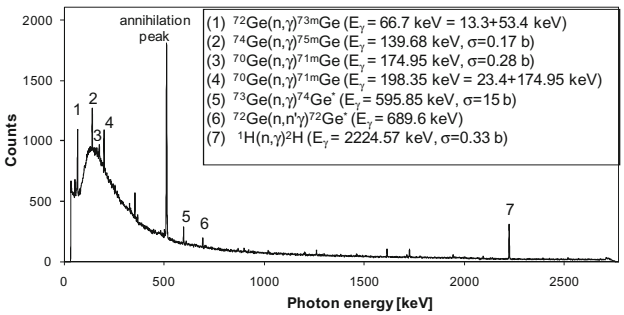

Fig. 2 Spectrum of gamma rays accompanying nuclear reactions of neutrons on germanium crystal and paraffin overlay.

The quantitative analysis of 595.85keV peak (marked as (5) in Figure 2), accompanying the nuclear reaction $^{73}Ge(n,\gamma)^{74}Ge^{*}$, was performed. This reaction involves slow neutrons (E_{mean}=0.21eV). Subsequently, using paraffin moderators with the thickness of 6 cm and 8 cm, fractions of intermediate and fast neutrons (E_{mean}=0.05MeV and E_{mean}=0.55MeV) were estimated. The shape and thickness of neutron energy moderators were adopted from [2].

The response of HPGe spectrometer was calibrated on the Pu-Be source with a known neutron fluence.

On the base of neutron fluence results, ambient dose equivalent H*(10) was estimated with the use of fluence-to-dose equivalent conversion coefficients $C_{F\text{-}D}$, calculated using the equation (1) given by AAPM Report 19 [3] and recalculated to SI units.

$$C_{F-D} = \frac{4.4\times10^{9}}{E_{mean}^{0.735}}\left[\frac{n/cm^2}{Sv}\right] \quad (1)$$

III. RESULTS

The results of ambient dose equivalent measurements are presented in Table 1 for the location of 50 cm from the accelerator room door and at the operator console panel. Data marked as HPGe were obtained from the analysis of prompt gamma neutron activation spectrum (Fig.2) with the use of equation (1). Data for LB123 are the direct indications of dosimeter. The uncertainty of the results for both methods used is comparable and is increasing for smaller H*(10) values.

Table 1 Neutron ambient dose equivalent rate as seen by two methods (LB123 and PGNAA) for four studied linacs working in 20 MV mode. The uncertainties are included in parenthesis.

Linac no.		**1**	**2**	**3**	**4**
S [m^2]		155	137	138	127
L [m]		8.17	8.05	7.98	7.98
H*(10) at 50 cm from the treatment room door [μSv/h]					
0°	**HPGe**	1.541(9%)	1.615(6%)	1.825(5%)	1.512(7%)
	LB123	0.833(2%)	1.020(4%)	2.500(6%)	1.940(2%)
90°	**HPGe**	0.531(14%)	1.499(8%)	0.827(6%)	1.576(7%)
	LB123	0.642(3%)	0.960(4%)	1.880(2%)	1.580(4%)
Φ at 50 cm from the treatment room door [cm^{-2}s^{-1}]					
0°	**HPGe**	47.3(9%)	66.2(6%)	83.1(5%)	62.6(7%)
90°	**HPGe**	28.8(14%)	50.9(8%)	72.2(6%)	57.8(7%)
H*(10) at the operator console [μSv/h]					
270°	**HPGe**	0.027(18%)	-	-	-
	LB123	0.029(20%)	0.056(4%)	0.017(15%)	0.016(19%)

Contribution of slow component in total neutron flux was from 64% to 87%, and the fast component was not registered at all, what is in agreement with the neutron spectrum presented in [4], as the fast component of neutron flux outside the door is inconsiderable and thus, could not be measured in our method.

Neutron fluence estimated in the last part of experiment shows the increase by 39% when the smallest (0.3×0.3 cm^2) and the decrease by 18% when the largest (40×40 cm^2) fields were set, in comparison with 10×10 cm^2 field size. The increase of the neutron dose outside the door by 21% and 35% was also observed when a wedge was used and the gantry was set at 270°, respectively.

IV. DISCUSSION

Neutron ambient dose equivalent 50 cm in front of the door increases as the dimensions of the linac room decrease. It is probably associated with slightly higher energy of neutrons leaving the treatment room, since the neutrons slowing down is directly connected with the scattering process realized on the wall surface. In more recent projects of the bunkers the care about lowering the dose at the operational console is noticeable, while the increase of H*(10) in the vicinity of the door is observed in comparison with older bunker projects. In the case of linac no 1 the neutron field is shaped differently because that room was adopted for 20 MV linac after the 23 MeV accelerator withdrawal.

The fluence of neutrons passing through the treatment room door and the ambient dose equivalent connected with it is decreasing when the therapeutic beam is directed at the wall opposite to the door (90°). Moreover, performed measurements suggest that a small or wedged therapeutic field and gantry position of 270° (beam directed on the pilot-house wall) increase the neutron dose outside the door. This confirms the results reporting the increase of neutron production with the complexity of shaping the irradiation field, e.g. [5]. Performed investigations have shown quantitatively this increase in terms of occupational neutron exposure.

V. CONCLUSIONS

In any of studied cases the annual dose limit for occupational exposure (6 mSv/y = 3 μSv/h) was not exceeded. Furthermore, at the operator's console the dose is 1-2 orders of magnitude lower than in front of the accelerator room door. This could be used as a clue, which positions should be avoided be the staff during operation of linac in high-energy mode.

Obtained results have shown that PGNAA of HPGe spectrometer could be used in characterization of low rate neutron radiation field in therapeutic facility in terms of occupational neutron exposure. This is confirmed either by the consistency with LB123 indications or by a good agreement with the results obtained by others with the use of different methods, found e.g. in [6]. For the comparison purposes, it should be noted that in the dose rate notation used in presented study period of 1 hour is equivalent to the emission of 36 000 monitor units (600 MU/min), since neutrons are present only during linac operation. PGNAA method based on neutron interactions with germanium crystal and moderation in paraffin overlay is able to roughly estimate the neutrons' energy. Since the activity induced in germanium crystal is short-lived (mostly excited states of stable nuclides are populated), there is no influence of such measurements on further operation of this spectrometer.

REFERENCES

1. Konefal A, Orlef A, Zipper W et al. (2001) Undesired neutron radiation generated by biomedical accelerators during high-energy X-ray and electron beam emission. Polish J Med Phys & Eng 7(4): 291-304.
2. Chao J H, Niu H (1997) Measurements of neutron dose by a moderating germanium detector. Nucl. Instrum. Meth. A 385: 161-165.
3. AAPM Report No.19 (1986). American Institute of Physics, New York.
4. Vega-Carrillo H R, Ortiz-Hernandez A, Hernandez-Davila V M et al. (2010) H*(10) and neutron spectra around linacs. J Radioanal Nucl Chem 283: 537-540.
5. Mesbahi A, Keshtkar A, Mohammadi E et al. (2010) Effect of wedge filter and field size on photoneutron dose equivalent for an 18 MV photon beam of a medical linear accelerator. Appl Radiat Isot 68(1): 84-89.
6. Donadille L, Trompier F, Robbes I et al. (2008) Radiation protection of workers associated with secondary neutrons produced by medical linear accelerators. Radiat Meas 43:939-943.

Author: Kinga Polaczek-Grelik
Institute: University of Silesia, Medical Physics Department
Street: Uniwersytecka 4
City: 40-007 Katowice
Country: Poland
Email: kinga.polaczek-grelik@us.edu.pl

CT Dose Index Test with Standard Phantoms

Nelda Kreislere and Aldis Balodis

Riga Technical University, Institute of Biomedical Engineering and Nanotehnology, Latvia

Abstract — **The aim of the study was to find out how the measured absorbed dose by using standard dose test method (with CT dose head and body phantoms) depends on the different axial scanning technologies and how they affect the measured value.**

The results show that using pencil type ionization chamber the measured absorbed dose distribution which determines value of CT dose index ($CTDI_{100}$) is not equable across the ionization chambers.

Uncertainty can reach 30 - 35% of the value during dose measurements of 100 mm long part of the head phantom and up to 50% of the value during measurements of the same length body phantom. It is considered that 5% uncertainty is acceptable during dose measurements in the 40 mm middle range of head phantom and 45 mm in the middle of the range in body phantom.

Keywords— **CT dose index (CTDI), head and body phantom, dose distribution, uncertainty.**

I. Introduction

Patient dose reduction in computed tomography is one of the key goals. [1] However, achievement of this objective requires more and more new approaches to determine the dose rate CT received by patients, and assessing the information provided by different manufacturers- the CT dose index (CTDI), which can be compared using standard methods. [2]

The base CT Dose Index (CTDI) values provided by Computed tomography manufacturers are highly dependent on scanning parameters and characteristics of the scanner. The scanner parameters which influence received radiation dose and depend on the hardware are: slice thickness, the distance between slices, interlayer, examination region, exposure factor and gantry tilt. In addition the beam collimation effects are important for multislice computed tomography.[5]

Image quality and scanning parameters affect absorbed dose by the patient and this is why it is not always possible to use CT dose test phantoms to quantitatively assess the absorbed dose precisely. Information regarding the CT dose that is delivered by a particular scanner is generally provided by the equipment manufacturers. It is calculated taking into account average image quality parameters and an average exposure time of patient examination. Manufacturers provide these values expressed as the weighted CT dose index ($CTDI_w$) and link those with the examination, using other dose descriptor - dose- length product (DLP). [3]

To compare scanners from different vendors one can use absorbed dose index $CTDI_{100}$ values provided in standard IEC 60601-2-44 [4]. For the measurements polymethylmetacrylate (PMMA) head and body phantoms of 16 and 32 cm in diameter and pencil ionization chamber or other measurement transformer are used. The measurements are made in the middle of the phantom or 1cm from the edge.

The absorbed dose index is calculated from the results of the measurements using the following formula:

$$CTDI_{100} = \frac{1}{N \cdot T} \int_{-50mm}^{+50mm} D(z)dz \qquad (1)$$

where T is the nominal beam collimation width at the isocenter, N is number of slices and D(z) is the dose profile perpendicular to the scan. The standard and the methodology defines that the length of the phantom is 14 cm and ionization chamber is at least 10cm long, but it does not say anything about the bounds in which value can change near the edges of the phantom which can be attributed to the scattering of the radiation near the edges. This gets important when selecting measurement type for calculation of $CTDI_{100}$ which can be acquired during consecutive rotations of the scanner or by using spiral scanning with wide slice (e.g. 10cm) or by using wide collimation with 20 cm at MDCT.

However, the literature data [6] inform that dose has "U"-type dependence on the coordinate. The attention is not typically paid to scattering process.

The aim of the study was to find out how during measurements the absorbed dose in phantoms depends on the different axial scanning parameters and how it changes across all phantom length and to examine differences between measured weighted CT dose index and the dose values provided by manufacturers.

II. Materials and Methods

The measurements were made in Riga Technical University, laboratory of Institute of Biomedical Engineering and Nanotehnology using single slice CT scanner Siemens

Y. Dekhtyar et al. (Eds.): *International Symposium on Biomedical Engineering and Medical Physics*, IFMBE Proceedings 38, pp. 142–144, 2013.
DOI: 10.1007/978-3-642-34197-7_37

Somatom AR.SP, by changing scanning parameters, pencil type ionization chamber Fluke Biomedical 6000-100, test device Victoreen 4000+, the CT Dose Phantom, which consists of 15 cm thick solid PMMA disks in 16 cm (head) and 32 cm (body) diameter.

It was identified how different scanning techniques based on various scanning parameters affect the measured absorbed dose over the phantom length, as well as the current test method was studied in more detail. .

All measurements were made according to IEC 60601-2-44 [4], by measuring the absorbed dose, and then calculating the CT dose index, according to equation (2),

$$CTDI_{100} = D \cdot K_1 \cdot \frac{L}{slice} \qquad (2),$$

where D- measured dose (mGy), K_1-calibration factor, L-ionization chamber - 100 mm active length (mm), slice (mm).

Ionization chamber during measurements was installed in the air and in the CT dose phantoms.

Measurements were made with a variety of slice thicknesses 2, 3, 5, 10 mm over the entire length of the ionization chamber, with the same table feed. As the reference point the table positions which are shown on scanner console panel weretaken.

Measurements were made of the CT head and body phantoms with the same scanning parameters, slice 5 mm, feed 5 mm, 130 kVp, 315 mAs to determine absorbed dose distribution over all phantom length.

III. Results and Discussion

Equable absorbed dose distribution over all phantom length was obtained during measurements when ionization chamber was positioned in the air without other absorbent (Fig.1). It was found that the measurements can be made anywhere in the ionization chamber and whether the scan plane passes through the ionization chamber middle or one of the ends does not change the final result. This also applies to any slice thickness. And difference between the results with each other at any slice thickness of slice does not exceed 1%.

Figure 1 also shows that $CTDI_{100}$ free in the air values at the slice thickness of 2, 3, 5 and 10 mm are close to each other, but scanning a 1 mm thick slice, gives almost double the value.

Unequal dose distribution over all phantom length was observed during absorbed dose measurements of the CT head and body phantoms. The obtained results show that the measured dose index $CTDI_{100}$ which was obtained by measuring a 100 mm long section of the phantom at the end of it gives 30 - 35% uncertainty in the head phantom (see Fig.2) and up to 50% uncertainty in the body phantom, when compared with the same measurement in the middle section of the phantom (see Fig.3).

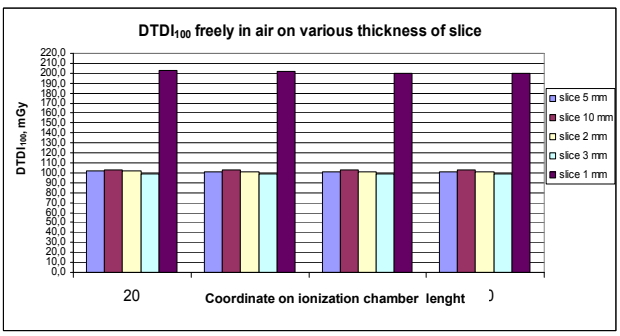

Fig. 1 $CTDI_{100}$ free in the air depending on thickness of slice over all ionization chamber length.

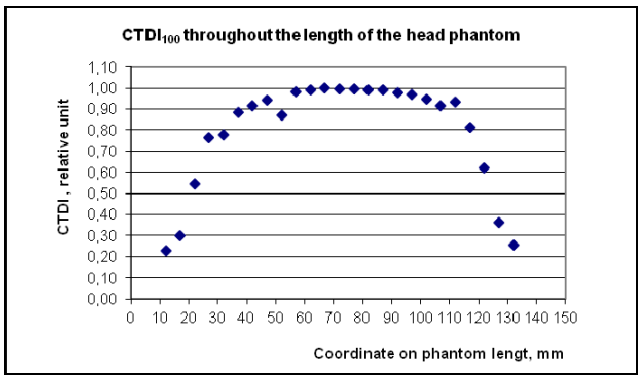

Fig. 2 Absorbed dose distribution of the head phantom with the slice thickness and table feed 5 mm; measured max value of $CTDI_{100}$ = 82,50 mGy.

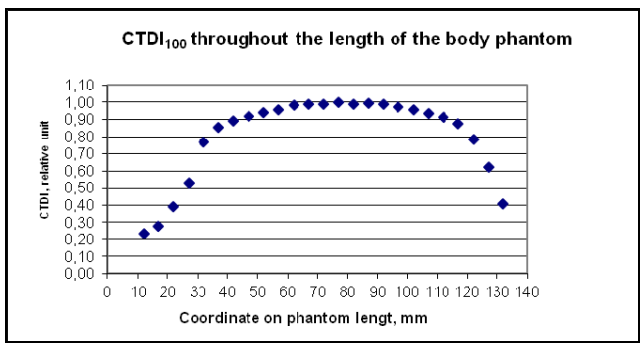

Fig. 3 Absorbed dose distribution of the body phantom with slice thickness and table feed 5 mm; measured max value of $CTDI_{100}$ = 39,77 mGy.

Analysis of the results (see Fig.2 and Fig.3) show that the 5% uncertainty in measurements is achievable in the 40 mm section in the middle of the head phantom (Fig.2) and 45 mm section in the middle of the body phantom. (Fig.3).

IV. Conclusions

The measurements of CT dose index $CTDI_{100}$ of 100 mm long section of the phantom as specified by the standard IEC 60601-2-44 can produce 30% - 35% uncertainty in the in the head phantom and up to 50% uncertainty in the body phantom when testing with ionization chambers over all active length. The study has shown that to not exceed 5% uncertainty of the absorbed dose, the measurements must be made along the 40mm section in the middle of the head phantom and along the 45 mm middle section in the body phantom.

References

1. Siemens launches dose reduction initiative at http://medicalphysicsweb.org/cws/article/research/43089
2. Xinhua Li, Da Zhang and Bob Liu (2011) A practical approach to estimate the weighted CT dose index over an infinite integration length. Physics in Medicine and Biology 56 2011 pp. Volume 56, Issue 18: 5789-5803
3. Bauhs J A, Vrieze T J, Primak A N et al. CT Dosimetry: Comparison of Measurement Techniques and Devices at http://radiographics.rsna.com/content/28/1/245.full
4. IEC 60601-2-44 Medical electrical equipment - Part 2-44: Particular requirements for the basic safety and essential performance of X-ray equipment for computed tomography (2009)
5. Prokop Mathias. Spiral and multislice computed tomography of the body.- Stuttgart; New York, Thieme, 2003.- 1090 lpp. (ISBN 3131164816 0865778701)
6. Jacius R A, Kambic G X. Measurement of Computed Tomography X-Ray Fields Utilizing the Partial Volume Effect. Medical Physics Jul/Aug 1980, Volume 7, No 4. 35-39.

Author: Balodis Aldis
Institute: Riga Technical University, Institute of Biomedical Engineering and Nanotehnology
Street: Ezermalas 6k
City: Riga
Country: Latvia
Email: balodisa@latnet.lv

X-Ray Radiation Statistics towards Quality Assurance in Digital Radiography

L.Bumbure[1], Y. Dekhtyar[1], A. Katashev[1], T. Kirsanova[1] and V. Zemite[1]

[1] Riga Technical University/TMF, BINI, Riga, Latvia

Abstract— **Most of diagnostic radiography today is digital. Therefore there is a great possibility to make an express check of an x-ray beam quality using digital approach. The flux of the x-ray photons detected is governed by the Poisson statistics. The deviation of the radiating technique modes leads from the Poisson statistics. Because the single element of a digital detector matrix produces the signal that is directly proportional to the number of the absorbed photons, the brightness distribution is in use to estimate the statistics of the photons. This is demonstrated to evaluate quality of x-ray beam of the digital x-ray diagnostic equipment.**

Keywords— **digital radiography QA, x-ray beam statistics.**

I. Introduction

Quality assurance (QA) of x-ray equipment is extremely important part of extensive quality control system in hospitals. Since most of diagnostic radiography is digital today, there is a great possibility to make an express quality check of x-ray equipment using fast digital approach.

When the point-like x-ray monochromatic source produces photons their statistical distribution in time obeys Poisson law [1] in any direction of radiation detection. Therefore, when a set of the equal detectors is located on the spherical surface surrounding the source symmetrically, all detectors are equivalent to record Poisson statistics of the photons, and each detector can be replaced logically with anyone. When the signal of the detector is directly proportional to the number of the detected photons, the distribution of the signals among the detectors of the entire set after its exposure obeys Poisson statistics too. If the distance from the detector set to the source is long, the spherical surface can be represented by its small sector approximated to the flat surface.

Digital detecting technologies are subdivided into two groups. The major difference between them is how the x-ray detection and readout are performed. There are systems that use storage-phosphor image plates with a separate image readout process which means an indirect conversion process [2]. In this case the image reproduces total number of the photons absorbed by each sensitive centre of detector.

The other technology converts absorbed x-rays photon energy into electrical charge by means of a direct readout process using TFT (Thin-film transistor) arrays [2].

The total charge collected is proportional to the X-ray photons received by the detector [3].

Because of the considered above detecting conditions and detectors' technique the brightness of the digital image obeys the Poisson statistics.

Any deviation from the above circumstances (x-ray tube focus, instability of voltage, quality of the detectors, etc.) leads to a shift from the Poisson statistics of the brightness. Generally, the statistics shifts to Gauss distribution

The present article is directed to explore a possibility to exploit this for quality assessment in x-ray digital radiography.

II. Matherials and methods

A. The acquisition of x-ray images

The x-ray device: digital x-ray machine "Digital Diagnost" was in use.

The digital detector: The digital flat-panel x-ray detector "Pixium 4600" detector was employed [4].

The exposure parameters: The x-ray images were acquired using a manual operation mode. The x-ray tube was provided with the high voltages equal to 66kV, 81kV and 96kV. The x-ray tube current was 80 mA and the exposure time was 10 ms. Both large and small focal spots (0.6 and 1.2 mm respectively) of the x-ray tube were employed.

The Source Detector Distance was 1m and the irradiated field was collimated to 7x7 cm for each exposure.

B. Acquisition and processing of the acquired data

A detected x-ray image was collected in the DICOM format and transferred further to TIFF format to analyze brightness distribution. The DICOM-TIFF transferring did not provide any observable changes in the images.

To process the images the specific software that digitalized brightness was developed. The brightness of each image pixel and the distribution over the brightness were used as the input and output, correspondingly.

Differently sized areas of the image were extracted for processing (Fig.1).

Y. Dekhtyar et al. (Eds.): *International Symposium on Biomedical Engineering and Medical Physics*, IFMBE Proceedings 38, pp. 145–148, 2013.
DOI: 10.1007/978-3-642-34197-7_38

The acquired statistic was verified to be the subject of the Poisson or Gauss distributions [5]. The Kolmogorov-Smirnov criterion was employed [6].

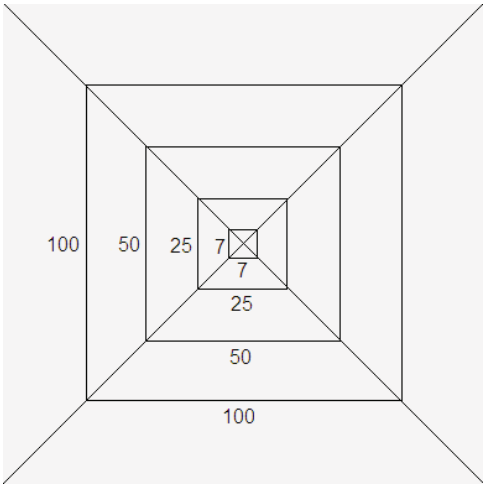

Fig. 1 The analyzed areas (sizes in pixels) of an image

For this the parameter lamda (λ), was calculated using formulae [7]:

$$\lambda = D_{max}\sqrt{N}, \text{ where} \quad (1)$$

$$D_{max} = x/N, \text{ where} \quad (2)$$

x – the maximal absolute difference between theoretical cumulative frequencies and experimental cumulative frequencies for the statistics, N – the number of pixels in the area.

The criterion λ was compared with the tabulated value λ_t at the significance level 0.05. If $\lambda < \lambda_t$ the hypotheses on the trusting statistics was accepted.

Thus the criterion λ was the index that statistics corresponds to the Poisson law (higher value of λ means that statistics less match the Poisson law).

The theoretical Poisson and Gauss distributions were derived employing the parameters calculated from the experiment (average, standard deviation).

III. Results

The cumulative distribution functions (CDF) brightness was found for different size areas for different kilovolts and focuses (Fig 2 – 6) on the brightness analyses base.

The results show that CDF conform Poisson distribution best when the x-ray image is acquired at 81kV, small focus and the 100x100 pixels large.

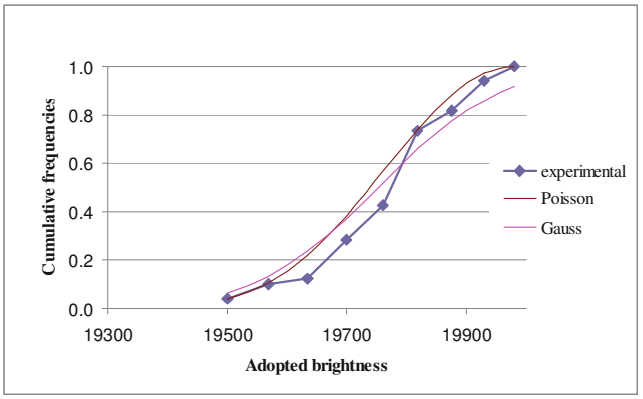

Fig. 2 The CDF for small focus, 81kV, 7x7 pixels area

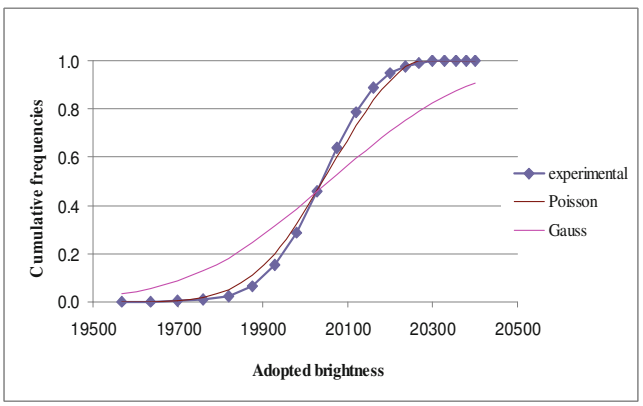

Fig. 3 The CDF for small focus, 81kV, 100x100 pixels area

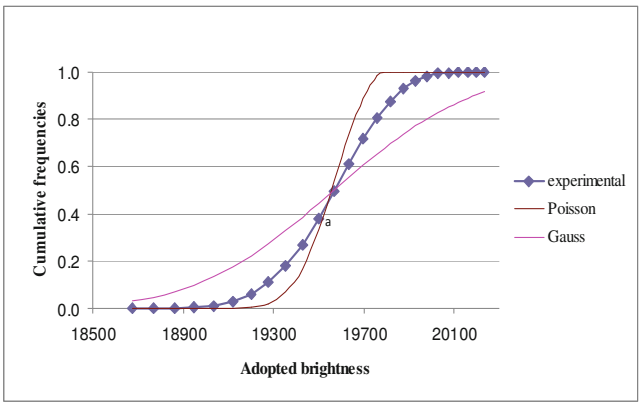

Fig. 4 The CDF for small focus, 61kV, 100x100 pixels area

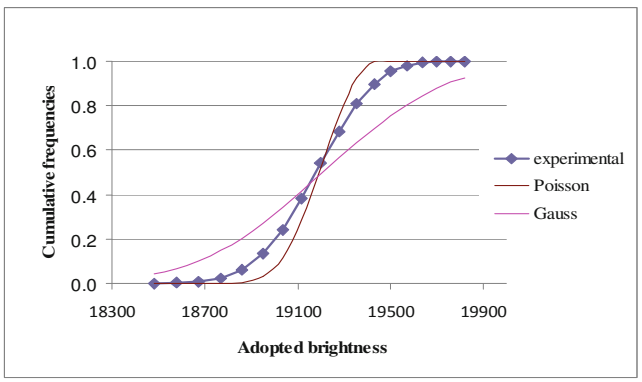

Fig. 5 The CDF for small focus, 96kV, 100x100 pixels area

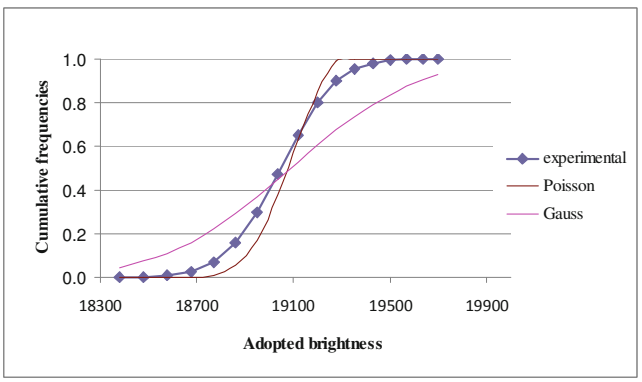

Fig. 6 The CDF for large focus, 81kV, 100x100 pixels area

The parameters λ for small and large focuses are shown in figures 7 - 9. The results show that the values of λ is smaller for small focus for all used kilovolts.

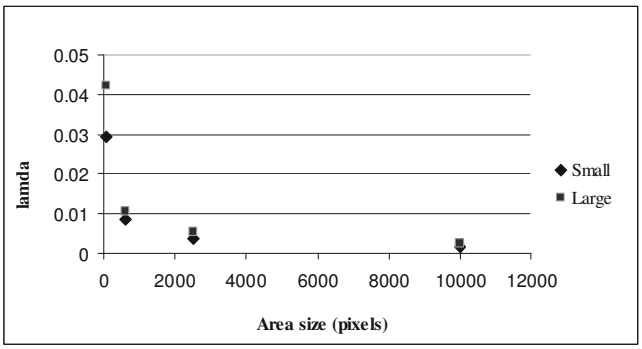

Fig. 7 Parameter λ for different focuses at 61 kV

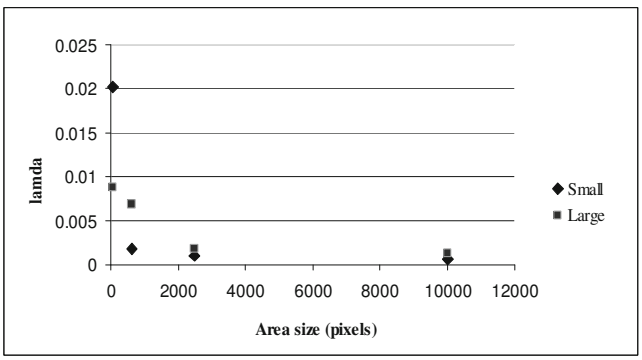

Fig. 8 Parameter λ for different focuses at 81 kV

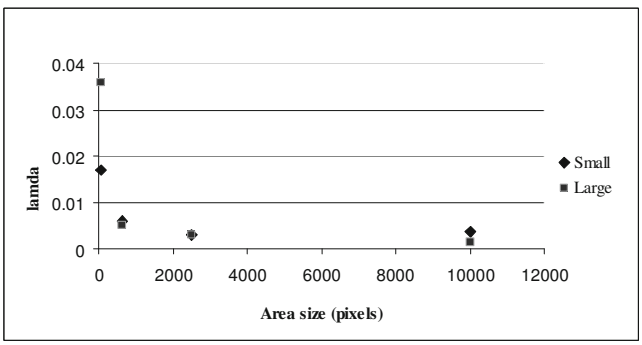

Fig. 9 Parameter λ for different focuses at 96 kV

When milliampers (mA) were enlarged the value of λ became smaller (Fig.10).

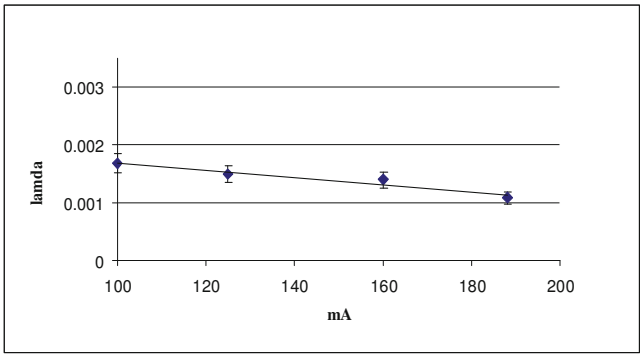

Fig. 10 Parameter λ in dependence on mA

IV. Conclusions

The Poisson statistics based approach to analyze brightness statistics of the digital image is demonstrated to estimate quality of x-ray digital radiography machines.

The approach could be in use by the medical staff for the express day-to-day monitoring of the x-ray digital radiography machines quality deviations.

References

1. Physics for diagnostic radiology; P.P.Dendy, B.Heaton; Bookcraft, UK, 1999, 446 p.
2. Digital radiography detectors - A technical overview: Part 1; L.Lanca, A.Silva, Elsevier, Radiography (2009) 15, 58-62
3. Digital radiography with large-area flat-panel detectors; E.Kotter, M.Langer; Springer, 2002
4. http://www.trixell.com/html-gb/products/interne/pixium_key.html##
5. Principles of statistics; M.G.Blumer; Dover publ., Inc., NY, 1979, 253 p.
6. Математическая статистика; В.М.Иванова, В.Н.Калинина и др.; Москва; Высшая школа; 1975 г.; 398 стр.
7. Методика статистической обработки емпирических данных; Комитет стандартов; Издательство стандартов; Москва; 1966 г.; стр. 28-29.

The address of the corresponding author:

Author: Lada Bumbure
Institute: Riga Technical University
Street: Ezermalas 6
City: Riga
Country: Latvia
Email: havanagila@inbox.lv

Time Dependent Deterioration of the X-Ray Dental Diagnostic Equipment

Yu. Dekhtyar[1], A. Kamenetskikh[2], M. Polakovs[3], and M. Sneiders[1]

[1] Institute of Biological Engineering and Nanotechnology, Riga Technical University, Riga, Latvia
[2] Mechanical Department, Specialty of Mechatronics, Ural State University of Railway Transport, Yekaterinburg, Russia
[3] Institute of Solid State Physics, University of Latvia, Riga, Latvia

Abstract — **Modern dental X-ray examinations are essential for diagnosis. The goal of this paper is to demonstrate time dependent behavior of dose providing parameters, which help to determine equipment's age effects on the x-ray machine parameters. Also the comparisons between two different dental X-ray generator equipment types *half-period* and *high frequency* was made.**

Keywords— **dental x-ray equipment, time, degradation.**

I. Introduction

The dental x-ray diagnostic is the most popular among x-ray diagnostics machines in Latvia (Tab. 1.).

Table 1 Distribution of the diagnostic x-ray equipment in Latvia.

Types of the diagnostic x-ray equipment	%
Dental	50
Radiographical	20
mobile radiographical	9
CT scanning	7
Other	14

Presented statistical data by NMS GRUPA Ltd. show dental diagnostic x-ray equipment (*further in text – dental x-ray*) spread in Latvian on year 2011 (fig 1.). There are two types of generators for dental x-ray:

- high frequency;
- half-period.

Statistics demonstrates that the Trophy ELITYS (25%) (*further in text* – ELITYS) is the most popular dental x-ray with high frequency and the Trophy IRIX 70 (13%) (*further in text* – IRIX 70) – with half-period generators in Latvia.

Time dependent degradation of x-ray machines gives a strong impact on quality of diagnostics. However, there are no data on time dependent degradation.

The goal of the paper is to explore time dependent behavior of dental x-rays ELITYS and IRIX 70 dose providing parameters such as:

- X-ray tube voltage [kV]. Quality of this parameter has an influence on a spectrum, image quality, and an absorbed dose.
- X-ray exposure time [ms]. - influences the absorbed dose.
- X-ray tube output [mGy/mAs] influences the absorbed dose.
- Air KERMA [mGy] – influences the absorbed dose. [1].

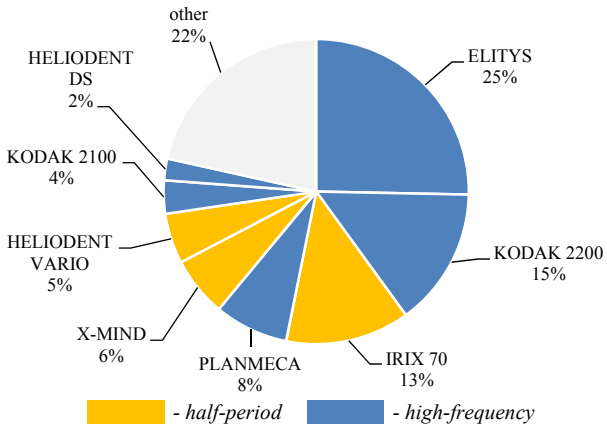

Fig. 1 Dental diagnostic x-ray equipment spread in Latvia year 2011 with *half-period* and *high-frequency* generator types.

II. Materials and Methods

The measurements data have been collected from NMS GRUPA Ltd. The number of the protocols was equal to 417 collected from year 2006 to 2011.

The expanded uncertainty of measurement of the parameters has also been taken from the above protocols (Tab. 2).

Table 2 The expanded uncertainty of measurement of the parameters.

Dose characterizing parameters	%
x-ray tube voltage [kV]	1.5
x-ray exposure time [ms]	1.0
air KERMA [mGy]	2.5

Y. Dekhtyar et al. (Eds.): *International Symposium on Biomedical Engineering and Medical Physics*, IFMBE Proceedings 38, pp. 149–152, 2013.
DOI: 10.1007/978-3-642-34197-7_39

The reported expanded uncertainty of measurement is stated as the standard uncertainty of measurement multiplied by the coverage factor k = 2, which for a normal distribution corresponds to a coverage probability of approximately 95%.

X-ray tube output at 1m [mGy/mAs] was calculated using equation 1:

$$TO = \frac{D}{I \cdot \Delta t \cdot k_{dist}} \quad (1)$$

where D is an ionizing radiation in terms of air KERMA dose, I – current of tube-head, Δt – x-ray exposure time, k_{dist} – distance correction.

Selection of the parameters has been done on the demands by the Republic of Latvia Cabinet of Ministers No. 97 of March 5, 2002 "Regulations on protection against ionizing radiation in medical exposure" [2].

Statistical processing of the collected data (arithmetic mean, experimental standard deviation) has been determined in accordance with EAL Publication EA-4/02 [3].

The correlation of the approximation of the x-ray machine parameters with respect to time has been verified by linear and polynomial (2nd and 3rd order) functions. The "least squares" method has been applied to confirm the best approximation.

III. Results and discussion

The results are presented in Figure 2.

The verification criteria for approximation are presented in Table 3 and 4 for high frequency and half-period generator type respectively, where:

- linear, polynomial 2nd order, polynomial 3rd order – type of approximation;
- t1, t2 or t3 – t-observed value;
- P(F) – the F statistic probability.

A. High Frequency Generator Type – ELITYS

The linear approximation has been confirmed for x-ray tube voltage. For x-ray exposure time, x-ray tube output and air KERMA the polynomial 2nd order approximation was confirmed.

Following this result x-ray tube voltage degrades in accordance with the linear correlation and during 8 years of exploitation decreases by 1.1%.

X-ray exposure increases in accordance with the polynomial 2nd order correlation and during 8 years of exploitation increases by 0.4%.

X-ray tube output and air KERMA follows the polynomial 2nd order correlation with a parameter maximum on equipment`s 5-6 year age, during first 4 years increases by 8.1% and 7.4% respectively. During next 4 years results decreases by 8.7% and 8.8% respectively.

Table 3 The approximation of the x-ray machine parameters.

Approximation		kV	ms	mGy	mGy/mAs
Linear	t1	**-2.48**	11.17	2.90	2.56
	P(F)	**0.01**	0.00	0.00	0.01
Polynomial 2nd order	t1	0.18	**-1.28**	**4.35**	**4.14**
	t2	-0.70	**3.67**	**-3.82**	**-3.69**
	P(F)	0.04	**0.00**	**0.00**	**0.00**
Polynomial 3rd order	t1	-0.42	-0.11	-0.51	-0.64
	t2	0.39	0.24	1.20	1.29
	t3	-0.48	0.23	-1.70	-1.77
	P(F)	0.08	0.00	0.00	0.00

B. Half-Period Generator Type – IRIX 70

The linear approximation has been confirmed for x-ray exposure time, x-ray tube output and air KERMA. For x-ray tube voltage the polynomial 2nd order approximation was confirmed.

Following this result x-ray tube voltage follows the polynomial 2nd order correlation with a parameter reaching its maximum value on equipment`s 6 year, during first 5 years it increases by 2.4%. During next 5 years results decrease by 3.3%.

X-ray exposure time increases in accordance with the linear correlation and during 10 years of exploitation increases by 0.5%.

Table 4 The approximation of the x-ray machine parameters.

Approximation		kV	ms	mGy	mGy/mAs
Linear	t1	-1.00	**1.72**	**-2.84**	**-3.66**
	P(F)	0.32	**0.09**	**0.01**	**0.00**
Polynomial 2nd order	t1	**1.83**	1.34	1.11	0.41
	t2	**-2.06**	-1.02	-1.70	-1.15
	P(F)	**0.08**	0.14	0.00	0.00
Polynomial 3rd order	t1	0.56	1.06	0.99	0.65
	t2	-0.32	-0.84	-0.92	-0.70
	t3	0.05	0.71	0.71	0.55
	P(F)	0.16	0.22	0.01	0.00

A. High Frequency Generator Type – ELITYS

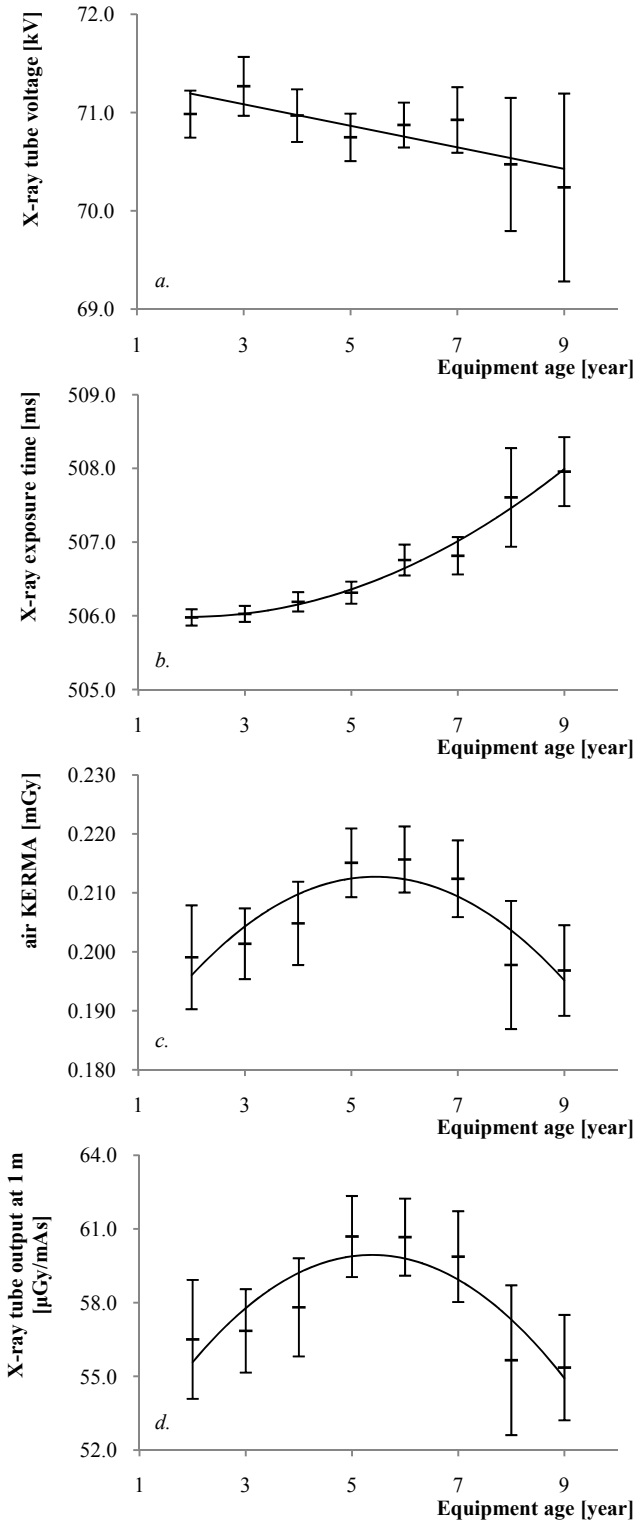

B. Half-Period Generator Type – IRIX 70

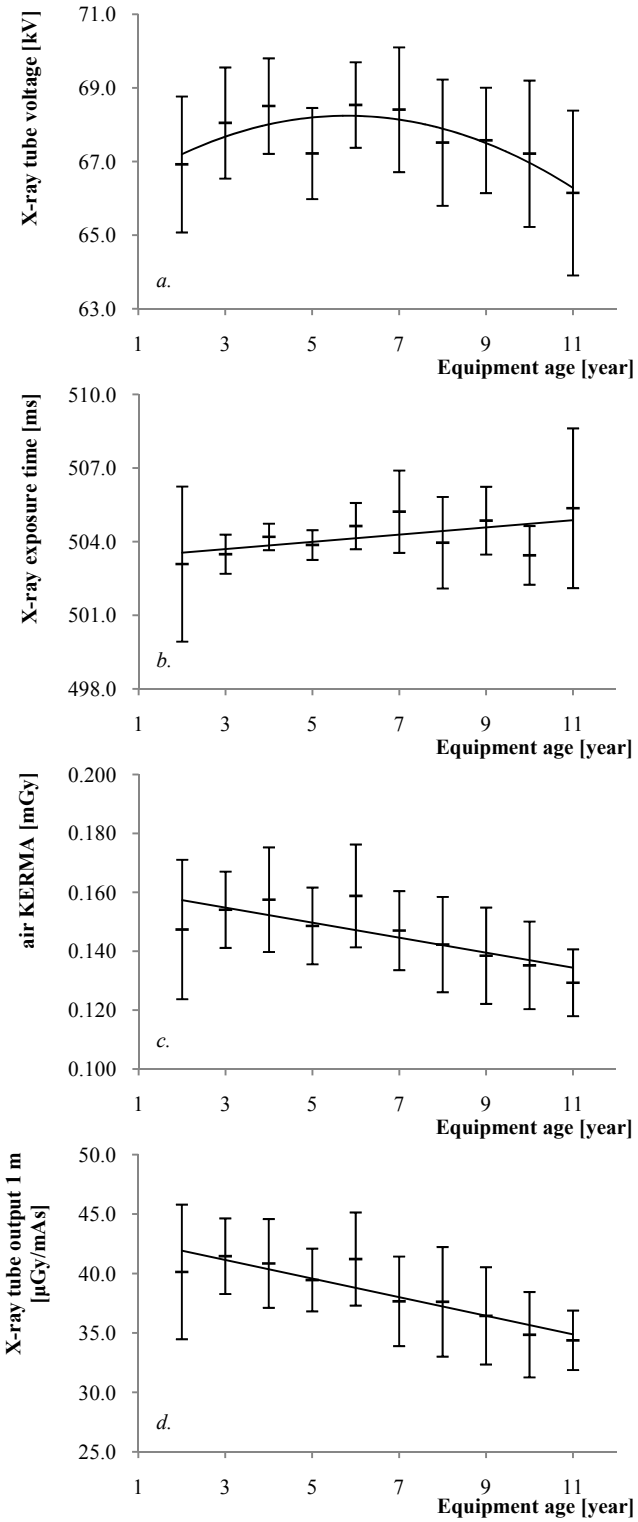

Fig. 2 The influence of the age of equipment on *a.* x-ray tube voltage, *b.* x-ray exposure time, *c.* air KERMA, *d.* x-ray tube output at 1m.

X-ray tube output and air KERMA follows the linear correlation and during 10 years decreases by 12.3% and 14.3% respectively.

IV. Conclusions

1. Degradation of dose characterizing parameters were explored for dental x-ray ELITYS with high frequency generator type for over 8 year of the equipment age.
2. Deviation of the parameters comparing first and last year (the 8 year of equipment exploitation) of studied equipment is shown in Table 5.

Table 5 Deviation of the parameters.

Dose characterizing parameters	Deviation, %
x-ray tube voltage [kV]	- 1.1
x-ray exposure time [ms]	+ 0.4
air KERMA [mGy]	- 1.0
x-ray tube output [mGy/mAs]	- 2.0

3. Degradation of dose characterizing parameters were explored for dental x-ray IRIX 70 with half-period generator type for 10 year of the equipment exploitation (Table 6).

Table 6 Deviation of the parameters.

Dose characterizing parameters	Deviation, %
x-ray tube voltage [kV]	- 1.2
x-ray exposure time [ms]	+ 0.5
air KERMA [mGy]	- 12.3
x-ray tube output [mGy/mAs]	- 14.3

Acknowledgment

The authors are indebted to NMS GRUPA Ltd. for provision of statistical information and protocols with measurement data.

References

1. Dehtjars Ju., Emzins Dz., Jurkevics Ar., et al. (2006) Radiation safety for radiology technologists. In Latvian: Radiācijas drošība radiologu asistentiem. RTU 336
2. Demands by the Cabinet of Ministers No. 97 of March 5, 2002 "Regulations on protection against ionizing radiation in medical exposure" at http://www.likumi.lv/
3. EAL Publication EA-4/02 at http://www.european-accreditation.org/

Author: Maksims Sneiders
Institute: Riga Technical University
Street: Ezermalas 6b, 248
City: Riga
Country: Latvia
Email: maksims.sn [at] gmail.com

On Criteria for Wide-Angle Lens Distortion Correction for Photogrammetric Applications

D. Celinskis and A. Katashev

Institute of Biomedical Engineering and Nanotechnologies / Faculty of Transport and Mechanical Engineering, Riga Technical University, Riga, Latvia

Abstract — **Photogrammetry is intensively used both in industrial applications and medicine. Extraction of various anthropometrical data, such as height, shoulder inclination or Kobb angle form single photograph could be implemented in mobile devices, used for health screening. To be able to get photo of standing individual when the space for observations is restricted, wide – angle lens has to be used. Unfortunately, such lenses demonstrate highly expressed radial distortion, thus image has to be corrected before it could be used for estimation the subject's dimensions. There are number of methods, proposed to correct lens radial distortion. Most of them use deviation of the imaged straight line from the real straight line as a criterion for image correction. Correction parameters are adjusted to minimize the deviation. When one have to select correction method for particular lens and particular application, it could be reasonable to choose method that provides minimal, comparing to others, residual deviation. Besides, this paper demonstrates, that such criterion does not guarantee that error of dimensions measurements will be minimal as well. In the present work, various radial distortion correction methods, including one, introduced by authors, were evaluated, using both straight line deviation and dimension measurement error. Obtained results allowed formulate recommendation for improvement of existing image correction methodology.**

Keywords — **photogrammetry, camera calibration, image distortion, wide-angle lens, correction.**

I. Introduction

Photogrammetry, as a method of obtaining object's dimensions form single photographic image, is widely used in a number of applications, such as human spine measurements [1], detection of musculoskeletal abnormalities [2], architectural measurements [3] etc. In most applications, rectilinear projection lenses are used to obtain object's image, because for such cameras simple pinhole projection model can be applied with reasonable accuracy. The pinhole projection "transforms" straight lines of the object into straight lines in the image plane, thus for the plane object, oriented parallel to the image plane, perspective distortion may be neglected and dimensions, measured in the image plane will be proportional to the object's dimensions. In reality this assumption is not absolutely true, since for images, obtained by rectilinear lenses, certain amount of distortion still exist and for high-precision photogrammetric applications camera image correction is required.

In turn, wide-angle lenses typically are not used for photogrammetric measurements. Their typical applications include cases when there is a need to get an image of the whole object form close distance or have as wide field of view as possible. Semiautomatic parking systems [4], robot vision or endoscopy [5] may be mentioned as examples. Indeed, comparing with rectilinear lenses, wide-angle lenses express much stronger radial distortion, that leads to significant bending of the object's straight lines in the image plane (fig.1 and 2). As the result, evaluation of the distance between two object's points by multiplying distance between corresponding image points on single calibration factor is no more valid. Therefore, one has to "correct" wide-angle lenses image to restore corrupted geometrical information before it may be used for photogrammetry. Such correction procedure often is referred as "calibration".

According to [6], radial distortion is responsible for about 90% of all distortion-related image deformities. Alongside, other forms of distortion, such as perspective distortion or color aberrations, are equally presented both in wide-angle and rectilinear lens-formed images (so, similar correction methods are used for both). That is why the present paper considers only radial distortion correction.

Until now, extensive work related to the radial distortion correction was done and, generally, two different approaches had been introduced [7]. The first one uses the correspondence between distorted and corrected images, introducing the matrix, where correct undistorted coordinates for each distorted image pixel are stored. Correction process does not involve any mathematical operations and pixels are simply transferred to correct positions. The main drawback of such approach is time-consuming process of matrix creation. Additionally, the method requires matrix equal to image size to be stored, so appropriate memory have to be provided.

Alternative approach uses parametric distortion model: the corrected position of image pixel is calculated, using some formula that has relatively few parameters. This

Y. Dekhtyar et al. (Eds.): *International Symposium on Biomedical Engineering and Medical Physics*, IFMBE Proceedings 38, pp. 153–158, 2013.
DOI: 10.1007/978-3-642-34197-7_40

approach save memory needed to store correction algorithm data, but requires calculation for each pixel.

For parametric methods, various approaches exist to find correction algorithm parameters. For example, in [7] image of calibration pattern made of periodically placed points was used. The relationship between points' coordinates obtained from the image and form the calibration pattern was used to calculate coefficients for particular parametric distortion model, that defines where each pixel must be transferred to make an image maximally similar to the one obtained through rectilinear projection.

More simple method uses iterative fitting of the correction algorithm parameters in a "goal seek" manner. For such an approach some measure of image "correctness" have to be introduced. Possible solution is to use image geometric invariants, like parallel lines, circles, etc. Examples of such approach, which is also called plumb line fitting method, can be found in [6] and [8]. The main idea is that points, which belong to the distorted straight line, are extracted from corrected image and fitted using equation of conic, polynomial or circle line. Such equation reduces into straight line equation when certain coefficients become equal to zero. Respectively, image correction model parameters are fitted until these coefficients becomes less then pre-selected level of tolerance level to make fitted function maximally close to the straight line equation.

A little bit different, but much often used approach [13] utilizes important feature of pinhole projection: it preserves straightness of lines. In other word, straight lines are projected into straight lines. Thus the sum of the squared displacements from a straight line is calculated and minimized for selected points that belong to the object's straight line on the corrected image. In practice, the sum is calculated over several lines, taken from different parts (center, periphery) of the image. Minimization of this sum allows finding parameters of the correction algorithm. Exactly this approach is evaluated within this work as most widely used.

The research in this field still continues and a new approach was introduced in [9]. Proposed method uses more geometric restrictions like parallelism and perpendicularities in addition to the line straightness. These restrictions are applied to the set of control points, distributed across the entire image. Local correction function is defined in vicinity of each control point. This method is a compromise between function – based and matrix-based correction approaches and its accuracy assessment could be the next step in the evaluation of achievable accuracy of wide-angle lenses in photogrammetric applications.

Although there are number of different radial distortion correction methods, no single method may be selected as the best one. Reviews [13] and [16] provided comparison of different correction methods and demonstrated that selection of the best method is camera-specific. In other words, for each particular lens – camera combination the optimal correction method and its parameters have to be selected individually.

For photogrammetric applications, that mainly require measurements of the object dimensions, preservation of distance between points by imaging system seems to be of the primary importance. Besides, as it was mentioned above, most of the correction methods are based on line straightness criteria. Thus the question arises: will the correction method, being the best in terms of line straightness, be as well the best in terms of point distance measurement accuracy? The present paper is attempting to answer this question.

It is necessary to mention additional problems related to the existing camera calibration software. Since wide-angle lenses were not often used in photogrammetry, accurate and applicable to any lens radial distortion correction software has not been founded yet. Moreover, according to [10] and [11], most of existing software traditionally use 3rd order polynomial correction functions, while in [4], [9], [12], [13], [14], [15] and [16] is stated, that this function in not able to correct highly expressed radial distortion and is more suitable for rectilinear lens calibration, since such lenses express weaker radial distortion. It gives additional support to the importance of validation and improvement of existing radial distortion correction approaches for wide-angle lenses.

II. Materials and methods

The study was carried out, using phantom object - pattern of 2×2 mm black points, placed in the nodes of rectangular net with cell size 10×10 mm (fig.1). Alongside, a stand with reference points (fig. 2) was constructed to perform evaluation of the measurement accuracy from a longer distance. The stand's width and height approximately corresponds to the more than medium human sizes. The distances pattern phantom - camera lens and stand - camera lens was 10 cm and 110 cm, correspondingly.

Images were acquired using USB CCD monochrome camera DMK 31BU03 (The Imaging Source®) with resolution 1024x768, equipped with 2,3 mm wide-angle lens T2314FICS-3 which have horizontal field of view 113,3°.

Although in practical applications set of calibration images, taken from different angles is used to account for different perspective distortion, in the present work the calibration phantom object was maximally accurately positioned in front of the camera to reduce perspective distortion to the negligible value. The accuracy of positioning was evaluated by checking whether the distance between leftmost and rightmost points of the horizontal rows, equally separated from the image center, are equal.

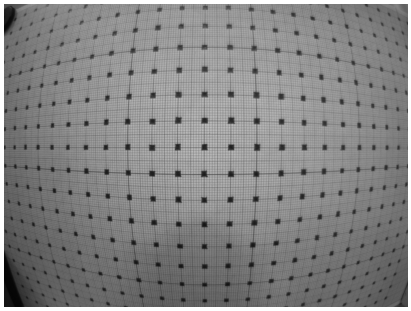

Fig. 1 Calibration pattern.

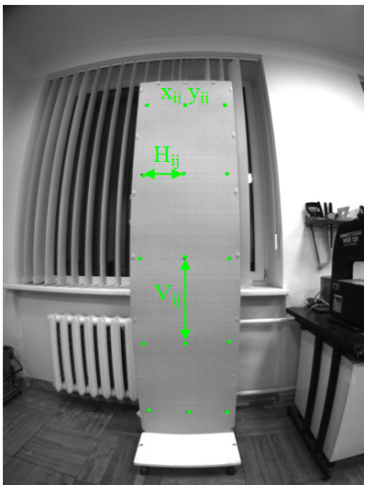

Fig. 2 Stand for measurement accuracy evaluation.

Correction algorithms were implemented using Delphi 7. The corrected (undistorted) image was created as follow. For each corrected image pixel (x_u, y_u), the distance from the principal point (x_c, y_c) was calculated:

$$r_u = \sqrt{(x_u - x_c)^2 + (y_u - y_c)^2} \tag{1}$$

Afterwards, the distance of the same object's point's image from the principal point at the distorted image r_d was calculated, using one of the distortion correction formulas $r_d = f(r_u)$. Coordinates x_d and y_d of the corresponding distorted image pixel, that have to be moved to the corrected image pixel (x_u, y_u,) are given by

$$x_d = (x_u - x_c) \times \frac{r_d}{r_u} \times C + x_c \tag{2}$$

$$y_d = (y_u - y_c) \times \frac{r_d}{r_u} \times C + y_c \tag{3}$$

where scaling factor C is chosen on the base of visual evaluation of the corrected image (its role is to crop corrected image to the rectangular area, cutting off deformed edges). Since coordinates (x_d, y_d) generally are not integer numbers, the brightness of the corresponding pixel was calculated by interpolation from 4 nearest points, following [17].

Distortion correction was carried out, using 10 different parametric distortion correction functions / models:

1. Equisolid projection [17]:

$$r_d = 2 \times K \times \sin\left(0{,}5 \times \arctan\left(r_u / K\right)\right) \tag{4}$$

2. Orthographic projection [17]:

$$r_d = r_u \Big/ \sqrt{1 + r_u^2 / K^2} \tag{5}$$

3. Fish-Eye Transform [13]:

$$r_d = K_1 \times \ln\left(1 + K_2 \times r_u\right) \tag{6}$$

4. Stereographic projection [17]:

$$r_d = 2 \times K \times \tan\left(0{,}5 \times \arctan\left(r_u / K\right)\right) \tag{7}$$

5. 3rd order odd polynomial [4]:

$$r_u = 1 + K_1 \times r_d^3 + K_2 \times r_d^5 + K_3 \times r_d^7 \tag{8}$$

6. Trigonometric-Polynomial:

$$r_u = \arctan\left(\frac{1 + K_1 \times r_d^2 + K_2 \times r_d^3}{1 + K_2 \times r_d^3}\right) \times r_d \tag{9}$$

7. Field-of-View model [13]:

$$r_d = 1 \Big/ K \times \arctan\left(2 \times r_u \times \tan\left(K/2\right)\right) \tag{10}$$

8. Field-of-View + parameters:

$$r_d = 1 \Big/ K \times \arctan\left(2 \times r_u \times \tan\left(K/2\right)\right) + \\ + K_1 \times r_u^3 + K_2 \times r_u^5 + K_3 \times r_u^7 \tag{11}$$

9. Equidistant Projection [4]:

$$r_d = K \times \arctan\left(r_u / K\right) \tag{12}$$

10. Equidistant Projection + parameters:

$$r_d = K \times \arctan\left(r_u / K\right) + K_1 \times r_u^3 + K_2 \times r_u^5 + K_3 \times r_u^7 \tag{13}$$

where K (whether indexed or not) denotes model parameters to be fitted. Function Nr.6 is original for this work, introduced as an attempt to combine widely used polynomial function with trigonometric functions. Coordinates of the principal point (x_c, y_c), in fact are the coordinate of the center of distortion, and have to be fitted as well.

For corrected image, the coordinates of the calibration pattern points were extracted using center of mass estimation method, based on the pixel intensity weighting process.

This method provided sub-pixel resolution in evaluation of the point position. Totally 294 points, grouped in 14 horizontal and 21 vertical lines, were extracted.

Then, two target values were calculated. The first one was the parameter of straightness: for each horizontal and vertical line, fit straight line was obtained and sum χ^2 of the squared displacement of the points from the fitted line was calculated, following [13]. Obtained value was divided by the length of the lines in pixels, and resulting values for all lines was added to give parameter in question $\sum(\chi^2/l)$. The second parameter was just the standard deviation *S* of the measured distance between two adjacent points, calculated over all available pairs. To calculate the measured distance, camera calibration factor *F* (in mm/pixel) was calculated by dividing calibration pattern net cell size (10 mm) by the average distance in pixel between adjacent points. The differences δ between measured and nominal distances was collected as well.

The distortion correction function's parameters *K* and position of the principal point (x_c, y_c) were iterated to minimize either first or the second parameter. Obtained parameters were used to correct the image of the stand. 10 different horizontal (H_{ij}, see fig.2) and 12 different vertical (V_{ij}, see fig.2) distances were measured form the image, using calculated calibration factor F. Then maximal deviation from known distance between stand marker sizes (V = 40 cm, H = 20 cm) Δ was determined and used as parameter of the measurement accuracy.

The above procedure was repeated for each model (4) – (13).

III. Results and discussion

Results of the distortion correction function optimization are summarized in the Table 1. Left side of the table shows residual values of the parameter of straightness and maximal deviation from real object's dimensions for the correction methods, fitted by minimizing parameter of straightness itself. Methods, numbered in accordance with the above list, are sorted in descending order, so the last method provides the smallest relative deviation from the straightness $\sum(\chi^2/l)$. Besides, the method Nr.4 demonstrates the smallest deviation Δ of the measured distance, although corresponding $\sum(\chi^2/l)$ is not minimal. Moreover, for the group of methods (methods 7, 8, 9 and 10), parameter $\sum(\chi^2/l)$ appears to be the same (with a given precision of calculation) that demonstrates poor usability of this value for the selection of the best method. Generally, this findings support supposition, that optimization of lines' straightness does not imply minimization of the distances measurement error.

Table 1 Distortion function evaluation results for parameters optimization by straightness criteria (left) and by minimization of the standard deviation of the inter - point distance (right).

Funct. Nr.	$\sum(\chi^2/l)$	Δ, mm (pix)	Funct. Nr.	$\sum(\chi^2/l)$	Δ, mm (pix)
3.	5,06	31,87 (6,29)	3.	34,69	5,45 (1,91)
2.	1,02	10,41 (3,04)	5.	1,87	5,02 (1,46)
1.	1,02	10,41 (3,04)	2.	6,78	4,20 (1,24)
5.	0,73	9,54 (2,75)	1.	6,78	4,20 (1,24)
4.	0,63		9.	0,81	4,15 (1,23)
9.	0,62	5,57 (1,64)	7.	0,80	4,15 (1,22)
10.	0,62	5,53 (1,63)	8.	0,80	4,14 (1,22)
7.	0,62	5,57 (1,64)	10.	0,81	4,13 (1,23)
8.	0,62	5,31 (1,56)	4.	0,70	4,11 (1,22)
6.	0,51	4,99 (1,17)	6.	0,53	4,03 (0,94)

At the right side of the Table 1, parameters $\sum(\chi^2/l)$ and Δ are presented for the case, when distortion correction function parameters was fitted, using standard deviation *S*. Generally, the distance measurement error is smaller, comparing with the data on the left side, so one may conclude, that higher accuracy may be achieved by use of the proposed coefficient optimization criteria, based on the minimization of the deviation of the measured linear sizes form the actual sizes. In the same time it can be noticed that models are sorted in different order, comparing with the cases of optimization on the base of straightness criteria. Moreover, the parameter $\sum(\chi^2/l)$ is noticeable higher in the right side of the table. This strengthens the conclusion, that minimization of the straight line criteria does not provide minimal distance measurement error as well, and the criteria based on minimization of Δ can provide more correct choice of the optimal distortion function.

Concerning the choice of the distortion correction function for the lens, used in the experiment, the highest measurement accuracy was reached by use of the Trigonometric-Polynomial function, for the first time introduced in the present paper. The maximal difference between real distance and distance, measured from the corrected image was 4,03 mm, what corresponds to the relative error of 2% as maximum. In comparison with the closest best function, namely, stereographic projection function, that provides the closest accuracy results (Δ = 4,11 mm), Trigonometric-Polynomial function requires to fit two coefficients instead of one. But the new method is simpler, comparing with more traditional polynomial functions, since most of them implements three or even more coefficients to get good enough distortion correction. Another aspect of evaluation of the functionality of the proposed correction function is estimation of the correction performance for a number of other types of wide-angle lenses, as it was done by other researches [12][13], as well as for rectilinear projection

lenses. This aspect has not been considered in the present paper, yet it is important because, as it was emphasized above, same functions perform differently for different lenses.

The proposed distortion correction approach directly includes determination of the center of distortion - principal point (x_c, y_c). One has to note, that correct identification of the center of distortion is absolutely crucial for the whole correction procedure, especially for the purposes of photogrammetry. For example, in the examined case, for the method Nr. 6, the displacement of the center of distortion from a correct position just for 0,40 pixels resulted in error increase from 4,03 mm to 4,25 mm. Several methods for determination of the center of distortion have been proposed previously (see, for instance, [15] and [18]), but it seems reasonably to fit position of the center by the same approach as other correction function parameters. This approach is based on the simple principle that highest accuracy can be achieved only with precisely determined center of distortion. Deviations of measured distances Δ, presented in the Table 1, correspond to the optimal distortion center position. As a result for all correction functions minimization provided distortion center coordinates with deviations only ±0,1 pixels. Respectively, an attempt to minimize $\sum(\chi^2/l)$ did not give so accurate results: deviations of the distortion center coordinates noticeably varied and reaches up to ±12 pixels for some functions. Consequently all results in the Table 1 are calculated, using distortion center coordinates, obtained by minimization of Δ, because observed measurement errors were much higher for centers obtained by $\sum(\chi^2/l)$ minimization.

Proposed optimization criteria - minimization of Δ – is especially convenient for photogrammetry applications, because it provides immediate possibility to evaluate measurement error of the developed system, thus estimating its usability. For the present case, for the majority of the used methods the error is about 4.5 mm. Such an error is acceptable for the measurement of the human height, since it varies by several centimeters during the day, or, for instance, evaluation of posture imbalance by measuring offset of the C7 vertebra over S1 vertebra in sagittal plane (pathology is indicated by the offset more then 40 mm, [19]). The accuracy of the method is, generally, compatible with one of the standard measuring stadiometers.

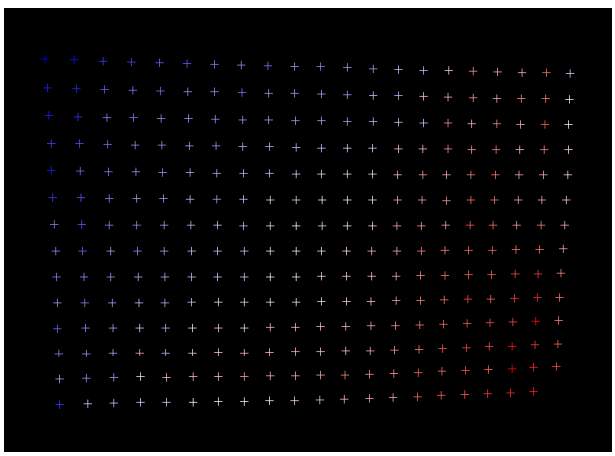

Fig. 3 Color scale coded error distribution for best correction function: Red max δ = 1,37 mm (4,59 pix), White δ = 0, Blue max δ = -1,49 mm (-5,01 pix).

The last question of interest for the present work was distribution of the distance measurement error over the image plane. For this, calibration pattern (fig.1) was used. Individual differences δ between measured and nominal distances between adjacent points was color-coded and depicted at the fig. 3. For all methods, the distribution of the errors over the image was the same – overestimation of the distances in the bottom – right corner and underestimation in the upper – left corner of the image. Moreover, the errors are increasing with the distance from the center and reach up to 15% at the image periphery. The most reasonable explanation of such behavior is influence of the perspective distortion. Since this distortion presented in the same extent in all calculation, it could not affect the conclusions concerning ranging of the methods. Besides, for practical applications, perspective distortion has to be corrected. One could suspect this will reduce measurement error. The other way to reduce error is to avoid use of the points close to the image borders, for instance, by restriction of the image area.

IV. Conclusions

In the present work, one has demonstrated that widely used criteria of the line straightness do not perform well for the wide–angle lens radial distortion correction. Alternative criteria, based on the minimization of the error of the distance measurement, could be more useful for photogrammetry purposes.

New, Trigonometric-Polynomial radial distortion correction function was introduced. This function demonstrates good characteristics and is the best for the lens – camera combination, used in the present work. The method implies simultaneous fitting of both distortion correction formula parameters and coordinates of the distortion center.

For the used camera, method allowed to achieve distance measurement precision of about 2%. This result is sufficient for anthropometrics measurements. Besides, only central part of the camera field of view has to be used, since at the image periphery relative error increases up to 15%.

One has to conclude that used calibration pattern positioning method does not exclude perspective distortion.

Although selection of the best correction method may be done despite of the residual perspective distortion, evaluation of the error, introduced entirely by lens and camera could not be made. Thus, perspective distortion has to be taken into account when calibrating camera.

Although proposed optimization parameter and correction method has shown good results for the used lens – camera combination, further research in needed to evaluate method's performance for other lenses.

Acknowlegements

This work has been carried out in the framework of the European Regional Development Fund Project "Development of New Mobile Telemedicine Screening Complex", agreement Nr.2011/ 0007/ 2DP/ 2.1.1.1.0/ 10/ APIA/ VIAA/ 008.

References

1. A. K. Chong, P. Milburn, R. Newsham-West, M. Voert (2009) High-accuracy photogrammetric technique for human spine measurement. The Photogrammetric Record: An International Journal of Photogrammetry, 24 (127). pp. 264-279. ISSN 0031-868X
2. J. Davidson, A. Miyashiro N. dos Santos, K. Maria B. Garcia et al. (2011) Photogrammetry: an accurate and reliable tool to detect thoracic musculoskeletal abnormalities in preterm infants, Physiotherapy, ISSN 0031-9406, DOI 10.1016/j.physio.2011.05.007.
3. R. Jiang, D. V. Jáuregui, K. R. White, Close-range photogrammetry applications in bridge measurement: Literature review, Measurement, Volume 41, Issue 8, October 2008, Pages 823-834, ISSN 0263-2241, DOI 10.1016/j.measurement.2007.12.005.
4. C. Hughes, M. Glavin, E. Jones, P. Denny, Wide-angle camera technology for automotive applications: a review, IET Intell. Transp. Syst., March 2009, Volume 3, Issue 1, p.19–31
5. J. P. Barreto, R. Swaminathan, J. Roquette, Non Parametric Distortion Correction in Endoscopic Medical Images, 3DTV Conference, 2007 DOI 10.1109/3DTV.2007.4379383
6. R. Wirza, Md. N. Bin Sulaiman et al. Establishing the Straightness of a line for radial distortion correction through conic fitting, 286 IJCSNS International Journal of Computer Science and Network Security, VOL.9 No.5, May 2009
7. L. Romero, C. Gomez (2007) Correcting Radial Distortion of Cameras with Wide Angle Lens Using Point Correspondences. Scene Reconstruction, Pose Estimation and Tracking, Book edited by: R. Stolkin, I-Tech, Vienna, Austria, pp. 530, June 2007
8. R. Strand, E. Hayman, Correcting Radial Distortion by Circle Fitting, In the Proceedings of the British Machine Vision Conference, Oxford, UK, 2005
9. C. Ricolfe-Viala, Antonio-José Sánchez-Salmerón, Correcting non-linear lens distortion in cameras without using a model, Optics & Laser Technology, Volume 42, Issue 4, June 2010, Pages 628-639, ISSN 0030-3992, DOI 10.1016/j.optlastec.2009.11.002.
10. F. Remondino, C. Fraser, Digital Camera Calibration Methods: Considerations and Comparisons, IAPRS Volume XXXVI, Part 5, September 2006
11. K. Peipe, W. Tecklenburg (2006) Photogrammetric camera calibration software - a comparison, Measurement Techniques, pp. 1-4.
12. W. Kim, C. Kim, An Efficient Correction Method of Wide-Angle Lens Distortion for Surveillance Systems, IEEE International Symposium on Circuits and Systems (ISCAS), pp.3206-3209, 2009
13. F. Devernay, O. Faugeras, Straight Lines Have to be Straight, Machine Vision and Application, Springer-Verlag, pp. 14-24, 2001
14. M. Friel, C. Hughes, M. Glavin, E. Jones, P. Denny, Automatic calibration of fish-eye cameras from automotive video sequences, IET Intell. Transp. Syst., Vol. 4, Iss. 2, pp. 136–148, 2010
15. R. I. Harley, Sing Bing Kang, Parameter-Free Radial Distortion Correction with Centre of Distortion Estimation, ICCV (2005) Proceedings of the Tenth IEEE International Conference on Computer Vision – pp. 1834 - 1841 Vol. 2, DOI 10.1109/ICCV.2005.184
16. C. Hughes, E. Jones, M. Glavin, P. Denny, Validation of Polynomial-based Equidistance Fish-Eye Models, IET Irish Signals and Systems Conference (ISSC), June 10-11, 2009
17. ALTERA, A Flexible Architecture for Fisheye Correction in Automotive Rear-View Cameras, White Paper, October 2008 at http://www.altera.com/literature-/wp./wp-01073-flexible-architecture-fisheye-correction-automotive-rear-view-cameras.pdf
18. A. Wang, T. Qiu, L. Shao, A Simple Method of Radial Distortion Correction with Centre of Distortion Estimation, J Math Imaging Vis, Vol. 35, pp. 165–172, 2009
19. Hebela, N. M., & Tortolani, P. J. Idiopathic Scoliosis in Adults: Classification, Indications, and Treatment Options. Seminars in Spine Surgery, 21(1), 16-23, 2009.

Authors: Dmitrijs Celinskis, Alexei Katashev, Dr.phys
Institute: Institute of Biomedical Engineering and Nanotechnologies, Riga Technical University
Street: 6k Ezermalas Street
City: Riga, LV-1006
Country: Latvia
Emails: dmitrijscelinskis@yahoo.co.uk, katashev@latnet.lv

Methods for Evaluation of Root Canal Curvatures

A.M. Pangica, C. Biclesanu, and A. Florescu

Faculty of Dentistry/Odontotherapy Department, Titu Maiorescu University, Bucharest, Romanie

Abstract — **Knowledge of root canal curvature is a important factor in successful endodontic treatment. The aim of this study was to check the possibility of including the data already known on the root canal anatomy into mathematical formulae which could lead to details not revealed by radiographies.**

Materials and methods: A total of 98 radiographs of were taken by periapical parallel technique and processed by automatic processing. 86% of the 98 root canals examined, were curved. Most angulation was 72 degree with a radius of curvature_of_2mm. The degree of canal curvature was measured at mesiodistal and bucco-lingual direction with Schneider method. The root curvature was assessed by using Corel Draw Graphics Suite Z5 and computer Sony VaioVPCEB4L1E.

Results:

The angles of curvature ranged from 0 degrees to 72 degrees in bucco-lingual vestibulo-oral radiographs and from 0 degrees to 65 degrees in mesio-distal radiographs . The highest range in vestibulo-oral incidence was 34.5 mm and in mesio-distal incidence, 49.2 mm.

Distomesial approach has been used for gathering information on root canal curvatures, which may not usually be obtained using radiographs taken in bucco-lingual incidence.

Conclusions: The results of this study suggest that Schneider method is reliable to determine the degree of rooth canal curvature. In this way the dentists can enhance endodontic therapy predictability and minimize errors during root canal obturation.

Keywords — **Root canal curvature, Schneider´method, X-ray, Curvature radius, Angle of curvature.**

I. Introduction

Endodontic treatment involves cleaning and shaping of the root canal and three-dimensional (3D) sealing of the canal space. For successful root canal treatment, the canal must be cleaned well, prepared, and filled completely [1]. Some of the most important factors that affect quality of root canal treatment are the anatomy of the canal, the presence of extra canals, and curve in the canal pathway [2].

In vivo evaluation of the root canal system involves the knowledge of its anatomy, its exploration with the root canal instruments and radiographying it. The working length is modified after root canal treatment, and very often the working length is decreased due to the movement of the curve towards the apex, followed by the impossibility to overcome this new obstacle. Sometimes, working length is modified by the fracture of the root instrument below this level, or NI-TI systems are under a lot of stress, or the root canal paste does not go past the curve because it is too abrupt or in a difficult to access area [3].

II. Aims

We wished to check the possibility of including the data already known on the root canal anatomy into mathematical formulae which could lead to details not revealed by radiographies or present knowledge.

We assumed that using geometric corrections, within Schneider's method, some improvements in the accuracy of the root curvature measurement can be achieved .

III. Materials and methods

A. Selection and Preparation of Specimen

The study was carried out on 98 extracted teeth stored in 75% ethanol folowing extraction. For each kind of tooth (except M3), 5 specimens have been randomly selected and investigated .We have excluded the teeth which could not be instrumented all the way to the apex or those with double curve (S).

Access openings were made using diamond burs (nr 837, Komet, Lemgo, Germany). Without initial root canal instrumentation, a 0,8 file (VDW, München, Germany) has been introduced into every root canal and gently pushed in until it was visible on the apical foramen.

86% of the 98 root canals examined, were curved and 62% showed an angle <27 degrees with radius <40 mm.

13% shown an angles between 27 and 35 degrees with radius <15 mm, and 9% of all canals shown angles >35 degrees with radius <13 mm. Most angulation was 72 degree with a radius of curvature of 2mm (table 1).

In order to be mathematically defined the canal curvature, angle, radius, and length of the curve must be in a mathematical relationship.

Y. Dekhtyar et al. (Eds.): *International Symposium on Biomedical Engineering and Medical Physics,* IFMBE Proceedings 38, pp. 159–162, 2013.
DOI: 10.1007/978-3-642-34197-7_41

B. *Radiographic Tehnique*

Radiographs are essential to practice of endodontic [4];

Table 1 Root canals analise.

0%		DIM<)	RADIUS
86% curved	62% angle	< 27°	<40 mm
	13% angle	27-35°	<15 mm
	9% angle	> 35	<13 mm
	2%	75°	2 mm
14%rectilineal			

In order to have the radiography done, the teeth have been aligned with respect to the long axis of the root canal and laid parallel to the film and as close as possible to the X-ray film. Each root canal radiography has been taken in buccal incidence (B-O view) and distal direction (D-M view). Exposure time was the same for all radiography.

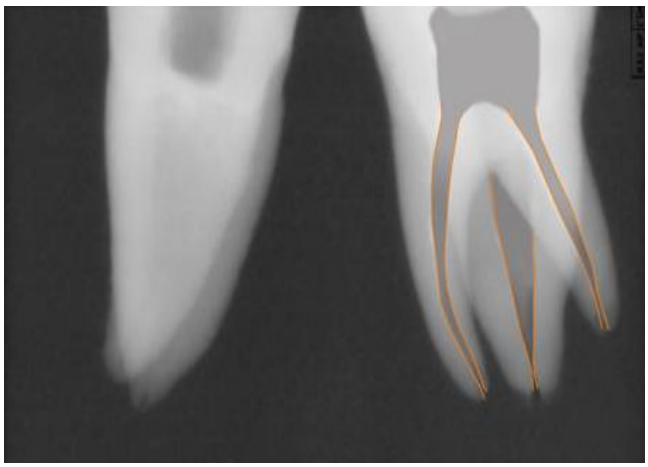

Fig. 1 Rx of the tooth.

The root curvature was assessed by using Corel Draw Graphics Suite Z5 and computer Sony VaioVPCEB4L1E. Digital radiographies were kept on it.

C. *Measurement of Canal Angulation*

The angle of curvature (α) has been determined for both incidence buccal-oral and disto-mesial, according to the method described by Schneider [5].

A bee line (a) was drawn along the file in the coronal right portion of the root canal, which was parallel to the longitudinal axis of the tooth. It was marked with A the point where the curvature of the root canal begins. The apical foramen was noted with B.

A second bee line (b) was drawn between the points A and B (fig. 2).

The angle of curvature is formed by the two lines „a" and" b" and the length S were measured with Corel Draw Graphics Z5.

The line (S) between points A and B represents the chord of a circle defining the hypothetic curved canal. The curved part of the canal between points A and B is represented as an hypothetical arc of a circle having a specified radius (r). The length of radius (r) could be calculated based on measured length of rope (S) between points A and B. Between the point A and point B the circle segment AB (which is actually the physical path that the tools used in mechanical treatment must go through) could be approximated by the corresponding chord of the circle (line AB).

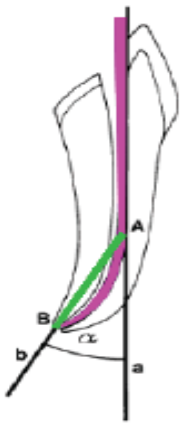

Fig. 2 Angle of curvature.

The radius was calculated geometrically within an isosceles triangle (Fig. 3). Since point A is the center circle and line A is a hypothetical tangent to this circle follows that

$$\alpha + ß = 90°$$

which means:

$$ß = 90° - \alpha \quad (1)$$

ß is the angle determined bu the Schneider method, hence

$$\cos\beta = \frac{\frac{s}{2}}{r} \quad (2)$$

which goes to:

$$r = \frac{s}{2\cos\beta} \quad (3)$$

Replacing ß from (1)

$$r = \frac{s}{2\cos(90-\alpha)} \quad (4)$$

it is possible to calculate the radius r:

$$r = \frac{s}{2\sin\alpha} \quad (5)$$

The length of the curved part of the root (K, between A and B) could be more accurate mathematically described, using the following formula:

$$k = \frac{4\pi\alpha}{360^\circ} \quad (6)$$

Using imaging system, the channel was watched by the point where the canal began to leave the root long axis (point A) to the apical end point (point B).

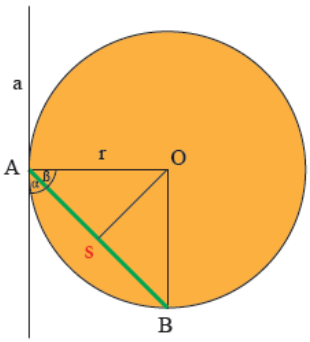

Fig. 3 The root curvature radius.

We considered the channels with an angle of 5 degrees or less, as straight. Finally, 20 curved roots were randomly selected in order to check the accuracy of the method used to determine the curvature (angle and length of the curved part) (fig. 4).

IV. Results

The angles of curvature ranged from 0 degrees to 72 degrees in mesio-distal radiographs and from 0 degrees to 65 degrees in radiographs. The highest range in bucco-lingual incidence was 34.5 mm and in mesio-distal incidence, 49.2mm (table2).

As the length of curved canal has been almost no difference between the calculated and the data obtained by image processing. For maxillary teeth mean difference was 4.7% and for mandibular teeth was 2.2%. Generally, the difference was smaller for the vestibulo- oral incidence than mesio-distal incidence.

Fig. 4 Application to geometrically determine the arc of the circle.

Table 2 Value of radius depending on the angle range.

	Curvature angle	Radius of curvature
MD Incidence	0-72°	49, 2mm
BL Incidence	0 - 65°	34, 5mm

As far as the length of the curved portion is concerned almost no difference has been observed between the mathematically calculated data and the one obtained by actual measurement through digital and image processing. For the maxillary teeth this length was 4.7% and for mandibular teeth it was 2.2%.

Generally, the difference was smaller for the vestibulo-oral incidence than for the mesio-distal one.

DM approach was used for gathering information regarding root canal curvatures, which is usually not obtained from radiographs made under VO incidence.

These unseen curves may play a significant role in the process of cleaning and shaping, as they may lead to loss of working length during root canal instrumentation or to the extension of a proximal canal curvature and thus eventually leading to severe channel thinning or even its perforation.

V. Discussions

Successful root canal instrumentation requires considerable knowledge of root canal curvature. Because the result is mechanical debridation, it significantly affects the radius of curvature and almost all types of teeth have shown that sometimes the bucco-lingual modification time

for the root canal curves can be much lower than the one described in mezio-distal time.

Due to the root canal angulation, it is of great importance for the outcome of root canal process the performance of studies to describe the root canal curves. These studies apply only one parameter to describe the curvature of a channel. Pruett *et al.* proposed that the assessment of canal curvature should be indicated by two measurements: the angle of curvature and the radius of curvature determined mathematically from radiographs [6]. There is a general shortage of clinical studies on canal curvature of maxillary anterior as most investigations have concentrated on the type and variation of the root canal system [7]. Few investigations have been conducted on the specific degree of canals curvature of the maxillary anterior teeth [8,9].

Pruett et al. has determined that it is not possible to define a curve after a root canal obturation based only on the angle in degrees measured according to Schneider method [5], because the channels may have the same angles but different curvature radii depending on the position of the point of maximum curvature and the length of the arc of circle [10].

As such, defining only the angle of curvature is ambiguous; the angle of curvature is independent of radius, and therefore channels with the same degree of curvature may have different radii. In order to enhance the comparability of different studies on the instruments used in curved canals, curvature should be described using the angle of the curve according to its radius and length.

Depending on the degree of curvature and length of the arc of circle it is perhaps possible to establish at least an estimated working length in cases where due to obstacles on the route canal it is not possible to be determined using the apexlocator [11].

VI. Conclusions

The root canal is three-dimensional and the curve and its location vs the apical foramen is usually determined using an X-ray film in two dimensions.

Disto-mesial approach has been used for gathering information on root canal curvatures, which may not usually be obtained using radiographs taken in bucco-lingual incidence. These unseen curves play a significant role in the process of cleaning and shaping, as they may lead to loss of working length during instrumentation or to the extension of a proximal curvature channel thus eventually leading to severe channel thinning or even its perforation.

The results of this study can enhance endodontic therapy predictability and minimize errors during root canal obturation. Proposed method may be valid for planning of endodontic treatment.

Acknowledgment

This research received no specific grant from any funding agency in the public, commercial, or not-for-profit sectors.

References

1. Tanomaru-Filho M, Bier CA, Tanomaru JM, Barros DB (2007) Evaluation of the thermoplasticity of different gutta-percha cones and the TC system. J Appl oral Sci, 15: 131-134.
2. Pérez Heredia M, Clavero González J, Ferrer Luque CM, González Rodríguez MP (2007) Apical seal comparison of low-temperature thermoplasticized gutta-percha technique and lateral condensation with two different master cones. Med Oral Patol Oral Cir Bucal 12, E175-179.
3. Hargreaves MK, Choen S (2011) Choen S Pathways of the Pulp, tenth Edition , Mosby Elsevier:150-153
4. Intraoral radiographic examination. In: Michael Pharaoh: Oral Radiology, 6th Edition. St.Louis: CV Mosby, 2009: pp.150.
5. Schneider SW, Blass B (1971). Comparison of the canal preparation in straight and curved root canals. Oral Surg., 32:271-5
6. Pruett JP, Clement DJ, Carnes DL Jr. (1997). Cyclic fatigue testing of nickel-titanium endodontic instruments. J Endod, 23:77-85
7. Zhu et all. (2003). Reliability of tho methods on measuring root canal curvature. Int.Chin.J Dent., 3:118-121
8. Naoum HJ, Chandler NP, Love RM. (2003). Conventional versus storage phosphor-plate digital images to visualize the root canal system contrasted with a radiopaque medium. J Endod, 29:349-52
9. Tao XL, Peng B, Bian Z, Fan MW. (2007). Survey of root canal curvature in maxillary anterior teeth. Hua Xi Kou Qiang Yi Xue Za Zhi., 25:135-8
10. Zheng QH, Zhou XD, Jiang Y, Sun TQ, Liu CX, Xue H, Huang DM (2009). Radiographic investigation of frequency and degree of canal curvatures in Chinese mandibular permanent incisors. J Endod;35:175-8
11. Martin B, Zelada G, Varela P et al. (2003) Factors influencing the fracture of NI-Ti rotary instruments. Int Endod., 36(4): 262-6

Author: Biclesanu Cornelia
Institute: Faculty of Dentistry
Street: 30, Ghe. Petrascu str. City: Bucharest
Country: Roumanie
Email: corneliabicle@yahoo.co

Required Lokomotor Robot Habilitation and Rehabilitation for Children with Cerebral Palsy during Sleep

E. Dukendjiev

Atypical Prosthetic Laboratory, Riga, Latvia

Abstract — **The child is cast into slow sleep phase (SSP) by exposure to monotonous action of the locomotor robot thus creating movement stereotypes during recurrent day sessions.**

Keywords — **sleep, habilitation, rehabilitation, locomotor robot.**

I. Introduction

Over the recent decades new rehabilitation methods have evolved that are based on exposure of patients to external energy in special brain conditions. *Leon Sazbon* successfully developed rehabilitation of adult patients in vegetative state (2001).

Patients with paediatric cerebral palsy (PCP) aged between 1.5 and 6 years should not be included into this brain state group, besides patients in this group lack muscular and controlling activity and movement stereotypes. The process of habilitation becomes possible only if the imperative acceleration of a child's locomotor activity is applied through exposure to external energy.

Application of the locomotor robot makes it possible to ensure controlled external energy and information flows. Sleep is characterised by inhibition of the organism's active exchange with the surrounding environment. Sleep makes the child available for corrective intervention. The subject of the research is habilitation during slow sleep phase (SSP) ensured by a biotechnical system „child – locomotor robot".

II. Methode and results

The child is cast into SSP by exposure to monotonous action of the locomotor robot thus creating movement stereotypes during recurrent day sessions.

For application of the method a locomtor robot is used [1], which consists of the reciprocal orthotic system that is put on the whole of the child's body; the system with the child placed inside is fastened to a verticalization device, which is mounted on the side frame of the treadmill. The patient's feet that rest upon the treadmill's lane are forced to move with the help of the active reciprocal mechanism. After the robot is switched on, forced alternate movement of the left and rights legs is started thus ensuring locomotive action. The trunk, arms and head are also forced to perform the balancing movements that accompany bipedal walking.

The first stage of SSP (hypnoidal state, drowsiness) quickly passes into the second and third stages that are characterised by development of a slow rhythm in delta range of the encephalogram with the frequency of up to 2 per 1 second. Duration of an individual sleep cycle is 1.5-2 hours on the average, which fully coincides with the duration of the locomotor session (up to 2 hours). To ensure initial resonance processes it is necessary to determine the length (pace) and frequency of step.

Step length ℓ[m] is calculated by Gavanga&Margaria formula at the pace speed on the moving lane

$$V_m \leq 2.7[m/s],\ \ell = 0.362 + 0.257\ V_m \quad (1)$$

Step length depends on the speed at which the lane is moving and the centre-to-centre spacing between the holders on the balance beams of the left and right tensioning.

Step frequency on the treadmill with the average speed of

$$V_m \leq 2.7[m/s] \quad (2)$$

is determined by Gavanga&Margaria formula

$$f\ [1/s] = V_m : 0.362 + 0.257\ V_m \quad (3)$$

The minimum robot treadmill speed is 0.1[m/s]. The average frequencies band is supplied in the table below.

Table 1 The average frequencies

V_m[m/s]	0.1	0.25	1	1.38
f [step/s]	0.24	0.6	1.36	2

Child's fatigue has no effect on the frequency and length of the step because the robot maintains all parameters at a fixed level.

Tests showed that during the sleep phase kids demonstrated appearance of motor reflexes, while brain kept

Y. Dekhtyar et al. (Eds.): *International Symposium on Biomedical Engineering and Medical Physics*, IFMBE Proceedings 38, pp. 163–164, 2013.
DOI: 10.1007/978-3-642-34197-7_42

functioning at the level consistent with a lower stage of ontogenesis. More significant changes in the sleep components were observed in children under 6 years old.

Cerebral conditions cause long-term sleep disorders – hypersomnia, and are mainly manifested by fits of day sleep (catalepsy). Idiopathic hypersomnia is characterised by diurnal drowsiness, which is quite frequently accompanied by the "sleep drunkenness" syndrome. These pathologic processes have also been taken into account and used in the clinical picture of the discussed method.

During "locomotor" sleep the brainstem-induced active inhibition is registered. These changes caused by presynaptic and post-synaptic inhibition of the activity of Gamma and Alpha motor neurons lead to hypomyotonia during SSP and sharp muscle suppression during the fast sleep phase (FSP).

Out of the three vestibular responses (somatic, sensor and vegetative) the somatic responses are the key components of the author's method because they have been secured evolutionarily and ensure preservation of space attitude of the body (spinal reflexes of striated muscles, reflexes). An individual supplements his/her spatial analysis by the visual one (during sessions the light is turned down low), proprioreceptive, tactile, acoustic analysers (during sessions there should be silence in the room). Due to monotonous action on the vestibular apparatus the thresholds of vestibulospinal reflexes of inhibition of sensorial and vegetative processes are reduced.

III. Conclusions

Application of monotonous forced mechanical movement of all body parts triggers the process that does not require rebuilding of the central nervous system (CNS) but merely marks a transition from the forced conditioned reflex to unconditioned reflex activity. The basis for such transition is shaped at the level of microstructure responsible for locomotion control – at the (active or forced) muscle excitatory stage, locomotion centres are released from inhibitory influence and become available for corrective intervention. Due to the links among motor neurons of various muscles and groups, spinal interaction is launched in the motor neuron pools of the spinal cord, which creates rhythmical movement of the step motion pattern.

Reference

1. Dukendjiev E, Rehabilitācijas lokomotora robots. Patenta pieteikums Nr.P-12-15, 30.10.2012

Author: Evgueni Dukendjiev
Institute: Atypical Prosthetic Laboratory
Street: 3 Liepayas Street
City: Riga
Country: Latvia
Email: bionika@zb.lv

Bionics in Planning of Habilitation for Children with Cerebral Palsy

E. Dukendjiev

Atypical Prosthetic Laboratory, Riga, Latvia

Abstract — **Assessment of integral deficit of muscular and controlling activity (which needs to be compensated by external energy and information) comes down to defining the difference between biomechanical and neurological activity in health and in disease by comparing a set of parameters of chronological age in health with the actual child's chronality parameters. The difference between these values creates the aggregate amount of deficit (Δ) followed by the amount of free time (D) and the amount of external energy (E) necessary for habilitation.**

Keywords — **bionics, time/energy, habilitation, cerebral palsy.**

I. Introduction

The process of habilitation of paediatric cerebral palsy is possible only through imperative locomotor activity of a child with the help of external energy and information, i.e., by using a locomotor robot [5]. The First Law of Chronodynamics states that with the help of external energy it is possible to change the chrono density within the local subspace (body), while the amount of the modified chrono density (d) will be equivalent to the amount of energy consumed by the system (ΔE), i.e., ΔE=h-d [1]. This serves the basis for assessing and planning habilitation of children according to the method that allows for compensation of muscular and controlling activity deficit with the help of external energy [2]. The Second Law of Chronodynamics states that the general internal (X) of the object's system is invariable and is determined by the sum of free (D) time (varies depending of the energy input) and linked (H) time, i.e., X=D+H. The subject of this research is determination of the amount of time and energy that are required for habilitation of children with cerebral palsy and cerebrospinal conditions.

II. Methode and results

Assessment of integral deficit of muscular and controlling activity (which needs to be compensated by external energy and information) comes down to defining the difference between biomechanical and neurological activity in health and in disease by comparing a set of parameters of chronological age in health with the actual child's chronality parameters. The difference between these values creates the aggregate amount of deficit (Δ) followed by the amount of free time (D) and the amount of external energy (E) necessary for habilitation.

According to the method suggested by G.Doman [3] the patient's neurological age is determined by two criteria – manual competency and mobility in actual reality and in comparison to those typical for a specific age. The difference Δ_{GD} [in months] between neurological and chronological age serves as quantitative indicator of the deficit of controlling activity. According to the author's method, biomechanical age is determined by several criteria: mass, height, amplitude of flexion-extension angles of the legs, legs shape, and proportions of the body dimensions in the course of growth, which are compared to chronological parameters. The difference Δ_{ED} between biomechanical and chronological age serves as quantitative indicator of the deficit of muscular activity. The overall deficit is determined by adding up the components

$$\Delta = \Delta_{GD} + \Delta_{ED}[\text{months}] \quad (1)$$

Table 1 Based on the data by G.Doman и E.Dukendjiev.

Locomotion type	Age [years]	Daily locomotion norm S [in meters]	
Crawling	1-2	68 ÷ 113	(S_1)
	3-6	75 ÷ 273	
Going on hands and knees	3-4	546 ÷ 720	(S_2)
	5-6	728 ÷ 910	
	from 7 years on	1456 ÷ 2184	
Bipedal walking	3-4	1435 ÷ 1893	(S_3)
	5-6	2184 ÷ 2730	
	from 7 years on	7207 ÷ 9000	

The lane of the locomotor robot [5] should move at the minimum speed of V=0.1 [m/s]. The overall distance is determined by the choice and combination of various locomotion types $S = S_1+S_2+S_3$ [meters]. Locomotive sessions should coincide with the time of consumption of external biochemical energy, i.e., there should be five of them. Duration of an individual session (d) is calculated as follows:

S[m]:V=0.1[m/s]=D[c]:5sessions=d[s]x60x60=d[hours] (2)

Y. Dekhtyar et al. (Eds.): *International Symposium on Biomedical Engineering and Medical Physics*, IFMBE Proceedings 38, pp. 165–166, 2013.
DOI: 10.1007/978-3-642-34197-7_43

If the deficit Δ can be compensated with the obtained parameters, a linear chart is drawn (Table 2).

Table 2 Obtained parameters.

Consumption of external bio-chemical energy		Consumption of external physical energy	
Feeding	Time	Session	Time
Breakfast	30 min	No 1	d_1 sec
Second breakfast	30 min	No 2	d_2
Lunch	40 min	No 3	d_3
Afternoon luncheon	30 min	No 4	d_4
Supper	40 min	No 5	d_5
Total: $t_ф$ =170 min		Total: $D={}_1\Sigma^5 d_i$	

To the functional time $t_ф$ the time for communication, bathroom, etc., in the amount of at least Δt_0=0.8 $t_ф$ should be added. After that the time balance for one day is calculated as follows:

$$t_ф + \Delta t_0 + D \leq 12 \text{ hours} \quad (3)$$

Change in the value of the components is possible providing that the overall resultant amount is constant depending on the condition of a child and the habilitation stage.

In case of the deficit exceeding 2 years (Δ=24 months) the computations are already made on the basis of minimum required time of sessions in one day. It is formally assumed that free time is equal to 12 hours and the number of physiologically required sessions is five. Then, the conditional duration of a session is calculated by the following formulas:

$$\Delta[\text{months}] \text{ x } 30 \text{ [days in one month]} = \Delta[\text{days}] \quad (4)$$

$$\Delta[\text{days}] \text{ x } 12[\text{hours}] \text{ x } 60 \text{ [min]} \text{ x } 60 \text{ [sec]} = \Delta[\text{sec}] \quad (5)$$

$$\Delta[\text{sec}] : 5 \text{ [sessions per day]} = d[\text{sec in one session}] \quad (6)$$

After that the chart is drawn that is patterned after Table 2 and the time balance for one day is obtained. In case of the late start of habilitation process and significant pathologies present the time balance may turn out negative. In that case it becomes necessary to increase the overall duration of habilitation process despite the fact that the obtained results are not going to achieve the intended effect.

For planning the process of habilitation and design of the robot it is necessary to determine the energy expenditure during locomotions on the robot. At a first step the net metabolic capacity ($Ë_в$) is determined, which corresponds to energy expenditure per time unit, where the amount of energy consumption during rest is subtracted from gross registered metabolic capacity by the formula suggested by Mahadeva A.O.

$$Ë_в \text{ [kcal/min]} = 0.047Q + 1.024 \quad (7)$$

where Q[kg] – the child's weight.

The formula is valid at the lane speed of up to 1.34[m/s]. Obtained values serve the basis for planning external biochemical energy – the child's feeding schedule. For calculation of the amount of external physical energy during walking on the lane the calculation table 22 designed by Zatsiorsky V.M. [4] is used. The pace speed of V = 0.1 ÷1.8 [m/s] requires net metabolic capacity $Ë_в$ from 1.13 to 9.97 [W/kg]. Accordingly, during the session that lasts d[sec] the amount of energy required is:

$$Ë_в[\text{W/kg}] \text{ x } d[\text{sec}] = E_{session}[\text{W/sec}] = 0.27E_{session}[\text{kW/hour}] \quad (8)$$

III. Conclusions

For compensation of the overall deficit the external energy for the biotechnical system "child-robot" is required E[kW/hour]= Δ[sec]. $Ë_в$ [W/sec]x 0.27.

References

1. Дюкенджиев Е, Система описания мира. И-во РТУ, Рига, 1996.
2. Дюкенджиев Е, Бионика в реабилитации Церебрального паралича и спиномозговых заболеваний. Том I. И-во РТУ, Рига, 2010.
3. Доман Г. Что делать если у вашего ребёнка повреждение мозга. VINDEX, Рига, 2007.
4. Зациорский В.М. и коллектив. Биомеханические основы выносливости. И-во "Физкультура и спорт", Москва, 1982.
5. Dukendjiev E, Rehabilitācijas lokomotora robots. Patenta pieteikums Nr.P-12-15, 30.10.2012

Author: Evgueni Dukendjiev
Institute: Atypical Prosthetic Laboratory
Street: 3 Liepayas Street
City: Riga
Country: Latvia
Email: bionika@zb.lv

Sole Hardness Effect on Typical Badminton Movement

J.B. Ma, W.W. Shen, and Q. Hao

Faculty of Sports Science, Ningbo University, Ningbo, China

Abstract — **In this study, we used biomechanics testing on the typical badminton movement to compare the shoe hardness effect on the body kinetics response. Six excellent badminton players participated in this test. Heels of ground reaction forces and landing time were collected through force-measuring system and video analysis system. Our results indicate that the peak ground reaction forces was less when wearing the badminton shoes with less hardness sole, but no statistically significant difference. Meanwhile, the heel landing time was less in the shoes with higher hardness sole. Badminton shoes are not only shall protect the foot joints and muscles in exercise or competition, but also possess the function to improve the athlete's reaction speed.**

Keywords — **Badminton shoes, sole hardness, heel landing.**

I. Introduction

Badminton is very popular among people of various ages and its popularity is still in increasing trend [1]. In order to further improve athletic training level of badminton, prevention sports trauma to ensure that the continuous movement of good development, sports biomechanics research is necessary to discuss the inherent theory and applied to daily training guidance [2]. With the badminton sport technology gradually mature, professional badminton shoes to improve the match performance is becoming increasingly important. Just during one match, the players need to do all kinds of complex movements, such as sudden stop, start, jumping and so on. Although there is no direct physical confrontation, but the complexity, sudden and persistent of the movement is very fierce [3]. However, in the competition include flexible mobile footwork and good sudden stop, jumping of technology the realization are dependent on the interaction of between sports shoes with the ground.

Badminton with high-intensity and prolonged exercise collision characteristics, can easily lead to lower extremity injury for badminton player. To analyze the damage situation of 56 athletes of 3 badminton teams in Guangzhou found that foot and ankle part of the damage came in second place (16.98%), the total probability of injury will be as high as 47.16%, if we add up all the injury on thigh, leg, knee, foot and ankle [4]. Although this investigation has regional limitations, but there is still a certain representativeness. There has been a large number of sports shoes research on the effects have shown that a impact on lower limb loading and kinematics of athletic shoes, indeed can change the technical features of the movement [5].

Based on the situation and development of the research, the main point is to take the most common classic badminton footwork of Right-court lunge step as an example to analyze the characteristic of Plantar Foot Pressure by using modern Biomechanics technology, while landing to the court. Simultaneously, comparing the different Biomechanical feature of badminton shoes, we want to go further on the point that the biomechanical characters of lower limbs would be effect by different badminton shoes and potential factors. Finally, we consider that this research about badminton shoes could give some theoretic support the badminton shoes design and material optimization in the future.

II. Methods

The subjects selected were highly skilled badminton players. A total of 6 professional male badminton players volunteered to participate in the present study and meet the criteria in Table 1 and their steady movement.

Table 1 Subject descriptive data (mean and standard deviation in brackets).

Age (years)	Height (cm)	Mass (kg)	Training age (years)
23(3)	174.5(5.6)	65(8.2)	6(3)

Fig. 1 Construction of testing badminton shoes, the difference only in sole hardness.

Soles hardness value according to the experiment, using Asker Durometer (Type C) hardness tester test, the soles hardness values were 58 and 68 (Fig.1). Two Badminton shoes that significant differed only in shoes sole hardness,

Y. Dekhtyar et al. (Eds.): *International Symposium on Biomedical Engineering and Medical Physics*, IFMBE Proceedings 38, pp. 167–169, 2013.
DOI: 10.1007/978-3-642-34197-7_44

in the sole design and other material application wasn't exist significant difference, and the weight of the shoe no obvious difference, were used in the present study. This study is to compare the heel landing time and vertical ground forces by the influence of different the shoes sole hardness of badminton, in the most common classic badminton footwork of Right Front-court Lunge Step in the process of action. The main biomechanical parameters are time and maximum ground vertical forces of contact with the ground to the whole feet fully touch of heel. Kinetic data were collected simultaneously with the kinematic data using a force platform (Kistler, Switzerland) that was placed in the center of the paly platform. Kinematic data of heel landing time were collected using a high-speed video camera at a sampling rate of 500 Hz.

When the testers given by the start instruction, they shall use their most vigorously energy to do Front-court Lunge Step by push the net before the ball, and step on the central region of the force platform. Kinematic data of heel landing time were collected using a high-speed video camera at a sampling rate of 500 Hz. All statistical tests were performed using SPSS (version 17.0) to statistic the data.

III. Results

Results of the ground maximum vertical force which found when wearing the soft soled shoes was slower than when wearing the harder soled shoes (Fig.2). No other significant differences in ground maximum vertical forces were observed between the soft soled shoes and harder soled shoes (p=0.08).

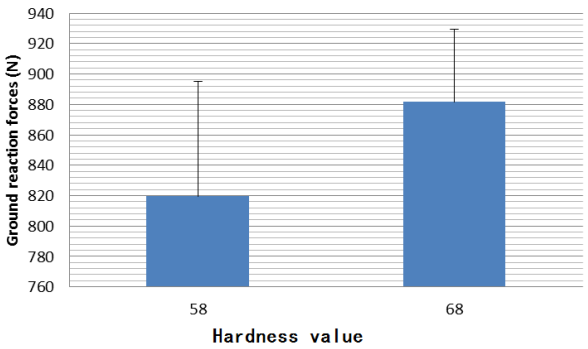

Fig. 2 Ground vertical force comparison in different hardness condition.

Statistics of the heel parts to achieve maximum ground vertical force used time which found wearing the soft soled shoes of the amount of time an average of 0.033 s and wearing the harder soled shoes of the amount of time an average of 0.028 s, soft soled shoes of the amount of time near the significantly greater than the harder soled shoes of the amount of time (Fig.3). Although weren't show statistically significant difference between the soft soled shoes and harder soled shoes (P=0.092). But when analysis to the sole hardness impact on the ground vertical force, this is also a factor cannot be ignored.

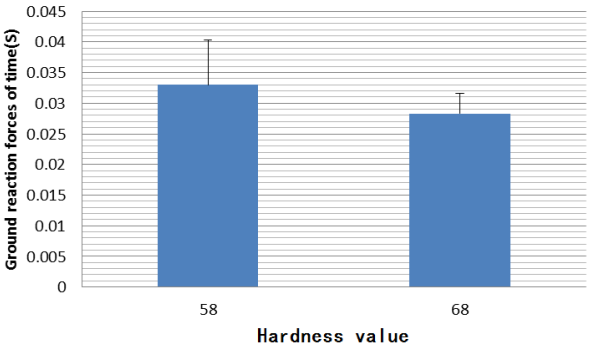

Fig. 3 Peak ground vertical force appearance time in different hardness condition.

Heel landing time is refers to contact with the ground to the whole feet fully touch of heel use time in Subjects completed classic badminton footwork of Right Front-court Lunge Step in the process of action. Statistics of the heel landing time which found when wearing the soft soled shoes was slower than when wearing the harder soled shoes (Fig.4). No other significant differences in heel landing time were observed between the soft soled shoes and harder soled shoes (p=0.535).

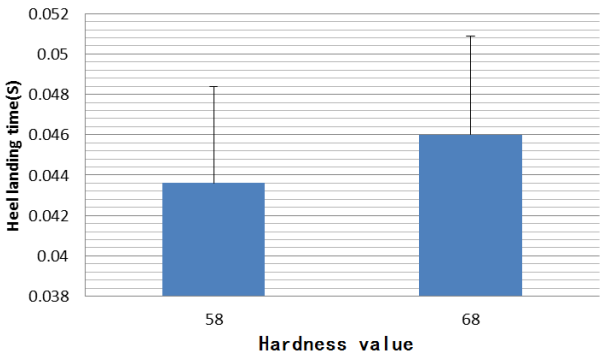

Fig. 4 Heel landing time in different hardness condition.

IV. Conclusions

This study found that the heel of the maximum ground vertical forces and the time of maximum ground vertical forces will change with various hardness badminton shoes

in the action of Right-court lunge step to catch net ball. The greater the hardness of the shoe sole, the ground vertical forces that the heel suffered will be larger, but in the study, it showed no significant difference, the result is same to the early research. After the test for the ground vertical forces when the subjects in walking state with hard and soft shoes, Tsai et al [6] found that the ground vertical forces what the hard shoe suffered is greater than the soft one , but it didn't show the significant difference. Miiani et al [7] also found the same results when he studied the relationship between different sole hardness and sense organs.

Above show that the difference of soles hardness can really change the range of ground vertical forces, the bigger of the soles hardness value, the ground vertical forces is high, and the buffer action will be smaller. But the study found that the changes of sole hardness is no significant difference to the influence of heel landing time, instead of the heel landing time of the low hardness of shoes is short, this is different from the traditional understand. But the results of this study are just from a small sample size explored. Further studies should to increase study subjects and more strict control of experiment action, eventually, find the most suitable of sole hardness needs of badminton sport, in order to provide reliable theoretical data of research and development badminton shoes.

ACKNOWLEDGMENT

This study was supported by Ningbo University's Discipline Project (XKW11D2029), and Research Innovation Foundation (G11JB022).

REFERENCES

1. Lo D, Stark K. (1991) The badminton overhead shot. Nation Strength and Conditioning Association Journal 13: 6–13
2. Tang H P (1993) Three dimensional cinemato-graphic analysis of the forearm movement during a badminton forehand smash. In Proceedings of the 1st world congress of science and racket sports, Liverpool UK
3. Wei Y. (2009) Effects of Sports Shoes on Metatarsophalangeal Joint and Rearfoot Motion in Typical Badminton Footwork. China Sports Science 10: 89-96
4. Yu X, Xu GQ (2005) The Study of Athletic Injuries for Badminton Athlete in Guangzhou. Journal of PLA Institute of Physical Education 24:100-102
5. Clarke TE, Frederick EC, Cooper LB (1983) The effects of shoe cushioning upon ground reaction forces during running. Int J Sports Med, 4: 247-251
6. Tsai YJ, Christopher M (2009) Increased shoe sole hardness results in compensatory changes in the utilized coefficient of friction during walking. Gait Posture 30: 303-306.
7. Miiani TL, Hennig EM, Laforturen MA (1997) Perceptual and biomechanical variables for running in identical shoe constructions with varying midsole hardness. Clin Biomech 12: 294-300

Author: Jiabing Ma
Institute: Ningbo University
Street: Fenghua Road
City: Ningbo
Country: China
Email: jiabingma@yahoo.cn

Novel Synthesis Method and Biomedical Applications of Doped and Undoped Hydroxyapatites and Fluoroapatites

G.V. Nechyporenko and V.F. Zinchenko

A.V. Bogatsky Physical-Chemical Institute of NAS of Ukraine/
Department of Chemistry of Functional Inorganic Materials, Odessa, Ukraine

Abstract — **An essentially new method of synthesis of apatite – based materials in saline melts at moderate temperatures (350-700°C) is developed. The method combines in itself the advantages of the ways of hyper-thermal hydrolysis (a "dry" method) and precipitation from aqueous solutions (a "wet" method). As a reaction media the melts of the equimolar NaCl-KCl system as well as eutectics of the $NaNO_3$ – KNO_3 composition were used. Silver-containing and Palladium-containing apatites were obtained. Those can be used as a materials with antimicrobial and antitumor properties. The obtained materials were identified with a method of the X-ray diffraction phase analysis, and IR – spectroscopy. The developed method of synthesis of the biocompatible nanoscale materials and composites from them is a rather effective and accessible way to practical usage in dentistry, orthopaedics and other areas of medicine.**

Keywords — **Calcium apatites, synthesis, saline melts, biomaterials.**

I. Introduction

The need for reliable and economically expedient biomaterials for treatment of changes and diseases of the musculoskeletal device increased during the last years. Calcium Hydroxyapatite (CaHAP, $Ca_{10}(PO_4)_6(OH)_2$) is the main mineral component of bone tissue and a synthetic form of one of most widely used biomaterials for skeleton reconstruction due to the lack of local or systematic rejection. Calcium Fluorapatite (CaFAP, $Ca_{10}(PO_4)_6F_2$) is an important component of tooth enamel, and materials on its basis are used for fight against caries and for tooth prosthetics [1-3.The main objectives of this work are:

-development of novel methods for the synthesis of apatites.

-improvement and simplification of routes of the synthesis of apatites.

-obtaining nanopowders and studying and biocompatible materials based on apatite.

II. Experimental part

A. Synthesis of Apatites in Saline Melts

Methods of reception of apatites by solid-phase synthesis ("dry" synthesis) and by interaction in aqueous solutions ("wet" synthesis) are well known [3]. Each of these ways possesses, alongside with advantages a number of lacks. We have developed a way of obtaining calcium hydroxylapatite (CaHAP) and calcium fluorapatite (CaFAP) in saline melts at moderate temperatures (500-700°C). Thus there an intensification of process of synthesis, due to acceleration of movement of particles in a melt in comparison to a solid, occurs. As medium for synthesis a chloride melt of NaCl-KCl of equimolar composition, having temperature of fusion 665°C, is used.

For carrying out synthesis of apatites in chloride melt [4] as initial components $CaCO_3$, CaO, $Ca(OH)_2$ (in case of CaHap) or CaF_2 (in case of CaFAP), $NaPO_3$ have been taken. It is shown that at interaction of $CaCO_3$, CaO, $Ca(OH)_2$, and CaF_2 with melt of NaCl-KCl, a decrease of temperature occurs due to formation of incongruently melting compounds $KCaCl_3$; interaction of $NaPO_3$ with NaCl-KCl melt leads to formation of glassy-like compound $Na_6P_4O_{13}$. At obtaining apatites the ratio batch mixture: saline melt 1:1. Synthesis is carried out in muffle furnace at temperature 700ºC during 2 hours. Interaction occurs on following schemes:

$$6NaPO_3+6CaO+3CaCO_3+Ca(OH)_2 \rightarrow Ca_{10}(PO_4)_6(OH)_2+3Na_2CO_3 \quad (1)$$

$$6NaPO_3+6CaO+3CaCO_3+CaF_2 \rightarrow Ca_{10}(PO_4)_6F_2+3Na_2CO_3 \quad (2)$$

To improve the conditions of synthesis in saline melts and increase opportunities for nanosized particles, we proposed a novel, low-temperature synthesis method in a saline melt. Synthesis was carried out in muffle furnace at temperature 350ºC in a saline melt of eutectics KNO_3-$NaNO_3$ during 2 hours [5]. Interaction occurs on following schemes:

$$6KPO_3+10Ca(OH)_2 \rightarrow Ca_{10}(PO_4)_6(OH)_2+6KOH+6H_2O\uparrow \quad (3)$$

$$6Na_3PO_4+CaF_2 \rightarrow Ca_{10}(PO_4)_6F_2+ 18NaF \quad (4)$$

Saline melts methods combining the main advantages of the "dry" (rapidity of process) and "wet" (completeness of reaction and a rather high degree of dispersion of products) methods. In this work the samples obtained through

Y. Dekhtyar et al. (Eds.): *International Symposium on Biomedical Engineering and Medical Physics*, IFMBE Proceedings 38, pp. 170–173, 2013.
DOI: 10.1007/978-3-642-34197-7_45

high-temperature synthesis at 700ºC and low-temperature synthesis at 350ºC are presented. The phase structure and lattices parameters of the obtained materials are determined by X-ray diffraction phase analysis (XRD) on the automated DRON– 3 apparatus by standard techniques.

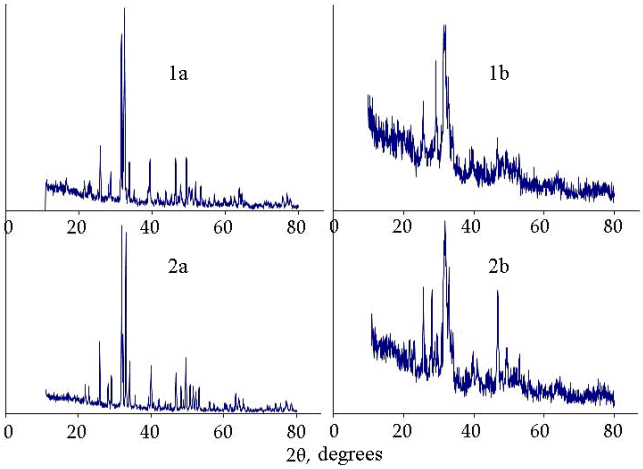

Fig. 1 The X-ray diffraction patterns of the samples of apatites synthesized in saline melts:
1–NaCl-KCl (700°C), 2 - $NaNO_3$ – KNO_3 (350°C);
a-CaHAP, b – CaFAP.

From the diffractograms it is possible to conclude that at a high temperature the synthesized apatites show a regular lattice and a clear separation of the various peaks. For the low temperature synthesis compounds diffraction peaks are broadened, diffuse, and the general background is high and an expressed "halo" is observed in the small angular range, corresponding to the presence of an amorphous (nanostructural) component. It shows the obvious signs of imperfection and small sized crystals (Fig. 1).

The IR – spectra (Fig. 2) of both samples have similar characteristics, namely: in the interval of 3300- 3700 cm^{-1} there is an intensive diffuse ("hydrate") band, and also characteristic bands in the intervals of 500- 1500 cm^{-1} and a 1500-1700 cm^{-1}, peculiar to the vibrations of atoms in PO_4^{3-} and CO_3^{2-} ions, respectively. Distinction consists of notedly lower intensity of a band of absorption of CO_3^{2-} (1410 cm^{-1}, 1464 cm^{-1}) of the samples synthesized in chloride melt (1a, 1b), as compared to such for the samples synthesized in nitrate melt (2a, 2b). It allows to assert about the partial substitution of PO_4^{3-} for CO_3^{2-}, thus, degree of substitution being higher in a case of the sample synthesized by a low- temperature method. A presence of carbonate groups in apatites is a rather useful property, as really in a bone apatite there is plenty enough of the phosphatic groups substituted by carbonate groups, that does it more biocompatible.

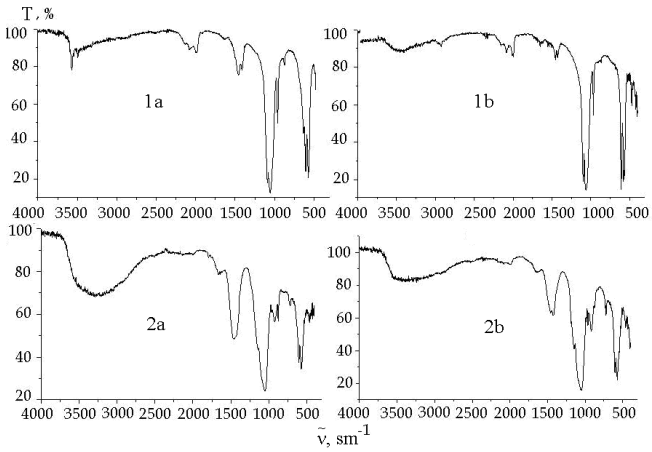

Fig. 2 The IR – spectra of the samples of apatites synthesized in saline melts:
1 – NaCl-KCl (700°C), 2 - $NaNO_3$ – KNO_3 (350°C);
a – CaHAP, b – CaFAP.

The possible application of nano-sized CaFAP(synthesis at 350°C) is the removal of the cause of hypersensitiveness of teeth [6]. In a clinical experiment human paronymous teeth were used known to be hypersensible in the cervical area that were remote on clinical testimonies. On the hypersensitive areas of the tooth a gel was applied with CaFAP nanoparticles sizing about 40-50 nm. After penetration of nanoparticles in the open cells of dentinal microtubules to the depth of a few micrometres - which occured during 15-20 min - the gel was removed. The specific zone was irradiated by a CO_2-laser in the periodic puls-mode with a pulse power of 300 mW. If necessary the irradiation was repeated several times. As a result the microtubules of the hypersensitive teeth were blocked by nanoparticles of CaFAP aggregated with one another and to the walls of microtubules due to the effect of coalescence. This must certainly result in a strong diminution of pain syndrome due to the removal of its initial reason, namely, the dentinal microtubules themselves.The above two microphotos (Fig. 3) show that cells of tubules blocked up from the surface with nanoparticles of fluorapatite material differs little in appearance from the basic material [6].

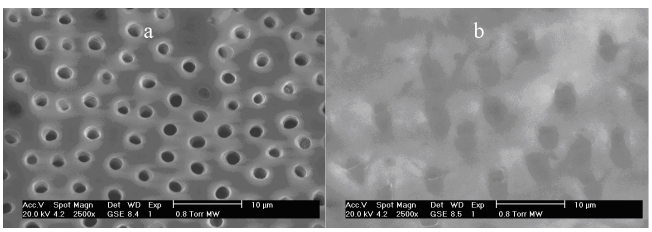

Fig. 3 Microphotos of a zone of a hyper sensitive dentine of tooth before (a) and after laser penetration (b)

B. Surface Modification of CaGAP CaFAP with Ag^+, and Pd^{2+} Ions

In this paper, Silver-containing apatites as promising biocompatible materials with antimicrobial properties, as well as Palladium-containing apatite as anticancer biocompatible materials and catalysts [7-9] are obtained. Usually, at Ag^+ adsorption from solution apatite samples are destroyed with the formation of silver phosphate. It is suggested that the combination of Ag^+ and Ln^{3+} ions, for which the following relations:

$$z_{Ag^+} + z_{Ln^{3+}} = 2z_{Ca^{2+}}, r_{Ag^+} + r_{Ln^{3+}} = 2r_{Ca^{2+}} \qquad (5)$$

where z and r are an ionic charge and radius, respectively, will make it possible to break a barrier of discrepancy and incompatibility of ions of "guest" and "owner". For optimization of the composition of the solution, the sorption of ions of a series of lanthanides is studied previously. Stability of CaHAP increases along Nd→ Eu→ Tb→ Er→ Tm→ Yb→ Lu series, and only for Yb^{3+} and Lu^{3+}, the decomposition of the sorbent doesn't occur. With other lanthanides of the studied series the sorption products to a greater or lesser extent contain silver phosphate, which implies sorbent decomposition. In order to prevent the undesirable process of structural decomposition of the apatites an $AgNO_3$ and $Lu(NO_3)_3$ mixture in solution is used with concentrations of 0,0096 and 0,018 mol/dm^3 respectively. Interaction of a CaHAP sorbent with the solution of the stated composition is observed, however visible destruction of the apatite structure it is not detected. Thus, an essential reduction of concentration of solution that speaks well for a successful sorption of its components, is revealed. In addition, occurence of absorption of a very high (F(R) ≈1) intensity, which correspond to electronic transitions in Ag^+ ions, on spectra of diffuse reflectance in an UV range testifies the process of a sorption. The products of sorption also reveal changes in lattice parameters, namely: an increase in the parameters *a* and *b* of CaHAP lattice. After thorough washing, they become close to those for the initial sample of CaHAP (Table 1). It should be noted that the lavage of the samples with water leads to the gradual ion desorption (leaching Ag^+), ions resulting in a significant decrease in the intensity of the absorption bands mentioned above. From the comparison of presented in Table 1 data one could see that, as a result of Ag sorption, parameters *a* and *b* of CaFAP lattice are markedly increased, and the parameter *c* is some reduced.

As in the case of CaHAP, as a result of sorption of Ag ions, in the spectrum of diffuse reflectance in an UV range appearance of a characteristic absorption band is observed. Reduction of Ag^+- modified apatites with hydrazine, according to the scheme:

$$4Ag^+ + N_2H_4 \rightarrow 4Ag\downarrow + N_2\uparrow + 4H^+ \qquad (6)$$

Results in a gray color of samples, and appearance of characteristic "halo" in the small-angle range of diffractograms, indicating the nanosized structure of particles of Ag (Fig. 4).

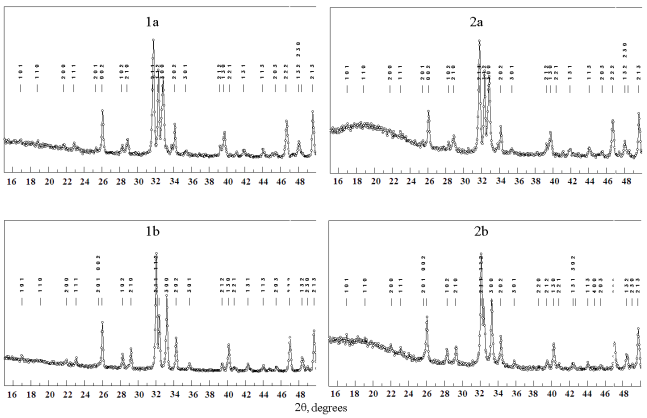

Fig. 4 Patterms of X-ray diffractograms of apatites: 1–before Ag^+ - modifying, 2 – after Ag^+ - modifying; a-CaHAP, b – CaFAP.

Considering important catalytic, antineoplastic and immunomodulatory properties the sorption by CaHAP of Pd^{2+} ions from a $Pd(NO_3)_2$ solution in water is investigated. As appears from Table 1, it appeared successful thanks to approximately equal sizes of the Pd^{2+} and Ca^{2+} ions (respectively, 1.00 Å and 1.14 Å). The sorption is studied on the sample of CaHAP which is synthesized in a low-temperature saline $NaNO_3 – KNO_3$ melt.

The sorption of Pd^{2+} results in some reduction of all parameters of a CaHAP crystal lattice owing to a specified above ratio of the ionic sizes. The sample of a sorbent have got the characteristic for Pd^{2+} ions brown-red color caused by 5d-5d electronic transitions; it is fixed on a diffusie reflectance spectra in the form of a dim band in an UV and visible ranges.

After reaction with hydrazine the sample turns to dark – gray, characteristic for thin-dispersed metallic palladium. Reduction of Palladium by hydrazine (7) occurs to the same scheme as previously stated for Silver (6):

$$2Pd^{2+} + N_2H_4 \rightarrow 2Pd\downarrow + N_2\uparrow + 4H^+ \qquad (7)$$

Table 1 Changes of the lattice parameters of Calcium apatites after sorption of Ag+, Lu3 +, and Pd2 + ions from aqueous solutions and consequent reduction.

Sample, N	The conditions processing	Parameters of lattices, Å a = b	c	Note (color)
1	CaHAP (synthesis in KCl-NaCl melt, 700ºC)	9.4718	6.8576	White
2	Sorption on a sample № 1 from $AgNO_3$+$Lu(NO_3)_3$ solution, drying	9.4789	6.8654	White. An intensive band of absorption in an UV interval is present
3	Processing of a sample № 2 with hydrazine, drying	9.4713	8.6578	Gray. The XRD didn't reveal Ag^+. On diffractograms "halo" in a small-angular range is present
4	CaFAP (synthesis in KCl-NaCl melt, 700ºC)	9.3435	6.8833	White
5	Sorption on a sample № 4 from AgNO +$Lu(NO_3)_3$ solution, drying	9.3719	6.8806	White. An intensive band of absorption in an UV interval
6	Processing of the sample № 5 with hydrazine, drying	9.3757	6.8814	The XRD didn't reveal Ag^+. On diffractograms "halo" in a small-angular range is present
7	CaHAP (synthesis in KNO_3-$NaNO_3$ melt, 350ºC)	9.4108	6.9078	White
8	Sorption on a sample № 7 from $Pd(NO_3)_2$ solution, washing, drying	9.3852	6.8875	Brown-red
9	Processing of the sample № 8 with hydrazine, drying	-	-	Dark – gray. The XRD didn't reveal Pd^{2+}.

III. Conclusions

In the addition to a previously proposed method of synthesis in the saline melt KCl-NaCl (700 ° C), a new, low-temperature method of synthesis from a nitrate saline melt, facilitates the formation of a product with a high content of apatite nanoparticles. It is shown that nano-dispersed CaFAP offers new paths in medical practice for the treatment of dentine hypersensitivity. Also the ion-sorption of Silver and Palladium ions by apatites from solutions, followed by reduction of obtained Silver and Palladium-apatites, can be called promising for medicine, in particular as antimicrobial and anticancer drugs.

References

1. Jarcho M. et al (1992) Retrospective analysis of hydroxyapatite development for oral implant applications. Dental Clinics of North America, vol. 36, pp. 19–26.
2. Tirrell M., Kokkoli E., and Biesalski M. et al (2002)The role of surface science in bioengineered materials. Surface Sci., vol. 500, pp. 61–83.
3. Haifeng Chen, Kai Sun, Zhiyong Tang, Law R., Mansfield J., and Clarkson B. et al (2006) Synthesis of Fluorapatite Nanorods and Nanowires by Direct Precipitation from Solution. Pub.Med. 6(6), pp.1504–1508. DOI: 10.1021/cg0600086.
4. Patent №69746A Ukraine. A way of the reception of hydroxyapatite / Zinchenko V. F., Efryushina N. P., Stamikosto O. V., Eryomin O. G., Kovalevska I. P. Publ. 15.09.2004 [in Ukrainian].
5. Patent №96862A Ukraine. A way of the reception of fluoroapatite / Nechiporenko G.V., Eryomin O.G., Zinchenko V. F., Barylyak A.Ya., Bobytskiy Ya. V. Publ.12.12.2011 [in Ukrainian].
6. Patent №54183 Ukraine. A method for treating dentin hypersensitivity. Barylyak A.Ya., Bobytskiy Ya., Vernish Yo., Vitner E., Zinchenko V. F., Moritz A., Nechiporenko G.V. Publ. 25.10.2010[in Ukrainian].
7. Diaz M., Barba F., Miranda M., Guitián F., Torrecillas R., Moya J. (2009) Synthesis and Antimicrobial Activity of a Silver – Hydroxyapatite Nanocomposite. J. Nanomater., vol. 2009, pp.6 DOI:10.1155/2009/498505.
8. Kohsuke M., Takayoshi H., Tomoo M., Kohki E., and Kiyotomi K. (2004) Hydroxyapatite-Supported Palladium Nanoclusters: A Highly Active Heterogeneous Catalyst for Selective Oxidation of Alcohols by Use of Molecular Oxygen. J. Am. Chem. Soc., vol. 126 (34), pp 10657–10666.
9. Perevodchikova N. (2000) Anticancer chemotherapy. Moscow [in Russian].

Author: Nechyporenko Ganna Vasilivna

Institute: Bogatsky Physical-chemical Institute of NAS of Uraine
Street: 86 Lustdorfska Doroga Str
City: Odessa, 65080
Country: Ukraine
Email: nechiporenkoanna@gmail.com

Author: Viktor Fedosiyovych Zinchenko

Institute: Bogatsky Physical-chemical Institute of NAS of Ukraine
Street: 86 Lustdorfska Doroga Str
City: Odessa, 65080
Country: Ukraine
Email: vfzinchenko@ukr.net

New Biphasic Calcium Phosphate in Orthopedic Surgery: First Clinical Results

S. Petronis[1,2], J. Petronis[1], V. Zalite[3], J. Locs[3], A. Skagers[2], and M. Pilmane[2]

[1] Riga 2nd Hospital, Riga, Latvia
[2] Riga Stradins University, Riga, Latvia
[3] Riga Technical University, Riga Biomaterials Innovation and Development Centre, Riga, Latvia

Abstract — **This study evaluated first results of biphasic phosphate (BCP) ceramic granules with hydroxyapatite (HAp)/ β-tricalcium phosphate (TCP) ratio of 90/10 as bone substitute for reconstruction of the bone defects in orthopedic surgery, such as fracture and fracture non union treatment, primary and revision arthroplasty and chronic osteomyelitis. We evaluated twelve clinical cases of patients who had undergone surgeries with BCP implantation. Follow up period range from 2 to 8 months, on average 4.5 months. The classification of results was based on clinical and radiographic assessments. The size of defects ranged from 32 cm to 1 cm, average 6.42 cm, median 3 cm. The best results were obtained from patients after elective orthopedic procedures and patients with bone defects less than 3 cm.**

Keywords — **Biphasic calcium phosphates, ceramics, bone defects, bone substitutes.**

I. Introduction

Biphasic calcium phosphate (BCP) as bone grafting substitute can be used in orthopedic and trauma surgery, to repair diaphyseal, calvarial and facial bone defects, and also for reconstruction of acetabulum, femoral, mandibular, dental bony and metaphyseal defects, tibial valgisation osteotomy, cervical spondylosis [1]. Porous hydroxyapatite (HAp) is suggested as possible bone graft substitute in maxillofacial surgery [2].

Numerous studies have already revealed the superior osteoinduction of implanted BCP bioceramics consisting of HAp and β-tricalcium phosphate (TCP) over pure HAp. Molecular and cellular interactions between host bone and calcium phosphate bioceramics may be realised by stimulation of bone formation through specific interactions of their surface with the extracellular fluids and cells, ionic exchanges, superficial molecular rearrangement and cellular activity [3]. Experimental and clinical data confirmed bioactivity of synthetic HAp in bone environment through activation of endogenous growth factors, remineralisation of atrophic host bone and integration in natural remodeling of bone [4]. Concerning attempts to find the optimum balance between the two phases in BCP, the results obtained by various researchers appear to differ [1]. It can be explained by the different preparation technologies and parameters like synthesis route and sintering temperature what leads to the differences in microstructure and surface roughness [5].

In current study the BCP ceramic granules with HAp/β-TCP ratio of 90/10 was selected as appropriate. It is supposed that the minor amount of β-TCP in the composition due to relatively faster resorbtion rate compared to HAp will ensure the initial burst of releasing calcium and orthophosphate ions into the biological medium, thus seeding new bone formation. The majority of HAp remaining after resorbtion of β-TCP will act as a tissue scaffold for the complete formation of new bone [6].

Objective of this study is to evaluate first results of BCP ceramic granules with HAp/ β-TCP ratio of 90/10 as bone substitute for reconstruction of the bone defects in orthopedic surgery.

II. Materials and Methods

A. Preparation of BCP Ceramic Granules

Calcium deficient hydroxyapatite (CDHAp) was synthesized by aqueous precipitation technique like described before [7] where calcium hydroxide and phosphoric acid was used as raw materials following the reaction $Ca(OH)_2 + H_3PO_4 \rightarrow Ca_{10-x}(HPO_4)_x(PO_4)_{6-x}(OH)_{2-x} + H_2O$. The filtered precipitates was formed in to the granules, dried and sintered at 1150 ^oC for 2 hours. The sintered granules were sieved using vibrational sieves to gain the granular fraction in sizes from 1 to 1.4 mm.

B. Characterization Technologies

The microstructure of CDHAp and BCP ceramics were investigated using field emission scanning electron microscope (SEM) Tescan Mira/LMU. A Fourier transformation infrared spectrometer (FT-IR) (Varian Scimitar 800) in the wave number range 4000–400 cm−1 was used for sample investigations in the transmission mode in a dry air atmosphere using the KBr pellet technology. For crystalline phase identification, X-ray diffraction (XRD) was measured on a powder X-ray diffractometer (PANalytical X'Pert Pro), using Cu radiation produced at 40 kV and 30 mA. The x-ray

Y. Dekhtyar et al. (Eds.): *International Symposium on Biomedical Engineering and Medical Physics*, IFMBE Proceedings 38, pp. 174–177, 2013.
DOI: 10.1007/978-3-642-34197-7_46

images were made with Philips Bucky Diagnost with digital processing device Philips PRC Eleva Corado.

C. Clinical Cases

This study is a retrospective evaluation of twelve randomly chosen clinical cases of patients who had undergone surgeries with BCP implantation. Follow up period range from 2 to 8 months, on average 4.5 months.

Three patients were male and nine female. Age ranged from 22 year to 84 year with mean age 62.2 years.

Bone defects were classified according to the etiology and morphology of the bone defect. Regarding cause of defects, they were divided into the following: (1) orthopedic defects- 5 patients, resulting from elective procedures such as arthroplasty (primary and revision), (2) traumatic defects- 4 patients, resulting from fractures and fracture non unions, (3) defects due to infection- 3 patients with osteomyelitis.

Table 1 Description of age, gender, affected bone and diagnosis

Gender	Age	Bone	Diagnosis
M	75	Tibia	Osteomyelitis
F	59	Humerus	Fracture
F	58	Tibia	Osteomyelitis
F	54	Tibia revision	Knee endoprothesis
F	76	Acetabulum	Hip osteoarthritis
F	73	Femur revision	Hip endoprosthesis
F	83	Humerus	Fracture
M	50	Tibia	Osteomyelitis
F	53	Tibia	Fracture
F	84	Femur revision	Hip endoprosthesis
M	22	Femur	Pseudarthrosis
F	60	Femur revision	Hip endoprosthesis

Regarding morphology, defects were divided into: (1) cavity bone defects- 6 cases and (2) segmental bone defects- 6 cases. Bone defects were measured on the digital x-ray images.

Surgical procedures were performed according to general principles used for bone defect treatment: traumatic cavities filled directly with bone substitute and in other cases debridement and necrectomy were performed prior to application of bioceramics. Patients with osteomyelitis were chronic cases and surgery was performed in remission phase.

D. Clinical and Radiographic Evaluation

The classification of results was based on clinical and radiographic assessments. For clinical evaluation, the functional treatment of the operated limb, without pain, were measured, and scores ranging from 0 to 3 were given as follows: 0- absence of movement of the operated limb, 1- up to 30% of normal function, 2- up to 60% of normal function and 3- preoperative or normal range of motion. The radiographic analysis consists of the presence of integration of the biomaterial and callus formation. The following scores were given: 0- no integration of bioceramics and no callus formation, 1- moderate callus formation and bioceramics integration, 2- good callus formation and bioceramics integration and 3- bone fully healed and very good bioceramics integration.

The final results represent combination of both parameter scores: 0-2 poor results, 3 moderate results, 4-5 good results and 6- excellent results. Classification and evaluation method is similar as in recent publications [8].

Tolerance of biomaterial and complications were recorded.

III. Results and Discussion

A. BCP Ceramic Bone Grafting Material

As it can be seen in Fig. 1, the CDHAp particles (Fig. 1 a) after precipitation are of rod shape form with 30 to 50 nm diameter and 150 to 200 nm length. The synthesized BCP ceramic granules are of irregular form (Fig. 1 b) with grains sizes around 500 nm and minor micro porosity with pore sizes around 200 nm (Fig. 1 c).

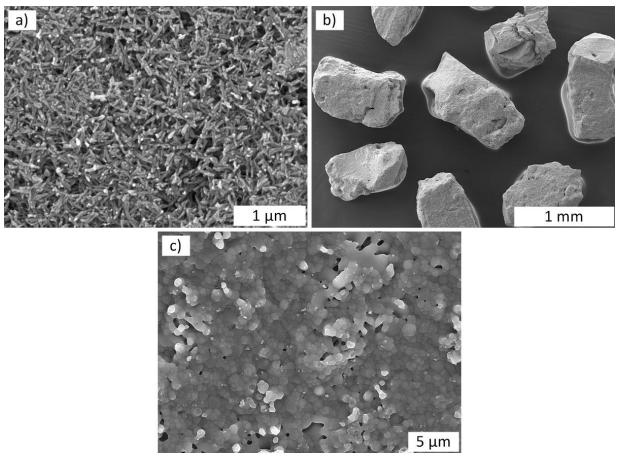

Fig. 1 SEM micrographs of: a) precipitated CDHAp particles; b) and c) BCP ceramic granules.

The XRD pattern (Fig. 2) of sintered BCP ceramics confirms the presence of two phases HAp and β-TCP in the sample with a mass ratio of 90 to 10. The β-TCP characteristic

maxima located at 2θ=31 and 34,5° are marked with arrows. The calibration curve for XRD was used for performing quantitative analysis and determination of the HAp/ β-TCP ratio. In the FT-IR spectra (Fig. 2) only the HAp and β-TCP characteristic absorption maximums can be seen.

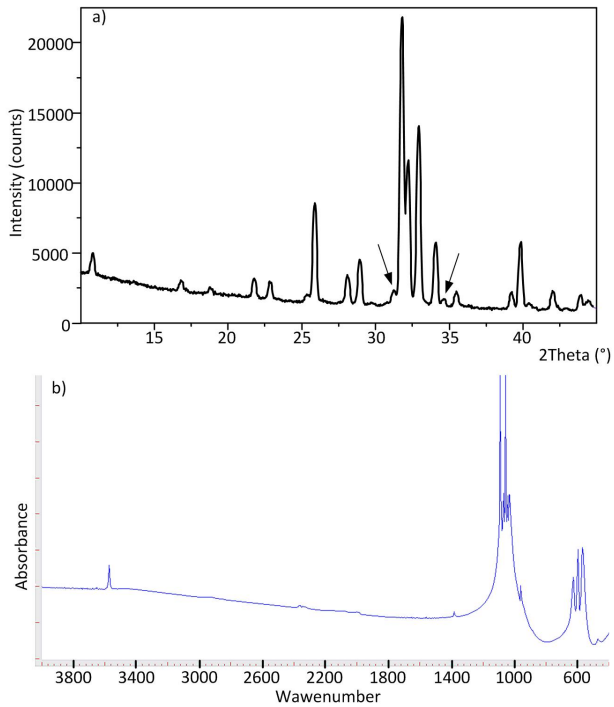

Fig. 2 XRD pattern (up) and FT-IR spectra (down) of BCP ceramics.

B. *Clinical Results*

From twelve procedures performed we found seven patients with good results (combined score 4-5), five patients with moderate results (combined score 3).

In the group of nine patients with orthopedic defects combined score average was 4.2 (range 3 to 5). In the group of four patients with traumatic defects combined score average was 4 (range 3 to 5). And in the group of three patients with osteomyelitis average score was 3.67 (range 3 to 5).

Regarding morphology of the bone defect from six cases with cavity defect combined score average was 4.3 (range 3 to 5) and in group of six patients with segmental defect combined score average was 4.2 (range 3 to 5). In five cases bone defect was more than 3 cm with combined score average 3.6 (range 3 to 5). From those two (40%) had good result (score 4 to 5) and three (60%) had moderate result (score 3). In seven cases bone defect was smaller than 3 cm with combined average score 4.17. From those five (70%) had good result (score 4 to 5) and two (30%) had moderate result (score 3).

The size of defects ranged from 32 cm to 1 cm, average 6.42 cm, median 3 cm.

The amount of bioceramics used to fill bone defects on average was 22.5 grams (range 5 g to 60 g).

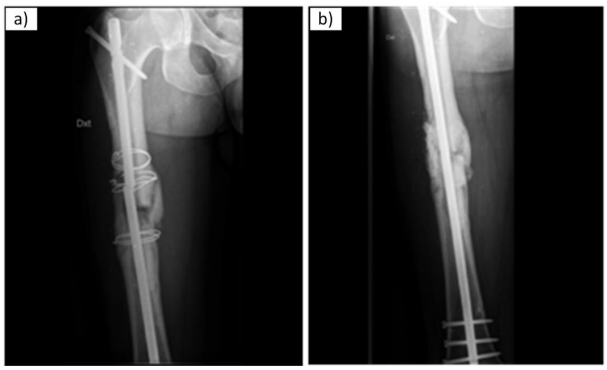

Fig. 3. X-ray image of non union of the femur: a) preoperative x-ray and b) follow up at 4 months after repeated surgery with BCP application.

Using combined score consisting of clinical and radiographic evaluation our overall results showed that in short term 7 out of 12 patients had good results and rest 5 patients had moderate results.

Comparing patients with different cause of bone defects we found that the best results are after elective orthopedic procedures with good results in four cases out of five. Trauma patients had good results in two cases out of four (Fig. 3 and 4). Among three cases with osteomyelitis one was with good and two with moderate results (Fig. 5).

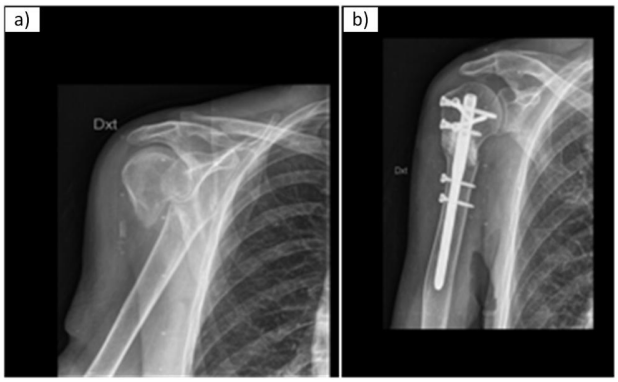

Fig. 4 X-ray image of fracture of the proximal humerus: a) before surgery and b) postoperative follow up at 5 months.

Regarding size of the bone defect we find better results for patients with bone defect less than 3 cm. In this group five out of seven had good results. We also should take into account that patients with bigger bone defects had more invasive surgery that influence overall result.

Two patients had minor complications- transient inflammation at surgical site. One was patient with osteomyelitis and one case was after complex fracture of tibia.

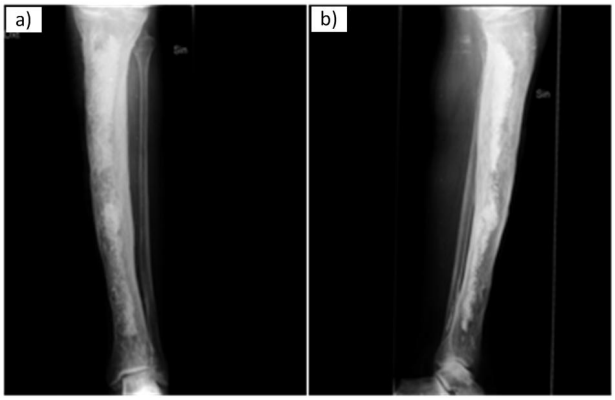

Fig. 5 X-ray image of (a) postoperative anterior and (b) lateral view after debridement and filling large bone defect with BCP in patient with chronic osteomyelitis of tibia shaft.

IV. Conclusions

This study showed efficacy of new BCP bioceramics HAp/b-TCP ratio of 90/10 in the reconstruction of the bone defects caused by trauma or associated with elective orthopedic procedures such as primary or revision arthroplasty. We also had positive experience using bioceramics to fill bone defects after osteonecrectomy in chronic osteomyelitis. And results even after treatment of very large bone defects (32 cm) are promising.

The best results were obtained from patients after elective orthopedic procedures and patients with bone defects less than 3 cm.

Our bioceramics is good alternative to fill small and large bone defects both in cortical and cancellous bone areas and could be good alternative for bone defect reconstruction.

First results are positive and we will keep follow up for these patients to collect late clinical data of bone defect healing and biomaterial osseointegration.

Acknowledgement

This work has been supported by the European Social Fund within the project "Multidisciplinary Research in Biomaterials Technology of New Scientist Group", No.2009/0199/1DP/1.1.1.2.0/09/APIA/VIAA/090.

References

1. S. V. Dorozhkin (2012) Biphasic, triphasic and multiphasic calcium orthophosphates. Acta Biomaterialia 8:963–977. doi:10.1016/j.actbio.2011.09.003.
2. R.E. Holmes, S.M Roser. (1987) Porous hydroxyapatite as a bone graft substitute in alveolar ridge augmentation: a histometric study. Int J Oral Maxillofac Surg 16:718-28
3. F. Barrere, van Blitterswijk CA,K. de Groot (2006) Bone regeneration: molecular and cellular interactions with calcium phosphate ceramics. Int J Nanomedicine 1:317-32
4. A. Skagers, I. Salma, M Pilmane, et al..Tripple confirmation for bioactivity of synthetic hydroxyapatite (Hap) in bony environement//Termis EU 2011 Annual Meeting Tissue Engineering&Regenerative Medicine International Society 7.-10. June 2011, Granada, Spain.
5. M. Bohner, L. Galea, N. Doebelin (2012) Calcium phosphate bone graft substitutes: Failures and hopes. J Eur Ceram Soc In press doi:10.1016/j.jeurceramsoc.2012.02.028
6. A. Kolk, J. Handschel, W. Drescher. (2012) Current trends and future perspectives of bone substitute materials - From space holders to innovative biomaterials. J Carnio Maxill Surg. In press. doi:10.1016/j.jcms.2012.01.002
7. K. Salma, Z. Irbe, D. Jakovlevs. et al. (2011) Advanced Materials Research 222:255-258. doi:10.4028/www.scientific.net/AMR.222.255
8. C.A. Garrido, S.E. Lobo, F.M. Turibio,et al..(2011) Biphasic calcium phosphate bioceramics for ohtopaedic reconstructions: clinical outcomes. Int J Biomater 2011:129727. doi:10.1155/2011/129727

Author: Sandris Petronis
Institute: Riga 2nd Hospital
Street: Gimnastikas 1
City: Riga
Country: Latvia
Email: sandris.petronis@apollo.lv

Autologous Fibrin Mixed with Biphasic Calcium Phosphate Bioceramic Granules Activates Encapsulation in Soft Tissue Environment

I. Salma[1], G. Salms[2], A. Skagers[2], M. Pilmane[3], and L. Feldmane[4]

[1] Riga Technical University, Riga Biomaterials innovation and development centre, Riga, Latvia
[2] Riga Stradins University, Department of Oral and Maxillofacial Surgery, Riga, Latvia
[3] Riga Stradins University, Institute of Anatomy and Anthropology, Riga, Latvia
[4] Riga Stradins University, Department of Pathology, Riga, Latvia

Abstract — **The physical, chemical and biological properties of both biphasic calcium phosphate (BCP) bioceramics and fibrin scaffolds may be cumulated for preparing advanced bone substitutes. Aim of experimental study was to evaluate histological response on implantation of synthetic biphasic HAp/TCP bioceramic granules mixed with autologous plasma derived fibrin scaffold in subcutaneous tissue of rabbits.**

Subcutaneus implantation of BCP granules with fibrin scaffold was performed in 6 experimental animals. BCP granules without fibrin scaffold were implanted on the control side.

After 6 weeks tissues were prepared for detection of apoptosis using TUNEL method. Routine histological method - staining with hematoxilin and eosin and evaluating with Leica BME microscopy was used for obtaining a review picture.

Routine histological examination after implantation of fibrin scaffold with BCP bioceramic granules showed increased number of cells, mainly plasmatic and gigantic cells also lymphocytes and eosinophils, pronounced angiogenesis and increased formation of fibrous tissue capsule compared with control side.

From our results we can conclude that plasma derived fibrin scaffold activates encapsulation of BCP bioceramic in soft tissue environment. This phenomenon may serve as a possibility for biological retention of drugs, growth factors and/or cells.

Keywords — **fibrin scaffold, calcium phosphate bioceramic, in vivo experiments, autologous plasma.**

I. Introduction

The combination of natural or synthetic polymers with bioceramics has demonstrated the ability to enhance cellular interaction, encourage integration into host tissue, and provide tunable material properties and degradation kinetics.

Fibrin is natural protein polymeric scaffold for invasion of inflammatory and repair cells into wound environments and in such way enables the retention of therapeutic proteins from fibrin matrices without additional enzymatic or synthetic cross linking factors [1] and serve as versatile scaffold for tissue engineering [2]. Bioceramics and comercial fibrin sealants composites have been widely used in various types of bone surgery because of their adhesive and haemostatic properties, but the role of fibrin sealants in bone healing is controversial. Fibrin sealants are biological adhesives that mimic the final step of the coagulation cascade. The components are extracted from human plasma, except for antifibrinolytic agent and calcium chloride.

The ideal bone substitute should be biocompatible, biodegradable at the expense of bone growth and mouldable, with sufficient mechanical properties to fill and restore bone defects [3]. The physical, chemical and biological properties of both biphasic calcium phosphate (BCP) bioceramic and fibrin scaffolds may be cumulated for preparing advanced bone substitutes.

In our study autologous rabbit plasma was used as a raw material for fibrin scaffold fabrication.

Plasma has all the essential characteristics to be an excellent support biomaterial – to interface with biological systems for the purpose of treating or replacing any type of tissue or organ. Plasma is well tolerated by patients and is replaced by tissue after integration.

Aim of experimental study was to evaluate histological response on implantation of synthetic biphasic HAp/TCP bioceramic granules mixed with autologous plasma derived fibrin scaffold in subcutaneous tissue of rabbits.

II. Materials and methods

A. Preparation of BCP Ceramic Granules

Calcium deficient hydroxyapatite (CDHAp) was synthesized by aqueous precipitation technique [4]. The filtered precipitates was formed in to the granules, dried and sintered at 1150 ^{o}C for 2 hours. In this study the BCP ceramic granules with HAp/b-TCP ratio of 30/70 were selected as appropriate. The sintered granules were sieved using vibrational sieves to gain the granular fraction in sizes from 0.5 to 1.0 mm (Fig.1).

Y. Dekhtyar et al. (Eds.): *International Symposium on Biomedical Engineering and Medical Physics*, IFMBE Proceedings 38, pp. 178–181, 2013.
DOI: 10.1007/978-3-642-34197-7_47

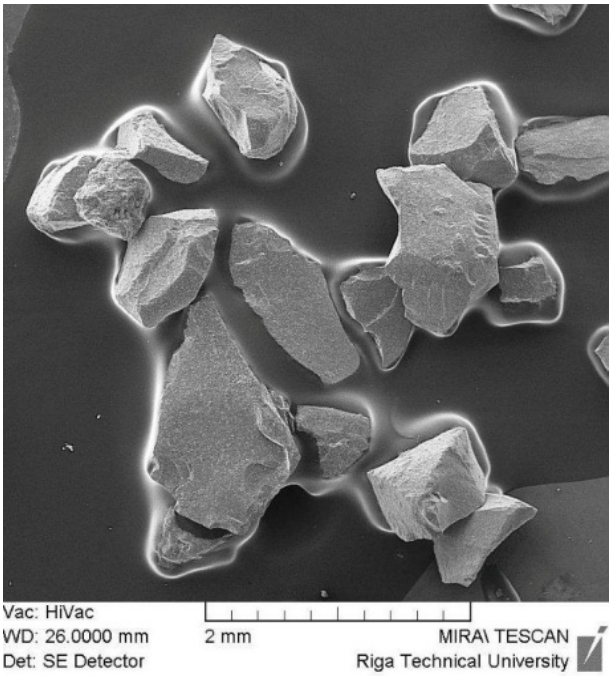

Fig. 1 Scanning electron microscopy of the granules.

B. *Preparation of Bioceramic and Plasma Derived Fibrin Scaffold Composites*

We slightly modified already existing method for plasma scaffold preparation [5]. To obtain the plasma, blood has been spinning for 10 minutes at 3000 rpm in the centrifuge Compact Star CS 4.

For the preparation of the bioceramic and plasma scaffold composites, antifibrinolytic agent tranexamic acid (Amchafibrin 500mg/5ml; Rottapharm) is dissolved in the autologous rabbit plasma and then calcium gluconate (Calcium Sopharma 8,94mg/ml; Sopharma) and 0.5g BCP ceramic granules are added.

The suspension obtained is stored in an incubator at 37^0 C for 20 minutes. Different tests have been made to obtain the best possible scaffold. The quantities of its components have been changed: plasma (0.5 ml and 0.8 ml; tranexamic acid (0.1ml and 0.2 ml); calcium gluconate (0.25ml and 0.5 ml). The following quantities yield the best results – gel form plasma derived fibrin scaffold: plasma 0.5 ml, tranexamic acid 0.2 ml and calcium gluconate 0.25ml (Fig.2).

C. *Implantation in Vivo and Evaluation of Histological Results*

The Animal Ethics Committee of Latvian Food and Veterinary Administration approved the use of 6 New Zealand male rabbits for this morphofuncional study. The rabbits

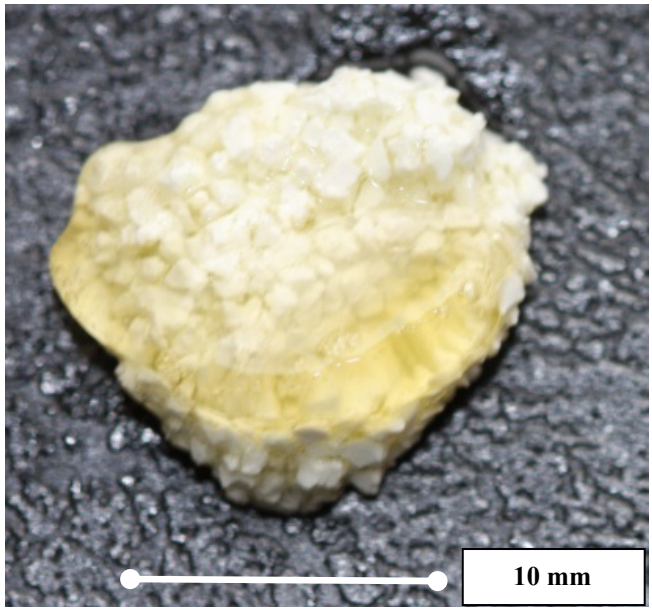

Fig. 2 Autologous plasma derived fibrin scaffold with BCP granules.

received general anesthesia with Ketamini 15 mg/kg and Midazolami 0.5 mg/kg i/m and additional local anesthesia with Sol. Lidocaini 2% (4 mg/kg). 2 cm incision was made on the right side of lumbar area and 0.5 g Hap/TCP granules with fibrin scaffold were implanted subcutaneously. 0.5 g Hap/TCP granules without fibrin scaffold were implanted on the control side.

The subdermal layer was closed with 4-0 vicryl and the skin with 4-0 prolene sutures. Animals were narcotized and euthanasia by air embolisation was performed after 6 weeks.

Blocks of soft tissue from experimental and control side were harvested and fixed in Stefanini solution. Then tissues were prepared for detection of apoptosis using TUNEL method (Roche Applied Science, Penzberg, Germany). In the chosen 5 visual fields positive apoptotic cells out of 100 total visual cells were counted. Apoptotic index was determined: apoptotic cell correlation to total cells. Routine histological method - staining with hematoxilin and eosin and evaluating with Leica BME microscopy was used for obtaining a review picture.

III. Results

Six weeks after the implantation of plasma derived fibrin scaffold with BCP bioceramic granules routine histological examination showed increased number of cells, mainly plasmatic and gigantic cells also lymphocytes and eosinophils and increased formation of fibrous tissue capsule (Fig. 3).

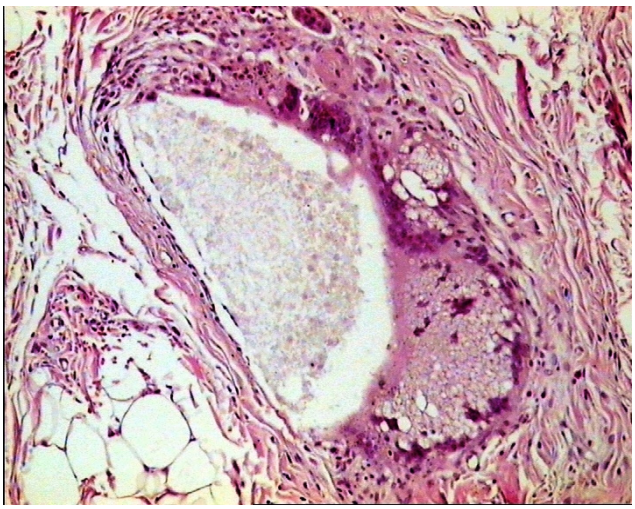

Fig. 3 Fibrous tissue capsule around BCP bioceramic granule with fibrin scaffold (h/eo, x 100).

BCP bioceramic with autologous plasma derived fibrin scaffold initiate pronounced angiogenesis around the implant (Fig. 4).

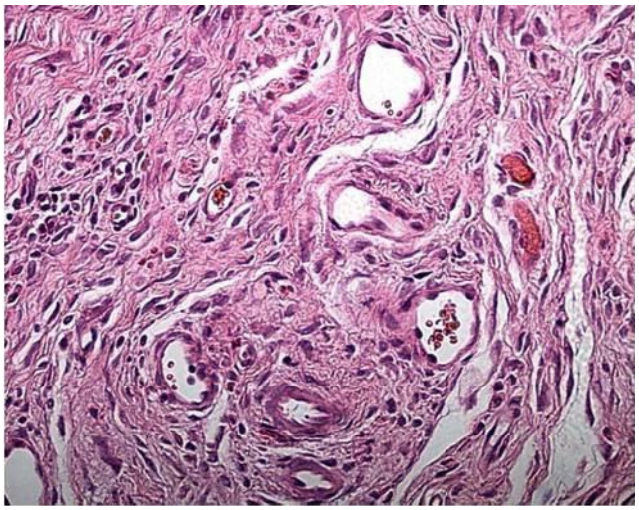

Fig. 4 Formation of new vessels in soft tissue around BCP bioceramic granule with fibrin scaffold (h/eo, x 200).

The evaluation of apoptosis in surrounding soft tissue 6 weeks after implantation of BCP bioceramic with fibrin scaffold showed apoptotic cells in moderate amount: apoptotic index– 0.424 (Fig. 5).

A large number of soft tissue cells were apoptotic after implantation of BCP bioceramic without fibrin scaffold: apoptotic index-0.761 (Fig. 6).

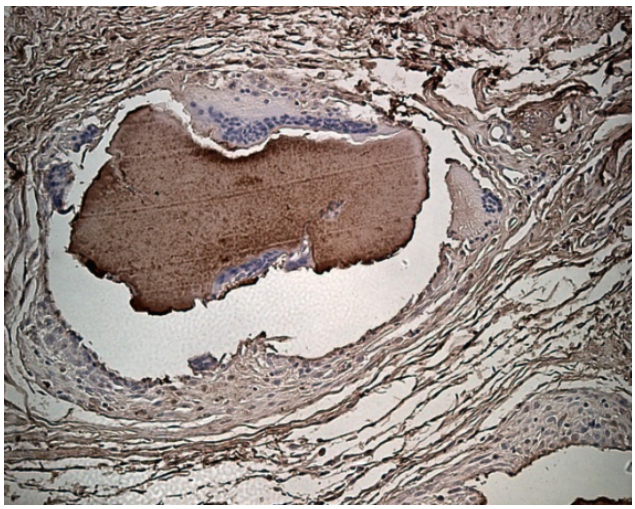

Fig. 5 Apoptosis (brown nuclei) in soft tissue around BCP bioceramic granules with fibrin scaffold (TUNEL, x 100).

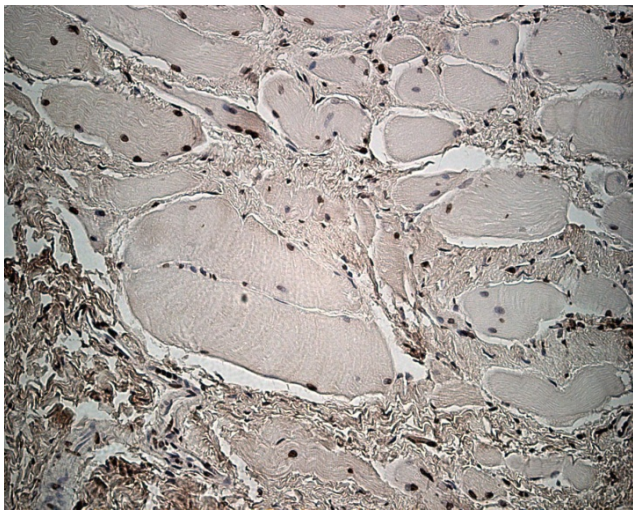

Fig. 6 Apoptosis (brown nuclei) in soft tissue around BCP bioceramic granules without fibrin scaffold (TUNEL, x 100).

IV. Discussion

The combination of fibrin scaffold and bioceramic may result in their properties being accumulated. The physical properties of this composite are enhanced, with better mechanical resistance than in ceramic alone [6, 7]. Combining bioceramic with fibrin scaffold provides a mouldable and self-hardening composite biomaterial. In our experiments we also achieved simply preparable gel form fibrin scaffold from autologous plasma. From blood collection until ready fibrin scaffold 25-30 minutes are required.

Furthermore, initial stability of this bone filler may be achieved through its adhesion to the walls of the bone defect. The biological properties might also enhanced, thanks to the positive role played by fibrin on vascularization and blood vessel growth in bone defects [8]. Fibrin mediates platelet and endothelial cell spreading, fibroblast proliferation and capillary tube formation [9]. In our experiments with fibrin scaffold implantation we found pronounced stimulation of angiogenesis.

Fibrin scaffold has double function in tissue engineering. First as scaffold for incorporation of cells, proteins, other biologic and pharmaceutical agents and second as immobilizier of different substances in other biomaterials to provide long time retention in site of clinical necessity and controlled release is in current evaluation.

V. Conclusions

Fibrin scaffold acts like a glue binding BCP granules improving handling during surgical procedure. From our results we can conclude that plasma derived fibrin scaffold activates encapsulation of BCP bioceramic in soft tissue environment. This phenomenon may serve as a possibility for biological retention of drugs, growth factors and/or cells. The intra-operative preparation of these composites makes it possible to add bone growth factors or autologous osteoprogenitor cells prior to bone reconstruction. The bone growth factors and autologous osteoprogenitor cells associated with the bioceramic-fibrin composites should provide surgeons with tissue engineered grafts with enhanced integrative properties. Our histological evaluation deals with early stage of autologous bio-scaffold integration in subcutaneous tissue of rabbit and can confirm only biocompatibility of such material in general. Possibility of osteoinduction and another signs of bioactivity may be evaluated in long-term experiment.

Acknowledgment

The European Social Fund within the project “Multidisciplinary Research in Biomaterials Technology of New Scientist Group”, No.2009/0199/1DP/1.1.1.2.0/09/APIA/VIAA/090.

References

1. Soon ASC, Stabenfeldt SE, Brown WE, Barker TH (2010) Engineering fibrin matrices: the engagement of polymerization pockets through fibrin knob technology for the delivery and retention of therapeutic proteins. Biomaterials 31:1944-54
2. Ahmed TA, Dare EV, Hincke M (2008) Fibrin: a versatile scaffold for tissue engineering applications. Tissue Eng Part B Rev 14:199-215
3. Bauer T, Muschler G (2000) Bone graft materials. An overview of the basic sciences. Clin Orthop Rel Res 371:10-27
4. Pelss J, Loca D et al (2011) Release of anticancer drug doxorubicin from biodegradable polymer coated porous hydroxyapatite scaffolds. Adv Mater Res 284-286:1770-1773
5. Negri S, Federici G, Farinato S, Fila C (2009) Human plasma as a dermal scaffold for the generation of a completely autologous bioengineered skin. J Clin Rehab Tissue Eng Res 13(47):9211-9216
6. Wittkampf A (1989) Fibrin sealant as sealant for hydroxyapatite granules. J Cranio Max-Fac Surg 17:179-181
7. Marini E, Valdinucci F et al (1994) Morphological investigations on bone formation in hydroxyapatite-fibrin implants in human maxillary and mandibular bone. Cells Mater 4:231-246
8. Nakamura K, Koshino T, Saito T (1998) Osteogenic response of the rabbit femur to a Hydroxyapatite thermal decomposition product fibrin sealant mixture. Biomaterials 19:1901-1907
9. Mosesson MW (2005) Fibrinogen and fibrin structure and functions. J Thromb Haemost 3(8):1894-904

Author: Ilze Salma
Institute: Riga Technical University, RBIAC
Street: Pulka3/3
City: Riga
Country: Latvia
Email: salma.ilze@gmail.com

Engineering of the Hydroxyapatite Cell Adhesion Capacity

Yu. Dekhtyar[1], V. Bystrov[2], A. Bystrova[2], A. Dindune[3], A. Katashev[1], I. Khlusov[4], E. Palcevskis[1], E. Paramonova[2], N.N. Polyaka[1], M. Romanova[1], R. Sammons[5], and D Veljović[6]

[1] Riga Technical University, Riga, Latvia
[2] Institute of Mathematical Problems of Biology, Pushchino, Russia
[3] Institute of Inorganic Chemistry, Riga Technical University, Salaspils, Latvia
[4] Tomsk Branch of «Russian Ilizarov Scientific Centre «Restorative Traumatology and Orthopedics», Tomsk, Russia
[5] University of Birmingham, Birmingham, UK
[6] University of Belgrade, Belgrade, Serbia

Abstract — **The general adhesion theory is the fundament to explain cell attachment to a bioimlplant surface in a human body. Electrical potential of the surface could be employed to control attachment. The paper demonstrates that the electrical potential may be engineered due to hydrogenation of hydroxyapatite. Such the procedure enhance attachment of osteoblast and generation of tissue. The Sr and Si doped hydrohyapatite demonstrates higher ability to be engineered by hydrogenation in contrast with undoped and Ag doped materials.**

Keywords — **hydroxyapatite, doped hydoxyapatite, osteoblasts, electrical charge engineering.**

I. Introduction

In spite of the high success in understanding of human cells interaction with bone replacing bioimplants in a human there are still biocompatibly problems. These often are connected with eligible human cells incapability for attachments to the implant surface that influence regeneration of bone tissue.

Following the general adhesion theory [1] attachment of the cell to the bioimplant is controlled in particulary by an electrostatic force contributing interaction between the cell and the implant. Generally the electrical communication could be engineered owing to a surface electrical potential of the implant. The potential could be supplied by the both external sources and the surface itself.

Hydroxyapatite (HAP) is the popular material for the bioimplants. The technologies that are typically in use to engineer the electrical charge of the HAP employ its electrical polarization due to the external electrical field [2] or because of radiation [3]. In both cases the opposite surfaces of the HAP based implant are acquiring the unlike (in sign) charges. Therefore differently charged implant surfaces could induce cell processes in the opposite directions, that is undesirable. Therefore the considered technologies are restricted.

However to reach the uniformity of the electrical charge distribution a reconstruction of the HAP ion subsystem of the entire surface layer could provide polarization vectored from/to the bulk. By this way the uninformety of the charge distribution could be reached.

To improve biocompatibility and stability of HAP properties the doping is applied.

The article is targeted to demonstrate a possibility of technology for electrically functionalization of the surfaces of differently doped HAP (Ar, Sr, Si).

II. Proton tunneling towards functionalyzation

The first principles methods to study proton transfer peculiarities in HAP were employed in [4]. *Ab initio* quantum-chemical calculations (with HyperChem and Gaussian98 code, HF, 6-31G(d)) were held to investigate the optimized HAP structure and energy barriers on possible proton transport ways.

The significant property of the HAP is an existence of OH^- chains [5] along crystallographic c-axes in columns formed by Ca-triangles and phosphate groups. HAP occurs in two crystallographic space groups – monoclinic P21/b and hexagonal P63/m, with known cell parameters [6]. In hexagonal phase OH dipoles in the same columnar channel may be oriented differently (disordered column model) or they may be oriented by the same way in the given column, however the orientation does not depend on the orientation in neighboring columns (ordered column model of the hexagonal phase). The Hartree-Fock (HF) method realized in GAUSSIAN 98 code [7] was is use to calculate energy barrier values on all possible ways of proton transport. The 6-31G(d) basis was employed. The proton transport was assumed along the columnar channel and consisted of two steps: the rotation of proton around the O2-(1), and proton movement to the nearest proton vacancy (2). The PO4 group influenced the potential energy profile for the possible

Y. Dekhtyar et al. (Eds.): *International Symposium on Biomedical Engineering and Medical Physics*, IFMBE Proceedings 38, pp. 182–185, 2013.
DOI: 10.1007/978-3-642-34197-7_48

proton transfer along the column throw the oxygen of the PO4 group.

The calculated energy barriers are provided in the Table 1.

Table 1 Energy barriers for proton transfer.

		Along c-axes			Through oxygen from PO_4		
		ΔE_1, eV	ΔE_2, eV	ΔE_{12}, eV	ΔE_1, eV	ΔE_2, eV	ΔE_{12}, eV
OH	monoclinic	3.38	2,65	0.71	4.09	0.81	3.28
	hexagonal ordered	2.86	1.76	1.1	5.21	1.09	4.12
	hexagonal disordered	0.68	0.84	0.15	2.89	1.0	1.89

The calculated energies demonstrated double well asymmetric potentials. The high energy barriers make impossible the proton transfer at the normal room or human body temperature conditions. However, such the stable situation could be exerted by the external forces.

III. Hydrogenation to Move the Proton

A. Approach

When HAP is disposed in a high pressure hydrogen atmosphere conditions, a strong gradient of the proton concentration directed from the bulk to the surface is supplied. As the result the proton of the HAP increased a probability to transfer from the surface location to the bulk, the stable, negative charge depositing on the surface.

B. Hydrogenation and Verification of Charge Deposition

To reach the above approach the HAP specimens were disposed in 6 MPa hydrogen atmosphere during 6 h.

To verify provision of the electrical charge the photoelectron emission electron work function (φ) was tested both before and after hydrogenation. The value of φ defined the energy that it is necessary to supply to an electron to escape it from a solid. The emitted electron is influenced by the electrical field of the surface charge that contributes φ, however the value of φ is directly proportional to the surface potential.

To measure φ, a photoelectron emission current (I) was induced by ultraviolet photons in a range of 3-6 eV under vacuum conditions (10^{-1} Pa). The value of φ was identified as the photon energy threshold when I=0. The measurements were provided using a photoelectron spectrometer [8].

The experiments demonstrated that hydrogenation is able to provide an increment of the φ value from 0.1 to 1 eV.

IV. Specimens

The HAP derived materials were prepared from HAP powders. The chemical interaction between calcium hydroxide and phosphoric acid was chosen as the most suitable and simplest method for synthesis of fine and stoichiometric hydroxyapatite [9]. The Sr, Ag and Si admixtures were provided for different batches of the specimens.

Chemical composition of HAP powders (content of Ca and P) was estimated by chemical analysis. The phase composition was estimated by X-ray diffraction analysis using Advance 4 (Bruker AXS, Germany) instrumentation.

The tablets (diameter - 12 mm, thickness- 3 mm) for sintering were axially pressed at a pressure of 85-86 MPa. The green compacts for microwave sintering were formed by cold isostatic pressing (CIP) of pure HAP powder at 400 MPa for 1 min at room temperature (25 ºC), using a steel die and hydraulic oil as the pressure medium. Conventional sintering was performed in a laboratory furnace NABERTHERM LHT 08/18 at a temperature of 1200 ºC for 2h (heating rate 200ºC/h). The isostatically pressed disc green compacts were sintered in a microwave laboratory furnace (Linn High Therm MHTD 1800-4,8/2,45-135) by heating to 1200 ºC at a heating rate of 20 ºC/min and maintaining the temperature for 15 min. The temperature was monitored continuously with an optical pyrometer at the top of the furnace.

Density and porosity of the sintered samples were determined by the hydrostatic method.

The implant models were provided for the biocompatibility test. The Ti disks (diameter of 12 mm, thickness of 1 mm) were electrochemically coated with the conventional HAP.

To estimate ability of the specimens to attach the cells the osteoblast were selected. The SAOS-2 human osteoblasts (ATCC Cat No. HTB-85™; LGC Standards, Teddington, UK) were cultured in McCoy's 5a medium (Gibco, Paisley, UK).containing 10% foetal calf serum (Sigma, UK), 2.5% Hepes (Gibco, Paisley, UK) and 1% Penicillin/Streptomycin (Gibco, Paisley, UK) until confluent, harvested using trypsin-EDTA (Gibco, Paisley, UK) and resuspended in the same medium at a concentration of 1 x 105 cells/ml. The cells were allowed to recover from the enzyme for 1h at 37 ºC and 1 ml of suspension was then added to each specimen in separate wells of a 24-well plate at 37 ºC in an incubator containing 5% CO2, for 30 min [17]. Experiments were terminated by removal of the cell suspension and washing three times in phosphate buffered saline to remove non-attached cells. Attached cells were then fixed

for 1 h in 2.5% glutaraldehyde in 0.1 M sodium cacodylate buffer, pH 7.3, dehydrated in alcohol and hexamethyldisilizane and gold-sputter coated in preparation for scanning electron microscopy (SEM). Secondary electron images were obtained using a Jeol lv3500 microscope at an accelerating voltage of 15 kV, working distance 13 mm (Fig 1.).

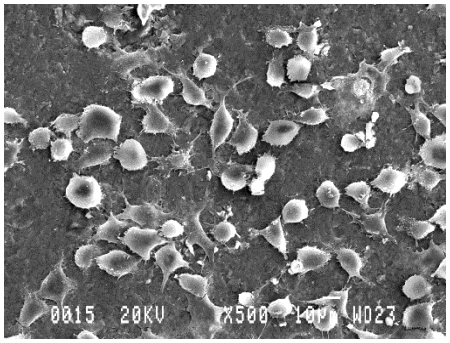

Fig. 1 Electron microscopy image of the osteoblat cell attached to HAP.

Images of five non-overlapping fields of view were captured using the SemAfore 4.0 programme (JEOL/ Skandinaviska, Sweden) at a magnification of 150x (image area = approximately 800 x 600 μm). The individual cells were counted in each image and the average number of cells per area +/- standard deviation was determined. Statistical analysis was carried out using a Mann Whitney U test.

The biocompatibility properties were evaluated due to experiments with animals. BALB/c male mice were in use for in vivo experiment. One implant models with applied syngeneic marrow column (average marrow area is 7.5 mm^2), taken from femur under aseptic conditions, were introduced subcutaneous into each animal (49 animals) under ether-anesthesia to estimate further ectopic osteogenesis phenomenon [10].

Bone marrow was cultivated for the adhesion on the substrate for 45 min in culture medium, containing 95 % of RPMI-1640 and 5% of embryonic bovine serum. The marrow was a source of mesenchymal stromal cell pull (MSCP) and growth factors. No generation of tissue plates under separate subcutaneous introduction of scaffolds or marrow fragments was noted in mice. The implants were released in 45 days. Standard methods of light thin slices microscopy were used for histological analysis of tissue plates.

V. Results and Discussion

A. Attachment of the Cells

The Fig. 2 demonstrates a correlation of the number of the cells attached to HAP in dependence on the hydrogenation forced increment of φ and doping of HAP.

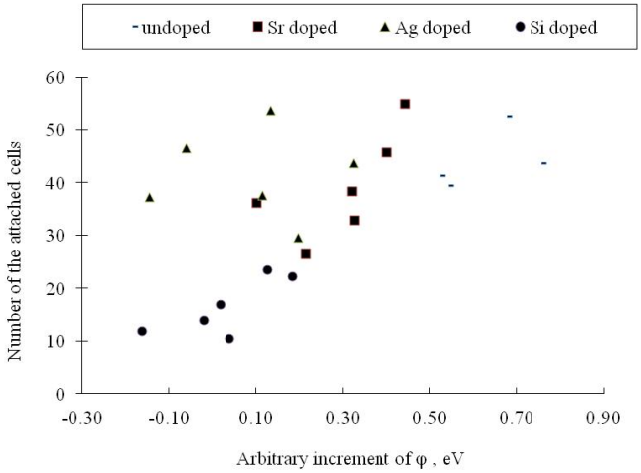

Fig. 2 Correlation of the number of the cells attached to HAP in dependence on electron work function increment and doping.

The results generally evidence that the number of the attached cells increases in dependence on φ increment. However the strongest correlation is demonstrated by Si and Sr doped HAP. Perhaps these materials are more advanced for surface charge engineering.

B. Experiment with the Animals

Hydrogenation of the implant model surface layer increased its φ on ~ 0.1 eV. As the result MSCP differentiation directions was influenced. Connective tissue growth was improved. Probability of following ossification with growth of the membrane reticulated bone was 20 %. Decrease of φ on the above value led to primary formation of the bone from the marrow MSCP.

V. Conclusions

1. The reached hydrogenation technology is able to engineer electrical charge of the HAP surface that has an influence on osteoblast attachment.
2. The Si and Sr doped HAP are more advanced materials for surface charge engineering
3. Hydrogenation of HAP based implant model influences directions of MSCP differentiation. Connective tissue growth is improved.
4. The hydrogenation technology could be employed for the controlled engineering of the HAP surface charge to enhance osteoinduction.

Acknowledgment

The research has been partially supported by the Eureka program project E!3033 (Latvia) and European regional

development fond (Latvia) project 2010/0288/2DP/ 2.1.1.1.0/10/APIA/VIAA/038, ESS2010/114.

REFERENCES

1. Derjaguin B.V., Landau L.D. (1941) Theory of the stability of strongly charged lyophobic sols and of the adhesion of strongly charged particles in solutions of electrolytes. Acta Physic Chimica (USSR), 14, 633-642
2. Ito S., Shinomiya K., Nakamura S., Kobayyashi T., Nakamura M/.Yamashita K. (2006) Effect of electrical polarization of hydroxyapatite ceramics on new bone formation. Journal of the Japanese Bio-Electrical Research Society, 20: 23-27.
3. Aronov D., Molotskii M., Rosenman G. (2007) Charge-induced wettability modification. Applied Phys. Let. 90: 104104-1-104104-1.
4. Bystrov V.S., Bystrova N.K., Paramonova E.V., Dekhtyar Yu.D. (2009) Interaction of charged hydroxyapatite and living cells.I. Hydroxyapatite polarization properties. Mathematical biology and bioinformatics, 2009. V. 4. № 2. 7-11.
5. Bystrov V. et al. Advanced materials forum III. (2006) *Mater. Science Forum.* V. 514-516. 1434-1437.
6. Hughes J. M. Cameron M, Crowley K D, (1990) *American Mineralogist*.. V. 75, 295-304.
7. Frisch M J et al. *Gaussian 98 Revision A.1x*. Pittsburg PA: Gaussian, Inc., 2001.
8. Akmene R J, Balodis A J, Dekhtyar Yu D, Markelova G N, Matvejevs J V, Rozenfelds L B, Sagalovičs G L, Smirnovs J S, Tolkačovs A A and Upmiņš A I (1993) *Poverhnost, Fizika,*Himija, Mehanika (Russian Journal), 8, 125-128
9. Sader M S, LeGeros R Z and Soares G A.(2009) J. Mater. Sci.: Mater. Med. 20 521.
10. Urist M.R. (1965). Bone: formation by autoinduction. Science 150: 893.

Author: Yuri Dekhtyar
Institute: Riga Technical University, Biomedical Engineering and Nanotechnologies Institute
Street: 1 Kalku
City: Riga LV1658
Country: Latvia
Email: dekhtyar@latnet.lv

In Vitro Evaluation of Osteoblast Cell Behavior and Antimicrobial Properties of Biphasic Calcium Phosphate Ceramics

D. Loca[1], A. Dubnika[1], A. Reinis[2], and N. Romancikova[3]

[1] Riga Technical University, Riga Biomaterials Inovation and Development Centre, Pulka 3/3, LV-1007, Riga, Latvia
[2] Riga Stradins University, Department of Biology and Microbiology, Dzirciema 6, LV-1007, Riga, Latvia
[3] Latvian Institute of Organic Synthesis, Aizkraukles 21, LV-1006, Riga, Latvia

Abstract — **Calcium phosphate ceramic materials in form of hydroxylapatite (HAp) and β-tricalcium phosphate (TCP) are good candidates for bone substitution and regeneration. Majority of methods used for biphasic calcium phosphate (mixture of HAp and TCP) preparation includes synthesis of calcium deficient apatite, not so often mechanical mixing of HAp and TCP is applied. The aim of this work was to evaluate the effect of HAp/TCP ratio as well as the impact of biphasic calcium phosphate (BCP) preparation technique on osteoblast cell behavior and ceramic antimicrobial properties. Results showed that BCP composite samples supported much higher proliferation rate of osteoblast cells as those of pure HAp or TCP. The best result was observed for BCP samples with HAp/TCP ratio 60/40. BCP preparation technique significantly does not affect the cell attachment on the surface of BCP samples, while influence on colonization intensity of bacteria was observed. Results indicated that the use of pure HAp or BCP ceramics as implant materials can cause less inflammatory risks compared to the pure TCP ceramics.**

Keywords — **biphasic calcium phosphate ceramics, bioceramics, hydroxyapatite, β-tricalcium phosphate.**

I. Introduction

Synthetic calcium phosphates (CaP) are chemically similar to the bone mineral phase, hence they are good candidates as bone substitution materials. Osteoconductivity and biocompatibility are the main advantages of CaP biomaterials [1, 2]. Mostly CaP bioceramic is used in form of hydroxylapatite (HAp, $Ca_{10}(PO_4)_6(OH)_2$), β-tricalcium phosphate (TCP, $Ca_3(PO_4)$) or biphasic calcium phosphates (BCP), which is mixture of HAp and TCP [3]. The use of BCP bioactive ceramics is based on an optimum balance between more stable phase – hydroxyapatite and more soluble phase – β-tricalcium phosphate [4]. Varying the ratio of HAp and TCP, bioactivity and resorbability of BCP can be controlled. BCP can be prepared by mechanically mixing of HAp and TCP in desired quantities or by synthesis of calcium deficient apatite [5].

The ability of microorganisms to infect and colonise implanted biomaterials or other appliances is still a common problem and serves as a risk factor for hospital infections leading to the use of aseptic and antiseptic methods [6]. Therefore, studies regarding to the risk of bacterial contamination of biomaterials and its effect on inflammation and immune reactions in implant surrounding tissues are of great interest.

Previous studies revealed that MG-63 osteoblast culture was a good model to estimate the behaviour and survival on the surface of the different composite scaffolds. It was shown that MG-63 cells attached, proliferated on the surface, and/or migrated into the pore walls, indicating biocompatibility of the bioceramic scaffolds [7-9].

In current research, the adhesion and colonization of bacteria as well as osteoblast cell adhesion on pure TCP, pure HAp and TCP/HAp compositions obtained by two different methods is investigated and BCP preparation method impact on its properties evaluated.

II. Materials and Methods

A. Preparation of Bioceramic Samples

The chemical synthesis of apatite and calcium-deficient apatites with different Ca/P ratios in range from 1.5 to 1.67 was carried out by wet precipitation method. The dried precipitate was milled to obtain a fine powder. The biphasic composition of ceramic was ensured using two methods: A) calcination and sintering of as-synthesized calcium-deficient apatites; and B) calcination and sintering of mechanical mixtures of as-synthesized powders with Ca/P ratio of 1.5 and 1.67. Before sintering, powders were uniaxially pressed. The sintering of the samples was carried out at 1150 °C for 2 h. Obtained samples were with the following HAp/TCP ratio: 100/0, 90/10, 60/40, 50/50 and 0/100. The open porosity of bioceramic samples was determined with Archimed method, microstructure was investigated using scanning electron microscopy (SEM) and phase composition was verified using X-ray diffractometry.

Y. Dekhtyar et al. (Eds.): *International Symposium on Biomedical Engineering and Medical Physics*, IFMBE Proceedings 38, pp. 186–189, 2013.
DOI: 10.1007/978-3-642-34197-7_49

B. Determination of Bacteria Adhesion and Colonization Intensity on the BCP Ceramic Surface

Reference cultures of *Ps.aeruginosa* ATCC 27853 and *S.epidermidis* ATCC 12228 were used in the research. Bacteria suspensions were prepared from the microbiological cultures in 1 ml of TSB (Triptycase soy broth, Oxoid, UK) with the concentrations of 10, 10^2, 10^3 CFU/ml (colony forming units). Samples were cultivated at 37 ^oC for 2 h for the determination of bacteria adhesion. Bioceramic samples were incubated in 1 ml of TSB for 24 h, to evaluate the level of microorganism colonization. Sonication-plate count method [10, 11] was used for determination of both bacteria adhesion and colonization. After incubation the unattached microorganisms were washed off. To separate the bacteria attached on the bioceramic surface, samples were treated in an ultrasonic bath for 1 min (with frequency of 45 kHz) and for 1 min in centrifuge *Vortex* at maximum rpm. The several subcultures were made on a TSA growth medium (Triptycase soy agar, Oxoid, UK), cultivated for 24 h in temperature of 37 ^oC, to determine the total count of microorganisms. For CFU calculations 1 mm^2 of the biomaterial sample surface was used. Samples for SEM analysis were fixed in a mixture of ether-ethanol (1:1).

C. Determination of Osteoblast Cell Behavior on the BCP Ceramic Surfaces

Cell line. MG-63 cell line, human osteoblast, was obtained from ATCC collection (CRL-1427) and maintained in culture medium DMEM containing 10 % fetal bovine serum and 2 mM L-glutamine. Cell line was incubated in thermostat at 37 °C with 5 % CO_2 in a humidified atmosphere. For the seeding the cells were washed with phosphate-buffered saline (PBS) and detached with 0.25 % trypsin EDTA solution at 37 °C for 2 minutes.

Stable GFP transfection. MG-63 cells were incubated with DOTAP reagent and plasmid pEGFP-N1 for 4 h in serum free medium. After 48 h MG63-GFP cells were selected in the presence of G418 culture medium (500 μg/ml).

Sample preparation. For biological investigations samples were sterilized for 30 min using UV irradiation. Each sample was plated into the well of 24-well tissue culture plate. MG63-GFP cells were seeded at density 2×10^4 cells per well. The wells without sample were taken as a control. Plates were grown in thermostat for 72 h at 37 °C with 5 % CO_2 and humidified atmosphere.

Cytotoxicity assay. Crystal violet (CV) staining of alive cells [12] on the surface of the samples was use for the determination of samples citotoxicity. For CV assay, cells were fixed for 15 min with a 0.1 % glutaraldehyde in phosphate buffer solution (PBS), stained for 30 min with a 0.1 % solution of CV, rinsed with distilled water. The dye was released from the cell membranes by 1:1 of 96^0 ethanol and citrate buffer (pH 4,2). Blank samples without cells were used as staining control. The absorbance of aliquot was measured at 540 nm using a microplate reader. All data are the mean of three independent experiments.

All analyses were performed in four wells including medium control. The results of cytotoxic effect were calculated by GraphPad Prizm 5.03 program, expressed as percentage of alive cells attached to the sample and compared to control - well without sample, which was assumed as 100 % of alive cells. All results were calculated to the complete well area for both, samples and control.

Microscopy. Fluorescent microscope ECLIPSE TE 300 NIKON equipped with digital camera NIKON Ds 5Mc and scanning electron microscope (SEM Mira\LMU) were used for osteoblast visualization.

III. Results and Discussion

Such properties as open porosity and surface morphology can affect the cell and microorganism behavior on the surface of bioceramic samples. Results showed that the open porosity of pure HAp is more than two times higher than that of pure TCP (see Fig. 1).

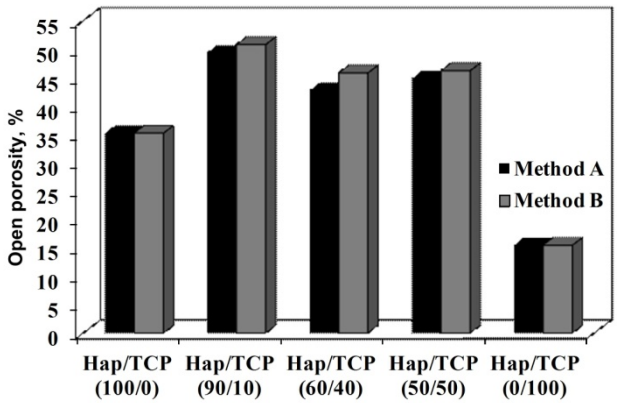

Fig. 1 Open porosity of bioceramic samples.

At the same time the open porosity of biphasic HAp/TCP compositions is higher than that of pure components. We suggest that such effect occurred due to the differences in grain sizes (see Fig. 2) and phase transition and sintering temperatures of HAp and TCP. The surface microstructure of all prepared BCP samples was similar. Calculations showed that open porosity of bioceramic samples is not significantly influenced by the preparation technique of HAp/TCP.

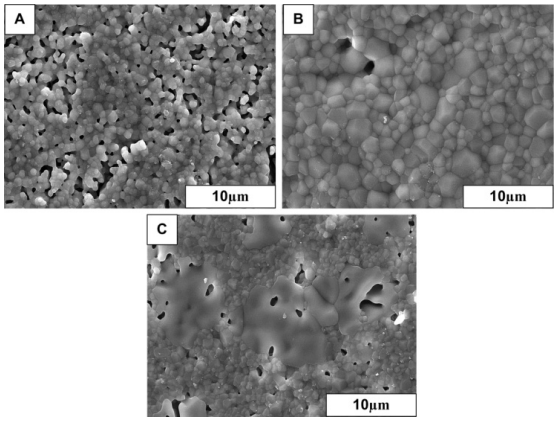

Fig. 2 SEM images of ceramic sample surfaces: A) HAp; B) TCP; C) HAp/TCP (60/40).

The antimicrobial properties of prepared samples were evaluated and the statistical evaluation of the results provided (standard deviation for the microorganism adhesion intensity results was in the range from 0.0005 up to 0.005 CFU/mm^2). Adhesion of S.*epidermidis* on HAp and TCP samples incubated in 10 CFU/ml, either did not occur, or was very low. The remaining samples were incubated in *S.epidermidis* suspension of concentrations 10^2 and 10^3 CFU/ml. The adhesion process of *Ps.aeruginosa* began at 10 CFU/ml of incubated samples and finally demonstrated around 20 times greater intensity than the adhesion of *S.epidermidis*, incubated in 10^3 CFU/ml (see Table 1). It was found that the colonization intensity of both bacteria on the surface of the biphasic samples obtained via method B was higher compared with samples prepared via method A (see Table 2).

Table 1 Microorganism adhesion intensity on HAp and TCP samples.

Bioceramic	Prep. meth.	Adhesion intensity, CFU/mm^2					
		S.epidermidis			Ps.aeruginosa		
		10	10^2	10^3	10	10^2	10^3
HAp/TCP (100/0)		-	-	0.028	-	0.042	0.704
HAp/TCP (90/10)	A	-	0.014	0.042	0.014	0.028	0.845
HAp/TCP (60/40)	A	-	0.028	0.056	0.028	0.042	0.915
HAp/TCP (50/50)	A	0.014	0.028	0.028	0.028	0.042	1.07
HAp/TCP (90/10)	B		0.028	0.042	0.014	0.028	0.873
HAp/TCP (60/40)	B		0.028	0.056	0.028	0.042	0.943
HAp/TCP (50/50)	B	0.014	0.028	0.056	0.028	0.042	1.056
HAp/TCP (0/100)		0.014	0.028	0.084	0.028	0.042	1.127

Table 2 Microorganism colonization intensity on HAp and TCP samples.

Bioceramic	Preparation method	S.epidermidis, CFU/mm^2	Ps.aeruginosa, CFU/mm^2
		10^2	
HAp/TCP (100/0)		16±0.85	24±0.83
HAp/TCP (90/10)	A	26±0.9	48±2.06
HAp/TCP (60/40)	A	70±1.3	120±2.8
HAp/TCP (50/50)	A	135±2.98	210±3.0
HAp/TCP (90/10)	B	30±0.9	50±2.1
HAp/TCP (60/40)	B	85±2.2	135±3.1
HAp/TCP (50/50)	B	120±2.8	200±3.2
HAp/TCP (0/100)		195±3.1	318±3.5

The effect of HAp/TCP ratio as well as the impact of BCP preparation technique on osteoblast behaviour was evaluated. It was observed that BCP preparation technique significantly does not affect the cell behaviour on the surface of bioceramic samples and more cells tend to attach the dense regions of the samples (see Fig. 3). In all cases cells attached to the samples had morphologically normal shape and size, corresponding to MG63-GFP culture in control wells.

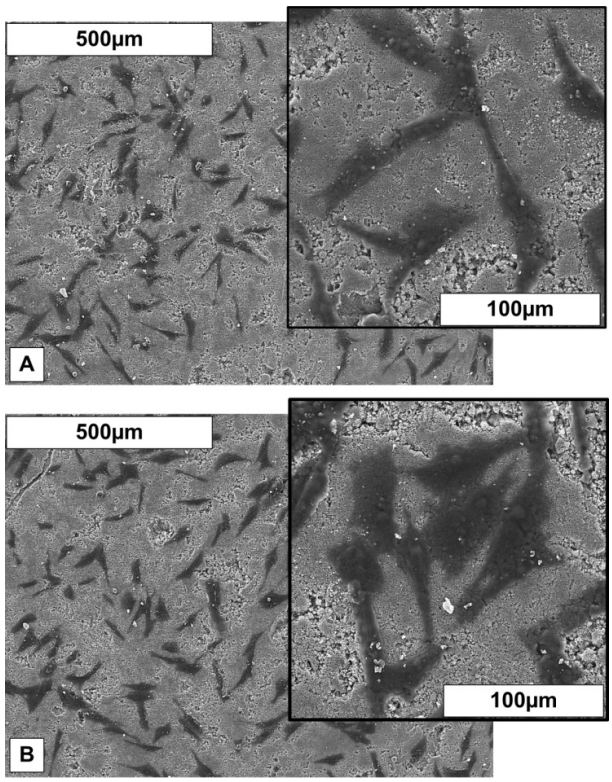

Fig. 3 SEM images of osteoblasts on BCP ceramic: (HAp/TCP ratio 60/40): (A) synthesized and (B) mechanical mixture.

Results showed that all tested samples are biocompatible and non cytotoxic. Moreover, the surface structure and composition of BCP samples increased the osteoblast cell MG63-GFP proliferation compared to pure HAp (see Table 3).

Table 3 Cell proliferation rate related to pure Hap.

Bioceramic	Prepared by method A (synthesized mixture)	Prepared by method B (mechanical mixture)
HAp/TCP (100/0)	reference	reference
HAp/TCP (90/10)	1.5	1.3
HAp/TCP (60/40)	**3.7**	**3.6**
HAp/TCP (50/50)	3.0	3.2
HAp/TCP (0/100)	0.4	0.4

Disadvantage of crystal violet staining in cytotoxic assay deals with the dye absorption by samples. Although we took this fact into account during calculations, some inaccuracy was possible. Nevertheless, crystal violet staining allowed detecting the cell membrane disruption in the process of MG63-GFP cells attachment and proliferation without special additional methods. The current research has shown that sample structure and composition with HAp/TCP ratio 60/40 was most *convenient* for osteoblast attachment, moreover, these samples induced intensive MG63-GFP cell proliferation, almost four-fold, compared to the control well, indicating that the use of such composite as implant material could have great advantage in bone tissue regeneration.

IV. Conclusions

The adhesion and colonization of bacteria as well as osteoblast cell behavior on the surface of the bioceramics is mostly dependent on the chemical and structural composition of the samples and only a small effect of preparation method can be observed.

The adhesion and colonization intensity of *Ps.aeruginosa* on the surface of the all samples was much higher than that of *S.epidermidis*, as well as the adhesion and colonization intensity of both bacteria was higher for the ceramics containing larger TCP amount.

BCP composite samples supported much higher proliferation rate of osteoblast cells as those of pure HAp or TCP. Cell adhesion and proliferation rate increased with increasing the TCP content in composites and reached the maximum at HAp/TCP ratio 60/40.

Acknowledgment

This work has been supported by the European Social Fund within the project "Multidisciplinary Research in Biomaterials Technology of New Scientist Group", No.2009/0199/1DP/1.1.1.2.0/09/APIA/VIAA/090.

References

1. Galbusera F, Bertolazzi L., Balossino R et al. (2009) Combined computational study of mechanical behaviour and drug delivery from a porous, hydroxyapatite-based bone graft. Biomech Model Mechanobiol 8:209-216.
2. Dorozhkin VS. (2010) Calcium orthophosphates as bioceramics: state of the art. J Funct Biomater 1:22-107.
3. Rameshbabu N, Rao KP. (2009) Microwave synthesis, characterization and in-vitro evaluation of nanostructured biphasic calcium phosphates. Curr Appl Phys 9:S29-S31.
4. Walsh WR, Vizesi F, Michael D et al. (2008) Beta-TCP bone graft substitutes in a bilateral rabbit tibial defect model. Biomaterials 29:266-271.
5. Emadi R, Esfahani SI, Tavangarian F. (2010) A novel, low temperature method for the preparation of ß-TCP/HAp biphasic nanostructured ceramic scaffold from natural cancellous bone. Mater Lett 64:993–996.
6. Hetrick EM, Schoenfisch MH. (2006) Reducing implant-related infections: active release strategies. Chem Soc Rev, 35:780-789.
7. Young HK, Dong SS, Lee JK. (2011) Biological behavior of MG63 cells on the hydroxyapatite surface bioceramics development and applications. Bioceramics Development and Applications, doi:10.4303/bda/D101126.
8. Zhang Y, Zhang M. (2002) Three-dimensional macroporous calcium phosphate bioceramics with nested chitosan sponges for load-bearing bone implants. J Biomed Mater Res.61:1-8.
9. Nath S, Kalmodia S, Basu B. (2010) Densification, phase stability and in vitro biocompatibility property of hydroxyapatite-10 wt% silver composites. J Mater Sci - Mater. Med 21:1273-1287.
10. Trampuz A, Piper KE, Jacobson MJ et al. (2007) Sonication of removed hip and knee prostheses for diagnosis of infection. N Engl J Med 357:654-663.
11. Sampedro MF, Huddleston PM, Piper KE et al. (2010) A biofilm approach to detect bacteria on removed spinal implants. Spine, 35:1218-24, doi: 10.1097/BRS.0b013e3181c3b2f3.
12. Saotome K, Morita H, Umeda M. (1989) Cytotoxicity test with simplified crystal violet staining method using microtitre plates and its application in injection drugs. Toxicol In vitro, 3:317-321.

Author: Dagnija Loca
Institute: Riga Technical University, Riga Biomaterials Inovation and Development Centre
Street: Pulka 3/3
City: Riga
Country: Latvia
Email: dagnija.loca@rtu.lv

Biogenic Nanosized Hydroxyapatite for Tissue Engineering Applications

K. Balázsi[1], H.-Y. Sim[2], J.-Y. Choi[3], S.-G. Kim[4], C.-H. Chae[5], and C. Balázsi[1]

[1] Institute for Technical Physics and Materials Science, Research Centre for Natural Sciences, Hungarian Academy of Sciences, Budapest, Hungary
[2] Department of Orthodontics, SMG-SNU Boramae Medical Center, Seoul, Korea
[3] Department of Biochemistry and Cell Biology, Kyungpook National University, Daegu, Korea
[4] College of Dentistry, Gangneung-Wonju National University, Gangwondo, Korea
[5] Department of Dentistry, Hallym University, Seoul, Korea

Abstract — **Hydroxyapatite (HAp) as resorbable porous bioceramics use as bone defect filling materials due to its remarkable biocompatibility and close chemical similarity to biological apatite present in bone tissues. One of perspective, non-expensive and environmental friendly material for hydroxyapatite preparation is eggshell. In this work, a simply method of HAp producing by mechanochemical activation from eggshells and the bone regeneration of HAp applied as bone tissue material were studied.**

Keywords — **eggshell, hydroxyapatite, attritor milling, in vivo, nanostructure.**

I. Introduction

Nanomaterials have wide-ranging implications in a variety of areas, including chemistry, physics or biomedical sciences.

Hydroxyapatite (HAp) has been widely used as an artificial bone substitute because of their high biocompatibility and good bioaffinity, as well as osteoconductability [1]. HAp is not only a main component of hard tissues, such as bones and teeth, but a material applied for bioceramics and adsorbents because it has an excellent affinity to biomaterials such as proteins [2]. HAp powders have been produced using bio products like corals [3], cuttlefish shells [4], natural gypsum [5], natural calcite [6], bovine bone [7]. Chemical analysis has shown that these products which are otherwise considered as bio-waste are rich sources of calcium in the form of carbonates and oxide. Several papers reported to produce the materials for implant or prosthesis purposes with chemical characteristics similar to HAp [8].

In this work, the HAp powder was prepared from a non-expensive and environmental friendly material – eggshell [9, 10]. The mechanochemical activation was used for HAp preparation. The bone regeneration of HAp successfully applied as material for tissue engineering applications were studied by in vivo experiments.

II. Experimental

A. Hydroxyapatite Preparation

The eggshells were collected and cleaned. The raw eggshells were calcinated at 900°C in air. The 3 hours thermal treatment resulted in calcium oxide formation from starting material. To synthesize calcium phosphate powders were crushed and milled by high efficient attritor mill (Union Process 01 HDDM). Milling parameters were 4000 rpm for 5 h, shell: H3PO4 ratio was 50: 50 wt% [3]. Small amount of milled HAp powder was heat treated at 900°C for 2 h in air.

The structure of HAp powder was characterized by scanning electron microscope (SEM, Jeol Inc., Toyko Japan) and transmission electron microscope (TEM, Philips CM-20). The phase composition was HAp powder determined by X-ray Diffractometry (XRD-Bruker Advance 8D). Semi-quantitative elemental analysis was performed by energy dispersive X-ray spectroscopy (EDS-JEOL JSMIII 25) with a Bruker Si(Li) EDS detector and Quantax system. Collection times were typically 25-60 minutes (live lime) using area scan mode on a single 1 mm^2 area.

B. In Vivo Experiment

General anesthesia was induced by intramuscular injection of a combination of 0.05ml of rompun and 0.05ml of zoletil. Micro-CT scanner is based on the same underlying physical principle as a clinical CT scanner. It produced 3D tomographic data at microscopic resolution. A dental-trephine bur was used under copious saline irrigation to create a one full-thickness calvarial defect. 3-mm-diameter defects were created. The graft – HAp was placed on calvarial defects. Some defects were kept as empty as a control. Postoperatively, the mouse received gentamicin 1mg/kg intramuscularly 1 times daily for 3 days. Each mouse was individually caged and received food and water.

Y. Dekhtyar et al. (Eds.): *International Symposium on Biomedical Engineering and Medical Physics*, IFMBE Proceedings 38, pp. 190–193, 2013.
DOI: 10.1007/978-3-642-34197-7_50

They were underwent a micro-computed tomogram the 4 weeks later. The anesthetized state of the mouse underwent micro CT using an Explored Locus SP micro CT scanner (GE Medical Systems, London, Ontario, Canada).

III. Results

From our previous studies, structural observations of the eggshells after the 3 h calcination process at 900°C showed the compact morphology with grain size of particles about 2-3 μm [9, 10]. The intensive milling caused the decreasing of particle size. As can be observed from SEM investigations, the average grain size is 10 times smaller, only 100 – 200 nm (Fig. 1a). The TEM observation showed the bimodal nanostructure of HAp powder (Fig. 1b). The average size of finer structure is ~ 40 nm, globular particles are ~ 200 nm.

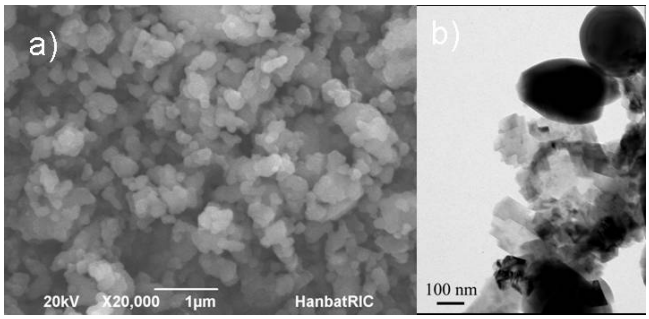

Fig. 1 Structural observation. a) SEM image of milled HAp powder, b) TEM image of bimodal HAp structure.

The phase composition of milled and post heat treated HAp powder were analysed by XRD measurements (Fig. 2). Milled HAp contains main lines of hydroxyapatite (JCPDSPDF 74-0565) phase and other minor phases as calcite ($CaCO_3$, JCPDS-PDF 05-0586), monetite ($CaHPO_4$, JCPDS-PDF 071-1760) and phosphoric acid (H_3PO_3, JCPDS-PDF 072-0518). The next heat treatment (900°C, 2h) caused the disappearance of most lines of the minor phases.

Table 1 Hydroxyapatite main elements (wt%).

Element	O	P	Ca	Mg
Milled HAp	42.05	16.01	41.01	0.45
Post treated HAp	31.76	18.34	48.98	0.47

The elemental composition of hydroxyapatite is showing the main and minor elemental.

The main elements are O, P, Ca ad Mg (Tab. 1). The minor elements are 0.05-0.08 wt% Na, 0.06-0.1 wt% Si, 0.1 wt% S, 0.01-0.03 wt% Cl, 0.06 wt% Zn and 0.14-0.16 wt% Zr. These elements are residuals from eggshell raw material and preparation process.

The important data is a magnesium trace element in HAp (0.45-0.47 wt%). Magnesium (Mg) has been known as one of the cationic substitutes for calcium in the HAp lattice [11,12]. The incorporation of Mg in synthetic HAp is limited (maximum of about 0.4wt% of Mg) unless other ions, such as carbonate or fluoride are simultaneously incorporated together with magnesium as paired substitutions [12].

Increasing concentration of Mg in HAp has the following effects on its properties: (i) decrease in crystallinity, (ii) increase in HPO_4^{2-} incorporation, and (iii) increase in extent of dissolution [12]. Mg is one of the main substitutes for calcium in biological apatites. Enamel, dentin and bone contain,respectively, 0.44, 1.23, and 0.72wt% of Mg [12]; Mg-substituted HAp materials (denoted hereafter as Mg- HAp) are expected to have excellent biocompatibility and biological properties [13]. 2.56 Ca / P ratio was measured in the case of milled HAp and 2.67 for post treated HAp (900°C, 2h).

In our former study we could confirm higher bone formation ability of hydroxyapatite made from eggshells, together with commercial synthetic hydroxyapatite (used as reference) than the unfilled control [14]. However, HAp from eggshell had significantly higher bone formation than the unfilled control at 8 weeks after the operation (P = .038) [14].

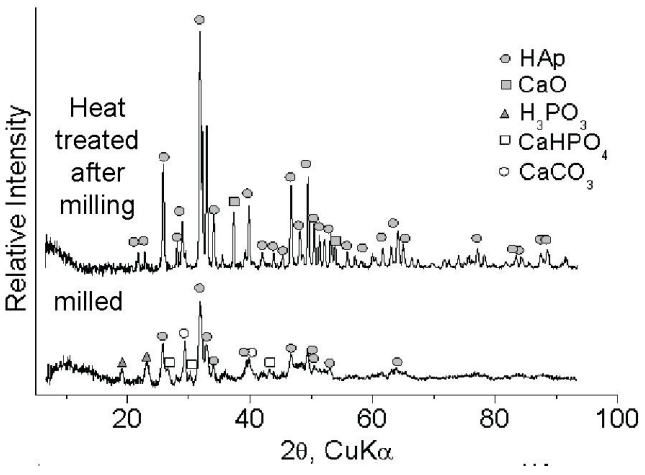

Fig. 2 XRD measurements of milled and heat treated HAp powders.

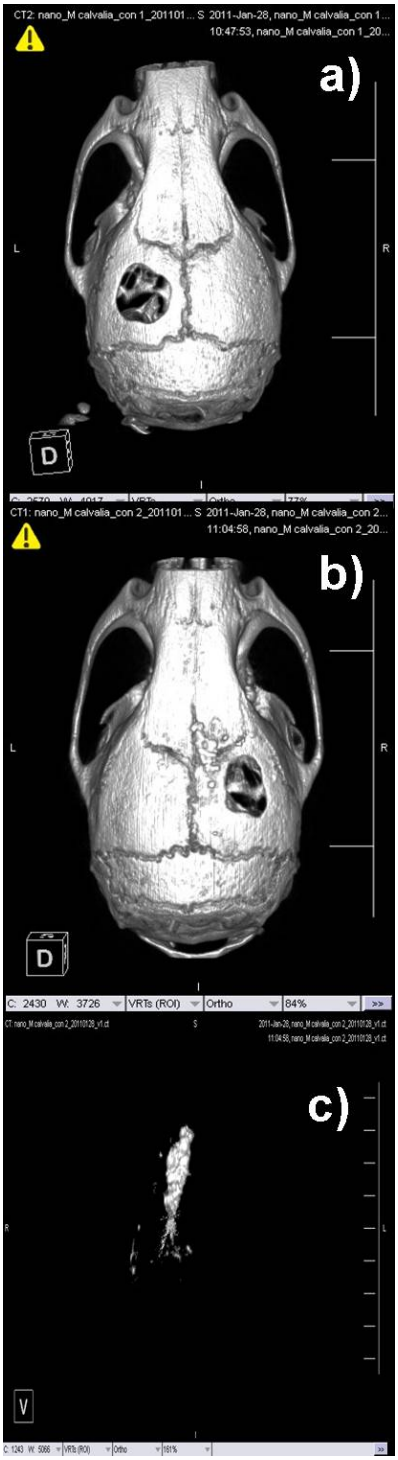

Fig. 3 Micro Computed tomogram (μ-CT) of mouse in vivo experiment. a) control, b) experiment, c) new bone after 4 weeks.

Bioceramics exert bone regeneration by self degradation, and the space formed by that degradation can be replaced by new bone [16]. Therefore smaller particles will have more advantages than larger particles. The cellular response to HAp particles depends on the particle size, morphology, crystallinity, and chemical composition [17].

White mouse was used for in vivo test of HAp biocompatibility (Fig. 3 and Fig. 4). The results of the μCT analysis are shown in Fig. 3. As it can be observed on the mouse calvaria, there are no healing observed in the control group at 4 weeks after the operation (Fig. 3a). New bone formation has been observed on the calvaria showed by μCT analysis (Fig. 3b). The new bone formation surprisingly occurred not only in defect side, but on the nearby region. This HAp graft was carried to the bone formation place very probable by blood stream. In the next experiments the graft adhesion should be further optimized. The standing alone new bone on the mouse calvaria formed by nanosized HAp after 4 week can be seen on Fig. 3c.

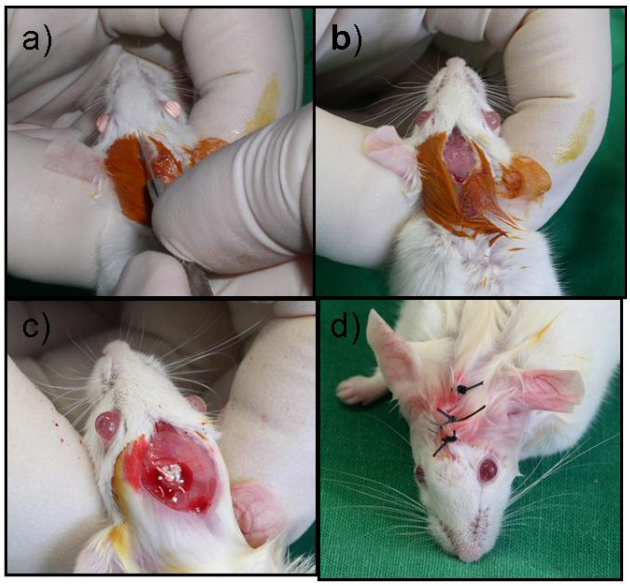

Fig. 4 White mouse in vivo experiment. a) start of experiment, b) calvaria defect, c) graft – HAp placed on calvarial defect, d) end of experiment.

This result is in good agreement wit our white rabbit in vivo experiment [18]. All measured variables of the μCT and histomorphometric analysis were significantly higher in the nanosized HAp grafted groups than in the unfilled control groups at 4 and 8 weeks after operation.

IV. Conclusions

Hydroxyapatite (HAp) as resorbable porous bioceramics use as bone defect filling materials due to its remarkable biocompatibility and close chemical similarity to biological apatite present in bone tissues. One of perspective, non-expensive and environmental friendly material for HAp preparation is the eggshell. HAp was successfully produced from recycled eggshells and phosphoric acid by attritor milling. The SEM investigations confirmed the average 100 nm particle size. The elemental composition showed 0.45-0.47 wt% magnesium content. μCT measurements prepared on white mouse after 4 weeks demonstrated the new bone formation. From in vivo results should be concluded that the nanosized HAp prepared from the eggshell can be good calcium source in bone formation.

Acknowledgment

This study was supported by OTKA 76181, BioGreen21 Program of Rural Development Administration, by the János Bolyai Research Scholarship of the Hungarian Academy of Sciences and OTKA PD 101453.

References

1. L.L. Hench, Sol-gel materials for bioceramic applications. Bioceramics. J. Am. Ceram. Soc. 81 (1998) 1705-1728.
2. Kikuchi M, Ikoma T, Itoh S, Matsumoto HN, Koyama Y, Takakuda K, et al. Biomimetic synthesis of bone-like nanocomposites using the self-organization mechanism of hydroxyapatite and collagen. Compos Sci Technol 2004;64:819–25.
3. R. Murugan, K.P. Rao, Controlled release of antibiotic from surface modified coralline hydroxyapatite, Trends Biomat. Artif. Organs 16 (2002) 43-45. Lock I, Jerov M, Scovith S (2003) Future of modeling and simulation, IFMBE Proc. vol. 4, World Congress on Med. Phys. & Biomed. Eng., Sydney, Australia, 2003, pp 789–792
4. J.H.G. Rocha, A.F. Lemos, S. Agathopoulos, P. Valério, S. Kannan, F.N. Oktar, J.M.F.Ferreira, Scaffolds for bone restoration from cuttlefish, Bone 37 (2005) 850
5. M.K. Herliansyah, E. Pujianto, M. Hamdi, A. Ide-Ektessabi, M.W. Wildan, A.E. Tontowi, Proc. ICPDM (2006) X-31–IX-36
6. M.K. Herliansyah, D.A. Nasution, M. Hamdi, A. Ide-Ektessabi, M.W. Wildan and A.E. Tontowi, Preparation and characterization of natural hydroxyapatite: A comparative study of bovine bone hydroxyapatite and hydroxyapatite from calcite, Mater. Sci. Forum 561–565 (2007) 1441 – 1444.
7. M.K. Herliansyah, M. Hamdi, A. Ide-Ektessabi, M.W. Wildan, J.A. Toque, The influence of sintering temperature on the properties of compacted bovine hydroxyapatite, Mater. Sci. Eng. C29 (2009) 1674 – 1680.
8. R. Rodrıguez, J. Coreno, V.M. Castano, repared by the sol-gel method, Adv. Compos. Lett. 5 (1996) 25 – 28.
9. C. Balázsi, F. Wéber, Z. Kövér, E. Horváth, C. Németh, Preparation of calcium – phosphate bioceramics from natural resources J Eur Ceram Soc 27 (2007) p. 1601
10. G. Gergely, F. Wéber, I. Lukács, A. L. Tóth, Z. E. Horváth, J. Mihály, C. Balázsi, Preparation and characterization of hydroxyapatite from eggshell , Ceram Inter 36 (2010) 803 – 806.
11. Elliott JC. Structure and chemistry of the apatites and other calcium orthophosphates. Amsterdam: Elsevier; 1994.
12. LeGeros RZ. Calcium phosphates in oral biology and medicine. Basel, Switzerland: Karger AG; 1991.
13. W.L. Suchanek, K. Byrappa et al. / Preparation of magnesium-substituted hydroxyapatite powders by the mechanochemical–hydrothermal methodBiomaterials 25 (2004) 4647–4657
14. Sang-Woon Lee, Seong-Gon Kim, Csaba Balázsi, Weon-Sik Chae, Hee-Ok Lee, Comparative study of hydroxyapatite from eggshells and synthetic hydroxyapatite for bone regeneration, Oral Surg Oral Med Oral Pathol Oral Radiol 113 (2012) 348-355.
15. Rezwan K, Chen QZ, Blaker JJ, et al: Biodegradable and bioactive porous polymer/inorganic composite scaffolds for bone tissue engineering. Biomaterials 27:3413, 2006.
16. Suzuki T, Hukkanen M, Ohashi R, et al: Growth and adhesion of osteoblast-like cells derived from neonatal rat calvaria on calcium phosphate ceramics. J Biosci Bioeng 89:18, 2000.
17. Kim HW, Lee EJ, Kim HE, et al: Effect of fluoridation of hydroxyapatite in hydroxyapatite/polycaprolactone composites on osteoblast activity. Biomaterials 26:4395, 2005.
18. H.Y. Kweon, K.G. Lee et al, Development of Nano-Hydroxyapatite Graft With Silk Fibroin Scaffold as a New Bone Substitute, Journal of Oral and Maxillofacial Surgery, 69(6) 2011, pp. 1578-1586.

The address of the corresponding author:

Author: Dr. Csaba Balázsi
Institute: Institute for Technical Physics and Materials Science, Research Centre for Natural Sciences, Hungarian Academy of Sciences
Street: Konkoly – Thege M. ut 29-33
City: 1121 Budapest
Country: Hungary
Email: balazsi.csaba@ttk.mta.hu

Ultrastructural Characteristics of Tissue Response after Implantation of Calcium Phosphate Ceramics in the Mandible of Rabbit

V. Zalite[1], V. Groma[2], D. Jakovlevs[1], J. Locs[1], and G. Salms[3]

[1] Riga Biomaterials Innovation and Development Centre, Riga Technical University, Riga, Latvia
[2] Institute of Anatomy and Anthropology, Riga Stradins University, Riga, Latvia
[3] Department of Oral and Maxillofacial Surgery, Riga Stradins University, Riga, Latvia

Abstract — **This study is undertaken in order to explore interaction between calcium phosphate bioceramics and surrounding tissues in the mandible of rabbit. The tissue response was evaluated 6 months after implantation of ceramics. Three kinds of porous bioceramics were studied: hydroxyapatite (HAp) and HAp mixture with β-tricalcium phosphate (95%HAp/5%β-TCP and 80%HAp/20%β-TCP). X-ray diffractometry (XRD), Fourier transform infrared spectroscopy (FT-IR) and scanning electron microscopy (SEM) were used to characterize porous bioceramic samples. Transmission electron microscopy (TEM), light microscopy and SEM examinations were applied for evaluation of interaction between tissues and bioceramics. The open porosity of obtained samples is in range between 50 to 60%. Pores have not specific form and mainly they are interconnected. The histological studies demonstrated appearance of a thick fibrous collagenous capsule formed around the pure HAp and presented by densely packed fibers and flattened fibrocytes, while addition of b-TCP evidenced highly vascularized adipose tissue.**

Keywords — **β-tricalcium phosphate, hydroxyapatite, ceramics, tissue, porous structure, cell, microstructure.**

I. Introduction

Inflammation, trauma, congenital malformations and tumours can cause bone defects. Various bone grafts, both exogenous and autogenous, along with different synthetically manufactured biomaterials, have been extensively used in animal studies [1-3].

The most popular for bone regeneration is calcium phosphate (CaP) ceramics, especially hydroxyapatite (HAp) and β-tricalcium phosphate (β-TCP) ceramics due to chemical similarity and crystallinity with mineral phase of natural bone [4, 5]. Porous CaP ceramic have been used in orthopaedic, dental and craniofacial surgery [6, 7]. Biomaterials with open and interconnected porosity have several advantages comparing to dense materials:

- more proteins and cells can attach because of larger surface area,
- open and interconnected porosity improves penetration of cells and body fluids into the structure,
- porous structure guarantees better vascularization,
- decrease resorption time [8-11]

HAp can be stabile in body enviroment for several decades, while pure β-TCP resorbes in 3 months. To reach better bioactivity, resorption and even drug release kinetics many scientific publications report, that mixture of both CaP shows better results comparing to single phase [12].

Studies over implants show that not only the structure of biomaterial, but also the character of surface affects the local tissue reaction [2, 13]. It was generally accepted that HAp coatings increase osteoblast attachment, cell proliferation, and differentiation. Recent studies have demonstrated that HAp as well as HAp coatings may enhance osseointegration despite similarities in average surface roughness [14]. During decades morphologic studies have been assumed to be useful in a complex evaluation of bone formation and regeneration [1, 15, 16]. This study was designed to detail the structural and ultrastructural features of the interfaces between pure HAp or biphasic calcium phosphates ceramics implants and their surrounding tissues.

II. Materials and Methods

A. Preparation of Porous Samples

Calcium phosphate powder was prepared in the Riga Biomaterials Innovation and Development Centre Riga Technical University laboratory by realizing wet precipitation reaction between $Ca(OH)_2$ suspension and H_3PO_4 solution. Three powders with different Ca and P ratio were obtained by varying value of end pH of synthesis. Obtained powders were mixed with glycerol (purity > 99.8%, Ltd. BIO-VENTA, Latvia), distilled water and ammonium bicarbonate NH_4HCO_3 (Ltg. Enola, ES/BASF). Thermal treatment in 1150°C for 2 hours was applied to achieve ceramic material. Three groups of porous samples with different phase composition were obtained, see Table 1.

Y. Dekhtyar et al. (Eds.): *International Symposium on Biomedical Engineering and Medical Physics*, IFMBE Proceedings 38, pp. 194–197, 2013.
DOI: 10.1007/978-3-642-34197-7_51

Table 1 Experimental samples.

Group	Phase
1st group	100% Hap
2nd group	95% HAp/5% β-TCP
3rd group	80% HAp/20% β-TCP

B. Examination of Porous Samples

The obtained CaP porous samples were analyzed by X-ray diffraction (XRD, *PANalytical X'Pert Pro*, Cu Kα1, 40 kV, 30mA) and Fourier transformation infrared spectrometry (FT-IR, *Varian Scimitar 800*) in the wavenumber range 4000–400 cm^{-1} to evaluate phase and chemical purity. The field emission scanning electron microscopy (FE-SEM, *Tescan Mira/LMU*) was used to study the microstructure after sintering. Porosity was determined by Archimedes method.

C. Morphologic Examination

The experiments were carried out in the laboratory for Electron microscopy Riga Stradins University. The tissue response was evaluated 6 months after implantation of ceramics in the mandible of rabbits. The approval for this performance was obtained from the Riga Stradins University Ethics Committee. For this study pure tablets of HAp (the 1st group), HAp: β-TCP with a mass-ratio 95/5 (the 2nd group), and HAp: β-TCP – 80/20 (the 3rd group) were implanted in the mandible of rabbits. The tissues surrounding HAp and biphasic ceramics implanted tablets and the insides of their pores were observed and analyzed with a light microscope and electron microscope six months after implantation. Tissue samples were fixed in 2.5% glutaraldehyde. For transmission electron microscopy (TEM), the samples were post fixed in 1% osmium tetroxide, dehydrated through a graded ethanol series, and embedded in Epon epoxy resin. 60nm-thick fine sections were cut with a LKB ultramicrotome, collected on 200-mesh formvar coated cooper grids, double stained with uranyl acetate and lead citrate, and examined with a JEM 1011 electron microscope at accelerating voltage 80-100kV at magnification x5000 – x50000. 1μm- thich sections were stained with toluidine blue and viewed using light microscope.

For scanning electron microscopy (SEM), tissue dehydration was performed using increasingly concentrated solutions of acetone (70%, 80%, 90%, and 99.9% acetone in water, concentration change every 10 min), dried by the critical point method using liquid CO_2, and coated with a thin layer of gold. The samples were analyzed by a scanning electron microscope JSM-6490LV. For observation in the SEM mode, the untitled specimens were examined at an accelerating voltage of 20 kV.

III. Results and Discussion

XRD patterns shows phase composition after thermal treatment in 1150°C for 2 hours (Fig 1). The sharp peaks indicate well crystalline calcium phosphate powder consisting of pure HAp and mixture of HAp and β-TCP phases. Black triangles denote position of β-TCP phase. According to XRD data, the phase composition is following: 1st group (Fig. 1 A) – 100% HAp, 2nd group (Fig. 1 B) - 95% HAp and 5% β-TCP and 3rd group (Fig. 1 C) – 80% HAp and 20% β-TCP.

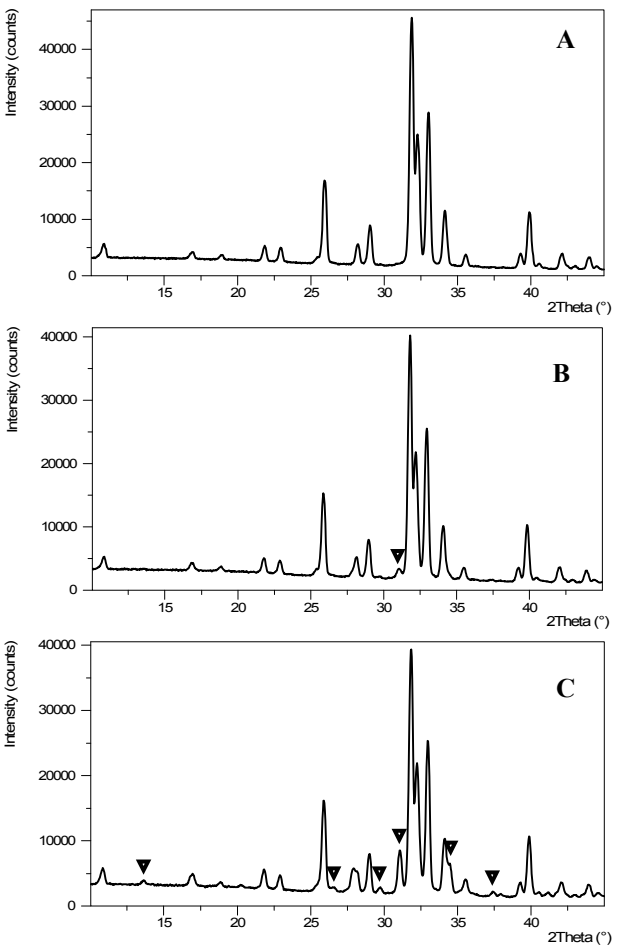

Fig. 1 X-ray diffractometry patterns: A – 1st group, B – 2nd group, C – 3rd group.

FTIR analyze was taken, to make sure, that used additives for production of porous samples do not affect chemical composition of resulting products. FTIR spectra (Fig. 2) showed only PO_4 (550-600, 962, 1020-1120 cm^{-1}) and OH (640, 3571 cm^{-1}) functional groups that characterize HAp and β-TCP phases.

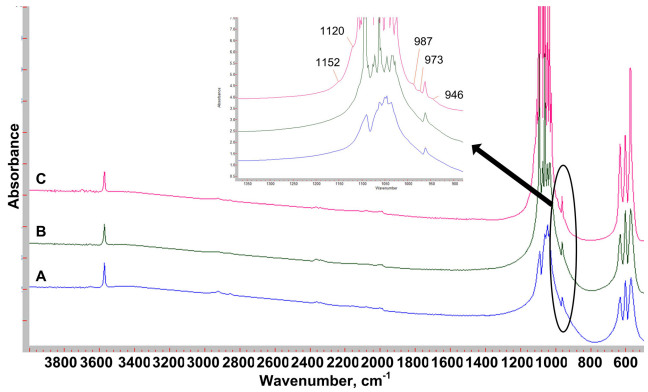

Fig. 2 FT-IR spectra: A - 1st group, B – 2nd group, C – 3rd group.

The evidence of peaks at 946 cm^{-1}, 973 cm^{-1}, 987 cm^{-1}, 1152 cm^{-1} and 1120 cm^{-1} wavenumber indicates formation of β-TCP phase. The intensity of those peaks increase from 1st to 3rd group.

As shown in Fig. 3, ceramics have highly porous structure (Fig. 3 A) forming 50 to 60 % open porosity.

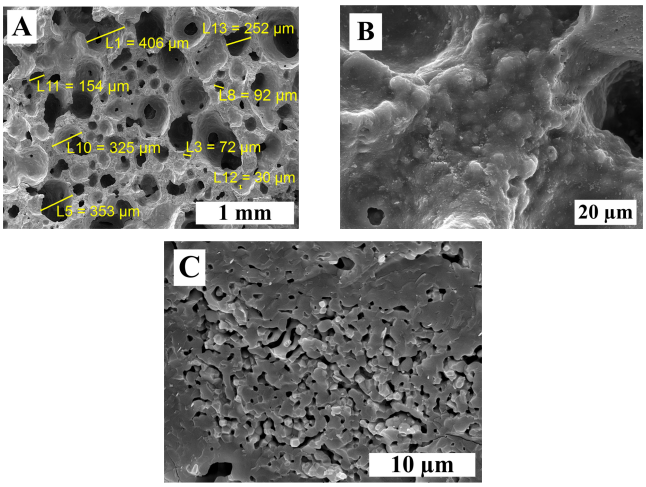

Fig. 3 SEM images of 1st group sample: A – fracture, B – pore walls, C – fracture surface of pore wall.

Pores are without a specific form. The size of macropores ranges between 30 and 400 µm (Fig. 3A). According to literature [10], it is promising for cell penetration and tissue forming. The surface of pore walls is rough (Fig. 3B) and grains have dense packing after sintering at 1150°C. There are partly connected micropores (< 10 µm) in the fracture of pore wall (Fig. 3C).

The outer layer of all implanted tablets was constituted by collagen fibers arranged in bundles (Fig. 4A) and connective tissue cells presented mostly by differentiated fibrocytes in TEM examination (Fig. 4B).

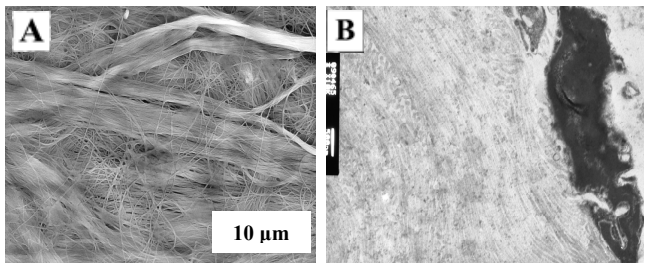

Fig. 4 A - SEM image revealing bundles of collagenous microfibrils; B - TEM picture demonstrating densely packed collagenous microfibrils collected in bundles and fibrocytes displaying finely differentiated cellular morphology. Original magnification x 10 000.

These were densely packed and surrounded by collagen fibers. Near the implant surface the collagen fibers ran parallel to biomaterial surface. The above mentioned findings were found to be in accordance with those evidenced by other authors [1, 3, 9]. Fat tissue was rather abundant, particularly, in the 2nd group (Fig. 5A). By contrast, thickening of fibrous capsule was not evident in the given group but was demonstrated in the 1st group (Fig. 5B).

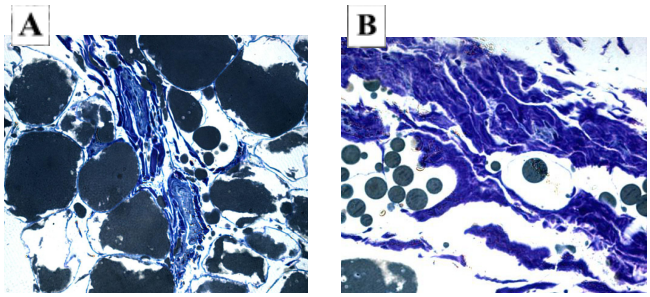

Fig. 5 Light microscopy. In epoxy resin embedded tissue sample stained with toluidine blue demonstrates: A- typical white adipose tissue morphology, sprouting vascular beds, pericytes and some flattened fibrocytes and B - a thick fibrous capsule around the sample of the 1st group. Original magnification x 400.

SEM examination revealed an intimate adhesion and spreading of cells immediately at the HAp tablet surface. These were much more less numerous at the samples obtained from the 3rd group, whereas, the samples of the 1st group displayed a remarkable tendency for cell clustering and aggregation seen in SEM studies. A vascular supply was well established. Inflammatory cells were not demonstrated. A loose and often reticular appearance of connective tissue cells was demonstrated within the calcium-phosphate ceramics pores. The interior of HAp pores of the samples obtained from the 1st and the 2nd group demonstrated a similar ultrastructure, commonly displaying a reticular 3-D appearance. Osteoblasts attached to the surface of bioceramics were regularly appearing (Fig. 6).

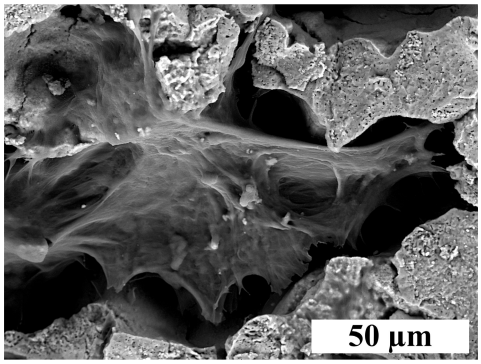

Fig. 6 SEM picture of fracture surface of sample obtained from the 1st group. The cells could be found through the entire pore.

IV. Conclusions

Studies conducted applying light, transmission and scanning electron microscopy. The results 6th months after implantation showed, a thick fibrous collagenous capsule formed around the pure HAp and presented by densely packed and flattened fibrocytes, while addition of β-TCP evidenced reduction of fibrous collagenous layer and expansion of highly vascularized adipose tissue. Collagen microfibrils predominantly showed ordered distribution and dense packaging.

Calcium phosphate porous ceramics obtained by gas-generating method is promising for bone tissue regeneration as showed histological studies. It has to be taken into account microstructure and phase composition of prepared ceramics to provide better new bone formation and resorption of implant material. The obtained porous structure is suitable for formation of blood vessels, which is an important factor for tissue regeneration processes. The examionation of resorption rate of studied materials will be the next investigation.

Acknowledgment

This work has been supported by the European Social Fund within the project "Multidisciplinary Research in Biomaterials Technology of New Scientist Group", No.2009/0199/1DP/1.1.1.2.0/09/APIA/VIAA/090.

References

1. Kunert-Keil Ch, Gredrange T, Mai R et al. (2009) Morphological evaluation of bone defect regeneration after treatment with two different forms of bone substitution materials on the basis of BONIT-matrix. J Physiol Pharmacol. 60: 57-60
2. Gauthier O, Muller R, von Stechow D et al. (2005) In vivo bone regeneration with injectable calcium phosphate biomaterial: A three-dimensional micro-computed tomographic, biomechanical and SEM study. Biomaterials 26:5444-53
3. Abrahamsson I, Zitzmann NU, Berglundh T et al. (2002) The mucosal attachment to titanium implants with different surface characteristics: an experimental study in dogs. J Clin Periodontol. 29:448-55.
4. Yoshikawa H, Tamai N, Murase T, Myoui A (2009) Interconnected porous hydroxyapatite ceramic for bone tissue engineering. J R Soc Interface 6:S341 – S348
5. Dorozhkin SV (2011) Medical application of calcium orthophosphate bioceramics. BIO 1:1-51
6. Matsumine A, Myoui A, Kusuzaki K, Araki N, Seto M, Yoshikawa H, Uchida A (2004) Calcium hydroxyapatite ceramic implants in bone tumor surgery. A long-term fllow-up study. J. Bone Joint Surg Br 86:719-725
7. Uchida A, Araki N, Shinto Y, Yoshikava H, Kurisaki E, Ono K (1990) The use of calcium hydroxyiapatite ceramic in bone tumour surgery. J Bone Joint Surg 72:298-302
8. Lee W-H, Zavgorodniy AV, Loo C-Y, Rohanizadeh R (2012) Synthesis and characterization of hydroxyapatite with different crystallinity: Effect on protein adsoption and release. J Biomed Mater Res Part A 100A:1539-1549
9. Li S-H, De Wijn JR, Layrolle P, de Groot K (2001) Synthesis of macroporous hydroxyapatite scaffolds for bone tissue engineering. J Biomed Mater Res 61(1):109-120
10. Osborn JF (1985) Implantatwerkstoff Hydroxylapatitkeramik, Quintessens Verlags
11. Petrov OE, Dyulgerova E, Petrov L, Popova R (2001) Characterization of calcium phosphate phases obtained during the preparation of sintered biphase Ca-P ceramics. Mater Lett 48:162–167.
12. Fariña NM, Guzón FM et al. (2007) In vivo behavior of two different biphasic ceramic implanted in mandibular bone of dogs. Journal of Materials Science 19(4):1565-1573
13. Lewandowski R, Rutowski R, Staniszewska-Kus J, Pielka S, Wnukiewicz B (2004) Tissue reaction after implantation of ceramic biomaterials with introduced electrokinetic zeta potential on surface. Polim Med 34:13-25
14. Hermida JC, Bergula A, Dimaano F et al. (2010) An in vivo evaluation of bone response to three implant surfaces using a rabbit intramedullary rod model. J Orthpaedic Surgery Res 5:57-65
15. Schupbach P, Hurzeler M, Grunder U (1994) Implant-tissue interfaces following treatment of peri-implantitis using guided tissue regeneration. A light and electron microscopic study. Clin. Oral Implants Res 5:55-65
16. Tete S, Mastrangelo F, Bianchi A et al. (2009) Collagen fiber orientation around machined titanium and zirconia dental implant necks: an animal study. Int J Oral Maxillofac. Implants 24:52-8.

Author: Vita Zalite
Institute: Riga Technical University Riga Biomaterials Innovation and Development Centre
Street: Pulka 3/3
City: Riga
Country: Latvia
Email: vita.zalite@rtu.lv

DLC Thin Films for Cardiovascular Stents

S.T. Shishiyanu[1], T.S. Shishiyanu[1], P.S. Stefanov[2], and V.K. Gueorguiev[3]

[1] Department of Microelectronics, Technical University of Moldova, 2004 Chisinau, Moldova
[2] ISMA Ltd., 1138 Sofia, Bulgaria
[3] Institute of Solid State Physics, Bulgarian Academy of Sciences, 1784 Sofia, Bulgaria

Abstract — **Diamond-like carbon films (DLC films) for cardiovascular implants have successfully been prepared by dual-target unbalanced magnetron sputtering and Rapid Photothermal Processing (RPP). It is found that the sputtering current of target plays an important role in the DLC film deposition. Deposition rate of 3.5 μm/h is obtained by using the sputtering current of 30 A. Rapid Photothermal Processing at 400°C essentially reduced the carbon content and have improved the surface morphology structure of deposited coatings, which depend on the intensity of the ion impingement on the growing interface.**

Keywords — **Diamond-like carbon, nanocomposite DLC, RPP.**

I. Introduction

Diamond-like carbon (DLC) films have found widespread application in biological coatings for implantable medical devices, as a result of their good chemical resistance, temperature stability and biocompatibility. The biological behavior of an implant can be tuned by modifying the element composition. DLC can be easily alloyed with other biocompatible materials such as titanium as well as toxic materials such as silver, copper and vanadium by normal co-deposition methods [1]. Nanocrystalline diamond-coated medical steel has shown a high level resistance to blood platelet adhesion and thrombi formation [2]. Diamond and DLC coatings have successfully been proposed for applications as artificial heart valves, prosthetic devices, joint replacements, catheters and stents, orthopedic pins, roots of false teeth, surgical scalpels and dental instruments [3-6].

II. Experimental

Pulsed direct current (p-DC) magnetron sputtering in combination with an unbalanced magnetron configuration has become a major technique in the deposition of advanced coatings during the last decade. It has the significant advantage over DC magnetron sputtering in suppressing arcing at the targets during reactive sputtering and in sputtering non-conductive materials.

In this paper we present the results of the microstructural control of Ti/DLC nanocomposite coatings with pulsed direct current (DC) magnetron sputtering. The sputtering system was configured of Ti target (99.7%), and graphite target (99.99%). The diameter of all the was 3 inches. All the power supplies for sputtering were operated at current regulation mode via a computer-controlled system. The thin metal layers were deposited on nonannealed and annealed stainless steel. Annealing was performed according the technology sequence for stents-electropolishing and high temperature annealing for grain enlargement and improving of the stents elasticity. A number of analytic methods were applied SEM, AFM and EDX.

The Ti/DLC films were deposited onto pre-etched non-annealed and high temperature annealed stainless steel type 316L. The morphological analyses demonstrated the essential grain enlargement. The high temperature annealing increased the grain size from 10 to 60 μm, which is necessary for the required elasticity of the arterial stents. The grain structure can influence the structure of the deposited biocompatible nanolayers, which is demonstrated further for deposited at high temperatures layers on stainless steel substrates.

The images of the grain structure of the pre-etched 316L type stainless steel annealed at high temperatures and the initial non-annealed sample are shown in Fig. 1.

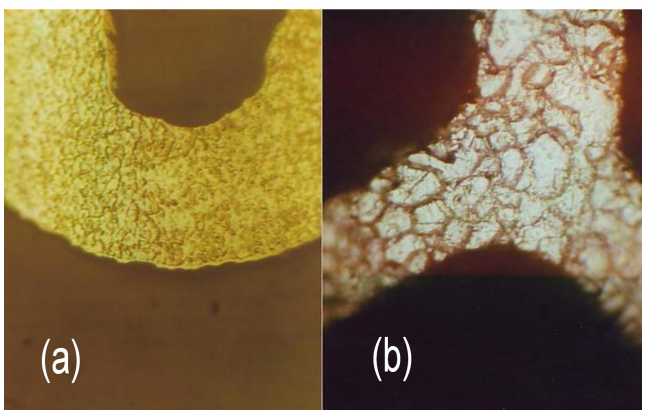

Fig. 1 (a,b) Grain structure of pre-etched high temperature annealed (a) and non-annealed (b) 316L type stainless steel.

Y. Dekhtyar et al. (Eds.): *International Symposium on Biomedical Engineering and Medical Physics*, IFMBE Proceedings 38, pp. 198–200, 2013.
DOI: 10.1007/978-3-642-34197-7_52

The investigated Ti/DLC nanocomposite films have been deposited onto the coronary stainless steel stent with the following dimensions: diameter 3mm, length 13mm fabricated by Company ISMA Ltd presented in Fig. 2.

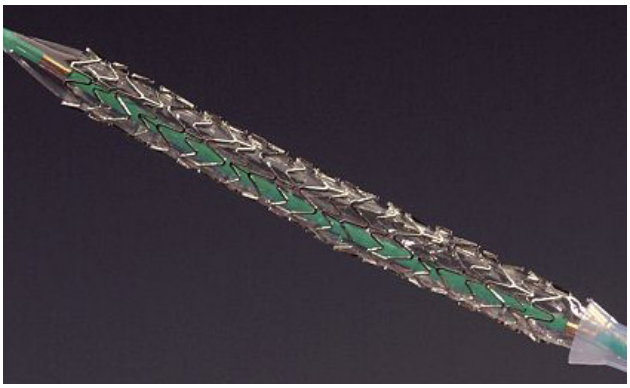

Fig. 2 Photography of the coronary stainless steel stent, diameter 3mm, length 13mm.

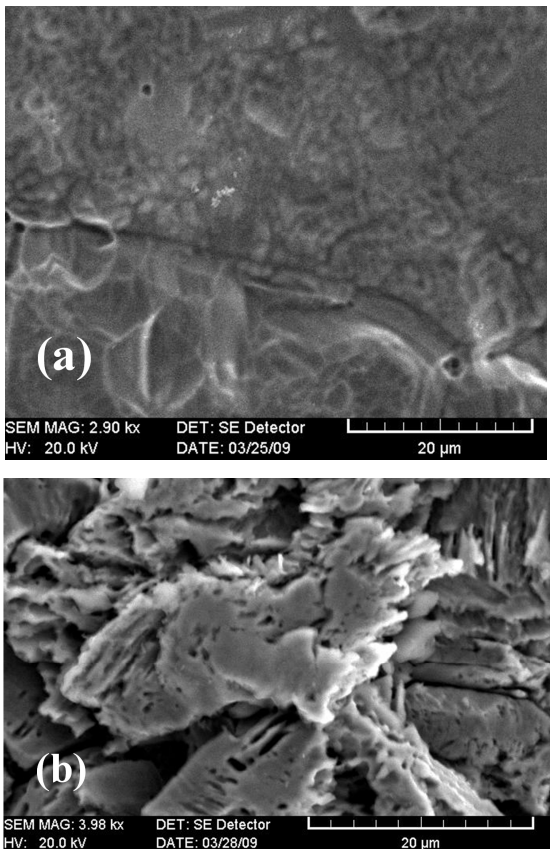

Fig. 3 (a,b) SEM of RPP DLC layers on stainless steel deposited at temperatures: a - 250°C, b - 270°C.

The SEM images of the DLC layers deposited on stainless steel at temperatures 250°C and 270°C, the RPP was performed at 300°C in vacuum, are presented in Fig. 3.

The thermal annealing of the stainless steel substrate during deposition at high temperatures do not change essential the elemental content of the substrate. Only a small oxidation is observed. But the surface and the structure of the deposited carbon layers is not smooth, as it is for layers deposited on the glass and these temperatures are not applicable for the stents technology.

AFM study images of the DLC layers deposited on stainless steel at 250°C, RPP 400°C are presented in Fig. 4.

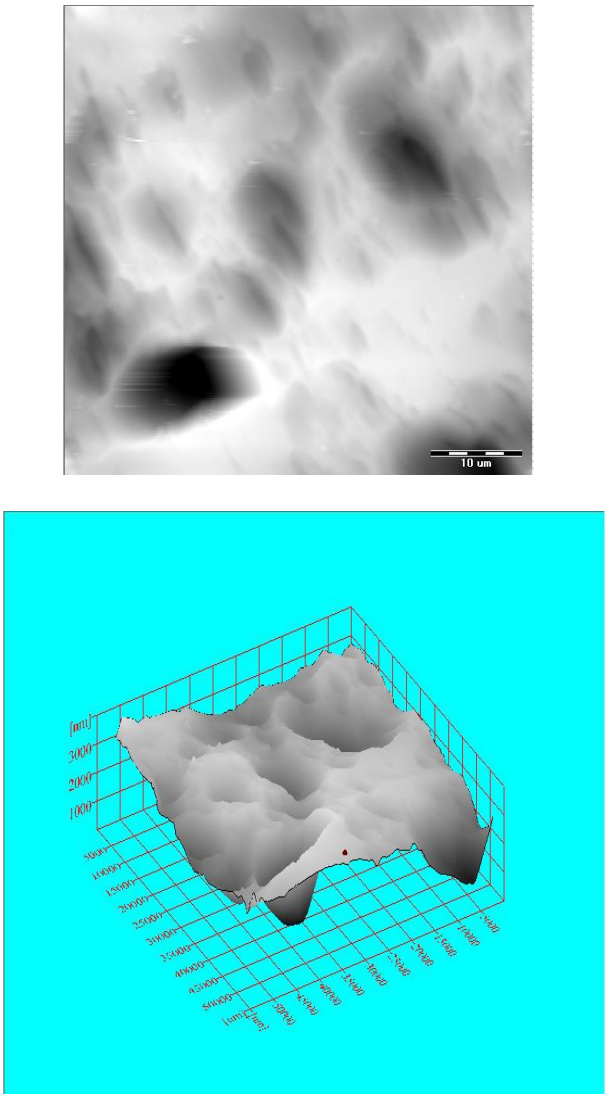

Fig. 4 (a,b) 2D and 3D AFM images of layer deposited at 250°C on nonannealed stainless steel.

The AFM study of DLC layers deposited at high temperatures on nonannealed and annealed stainless steel have shown that the roughness of the layers is up to 300 nm on nonannealed substrates and up to 3500 nm on annealed substrates. The roughness on nonannealed samples is due to the nonpolished surface, wile on the annealed substrates-to the much larger grain size after annealing.

Table 1 Influence of Rapid Photothermal Processing on the carbon content in DLC film.

Element	Non annealed		Furnace 400°C 3 min		RTP 300°C 3 min		RTP 300°C 1 min + 400°C 1 min	
	W%	A%	W%	A%	W%	A%	W%	A%
C	27.51	39.4	28.2	39.6	30.3	42.9	16.5	25.45

The Rapid photothermal processing has been performed at the following temperatures: 300°C, 350°C, 400°C, 450°C, 500°C, 600°C, 700°C in vacuum and N2. The RPP at 300°C and the furnace annealing at 400°C up to 3 min do not change essentially the carbon content, but RPP at higher temperature 350°C-450°C even up to 1 min essentially change/reduce the carbon content.

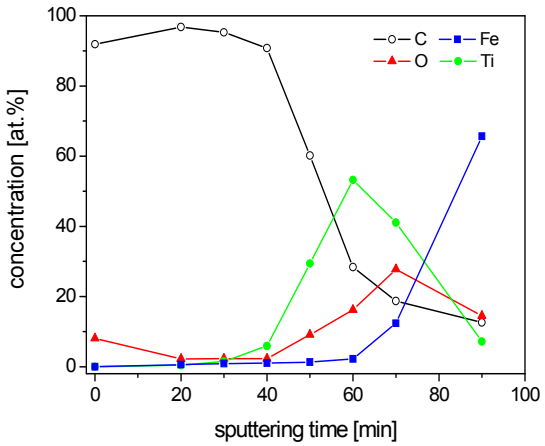

Fig. 5. Auger depth analysis for 65min deposition of DLC.

Auger depth analysis of DLC layers deposited on stainless steel for different deposition times at low plasma densities were also carried out, and the Auger spectra are presented in Fig. 5. The Auger analyses have shown existence of relative thick carbon layer, thin transition C/Ti layer and thin Ti layer.

III. Conclusions

The reliable technology for magnetron deposition of biocompatible Ti/DLC nanolayers for coating of implantable medical devices has been established. RPP at 400°C improved the microstructure and properties of deposited coatings, which strongly depend on the intensity of the concurrent ion impingement on the growing interface.

Acknowledgements

Authors gratefully acknowledge ISMA Ltd. Sofia for providing the magnetron sputtering system and the cardiovascular STENTs produced by ISMA Ltd. Sofia, Bulgaria. Authors also gratefully acknowledge Dr. E.Monaico, Dr. M.Enachi and National Center for Materials Study and Testing for carefully provided SEM and AFM measurements.

References

1. Scheerder I.D., et al. (2000) The Biocompatibility of Diamond-Like Carbon Nano Films. J. Invasive Cardiology 12:389–394
2. Okroj W., Kamińska M., Klimek L., Szymański W., Walkowiak B. (2006) Blood platelets in contact with nanocrystalline diamond surfaces. Diamond & Related Materials 15, 10:1535-1539
3. Grill A. (2003) Diamond-like carbon coatings as biocompatible materials—an overview. Diamond & Related Materials 12, 2:166-170
4. Hauert R. (2003) A review of modified DLC coatings for biological applications. Diamond & Related Materials 12, 3-7:583-589
5. Freitas R.A. (1999) Foresight Update, 39 Foresight Inst. Palo-Alto, CA, USA
6. Dearnley P.A. A review of metallic, ceramic and surface treated metals used for bearing surfaces in human joint replacements. Proc. of Institution of Mechanical Engineers. Part H, Engineering in Medicine, vol. 213, 1999, pp107-135.

Bone Marrow Multipotent Mesenchymal Stromal Cells Transplantation Effects after Experimental Polytrauma in Rats

G. Krumina[1], D. Babarykin[1], Z. Krumina[1], I. Paegle[2], O. Suhorukov[2], G. Makarenkova[3], S. Nikulshin[4], and I. Folkmane[3]

[1] Institute of Innovative Biomedical Technology, Riga, Latvia
[2] Riga Hospital of Traumatology and Orthopedics, Riga, Latvia
[3] University of Latvia, Riga, Latvia
[4] University Children's Hospital, Riga, Latvia

Abstract — **The aim of this study was to evaluate impact of transplantation of bone marrow mesenchymal stromal cells on recovery after polytrauma and bone fracture repair.**

27 Wistar-Kyoto rats were divided into 3 groups (n=9): normal control (A), polytrauma (B), and polytrauma treated with BM MMSCs transplantation (C). The experimental polytrauma model was made on male rats by causing multiple fractures and hemorrhagic shock. At 36 hours and nine days after surgery 9 rats received syngeneic BM MMSCs ($1x10^6$ cells/kg) intravenously. In 30 days post-surgery period changes in animals' body temperature, weight and locomotor behavior as well as blood parameters were recorded. At day 30 rats were euthanized and macroscopic and histological observations of rats lower extremities was performed.

The treated animals showed faster weight gain, as well as regaining their physical activity earlier. These outcomes were associated with locomotor activity test results, blood glucose and lactate ratios and less marked muscle atrophy.

Rat treatment with BM MMSCs transplantation stimulated bone fracture healing – bone edge consolidation and enhanced callus formation, as well as the size and maturity of newly formed trabeculae.

Red blood analysis results showed delayed recovery after hemorrhage in the rats receiving BM MMSCs: restoration of RBC counts, hematocrit and HGB level velocity was less than in the untreated animals.

BM MMSCs transplantation improved rats rehabilitation scores after experimental polytrauma.

Keywords — **Bone marrow multipotent mesenchymal stromal cells, polytrauma.**

I. Introduction

Despite technological progress, improvements in working conditions and road safety trauma is one of the leading cause of death and disability [1]. Military operations, terror acts and natural disasters in the last years have increased the number of trauma and polytrauma victims [2]. Polytrauma is characterized not only by damage to certain parts of the body, but also by serious systemic changes, including ischemia, hypoxia and inflammation. They require complex treatment that involves multiple management procedures [3,4].

During the last decade fast developing regenerative medicine in treatment of tissue and organ injury has lead to more wide-spread use of cell technology, including embryonic, fetal stem cells, and mesenchymal stem cells (MSCs) transplantation [6]. Bone marrow multipotent mesenchymal stromal cells (BM MMSCs) are being used more frequently, because they are easy to access for isolation and cultivation [8]. Diversity of MSCs' therapeutic efficacy is provided not only by their capability to differentiate within its mesenchymal lineage and promote bone, cartilage, muscles, tendon and fat tissue reparation [9], but also by its potency to transdifferentiate into an ectodermal cell lineage, as well as immunomodulation and paracrine effects [10,11,12].

Potential effects of MSCs transplantation in the case of polytrauma have not been widely published. MSCs transplantation could have a positive effect not only on fracture repair, but also on some other polytrauma components such as hemorrhagic shock, ischemia and hypoxia. [13,14,15]. There is reason to suppose, that the fate of transplanted cells in case of polytrauma will differ from situations when tissue injury is local. Considering the pathophysiological mechanisms of trauma and the ability of systemically transplanted MSCs to migrate to sites of injury [16], it would be logical to use MSCs in polytrauma treatment by infusing cells into patients intravenously.

The aim of our study is to investigate the effects of BM MMSCs transplantation on bone fracture repair in rats exposed to experimental polytrauma.

II. Materials and Methods

A. Animals

Male Wistar-Kyoto rats (190±11 g) were maintained on a standard rat diet and water *ad libitum*.

They were randomly divided into 3 groups (n=9): A – intact animals - control, B – animals with experimental polytrauma, C – animals with polytrauma and syngeneic BM MMSCs post-surgery transplantation.

The experiment was approved by the local Animal Ethics Committee. The rats' weight and rectal temperature was

Y. Dekhtyar et al. (Eds.): *International Symposium on Biomedical Engineering and Medical Physics*, IFMBE Proceedings 38, pp. 201–206, 2013.
DOI: 10.1007/978-3-642-34197-7_53

measured every other day during the 30 days of the experiment.

At 10, 20 and 30 days after surgery, the rats' locomotor behavior was assessed in an open field test, according to a published method [17].

B. Polytrauma Model

Polytrauma was induced by causing multiple fractures and hemorrhagic shock under general anesthesia with intraperiotenal injection of ketamine/medetomidine/ atropine (75/0.5/0.5 mg/kg). Fractures were provoked by clamping both femurs and the right tibia. No fixation of fractures was used during recovery. Hemorrhagic shock was induced by 3.5 - 4 ml withdrawal of blood from the sublingual vein. After 60 min animals receive fluid resuscitation by infusing 2 ml of saline. Thereafter, the rats were maintained on water containing 0.15 mg/ml ibuprofen for at least 2 weeks.

C. Isolation, Expansion and Transplantation of BM MMSCs

The BM MMSCs were isolated from femurs and tibias of 130-150 g male Wistar-Kyoto rats (n=54) and expanded as described previously [18]. The adherent cells after 3 passages were used for MSCs. They were CD90 positive and CD45 negative detected by flow cytometry [18] as well as showed ability for osteogenic and adipogenic differentiation [19].

Thirty-six hours and nine days after surgery rats received saline (0.2 ml, group B) or syngeneic BM MMSCs ($1x10^6$ cells/kg in saline, group C) injected into the lateral tail vein.

D. Blood Analysis

At the 3rd and 10th day of the experiment venous blood from each rat was analyzed using a blood gas analyzer RapidLab® 1265 (Siemens, Germany).

In addition, the day before the operation and at day 3 and 10 as well as at the end of the experiment, heparinized blood was drawn for blood element analysis on Cell-Dyn® 3700 (Abbott, USA).

At the end of experiment 2 ml of blood was collected for biochemical analyses (blood serum creatinine, urea, alanin aminotransferase (ALT) and aspartate aminotransferase (AST)) performed on ILAB 300+ (Instrumentation Laboratory, USA).

E. Macroscopic Observations of Rats' Lower Extremities

The rats were euthanized 30 days after surgery by trans-cervical dislocation and the lower extremities from three animals in each group were taken for muscle and callus macroscopic examination as well as for histological observation. Muscles together with their tendons were weighed immediately following dissection.

F. Histological Preparation of the Bones

The bones were fixed in 4% paraformaldehyde and then decalcified using Shandon TBD-2 Decalcifier (Fisher Scientific, USA) and embedded in paraffin. Bone histological sections were stained with hematoxilin and eosin.

G. Statistical Analysis

Statistical analysis was performed using *Excel* 2003. All results are expressed as mean ± standard deviation of the mean of three or more measurements. A two-sided, paired t test was used, and differences were considered significant at $p < 0.05$.

III. Results

A. Changes in Body Weight Following Polytrauma

In our experiment, a body weight decrease of (7.4±1.5 g) was observed in the operated animals as early as 24 h after surgery. Thereafter, the rats' body weight in both animal groups operated on increased similarly as in the control group (Fig. 1). At the 4th day after polytrauma, the weight in groups B and C was similar, but soon after, the rats' weight

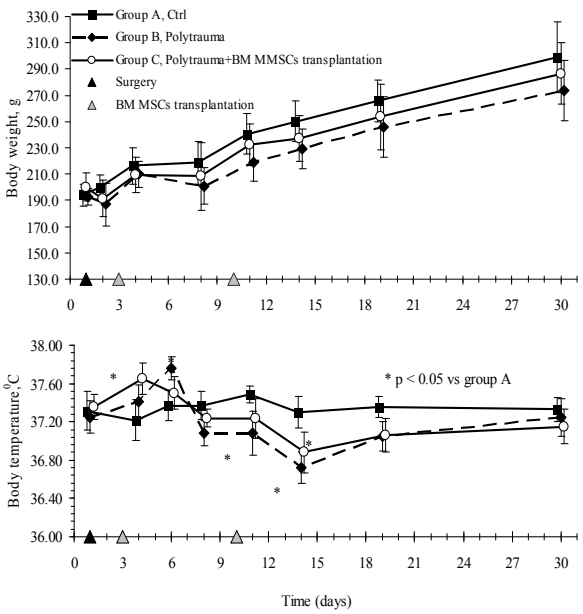

Fig. 1 Body weight and temperature dynamics in rats with experimental polytrauma and bone marrow multipotent mesenchymal stromal cells transplantation (mean ± SD).

gain in group C increased more than in group B and at the end of the experiment, the weight gain since the first day in group C was 105.1±6.5 g, however, in group B, it was – 80.5±5.2 g ($p<0.05$).

B. Temperature Alterations

In the 1st week after surgery, the rats' rectal temperature increased slightly in both operated animal groups (Fig. 1). At the end of the 2nd week after surgery, the rats' body temperature in both the operated animal groups decreased – group B 36.72±0.26 °C, group C 36.88±0.31 ^{0}C (NS).

C. Macro-morphological Changes in Fractured Extremities

No substantial differences in skeletal muscles between groups A and C was seen in their macroscopic observation except some deformities in the latter. Muscle mass was similar between these two groups, but in group B animals it was approximately 20% less (Table 1).

Table 1 Polytrauma and bone marrow multipotent mesenchymal stromal cell transplantation effects on rats hindlimbs muscle's weight (g) in 29 days after surgery (mean ± SD).

	A Control	*B Polytrauma*	*C Polytrauma + BM MMSCs transplantation*
M. biceps femoris	1.81±0.03	1.45±0.04*	1.78±0.04†
M. quadriceps femoris	2.41±0.04	1.93±0.03*	2.36±0.03†
M. gastrocnemius	0.68±0.02	0.49±0.02*	0.65±0.03†
M. tibialis anterior	0.57±0.05	0.46±0.02*	0.55±0.02†

* $p < 0.05$ vs. control group A
† NS vs. control group A.

After dissecting the muscles, it was seen that practically all the fractured bones were healing with dislocations. In two cases from group C it was a side' to side consolidation, in the others the consolidation was angulated. For that reason, some shortening, mainly in femoral bones, took place. In group C consolidation was characterized by large callus area that fixated and stabilized the fracture in comparison to group B, where the callus size was smaller. It was also seen that animals in group C regained functional capacities of their extremities earlier than in group B (Fig 2).

D. Histological Findings

Histological examination of fractured bones (group B) showed that repair developed in accordance with a classic scenario: 30 days after the fracture, active bone repair was observed both periostally and endostally while in control group A there were no signs of osteoblast activity (Fig. 3).

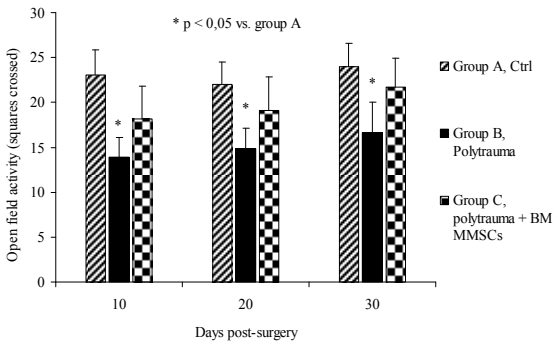

Fig. 2 Open field testing over a 30 days period following surgery in rats from groups B (polytrauma), C (polytrauma with following bone marrow multipotent mesenchymal stromal cells transplantation) and A (control) (mean ± SD).

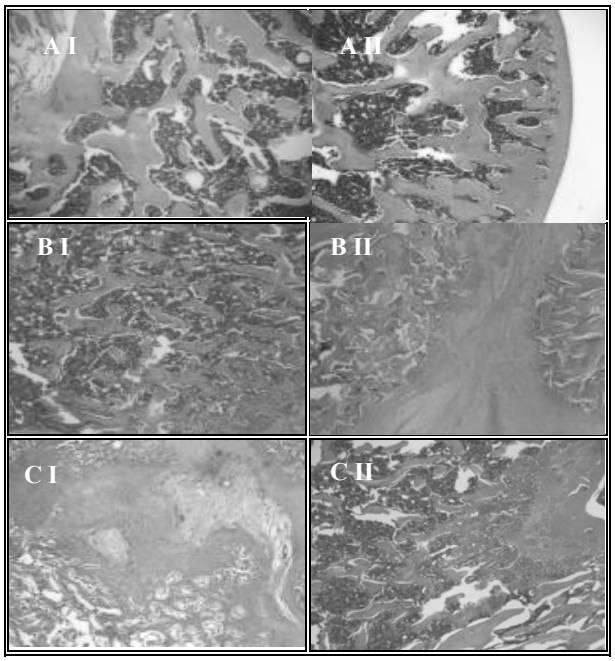

Fig. 3 Stain: He/Eo. Magnification: x100. **A** - Group A (intact rats). Normal structure of tubular bone. Mature bone with no osteoblast activity. Bone marrow hemopoietic activity complies with animals' age. A**I** Bone structure in diaphysis. A**II** Bone structure in femur distal metaphysis. **B** - Group B (rats with polytrauma). Bone marrow hemopoietic activity elevated. Configuration and placement of bone trabeculae uneven and chaotic. High osteoblasts activity but trabeculae maturity level low with remained cartilage inclusions. B**I** New bone tissue in fracture site. B**II** Pseudoarthrosis in tibia. **C** - Group C (rats with polytrauma+syngeneic BMMSCs transplantation). Osteoblasts activity is very high. Trabeculae maturity degree is high; size and orientation are indistinguishable with control group animals, in some cases trabeculae size exceeds control one. Bone marrow hemopoietical activity elevated. C**I** Fracture site in femur. C**II** New bone tissue in fracture site.

Fibroplasy and chondroplasy as well as ossification at the fractured bone edges were unevenly marked. Trabeculae in newly formed bone tissues were small in size, immature with retained cartilage inclusions and their architecture within bone was uneven. Bone marrow hematopoietic activity was elevated (Fig. 3).

In group C, active subperiostal and endostal osteoplasy was seen. In some places, newly formed bone trabeculae were enclosed with many layers of osteoblasts. Unlike in group B bone trabeculae were mature, their size conformed to the norms. In fibrous tissue and cartilage of fracture lines, bone regeneration was active, ensuring stable fragments' fixation. Similarly in group B, bone marrow hematopoietic activity was elevated (Fig. 3).

E. Changes in Blood Parameters

The creatinine level as well as the ALAT and ASAT 30 days after the beginning of the experiment was similar in all operated and non-operated animals (Table 2). A difference in blood urea levels between groups was not statistically significant; however, it had a tendency to increase in the untreated polytrauma group (B; 5.47±0.33 mmol/l) in comparison to the control group (A; 5.11±0.39 mmol/l) and animals which received BM MMSCs injections (4.90±0.26 mmol/l).

We also measured glucose and lactate concentrations in the rats' blood 10 days after surgery. In group B, the animals' lactate level had decreased (2.83±0.59 mmol/l; NS) in comparison with control group (3.69±0.57 mmol/l), but glucose had risen - 4.5±1.91 mmol/l vs control – 3.70±1.83 mmol/l. The lowest blood glucose level was in group C (2.32±0.88 mmol/l), but lactate concentration was the same as in control group (3.68±0.87 mmol/l).

Three days after surgery, group B and C animals' pO_2 was lower than in control group A. The pCO_2 was increased above the normal level and blood pH was decreased, which indicated hypoventilation and respiratory acidosis. HCO_3^- in traumatized animals had a tendency to increase due to metabolic compensation.

On 10th day after surgery, the blood acid-base balance parameters in all animal groups had returned to normal range. There were no statistically significant differences between the two poly-trauma groups (Table 3).

Table 2 Blood serum biochemical parameters at day 30th in rats with polytrauma (mean ± SD).

Groups	*A - Control*	*B - Polytrauma*	*C - Polytrauma + BM MMSCs transplantation*
Creatinine, mmol/l	0.05±0.01	0.05±0.02	0.05±0.03
ALAT, U/l	46.3±11.5	49.0±5.6	41.6±4.4
ASAT, U/l	179.4±25.8	186.7±43.1	180.3±39.3

Table 3 Acid/base balance and gas parameters dynamics (day 3rd and 10th) in rats with polytrauma (mean ± SD).

Groups	*A - Control*		*B - Polytrauma*		*C - Polytrauma + BM MMSCs transplantation*	
pH	7.43 ±0.02	7.40 ±0.07	7.2 ±0.02*	7.35 ±0.01**	7.28 ±0.03*	7.33 ±0.05**
pO_2, mmHg	41.6 ±2.6	41.9 ±6.3	34.9 ±4.9*	39.5 ±2.6**	35.3 ±3.9*	40.3 ±6.0**
pCO_2, mmHg	50.3 ±4.7	51.1 ±3.2	54.3 ±5.2	47.7 ±3.6	54.3 ±3.6	46.5 ±4.0
HCO_3, mmol/l	23.5 ±3.4	21.9 ±1.5	26.7 ±3.1**	25.1 ±1.7	25.4 ±3.2**	23.5 ±1.6

* $p < 0.05$; vs. group A (control).
** NS; vs. group A.
† $p < 0.05$ vs. group B (polytrauma).

Due to a blood loss RBC count as well as the HGB and HCT levels was noticeably decreased 3 days after surgery (Table 4). The cell count increased thereafter, but some differences in the speed of recovery between group B and C were fixed. The increase in RBC count in group B was 1.21 $x10^6/mm^3$ while in group C – it was 0.81 $x10^6/mm^3$ in 7 days. The same tendencies were seen in hemoglobin concentration and hematocrit gain (2.36 g/dL vs. 1.2 g/dL , i.e. 10.37% vs. 5.37% in 7 days). Although at the 30th day after surgery these parameters in both group B and C returned to baseline values, in group C the results still remained a little lower than in group B.

Table 4 Red blood indices dynamics of the rats with polytrauma and syngeneic BM MMSC transplantation (mean ± SD).

	Day of exp.t	*A Control*	*B Polytrauma*	*C Polytrauma + BM MMSCs transplantation*
RBC, $x10^6/mm^3$	3rd	8.13±1.3	6.32±1.1	6.82±1.0
	10th	8.05±1.0	7.53±1.2*	7.63±1.4*
	30th	8.70±1.0	8.76±1.3	8.60±1.5
HGB, g/dL	3rd	15.53±0.8	12.87±1.2*	13.63±0.9*
	10th	15.13±0.5	15.23±0.8	14.83±1.0
	30th	15.58±0.4	16.67±0.3	16.30±0.5
HCT, %	3rd	50.05±2.8	41.63±2.9*	44.26±2.7*
	10th	48.53±3.1	48.91±4.2	48.00±3.0
	30th	49.05±2.7	51.38±3.1	50.42±2.4

- $p < 0.05$ vs. group A (control).

Rats in groups B and C had a decrease in the leukocyte count by 17% 3 days after surgery. At day 10 it was elevated by 30% above the normal level. At the end of the experiment the WBC count in group C rats was 16% less than in control (Fig. 4).

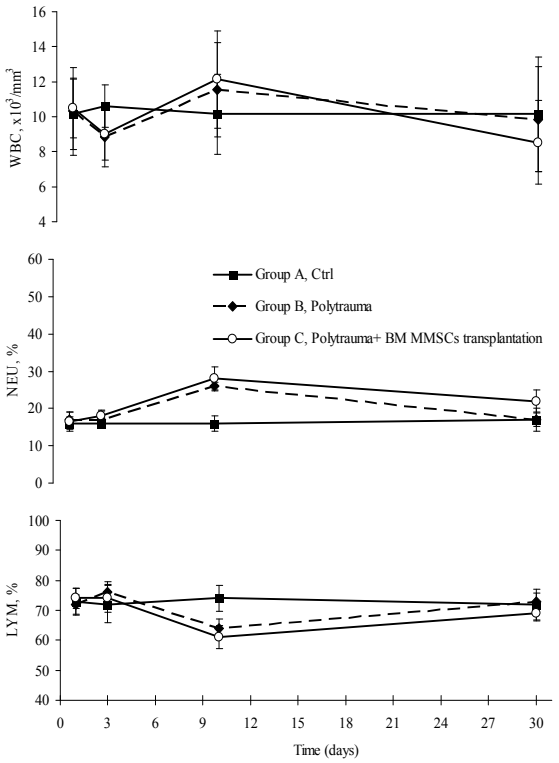

Fig. 4 Dynamics of white blood cell counts (WBC) and neutrocytes (NEU) and lymphocyte (LYM) percentage in rats after polytrauma and bone marrow multipotent mesenchymal stromal cell transplantation (mean ± SD).

Decline in lymphocyte counts was seen 10 days after surgery in group B and group C (64% and 61% respectively), however, neutrocyte counts, especially in group C, was rising (Fig. 4). Blood monocyte counts in B and C group rats was decreased on the 3rd day after polytrauma and increased at day 10. Eosinophile and basophile counts did not change significantly during the experiment.

IV. Discussion

The aim of this study was to evaluate the outcome of BM MMSCs transplantation in rats after experimental polytrauma, with 3 bone fractures and acute hemorrhage.

In our study, the main systemic changes influenced by polytrauma were body weight gain, temperature, blood acid/base and gas balance as well as blood cell counts.

Weight gain is one of the indicators of animal recovery. Rats, which underwent polytrauma, showed weight gain soon after surgery. That indicated that the studied animals had no irreversible stress after surgery. However total gain of weight in rats that received BM MMSCs treatment was larger than in the untreated polytrauma group. This may mean that rats' treatment with BM MMSC transplantation leads to faster recovery after trauma and better rehabilitation process outcomes.

In our experiment, body temperature increase in rats, that received BM MMSCs (37.65±0.41 ^{0}C) was detected 24 h after cell transfusion (4 days after surgery), however, in the polytrauma group (37.76±0.42^0 C) – this occurred only 6 days after the trauma. This may indicate the immunological reaction in response to the cell transfusion that often occurs after blood cell transfusion [20].

Animals treated with BM MMSCs transplantation regained functional capacities of their extremities earlier than the untreated group. Macroscopic observations showed that rats from the cell treated group had larger sizes of callus that could ensure stability and functionality of broken extremities.

Transplantation of BM MMSCs improved healing of rats' long bone fractures by enhancing osteoblast activity and their function (bone matrix development and mineralization) and accelerating trabeculae formation and maturation.

Obviously fractures affected not only bone and cartilage tissues, but also stimulated hematopoietic bone marrow cell proliferation which was seen in both operated rat groups. One of the factors that may activate hematopoiesis is an increase in bone blood flow as a response to mechanical disruption [21].

Usually, during hemorrhagic shock there is an elevation of the blood lactate concentration due to tissue metabolism change to anaerobia caused by ischemia [22]. The discrepancy in our results (the tendency of lactate to rise) may be explained by a 10 day delay between polytrauma with hemorrhagic shock and lactate measurement. The differences in blood glucose and lactate concentration dynamics between polytrauma and polytrauma + BM MMSCs transplantation group could also be explained by differences in the animals' physical activity level: rats treated with BM MMSCs infusion were more mobile. This explanation is supported by the fact that the rats with polytrauma lower extremity muscles had atrophied (Table 1) as well as by the locomotor activity test results: locomotor activity of polytraumatized rats treated with BM MMSCs infusion in the open field test for all three measurements was higher than in nontreated polytrauma group (NS) (Fig. 2). There were some differences in other blood serum biochemical indices dynamics between the animal groups, as well. Blood urea had a tendency to increase in untreated animals in comparison with the control and polytrauma with BM MMSCs group, however, the creatinine level was stable. Differences in ALT and AST activities between groups indicate that liver function was slightly negatively influenced by poly-trauma (Table 2), but BM MMSCs infusion had a stabilizing effect (NS).

Changes in acid-base balance induced by hypovolemic shock and hypoperfusion are characteristics for trauma

patients [23]. In our study's operated animals blood parameters showed hypoventilation and respiratory acidosis with metabolic compensation in operated animals 3 days after surgery. On 10th day after surgery, the blood acid-base parameters in all animal groups had returned to normal range. There were no statistically significant differences between the two poly-trauma groups (Table 3) indicating that BM MMSCs transplantation did not have any impact on this part of the poly-trauma pathophysiological process.

Production of new red blood cells after acute anemia in animals who received BM MMSCs transplantation was impaired as indicated by RBC count as well as the HGB and HCT levels. The reasons for this are unclear.

Certain responses to surgery and cell infusions have been developed also in the leukocyte formula. Rats that underwent surgery had decrease in the leukocytes count by 17% three days after surgery that was caused by blood loss, at day 10 it was elevated by 30% above the normal level, which evidently shows inflammation caused by polytrauma. At the end of the experiment the WBC number in BM MMSCs treated rats was for 16% less than in control. This phenomenon may be explained by MSCs-mediated inhibition of lymphocytes proliferation [24].

V. Conclusion

BM MMSCs transplantation improved rat rehabilitation scores after experimental poly-trauma. The treated animals showed faster weight gain, as well as regaining their physical activity earlier than untreated rats. These outcomes were supported by locomotor activity test results, blood glucose and lactate ratios and less marked skeletal muscle atrophy.

Rat treatment with BM MMSCs transplantation stimulated bone fracture healing – bone edge consolidation and enhanced callus formation, as well as the size and maturity of newly formed trabeculae.

Transplantation of BM MMSCs caused delayed recovery after hemorrhage: restoration of RBC counts, hematocrit and HGB level velocity was less than in the untreated animals.

All consequences of polytrauma can not be treated only with cell transplantation. To enhance poly-trauma treatment efficacy with BM MMSCs systemic injections, cell transplantation has to be combined with an additional technology that would have impact on fate and functions of transplanted cells.

References

1. Lecky FE, Bouamra O, Woodford M, et al. (2010) Epidemiology of polytrauma. In: Pape, H.-C.; Peitzman, A.B.; Schwab, C.W.; Giannoudis, P.V. eds. Damage Control Management in the Polytrauma Patient. Springer, 13-23

2. Lopez AD, Mathers CD, Ezzati M, et al. (2006) Global and regional burden of disease and risk factors, 2001: systematic analysis of population health data. Lancet 367(9524):1747-57

3. Gebhard F, Huber-Lang M. (2008) Polytrauma--pathophysiology and management principles. Langenbecks Arch Surg 393(6):825-831

4. Clark ME, Scholten JD, Walker RL, et al. (2009) Assessment and treatment of pain associated with combat-related polytrauma. Pain Med 10(3):456-469

6. FuchsE, Segre JA. (2000) Stem cells: a new lease on life. Cell 100(1):143-155

8. Pountos I, Giannoudis PV. (2005) Biology of mesenchymal stem cells. Injury 36S(3):S8-S12.

9. Chamberlain G, Fox J, Ashton B, et al. (2007) Concise review: mesenchymal stem cells: their phenotype, differentiation capacity, immunological features, and potential for homing. Stem Cells 25(11):2739-2749

10. Lin W, Chen X, Wang X, et al. (2008) Adult rat bone marrow stromal cells differentiate into Schwann cell-like cells in vitro. In Vitro Cell Dev Biol Anim 44(1-2):31-40

11. Patel SA, Sherman L, Munoz J, et al. (2008) Immunological properties of mesenchymal stem cells and clinical implications. Arch Immunol Ther Exp (Warsz) 56(1):1-8

12. Arthur A, Zannettino A, Gronthos S. (2009) The therapeutic applications of multipotential mesenchymal /stromal stem cells in skeletal tissue repair. J Cell Physiol 218(2):237-245

13. Plaschke K. (2009) Human adult mesenchymal stem cells improve rat spatial cognitive function after systemic hemorrhagic shock. Behav Brain Res 201(2):332-337

14. Hoffmann J, Glassford AJ, Doyle TC, et al. (2010) Angiogenic effects despite limited cell survival of bone marrow-derived mesenchymal stem cells under ischemia. Thorac Cardiovasc Surg 58(3):136-142

15. Abdollahi H, Harris LJ, Zhang P, et al. (2011) The role of hypoxia in stem cell differentiation and therapeutics. J Surg Res 165(1):112-117.

16. Hosogane N, Huang Z, Rawlins BA, et al. (2010) Stromal derived factor-1 regulates bone morphogenetic protein 2-induced osteogenic differentiation of primary mesenchymal stem cells. Int J Biochem Cell Biol 42(7):1132–1141

17. Weaver Ian CG, Meaney MJ, Szyf M. (2006) Maternal care effects on the hippocampal transcriptome and anxiety-mediated behaviors in the offspring that are reversible in adulthood. PNAS 103(9):3480–3485.

18. Krievina G, Bezborodovs N, Makarenkova G, et al. (2008) The Influence of Cultivation Conditions on the Proliferation and Differentiation of Rat Bone Marrow Multipotent Mesenchymal Stromal Cells. IFMBE Proc. Vol. 20, pp. 41-44

19. Freshney RI, Stacey GN, Auerbach JM. (2007)Culture of Human Stem Cells. Wiley, New Jersy

20. Zimring JC. (2010) Recent developments and future directions of alloimmunization to transfused blood products. Clin Lab Med 30(2):467-473

21. Van Dyke D, Harris N. (1969) Bone marrow reactions to trauma. Stimulation of erythropoietic marrow by mechanical disruption, fracture or endosteal curettage. Blood 34(3):257-275

22. Kovach AGB, Rosell S, Sandor P, et al. (1970) Blood flow, oxygen consumption, and free fatty acid release in subcutaneous adipose tissue during hemorrhagic shock in control and phenoxybenzamine-treated dogs. Circ Res 26:733-741

23. Kaplan LJ, Frangos S. (2005) Clinical review: Acid-base abnormalities in the intensive care unit - part II. Crit Care 9(2):198-203

24. Uccelli A, Moretta L, Pistoia V. (2008) Mesenchymal stem cells in health and disease. Nat Rev Immunol 8:726-736

Author: Guntra Krumina
Institute: Institute of Innovative Biomedical Technology
Street: Inchukalna street 2, LV-1014
City: Riga
Country: Latvia
Email: guntra.krumina@gmail.com

Transmyocardial Laser Revascularization: Single-Institution Experience

Edgars Freilibs, Romans Lacis, and Uldis Strazdins

Pauls Stradins Clinical University Hospital/ Center of Cardiac Surgery, Riga, Latvia

Abstract — **Objective: The standard revascularisation methods have not proved effective enough in situations of very diffuse coronary artery disease (CAD). One of the methods to solve this situation is transmyocardial laser revascularization (TMLR). Methods and results: 35 patients have undergone surgical treatment since November 2003. All operations had done TMLR as an adjunct to coronary artery bypass graft surgery (CABG).All patients had 3 vessels disease. At a median follow up 6 months after operation 78 % of patients were free of angina pectoris. All patients before operation were in III and IV Canadian Cardiovascular Society (CCVS) angina class, after operation at follow up time were in class 0 – II CCVS. Myocardial perfusion scintigraphy shows significant improvement of myocardial perfusion. In control group were 50 patients with three vessels disease, all of the patients underwent isolated CABG surgery on pump. No statistical significant differences were found in Troponin I level, postoperative bleeding compared with isolated CABG. Conclusions: TMLR is minimally traumatic and effective treating method in combination with CABG.**

Keywords — **transmyocardial laser revascularization, coronary artery disease, coronary artery bypass graft surgery, Canadian cardiovascular society angina class.**

I. Introduction

Coronary artery disease is the leading cause of death worldwide. Cardiovascular diseases cause 42% of all deaths in the European Union (EU): 46% of deaths (women) and 38% deaths (men). 4 million Europeans are dying each year from cardiovascular diseases [7].

There are three main treating methods for CAD: medical therapy, percutaneous interventions (PCI), and coronary artery bypass graft surgery (CABG). In patients with severe diffuse coronary artery atherosclerosis it is not possible to do complete revascularisation with PCI or CABG (we can predict it in coronary angiography).If these patients have severe angina that persists despite maximal medical therapy we have to look at other treating methods. One option is TMLR. The first time TMLR was done by Mirhoseini et al. to animals in 1981 [2-4]. It was done for the first time to people by Okada et al. in 1986 [2-4].

The technical idea of method is to create the channels through myocardium with laser energy. Hypothesis of TMLR are – blood flow to the myocardium through channels and initiate the wound healing process with associated angiogenic response (angiogenesis) and (or) regional myocardial denervation. [1] Mechanism of revascularization with TMLR is still unclear. Several randomized, controlled, multicentral trials have established the clinical efficacy of sole therapy TMLR [2-6]. Our aim is to do TMLR as an adjunct to CABG and to assess the effect of operation.

II. Materials and methods

35 patients were operated on in our hospital by TMLR plus CABG. The operations took place from November 2003 to 2012. 17 patients were women and 18 men. The average age was 65 years old (46- 75) .All patients had three vesels severe diffuse coronary artery atherosclerosis disease. One or two main coronary arteries were non amenable for PCI or CABG. It was diagnosticed preoperatively angiographically or intraoperatively. For TMLR we use Cardiogenesis „TMR 2000„ Holmium: yttrium – aluminum – garnet (Ho: YAG). Ho: YAG is pulsatil mid – infrared laser. The average amount of channels was 10 to a patient. Mostly channels were done to anterior wall of the left chamber.

77 % of patients were examinated with myocardial perfusion scintigraphy, 10 patients were examinated with magnetic resonance imaging (MRI), almost all were examinated with echocardiography before and 6 months after procedure. Patients were checked for their CCVS class pre and 6 months postoperatively.

We controlled Troponin I postoperatively.

We checked postoperative bleeding.

In control group were 50 patients with three vesels disease, all patients were after isolated CABG operated on pump.

III. Results

Survival after operations was 97%. 1 patient died 9 days after the operation; the cause was acute respiratory virus infection (ARVI). All patients were in class III-IV CCVS preoperatively. After operations 78 % of patients were graded as class 0 (CCVS), 11 % as class I, 11% as class II 6 months after the procedure.

Y. Dekhtyar et al. (Eds.): *International Symposium on Biomedical Engineering and Medical Physics*, IFMBE Proceedings 38, pp. 207–208, 2013.
DOI: 10.1007/978-3-642-34197-7_54

Average Troponin I after operations was 23.3 ng/ml. Average Troponin I in the control group was 15.5 ng/ml.

Echocardiography did not show statistically significant increase of ejection fraction after the procedure in both groups.

No reoperations caused by postoperative bleeding in both groups.

Myocardial perfusion scintigraphy showed perfusion improvement in myocardium after operation; however some patients still had ischemic regions in myocardium.

IV. Conclusions

TMLR in combination with CABG is an effective treating method at the end stage medically refractory coronary artery disease.

It is not easy to conclude that the improvement of angina and myocardial perfusion due to TMLR was because we did TMLR in combination with CABG.

TMLR is a minimal traumatic method - no reoperations due to bleeding, the Troponin I level and incidence of myocardial infarction postoperatively was approximately the same in the control group.

References

1. Charles R.Bridges, Keith A.Horvath, Ray Chu-Jeng Chiu (2006). Myocardial laser revascularization. Blackwell
2. Schofield PM, Sharples LD, Caine N, et al. Transmyocardial laser revascularization in patients with refractory angina: a randomized controlled trial. Lancet 1999; 353:519-24
3. Jones JW, Schmidt SE, Richman BW, et al. Holmium: YAG laser transmyocardial revascularization relieves angina and improves functional status. Ann Thorac Surg 1999; 67:1596-601
4. Frazier OH, March RJ, Horvath KA. Transmyocardial revascularization with a carbon dioxide laser in patients with end-stage coronary artery disease. M Engl J Med 1999:341:1021-8
5. Allen KB, Dowling RD, Fudge TL, et al., Comparison of transmyocardial revascularization with medical therapy in patients with refractory angina. N Engl J Med 1999; 341:1029-36
6. Burkhoff D, Fisher PE, Apfelbaum M, et al. Histological appearance of transmyocardial laser channels after 4_weeks. Ann Thorac Surg 1996; 61:1532-6
7. Coronary Heart Disease Statistics at http://www.annecollins.com/nutrition/heart-facts.

Author: Edgars Freilibs
Institute: Pauls Stradins Clinical University Hospital/ Center of Cardiac Surgery
Street: Pilsonu Street 13
City: Riga
Country: Latvia
Email: edgars.freilibs@inbox.lv

Chemically Inert Nanoparticles Affect Hemopoietic and Stromal Cells Microenvironments in Vitro

I.A. Khlusov[1,3], T.A. Feduschak[2], and M.Yu. Khlusova[1]

[1] Scientific Educational Center "Biocompatible Materials and Bioengineering", Tomsk Polytechnic University, Siberian State Medical University, Institute of Strength Physics and Materials Science, Siberian Branch, Russia Academy of Sciences, Tomsk, Russia
[2] Institute of Petroleum Chemistry, Siberian Branch, Russia Academy of Sciences, Tomsk, Russia
[3] Limited Company "Bioconstructor-S", Tomsk, Russia

Abstract — **Cellular and molecular processes developing in vitro during direct contact of chemically inert nanoparticles with mice HI and artificial niches for osteogenic differentiation of human stromal stem cells (SSC) were evaluated. Nano-sized carbon encapsulated iron powders Fe(C) (diameter <10 nm) and FeSi(C) (diameter < 20 nm) were prepared. Pure titanium discs (diameter 12 mm, thickness 1 mm) with bilateral CP coatings were used as the source of surface with artificial osteogenic niches. Chemical inertness of iron and composite nanoparticles with carbon covering was evident. Reactive oxygen species production caused by Fe(C) or FeSi(C) was insufficient to destroy cells and their microenvironment. However, low doses of chemically inert nanopowders were capable to diminish morphofunctional status and humoral cooperation of SSC with hemopoietic cells** and CP coatings**. For all this, different heat generation (Q) for Fe(C) and FeSi(C) specimens has been revealed. We proposed thermodynamic functioning of interfaces between both different stem cells and CP surfaces.**

Keywords — **artificial specimens, hemopoietic islets, stromal stem cells, cytokines, surface free energy.**

I. Introduction

To explain a fundamental and contradictory phenomenon of self-maintenance and differentiation processes of hemopoietic stem cells (HSC) R.Schofield put forward a hypothesis on a hemopoietic niche (specialized stem cell microenvironment) as an essential matter for the maintenance of stem cell phenotype [1]. Outside the niche HSC differentiate into committed hemopoietic precursors in the specific microterritory, so-called hemopoietic islets (HI) [2].

Current trends lead to asking the question: What does the concept of the stem cell niche really mean today? [3]. Our point of view allows selecting achievements in this field. First of all, there are proposed a hierarchy of niches for HSC self-maintenance, proliferation or differentiation [4] and their some topographical localization [5]. So, osteoblastic (endosteal) niches promote "quiescent" HSC state and perivascular ones do an active hemopoietic cells proliferation [6]. In this connection, HI as bone marrow structural and functional units for HSC proliferation and differentiation [2] can be also considered as specific niches with final sizes of stem and progenitor cells microterritory. Besides, there are the attempts of stem cell niches designing by means of artificial materials [7]. Nevertheless, no delicate mechanisms of niches functioning are known. Recently we have simulated in vitro artificial niches for osteogenic differentiation of human stromal stem cells and established their pilot quantitative parameters [8]. We hope it is our first step to study physical, chemical and biological features of stromal and hemopoietic niches and to design them according to biomimetic principles.

Stem cell fate is controlling by microenvironment nanotopography [9]. Nanoparticles with a diameter < 50 nm penetrate through marrow barrier [10] and can be toxic for bone marrow cells [11]. So, some mechanisms of stem cell and microenvironment interconnection can be revealed with the help of well known nanoparticles as nanoirritants of hemopoietic and stromal cells microenvironment.

In this regard, we evaluated cellular and molecular processes developing in vitro during direct contact of nanoparticles with mice HI and artificial niches for osteogenic differentiation of human stromal stem cells (SSC).

II. Specimens

A. Nanoparticles Preparation

Nano-sized carbon encapsulated iron powders Fe(C) (diameter<10 nm) and FeSi(C) (diameter<20 nm) were prepared in Institute of Metal Physics (Ural Branch of Russia Academy of Sciences, Ekaterinburg, Russia) by dint of metal evaporation with its following condensation in flow of inert gas containing hydrocarbons. High-temperature hydrocarbon pyrolysis occurs in process of gas-cycle synthesis on particles' surface. Carbon cover with thickness of 1-2 nm being produced by this process precipitates on particles' surface.

Infrared (IR) spectra were received on IR-Fourier spectrometer Nexus Nikolet N5700 in tablets with KBr to show functional groups on nanoparticles surface. Concentration

Y. Dekhtyar et al. (Eds.): *International Symposium on Biomedical Engineering and Medical Physics*, IFMBE Proceedings 38, pp. 209–212, 2013.
DOI: 10.1007/978-3-642-34197-7_55

of acid sites on surface of ferromagnetic nanoparticles was determined by the method of temperature-programmed desorption of ammonia gas.

Catalytic activities of nanopowders and titanium disks with calcium phosphate (CP) coatings relative to reactions running according to free radical mechanism were estimated on model reaction of initiated oxidation of isopropylbenzene (cumene) under 60 ^{0}C (azobisisobutyronitrile ($C_8H_{12}N_4$) homogenous initiator, initiation rate $w_i=6.8\times10^{-8}$ l/mole×s, heat flow power 660×10^{-5} Joule/s) by means of kinetic method developed in Institute of Chemical Physics (Moscow). Sensitivity of heat flow registration was 10^{-6} Joule/cm.

B. Titanium Specimens with Calcium Phosphate Coating

Pure titanium specimens (diameter 12 mm, thickness 1 mm) with bilateral CP coating were used as artificial substrate for stromal stem cells cultivation. Coatings were applied on titanium by means of anode-spark (microarc) oxidation method in 10 % phosphoric acid solution containing suspension of nano-sized (20 – 40 nm) synthetic HAP particles with stoichiometric composition $Ca_{10}(PO_4)_6(OH)_2$ [12].

C. Hemopoietic Islets Techniques

Quantitative composition of hemopoietic islets (HI) was investigated by means of [2] method. Marrow from Balb/c mice femurs was eluated into tubes with 1ml of RPMI-1640 medium. 0.9 % sodium chloride (NaCl) nanodispersions of Fe(C) or FeSi(C) in final concentration of 3 mg/l (10 maximum tolerated dose) was added to some tubes. Myelokaryocytes suspension (1 ml) with 100 µl of NaCl solvent served as negative control of toxicity.

Hydrogen peroxide (H_2O_2) with 1 mM final dilution was selected as positive toxic control. Components were mixed through needle with diameter of 1 mm and cultivated under 37^{o}C during 1 hour. Then, cell suspension was pipetted again, mixed with 0.1% neutral red solution in proportion 1:1. Quantity of HI with stained and unstained central elements was counted into Goryaev's camera before and after cultivation. Cell associations containing more than 3 myelokaryocytes connected with centrally placed monocyte/macrophage or stromal mechanocyte were taken as HI. The numbers of apoptotic and necrotic cells and intracellular levels of reactive oxygen species (ROS) were determined as described earlier [13].

D. Stromal Stem Cells Cultivation

Culture of human lung prenatal stromal cells (HLPSC, "Stem cells bank" Co Ltd., Tomsk) was used in experiments as SSC source. HLPSC are the cells with different shapes and sizes, keeping stable karyotype by passages and carcinogenically safe. After unfreezing, 91-93 % cells viability was determined according to ISO 10993-5 in test with 0.4 % trypan blue. HLPSC differentiation into alkaline phosphatase (ALP) positive cells secreting osteocalcin was established by us earlier [8].

For HLPSC cultivation on titanium discs with CP coating we used following medium's composition: beta-glycerophosphate (10 mM), ascorbic acid (50 µg/ml), dexamethasone (10^{-6} M), L-glutamine (280 mg/l), gentamicin sulphate (50 mg/l), HEPES buffer (10 mM), 20% fetal bovine serum, 80% DMEM/F12 (1:1) medium.

Discs were placed in plastic wells (area 1.77 cm^2) of 24-well plate (Orange Scientific, Belgium). Cell suspension (1 ml) in concentration of $3x10^4$ viable karyocytes was added. Nanodispersion (3 mg/l) of Fe(C) nanoparticles was dropped into selected wells.

Discs with cells seeded were removed in 4 days and air-dried. Fixation of adherent cells was carried out in formalin vapor during 30 sec for ALP staining. An intracellular activity of ALP was determined according to [14] with fast garnet dye.

Computer morphometry was applied for detection of cell quantity parameters by means of measurement of their optical characteristics. Area (S) and optical density (D) of ALP stained cells were estimated as described earlier [8] by means of ImageJ program tools. Area was expressed in square nanometers, optical density – in standard units of optical density (s.u.o.d.). TNF-alpha and interleukins (IL-2, IL-4) concentrations were measured in cell culture supernatants by "sandwich" ELISA.

Statistical analysis was made by means of variation statistics methods with the use of Mann-Whitney U-test.

III. Results and Discussion

A. Specimens Physical-Chemical Examination

Questions concerning interconnection of physical-chemical properties of metal nano-sized powders and their biological activity are not widely covered in modern literature. Set up of experiment in this work was planned as an effort to move forward in understanding of chemical and/or physical state of nanoparticles surface and its biological properties.

According to thermal desorption spectra of thermoprogrammed ammonia desorption, NH_3 molecules didn't sorb onto heterogenous surface of nanopowders used.

No iodine and potassium iodide water solutions changed their color during interaction with nanopowders as a test for the presence of redox centers. Qualitative reaction of sulphosalicylic acid with surface iron ions was negative. It

proved an intactness of carbon covering iron nucleus of nanoparticles tested.

IR spectrums of nanopowders didn't show bands of functional groups. Consequently, Fe(C) and FeSi(C) nanoparticles indicates an absence of active centers which can determine display of reactivity in chemical reactions.

Thermal effects of nanopowder specimens in model reaction of isopropylbenzol oxidation can be corresponded to physical processes of wettability and adsorption, but they are not connected with free radical reaction.

In this regard, possible cellular affects of nanoparticles can be correlated with their physical properties. In particular, heat flow power achieved to $(11\pm2)\times10^{-5}$ and $(22\pm2)\times10^{-5}$ Joule/s ($p<0,01$) for Fe(C) and FeSi(C) specimens, respectively. It testified the different levels of heat generation (Q) and surface free energy for chemically inert nanoparticles.

Further, specimens showed Q in a range of 2.1-7.8 (CP coating), 35-134 (Fe(C)) and 198 (FeSi(C)) Joule/g. There is evident relationship between specimen's wettability and cell behavior through surface free energy modification [15]. For all this, thermodynamic action of nanoparticles on cell-substrate interaction can't be excluded.

B. Nanoparticles Effect on Stem Cell Niches

Stromal cells (fibroblasts, osteoblasts) produced by SSC are positive stained for ALP. Some authors consider significant staining for ALP as cytochemical characteristic of osteoblasts [16].

CP surface relief imitates SSC microterritories (niches) [8] which are a base of HSC niches [5]. No short-term HLPSC culture achieved confluent status in our experiments. Cell density was equal on the CP and plastic surfaces. According to data of computer morphometry, average density of distribution (adhesion) of ALP stained cells was approximately 15-34 cells per 1 mm^2 of CP coating (Table 1). Decrease in S index and significant elevation of D occurred under cells contact with selected regions (niches) of CP rough surfaces (Fig.1). Fe(C) nanoparticles enhanced this HLPSC morphofunctional modification (Table 1).

Cell shape changes have to be accompanied by modification of secretory activity. Fe(C) nanoparticles statistically reduced both IL-2 and IL-4 intercellular concentrations (Fig.2).

In this connection, increasing optical density of cells processed by Fe(C) could be connected with cellular fixation of nanoparticles actively absorbing light in visible part of spectrum.

Bone marrow osteoblasts form HSC niche for their B-lymphocytes differentiation [6]. Thus, low doses of chemically inert nanopowders are capable to destroy morphofunctional status and cytokine cooperation of SSC and HSC niches.

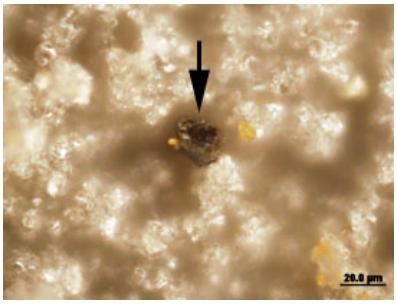

Fig. 1 ALP stained HLPSC on CP surface.

Table 1 Morphometric indices of HLPSC stained for ALP, X±SD.

Groups, n=3	Number of stained cells per 1 mm^2 of surface	ALP staining area (S), μm^2	Cell optical density (D), s.u.o.d.
Plastic wells	34.50±23.00 n_1=10	145.11±5.18 n_2=22	5.19±1.57 n_2=22
Disc+ Cells	14.48±5.18 n_1=27	92.28±82.14* n_2=33	20.26±7.72* n_2=33
Disc+ Cells+Fe(C)	18.51±9.78 n_1=18	71.75±51.13* n_2=29	24.66±6.0*** n_2=29

*) $p<0.05$ with cells on plastic wells; **) – with cells on discs according to U-test; n – specimens number; n_1 – counted fields of vision; n_2 – counted cells.

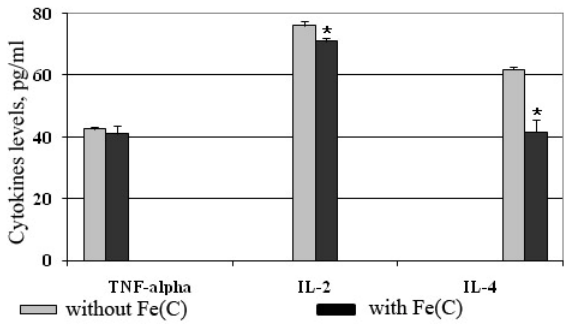

Fig. 2 Cytokines secretion in HLPSC culture.

C. Nanoparticles Effect on Hemopoietic Islets

HI number in femur is individual for every mouse. Obtained numerals were converted to percents from initial value (before 1-hour marrow cultivation) for lightening the results analysis.

No increase in the number of apoptotic and necrotic cells was revealed after 1-hour incubation of bone marrow with Fe(C) or FeSi(C) nanodispersions. It emphasizes an absence of nanoparticles direct cytotoxic influence. On the other hand, only FeSi(C) exposition led to essential depression of HI number (Table 2). However, oxidative stress mediated by ROS intracellular growth was equal for Fe(C) or FeSi(C) administration (up to 325-350 % of negative toxic control).

Table 2 HI amount (% of initial value) in mice marrow suspension after 1-hour nanopowders exposition, X ± m.

Groups, n=5	Stained HI	Unstained HI	Total number of HI
Negative toxic control	126.15±15.27	224.38±28.27	161.06±14.42
Fe(C)	137.35±22.35#	175.17±8.66	153.30±15.20#
FeSi(C)	72.48±9.08***	117.14±38,55	88.14±14,48***
Positive toxic control	69.03±16.21*	142.18±30.51	92.78±10.74*

*) $p<0.05$ with negative toxic control; **) $p<0.05$ with Fe(C); #) $p<0.05$ with positive toxic control according to U-test; n – specimens number.

Destroying stromal and hemopoietic cells associations are not connected with oxidative stress dependent on ROS caused by chemically inert nanoparticles. There are diverse Q indices for Fe(C) and FeSi(C) nanodispersions (see above). So, we can not exclude nanoparticles thermodynamic affect on HI as specific niches for stem and progenitor hemopoietic cells.

IV. Conclusions

Chemical passivity of iron and composite nanoparticles with carbon covering is evident. ROS production caused by Fe(C) or FeSi(C) nanodispersions is insufficient to destroy cells and their microenvironment. However, low doses of chemically inert nanopowders were capable to diminish morphofunctional status and humoral cooperation of SSC with HSC and CP coatings. For all this, different heat generation (Q) for Fe(C) and FeSi(C) specimens has been revealed. We proposed thermodynamic functioning of interfaces between both different stem cells and CP surfaces. Niches design for SSC and HSC on a base of development of "niche-energy" concept may be useful for bone tissue and bone marrow engineering.

Acknowledgment

The authors are deeply indebted to: professor A.Ye. Yermakov and PhD V.A. Uimin (Institute of Metal Physics, Ekaterinburg, Russia) for nanoparticles production; professor Yu.P. Sharkeev and PhD E.V. Legostaeva (Institute of Strength Physics and Materials Science, SB of RAS, Tomsk, Russia) for designing titanium specimens with CP coating; Scientific Educational Center of Molecular Medicine of Siberian State Medical University for ROS estimation.

References

1. Schofield R (1978) The relationship between the spleen colony-forming cell and the haemopoietic stem cell. Blood Cells 4:7-25
2. Crocker PR., Gordon MY (1985) Isolation and characterization of resident stromal macrophages and hematopoietic cell clusters from mouse bone marrow. J Exp Med 162:993-1014
3. Lander AD, Kimble J, Clevers H et al. (2012) What does the concept of the stem cell niche really mean today? BMC Biology 10:19 DOI 10.1186/1741-7007-10-19
4. Dellatore SM, Garsia AS, Miller WM (2008) Mimicking stem cell niches to increase stem cell expansion. Curr Opin Biotechnol 19:534-540
5. Purton LE, Scadden DT (2008) The hematopoietic stem cell niche. StemBook/Ed. L.Silberstein. The Stem Cell Research Community DOI 10.3824/stembook.1.28.1
6. Yin T, Li L (2006) The stem cell niches in bone. Journal of Clinical Investigation 116(5):1195-1201
7. Lutolf MP, Gilbert PM, Blau HM (2009) Designing materials to direct stem-cell fate. Nature 462:433-441
8. Khlusov IA, Khlusova MYu, Zaitsev KV et al. (2011) Pilot *in vitro* study of the parameters of artificial niche for osteogenic differentiation of human stromal stem cell pool. Bull Exp Biol Med 150(4):535-542
9. Sniadecki NJ, Desai RA, Ruiz SA, Chen CS (2006) Nanotechnology for cell-substrate interactions. Annals of Biomedial Engineering .34:59-74
10. Medina C, Santos-Martinez MJ , Radomski A et al. (2007) Nanoparticles: pharmacological and toxicological significance. Br J Pharm 150:552–558
11. LaConte L, Nitin N, Gang Bao (2005) Magnetic nanoparticle probes. Nanotoday 3:32-39
12. Sharkeev YuP, Legostaeva EV, Eroshenko AYu et al. (2009) The structure and physical and mechanical properties of a novel biocomposite material, nanostructured titanium-calcium-phosphate coating. Composite Interfaces 16:535-546
13. Novitsky VV, Khlusov IA, Ryazantseva NV et al. (2011) Structural and functional state of the bone marrow during its in vitro interaction with ferromagnetic nanoparticles. Bull Exp Biol Med 151(4):473-476
14. Hayhoe FGJ, Quaglino D (1980). Hematological cytochemistry. Churchill Livingstone, Edinburgh, London & N.Y.
15. Ponsonnet L, Reybier K, Jaffrezic N et al. (2003) Relationship between surface properties (roughness, wettability) of titanium and titanium alloys and cell behaviour. Materials Science and Engineering C 23:551–560
16. Riggs BL, Melton III LJ (1996). Osteoporosis. Etiology, diagnosis, and management. Second Edition. Lippincott-Raven Publ., Philadelphia, N.Y.

Author: Igor A. Khlusov
Institute: Siberian State Medical University
Street: Moskovsky tract 2
City: Tomsk
Country: Russia
Email: khlusov63@mail.ru

Sources of Radiotoxicity in Spent Nuclear Fuel

G. Adlys

Kaunas University of Technology, Physics Department, Studentu g. 50, Kaunas, Lithuania

Abstract — **Spent nuclear fuel is an important component of the nuclear waste in nuclear energy sector. It consists of fission products, and actinides. The composition and quantity of radionuclides in spent nuclear fuel depends on nuclear fission yields, initial nuclear fuel composition and the fuel burn-up. Due to the complicated physical phenomenon that take place during irradiation of nuclear fuel by neutrons special neutron code APOLLO is used for the fuel composition calculations and the fuel depletion code PEPIN. Radiation hazard related to the production of radionuclides depends on the type of radioactivity and on the energy of emitted particles. Radiation hazard is defined by the radiotoxicity of elements entering environment. Present paper discusses production processes of radiotoxic materials and provides the results of radiotoxicity analysis in the spent nuclear fuel of RBMK type reactor.**

Keywords — **Spent nuclear fuel, fission products, actinides, code APOLLO, code PEPIN, radiotoxicity.**

I. Introduction

About one third of all the electricity produced in the European Union is nuclear–generated [1]. Nuclear energy as a part of energy mixture is defined as a stable, non-emitting CO_2 kind of energy. Nuclear energy plays an important role in the countries with a poor domestic fuel sector, since the economy is very\ sensitive to the fuel price variations.

Ignalina Nuclear Power Plant (Ignalina NPP) in Lithuania was the most important energy supplier not only for Lithuania, but also for neighboring countries: Latvia, Estonia, Belarus and Kaliningrad region during last 25 years. Two RBMK-1500 reactors were designed at the Ignalina NPP with a capacity of 1500 MWe each. The first reactor was commissioned late in December 1983, the second one in August 1987. Their design lifetime was projected out to 2013 – 2017[2]. However, one of the key conditions for Lithuania's accession to European Union was a requirement that the first RBMK-1500 reactor must be closed by the end of 2004 and the second one – by the end of 2009. These requirements were fulfilled, and since 31 December, 2009, 20:54 (UTC) Lithuania changed from the country generating some 75 - 80 % of its electricity in nuclear sector and exporting the energy to the neighboring countries to electricity importing country. Construction of the new regional Visaginas nuclear power plant next to the Ignalina site is planned for the nearest future. [3].

II. Actinides

Nuclear energy is based on nuclear fission of heavy nuclei which is followed by the appearance of two lighter nuclei. The probability that fission or any another neutron-induced reaction will occur is described by the neutron cross-section. Uranium ^{235}U is the only naturally occurring isotope which is used for the production of nuclear energy. The fission cross-section of uranium ^{235}U becomes very large at the thermal energies. Thermal equilibrium with the surrounding nucleus could be achieved when neutrons are slowed down. Since the concentration of uranium ^{235}U in natural uranium ore is only 0.7 percent, other fissile heavy nuclei - ^{239}Pu and ^{241}Pu - could be used. Each of these plutonium isotopes is produced artificially in a nuclear reactor, from the fertile nuclei ^{238}U and ^{240}Pu respectively. Uranium ^{238}U is the main naturally-occurring fertile isotope.

The neutron capture by ^{238}U during reactor operation is followed by two successive β^- decays from ^{239}U to ^{239}Np and to ^{239}Pu. This way is the main path of ^{239}Pu formation:

$$^{238}_{92}U + n \xrightarrow{\beta^-} {}^{239}_{93}Np \xrightarrow{\beta^-} {}^{239}_{94}Pu$$

Through consecutive neutron capture by ^{239}Pu other plutonium isotopes ^{240}Pu, ^{241}Pu, ^{242}Pu are produced. Due to this uranium and plutonium are the major actinides in the nuclear fuel while ^{237}Np, curium $^{242\text{-}244}$Cm and americium ^{241}Am, ^{243}are known as the minor actinides. Plutonium and minor actinides are responsible for the radiotoxicity of the spent nuclear fuel.

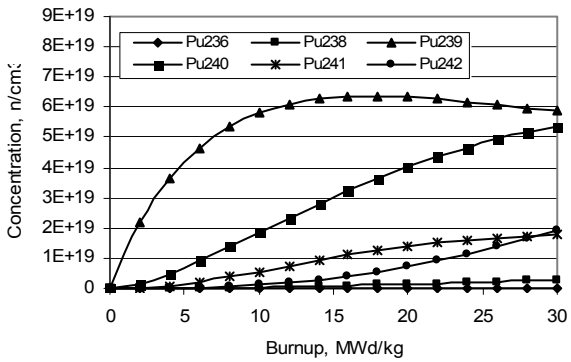

Fig. 1 Accumulation of plutonium isotopes during fuel burn up in RBMK reactor [5].

Y. Dekhtyar et al. (Eds.): *International Symposium on Biomedical Engineering and Medical Physics*, IFMBE Proceedings 38, pp. 213–216, 2013.
DOI: 10.1007/978-3-642-34197-7_56

Accumulation of plutonium isotopes during burn up of nuclear fuel are shown in Fig.1. Radionuuclide concentrations were calculated by means of APOLLO1code [4] for RBMK-1500 reactor.

Americium appears in the system through beta decay of ^{241}Pu and through neutron capture on ^{242}Pu. The neutron capture by americium leads to the production of curium Fig.2 presents accumulation of minor actinides (americium and curium) depending on fuel burn up.

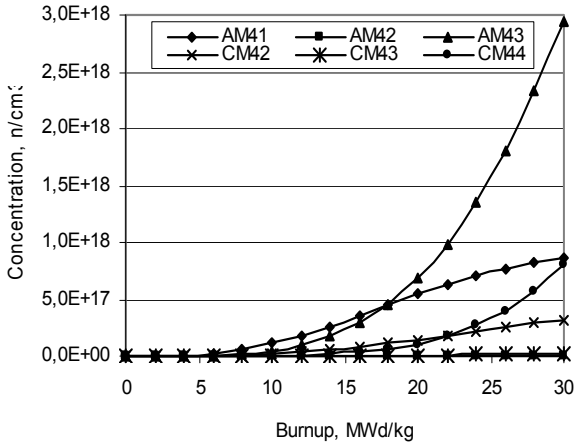

Fig. 2 Accumulation graphs of minor actinides in dependence on fuel burn up [5].

Uranium oxide UO_2 nuclear fuel is used in RBMK reactors. Nuclear fuel containing more than one oxide of fissile nuclide is referred as mixed oxide or MOX fuel. It can be manufactured using weapons-grade plutonium. In such a case MOX contains more than 70 w/o ^{239}Pu as compared to total plutonium amount. Another option for the production of MOX is to use reprocessed plutonium from spent UO_2 fuel [6]. In this case fabricated fuel, ready for power production, contains typically 5-9 w/o ^{239}Pu. MOX fuel is an alternative to the low-enriched uranium fuel which is used in the light water reactors. Typical MOX fuel composition is shown in Fig.3

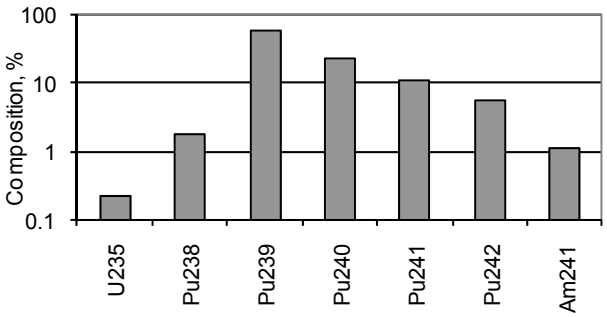

Fig. 3 Composition of MOX fuel.

III. Fission products

Another source of radiotoxicity in spent nuclear fuel is fission products. Binary fission, which is most probable, creates two nuclei with different masses. 699 fission products with mass numbers ranging from 60 to 170 that were created in neutron irradiated nuclear fuel have been analyzed with the depletion code PEPIN [7].

Fission of heavy nucleus produces a different set of fission products that are statistically predictable. Mass distribution of fission products is characterized by an asymmetric curve, which represents two maxima and valley between separating groups. The quantity of any particular nuclide produced per fission is called its yield.

Distribution of masses of fission products in spent nuclear fuel of RBMK reactor are shown in Fig.4 according to calculations performed with computer code PEPIN.

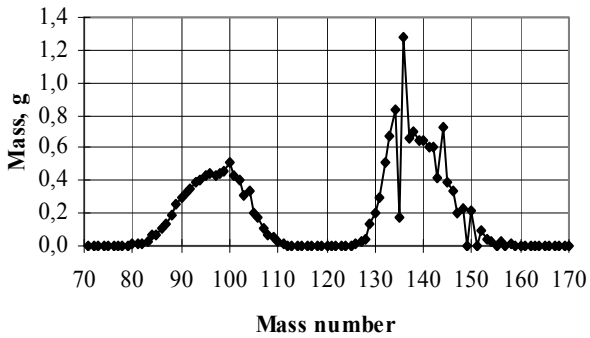

Fig. 4 Distribution of RBMK reactor spent nuclear fuel fission product masses.

When the energy of neutrons increases, the valley between the two peaks becomes shallow. At very high neutron energies and for very heavy elements the mass yield becomes more symmetrical. The number of isotopes produced during fission process of fissile elements is shown in Fig.5.

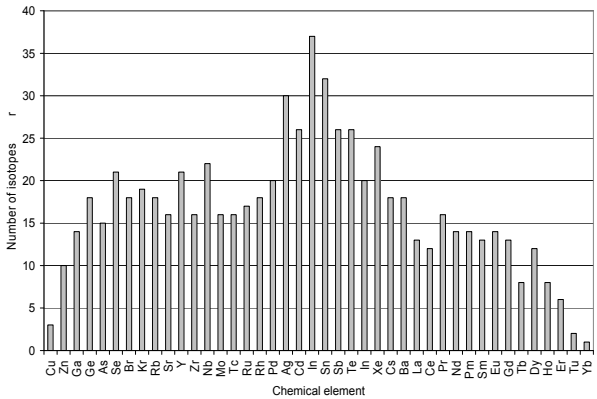

Fig. 5 Number of chemical element isotopes in fission products.

It could be seen that the biggest number of isotopes are produced by Ag, In and Sn. Nuclides that undergo fission are neutron rich and the initial fission products are more neutron-rich than the stable nuclides of the same mass. This is the reason why some fission products may be unstable. Most of these fission products are initially unstable and short-lived and decay within a few hours emitting beta, gamma or neutron radiation.

IV. RADIOTOXICITY

The concept of radiotoxic inventory and the term of potential radiotoxicity are used for evaluation of the harmful potential of a certain quantity of radioactive material [5]. The radiotoxicity of a nuclide is determined by its effective dose coefficient *e(T)* or DPUI (dose per unit intake). Effective dose coefficient corresponds to the dose resulting from the intake of 1 Bq of a specific radionuclide. It considers the metabolism of radionuclides in the organism once ingested or inhaled, the energy and type of the emitted radiation as well as the effect of radiation upon the specific tissue or organ. The quantity T is the integration time in years following intake. For adults, the integration time is 50 years [7]. Actinides have the higher impact than the fission products for the same radioactivity level. The radiotoxicity resulting from the intake of a particular nuclide is given as a product of the effective dose coefficient and the nuclide's activity:

$$Radiotoxicity = Activity \times e(50)$$

Effective dose coefficients are evaluated using models describing the movement of radionuclides through the different organs of the body and are regularly updated by the International Commission on Radiological Protection.

Table 1 DPUI values of ingestion by an adult [8].

	Nuclide	DPUI, Sv/Bq
Actinides	Uranium 238	4.5×10^{-8}
	Plutonium 239	2.5×10^{-7}
	Americium 241	2.0×10^{-7}
	Neptunium 237	1.1×10^{-7}
Fission products	Zirconium 93	1.1×10^{-9}
	Technecium 99	6.4×10^{-10}
	Samarium 151	9.8×10^{-11}
	Strontium 90	2.8×10^{-8}
	Iodine 131	2.2×10^{-8}
	Caesium 137	1.3×10^{-8}

Modeling results obtained using depletion code PEPIN1 show that the total activity decreases with a time due to short-lived nuclides decays. Maximum number of radionuclides could be found at the stopping moment of the reactor, however the contributions are small and for almost all radionuclides vary from 0.001 % to 0,1 %. Only 15 radionuclides contribute to the total activity with more than 1 %.

Table 2 provides the data of PEPIN calculations for radionuclides contributing to the total activity with more than 0.01 %. Cursive script in the table corresponds to the radionuclides contributing with more than 1 % to the total activity and boldfaced script indicates radionuclides with more than 10 % of total activity. After 1 year of fuel cooling the main activity contributors are ^{95}Nb, ^{106}Ru, ^{106}Rh, ^{144}Ce, ^{144}Pr After 10 to 100 years of fuel cooling ^{90}Sr, ^{90}Y, ^{137}Cs, ^{137m}Ba are the most important radionuclides according to their activity; after 50 year cooling most important nuclides are ^{85}Kr, ^{90}Sr, ^{90}Y, ^{99}Tc, ^{121m}Sn, ^{121}Sn, ^{137}Cs, ^{137m}Ba, ^{151}Sm, ^{155}Eu. It is to point out that the activity calculations were performed for spent nuclear fuel of RBMK-1500 reactor, when the fuel burn up was 18 MWd/kg.

Table 2 Importance of radionuclides according to total activity in spent nuclear fuel.

Cooling time	Nuclides
1 y	Kr85, *Sr89, Sr90 Y90, Y91*, *Zr95*, **Nb95**, Ru103, Rh103m, **Ru106, Rh106**, Sn123, Te125m, Te127m, Te127, Te129m, Te129, Cs134, *Cs137*, Ba137m, Ce141, **Ce144**, **Pr144**, *Pm147*, Eu155.
10 y	*Kr85*, **Sr90**, **Y90**, Ru106, Rh106, Sn121m, Sn121, Sb125, Te125m, Cs134, **Cs137**, **Ba137m**, Ce144, Pr144, *Pm147*, Sm151, Eu155.
50 y	Kr85, **Sr90**, **Y90**, Tc99, Sn121m, Sn121, **Cs137**, **Ba137m**, *Sm151*, Eu155.
100 y	Kr85, **Sr90**, **Y90**, Tc99, Sn121m, Sn121, **Cs137**, **Ba137m**, *Sm151*.

The total activity and radiation power of fission products decreases with a time (Fig.6.) and the influence of long – lived fission products is growing up.

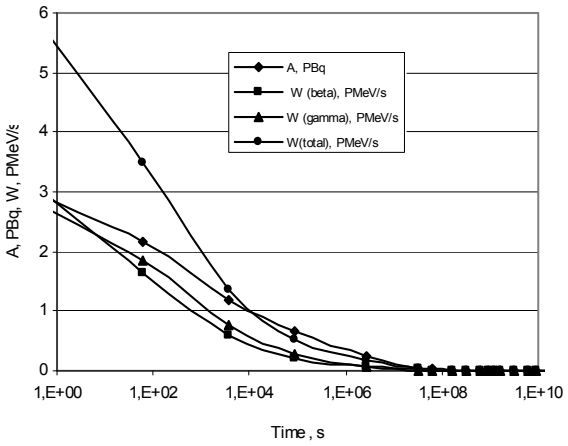

Fig. 6 Activity and radiation power of fission products versus cooling time.

When cooling time increases from 1 year to 100 years, the number of radionuclides contributing to the total activity with more than 1% decreases from 12 to 4. During this time period only 4 radionuclides contribute to the total activity with more than 10 %. After 1000 years of fuel cooling 6 nuclides contribute with more than 1 %, 3 nuclides – with 5 % and only one nuclide contributes with more than 50 % of total activity.

The strongest radiation power sources are ^{134}I (3,88 %), ^{138}Cs (3,58 %), ^{142}La (3,10 %), ^{140}La (2,84 %), ^{94}Y (2,37 %), ^{93}Sr (2,22 %), ^{95}Y (2,10 %), ^{132}I (2,07 %), 104Tc (2,03 %) after 1 min of the fuel cooling. After 1 hour of cooling the contribution to radiation power of some nuclides increases: ^{140}La (7,31 %), ^{134}I (6,96 %), ^{142}La (5,76 %), ^{132}I (5,30 %), ^{135}I (4,40 %), ^{138}Cs (3,97), ^{92}Y (3,27 %). After 24 hours of cooling contribution of particular radionuclides to total radiation power became more important: ^{140}La (18,63 %), ^{132}I (11,34 %), ^{144}Pr (5,97 %), ^{95}Zr (5,29 %), ^{95}Nb (5,08 %), ^{135}I (3,43 %). Due to the small gamma radiation components ^{144}Pr, ^{106}Rh, ^{90}Y are thoroughly beta radiation sources within this time period. At this time ^{134}Cs, ^{137m}Ba, ^{95}Nb, ^{95}Zr are the main gamma radiation sources.

Comparison of generated radiation power after 5 years cooling for the fuel burn up 10 MWd/kg and 20 MWd/kg are provided in Fig.7. Nuclear fuel of RBMK-1500 reactor enriched with 2.4 % ^{235}U and 0.41% of Er was used in calculations.

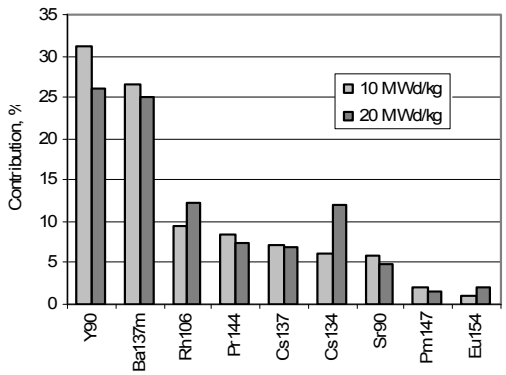

Fig. 7 Contribution of radionuclides to the total radiation power in the case of two different fuel burn-up after 5 years cooling.

It is to assume, that when fuel burn-up increases from 10 MWd/kg to 20 MWd/kg, the contribution of ^{90}Y and ^{137m}Ba decreases, but contribution of ^{106}Rh and ^{134}Cs increases. Comparing the results of calculations after 50 year cooling period it is evident that ^{106}Rh, ^{144}Pr, ^{134}Cs and ^{147}Pm losses their influence and the influence of ^{85}Kr and ^{151}Sm is growing up. Almost all fission products belong to the decay chains where genetic pairs of short-lived nuclides and long-lived nuclides are formed: ^{90}Sr (28.78 y) and ^{90}Y (58.51 d); ^{106}Ru (373.59d) and ^{106}Rh (29.80 s); ^{137}Cs (30.07 y) ir ^{137m}Ba (2.552 min).

References

1. Adlys G., Adlienė D., Tulonen S. Tendencies of nuclear energy development in Europe. Proceedings of the Int. Conf. ECT2008, Kaunas, Lithuania, 2008 pp.168-171
2. Adlys G., Adlienė D. Baltic nuclear projects. Jahrestagung Kerntechnik 2009 May 12-14, 2009, Dresden, Germany, pp. 1004-1007
3. Adlys G., Adlienė D. (2008) From nuclear to nuclear - Lithuanian experience, ATW-International Journal for Nuclear Power 53 (2): 86-91
4. Le C.G., Mathonniere G. APOLLO1: Notice d'utilisation, Rapport DMT/SERMA/LENR, CEA (1995)
5. Adlys G. Radiotoxicity of nuclear fuel. Proceedings of the Int. Conf. Medical Physics, Kaunas. Lithuania, 2008, pp. 45-48
6. Dennis M.L., Usman Sh. (2010). Feasibility of 106Ru peak measurement for MOX fuel burnup analysis. Nuclear Engineering and Design 240: 3687-3696.
7. Nimal J.C., Nimal B., Duchemin B.. Note de principe du code PEPIN. Rapport DEMT 86/050 –SERMA/LEPF/86/760 (1986)
8. Magill J., Berthou V., Haas D., et all (2003) Impact limits of partitation and transmutation scenarios on the radiotoxicity of actinides in radioactive waste. Nuclear energy 42 (5): 263-277.

Author: G.Adlys
Institute: Kaunas University of Technology
Street: Studentu g. 50
City: Kaunas
Country: Lithuania
Email: gediminas.adlys@ktu.

Author Index

Keyword Index